The 29ᵗʰ European Symposium on Ultrasound Contrast Imaging

- An ICUS-Endorsed Conference -

JAM visual thinking
– www.jamvisualthinking.com
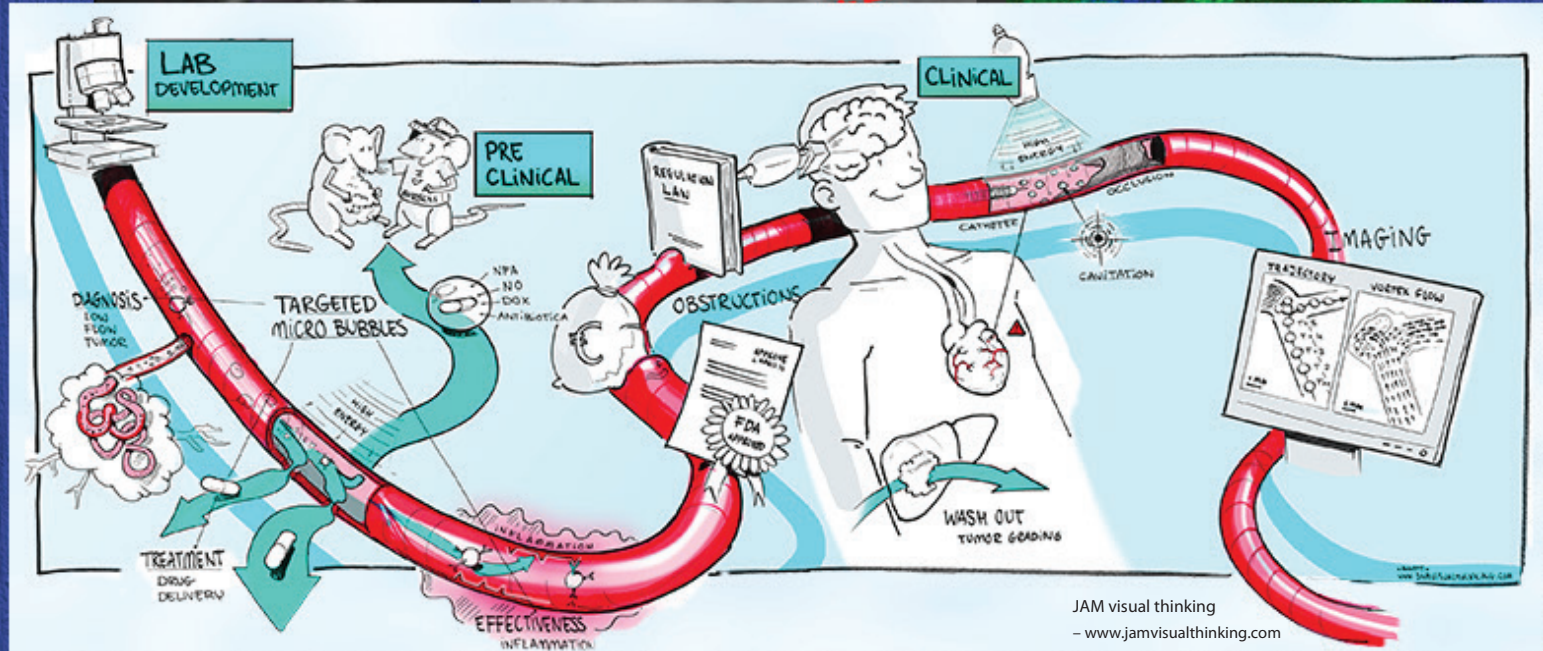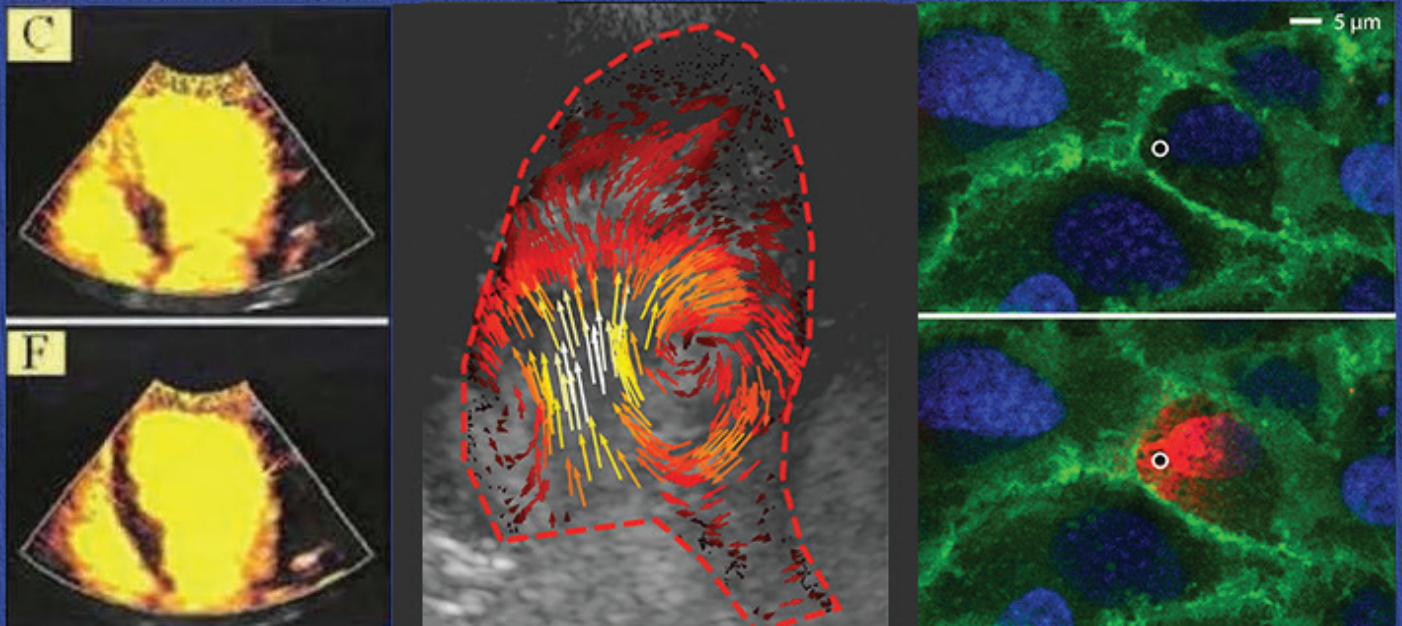
Abstract book

18-19 January 2024, Rotterdam, the Netherlands

Organised by Rik Vos, Klazina Kooiman, Annemien van den Bosch, Folkert ten Cate and Nico de Jong

Erasmus MC Rotterdam

Conference Dinner

Thursday January 18th, 2024

Time: starting at 18:30 hrs

Address: Wereldmuseum

Willemskade 25, 3016 DM Rotterdam

Only 10 minutes walking distance from Mainport Hotel

THE 29TH EUROPEAN SYMPOSIUM ON ULTRASOUND CONTRAST IMAGING
January 18-19, 2024
Rotterdam

Pre-program events

<u>TUESDAY, 16 January 2024</u>

13.00   PhD defence Luxi Wei: Volumetric Contrast-enhanced Echocardiography with Sparse Arrays
               Location: Professor Andries Querido zaal, Erasmus MC, Dr. Molewaterplein 40, Rotterdam

<u>WEDNESDAY, 17 January 2024</u>

10.30   PhD defence Geraldi Wahyulaksana: High-frame-rate Contrast-Enhanced Echography
               for Myocardial Perfusion Assessment
               Location: Professor Andries Querido zaal, Erasmus MC, Dr. Molewaterplein 40, Rotterdam

Welcome drinks

<u>WEDNESDAY, 17 January 2024</u>

17.30 – 19.30 Welcome Drinks at the conference location: Mainport Hotel, Leuvehaven 77, Rotterdam
               + Registration

THE 29TH EUROPEAN SYMPOSIUM ON ULTRASOUND CONTRAST IMAGING
January 18-19, 2024
Rotterdam

THURSDAY, 18 January 2024

08.00 – 09.00	Registration

Oral program

09.00 – 09.10 **Introduction and opening** by Rudolf de Boer, head Cardiology Erasmus MC, Rotterdam ....
.... *Chairperson: Annemien van den Bosch*

09.10 – 10.10 THERAPY: TOWARDS CLINICAL USE I ....*Chairpersons: Annemien van den Bosch and Eleanor Stride*

10.10 – 11.40	Coffee & parallel poster sessions A + B

11.40 – 12.30 THERAPY: TOWARDS CLINICAL USE II .... *Chairpersons: Christy Holland and Mike Averkiou*

12.30 – 13.45	LUNCH

13.45 – 14.15 THORAX LECTURE .... *Chairperson: Klazina Kooiman*

14.15 – 15.25 IMAGING: NEW DIRECTIONS .... *Chairpersons: Dan Adam and Michel Versluis*

15.25 – 16.00	Intermission

16.00 – 17.20 CLINICAL IMAGING.. *Chairpersons: Folkert ten Cate and Ton van der Steen*

18.30 – 22.30 EVENING PROGRAM AT WERELDMUSEUM, Willemskade 25, Rotterdam (Incl. Dinner buffet)
Gather at main lecture room at 18:15 to walk there together

<u>FRIDAY, 19 January 2024</u>

07.30 – 08.00 Registration

Oral program

08.00 – 09.30   PARALLEL SHORT ORAL SESSION I (poster room "Maas") and SESSION II (main lecture room)
N.B. Walking breakfast provided

09.30 – 09.50   Intermission + hotel check-out

11.10 – 12.40   Coffee & parallel poster sessions C + D

12.40 – 13.50   LUNCH

14.40 – 15.00   Intermission

16.30 – 16.40   CLOSING REMARKS .... *Klazina Kooiman and Rik Vos*

16.40   ANNOUNCEMENT OF THE WINNERS OF THE COMPETITION AND POSTER PRIZES

+ FAREWELL DRINKS

Organised by: Rik Vos, Klazina Kooiman, Annemien van den Bosch, Folkert ten Cate, Nico de Jong
Scientific board: Mike Averkiou, Mark Borden, Olivier Couture, Beat Kaufmann, Eleanor Stride, Flordeliza Villanueva

THE 29TH EUROPEAN SYMPOSIUM ON
ULTRASOUND CONTRAST IMAGING
January 18-19, 2024
Rotterdam

Poster sessions THURSDAY, 18 January 2024

Thursday 10.10-11.40 POSTER SESSION A: MICROBUBBLE PRODUCTION AND ULTRASOUND IMAGING ....
....*Chairperson: Mike Averkiou*

Location: Poster room "Maas"; with 2-minute poster pitches starting at 10.10

Thursday 10.10-11.40 POSTER SESSION B: CANCER THERAPY .... *Chairperson: Flordeliza Villanueva*
Location: Poster room "Haven"; with 2-minute poster pitches starting at 10.10 in the main lecture room

Organised by: Rik Vos, Klazina Kooiman, Annemien van den Bosch, Folkert ten Cate, Nico de Jong

Scientific board: Mike Averkiou, Mark Borden, Olivier Couture, Beat Kaufmann, Eleanor Stride, Flordeliza Villanueva

THE 29TH EUROPEAN SYMPOSIUM ON ULTRASOUND CONTRAST IMAGING
January 18-19, 2024
Rotterdam

Parallel short oral sessions FRIDAY, 19 January 2024

Organised by: Rik Vos, Klazina Kooiman, Annemien van den Bosch, Folkert ten Cate, Nico de Jong

Scientific board: Mike Averkiou, Mark Borden, Olivier Couture, Beat Kaufmann, Eleanor Stride, Flordeliza Villanueva

Poster sessions FRIDAY, 19 January 2024

Organised by: Rik Vos, Klazina Kooiman, Annemien van den Bosch, Folkert ten Cate, Nico de Jong

Scientific board: Mike Averkiou, Mark Borden, Olivier Couture, Beat Kaufmann, Eleanor Stride, Flordeliza Villanueva

Erasmus MC
THORAX CENTRUM

Ultrasound image-guided catheter-directed therapy to treat peripheral arterial disease

Christy K. Holland[1,2], Sonya R. Kennedy[2], Kevin J. Haworth[1,2], Daniel Suarez Escudero[1], Maxime Lafond[1], Brion Frierson[3], Shaoling Huang[3], Melvin E. Klegerman[3], Tao Peng[3], David D. McPherson[3], Curtis Genstler[4]

[1]*Department of Internal Medicine, Division of Cardiovascular Health and Disease, University of Cincinnati, Cincinnati, OH, USA*
[2]*Department of Biomedical Engineering, University of Cincinnati, Cincinnati, OH, USA*
[3]*Department of Internal Medicine, The University of Texas Health Science Center at Houston, Houston, TX, USA*
[4]*Boston Scientific, Maple Grove, MN, USA.*
Corresponding author: Christy.Holland@uc.edu

Introduction

Peripheral arterial disease (PAD) represents a challenging clinical problem affecting 15–20% of people over 70 years of age due to the diffuse nature of atheroma deposition throughout the arterial bed [1]. Atherosclerotic PAD affects 202 million people worldwide and leads to serious health complications, including limb amputation [2]. PAD stent implantation ameliorates flow, but ~15% of patients lose patency a year following treatment due to in-stent and peri-stent restenosis [3-8]. Studies of drug eluting stents in PAD have reported disappointing long-term results [9]. The development of a methodology to stabilize the vascular bed at stent implantation to obviate neointimal hyperplasia, a major cause of stent restenosis, is needed. Pioglitazone (PGN) is a peroxisome proliferator activated receptor-gamma (PPARγ) agonist that reduces pro-inflammatory cytokines [10-12] and generates anti-inflammatory and anti-arteriosclerotic effects [13-15]. Ultrasound-mediated delivery of PGN to the arterial bed was observed in a swine atheroma model [16-18]. To explore the mechanism of enhanced PGN delivery, the purpose of this collaborative study was to determine if PGN-loaded echogenic liposomes (PGN-ELIP) infused through an EKOS™ catheter (Boston Scientific, Maple Grove, MN, USA) nucleated sustained inertial and stable cavitation. The EKOS™ Endovascular System is an FDA-cleared catheter for ultrasound-mediated infusion of physician-directed therapeutics into the peripheral vasculature and pulmonary arteries [16,18-20].

Methods

Echogenic Liposome Formulation:

Pioglitazone-loaded echogenic liposomes (PGN-ELIP) conjugated to a fibrin-binding peptide, PAFb, or gly-pro-arg-pro-pro-gly-gly-gly-cys, were manufactured at UT Health Sciences Center, Houston and shipped on ice packs to University of Cincinnati (Fig. 1). The amino-terminal pentapeptide binds to fibrin [18,21-23], which is a marker for late-stage atheroma [24]. This peptide is not expected to be immunogenic or to elicit foreign protein reactions by patients and is thus an innovative targeting strategy [18].

Figure 1. Schematic of PGN-loaded echogenic liposome structure.
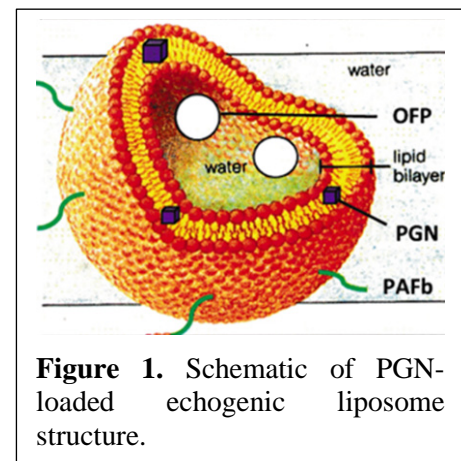
PGN-ELIP characterization: The size distribution, acoustic attenuation, and PGN dose of PGN-ELIP were evaluated before and after infusion through EKOS™ catheters (Fig. 2) [25]. The PGN-ELIP size ranged from 0.6 to 3.0 μm and before infusion the peak number density was $5.0 \pm 0.6 \times 10^8$ ELIP/mL, which is consistent with previous measurements of therapeutic-loaded ELIP [26-28]. Acoustic attenuation of PGN-ELIP decreased after infusion through the EKOS™ catheter [25]. Using high-performance liquid chromatography, PGN doses of 432.0 ± 128.3 μg and 202.0 ± 51.2 μg were quantified before and after infusion through quiescent EKOS™ catheters, respectively, indicating the PGN can traverse the catheter [25].

Passive Cavitation Imaging:
Passive cavitation imaging was used to quantify and map bubble activity originating from DEFINITY® or PGN-ELIP infused through an EKOS™ catheter with therapeutic ultrasound (TUS) transducers (Fig. 2) operated at fixed acoustic output pressure amplitudes in a flow phantom mimicking porcine femoral arterial flow (Fig. 3) [19,20,25].

Figure 2. Schematic of EKOS™ catheter with 12 pairs of 2-mm long, 2.25 MHz therapeutic ultrasound (TUS) transducers. The first six TUS transducer pairs were quiescent while the distal six TUS transducer pairs were active and sonicated the microbubbles. The first six drug delivery holes were located proximal to the active transducers, enabling localized release of microbubbles and drug for ultrasound-mediated pioglitazone delivery [19,20,25].

Results and Discussion

Fig. 4 displays the spatial distribution of echogenicity and cavitation energy within the arterial flow phantom tube lumen when either DEFINITY® or PGN-ELIP were infused through EKOS™ catheters. Cavitation was sustained during 3-min infusions for both agents along the entire distal 6 cm treatment zone of the catheter. Ultraharmonic and inharmonic emissions indicative of stable and inertial cavitation were detected along the catheter treatment zone at drive pulse powers of 9, 18 and 47 W (peak rarefactional pressures of 0.67, 0.95, and 1.47 MPa at the surface of the catheter, or MIs from 0.28 to 0.93). For PGN-ELIP infusions at drive pulse powers above 9 W, ultraharmonic and inharmonic energies were similar and observed throughout the lumen. DEFINITY® nucleated approximately an order of

Figure 3. Schematic of flow phantom setup for passive cavitation acquisitions. Saline at 37°C was circulated from the reservoir, over the catheter, and back to the reservoir. The L11-5v array imaging plane included the first proximal active EKOS™ TUS transducer pair [19,20,25].

magnitude more cavitation activity than PGN-ELIP [25] and thus infusion of this echo contrast agent with a dilute non-targeted solution (without liposomal encapsulation) of PGN may augment drug delivery into the arterial wall, though may come with added risk of damage both to the endothelium and distal capillary bed if infused intraarterially. Note that PGN, a lipophilic drug, has very low solubility in aqueous solutions (46.85 μg/mL at 25°C) [29]. Thus, only a limited PGN dose would be possible without liposomal
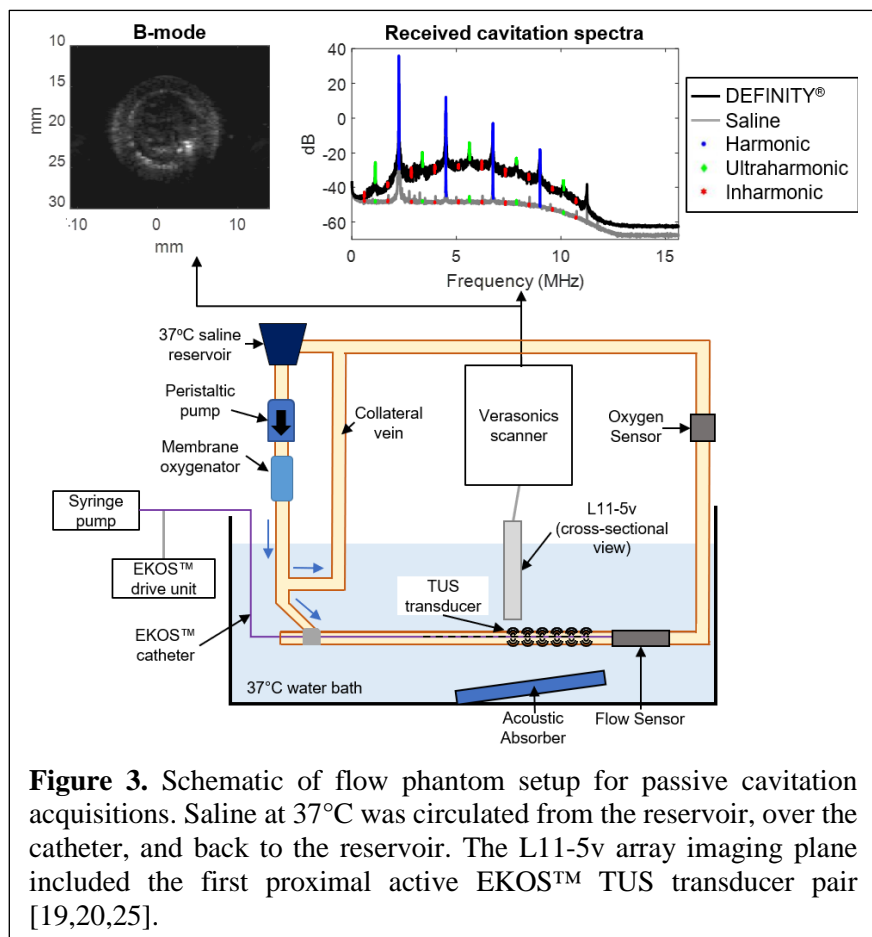
encapsulation. Without fibrin targeting, direct infusion of a dilute solution of PGN 46.85 mg/L [29] through stented arterial tissue may not achieve the needed dose to achieve prevention of peri-stent restenosis.

Figure 4 Composite PCI and B-Mode images of ultraharmonic (green) and inharmonic (red) emissions from cavitation nucleated by infused DEFINITY® or PGN-loaded echogenic liposomes insonified by one pair of EKOS™ transducers driven with 4, 9, 18, or 47 W electrical pulse power. The B-mode images (visualizing echogenicity alone) are shown in rows 1 and 3, and the corresponding composite images are shown in rows 2 and 4 [25]. Passive cavitation image overlays map ultraharmonic energy in green (stable cavitation) and inharmonic energy in red (inertial cavitation). Yellow represents an equal combination of ultraharmonic (green) and inharmonic energies (red).

Conclusion

These studies demonstrate PGN-ELIP can traverse the catheter at a therapeutically effective concentration for ultrasound-mediated delivery to the arterial bed. Though the EKOS™ catheter was not designed specifically for cavitation nucleation, infusion of PGN-ELIP or DEFINITY® can be employed with an active EKOS™ catheter to trigger and sustain bubble activity for enhanced intravascular drug delivery.

References

[1]   Olin JW, Sealove BA. Peripheral Artery Disease: Current Insight Into the Disease and Its Diagnosis and Management. Mayo Clinic Proceedings. 2010; 85(7):678-92.

[2]   Selvin E, Erlinger TP. Prevalence of and risk factors for peripheral arterial disease in the United States - Results from the National Health and Nutrition Examination Survey, 1999-2000. Circulation. 2004; 110(6):738-43.

[3]   Abdulhannan P, Russell DA, Homer-Vanniasinkam S. Peripheral arterial disease: a literature review. British Medical Bulletin. 2012; 104(1):21-39.

[4]   Duda SH, Pusich B, Richter G, Landwehr P, Oliva VL, Tielbeek A, et al. Sirolimus-eluting stents for the treatment of obstructive superficial femoral artery disease. Circulation. 2002; 106(12):1505-9.

[5]   Duda SH, Bosiers M, Lammer J, Scheinert D, Zeller T, Tielbeek A, et al. Sirolimus-eluting versus bare nitinol stent for obstructive superficial femoral artery disease: the SIROCCO II trial. J Vasc Interv Radiol. 2005; 16(3):331-8.

[6]   Lammer J, Bosiers M, Zeller T, Schillinger M, Boone E, Zaugg MJ, et al. First clinical trial of nitinol self-expanding everolimus-eluting stent implantation for peripheral arterial occlusive disease. Journal of Vascular Surgery. 2011; 54(2):394-401.

[7]   Liistro F, Angioli P, Porto I, Ducci K, Falsini G, Ventoruzzo G, et al. Drug-Eluting Balloon Versus Drug-Eluting Stent for Complex Femoropopliteal Arterial Lesions The DRASTICO Study. Journal of the American College of Cardiology. 2019; 74(2):205-15.

[8] Mosarla RC, Secemsky EA. From IMPERIALism to EMINENence: The Noble Rise of the Second-Generation Peripheral Drug-Eluting Stent. Circulation. 2022; 146(21):1577-80.

[9] Li M, Tu H, Yan Y, Guo Z, Zhu H, Niu J, Yin M. Meta-analysis of outcomes from drug-eluting stent implantation in femoropopliteal arteries. PLoS One. 2023; 18(9):e0291466.

[10] Buchanan KD, Huang SL, Kim H, McPherson DD, MacDonald RC. Encapsulation of NF-κB decoy oligonucleotides within echogenic liposomes and ultrasound-triggered release. Journal of Controlled Release. 2010; 141(2):193-8.

[11] Li AC, Brown KK, Silvestre MJ, Willson TW, Palinski W, Glass CK. Inhibitory effects of peroxisome proliferator-activated receptor gamma ligands on the development of atherosclerosis in low density receptor-deficient mice. Circulation. 2000; 102(18):221-.

[12] Li AC, Palinski W. Peroxisome proliferator-activated receptors: How their effects on macrophages can lead to the development of a new drug therapy against atherosclerosis. Annual Review of Pharmacology and Toxicology. 2006; 46:1-39.

[13] Beckman J, Raji A, Plutzky J. Peroxisome proliferator activated receptor gamma and its activation in the treatment of insulin resistance and atherosclerosis: issues and opportunities. Current Opinion in Cardiology. 2003; 18(6):479-85.

[14] Ishibashi M, Egashira K, Hiasa K, Inoue S, Ni WH, Zhao QW, et al. Antiinflammatory and antiarteriosclerotic effects of pioglitazone. Hypertension. 2002; 40(5):687-93.

[15] Plutzky J. PPARs as therapeutic targets: Reverse cardiology? Science. 2003; 302(5644):406-7.

[16] Kee PH, Moody MR, Huang SL, Kim H, Yin X, Peng T, et al. Stabilizing Peri-Stent Restenosis Using a Novel Therapeutic Carrier. Jacc-Basic to Translational Science. 2020; 5(1):1-11.

[17] Klegerman M, Moody M, Peng T, Laing ST, Huang S, Govindarajan V, et al. Ultrasound-Enhanced Therapeutic Vascular Delivery. Journal of the American College of Cardiology. 2022; 79(9):1754-.

[18] Klegerman ME, Moody MR, Huang SL, Peng T, Laing ST, Govindarajan V, et al. Demonstration of ultrasound-mediated therapeutic delivery of fibrin-targeted pioglitazone-loaded echogenic liposomes into the arterial bed for attenuation of peri-stent restenosis. Journal of Drug Targeting. 2022; 31(1):109-18.

[19] Lafond M, Salido NG, Haworth KJ, Hannah AS, Macke GP, Genstler C, Holland CK. Cavitation Emissions Nucleated by Definity Infused through an Ekosonic Catheter in a Flow Phantom. Ultrasound Med Biol. 2021; 47(3):693-709.

[20] Suarez Escudero D, Lafond M, Salido NG, Haworth KJ, Hannah AS, Genstler C, Holland CK. Corrigendum to "Cavitation emissions nucleated by Definity® infused through an EkoSonic® catheter in a flow phantom". Ultrasound Med Biol. 2022; 49:410-4.

[21] Laudano AP, Doolittle RF. Synthetic Peptide Derivatives That Bind to Fibrinogen and Prevent Polymerization of Fibrin Monomers. P Natl Acad Sci USA. 1978; 75(7):3085-9.

[22] Aruva MR, Daviau J, Sharma SS, Thakur ML. Imaging thromboembolism with fibrin-avid Tc-99m-peptide: Evaluation in swine. J Nucl Med. 2006; 47(1):155-62.

[23] McCarthy JR, Patel P, Botnaru I, Haghayeghi P, Weissleder R, Jaffer FA. Multimodal Nanoagents for the Detection of Intravascular Thrombi. Bioconjugate Chemistry. 2009; 20(6):1251-5.

[24] Gargiulo S, Gramanzini M, Mancini M. Molecular Imaging of Vulnerable Atherosclerotic Plaques in Animal Models. International Journal of Molecular Sciences. 2016; 17(9).

[25] Kennedy SR, Lafond M, Haworth KJ, Escudero DS, Ionascu D, Frierson B, et al. Initiating and imaging cavitation from infused echo contrast agents through the EkoSonic catheter. Scientific Reports. 2023; 13(1).

[26] Shekhar H, Bader KB, Huang SW, Peng T, Huang SL, McPherson DD, Holland CK. In vitro thrombolytic efficacy of echogenic liposomes loaded with tissue plasminogen activator and octafluoropropane gas. Physics in Medicine and Biology. 2017; 62(2):517-38.

[27] Shekhar H, Kleven RT, Peng T, Palaniappan A, Karani KB, Huang SL, et al. In vitro characterization of sonothrombolysis and echocontrast agents to treat ischemic stroke. Sci Reports. 2019; 9.

[28] Raymond JL, Haworth KJ, Bader KB, Radhakrishnan K, Griffin JK, Huang SL, et al. Broadband Attenuation Measurements of Phospholipid-Shelled Ultrasound Contrast Agents. Ultrasound in Medicine and Biology. 2014; 40(2):410-21.

[29] PubChem. Pioglitazone (Compound), 3.2.4 Solubility]. Available from: https://pubchem.ncbi.nlm.nih.gov/compound/Pioglitazone#section=Solubility.

Magnetic Resonance Imaging of Focused Ultrasound-Mediated Blood-Brain Barrier Opening in Grey and White Matter

Alessandro De Maio[1,2], Yuexi Huang[1], Fa-Hsuan Lin[1,2], Bojana Stefanovic[1,2], Greg Stanisz[1,2], Meaghan O'Reilly[1,2]

[1] *Physical Sciences Platform, Sunnybrook Research Institute, Toronto, Canada*
[2] *Department of Medical Biophysics, University of Toronto, Toronto, Canada*
Corresponding author: alex.demaio@mail.utoronto.ca

Introduction

Focused ultrasound (FUS)-mediated blood-brain barrier (BBB) opening is an image-guided treatment modality for local drug delivery to the central nervous system. In vivo treatment monitoring is achieved via contrast-enhanced magnetic resonance imaging (MRI); however, in the grey matter (GM) contrast uptake is 3-5 times greater than in the white matter (WM)[1], when identical acoustic parameters are used. Differences in WM and GM BBB opening have been reported in both animal models (rats [2], dogs [3], non-human primates [4]) and humans [5], possibly due to greater extravascular spaces and 8x lower vascular densities in the WM [6].

The objective of this study is to characterize BBB-opening in GM and WM following single and repeated FUS exposures and to correlate the achieved drug distribution to MRI measures of BBB opening.

Methods

Experiments were conducted in rats using a preclinical treatment platform, and in pigs on a clinical MRI guided FUS system. On the preclinical system (LP-100, FUS instruments), six Fischer-344 rats underwent repeated FUS BBB opening sessions. The procedure included the use of feedback-controlled pressures [7] and the following acoustic parameters: 580 kHz, 10ms burst, 1Hz pulse repetition frequency, 2 min duration. A clinical system (ExAblate Neuro MRgFUS) was used in a cohort of four Yorkshire pigs. The procedure differed in the use of a feedback-controlled power algorithm [8] with the following parameters: 220 kHz, 5ms burst, 1Hz pulse repetition frequency, 2 min duration. The prescribed cavitation dose, based on prior human studies [8], was 0.3 with a maximum power of 30W.

In both rat and pig experiments, each treatment was repeated at 30-minute intervals targeting the unilateral internal capsule and thalamus. Definity microbubbles were administered intravenously for each sonication, as a bolus in rats (20μL/kg), and as a continuous infusion throughout the exposure duration in pigs (0.8μL/kg/min). Bevacizumab, an anti-tumoral monoclonal antibody, was delivered intravenously, and in the case of the rat experiments it was conjugated with a fluorophore for later characterization with light-sheet microscopy. Following FUS exposure, 0.1ml/kg Gadovist was administered intravenously. Images were acquired at baseline and after each treatment, with analyses performed following registration to a brain atlas. T_1-mapping (via the Barral equation model) and T_1-weighted images were employed to measure contrast-enhanced signal changes, while T_2^*-weighted images were used to assess tissue damage.

Following necropsy, drug deposition was measured. Two rat brains were extracted and cleared in CUBIC solution for imaging via light sheet fluorescence microscopy (LSFM). Treated and contralateral control areas of four pig brains were homogenized for drug concentration quantification via enzyme-linked immunosorbent assay (ELISA).

Results

In rats, following the first treatment, the post-contrast change in T_1 relaxation time was $-3.7 \pm 1.1\%$ (normalized to the contralateral hemisphere) in the GM, and $+0.28 \pm 0.1\%$ in the WM ($p<.001$). After a second sonication, the change in T_1 in the treated hemisphere was $-11.9 \pm 3.6\%$ in GM and $-12.6 \pm 3.8\%$ in WM ($p=0.465$). LSFM revealed the fluorescent drug signal was highest in the focus regions with intensities,

relative to contralateral, of 267.7±35.3 in the cortex, 355.0±45.1 in the thalamus and 251.9±40.3 in the WM; decreasing with distance and detectable up to 4.5mm from the focus.

In pigs, to ensure an equal cavitation dose at each target tissue, the delivered power was automatically adjusted in real-time, resulting in 9.00±3.36 W for GM and 12.90±5.28 W for WM (p<.001). Following a single treatment, contrast enhancement measured on T_1-weighted images in the GM and WM was 20.5±11.1% and 21.5±8.6% (p=.360), respectively decreasing to 6.1±3.3% and 5.4±4.2% (p=.220) at 70 minutes. After a second exposure, enhancement was 19.7±12.5% in GM and 21.8±8.8% in WM (p=.470), while 15.3±8.4% in GM and 18.3±5.2% in WM (p=.064) after a third exposure, with no statistical differences between each session. No differences in bevacizumab deposition were found between GM and WM, however, a linear relationship for total drug deposition was determined, accounting for tissue types and total administered ultrasound power over multiple treatment sessions (R^2 = .514).

T_2* effects, suggestive of tissue damage, were absent in both animal models.

Conclusions

In rats, on a preclinical system, contrast enhancement following FUS-induced BBB-opening quantitatively demonstrated the need for a second sonication in the white matter to obtain similar levels of permeabilization to the grey matter.

In pigs, on a clinical system, the larger brain and white matter structures enabled individual targeting of each tissue type. It was observed that to achieve an equal cavitation dose, higher ultrasound power was required in the white matter. Contrast T1-weighted imaging showed similar signal changes between tissues following either single or repeated treatments. At 70 min. following a single sonication, the signal in the treated region returned to almost baseline, while repeated exposures at 30-minute intervals enabled sustained BBB permeability to imaging contrast.

These results quantitatively demonstrate the necessity of tissue-specific acoustic parameters and treatment strategies to achieve BBB-opening in both small and large animal models.

References

[1]. Karakatsani MEM, Samiotaki GM, Downs ME, Ferrera VP, Konofagou EE., Targeting Effects on the Volume of the Focused Ultrasound-Induced Blood-Brain Barrier Opening in Nonhuman Primates In Vivo, IEEE Trans. Ultrason. Ferroelectr. Freq. Control, 64(5), 798–810, 2017;

[2]. Smith P, Ogrodnik N, Satkunarajah J, O'Reilly MA., Characterization of ultrasound-mediated delivery of trastuzumab to normal and pathologic spinal cord tissue, Sci Rep, 11, 4412, 2021

[3]. O'Reilly, M. A., Jones, R. M., Barrett, E., Schwab, A., Head, E., & Hynynen, K. (2017). Investigation of the Safety of Focused Ultrasound-Induced Blood-Brain Barrier Opening in a Natural Canine Model of Aging. *Theranostics*, *7*(14), 3573–3584.

[4]. McDannold, N., Arvanitis, C. D., Vykhodtseva, N., & Livingstone, M. S., Temporary disruption of the blood-brain barrier by use of ultrasound and microbubbles: safety and efficacy evaluation in rhesus macaques. Cancer research, 72(14), 3652–3663.

[5]. Asquier, N., Bouchoux, G., Canney, M., Martin, C., Law-Ye, B., Leclercq, D., Chapelon, J. Y., Lafon, C., Idbaih, A., & Carpentier, A. Blood-brain barrier disruption in humans using an implantable ultrasound device: quantification with MR images and correlation with local acoustic pressure, Journal of Neurosurgery, vol. 132, no. 3. pp. 875–883, 2020;

[6]. P. S. Tsai et al., (2009). Correlations of neuronal and microvascular densities in murine cortex revealed by direct counting and colocalization of nuclei and vessels, J. Neurosci., 29(46), 14553–14570.

[7]. O'Reilly, M. A., & Hynynen, K. (2012). Blood-brain barrier: real-time feedback-controlled focused ultrasound disruption by using an acoustic emissions-based controller. *Radiology*, *263*(1), 96–106.

[8]. Huang, Y., Meng, Y., Pople, C. B., Bethune, A., Jones, R. M., Abrahao, A., Hamani, C., Kalia, S. K., Kalia, L. V., Lipsman, N., & Hynynen, K., Cavitation Feedback Control of Focused Ultrasound Blood-Brain Barrier Opening for Drug Delivery in Patients with Parkinson's Disease, Pharmaceutics, vol. 14, no. 12, 2607, 2022

Life After a Poke: How Can Sonoporation Disrupt Cellular Development?

Xinxing Duan[1,2], Alfred C. H. Yu[1]

[1]*Schlegel Research Institute for Aging, University of Waterloo, Waterloo, ON, Canada*
[2]*State Key Laboratory of Ultrasound in Medicine and Engineering, Chongqing Medical University, Chongqing, China*
Corresponding author: alfred.yu@uwaterloo.ca

Introduction

Sonoporation has demonstrated potential in transiently perforating cell membrane to facilitate drug delivery. However, the multitude of cellular bioeffects that may be induced by sonoporation has not been properly substantiated with convincing evidence, and such lack of knowledge has hampered the design of efficient sonoporation protocols for drug delivery applications. One caveat with the majority of ultrasound-mediated drug delivery experiments is that cells sonicated in the presence of microbubbles were presumed to be all sonoporated, but this is not necessarily true. In recent years, we have actively investigated how sonoporation may disrupt cellular development in ways that are distinguished from the bioeffects observed in other sonicated and unsonoporated cells.

Methods

A population-based experiment protocol has been meticulously devised to specifically identify cell groups of interest attributed to different forms of sonication exposure. This protocol involved the use of an immersion-based exposure setup with in-situ field calibrations (0.5MPa average peak negative pressure in-situ). Its transducer delivered 1-MHz ultrasound pulses (100-cycle duration, 1 kHz PRF, 30 s exposure period, 29.1 J/cm2 acoustic energy density) to the cell chamber, which was a 0.6mL-volume sealable labware with cover layers thinner (0.13-0.18 mm) than the ultrasound wavelength. In each trial, different cell types (leukomeia cells, leukocytes, etc.) and microbubbles (2e7/ml, 1:1 cell-bubble ratio) were suspended in medium and were added to the cell chamber together with calcein (sonoporation tracer). After 30s exposure, the cells were sorted using flow cytometry that analyzed the fluorescence of calcein and PI (viability indicator; added after exposure). Two cell groups were thus isolated: sonoporated (SNP+) (calcein+) and unsonoporated (SNP-) (calcein-). Two bioassays – cell proliferation (CCK-8), apoptosis (Annexin-V/PI flow cytometry) – were conducted on SNP+ and SNP- groups at 3, 8, 12, 24h after exposure. Real-time qPCR analysis was also performed on cells 3 h after exposure to study the genetic expression of heat shock proteins and other signaling pathways that were activated during cellular stress.

Results

SNP+ and SNP- groups exhibited different downstream bioeffects. Over 24 h, the SNP+ group barely restored a cell proliferation trend (24-h proliferation rate: 0.56) and showed significant apoptosis (54.6% of SNP+ cells were PI+). In contrast, the SNP- group had limited apoptosis (16.8%) and restored cell proliferation 8h after exposure (24-h proliferation rate: 1.31). Genes of HSP70 (HSPA1A, HSPA1B, HAPA6) were significantly upregulated for the SNP+ group after 3 h, whereas the corresponding genes had no significant change for the SNP- group.

Conclusions

Our investigation has served well to underscore how sonoporation may instigate a variety of cellular impact over time. This new body of mechanistic knowledge can be leveraged in different ways. For instance, in sonoporation-mediated chemotherapy, where the ultimate outcome is cell death, the intended drug action can be designed to synergize with the antiproliferation impact induced by sonoporation. In other drug delivery applications where cell survival is desired, efficiency may be improved by targeting HSP-70 signaling as a potential modulation pathway to boost the cytoprotective response of sonoporated cells, since our investigation has revealed that HSP-70 genes were upregulated as a cytoprotective maneuver to promote post-sonoporation cell recovery.
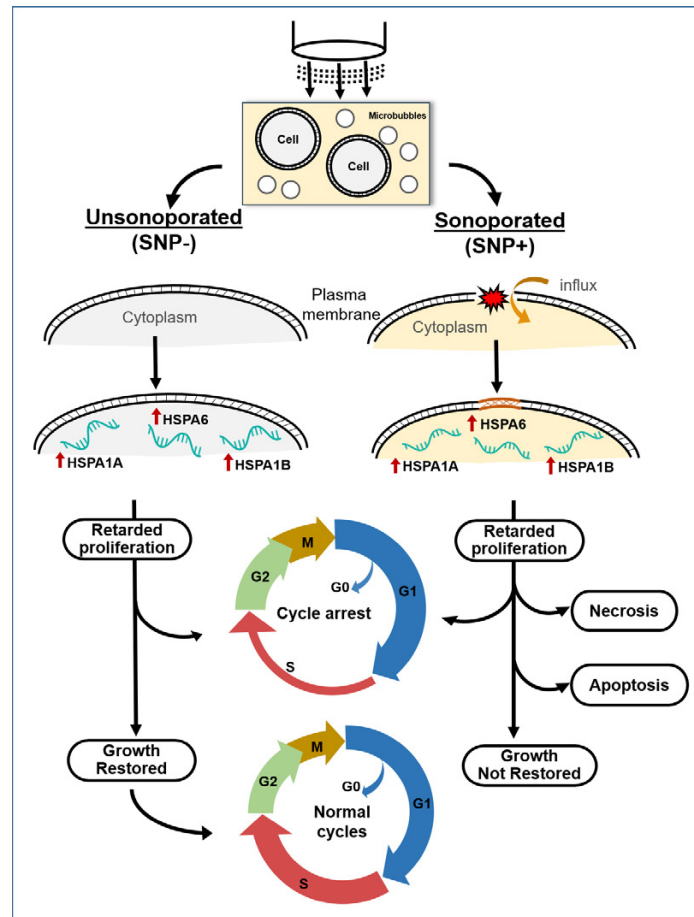
Figure 1. Downstream cellular impact observed in unsonoporated cells (left) and sonoporated cells (right), as derived from the experimental findings. (Adopted from [1])

References

[1]. Sonoporation generates downstream cellular impact after membrane resealing. *Scientific Reports*, 11: 5161, 2021.

Adverse post-infarct cardiac remodeling is attenuated by ultrasound targeted microbubble cavitation-mediated delivery of antimiR-92a

Soheb A. Mohammed,* Muhammad W.B. Amjad,* Anurag N. Paranjape, John J. Pacella, Xucai Chen, Flordeliza S. Villanueva

*contributed equally
Center for Ultrasound Molecular Imaging and Therapeutics, Division of Cardiology, Vascular Medicine Institute, University of Pittsburgh School of Medicine, Pittsburgh, PA, USA
Corresponding author: villanuevafs@upmc.edu

Introduction

Progressive adverse left ventricular (**LV**) remodeling after acute myocardial infarction (**AMI**) is a common and severe complication leading to heart failure, frequent hospitalization, and death.[1] It is characterized by infarct expansion (infarct dilation and thinning) occurring within hours after AMI. This is followed by LV dilation, hypertrophy, and fibrosis in <u>both</u> the post-ischemic and remote non-ischemic beds over the ensuing months, culminating in systolic dysfunction disproportionate to the initial infarct size. Current pharmacologic treatments merely delay progression and do not incorporate contemporary insights into dysregulated gene expression driving post-AMI remodeling. There is thus a vital unmet need for treatment strategies that target newly identified pathways, such as the role of microRNAs (**miR**), in the development of adverse remodeling.[2] miRs are endogenous single-stranded short non-coding RNAs that regulate normal gene expression by complementary binding to target messenger RNAs (**mRNAs**), causing mRNA degradation or translational repression.[2] However, miRs can be abnormally expressed in cardiovascular diseases, such as adverse remodeling. As such, delivery of oligonucleotide miR mimics or inhibitors is a promising approach to modulate expression of dysregulated miRs implicated in LV remodeling. For example, miR-92a inhibition with an antisense oligonucleotide (**antimiR**) that binds to miR-92a has cardioprotective effects on AMI and remodeling.[3] Unfortunately, delivery of RNA therapies is a major hurdle, with standard non-targeted strategies showing poor efficacy and off-target effects.[4] To overcome this hurdle, we have developed ultrasound-targeted microbubble cavitation (**UTMC**), a theranostic ultrasound-based targeted approach for delivery of RNA therapies. We hypothesize that UTMC-mediated cardiac antimiR-92a delivery will mitigate adverse cardiac remodeling post-AMI.

Methods

Lipid microbubbles (**MB**) loaded with antimiR-92a (**antimiR-92a-MB**) or negative control antimir (**antimiR-NC-MB**) were synthesized as previously described.[5-7] Anesthetized Wistar rats underwent thoractomy, then 60 min occlusion of the left anterior descending coronary artery (LAD) followed by reperfusion. Upon reperfusion, rats received intravenous <u>or</u> UTMC-mediated delivery of antimiR-92a (0.1mg/Kg) or UTMC delivery of antimiR-negative control during 15 minute infusion and UTMC delivery. UTMC was implemented using a clinically available scanner (SONOS 7500, Philips) and probe (S3, f=1.3MHz, MI 1.0, 4 frames/burst, 1 burst/second). Other rats received either no LAD occlusion (no AMI) or LAD occlusion/reflow only (AMI, no treatment) (n=3 rats per group). qPCR of heart and kidney, and 2D echo were performed 2 or 7 days later, respectively.

Results

At 7 days post AMI, echo showed normal LV cavity dimensions and restored anterior wall (LAD territory) contraction in antimiR-92a-MB + UTMC treated rats; there was persistent LV dilatation and anterior hypokinesis in those receiving no treatment, antimiR-NC + UTMC delivery, or i.v. antimiR-92a. Infarct size (TTC staining) was smallest in the antimiR-92a + UTMC rats compared to untreated and

antimiR-NC + UTMC treated rats. qPCR showed a beneficial effect of inhibiting abnormally elevated cardiac miR-92a levels during ischemia, and consequent de-repression of its cardioprotective target gene, Itgα5, by UTMC delivery of antimiR-92a, which was not seen in the other groups.

To assess off-target effects from systemic circulation of free antimiR-92a, we evaluated miR-92a and Itgα5 expression in the kidney. Unlike what we saw in the heart after antimiR-92a-MB + UTMC, there appeared to be no major change in renal miR-92a nor Itgα5 levels. This suggests low systemic circulation of free antimiR-92a after UTMC cardiac delivery, and that UTMC concentrated antimiR-92a preferentially in the heart.

Conclusions

In this rodent model of AMI and post infarct remodeling, our data suggest that UTMC-mediated antimiR-92a delivery to the heart is therapeutically effective and outperforms i.v. delivery with respect to: (1) attenuation of remodeling and preservation of LV function; (2) reduction in infarct size; (3) downregulation of abnormally elevated cardiac miR-92a with ischemia, resulting in therapeutic cardiac de-repression of target genes; and (5) preferential delivery to the heart, while sparing extra-cardiac tissue. UTMC-mediated delivery antimiR-92a is a promising approach to averting adverse sequelae of AMI; this platform may be generalizable to the delivery of other therapeutic oligonucleotides directed towards otherwise "undruggable" genes that drive cardiovascular disease.

References

[1]. Leanca SA, Crisu D, Petris AO, Afrasanie I, Genes A, Costache AD, Tesloianu DN, Costache, II. Left Ventricular Remodeling after Myocardial Infarction: From Physiopathology to Treatment. Life (Basel). 2022;12(8). Epub 20220724. doi: 10.3390/life12081111. PubMed PMID: 35892913; PMCID: PMC9332014.

[2]. Latronico MV, Condorelli G. MicroRNAs and cardiac pathology. Nat Rev Cardiol. 2009;6(6):419-29. doi: 10.1038/nrcardio.2009.56. PubMed PMID: 19434076.

[3]. Hinkel R, Penzkofer D, Zuhlke S, Fischer A, Husada W, Xu QF, Baloch E, van Rooij E, Zeiher AM, Kupatt C, Dimmeler S. Inhibition of microRNA-92a protects against ischemia/reperfusion injury in a large-animal model. Circulation. 2013;128(10):1066-75. Epub 20130729. doi: 10.1161/CIRCULATIONAHA.113.001904. PubMed PMID: 23897866.

[4]. Winkle M, El-Daly SM, Fabbri M, Calin GA. Noncoding RNA therapeutics - challenges and potential solutions. Nat Rev Drug Discov. 2021;20(8):629-51. Epub 20210618. doi: 10.1038/s41573-021-00219-z. PubMed PMID: 34145432; PMCID: PMC8212082.

[5]. Kopechek JA, Carson AR, McTiernan CF, Chen X, Hasjim B, Lavery L, Sen M, Grandis JR, Villanueva FS. Ultrasound Targeted Microbubble Destruction-Mediated Delivery of a Transcription Factor Decoy Inhibits STAT3 Signaling and Tumor Growth. Theranostics. 2015;5(12):1378-87. Epub 20151016. doi: 10.7150/thno.12822. PubMed PMID: 26681983; PMCID: PMC4672019.

[6]. Kopechek JA, McTiernan CF, Chen X, Zhu J, Mburu M, Feroze R, Whitehurst DA, Lavery L, Cyriac J, Villanueva FS. Ultrasound and Microbubble-targeted Delivery of a microRNA Inhibitor to the Heart Suppresses Cardiac Hypertrophy and Preserves Cardiac Function. Theranostics. 2019;9(23):7088-98. Epub 20190921. doi: 10.7150/thno.34895. PubMed PMID: 31660088; PMCID: PMC6815962.

[7]. Feroze R, Kopechek J, Zhu J, Chen X, Villanueva F. Ultrasound-Induced Microbubble Cavitation for Targeted Delivery of MiR-29b Mimic to Treat Cardiac Fibrosis. Ultrasound Med Biol. 2023;49(12):2573-80. doi: 10.1016/j.ultrasmedbio.2023.08.025.

Evaluation of Hepatocellular Carcinoma Microenvironment following Microbubble and Phase Change Droplet Cavitation

Hebah A. Falatah[1,2,3,4], Quezia Lacerda [4], Corinne E. Wessner [4],
Ji-Bin Liu [4], John R. Eisenbrey[4]

[1] *College of Applied Medical Sciences, King Saud Bin Abdulaziz University for Health Sciences, Jeddah 22384, Saudi Arabia*
[2] *King Abdullah International Medical Research Center, Jeddah 22384, Saudi Arabia*
[3] *Ministry of the National Guard-Health Affairs, Jeddah 22384, Saudi Arabia*
[4] *Department of Radiology, Thomas Jefferson University, Philadelphia, PA 19107, USA*

Corresponding author: John.Eisenbrey@jefferson.edu

Introduction

In 2020, primary liver cancer accounted for a significant number of cancer-related deaths worldwide, with hepatocellular carcinoma (HCC) comprising between 75% and 85% of cases[1]. Unfortunately, treatment options for HCC remain limited and largely depend on the tumor stage and the patient's overall health. Due to the late diagnosis of the disease and the limited treatment options available, the prognosis for HCC is generally poor. Local radiotherapy has shown limited success in treating HCC in the early and mid-stages of the disease. However, promising results have been obtained with the use of ultrasound-stimulated microbubbles (USMB), which have been shown to target the tumor vasculature and improve the efficacy of both chemotherapy and radiation therapy[2]. Clinical trials using these combination treatments have shown encouraging results[3, 4]. While the size of microbubbles (1-8 μm) allows them to pass through the pulmonary capillaries, they are still restricted to the vasculature[5]. In contrast, phase change nano-droplets(ND), which are smaller than 200 nm, can extravasate into the interstitial tumor space due to their size and the enhanced permeability and retention effect (EPR)[6]. Consequently, the purpose of this work was to evlauate changes to the HCC microenivornment following either microbubble- or ND destruction in a syngeneic preclinical model.

Methods

Definity, an ultrasound contrast agent manufactured by Lantheus Medical Imaging in North Billerica, MA, USA, was employed to prepare ND using a well-established protocol available in the literature[7]. The Definity vial was agitated for 45 seconds using a Vialmix following the manufacturer's instructions. After activation, ND were prepared in a 10 mL syringe with a 0.1 mL Definity/mL concentration.

All animal work was performed under protocol 22-12-613 and approved by the IACUC of Thomas Jefferson Univeristy. The RIL-175 hepatocellular carcinoma cell line was implanted subcutaneously into the right flank of 30 C57BL/8J mice. Upon tumors growing to an approximate volume of 250 mm^3, animals (n=4) were assigned to one of the treatment groups (ND +/- ultrasound disruptive pulse (USDP), MB +/- USDP, and +/- USDP control groups). A clinical ultrasound scanner, ACUSON Sequoia scanner (Siemens Medical Solutions USA, Inc., Issaquah, WA, USA), was used with a 10L4 linear transducer to acquire B-mode and contrast mode images. A destructive pulse was applied to destroy agents (MI of 1.4, 3.05 MPa) followed by 10 seconds of low MI imaging to allow MB/ND perfusion within the tumor. Multiple destructive pulses were applied for 5-9 minutes for the duration of observed signal. Volumetric photoacoustic and power Doppler imaging were performed using a Vevo 3100 system (VisualSonics, Toronto,ON, Canada) before and after treatment to analyze changes in tumor vascularity and oxygen saturation. Tumors were harvested 24 h post-treatment and immunohistochemistry staining was performed to quantify, CD31, Caspase-3, and CD45 to investigate the impact of ND on tumor vascularity, cell apoptosis, and immune response within the tumor after treatment.

Results

The study found that the activation of ND and microbubbles was clearly visible in the tumor after ultrasound triggering. It was observed that imaging with a mechanical index of 0.2 allowed activation of ND and particle enhancement roughly 7 minutes. Alternatively, MB signal was observed with a MI of 0.1 MI and present for 5 minutes (Figure 1).

When looking at imaging-based parameters of the tumor microenivronment, it was shown that using ND + USDP in mice lead to a significant reduction in tumor vascularity (p = 0.0001), as seen in Figure 2. The percent change in fractional vascularity was normalized to baseline (pre-treatment) values. The percent decrease in the tumor vascularity after treatment was -44.3% for ND (P = 0.001) and 18.4% for MB (P = 0.021) combined with USDP compared to the untreated group. In contrast, other treatment methods showed an increased in vascularity following the treatment, presumably due to the presence of inactivated/undestroyed contrast agents which increase overall Doppler signals. In terms of tumor oxyengation, there was no significant change observed in hemoglobin oxygenation across the treatment groups (p = 0.45) (Figure 2).
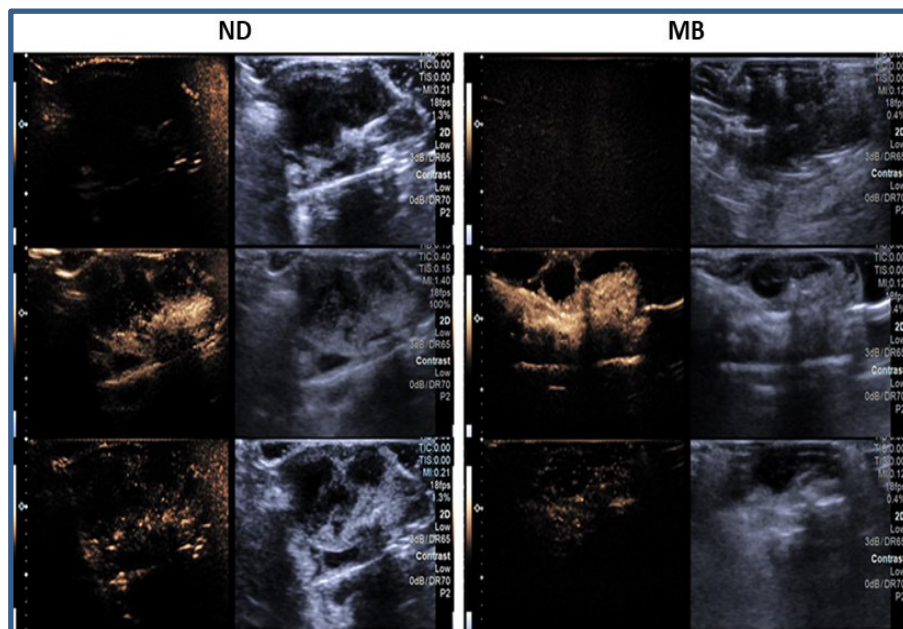
Figure 1. Example of contrast enhancement on the left and grayscale imaging on the right in an HCC syngeneic mouse model, showing phase change contrast agent (ND) and microbubble (MB) pre (top row), during (middle row), and post-activation (bottom row).
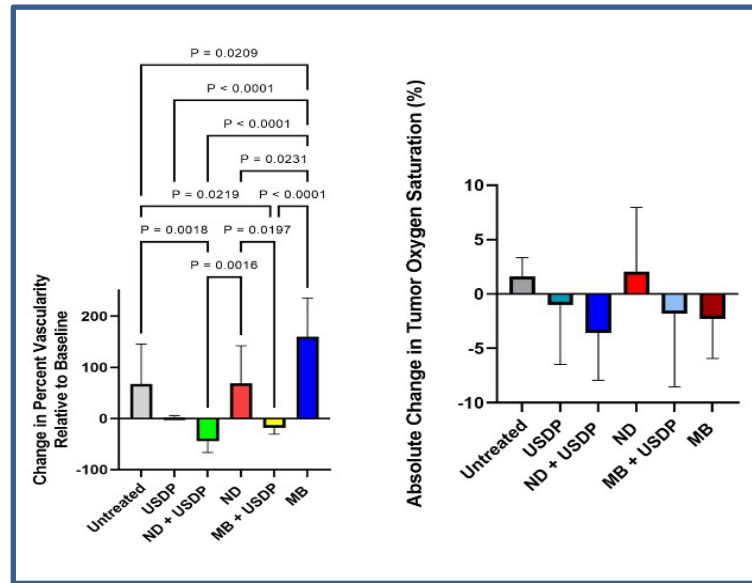
Figure 2. Analysis of power Doppler and photoacoustic imaging showing the relative percentage change in tumor vascularity (p < 0.0001) among the treatment groups: untreated, US only, ND + USDP, ND, MB + USDP, and MB. Data is presented as fractional vascularity change relative to baseline (pre-treatment).

When examining pathology data, results showed that CD31 expression was decreased to 0.28 % ± 0.2 in the group treated with ND and also decreased when tumors were treated with MB to 1.3% ± 0.2 when combined with USDP compared to the control (3.8% ±1.1). Cell apoptosis demonstrated the highest expression of (29.6 ± 8.3%) in the group treated with ND + USDP while the maximum expression in the MB + USDP group was 12.8 ± 3.4%. CD45 staining results showed a notable contrast between the group that received ND (p = 0.04) in the presence of USDP as compared to the control groups. The mean observed for the ND group with USDP was 5.5 ± 6.8 %, which was higher than the MB group that was only 4.9 ± 5.5% (Figure 3). No other statically significant differences between the groups were observed, indicating that the immune response may be enhanced by ND activation.
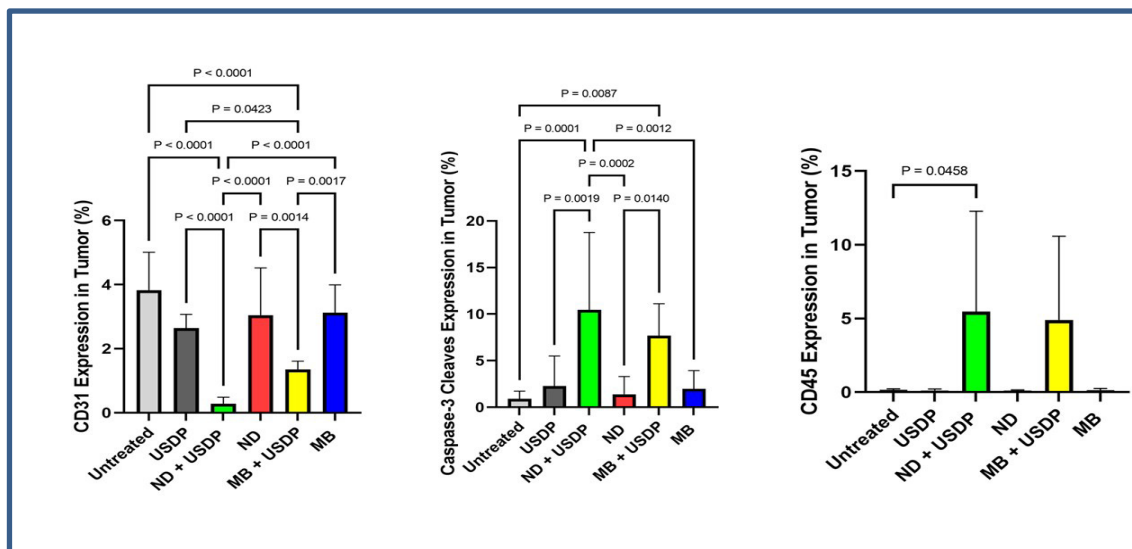
Figure 3. Quantification of endothelial cell numbers as a vascular marker (CD31), apoptosis (Caspase-3), and immune response (CD45) in a syngeneic HCC model.

Conclusions

This study shows that the use of both microbubbles or ND mediated by ultrasound has an impact on the HCC tumor environment. These finding warrant additional research to determine if ND may further enhance radiosensitivity of tumors relative to microbubbles.

References

[1]. Sung H. et al. CA. Cancer J. Clin. 2021; 71(3): 209-249

[2]. Al-Mahrouki, A. et al. PLOS ONE. 2017;12(7):e0181951

[3]. Daecher, A. et al. Cancer Lett. 2017: 411:100-105

[4]. Eisenbrey, J. et al. Radiology. 2021;298(2):450-457

[5]. Reznik N. et al. Ultrasound Med. Biol. 2013:40(6): 1379-1384

[6]. Campbell, R. Anticancer Agents Med. Chem. 2006;6(6):503-512

[7]. Choudhury, F. J. Am. Soc. Echocardiogr. Off. Publ. Am. Soc. Echocardiogr. 2017;30(2):189-197

Microbubbles decorated with rt-PA enhance fibrin degradation within *Staphylococcus aureus* pacemaker lead biofilms

Joop J.P. Kouijzer[1], Kirby R. Lattwein[1], Hongchen Li[1], Gonzalo Collado Lara[1], Mariël Leon-Grooters[1], Willem J.B. van Wamel[2], Alexander L. Klibanov[3], Klazina Kooiman[1]

[1] Department of Biomedical Engineering, Thoraxcenter, Erasmus MC, Rotterdam, the Netherlands
[2]Department of Medical Microbiology and Infectious Diseases, Erasmus MC, Rotterdam, the Netherlands
[3]Cardiovascular Division, Department of Medicine, University of Virginia, Charlottesville, Virginia, United States of America
Corresponding author: k.lattwein@erasmusmc.nl

Introduction

The increasing prevalence of cardiovascular diseases and an aging population has led to a surge in the use of cardiac implantable electronic devices (CIEDs), such as implantable cardioverter defibrillators and pacemakers. These life-saving devices pose a risk for cardiovascular infection, with an associated in-hospital mortality rate between 3.7 and 11.3% [1]. Managing patients with CIED infections necessitates lead extraction. However, not all individuals are suitable for device removal due to existing comorbidities, with 3-15% of the population declining or deemed unsuitable for CIED removal [2]. *Staphylococcus aureus* (*S. aureus*) is the most prominent causative microbe of CIED infections [3], which involves particularly fibrin-rich biofilm formation. The presence of fibrin hampers immune system infection clearance and antibiotic effectiveness. Fibrinolytic enzyme rt-PA, known for its high specificity and sensitivity to fibrin, presents a potential solution. While conventionally used for ischemic strokes, its systemic application in infective endocarditis is limited due to the high risk of intracranial hemorrhage [4]. We propose the development of rt-PA-decorated microbubbles for targeting cardiovascular biofilms, which can be utilized to locally provide the fibrinolytic effects to degrade *S. aureus* biofilms while reducing systemic risks. This proof-of-principle study details the coupling of rt-PA to microbubbles, their ability to adhere to fibrin-containing biofilms, and the evaluation of their therapeutic potential with and without ultrasound insonification using a new fibrin-based *S. aureus* biofilm model on a silicone pacemaker lead.

Methods

Recombinant tissue plasminogen activator (rt-PA) was chemically modified and coupled to maleimide microbubbles (DSPC (83.2 mol%), PEG-40 stearate (8.0 mol%), and DSPE-PEG3400-maleimide (8.8 mol%)) with a perfluorobutane (C_4F_{10}) gas core, resulting in fibrin-targeting rt-PA-decorated microbubbles. Control microbubbles (cMBs) did not contain rt-PA. The conjugation of functional rt-PA was validated with a tissue plasminogen activator chromogenic substrate assay, and coupling was confirmed with a FITC-labeled tissue plasminogen activator antibody visualized using confocal microscopy. A new fibrin-based biofilm model was developed on a silicone pacemaker lead using human plasma, a CIED clinical *S. aureus* isolate, and Alexa Fluor 647 fluorescently-labeled human fibrinogen conjugate. Infected pacemaker leads were secured with agar within IbiTreat Luer 3D μ-slides and filled with human plasma containing fluorophore SYTO 9 to stain living bacteria and propidium iodide for dead bacteria. Using a syringe pump, 2.4×10^7 microbubbles were delivered to the infected lead and allowed to adhere for 5 min. Subsequently, flow at 5.4 dyn/cm² (9 mL/min) for 30 s was applied to remove unattached microbubbles. The amount of fibrin within the biofilms and the number of microbubbles that remained bound to the biofilm was monitored for 60 min with confocal time-lapse microscopy. At 15 min, a single ultrasound burst (2 MHz, 250 kPa,

5,000 or 10,000 cycles) was applied. The number of microbubbles was determined manually using NIS-Elements software and biofilm reduction was quantified by fibrin intensity using Fiji software.

Results

Confocal microscopy revealed living *S. aureus* clusters in a fibrin matrix attached to the pacemaker leads. Presence of rt-PA on the microbubble shell was confirmed and found to have a heterogenous distribution. The concentration of rt-PA on the decorated microbubbles varied by batch (n=3) from 2.09-3.46 µg per clinical dose of microbubbles (1×10^9 microbubbles). The rt-PA-decorated microbubbles (35.2 ± 4.2; mean ± SD; n=6 fields-of-view) specifically remained bound to the infected lead model after applying physiological shear stress (5.4 dyn/cm^2) compared to cMBs (6.6 ± 5.3; n=9 fields-of-view). The impact of rt-PA-decorated microbubbles, ultrasound, and their combination on fibrin dissolution was assessed. After 60 mins, the combined treatment of rt-PA-decorated microbubbles with ultrasound showed the highest percentage of fibrin reduction (60.8% ± 34.4%). Without ultrasound insonification, rt-PA-decorated microbubbles only resulted in a reduction in fibrin intensity of 31.9% ± 15.1%, while this was 13.5% ± 4.6% for free rt-PA only (0.35 µg/mL; corresponding to the highest concentration of rt-PA on the decorated microbubbles). A significant positive correlation (r = 0.768, p = 0.002) was found between the quantity of rt-PA-decorated microbubbles bound during ultrasound treatment and the dissolution of fibrin.

Conclusions

This study confirms the successful production of rt-PA-decorated microbubbles with demonstrated efficacy in dissolving fibrin within *S. aureus* biofilms on infected pacemaker leads. The findings highlight the promising potential of this targeted therapeutic approach, combining rt-PA-decorated microbubbles with ultrasound, to locally and effectively treat cardiovascular device biofilms.

Acknowledgements

References

[1]. Polyzos KA, Konstantelias AA, Falagas ME. Risk factors for cardiac implantable electronic device infection: a systematic review and meta-analysis. Europace. 17(5):767-77, 2015.

[2]. Sandoe JA, Barlow G, Chambers JB, Gammage M, Guleri A, Howard P, et al. Guidelines for the diagnosis, prevention and management of implantable cardiac electronic device infection. Report of a joint Working Party project on behalf of the British Society for Antimicrobial Chemotherapy (BSAC, host organization), British Heart Rhythm Society (BHRS), British Cardiovascular Society (BCS), British Heart Valve Society (BHVS) and British Society for Echocardiography (BSE). The Journal of antimicrobial chemotherapy. 70(2):325-59, 2015.

[3]. Gomes S, Cranney G, Bennett M, Li A, Giles R. Twenty-year experience of transvenous lead extraction at a single centre. Europace. 16(9):1350-5, 2014.

[4]. Ong E, Mechtouff L, Bernard E, Cho TH, Diallo LL, Nighoghossian N, et al. Thrombolysis for stroke caused by infective endocarditis: an illustrative case and review of the literature. Journal of Neurology. 2013;260(5):1339-42, 2013.

Simultaneous imaging and monitoring of Immunomodulation and drug delivery using focused ultrasound and microbubbles towards the treatment of neurodegenerative disease and brain tumors

Elisa E. Konofagou[1,2,3], Sua Bae[1], Robin Ji[1], Keyu Liu[1], Maria Eleni Karakatsani[1], Antonios Pouliopoulos[1], Alina Kline-Schoder[1], Zachary Englander[3], Stergios Zacharoulis[4], Alexander Berg[5], Cheng-Chia Wu[5] and Lawrence Honig[6]

Departments of [1]Biomedical Engineering, [2]Radiology (Physics), [3]Neurosurgery, [4]Pediatrics, [5]Radiation Oncology and [6]Neurology,
630 West 168th street, Columbia University, New York, NY, USA

Introduction

The blood-brain barrier (BBB) poses a formidable impediment to the treatment of adult-onset neurodegenerative disorders preventing most drugs from gaining access to the brain parenchyma. Focused ultrasound (FUS), in conjunction with systemically administered microbubbles, has been shown to open the BBB locally, reversibly and non-invasively.

Methods

The objective is to induce localized drug or gene delivery in deep seated regions in the brain, such as the hippocampus and the substantia nigra. This BBB opening has allowed the transport of compounds, endogenous or exogenous, that would help treat the afflicted brain regions. Over these past few years, our group has demonstrated that FUS was capable of generating highly focused and transient BBB openings in murine and non-human primate (NHP) brains through the intact skull and skin in vivo; therefore, completely noninvasively. We have also identified the mechanism by which the BBB opens involving transcellular diffusion at low FUS pressures and tight-junction disruption at higher pressures.

Results

By optimizing this novel drug delivery system such as neurotrophic factors through protein or gene delivery for effective neuronal restoration in deep-seated brain regions such as the substantia nigra at the early stages of Parkinson's disease as well as inducing an immune response for reduction of the amyloid plaque and tau load in the hippocampus and the substantia nigra. In this presentation, we will emphasize the theranostic application of FUS together with ultrafast localization microscopy (ULM) that both utilize bubbles to treat and image, respsectively. We will demonstrate that simultaneous ULM can detect the region of the opening and the contraction of the blood vessels at the same time as visualizing any dedema. We will also demonstrate application of FUS BBB opening the early stages of neurodegenerative disease, such as Alzheimer's and Parkinson's in conjunction with neurotrophic drug (protein or gene) delivery as well as glioblastoma and pontine glioma treatment in conjunction with chemotherapeutic treatment will be presented. Finally, in preliminary clinical studies, the same FUS system will be shown capable of reducing amyloid load in early Alzheimer's patients.

Conclusion

The full potential of ultrasound for both imaging and treating with microbubbles will be explored and its translation capabilities together with cavitation mapping will also be demonstrated.

Contrast enhanced ultrasound molecular imaging for assessment of vascular inflammation in atherosclerosis

Beat A. Kaufmann[1,2]

[1]Cardiovascular Molecular Imaging, Department of Biomedicine, University of Basel and University Hospital of Basel, Switzerland
[2]Cardiology, Heart Center, Universyty Hospital of Basel, Switzerland
beat.kaufmann@usb.ch

Atherosclerosis is an inflammatory disease that progresses silently for decades before resulting in clinically apparent consequences such as myocardial infarction or stroke. Currently available methods for risk stratification place a large proportion of individuals in an intermediate risk category, for which management is not well defined. At the same time, novel but costly treatment options such as PCSK-9 inhibitors (monoclonal antibodies, siRNA) and glucagon-like peptide (GLP-1) receptor agonists have become available within the last decade. Thus, there is (1) a need for clinical translation of tools for improved risk stratification in intermediate risk populations, and (2) a need for better understanding of the effect of novel therapies that have an effect on cardiovascular outcomes.

Nanobodies or single domain antibodies are antibody fragments consisting of a single monomeric variable antibody domain derived from heavy-chain-only antibodies that are by nature present in camelids. Nanobodies are the smallest possible (10-15 kDa) antibody-derived polypeptide structure that bind to a specific antigen. Nanobodies possess advantages over conventional antibodies for clinical applications. They lack an Fc region and therefore do not induce complement-triggered cytotoxicity nor bind to Fc receptors on immune and other type of cells. In addition, there is homology between camelid and human antibody heavy chains, which makes humanization of nanobodies unproblematic. We developed and tested a microbubble (MB) contrast agent using a nanobody ligand directed against Vascular cell adhesion molecuole 1 (VCAM-1), a cell adhesion molecule involved in vascular inflammation that drives the development oif atherosclerosis. MBs with a nanobody targeting VCAM-1 ($MB_{cAbVcam1-5}$) and MB with a control nanobody (MB_{VHH2E7}) were characterized *in vitro*. Attachment efficiency to VCAM-1 under continuous was investigated. *In vivo* contrast enhanced ultrasound molecular imaging (CEUMI) of the aorta was performed in atherosclerotic double knockout (DKO; Ldlrtm1Her Apobtm2Sgy) and wild-type (WT) mice after injection of $MB_{cAbVcam1-5}$ and MB_{VHH2E7}. *Ex vivo* CEUMI of human endarterectomy specimens was performed in a closed-loop circulation model. The surface density of the nanobody ligand was 3.5×10^5 per MB. Compared to MB_{VHH2E7}, $MB_{cAbVcam1-5}$ showed increased attachment under continuous flow with increasing shear stress of 1-8 dynes/cm^2. CEUMI in DKO mice showed signal enhancement for $MB_{cAbVcam1-5}$ in early (p=0.0003 vs. MB_{VHH2E7}) and late atherosclerosis (p=0.007 vs. MB_{VHH2E7}); in WT mice there were no differences between $MB_{cAbVcam1-5}$ and MB_{VHH2E7}. CEUMI in human endarterectomy specimens showed a 100% increase in signal for $MB_{cAbVcam1-5}$ vs MB_{VHH2E7}. Thus, imaging of endothelial inflammation with a clinically translatable MB is feasible.

Randomized clinical studies have shown a reduction in cardiovascular outcomes with the GLP-1 receptor agonist liraglutide with the hypothesized mechanisms being an underlying effect on atherosclerosis. We therefore determined the effect of liraglutide on the endothelial surface expression of VCAM-1 and vascular inflammation in a mouse model of atherosclerosis. Apo E -/- mice received daily subcutaneous injections with liraglutide or vehicle. CEUMI using MBs targeted to VCAM-1 (MB_{VCAM-1}) and control MBs (MB_{Ctr}) was performed and blood cytokines, glucose, glycated hemoglobin (HbA1c) and lipids were measured. CEUMI showed an increase in endothelial surface VCAM-1 signal in vehicle treated animals, whereas in the liraglutide treated animals the signal remained low throughout the study. In liraglutide treated animals, inflammatory cytokines were reduced. Plasma glucose and blood HbA1c levels were not affected by liraglutide

treatment. Aortic plaque lesion area and luminal VCAM-1 expression on immunohistology were reduced under liraglutide treatment. Thus, liraglutide treatment reduced aortic endothelial VCAM-1 expression in a murine atherosclerosis model independent of glucose levels. Combined with the reduction in cytokine levels, this suggests that liraglutide attenuated vascular inflammation and atherosclerosis development.

In conclusion, CEUMI of vascular inflammation holds promise for clinical translation and use as a risk stratification tool. In addition, CEUMI can be used to assess the effect of novel compounds on vascular inflammation and thus on the pathogenesis of atherosclerosis.

A physically realistic contrast-enhanced ultrasound simulator

Nathan Blanken[1], Baptiste Heiles[2], Alina Kuliesh[2], Michel Versuis[1],
Kartik Jain[3], David Maresca[2], Guillaume Lajoinie[1]

[1]*Physics of Fluids Group, MESA+ Institute for Nanotechnology and Technical Medical*
(TechMed) Centre, University of Twente,
[2]*Department of Imaging Physics, Delft University of Technology*
[3]*Department of Thermal and Fluid Engineering, Faculty of Engineering Technology,*
University of Twente

Corresponding authors: g.p.r.lajoinie@utwente.nl, k.jain@utwente.nl, d.maresca@tudelft.nl

Introduction

Ultrasound is a cost-effective and safe clinical modality used in daily practice to assess the function of organs. Blood echogenicity can be increased significantly with intravascular ultrasound contrast agents (UCAs). These microbubbles can resonate, provided that their size is matched to the transmitted ultrasound frequency, which further enhances their echogenicity. Furthermore, resonant microbubbles are also nonlinear scatterers even at low acoustic pressure [1] which I often used to further boost the contrast-to-tissue ratio. In recent years, advances in contrast-enhanced ultrasound have mostly followed three directions: (1) improving microbubbles themselves (e.g., by making them monodisperse [2-4]), (2) designing new pulse sequences and imaging strategies (e.g., echo particle image velocimetry (echoPIV) [5-8], and (3) breaking the diffraction limit in vascular imaging with ultrasound localization microscopy (ULM) [9-14]. The experimental development of contrast-enhanced ultrasound imaging techniques is time and resource-intensive. Furthermore, it is difficult to get an objective account of \emph{in vivo} performance due to the lack of a ground truth. Several open- and close-source simulation tools have been developed to investigate specific aspects of ultrasound imaging [15-19]. These tools have been used to simulate contrast enhance ultrasound imaging data [20-22]. Yet, notwidthstanding their research vale, none of these simulations combine all the necessary ingredient of ultrasound contrast imaging: 3D ultrasound probes, 3D nonlinear wave propagation, nonlinear microbubbles scattering, and physiological blood flow in realistic vasculatures. Here we introduce PROTEUS, a physically realistic contrast-enhanced ultrasound simulator. PROTEUS combines a lattice Boltzmann flow solver [23, 24], an ultrasound wave propagation toolbox [15], an ODE solver to simulate nonlinear scattering and acoustic interactions of microbubbles [25], and a strealine generator to determinethe bubble trajectories. PROTEUS is open-source and available to the scientific community

Methods

the architecture of PROTEUS consists of four interconnected simulation modules that, together, capture the physics of contrast-enhanced ultrasound imaging. The fluid dynamics simulation module solves the fluid dynamics in a chosen vasculature. The microbubbles trajectory module computes the intravascular microbubbles trajectories based on the user-selected imaging settings (e.g. framerate, pulsing scheme, etc...) and on the result of the computational fluid dynamics (CFD) model. A virtual medical transducer array is simulated within the wave propagation module and used to transmit ultrasound waves in a virtual medium that contains the selected vascular structure perfused with microbubbles. Transmitted ultrasound waves elicit nonlinear microbubbles scattering, which is computed with the microbubble dynamics module. Finally, echoes are back- propagated to the virtual transducer surface using the wave propagation module. The output of these simulations consists of synthetic RF data containing microbubbles signals. These synthetic RF data can then be beamformed to reconstruct ultrasound images. PROTEUS includes two complementary computation frameworks for microbubbles scatter. The "full" PROTEUS simulator architecture accounts for both microbubbles-microbubbles interactions and microbubbles-tissue interactions (scatter and attenuation) based on k-Wave sub-simulations. The reduced order simulator architecture was optimized for speed and computes microbubbles-microbubbles interactions and microbubbles scatter back-propagation assuming a dissipative homogeneous medium.

Results

To demonstrate the potential of PROTEUS, we first simulated nonlinear ultrasound imaging of microbubbles using established pulse sequences. Second, we compared side-by-side non-linear imaging of polydisperse and monodisperse microbubbles suspensions. Third, we show how PROTEUS can serve to evaluated the accuracy of ultrasound particle image velocimetry (echoPIV) in a macroscopic flow model. And fourth, we conceived a case study investigating the impact of microbubbles size distribution on ULM.
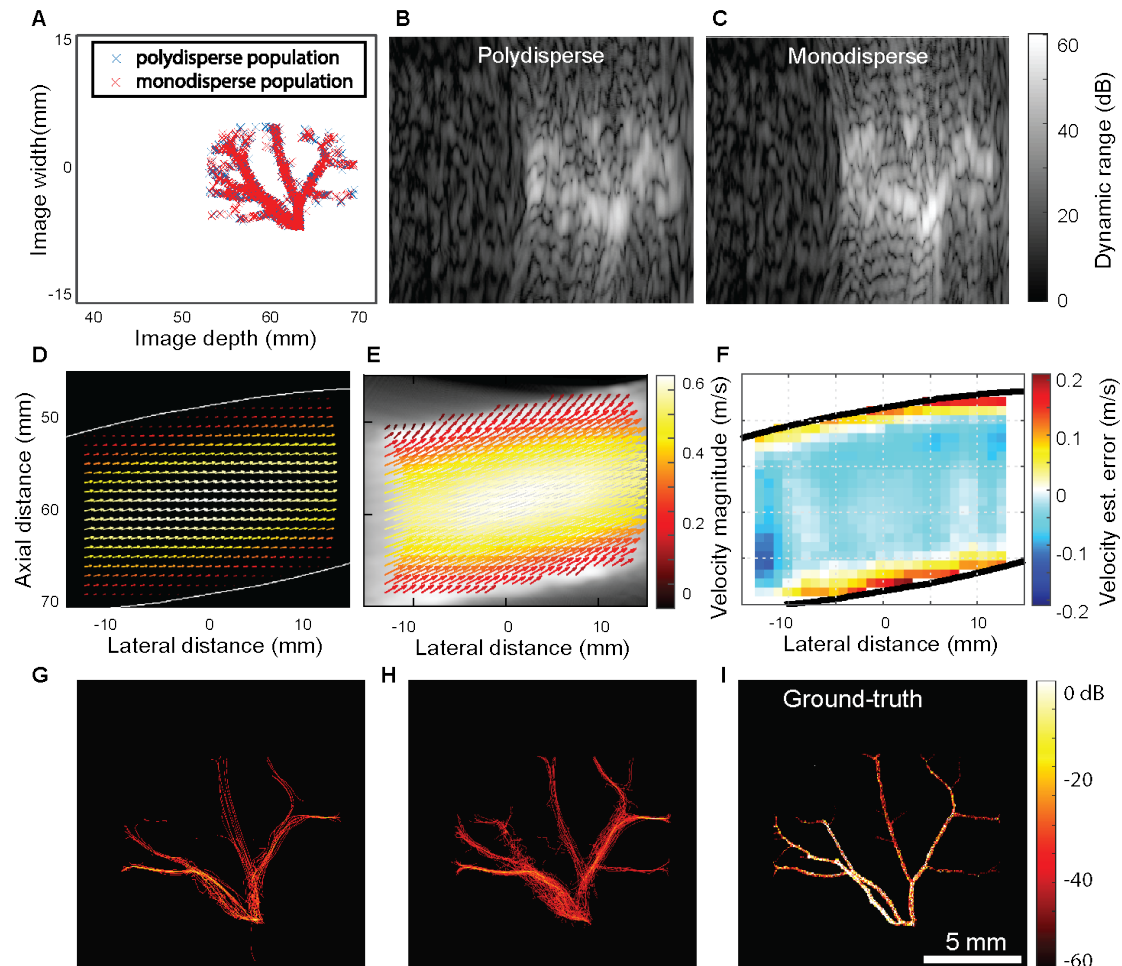
Figure 1: A.-C. Amplitude modulation with polydisperse (B) and monodisperse (C) microbubbles. The ground truth bubble locations are shown in A. In each case, the vasculatir contains 1,000 microbubbles. D.-F. Ultrasound vector flow imaging. We simulate contrast agents flowing in a 2 cm-diameter pipe. The ground truth velocity field from the CFD simulation is shown in D, and the velocity recovered from the PIV processing of the ultrasound images is shown in E. F. shows the accuracy of the echoPIV analysis. G.-I. Ultrasound localization microscopy. Density maps recovered for polydisperse (G) and monodisperse (H) microbubbles across 15,000 simulated frames. The ground truth density is shown in I.

Conclusions

We have developed PROTEUS, an effective and versatile open simulator to investigate existing and emerging applications in the field of contrast-enhanced ultrasound imaging. It enables comparative imaging studies and benchmarks that would be experimentally challenging. In the specific field of ULM, it will equip scientists with a tool to generate data and train AI-based computational imaging methods. For vector flow imaging (or echoPIV), PROTEUS will accelerate the development of more accurate approaches. PROTEUS capabilities extend beyond examples reported here and will lead to a wave of new imaging innovations.

References

[1] Michel Versluis, Eleanor Stride, Guillaume Lajoinie, Benjamin Dollet, and Tim Segers. Ultrasound contrast agent modeling: A review. Ultrasound Med. Biol., 46(9):2117–2144, 2020.

[2] Benjamin van Elburg, Gonzalo Collado-Lara, Gert-Wim Bruggert, Tim Segers, Michel Versluis, and Guillaume Lajoinie. Feedback-controlled microbubble generator producing one million monodisperse bubbles per second. Rev. Sci. Instrum., 92(3):035110, 2021.

[3] Tim Segers, Anne Lassus, Philippe Bussat, Emmanuel Gaud, and Peter Frinking. Improved coalescence stability of monodisperse phospholipid-coated microbubbles formed by flow-focusing at elevated temperatures. Lab Chip, 19(1):158–167, 2019.

[4] Tim Segers, Emmanuel Gaud, Gilles Casqueiro, Anne Lassus, Michel Versluis, and Peter Frinking. Foam-free monodisperse lipid-coated ultrasound contrast agent synthesis by flow-focusing through multi-gas-component microbubble stabilization. Appl. Phys. Lett., 116(17):173701, 2020.

[5] Stefan Engelhard, Majorie van Helvert, Jason Voorneveld, Johan G. Bosch, Guillaume Lajoinie, Michel Versluis, Erik Groot Jebbink, and Michel M. P. J. Reijnen. Us velocimetry in participants with aortoiliac occlusive disease. Radiology, 301(2):332–338, 2021.

[6] Astrid M. Hoving, Jason Voorneveld, Julia Mikhal, Johan G. Bosch, Erik Groot Jebbink, and Cornelis H. Slump. in vitro performance of echopiv for assessment of laminar flow profiles in a carotid artery stent. J. Med. Imaging, 8(1): 1–16, 2021.

[7] Javier Brum, Miguel Bernal, Nicasio Barrere, Carlos Negreira, and Cecilia Cabeza. Vortex dynamics and transport phenomena in stenotic aortic models using echo-PIV. Physics in Medicine &amp Biology, 66(5):055026, 2021.

[8] Jorgen A. Jensen, Svetoslav Nikolov, Alfred C.H. Yu, and Damien Garcia. Ultrasound vector flow imaging: I: Sequential systems. IEEE Transactions on Ultrasonics, Ferroelectrics, and Frequency Control, pages 1–1, 2016.

[9] Claudia Errico, Juliette Pierre, Sophie Pezet, Yann Desailly, Zsolt Lenkei, Olivier Couture, and Mickael Tanter. Ultrafast ultrasound localization microscopy for deep super-resolution vascular imaging. Nature, 527(7579):499–502, 2015.

[10] Charlie Demené, Justine Robin, Alexandre Dizeux, Baptiste Heiles, Mathieu Pernot, Mickael Tanter, and Fabienne Perren. Transcranial ultrafast ultrasound localization microscopy of brain vasculature in patients. Nature biomedical engineering, 5(3): 219–228, 2021.

[11] Jipeng Yan, Biao Huang, Johanna Tonko, Matthieu Toulemonde, Joseph Hansen-Shearer, Qingyuan Tan, Kai Riemer, Konstantinos Ntagiantas, Rasheda A Chowdhury, Pier Lambiase, Roxy Senior, and Meng-Xing Tang. Transthoracic superresolution ultrasound localisation microscopy of myocardial vasculature in patients, 2023.

[12] Nathan Blanken, Jelmer M. Wolterink, Hervé Delingette, Christoph Brune, Michel Versluis, and Guillaume Lajoinie. Super-resolved microbubble localization in single-channel ultrasound rf signals using deep learning. IEEE Transactions on Medical Imaging, pages 1–1, 2022.

[13] Jihun Kim, Mathew R Lowerison, Nathiya V Chandra Sekaran, Zhengchang Kou, Zhijie Dong, Michael L Oelze, Daniel A Llano, and Pengfei Song. Improved ultrasound localization microscopy based on microbubble uncoupling via transmit excitation. IEEE transactions on ultrasonics, ferroelectrics, and frequency control, 69(3): 1041–1052, 2022.

[14] Xi Chen, Matthew R Lowerison, Zhijie Dong, Nathiya Vaithiyalingam Chandra Sekaran, Daniel A Llano, and Pengfei Song. Localization free super-resolution microbubble velocimetry using a long short-term memory neural network. IEEE Transactions on Medical Imaging, 2023.

[15] Bradley E Treeby and Benjamin T Cox. k-wave: Matlab toolbox for the simulation and reconstruction of photoacoustic wave fields. Journal of biomedical optics, 15(2): 021314–021314, 2010.

[16] F. Varray, A. Ramalli, C. Cachard, P. Tortoli, and O. Basset. Fundamental and second-harmonic ultrasound field computation of inhomogeneous nonlinear medium with a generalized angular spectrum method. IEEE Transactions on Ultrasonics, Ferroelectrics and Frequency Control, 58(7):1366–1376, 2011.

[16] François Varray, Olivier Basset, Piero Tortoli, and Christian Cachard. CREANUIS: A non-linear radiofrequency ultrasound image simulator. Ultrasound in Medicine &amp Biology, 39(10):1915–1924, 2013.

[17] Damien Garcia. SIMUS: An open-source simulator for medical ultrasound imaging. Part I: Theory & examples. Computer Methods and Programs in Biomedicine, 218: 106726, 2022.

[18] J.A. Jensen and N.B. Svendsen. Calculation of pressure fields from arbitrarily shaped, apodized, and excited ultrasound transducers. IEEE Transactions on Ultrasonics, Ferroelectrics and Frequency Control, 39(2):262–267, 1992.

[19] JENSEN J. A. Field: A program for simulating ultrasound systems. 10th Nordic-Baltic Conf. Biomedical Imaging, 1996.

[20] Baptiste Heiles, Arthur Chavignon, Vincent Hingot, Pauline Lopez, Eliott Teston, and Olivier Couture. Performance benchmarking of microbubble-localization algorithms for ultrasound localization microscopy. Nature Biomedical Engineering, February 2022. ISSN 2157-846X. doi: 10.1038/s41551-021-00824-8.

[21] Marcelo Lerendegui, Kai Riemer, Bingxue Wang, Christopher Dunsby, and Meng- Xing Tang. BUbble Flow Field: a Simulation Framework for Evaluating Ultrasound Localization Microscopy Algorithms. November 2022.

[22] Hatim Belgharbi, Jonathan Poree, Rafat Damseh, Vincent Perrot, Leo Milecki, Patrick Delafontaine-Martel, Frederic Lesage, and Jean Provost. An Anatomically Realistic Simulation Framework for 3D Ultrasound Localization Microscopy. IEEE Open Journal of Ultrasonics, Ferroelectrics, and Frequency Control, 3:1–13, 2023. ISSN 2694-0884.

[23] Harald Klimach, Kartik Jain, and Sabine Roller. End-to-end parallel simulations with apes. In Parallel Computing: Accelerating Computational Science and Engineering (CSE), volume 25, pages 703–711, 2014.

[24] Manuel Hasert, Kannan Masilamani, Simon Zimny, Harald Klimach, Jiaxing Qi, Jörg Bernsdorf, and Sabine Roller. Complex fluid simulations with the parallel tree-based lattice boltzmann solver musubi. Journal of Computational Science, 5(5):784–794, 2014.

[25] Philippe Marmottant, Sander Van Der Meer, Marcia Emmer, Michel Versluis, Nico De Jong, Sascha Hilgenfeldt, and Detlef Lohse. A model for large amplitude oscillations of coated bubbles accounting for buckling and rupture. The Journal of the Acoustical Society of America, 118(6):3499–3505, 2005.

Super Resolution Imaging with NanoDroplets (SRUI-NDs) in a Chicken Embryo Model

Alexis Vivien, Mina Lykakis, Redouane Ternifi, Romain Melich, Emmanuel Gaud

Bracco Suisse SA, CH-1228 Plan-les-Ouates, Geneva, Switzerland
Corresponding author: Alexis.Vivien@bracco.com

Introduction

The recent enthusiasm of the ultrasound community to improve the resolution of images has led to the Super Resolution (SR) framework, which can be separated in two parts, SR Ultrasound Imaging with MicroBubbles (SRUI-MBs) and with NanoDroplets (SRUI-NDs).

NDs are smaller than their MBs counterparts and invisible to ultrasound, they can circulate smaller vessels and be activated *in-vivo* into MBs to resolve the finer vasculature. NDs also possess the advantage of a longer circulation time over MBs. As described in [3], NDs are potentially the best solution to the trilemma between image fidelity, acquisition speed and resolution that exist with MBs.

In order to answer this problematic by exploiting the NDs characteristics, a model of chicken embryo called the Chorio-Allantoic Membrane (CAM) was developed in house. The CAM model offers a profusely vascularized US-transparent media, easy to culture, which follows the 3R principles (replace, reduce, refine) and considered as an alternative to an animal model, therefore of great quality to investigate SRUI-NDs.

Two Super Resolution ultrasound sequences, respectively with and without ND pre-vaporization, were used on the CAM model, the results are presented in this study.

Methods

The imaging of the CAM model was performed between Embryonic Development Day (EDD)12 and EDD14. The chicken embryo, which has been developed on a weighting boat (*ex ovo* culture), was placed in a small incubator to maintain suitable temperature and humidity. Furthermore, the probe was placed parallel to the weighting boat in order to image only the CAM vasculature, and a binocular lens was used to facilitate the NDs intravenous injections (Figure 1).

The injection volume was defined to 30µL of ND suspension, which yielded a number concentration of about $3 \cdot 10^7$ NDs per mL when diluted in the 1.5 to 2 mL CAM blood pool.
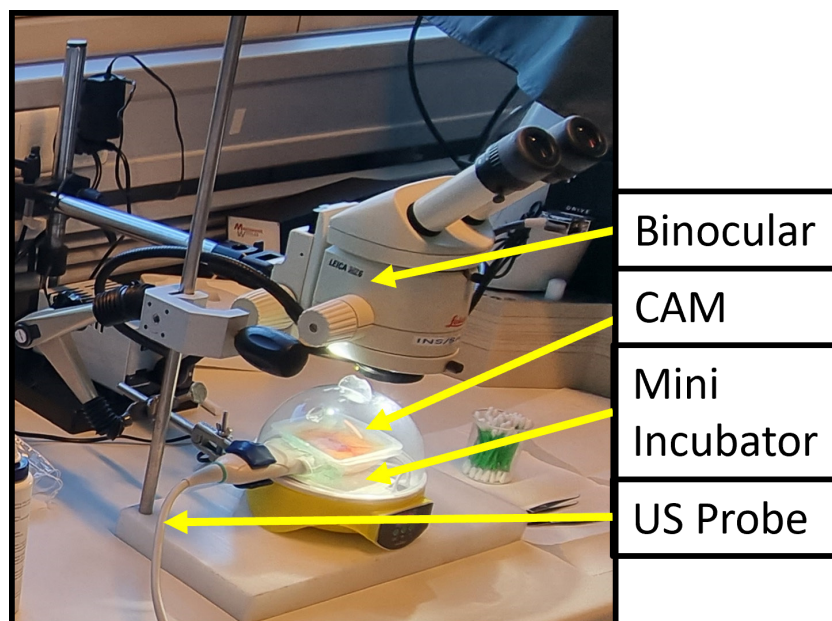
Figure 1 – Super Resolution in the Chorio-Allantoic Membrane Model

The ultrasound sequences were inspired from the AWSALM and FAST-AWSALM sequences popularized by Zhang et al. [1, 2] and will be refered to as Pre-Activation (PA) and Simultaneous Activation (SA) sequences.

For the PA sequence, 8 successive activation-imaging cycles (1 activation pulse + 200 imaging frames) were used to vaporize and image NDs with the L11-5v and the Vantage 256 platform (both Verasonics Inc., Kirkland, WA). The parameters of the sequence are summarized on Table 1.

Table 1. "Pre Activation" Sequence Parameters

State	Frequency [MHz]	Pulse Length [Cycles]	PNP [MPa]	MI
Activation	6	10	5 - 8	2.04 – 3.27
Imaging	7.42	1	0.4	0.15

PNP: Peak-negative acoustic pressure

MI: Mechanical Index

The SA sequence is an upgrade of the PA sequence as it activates and images NDs within the same ultrasound pulse, removing the need for a dedicated activation pulse, and therefore allowing for a faster acquisition. Thus, a single imaging sequence of 500 imaging frames was acquired with the same setup as for the PA sequence. The settings are specified below in Table 2.

Table 2. "Simultaneous Activation" Sequence Parameters

State	Frequency [MHz]	Pulse Length [Cycles]	PNP [MPa]	MI
Imaging/Activation	7.42	1	1.5 - 2	0.55 - 0.73

A dedicated ND formulation was prepared for each sequence type. Bracco proprietary condensed lipid-shelled nanodroplets containing a perfluorinated gas (C_4F_{10} (bp -1.7°C) for PA and a mixture of C_3F_8 (bp -36.7°C) and C_4F_{10} for SA) were used. In the latter, thanks to the use of a very low boiling point gas, namely C_3F_8, the NDs needed less acoustic power to vaporize, hence their use with the SA sequence.

Results

As highlighted in Figures 2 and 3, the experiments resulted in clear SR density maps of the larger vessels in the probe Field-of-View [FoV]. For the SA sequence, vessels as small as 130 µm in diameter were imaged while for PA the smallest detected vessel was 160 µm in diameter.

Figure 2 - Side-by-side of SR density map and microscope snapshot ("Pre Activation" Sequence). The star indicates the vaporization spot and the arrow the flow direction.

Experimentation was also facilitated by the SA sequence, used with the Perfluorocarbon mixture, due to the possibility to vaporize on the whole image, greatly reducing the time spent to find a major vessel, unlike for PA, and helping a great deal to retrieve extensive vascularization in the vaporization maps.
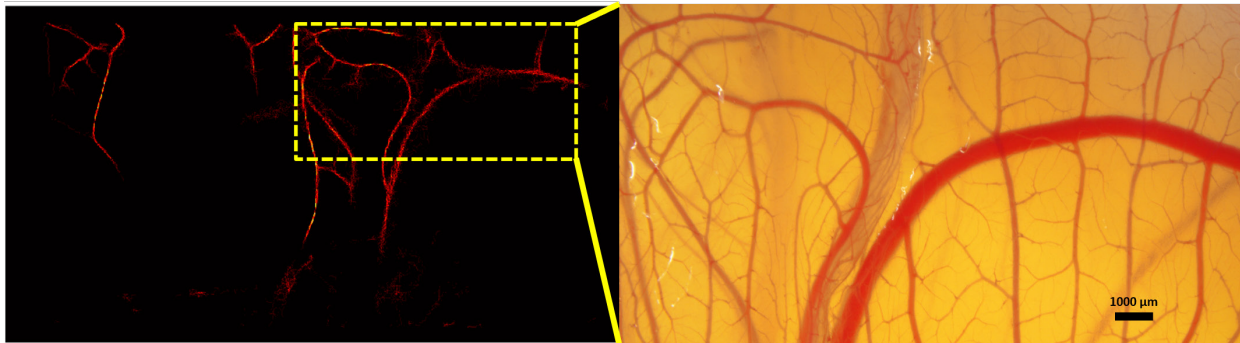
Figure 3 - Side-by-side of SR density map and microscope snapshot ("Simultaneous Activation" Sequence)

Conclusions

A high-quality imaging framework for SRUI-NDs was adapted to the CAM model. An alternative to animal testing, that proved to be of great interest and convenient use. Both PA and SA sequences resulted in high-fidelity density maps. In addition, as expected SA allows the detection of smaller vessels. Indeed, the ability to vaporize NDs in plane-wave eliminates the issue of finding a major vessel for vaporization like for PA which then confines newly created MBs to large vessels only.

Moreover, the straightforward experimentation as well as the easy NDs preparation can pave the way for a potential formulation screening. One could also consider using a clinical scanner in place of the Verasonics system, as the versatility of the setup allows for an easy change of probe and because the SA imaging parameters are close to clinical settings.

Finally, the CAM model attracts a great deal of interest in pharmaceutical and biological research because it is an efficient, and cost-effective alternative model compared to animal model and well suited to evaluate NDs behavior for SR applications.

References

[1]. Ge Zhang, Sevan Harput, Shengtao Lin, Kirsten Christensen-Jeffries, Chee Hau Leow, Jemma Brown, Christopher Dunsby, Robert J. Eckersley, Meng-Xing Tang; Acoustic wave sparsely activated localization microscopy (AWSALM): Super-resolution ultrasound imaging using acoustic activation and deactivation of nanodroplets. *Appl. Phys. Lett.* 2 July 2018; 113 (1): 014101. https://doi.org/10.1063/1.5029874.

[2]. Zhang G, Harput S, Hu H, Christensen-Jeffries K, Zhu J, Brown J, Leow CH, Eckersley RJ, Dunsby C, Tang MX. Fast Acoustic Wave Sparsely Activated Localization Microscopy (fast-AWSALM): Ultrasound Super-Resolution using Plane-Wave Activation of Nanodroplets. IEEE Trans Ultrason Ferroelectr Freq Control. 2019 Mar 25. doi: 10.1109/TUFFC.2019.2906496. Epub ahead of print. PMID: 30908211.

[3]. Zhang G et al., NanoDroplet-Based Super-Resolution Ultrasound Localization microscopy, ASC Sens. 2023, 9, 9, 3294-3306. Publication Date: August 22, 2023. https://doi.org/10.1021/acssensors.3c00418

Neonatal cerebral vascular reorganization during neurovascular interventions observed with Ultrasound Localization Microscopy

Louise Denis[1], Simone Schwarz[2], Emmanuel Nedoschill[3], Adrian Buehler[3], Vera Danko[3], Henriette Mandelbaum[3], Francisco Brevis Nuñez[2], Nikola Reinhard Dürr[4], Martin Schlunz-Hendann[4], Friedhelm Brassel[4,5], Ursula Felderhoff-Müser[6,7], Joachim Woelfle[3], Jörg Jüngert[3], Christian Dohna-Schwake[6,7], Nora Bruns[6,7], Adrian P. Regensburger[3], Olivier Couture[1], Ferdinand Knieling*

[1] *Laboratoire d'Imagerie Biomédicale, Sorbonne Université, CNRS, INSERM ; Paris, 75006, France.*
[2] *Clinic for Neonatology and Pediatric Intensive Care Medicine, Sana Clinics Duisburg; Duisburg, 47055, Germany.*
[3] *Department of Pediatrics and Adolescent Medicine, University Hospital Erlangen; Erlangen, 91054, Germany.*
[4] *Clinic for Radiology and Neuroradiology, Sana Clinics Duisburg; Duisburg, 47055, Germany.*
[5] *Center for Pediatric Interventional Radiology/Neuroradiology and Interventional Treatment of Vascular Malformations, Sana Clinics Duisburg; Duisburg, 47055, Germany.*
[6] *Clinic for Pediatrics I, University Hospital Essen, University of Duisburg-Essen; Essen, 45147, Germany.*
[7] *Centre for Translational Neuro- and Behavioural Sciences, University Hospital Essen, University of Duisburg-Essen; Essen, 45147, Germany.*

*Corresponding author. Email: ferdinand.knieling@uk-erlangen.de

Introduction

During the first days of neonatal growth, the central nervous system (CNS) develops self-regulatory mechanisms to ensure constant cerebral perfusion [1]. However, this vascular neogenesis takes place on a microscopic scale that cannot be observed with current clinical imaging methods. Until now, computed tomography (CT) or magnetic resonance imaging (MRI) are regularly used for the observation of cerebral perfusion [2] lacking the ability to visualize microcirculatory processes. On the other hand, ultrasound (US) in newborns through the fontanelle is used in clinical routine. Other studies using Contrast Enhanced Ultrasound Sequences (CEUS) realized with an injection of gas microbubbles intraveinously, allowed the observation of the kinetics of microbubble flow in cerebral vasculature of neonates [3-5]. More recently, the tracking of individual microbubbles allowed for super resolution imaging, so called ultrasound localization microscopy (ULM). By detecting subwavelength acoustic scattering of microbubbles, ULM can provide microvascular information in the adult human organs [6-13].

Therefore, we aimed to support the hypothesis that it is possible to monitor microvascular changes following therapeutic interventions performed on the brain of newborns using ULM. We studied subjects suffering from Vein of Galen (aneurysmal) malformation (VGAM) – a rare disease that is caused by direct connections between the intracranial arterial and venous systems [14,15] and which requires urgent endovascular treatment for stabilization [16].

Methods

For this prospective single center, cross-sectional diagnostic trial ethical and regulatory approval was obtained (Reference number: 2021435). All parents or guardians signed informed consent and the trial was registered (drks.de Identifier: DRKS00030052). Consecutive patients were recruited from July 2022 to February 2023 prior to neurovascular interventions. We included n = 7 neonates diagnosed with VGAM. All neonates received endovascular therapy at a median postnatal age of 2 days (range 2-9 days).

CEUS coronal imaging was performed transfontannely at three time points with an injection of ultrasound contrast agent (Sonovue®, Bracco, Italy) **(Fig. 1A, Fig. 1B)**, with a high-end ultrasound system

(GE Logiq E10s R3, GE Healthcare, Boston MA, USA) together with a micro curved array probe (C3-10, GE Healthcare, Boston MA, USA), a low mechanical index (MI: 0.07), a frequency of 4 MHz and a frame rate of 14 Hz.

ULM was realized using the CEUS acquisitions split into blocks of 200 frames each. We applied a spatiotemporal filter (SVD) with a threshold of 5/200 eigenvalues to enhance microbubbles signal. We localized the center of microbubbles with the radial symmetry method and tracked them with the simple tracker toolbox [17]. By interpolating and accumulating all the tracks, we reconstructed a microvascular ULM density map with a final grid 10 times more resolved then the original one, i.e. final pixel size of 10 μm. We manually segmented brain areas and performed tracks quantification. The number of localizations corresponds to the number of localized microbubbles in each area. The length of tracks corresponds to the number of localizations constituting a track. And the mean speed corresponds to the mean value of all the tracks speed.

Results

ULM density maps showed the microvessels reconstruction along the three time points in patient 2 (**Fig. 2A**). The dashed lines correspond to the zoomed areas in the right hemisphere where the white matter (blue) and the subarachnoid space (red) were manually segmented (**Fig. 2B**). In **Fig. 2B**, we could observe specific connections from the skull/venous system to the brain inside the subarachnoid space. These tracks seemed to have less localizations, to be shorter and to be faster than in the white matter (**Fig. 2C**). The third time point seemed to have more localizations, longer tracks and higher velocity then the first one, regardless of the ROI. Analyses need to be continued on other patients before statistical analyses can be carried out.

Conclusions

In this study, ultrasound localization microscopy was used to observe that neurovascular treatment of neonatal malformations caused remodeling and reorganization of cerebral vascularization. ULM enabled us to track microstructural vascular changes in human neonates with unprecedented spatio-temporal resolution. In the future, we hope that ULM could guide the selection of patients for endovascular specific interventions and for other large-scale applications, particularly in very young patients.
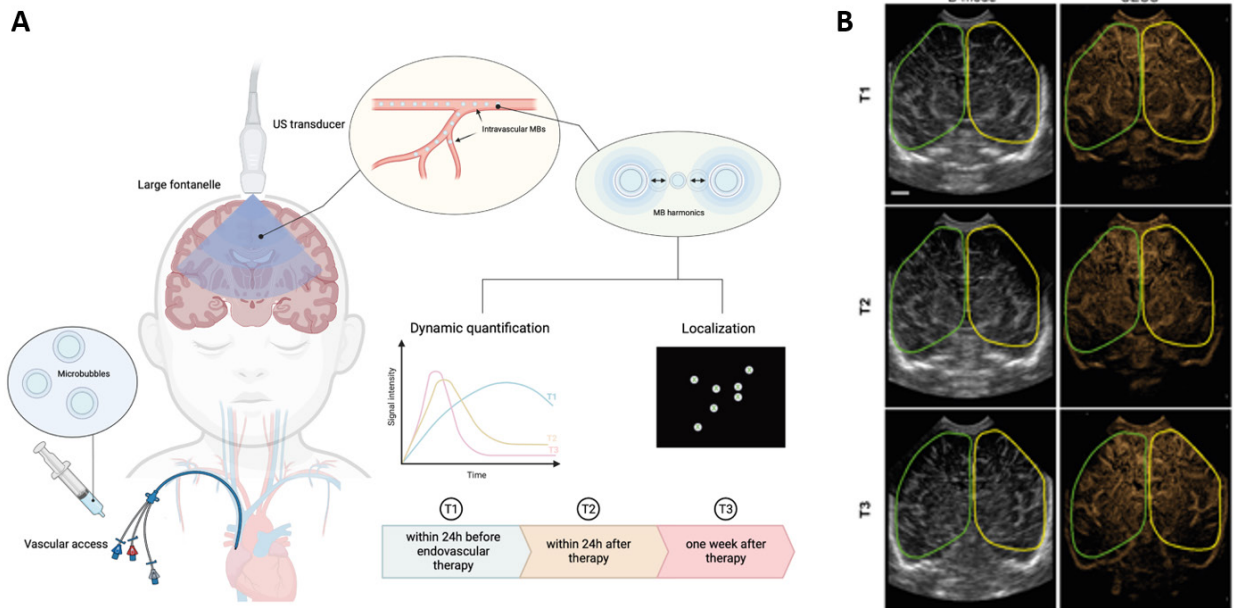
Figure 1. CEUS acquisition. (A) Schematic illustration of the proposed imaging approach using ultrasound contrast agents and imaging through the large fontanelle at 3 different timepoints during therapy. (**B**) Acquisition of Bmode ultrasound (US) and contrast-enhanced ultrasound (CEUS) along the 3 time points.
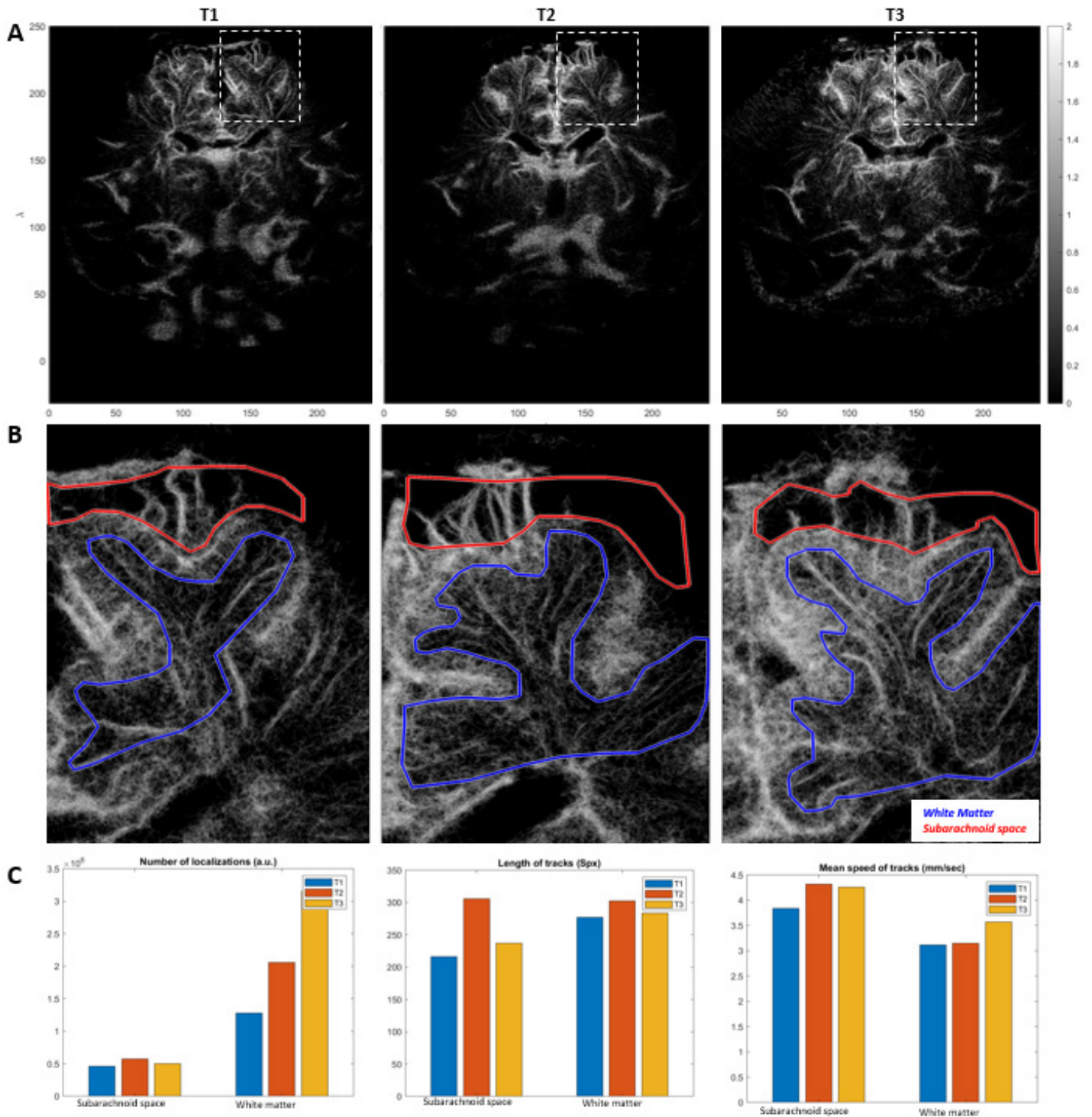
Figure 2. ULM density maps and quantification. (A) ULM density maps on patient 2 at the three time points. Scales are in lambda. Colormap is in arbitrary unit and corresponds to a count of tracks per pixel. (**B**) Zoom of the right upper hemisphere (dashed areas highlighted in **A**). Red regions correspond to subarachnoid space and blue areas represent the white matter. (**C**) Tracks quantification in both segmented areas in **B** along the three time points : number of localizations (in arbitrary unit), length of tracks (in superpixel units) and mean speed (in mm/sec).

References

[1]. R. C. Tasker, Brain vascular and hydrodynamic physiology. *Semin Pediatr Surg* **22**, 168-173 (2013).

[2]. J. Demeestere, A. Wouters, S. Christensen, R. Lemmens, M. G. Lansberg, Review of Perfusion Imaging in Acute Ischemic Stroke: From Time to Tissue. *Stroke* **51**, 1017-1024 (2020).

[3]. F. Knieling *et al.*, Transfontanellar Contrast-Enhanced Ultrasound for Monitoring Brain Perfusion During Neonatal Heart Surgery. *Circ Cardiovasc Imaging* **13**, e010073 (2020).

[4]. F. Knieling *et al.*, Transfontanellar Contrast-enhanced US for Intraoperative Imaging of Cerebral Perfusion during Neonatal Arterial Switch Operation. *Radiology* **304**, 164-173 (2022).

[5]. A. Ruffer *et al.*, Equal cerebral perfusion during extended aortic coarctation repair. *Eur J Cardiothorac Surg* **61**, 299-306 (2022).

[6]. C. Errico *et al.*, Ultrafast ultrasound localization microscopy for deep super-resolution vascular imaging. *Nature* **527**, 499-502 (2015).

[7]. B. Heiles *et al.*, Performance benchmarking of microbubble-localization algorithms for ultrasound localization microscopy. *Nat Biomed Eng* **6**, 605-616 (2022).

[8]. C. Huang *et al.*, Super-resolution ultrasound localization microscopy based on a high frame-rate clinical ultrasound scanner: an in-human feasibility study. *Physics in medicine and biology* **66**, (2021).

[9]. C. Demene *et al.*, Transcranial ultrafast ultrasound localization microscopy of brain vasculature in patients. *Nat Biomed Eng* **5**, 219-228 (2021).

[10]. L. Denis *et al.*, Sensing ultrasound localization microscopy for the visualization of glomeruli in living rats and humans. *EBioMedicine* **91**, 104578 (2023).

[11]. P. Lasjaunias *et al.*, Cerebral arteriovenous malformations in children. Management of 179 consecutive cases and review of the literature. *Childs Nerv Syst* **11**, 66-79; discussion 79 (1995).

[12]. Song, P., Rubin, J. M., & Lowerison, M. R. (2023). Super-resolution ultrasound microvascular imaging: Is it ready for clinical use?. *Zeitschrift für Medizinische Physik*.

[13]. Christensen-Jeffries, K., Couture, O., Dayton, P. A., Eldar, Y. C., Hynynen, K., Kiessling, F., ... & Van Sloun, R. J. (2020). Super-resolution ultrasound imaging. *Ultrasound in medicine & biology*, *46*(4), 865-891.

[14]. P. Lasjaunias *et al.*, Cerebral arteriovenous malformations in children. Management of 179 consecutive cases and review of the literature. *Childs Nerv Syst* **11**, 66-79; discussion 79 (1995).

[15]. P. L. Lasjaunias *et al.*, The management of vein of Galen aneurysmal malformations. *Neurosurgery* **59**, S184-194; discussion S183-113 (2006).

[16]. M. J. Cory *et al.*, Vein of Galen aneurysmal malformation: rationalizing medical management of neonatal heart failure. *Pediatr Res* **93**, 39-48 (2023).

[17]. B. Heiles *et al.*, Performance benchmarking of microbubble-localization algorithms for ultrasound localization microscopy. *Nat Biomed Eng* **6**, 605-616 (2022).

Early Detection of postinterventional Complications after EVAR:
Comparison of Contrast-enhanced Ultrasound (CEUS) and CTA

R. Kubale[1], D. Kerner[1], F. Frenzel[1], D. Driulini[1], P. Freiburger[3], B. Stange[2], A. Gurung[3], A.Massmann[1], M. Leist[1]

[1]*Klinik für Diagnostische und Interventionelle Radiologie, Homburg/Saar, Germany*
[2]*Klinik für Allgemeine Chirurgie, Viszeral-, Gefäß- und Kinderchirurgie, Homburg/Saar, Germany*
[3]*Siemens Healthineers Ultrasound Division, Issaqua, WA, USA*

Corresponding author: Kubale@mac.com

Introduction

Endovascular aneurysm repair is a well-established treatment for abdominal aortic and intestinal aneurysms, utilizing various endograft types (1-3). Surveillance is crucial for early detection of postinterventional complications, such as endoleaks and stent position shifts due to disease progression. Methods of first choice are CTA and increasingly CEUS (3-7). Aim was to describe the development and the clinical use of CEUS for EVAR during the last 25 years in comparison with CT and CTA. Possibilities and limitations and how to avoid artifacts and pitfalls are discussed.

Methods

CEUS was performed before 2000 using Quantum and Elegra (n=35), and later with Acuson S2000 (n=101), S2000 HELXTM Evolution (n=280) and Sequoia (n=60) ultrasound units (Siemens Healthineers, Erlangen, Germany), alongside SonoVue® contrast agent (Bracco Imaging, Milano, Italy). The average dose of contrast agent was 1.51±0.23 ml (range 1.2-2.0 ml), followed by a 10 ml normal saline flush. With the Sequoia (VA40A), only 0.6-1.0 ml was necessary. Quantitative evaluation was conducted using software from Bracco (VueBox). Multi-slice CTA was performed using commercially available CT scanners (SOMATOM Definition AS 64, SOMATOM Edge or Force; Siemens Healthineers, Erlangen, Germany). Table 1 shows the distribution. All ultrasound measurements were performed without prior knowledge of CTA results.

Combined examinations on the same day were possible in 260 patients, allowing for a comparison of the detection capabilities for complications and artifacts.

Examinations (Patients)	Available US Devices	Contrast Medium
1996-2001 (n= 35)	Quantum, Elegra, Sequoia I (Acuson)	SHU-504, Levovist
2002-2022 (n=441) more than 2300 exams	S2000® and S2000®HELX, Sequoia® (Siemens)	Optison, SonoVue

Results

The first detection of endoleaks using Levovist occurred in 5 patients. With the transition to Low-MI techniques, the feasibility of CEUS examinations increased to 60% (2001-2015) and since 2016 with increasing sensitivity of US devices to 92% since 2016. Detected complications included hematoma and pseudoaneurysm in the groin in <4% of cases, and restenosis and occlusion of prosthetic limbs in 1.5%. Two patients experienced a dislocation of the occluder system. One case presented a dorsal perforation of the prosthesis, detected primarily with CEUS, three years post-implantation. Four cases involved a dislocation of the limb with a high-flow endoleak. One case showed a partial kidney infarction (Fig. 1).

From 2012-2022, 245 patients with EVAR, including hybrid techniques using chimneys/periscopes and double-barrel techniques, underwent combined CTA/CEUS examinations on the same day during their first year. Endoleaks were detected with CT in 45% of cases and with CEUS in 51%. Mismatches in CT were due to very late and weak endoleaks in 5 cases and beam hardening artifacts from embolization material in 4 cases. In 3 cases, a dorsal endoleak was obscured by artifacts in CEUS. One endoleak was falsely identified by CEUS due to residual small air inclusions immediately after the intervention. In 12 out of 21 patients, quantification of endoleak dynamics (Fig. 2) was possible (Time to Peak, Rise Time).

Conclusions

Diagnosing and stratifying endoleaks can be challenging, with wide heterogeneity in follow-up strategies among EVAR centers (8).

1. Although the feasibility of CEUS in the early phase (3 days post-intervention) is limited due to abundant bowel gas and limited ultrasound transmission through prosthesis material, after this period, CTA and CEUS are comparable in detecting endoleaks after aortic and celiac endovascular repair. With increasing beam hardening artifacts due to multiple interventions (e.g., coiling, embolization material), CEUS proves superior to CTA.
2. Preliminary results from VueBox suggest that differences in time to peak, combined with rise time, can be useful in differentiating between type II and types I/III endoleaks and in evaluating the prognosis of endoleaks.
3. Strategies, optimization of system settings, and ways to avoid typical artifacts and pitfalls are discussed in more detail (9).

References

[1]. Greenhalgh RM, Brown LC, Kwong GP, Powell JT, Thompson SG, participants Et. Comparison of endovascular aneurysm repair with open repair in patients with abdominal aortic aneurysm (EVAR trial 1), 30-day operative mortality results: randomised controlled trial. Lancet. 2004;364(9437):843-8.

[2]. Frenzel F, Bucker A, Paprottka P, Nadjiri J, Mahnken AH, Massmann A, et al. DeGIR Quality Report 2019: Report on the treatment quality of minimally invasive methods - Interventional therapy (EVAR) of abdominal aortic aneurysms. Rofo. 2022;194(1):49-61.

[3]. Clevert DA, Gurtler VM, Meimarakis G, D'Anastasi M, Weidenhagen R, Reiser MF, et al. Classification of endoleaks in the follow-up after EVAR using the time-to-peak of the contrast agent in CEUS examinations. Clin Hemorheol Microcirc. 2013;55(1):183-91.

[4]. Cantisani V, Grazhdani H, Clevert DA, Iezzi R, Aiani L, Martegani A, et al. EVAR: Benefits of CEUS for monitoring stent-graft status. Eur J Radiol. 2015;84(9):1658-65.

[5]. hung J, Kordzadeh A, Prionidis I, Panayiotopoulos Y, Browne T. Contrast-enhanced ultrasound (CEUS) versus computed tomography angiography (CTA) in detection of endoleaks in post-EVAR patients. Are delayed type II endoleaks being missed? A systematic review and meta-analysis. J Ultrasound. 2015;18(2):91-9.

[6]. Gabriel M, Tomczak J, Snoch-Ziolkiewicz M, Dzieciuchowicz L, Strauss E, Oszkinis G. Comparison of Superb Micro-Vascular Ultrasound Imaging (SMI) and Contrast-Enhanced Ultrasound (CEUS) for Detection of Endoleaks After Endovascular Aneurysm Repair (EVAR). Am J Case Rep. 2016;17:43-6.

[7]. Harky A, Zywicka E, Santoro G, Jullian L, Joshi M, Dimitri S. Is contrast-enhanced ultrasound (CEUS) superior to computed tomography angiography (CTA) in detection of endoleaks in post-EVAR patients? A systematic review and meta-analysis. J Ultrasound. 2019;22(1):65-75.

[8]. Tse DM, Tapping CR, Patel R, Morgan R, Bratby MJ, Anthony S, et al. Surveillance after endovascular abdominal aortic aneurysm repair. Cardiovasc Intervent Radiol. 2014;37(4):875-88.

[9]. 9. Frenzel F, Kubale R, Massmann A, Raczeck P, Jagoda P, Schlueter C, et al. Artifacts in Contrast-Enhanced Ultrasound during Follow-up after Endovascular Aortic Repair: Impact on Endoleak Detection in Comparison with Computed Tomography Angiography. Ultrasound Med Biol. 2021;47(3):488-98.
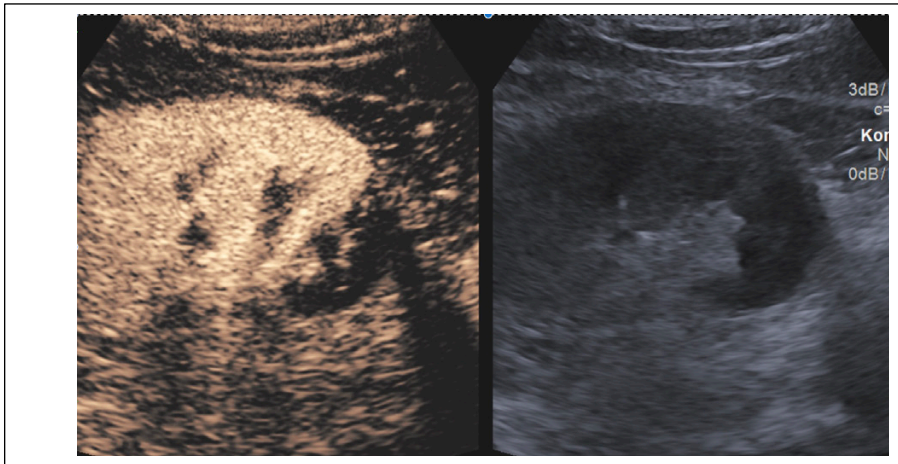
Fig. 1: CEUS of the left kidney with infarction of the inferior pole
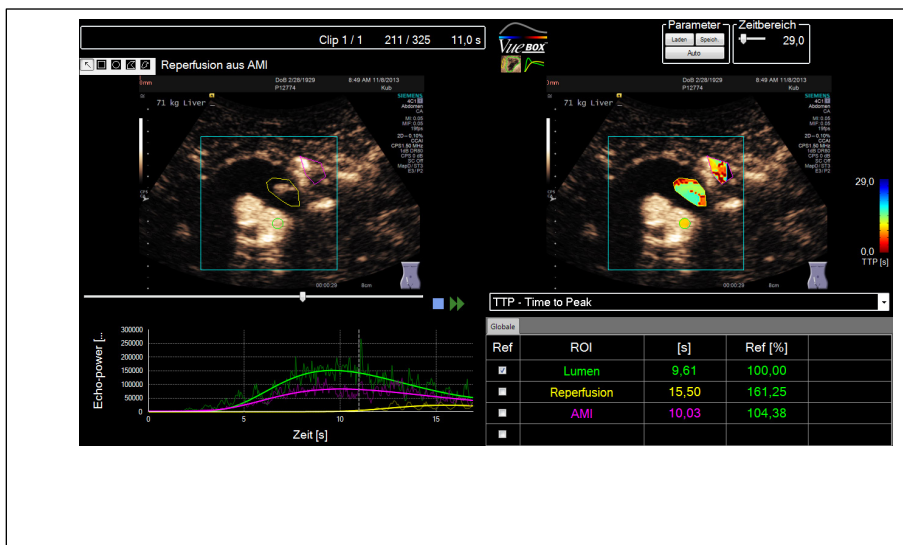
Fig. 2: Dynamic evaluation of an endoleak (Type II) caused by the inferior mesenteric artery
More than 7 sec after contrast in the aortic stent retrograde flow from the AMI appears with
A very long rise time. Spontaneous occlusion of the endoleak after 3 months.

Reduced **Mi**crovascular Blood Volume as a Driver of **Cor**onary Microvascular **Dis**ease in Patients with Angina and Non-Obstructive Coronary Artery Disease: The MICORDIS-study

Caitlin E.M. Vink[1], Elize A.M. de Jong[1,2], Janneke Woudstra[1], Mitchel Molenaar[1], Otto Kamp[1], Tim P. van de Hoef[2], Steven A.J. Chamuleau[1], Yolande Appelman[1]*, Etto C. Eringa[3,4]*
* Appelman and Eringa contributed equally to this work.

1. _Amsterdam UMC Heart Centre, Department of Cardiology, Amsterdam Cardiovascular Sciences, Amsterdam, the Netherlands._
2. _Department of Cardiology, University Medical Center Utrecht, The Netherlands._
3. _Amsterdam UMC, Amsterdam Cardiovascular Sciences, Department of Physiology, Amsterdam UMC, Amsterdam, the Netherlands._
4. _Maastricht University, Cardiovascular Research Institute Maastricht, Department of Physiology, Maastricht, the Netherlands._
Corresponding author: c.vink@amsterdamumc.nl

Introduction

Angina with Non-Obstructed Coronary Arteries (ANOCA) is a condition marked by abnormal vasomotor responses. Current diagnostic guidelines focus on coronary flow reserve (CFR) and microvascular resistance, as a cause of reduced myocardial oxygen supply. However, CFR is limited since it only includes information about myocardial blood flow (MBF). Apart from flow, myocardial blood volume (MBV) might play an independent role. The response of MBV is independent from flow, and linked to myocardial oxygen consumption, and regulated by stress, exercise and hyperinsulinemia. Myocardial contrast echocardiopgraphy (MCE) enables assessment of the myocardial perfusion. The aim of this study is to investigate the rol of MBV in ANOCA, by evaluating MBV under different physiological conditions using MCE.

Methods

The MICORDIS-study is a single-center observational cross-sectional cohort study focused on assessing MBV in patients with long-standing angina and documented non-obstructive coronary artery disease compared with matched healthy controls in terms of sex and age. ANOCA patients were instructed to withold from vasodilator medication, and underwent a coronary angiogram with invasive coronary function testing (ICFT) to identify coronary spasm and coronary microvascular dysfunction. All subjects underwent MCE to measure MBV and MBF. MCE was performed using a Philips iE33 ultrasound machine during constant intravenous infusion of gas-filled contrast microbubbles, and analysed using the Region of Interest (ROI) plug-in from QLAB [Figure 1]. The MBV and MBF were calculated according to Vogel et al. (1).

Results

This study included 28 ANOCA patients (21.4% men, 56.8 ±8.6 years) and 28 matched healthy controls (21.4 % men, 56.5 ±7.0 years). The ANOCA patients had a significant higher BMI (27.6 ±4.5 $vs.$ 24.0 ±2.6, $p < 0.01$), more hypertension (16% $vs.$ 0%, $p < 0.01$) and hyperlipidemia (14% $vs.$ 0%, $p < 0.01$). During ICFT 2 patients (10.7%) were diagnosed with epicardial vasospasm according to the COVADIS-criteria (2), 11 patients (39.3%) showed microvascular vasospasm according to the COVADIS-criteria (3), 9 patients had an inconclusive test (32.1%) and 5 patients (17.9%) had a negative ICFT. ANOCA patients had a significantly lower insulin sensitivity (M-value 36.8 μmol/kg/min $vs.$ 69.1 μmol/kg/min, $p < 0.01$), a

significantly lower heart rate reserve (54.8 ±21.6 *vs* 67.1 ±11.9, $p < 0.01$), and a tendency towards a reduced rate pressure product (16928 ±5024 *vs.* 16997 ±2878, $p = 0.09$). At baseline, ANOCA patients tended to have a lower MBV compared to healthy controls (0.38 ±0.08 *vs.* 0.43 ±1.0, $p = 0.058$). A significant lower MBV was found between the ANOCA patients and the healthy controls during hyperinsulinemia (0.40 ±0.07 *vs.* 0.44 ±0.08, $p = 0.046$) and during dobutamine-induced stress (0.39 ±0.13 *vs.* 0.48 ±1.0, $p = 0.014$). We did not find a significant difference in the capillary recruitment (ΔMBV) between patients and matched healthy controls in both conditions compared to baseline (ΔMBV$_{insulin}$ 0.009 ±0.08 *vs.* 0.007 ±0.09, $p = 0.92$, and ΔMBV$_{dobutamine}$ -0.004 ±0.15 *vs.* 0.035 ±0.13, $p = 0.35$).

Conclusions

In this study we observed a difference between MBV during hyperinsulinemia and dobutamine-induced stress between ANOCA patients and matched healthy controls. However, no difference in capillary recruitment was found. The remarkable differences in regards to BMI, hypertension, hyperlipidemia and insulin sensitivity between patients and healthy subjects suggests that disrupted metabolism contributes to the pathophysiology of ANOCA. Further research is needed to elucidate this aspect.
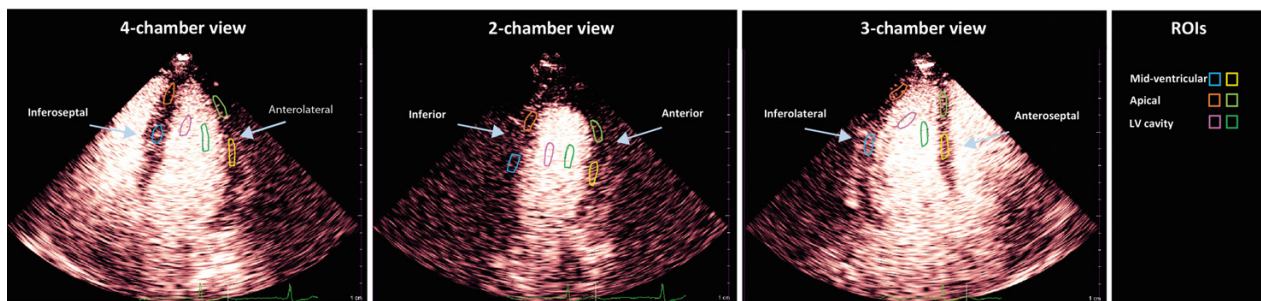
Figure 1. Myocardial contrast echocardiography was performed in apical 4-chamber, 2-chamber and 3-chamber views, of which regions of interest were derived in corespondence with the perfusion areas of the main coronary arteries. Abbreviations: ROIs; Region of interest, LV; Left Ventricle

References

[1]. Vogel R, Indermühle A, Reinhardt J, Meier P, Siegrist PT, Namdar M, et al. The quantification of absolute myocardial perfusion in humans by contrast echocardiography: algorithm and validation. J Am Coll Cardiol. 2005;45(5):754-62.

[2]. Beltrame JF, Crea F, Kaski JC, Ogawa H, Ong P, Sechtem U, et al. International standardization of diagnostic criteria for vasospastic angina. Eur Heart J. 2017;38(33):2565-8.

[3]. Ong P, Camici PG, Beltrame JF, Crea F, Shimokawa H, Sechtem U, et al. International standardization of diagnostic criteria for microvascular angina. Int J Cardiol. 2018;250:16-20.

Combining early MCE and strain imaging to predict final infarct size and left ventricular function in STEMI patients with MVO

S. El Kadi [1], M.C. van de Veerdonk [1], S. Li [2], E. Spoormans [1], N.W. Verouden [1], F. Xie [2], A.C. van Rossum [1], T.R. Porter [2], O. Kamp [1]

[1]_Amsterdam Cardiovascular Sciences, Amsterdam University Medical Centers - location Vrije Universiteit, Amsterdam, Netherlands_
[2]_Department of Cardiovascular Sciences, University of Nebraska Medical Center, Omaha, Nebraska, United States_
Corresponding author: s.elkadi@amsterdamumc.nl

Introduction

Microvascular obstruction (MVO) is frequently observed in patients with ST-elevation myocardial infarction (STEMI) after treatment with primary percutaneous coronary intervention (PCI) and is associated with adverse left ventricular remodeling, heart failure and mortality (de Waha et al., 2017; Nijveldt et al., 2009). Infarct size (IS) on follow up cardiac magnetic resonance (CMR) imaging is greater in STEMI patients with MVO, however, the temporal and spatial evolution of MVO after PCI is highly dynamic (Rochitte et al., 1998) and restoration of border zone perfusion in the hours following PCI could mitigate final infarct size. Similarly, myocardial contractility as assessed with left ventricular ejection fraction (LVEF) or global longitudinal strain (GLS) can vary over time due to myocardial stunning (Braunwald & Kloner, 1982). The aim of this study was to evaluate the combined predictive value of myocardial perfusion using myocardial contrast echocardiography (MCE) and GLS in relation with final IS and LVEF on follow up CMR in STEMI patients with MVO.

Methods

STEMI patients with electrocardiographic MVO (incomplete ST-resolution ($\leq$70%) on the electrocardiogram (ECG) after PCI) who underwent MCE one to three hours following primary PCI and CMR at two months follow up were prospectively included. Myocardial perfusion score (MPS) was semi-quantitatively graded by a blinded reviewer using a 17-segment model. Score 1 was given for normal replenishment (within 4 seconds of a high mechanical index (HMI) pulse), 2 for a delayed replenishment (> 4 seconds), and 3 in case of absent replenishment (up to 10 seconds after an HMI pulse). MVO was assessed on a segmental basis and was reported as such in case of absent replenishment up to 10 seconds after an HMI pulse. End-systolic GLS was calculated with TomTec Arena software (Tomtec imaging system, Unterschleissheim, Germany). IS was calculated with late gadolinium-enhanced CMR using the full-width at half-maximum method and expressed in absolute (grams) and relative (% of left ventricular mass) values.

Results

In total, 53 STEMI patients with MVO have been included in the analyses. Mean age was 62 ($\pm$ 12) and 48 patients (91%) were male. Culprit artery in patients was LAD in 42 patients (79%), right coronary artery in 7 patients (13%) and circumflex artery in 4 patients (8%). GLS and number of segments with MVO were statistically significantly associated with absolute final IS ($R^2 = 0.12$, p = 0.02; $R^2 = 0.16$, p < 0.01). GLS and number of segments with MVO on MCE were also associated with relative final IS ($R^2 = 0.20$, p < 0.01; $R^2 = 0.13$, p = 0.02). Patients with GLS > -13% and MVO in at least 4 segments had significantly higher IS and worse LVEF on follow up MRI as compared with patients who had only GLS > -13% or MVO in at least 4 segments or none of both (IS: 9.1$\pm$6% vs. 14$\pm$9% vs. 23$\pm$10%, p < 0.01; LVEF: 43$\pm$8% vs. 50$\pm$10% vs. 53$\pm$7%, p < 0.01).

Conclusions

Combining GLS on conventional echocardiography with MVO on MCE predicted significant differences in final IS and LVEF on CMR at two months follow up. The incremental value of a combined mechanical and perfusional assessment could improve current risk stratification of STEMI patients with MVO.
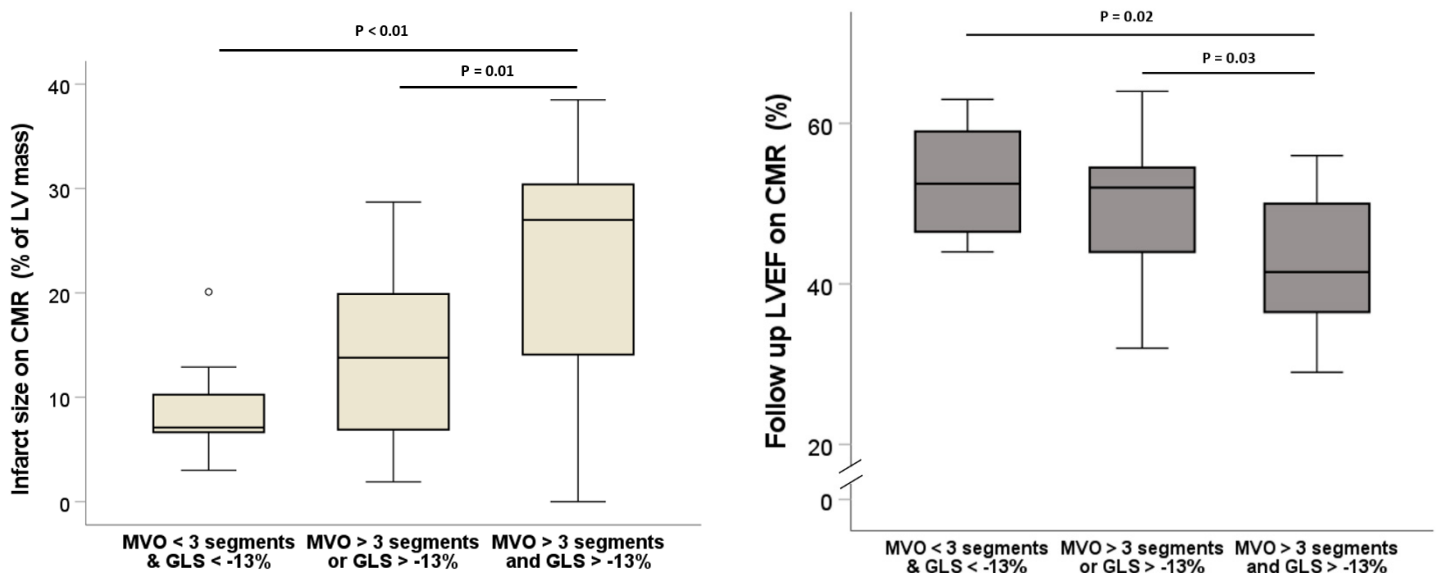
References

[1]. Braunwald, E., & Kloner, R. A. (1982). The stunned myocardium: prolonged, postischemic ventricular dysfunction. *Circulation, 66*(6), 1146-1149. doi:10.1161/01.CIR.66.6.1146

[2]. de Waha, S., Patel, M. R., Granger, C. B., Ohman, E. M., Maehara, A., Eitel, I., . . . Stone, G. W. (2017). Relationship between microvascular obstruction and adverse events following primary percutaneous coronary intervention for ST-segment elevation myocardial infarction: an individual patient data pooled analysis from seven randomized trials. *Eur Heart J, 38*(47), 3502-3510. doi:10.1093/eurheartj/ehx414

[3]. Nijveldt, R., Hofman, M. B., Hirsch, A., Beek, A. M., Umans, V. A., Algra, P. R., . . . van Rossum, A. C. (2009). Assessment of microvascular obstruction and prediction of short-term remodeling after acute myocardial infarction: cardiac MR imaging study. *Radiology, 250*(2), 363-370. doi:10.1148/radiol.2502080739

[4]. Rochitte, C. E., Lima, J. A. C., Bluemke, D. A., Reeder, S. B., McVeigh, E. R., Furuta, T., . . . Melin, J. A. (1998). Magnitude and time course of microvascular obstruction and tissue injury after acute myocardial infarction. *Circulation, 98*(10), 1006-1014. doi:10.1161/01.CIR.98.10.1006

The use of Subharmonic-Aided Pressure Estimation (SHAPE) and Shear Wave Elastography (SWE) of Pancreatic Adenocarcinoma Patients Undergoing Chemotherapy with Sonoporation to Evaluate Treatment Response

__Priscilla Machado__[1], Hailee Mayer[1], Trang Vu[1], John R. Eisenbrey[1], James Posey III[1], Spiros Kotopoulis[2], Babar Bashir[1], Patrick Mille[1], Atrayee Basu-Mallick[1], Daniel Lin[1], Rajan Singla[1], Ingrid Nordaas[2], Audun M. Trelsgard[2], Georg Dimcevski[2], Odd Helge Gilja[2], Kirk Wallace[3], Flemming Forsberg[1]

[1]*Thomas Jefferson University, Philadelphia, PA, USA*
[2]*Haukeland University Hospital, Bergen, Norway*
[3]*GE HealthCare, Niskayuna, NY, USA*

Corresponding Author: Priscilla.Machado@jefferson.edu

Introduction

Pancreatic ductal adenocarcinoma (PDAC) is 3% of cancers diagnosed in the United States with 64,050 new cases expected in 2023, but it is the fourth leading cause of cancer-related deaths with 50,550 expected deaths in 2023 and five year survival rates at around 5-9% [1-3]. One of the reasons for this high mortality is that only around 15 to 20% of patients with PDAC present with resectable tumors at the time of diagnosis [2-5]. Pancreatic ductal adenocarcinoma (PDAC) is notoriously unresponsive to chemotherapy, due to a dense desmoplastic stroma and poor blood supply [4, 6], though perfusion is sufficient to observe significant contrast enhanced ultrasound (CEUS) signal [4, 7]. Despite the "curative" intent of treatment for those patients who present with surgically amenable PDAC and undergo resection followed by adjuvant systemic therapy (with or without radiation) their median overall survival is around 15.5 to 24 months [8]. The five year overall survival for these resected patients is 25 to 30% for those with lymph node negative disease and only 10% in patients with lymph node positive disease. Hence, there is a considerable clinical need to develop innovative strategies for effective drug delivery and treatment monitoring, resulting in improved outcomes for patients with PDAC.

Sonoporation is a novel method that can enhance the therapeutic efficacy of co-administered chemotherapy by localized contrast-enhanced ultrasound imaging (CEUS) of gas-filled microbubbles (ultrasound contrast agent; UCA), which temporarily changes the tumor vascular microenvironment by increasing leakage from angiogenic vessels through microstreaming, shockwaves and the activation of various intracellular signaling responses [4, 5, 9]. Our Phase I clinical trial of sonoporation in 10 PDAC patients treated with Gemcitabine demonstrated no additional toxicity and an increase in median survival compared to the standard of care treatment (8.9 vs 17.6 months; p = 0.011) [4].

Subsequent, animal studies investigated 4 commercial UCAs under 2 different acoustic regimes and established the optimal UCA (Sonazoid; GE HealthCare, Oslo, Norway) as well as acoustic settings for sonoporation of PDAC [10].

There are two major chemotherapeutic regimens for the treatment of non-resectable PDAC, a combination of Leucovorin, Fluorouracil, Irinotecan and Oxaliplatin (FOLFIRINOX), considered the first line treatment, or a combination of Gemcitabine with a nanoparticle formulation of Paclitaxel (Nab-Paclitaxel), the second line treatment. These regiments result in a median overall survival of approximately 11 and 8-9 months.

An ongoing Phase II clinical trial aims to improve standard of care (SoC) chemotherapy treatment of PDAC by adding sonoporation (i.e., augmenting the SoC treatment with CEUS and microbubbles). As part of this study, a noninvasive ultrasound technique, subharmonic-aided pressure estimation (SHAPE), was used to estimate intra-tumoral pressure measurements [11]. Also, the tumor stiffness was assessed using shear wave elastography (SWE) during the sonoporation treatment. The objective of this study was to use SHAPE during the chemotherapy with sonoporation treatment to evaluate changes in treatment response of PDAC and to compare SWE measurements of tumor stiffness during sonoporation treatment in order differentiate treatment responders from non-responders.

Materials and Methods

This Phase II clinical trial aims to improve SoC chemotherapy treatment by adding sonoporation (i.e., augmenting the SoC treatment with CEUS and microbubbles). Two sites (one in the USA and one in Norway) will enrol a total of 120 subjects recently diagnosed with PDAC stages II, III or IV and who are scheduled to undergo chemotherapy as their first line of treatment were eligible to be enrolled in this ongoing, IRB-approved study (NCT04821284). All the enrolled subjects underwent their scheduled standard of careSoC chemotherapy treatment, which it is a choice between FOLFIRINOX or Gemcitabine/Nab-Paclitaxel treatment regimen, chosen on the discretion of the clinical oncology team. Exclusion criteria include medically unstable patients, pregnant persons or anyone with known allergies to the UCA. The primary objective is to evaluate the safety and therapeutic efficacy of sonoporation on PDAC SoC treatment based on local progression-free and overall survival. The Oncology teams at each site are responsible for the SoC chemotherapeutic treatment and decide whether the patient is to receive Gemcitabine/Nab-Paclitaxel or FOLFIRINOX as SoC, using the same decision making parameters as would be done if the patient was not included in the study.

In the experimental group the optimal CEUS and microbubble conditions will be applied to a single PDAC tumor imaged by ultrasound. Treatment will follow the timeline and guidelines of the SoC chemotherapeutic treatment for PDAC, with sonoporation performed immediately following each infusion of chemotherapy. The sonoporation treatment consisted of 20 min of ultrasound imaging sweeping through the tumor area performed at each chemotherapy visit. A Logiq E10 ultrasound scanner (GE HealthCare, Waukesha, WI) with a C1-6 probe was used to image, target and induce sonoporation.

SHAPE data: This system was also used to acquire SHAPE pressure measurement values (subharmonic signals in dB with an inverse linear relationship to pressures in mmHg) with the mean difference between the values acquired with and without microbubbles used in the final analysis. The data was acquired by first determining the optimal acoustic power on a individual basis. Once the presence of UCA in the imaging plane was established, the SHAPE optimization algorithm was activated and the acoustic power adjusted to produce the maximum change in subharmonic amplitudes (i.e., maximizing the sensitivity of SHAPE). Figure 1 shows in Panel A the optimization curve that is acquired after the run of the optimization algorithm, where a ROI is draw around the tumor and the optimization curve of the ROI provides the optimal acoustic power. Then the corresponding subharmonic imaging data was acquired with and without UCA at the optimal acoustic power setting in three to five digital clips of five seconds each

SWE data: The same system was also used to obtain mean SWE measurements values in kPa from the PDAC (averaged across 12 measurements).

Subjects were divided into responders and non-responders with their SHAPE and SWE values compared at three time points: first, third and last cycles of chemotherapy using t-tests. SHAPE and SWE values were compared using linear regression.

Results

To date, 8 of the 43 subjects enrolled in this ongoing study completed their first line chemotherapy treatment and had both their SHAPE pressure and SWE data analyzed. The mean age of the subjects was 62 years (range: 43-77 years). Subjects were divided into responders (n = 2) and non-responders (n = 6) to their treatment regimen.

SHAPE Analysis: First cycle mean dB pressure values and SD values were -1.97 ± 2.91 dB for responders and -6.08 ± 1.06 dB for non-responders (p = 0.01). Third cycle mean dB pressure values and SD values were 2.39 ± 3.41 dB for responders and -4.62 ± 1.05 dB for non-responders (p = 0.002). Last cycle mean dB pressure values and SD values were -3.91 ± 2.36 dB for responders and -2.38 ± 0.65 dB for non-responders (p = 0.20). The comparison between the cycles for responders showed no significant statistical difference for first cycle versus last cycle (p = 0.28) and for first cycle versus third cycle (p = 0.06). However, a significant statistical difference was seen for third cycle versus last cycle (p = 0.001). The comparison between the cycles for non-responders observed significant statistical difference for first cycle versus last cycle (p = 0.0002) and for third cycle versus last cycle (p = 0.009), but no significant statistical difference was seen for first cycle versus third cycle (p = 0.06).
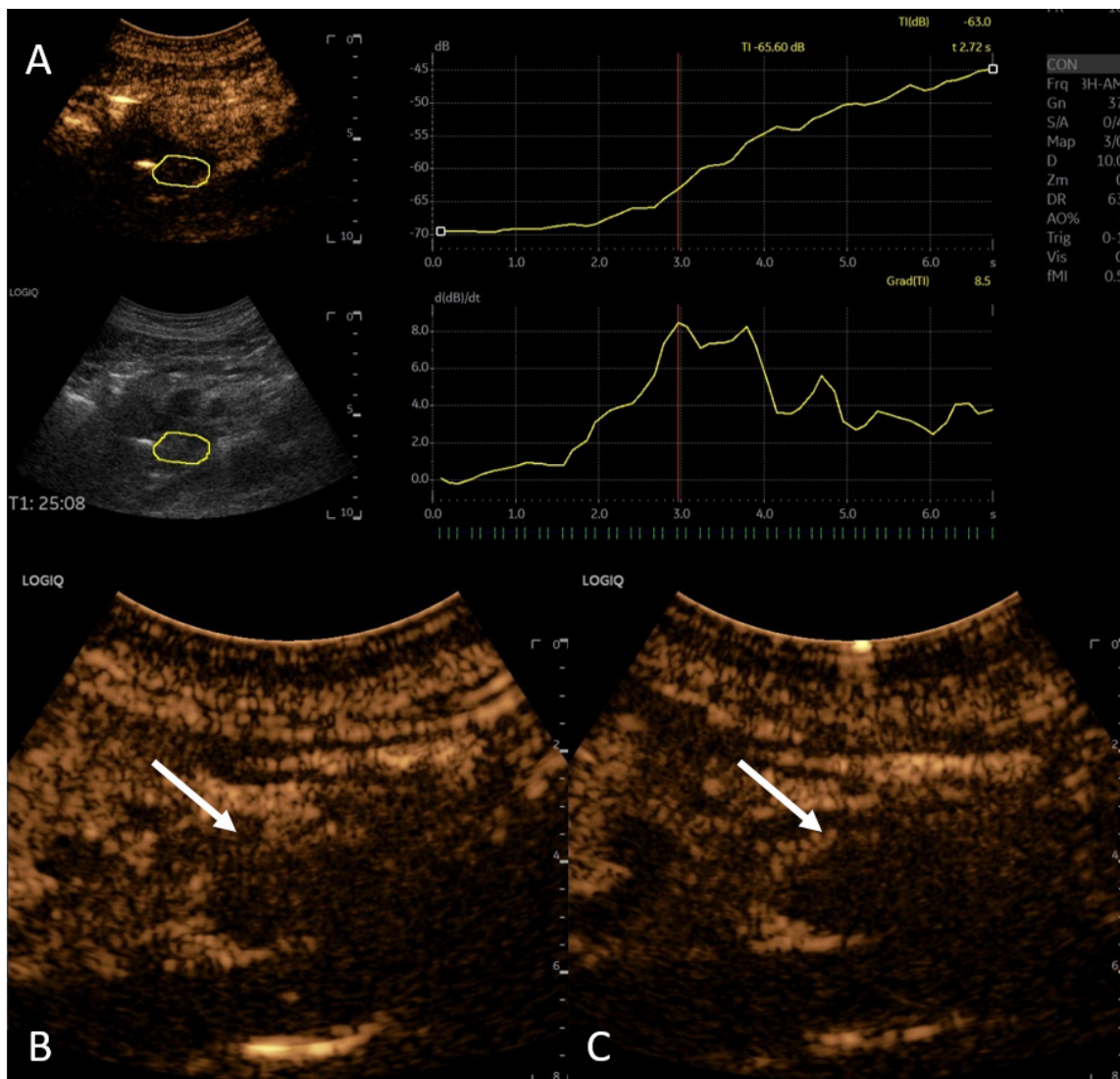
Figure 1: Example of a SHAPE study and SHI imaging in a pancreatic tumor. Panel A shows the optimization curve used to determine the optimal mechanical index (MI) which corresponds to the optimal acoustic power to acquire the SHAPE data. Panel B shows a SHI imaging where the arrow shows CEUS enhancement inside the tumor. Panel C shows a SHI imaging where the arrow shows no CEUS enhancement inside the tumor.

SWE Analysis: First cycle SWE mean and SD values were 11.57 ± 4.06 kPa for responders and 5.75 ± 0.78 kPa for non-responders (p = 0.001). After the third chemotherapy cycle SWE mean and SD values changed to 6.50 ± 2.00 kPa for responders and 7.30 ± 0.68 kPa for non-responders (p = 0.27). Last cycle SWE mean and SD values were not statistically significant 7.31 ± 2.39 kPa for responders and 7.14 ± 1.03 kPa for non-responders (p = 0.83). The comparison between the cycles for responders showed significant statistical difference for first cycle versus last cycle (p = 0.005) and for first cycle versus third cycle (p = 0.001); no significant statistical difference was seen for third cycle versus last cycle (p = 0.38). The same behavior was observed for non-responder with a significant statistical difference seen for first cycle versus last cycle (p = 0.001) and for first cycle versus third cycle (p < 0.0001), but with no significant statistical difference for third versus last cycle (p = 0.66).
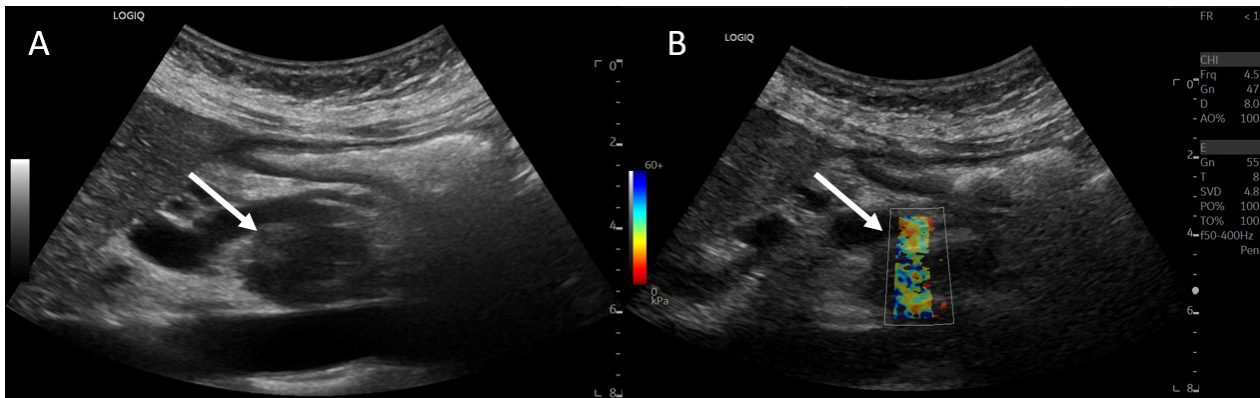
Figure 2: Example of a study case. Panel A shows a b-mode imaging where the arrow shows the pancreatic tumor. Panel B shows a SWE imaging where the arrow shows the pancreatic tumor and the SWE box.

The comparison between SHAPE and SWE values divided into responders and non-responders compared at three time points: first, third and last cycles of chemotherapy using linear regression showed no correlation except for the first cycle responders ($r^2 = 0.70$).

Conclusions

This was an initial analysis of SHAPE intra-tumoral pressure measurements and SWE stiffness measurements between responders and non-responders to SoC chemotherapy treatment augmented with sonoporation. The SHAPE data analysis showed that the mean dB values for responders decreased in SHAPE intra-tumoral measurements (indicating a pressure increase) from the first to the last cycleand that the mean dB values for non-responders increased in SHAPE intra-tumoral measurements (indicating a pressure decrease) from the first to the last cycle. Most importantly, results showed that between responders and non-responders there was significant statistical difference for the first cycle and third cycle. These preliminary results suggest that SHAPE intra-tumoral pressure measurements may be used to indicate chemotherapy response. The SWE data analysis showed that the mean values showed for responders decreased in tumor stiffness from the first to the last cycle, whereas for non-responders there was increase in tumor stiffness from the first to the last cycle. The results also showed that between responders versus non-responders there was significant statistical difference for the first cycle (p = 0.001). These initial results suggest that PDAC stiffness may be used to indicate chemotherapy response. A comparison between the SHAPE and SWE results showed that SHAPE and SWE correlation except for the first cycle responders ($r^2 = 0.70$). The use of non-invasive imaging modalities to evaluate chemotherapy response could help with patient care by providing a more precise indication of the tumor response to treatment.

References

[1]. Siegel, R.L., et al., *Cancer statistics, 2023.* CA: a cancer journal for clinicians, 2023. 73(1): p. 17-48.

[2]. Klein, A.P., *Identifying people at a high risk of developing pancreatic cancer.* Nature Reviews Cancer, 2013. 13(1): p. 66-74.

[3]. Rawla, P., T. Sunkara, and V. Gaduputi, *Epidemiology of pancreatic cancer: global trends, etiology and risk factors.* World journal of oncology, 2019. 10(1): p. 10.

[4]. Dimcevski, G., et al., *A human clinical trial using ultrasound and microbubbles to enhance gemcitabine treatment of inoperable pancreatic cancer.* Journal of Controlled Release, 2016. 243: p. 172-181.

[5]. Kotopoulis, S., et al., *Sonoporation-enhanced chemotherapy significantly reduces primary tumour burden in an orthotopic pancreatic cancer xenograft.* Molecular imaging and biology, 2014. 16: p. 53-62.

[6]. Kotopoulis, S., et al., *Sonoporation with Acoustic Cluster Therapy (ACT®) induces transient tumour volume reduction in a subcutaneous xenograft model of pancreatic ductal adenocarcinoma.* Journal of Controlled Release, 2017. 245: p. 70-80.

[7]. Wang, Y., et al., *Clinical Value of Contrast-Enhanced Ultrasound Enhancement Patterns for Differentiating Focal Pancreatitis From Pancreatic Carcinoma: A Comparison Study With Conventional Ultrasound.* Journal of Ultrasound in Medicine, 2018. 37(3): p. 551-559.

[8]. Mintziras, I., et al., *Postoperative morbidity following pancreatic cancer surgery is significantly associated with worse overall patient survival; systematic review and meta-analysis.* Surgical Oncology, 2021. 38.

[9]. Kotopoulis, S., et al., *Treatment of human pancreatic cancer using combined ultrasound, microbubbles, and gemcitabine: a clinical case study.* Medical physics, 2013. 40(7).

[10]. Kotopoulis, S., et al., *SonoVue® vs. Sonazoid™ vs. Optison™: Which Bubble Is Best for Low-Intensity Sonoporation of Pancreatic Ductal Adenocarcinoma?* Pharmaceutics, 2022. 14(1): p. 98.

[11]. Nam, K., et al., Monitoring neoadjuvant chemotherapy for breast cancer by using three-dimensional subharmonic aided pressure estimation and imaging with US contrast agents: preliminary experience. Radiology, 2017. 285(1): p. 53-62.

Contrast-enhanced ultrasound (CEUS) for a more accurate diagnosis of adenomyosis: a pilot study

E.J.E. de Bock[1,2], F.I. Kandi[3], B. Stoelinga[1,2], C. Schmitt[3], S. Turco[3], N.B. Burger[1,2], C. Dinis Fernandes[3], L.J.M. Juffermans[1,2], M. Mischi[3], J.A.F. Huirne[1,2]

[1]*Department of Obstetrics and Gynecology, location Vrije Universiteit Medical Center, Amsterdam, The Netherlands*
[2]*Amsterdam Reproduction and Development research institute, Amsterdam, The Netherlands*
[3]*Biomedical Diagnostics lab, Electrical Engineering, Eindhoven University of Technology, Eindhoven, The Netherlands*
Corresponding author: e.j.e.debock@amsterdamumc.nl

Introduction

Heavy and painful menstruations, as well as subfertility, profoundly affect the lives of many people [1]. Adenomyosis, a benign condition in which the endometrium grows into the myometrium, may be a root cause of these symptoms. Current estimates of adenomyosis prevalence vary widely (5-70%) [2], likely caused by diagnostic challenges due to adenomyosis' diffuse aspect on B-mode ultrasound and MRI.

Adenomyosis has been shown to be associated with abnormal vascularization, which may be due to increased angiogenesis [3]. Therefore, a potential starting point for improving diagnosis may be imaging the uterine microvascularization using contrast-enhanced ultrasound (CEUS). This study hypothesizes that differences in microvasculature between healthy and adenomyotic uterine tissue can be visualized using CEUS. Besides CEUS time-intensity curve fitting, a quantitative analysis of *pixel-based spatial similarity* can be performed using contrast-ultrasound dispersion imaging (CUDI) [4], resulting in metrics such as *spectral coherence (ρ), correlation (r),* and *mutual information (I)* [5]. These metrics are inversely proportional to dispersion: the higher the local *r, ρ and/or I*, the lower the local dispersion. A lower dispersion is associated with higher vascular density, tortuosity, and irregularity of the microvasculature, potentially indicative of angiogenic processes. The objectives of this pilot study were to 1) determine optimal machine settings and feasibility of uterine CEUS, 2) visualize and describe the adenomyotic uterus on CEUS both qualitatively and quantitatively.

Methods

Adult women (n=15) visiting the tertiary referral Uterine Repair Center, Amsterdam UMC, presenting with prominent sonographic features of adenomyosis, e.g., hyperechoic islands and myometrial cysts, and a healthy control (n=1) were included in the study. They underwent a two-dimensional (2D) CEUS examination by bolus-tracking of SonoVue™ (Bracco, Geneva) with a HERA W10 (Samsung Medison, Republic of Korea) ultrasound system, using an endovaginal EV3-10A or EV2-10B probe. This platform had not been optimized for uterine CEUS yet. Therefore, machine settings, such as *gain, dynamic range* and *mechanical index*, were varied across patients in order to optimize the acquisition for uterine CEUS. A custom transvaginal probe fixture was used to minimize uterine motion during the five-minute recordings.

Enhancement patterns of the resulting scans were analyzed qualitatively and quantitatively. Firstly, signal intensity of the discernible structures relative to each other, as well as the homogeneity of the myometrium enhancement, were visually assessed. Secondly, time-intensity analysis of the ultrasound contrast agent wash-in and wash-out was performed using VueBox^{TM} (Bracco, Geneva). In VueBox^{TM}, regions-of-interest (ROIs) were created for the uterine corpus, adenomyotic-appearing regions (i.e. regions that appeared adenomyotic on B-mode), adjacent healthy-appearing myometrium and endometrium on the 2D CEUS images based on the corresponding 2D B-mode images. VueBox^{TM} proprietary motion correction was applied to the scans. Time-intensity curves (TIC) were fitted to the measured CEUS intensities and wash-in (i.e. rise time and time-to-peak) and wash-out time parameters (i.e. fall time) were extracted.

Pixel-based spatial similarity analysis was performed using the CUDI [4] framework. In this analysis, the kernel of choice is an annulus of pixels with an inner and outer diameter (in the range of millimeters), to which the central pixel (i.e., located at the center of this annulus) is compared. For quantification of spatial similarity, ρ, r and I were computed between the TIC of the central pixel and those of the pixels in the kernel. To visualise these results, parametric maps of these metrics were generated over the ROIs.

Results

Fifteen adenomyosis patients and one healthy control were included in this pilot study, of which ten adenomyosis patients and the healthy control could be quantitatively analyzed. Uterine CEUS was straightforward to perform and well-accepted by all patients. The optimal settings for 2D CEUS resulted to be a *gain* of 30 dB, *dynamic range* of 45 dB, and *mechanical index* of 0.1. Upon visual inspection of the CEUS scans, the myometrium of the healthy control was homogeneously enhanced and the endometrium was hypo-enhanced. In the adenomyosis patients, the myometrium that appeared adenomyotic on B-mode showed heterogeneous enhancement, featuring both hyper- and unenhanced spots and the endometrium was hypo-enhanced. There was a large variation in CEUS enhancement patterns across patients (see Fig. 1).

Based on VueBox^{TM} analysis, wash-in and wash-out times appeared to be extended in adenomyotic-appearing regions when compared to adjacent healthy-appearing myometrium and to the myometrium of the healthy control.
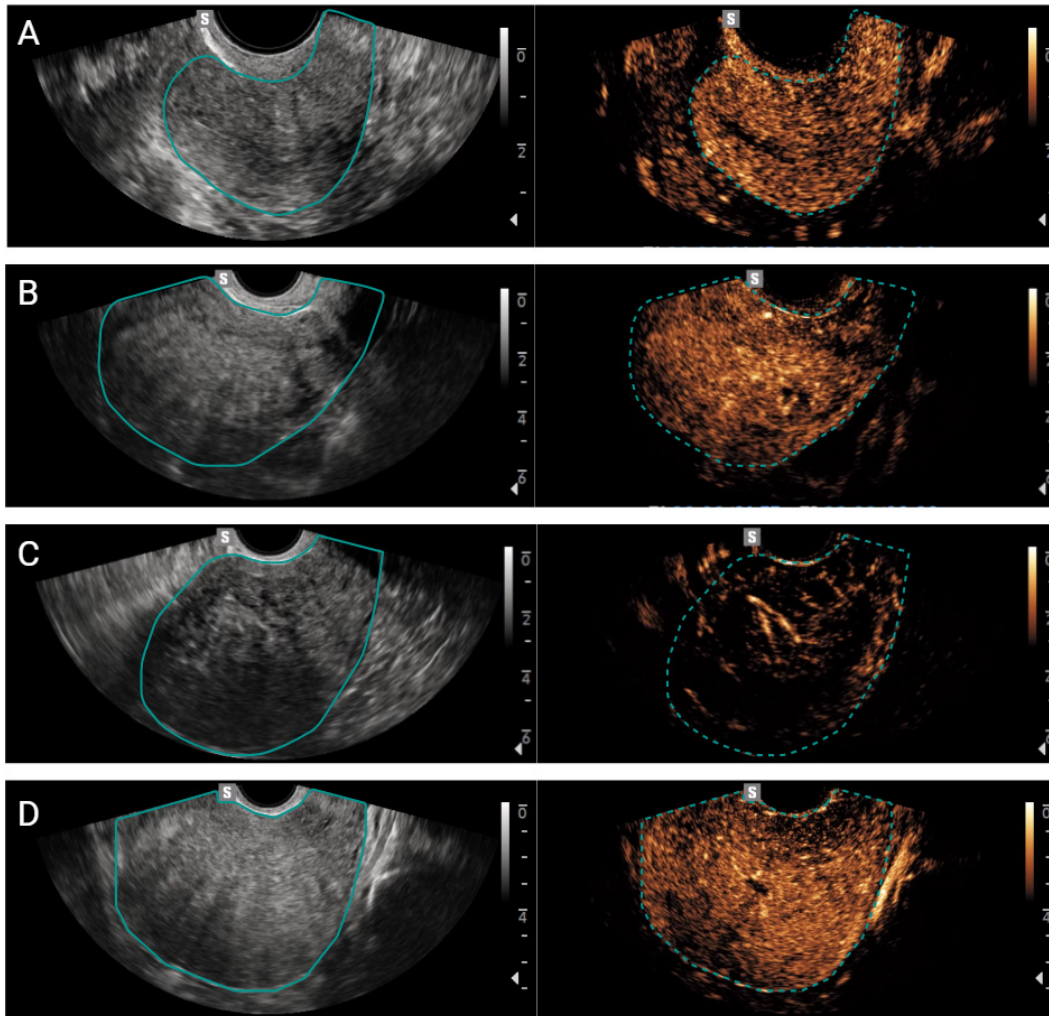
Figure 1. B-mode (left) and CEUS (right) of a sagittal section of the uterus (solid and dashed delineation) at peak intensity for the healthy control (A) and three adenomyosis patients (B, C, D). These images were all acquired at the optimal settings of *gain* = 30 dB, *dynamic range* = 45 dB, *mechanical index* = 0.1.

The CUDI parametric maps of the spatial similarity metrics reflect the enhancement behavior, most prominently when considering the *I* metric. The ρ, *r* and *I* all show higher values and a high heterogeneity in the adenomyotic myometrium, hence associated with heterogeneity in the local dispersion. The performance of these spatial similarity metrics is heavily influenced by the optimization of the used annular kernel, which should be optimized such that minute changes, stemming from early angiogenic processes, can be detected. The results presented here are preliminary and the optimal kernel settings are yet to be defined. The heterogeneity of ρ, *r* and *I* seems to coincide with the tissue heterogeneity of adenomyosis, hence they are potentially relevant features and warrant further investigation. Representative CUDI parametric maps of an adenomyotic uterus and for comparison those of a healthy uterus can be observed in Fig. 2 and Fig. 3, respectively. Observe the expected lower degree of heterogeneity in the healthy uterus, presented through all spatial similarity metrics.
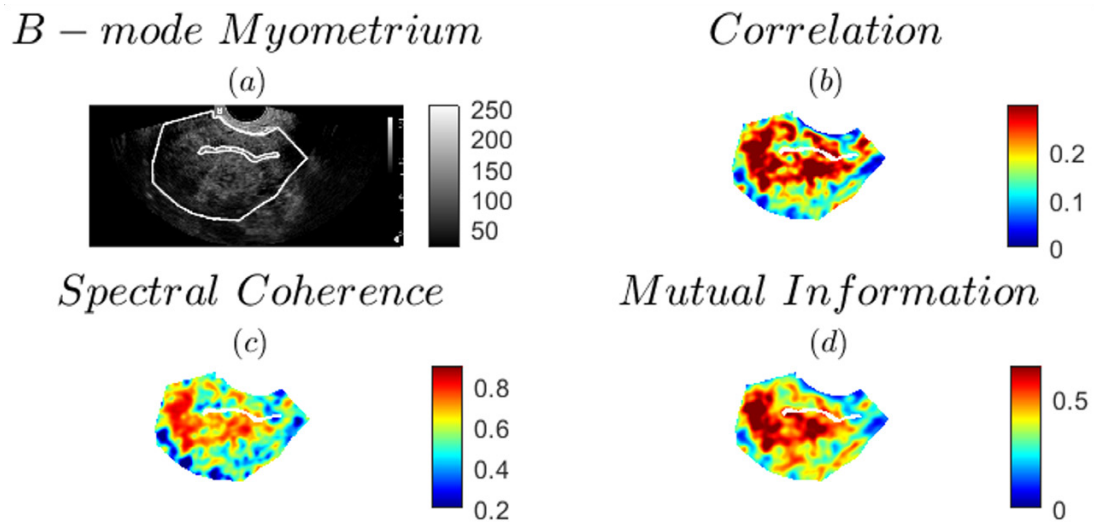
Figure 2. B-mode ultrasound and corresponding CUDI spatial similarity parametric maps of an adenomyotic uterine corpus. On the B-mode, the uterine corpus and there within the endometrium are delineated.
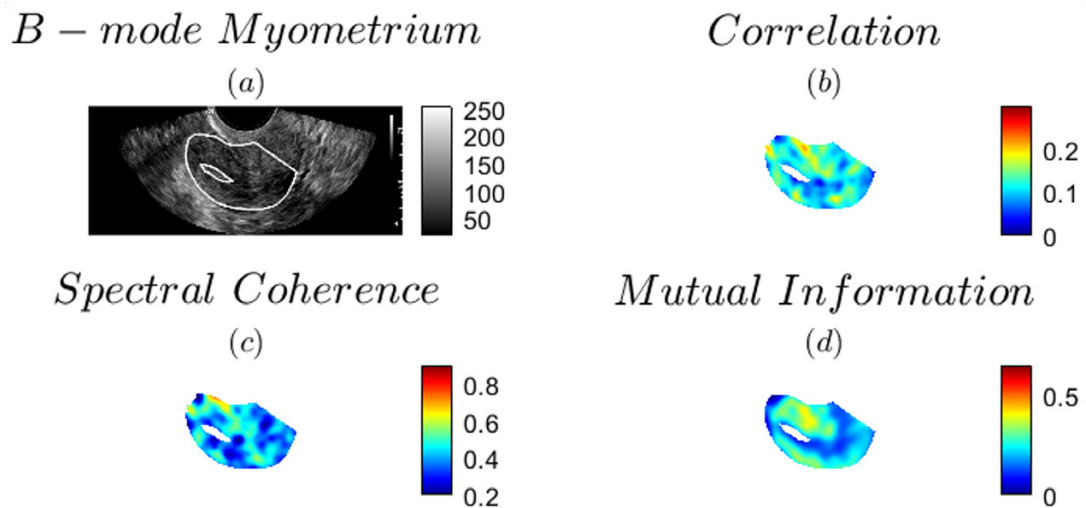
Figure 3. B-mode ultrasound and corresponding CUDI spatial similarity parametric maps of a healthy uterine corpus. On the B-mode, the uterine corpus and there within the endometrium are delineated.

Conclusion

Uterine CEUS is a feasible technique to image microvascular structures in the adenomyotic uterus. The promising results from the TIC and CUDI spatial similarity analyses warrant a large prospective study to accurately characterize and discriminate adenomyotic from healthy tissue.

References

[1]. Schoep, M. E., Adang, E. M., Maas, J. W., De Bie, B., Aarts, J. W., & Nieboer, T. E. (2019). Productivity loss due to menstruation-related symptoms: a nationwide cross-sectional survey among 32 748 women. BMJ open, 9(6), e026186.

[2]. Lydia Garcia and Keith Isaacson. "Adenomyosis: Review of the Literature". In: Journal of Minimally Invasive Gynecology 18 (2011), pp. 428–437. doi: 10.1016/j.jmig.2011.04.004.

[3]. Harmsen, M. J., Wong, C. F., Mijatovic, V., Griffioen, A. W., Groenman, F., Hehenkamp, W. J., & Huirne, J. A. (2019). Role of angiogenesis in adenomyosis-associated abnormal uterine bleeding and subfertility: a systematic review. Human Reproduction Update, 25(5), 647-671.

[4]. Kuenen, M.P.J., Saidov, T.A., Wijkstra, H., Mischi, M. (2013). Contrast-Ultrasound Dispersion Imaging for Prostate Cancer Localization by Improved Spatiotemporal Similarity Analysis. Ultrasound in Medicine & Biology, 39(9), pp. 1631-1641.

[5]. Schalk, S. G., Demi, L., Bouhouch, N., Kuenen, M. P., Postema, A. W., De La Rosette, J. J., ... & Mischi, M. (2016). Contrast-enhanced ultrasound angiogenesis imaging by mutual information analysis for prostate cancer localization. IEEE Transactions on Biomedical Engineering, 64(3), 661-670

Microbubble jetting from low-amplitude ultrasound driving

Marco Cattaneo[1], Louan Presse[1], Gazendra Shakya[1], Bratislav Lukić[2], Alexander Rack[2], <u>Outi Supponen[1]</u>

[1]*Institute of Fluid Dynamics, ETH Zürich, Zürich, Switzerland*
[2]*ESRF - The European Synchrotron Radiation Facility, Grenoble, France*
Corresponding author: outis@ethz.ch

Introduction

Ultrasonically driven microbubbles have been promoted as agents in targeted drug delivery thanks to their ability to exert mechanical action on the surrounding cell and tissues and to enhance their permeability to drugs. The mechanical stresses generated by the oscillation of microbubbles in contact with cells can result in the perforation of the cell membrane, a phenomenon known as sonoporation. However, the exact physical mechanisms causing sonoporation at clinically relevant acoustic driving are still unclear. We have recently observed contrast agent microbubbles forming repeated jets that can hit a nearby substrate, and believe them to play a major role in sonoporation [1]. These jets are different from the previously reported inertial jets [2] formed at high amplitudes (~MPa) from bubbles that get quickly destroyed in that here, the jet originates from nonspherical shape oscillations [3] and can hit the same spot several times within an ultrasound burst. Here, we investigate the physics behind jet formation of larger bubbles driven ultrasonically near a substrate leveraging high-speed phase-contrast X-ray and visible light shadowgraphy imaging. These experiments confirm that shape modes are responsible for generating repeated jets against a substrate at remarkably low acoustic pressures [4]. Lipid coating of the bubble is found to further reduce the jetting threshold pressure.

Methods

A rising stream of monodisperse bubbles within a size range of 10-100 µm is generated using custom-made polydimethylsiloxane (PDMS) microfluidic chips consisting of a T-junction between the continuous phase (water for uncoated bubbles), and the dispersed phase (air), and a secondary sheath flow, assisting the bubble separation by increasing the flow rate. Lipid-coated bubbles are produced using a lipid solution as the continous phase, containing DSPC and DSPE-PEG2000 in a 9:1 molar ratio, with a concentration of 10 mg/ml. One of these micrometric air bubbles is diverted from the stream and placed to rest on a flat glass substrate immersed in water. We subject the bubble to a 30-kHz or 100-kHz acoustic pulse (for which resonant bubble sizes are 110 and 33 µm, respectively) from an ultrasound transducer with pressure amplitudes ranging between 0.1 and 30 kPa. We use side-view microscopy with 20× or 30× magnification, coupled with a high-speed camera, to temporally resolve the bubble response at frame rates ranging from 100 kfps to 1 Mfps. In complement to shadowgraphy, we also leverage synchrotron X-rays (30 keV) that enable propagation-based phase-contrast imaging at ultra-high frame rates on the 150-m long ID19 beamline of the European Synchrotron Radiation Facility to obtain an undistorted view on interfaces and, in particular, jet formation within bubbles. The water chamber is equipped with sliding window tubes on two opposing sides to minimise the distance the X-rays travel within the attenuating water, all while preserving enough space for the undisturbed propagation of the ultrasound pulse (10 mm).

Results

An example of an ultrasonically driven 36-µm microbubble forming repeated jets near a substrate at a pressure amplitude of 12 kPa is shown in Fig. 1(a). Ultrasound driving initially induces spherical oscillations of the bubble. This so-called breathing mode then triggers the well-known Faraday instability, which causes axisymmetric interface deformations. Initially, this zonal shape mode follows the driving frequency, making it harmonic (see frames 50-70 µs). After some time, the shape mode becomes half-harmonic manifesting a period-doubling behaviour (see frames from 200 µs). The mode amplitude then increases and eventually

results in a so-called *Longuet-Higgins* jet (230 µs) - known from jets forming from standing surface waves [5]- hitting the surface at every shape mode cycle, i.e., at every second ultrasound cycle. Eventually, the bubble may lose its axisymmetry through the appearance of non-zonal shape modes and the jetting stops (in this particular case, after 11 shape mode cycles). From these visualisations it is clear that shape modes can drive repeated jetting to the same spot on the surface, even at very low ultrasound amplitudes, making them a potential damage mechanism in sonoporation.

At higher pressure amplitudes, as shown in Fig. 1(b) (at 28 kPa and 23-µm bubble size), the bubble's response is quick and intense. Also here a Longuet-Higgins jets forms as a result of the conical collapse of the tip of the bubble (14 µs). However, the mode amplitude becomes so large that upon shape reversal it causes a cylindrical collapse of the bubble, which in turn generates two so-called *Worthington* jets - known from jets forming from objects hitting a pool of liquid [6] - one upwards (towards the substrate) and one downwards from the location of the cylindrical collapse (24 µs). Such dynamics repeats itself in the following ultrasound cycles but the shape of the bubble gets quickly perturbed, weakening the jets. It is therefore clear that, at large amplitudes, we can get very strong jetting against the substrate, yet it is not sustained over several cycles and the bubbles may get quickly destroyed.
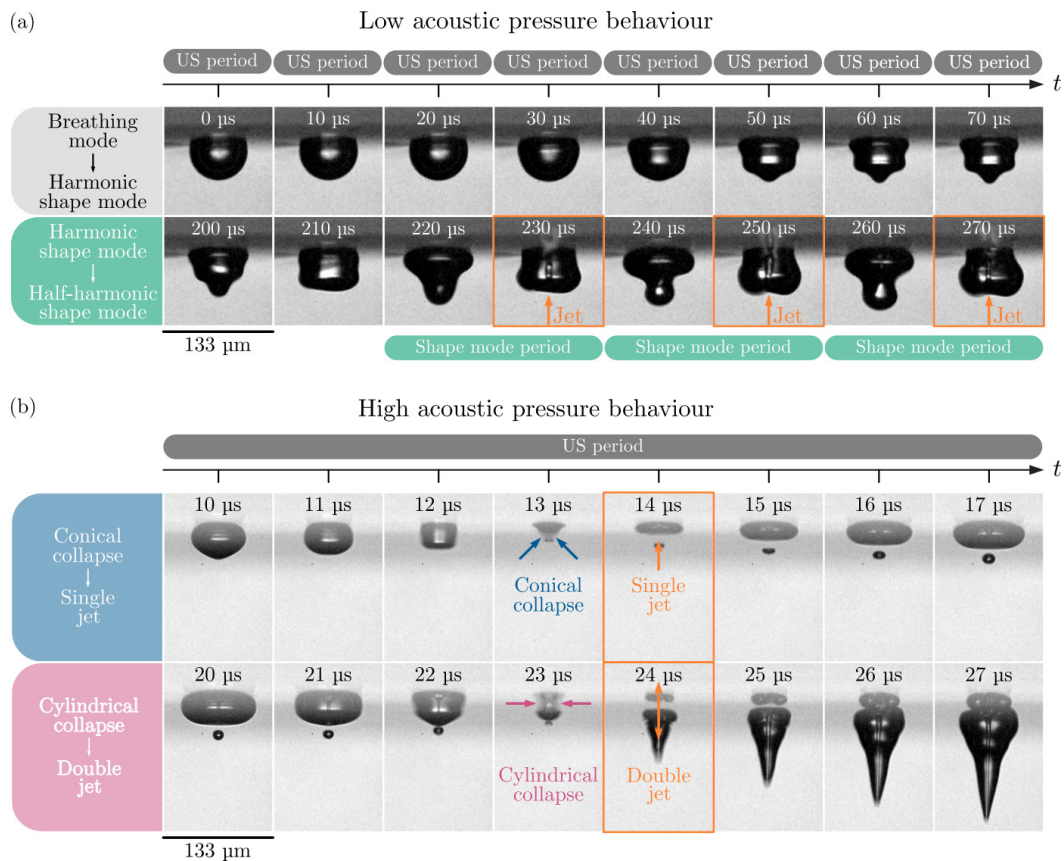
Figure 1. Shadowgraph microscopy images of the dynamics of air bubbles near a rigid substrate subject to 100-kHz ultrasound at (a) 12 kPa and (b) 28 kPa.

From our visualisations, we find that the the main lobe of the zonal shape mode that is first developed is most likely to produce a jet. By leveraging X-rays, which circumvent light refraction issues at curved interfaces, as depicted in Fig. 2(a), we find a clear threshold for the maximum acceleration of this lobe (a_{th} = 5×10^5 m s^{-2}) for it to produce a jet across a wide range of bubble sizes and shape mode orders, as shown in Fig. 2(b).

(a)

(b)
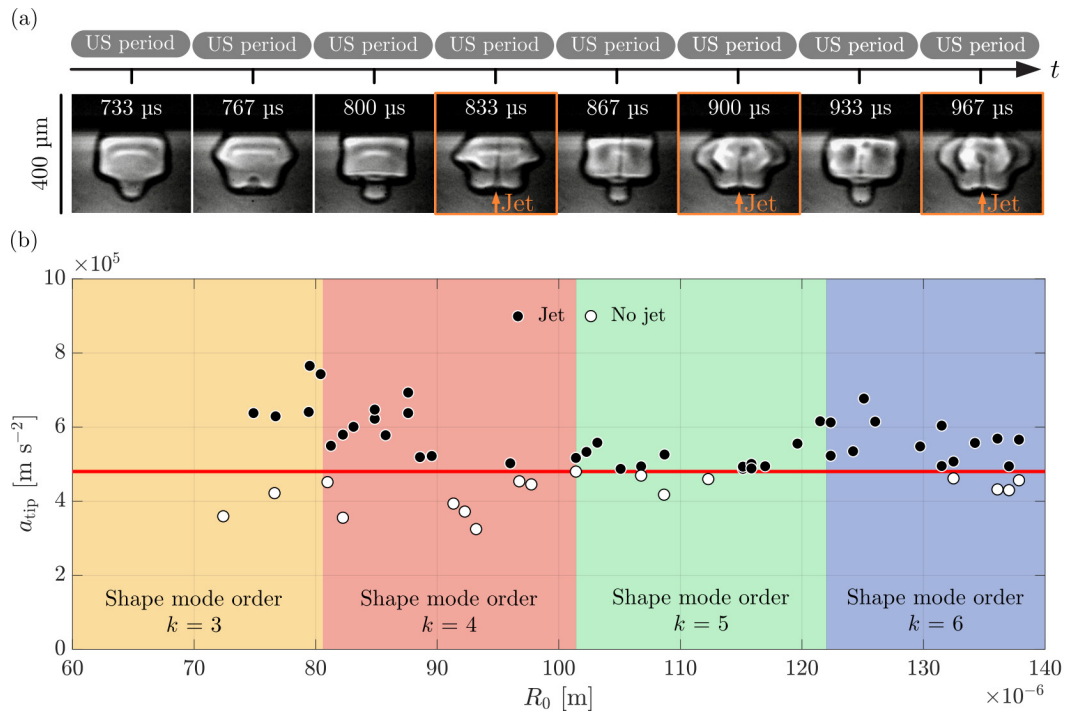
Figure 2. (a) X-ray images of the jetting dynamics of a bubble driven at 30 kHz and 11 kPa. (b) Measured maximum tip acceleration for bubbles across a range of bubble sizes and shape mode orders. The red solid line represents the apparent tip acceleration threshold for jetting.

The question arises whether the observed dynamics for these large, uncoated bubbles near a hard glass substrate is the same as that expected at microscale near soft substrates and cells, and whether it is relevant for sonoporation. The main difference is a higher pressure thershold for ultrasound contrast agent microbubbles, which may start jetting at ~100 kPa at their resonance frequency in the MHz range [1]. This is caused by the acoustic frequency: the higher the frequency, the higher the pressure needed to drive high-amplitude bubble oscillations (similarly to the cavitation effects predicted by the mechanical index). As for the coating, for large micrometric bubbles such as here, the coating decreases the pressure threshold to levels even below 1 kPa. Figure 3 directly compares the dynamics of a coated and an uncoated bubble at < 5 kPa, showing how the coating facilitates shape mode and jet formation. Therefore, without the coating, ultrasound contrast agent microbubbles would probably require prohibitively high pressures to jet. Finally, we have observed the same dynamics also with ultrasound contrast agent microbubbles near soft substrates, as well as near endothelial cells [7].

(a)

(b)
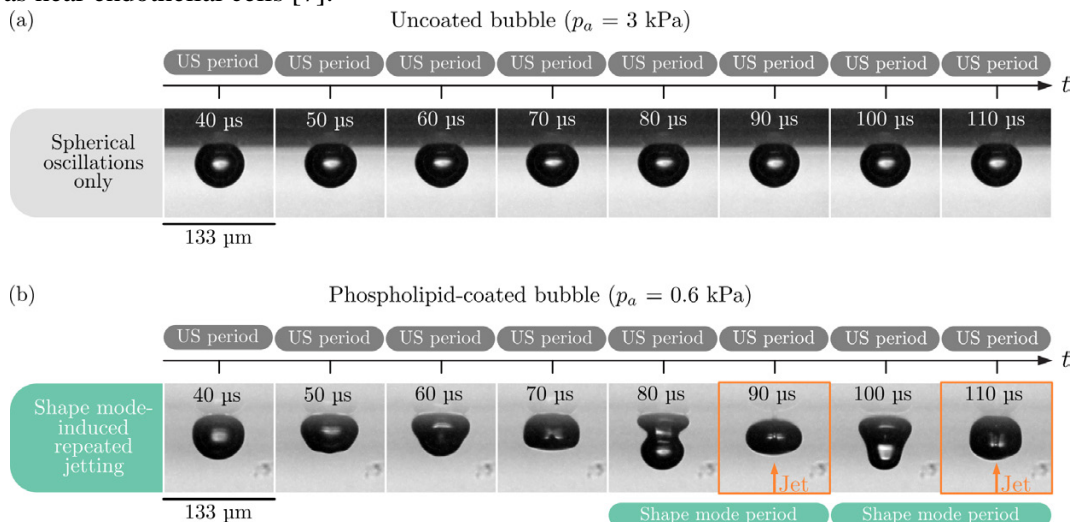
Figure 3. Comparison of the dynamics of (a) an uncoated and (b) a coated 28-µm bubble under 100-kHz ultrasonic excitation.

Conclusions

We have identified a low-pressure amplitude range (5 − 15 kPa) in which modal dynamics enable repeated jets onto a substrate from bubbles of the size range 10-100 μm driven at 30 or 100 kHz. We also find a jetting criterion based on the acceleration of the tip of the main lobe. Coating of the bubble further lowers the jetting threshold to below 1 kPa. Higher acoustic pressures (> 15 kPa) can also form strong jets which, however, are not sustained over many cycles. The shape deformations fostering repeated, sustained bubble jetting on a substrate is a plausible explanation for sonoporation to occur at the clinical acoustic parameters.

References

[1]. Cattaneo M, Shakya G, Supponen O, Jetting Behaviour of Ultrasound-driven Microbubbles in Contact with a Soft Substrate, IEEE International Ultrasonics Symposium (IUS), Montreal, QC, Canada, 2023, pp. 1-4, 2023.

[2]. Prentice P, Cuschieri A, Dholakia K, Prausnitz M, Campbell P, Membrane disruption by optically controlled microbubble cavitation, Nature Physics, 1.2, 2005.

[3]. Vos H J, Dollet B, Versluis M, de Jong N, Nonspherical shape oscillations of coated microbubbles in contact with a wall, Ultrasound in medicine & biology, 37(6), 935-948, 2011.

[4]. Cattaneo M, Presse L, Shakya G, Supponen O, V0076 Jet formation of ultrasound-driven microbubbles near a substrate, 76th Annual Meeting of the APS Division of Fluid Dynamics. 2014.

[5]. Zeff B W, Kleber B, Fineberg J, Lathrop D P, Singularity dynamics in curvature collapse and jet eruption on a fluid surface, Nature, 403(6768), 2000.

[6]. Gekle S, Gordillo J M, van der Meer D, Lohse D, High-Speed Jet Formation after Solid Object Impact, Physical Review Letters, 102(3), 2009.

[7]. Cattaneo M, Shakya G, Guerriero G, Krattiger L, Supponen O, Jetting behaviour of ultrasound-driven microbubbles in contact with a cell monolayer, The 29th European symposium on Ultrasound Contrast Imaging, 2024.

Are monodisperse phospholipid-coated microbubbles 'mono-acoustic'?

Sander Spiekhout[1], Benjamin van Elburg[2], Jason Voorneveld[1], Nico de Jong[1,3], Michel Versluis[2], Johannes G. Bosch[1], and <u>Tim Segers</u>[4]

[1]*Biomedical Engineering, Erasmus Medical Center, Rotterdam, The Netherlands*
[2]*Physics of Fluids Group, University of Twente, Enschede, The Netherlands*
[3]*Laboratory of Medical Imaging, Delft University of Technology, Delft, The Netherlands*
[4]*BIOS / Lab on a Chip Group, Max Planck Center Twente for Complex Fluid Dynamics, University of Twente, Enschede, The Netherlands*

Corresponding author: t.j.segers@utwente.nl

Introduction

Narrowing down the ultrasound-driven response of a suspension of lipid-coated microbubbles is a promising pathway to the use of bubbles for functional ultrasound sensing, e.g., for blood pressure sensing and molecular imaging using targeted bubbles. The first hurdle toward a uniform acoustic bubble response has recently been cleared by allowing stable microfluidic monodisperse bubble formation. The remaining and most pressing question that we address here is: Are monodisperse lipid-coated microbubbles 'mono-acoustic'? In other words, do they have uniform shell properties and therefore a uniform acoustic response?

Methods

The monodisperse microbubble suspension characterized in the present work was formed in a flow focusing device (Fig. 1A) using our standard lipid mixture (DSPC / DPPE-PEG5000, 9:1 molar ratio) [3,4]. The uniformity of the shell properties was investigated by, first, adding 0.01 mol% of lipophilic fluorescent dye (Rhodamine-DHPE, ThermoFisher Scientific) to the lipid formulation to visualize potential phase separation of condensed and expanded domains in the shell. Second, the viscoelastic shell properties of the
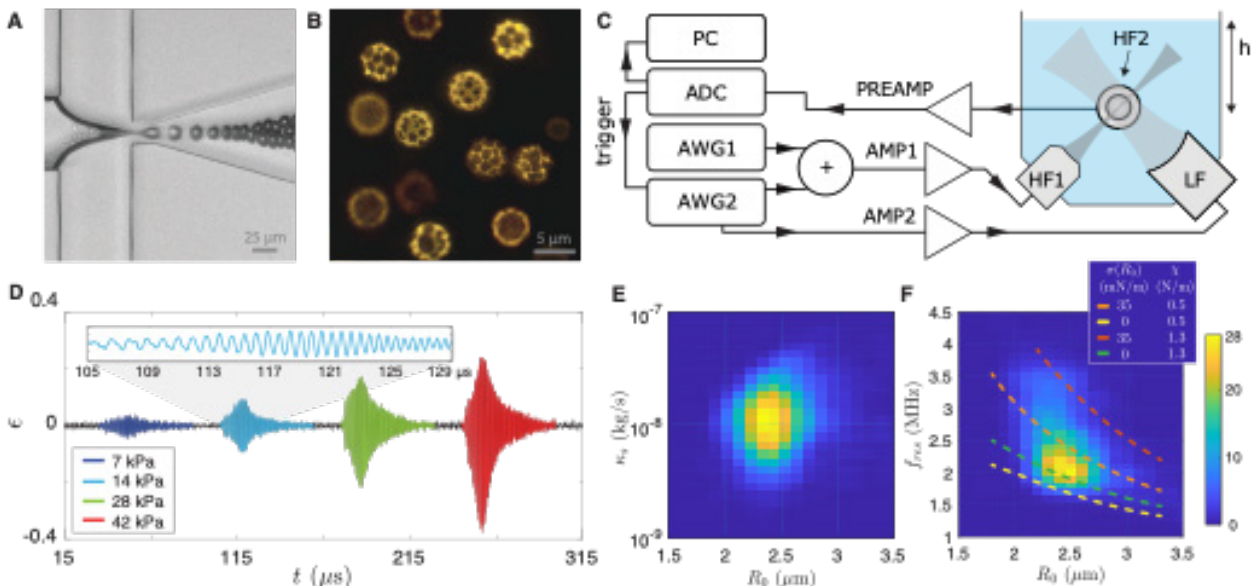
Figure 1. (A) Flow focusing device for monodisperse bubble production. (B) The shell of monodisperse lipid-coated microbubbles has phase-separated microstructures that are nonuniform across the bubble population. (C) Acoustical Camera (AC) setup employed to measure resonance curves of nearly 2000 individual freely floating microbubbles. (D) Typical strain response of a 2.3-µm radius bubble. (E) The obtained shell viscosity values of the monodisperse bubbles varied over as much as one order of magnitude and (F) their resonance frequencies varied by a factor of two.

monodisperse bubbles were characterized by measuring resonance curves of individual freely floating bubbles using a high-frequency (HF) off-resonance geometrical acoustic scattering technique named the 'acoustical camera' (AC). The AC setup consists of a water tank (Fig. 1C, h = 26 cm) with 3 confocally aligned and perpendicularly mounted transducers: HF1, HF2, and LF. The tank was filled with a highly diluted microbubble suspension, which was continuously stirred such that microbubbles passed one-by-one through the confocal transducer zone. Once detected, the bubble was insonified by four successive linear chirps (1 – 5 MHz) transmitted by transducer LF. Each chirp had a constant acoustic pressure amplitude which successively was 7, 14, 21, and 42 kPa. The strain response of the bubble was measured by amplitude demodulation of the geometrical scattering of the 25 MHz probing singnal transmitted by HF1 and received by HF2 (Fig. 1D). The resting radius R_0 of the bubble was obtained through phase demodulation of the HF scattering signal [1]. The viscoelastic shell properties of nearly 2000 individual bubbles were obtained by fitting the linearized Marmottant model [2] to the measured strain envelopes.

Results

The distributions of the shell viscosity κ_s and the resonance frequency f_{res} as a function of R_0 for all characterized bubbles are plotted in Fig. 1E and F, respectively. The figures demonstrate that for the narrow-sized bubble suspension with a mean radius of 2.4 μm that was characterized in the present work, remarkably, κ_s varied over as much as one order of magnitude, from 2×10^{-9} up to 2×10^{-8} kg/s, and f_{res} by a factor of 2, from 1.7 MHz up to 3.5 MHz. Thus, the microfluidically formed monodisperse bubbles characterized in this work are not mono-acoustic due to a variation in the bubble shell viscoelastic properties.

The range of κ_s values corresponds to a decreased resonance frequency by 1 to 9% ($f_{res} = f_0 \sqrt{(1-\delta_{tot}^2/2)}$, with δ_{tot} the total damping). Thus, the measured variation in f_{res} by a factor of two must have mainly resulted from variations in χ and/or $\sigma(R_0)$. To disentangle the effects of χ and $\sigma(R_0)$, we solved the full non-linear Marmottant model to obtain f_{res} using the same chirp driving pulse as in the measurements. We first use a constant value for χ of 0.5 N/m while $\sigma(R_0)$ was either set to 35 mN/m or zero, see the orange and yellow dashed curves in Fig. 1F, respectively. A χ of 0.5 N/m was selected as it is the shell elasticity obtained for a suspension of bubbles with a very similar shell composition. Note that the higher range of measured f_{res} is not captured by a χ of 0.5 N/m. As such, second, we plot numerically obtained curves for a χ of 1.3 N/m while again, $\sigma(R_0)$ is either set to 35 mN/m or zero, see red and green dashed curves, respectively. A comparison between the modeled curves and the measured spread in f_{res} demonstrates that the spread in f_{res} cannot be explained by either a variation in χ or $\sigma(R_0)$ alone. Thus, across the bubble population, the microfluidically formed bubbles in the present work had not only a range of shell viscosities, but also a range of shell elasticities, as well as a range of initial surface tensions.

Conclusions

We demonstrate that DSPC and DPPE-PEG5k (9:1 molar ratio) coated monodisperse microbubbles formed by microfluidic flow focusing using our protocols [3,4] have (i) nonuniform phase separated shell microstructures, (ii) nonuniform viscoelastic shell properties, and (iii) nonuniform acoustically driven dissolution behavior. These intriguing conclusions raise many questions and more work is needed to elucidate (i) the nucleation and growth of shell domains, (ii) whether the spread in the obtained shell properties originates from the inhomogeneous shell microstructures, and (iii) how bubble stability can be enhanced.

References

[1]. S. Spiekhout, J. Voorneveld, B. Van Elburg, G. Renaud, T. Segers, G. P. Lajoinie, M. Versluis, M. D. Verweij, N. De Jong, and J. G. Bosch, The J. Acous. Soc. Am. 151, 3993 (2022).

[2]. P. Marmottant, S. Van Der Meer, M. Emmer, M. Versluis, N. De Jong, S. Hilgenfeldt, and D. Lohse, J. Acoust. Soc. Am. 118, 3499 (2005).

[3]. T. Segers, A. Lassus, P. Bussat, E. Gaud, and P. Frinking, Lab. Chip 19, 158 (2019).

[4]. T. Segers, E. Gaud, G. Casqueiro, A. Lassus, M. Versluis, and P. Frinking, Appl. Phys. Lett. 116, 173701 (2020).

Characterizing the subharmonic ambient pressure sensitivity of single microbubbles

Sander Spiekhout[1], _Yuchen Wang[1]_, _Tim Segers[2]_, _Klazina Kooiman[1]_, _Michel Versluis[3]_, _Jason Voorneveld[1]_, _Nico de Jong[1,4]_, _Johannes G. Bosch[1]_

[1]_Biomedical Engineering, Erasmus Medical Center, Rotterdam, The Netherlands_
[2]_BIOS / Lab on a Chip Group, University of Twente, Enschede, The Netherlands_
[3]_Physics of Fluids Group, TechMed Center, University of Twente, Enschede, The Netherlands_
[4]_Department of Imaging Physics, Delft University of Technology, Delft, The Netherlands_
Corresponding author: s.spiekhout@erasmusmc.nl

Introduction

Microbubble response at half the insonification frequency (f/2) is sensitive to ambient pressure. However, different studies[1,2] show very different subharmonic responses as a function of ambient pressure. Some report increase of subharmonics for increasing ambient pressure (i.e., positive ambient pressure sensitivity)[2], while others show a decrease (i.e. negative sensitivity)[1]. In this study, we measured the change in subharmonics from single monodisperse microbubbles undergoing a dynamic ambient pressure change and numerically investigated why some of these bubbles exhibited positive sensitivity and others negative sensitivity under the same driving conditions.

Methods

Monodisperse lipid-coated microbubbles with a perfluorobutane gas core were generated in a microfluidic chip[3] from a lipid mixture of DSPC:DPPE-PEG5000:Pluronic F68 in a 81:9:10 molar ratio. Microbubbles were collected in a gas-tight vial and stored for two days. These were then sized in a Coulter counter (Multisizer 3, Beckman Coulter, Mijdrecht, The Netherlands), shown in Fig. A. Approximately 700 single bubbles were measured in an 'acoustical camera' setup extended with a speaker to induce a dynamic ambient pressure P_{amb} during the measurement of a single bubble (shown in Fig. E). Bubbles were driven into volumetric oscillation by an acoustic pulse of 1125 cycles with a frequency f of 4.5 MHz and 100 kPa pressure amplitude. The radial oscillation amplitudes of the vibrating bubbles were measured from high-frequency (HF; 25 MHz) scattering as in[4]. The dynamic ambient pressure P_{amb} comprised a 5-cycle 20 kHz wave of 2.7 kPa (40 mmHg peak-to-peak) around a static pressure of 104 kPa.

The subharmonic (f/2) amplitude $SubH$ was extracted by bandpass filtering the bubble's radial strain signal around f/2 with a 50 kHz bandwidth, which can increase or decrease with respect to P_{amb}, as shown in (Fig. B). To quantify the change in subharmonic amplitude it was linearly fit to P_{amb} by:

$$SubH = S_{subH}*P_{amb} + a_{subH},$$

where S_{subH} is the sensitivity of the subharmonic to ambient pressure and a_{subH} the subharmonic level at $P_{amb}=0$.

To understand how resting radius R_0 and initial surface tension $\sigma(R_0)$ influence the S_{subH} and a_{subH}, simulations were performed using the full Rayleigh-Plesset solution with the elasticity described by the Marmottant model[5] using a shell stiffness of 0.65 N/m, with R_0 ranging from 1.6 to 2.4 μm to include the entire monodisperse bubble population, and $\sigma(R_0)$ from 0 to 31 mN/m.

Results

One hundred and fifteen bubbles showed $a_{subh} > 0.5\%$ and 92 had an absolute sensitivity > 0.005 %/mmHg. Of the microbubbles having a absolute sensitivy, 62/92 showed positive S_{subH}. The measured sensitivity values for negative sensitivity ryesponses were grouped together and shown in Fig. B. The positive sensitvity responses are shown in Fig. C. For the negative responses, $SubH$ was more stable over time. The $SubH$ is also shown as a function of P_{amb} in Fig. D, which shows that responses exhibiting positive sensitivity have a higher S_{subh}, but a lower a_{subH}.

Simulated sensitivity values S_{subH} are shown on a false color scale histogram in Fig. F, with red indicating positive and blue indicating negative sensitivity. Simulated a_{subH} values are shown on the false color scale image of Fig. G. Regions of high absolute $Ssubh$ overlap with regions where a_{subh} is relatively low. The simulated positive sensitivity values are found in a narrow diagonal band ranging from $\sigma(R_0)$ of 0 mN/m and R_0 of 1.7+-0.05 μm, to $\sigma(R_0)$ of 31 mN/m and R_0 of 2.3+-0.1 μm. The simulated negative sensitivity values are found at nearly the entire bottom right corner of Fig. G from $\sigma(R_0)$ of 0 mN/m and R_0 values of 1.8 to $\sigma(R_0)$ of 12 and R_0 of 2.4 μm.

Conclusions

Single bubbles vibrating subharmonically can increase or decrease in subharmonic amplitude with ambient pressure. For the narrow size distribution measured here more bubbles exhibited positive sensitivity which also had a higher sensitivity magnitude. Responses exhibiting negative sensitivity had stronger subharmonics and were more stable. Simulations show that the parameter space where positive sensitivity is expected is narrower than the region where negative sensitivity is expected, and that low sensitivity is expected at higher subharmonic levels.
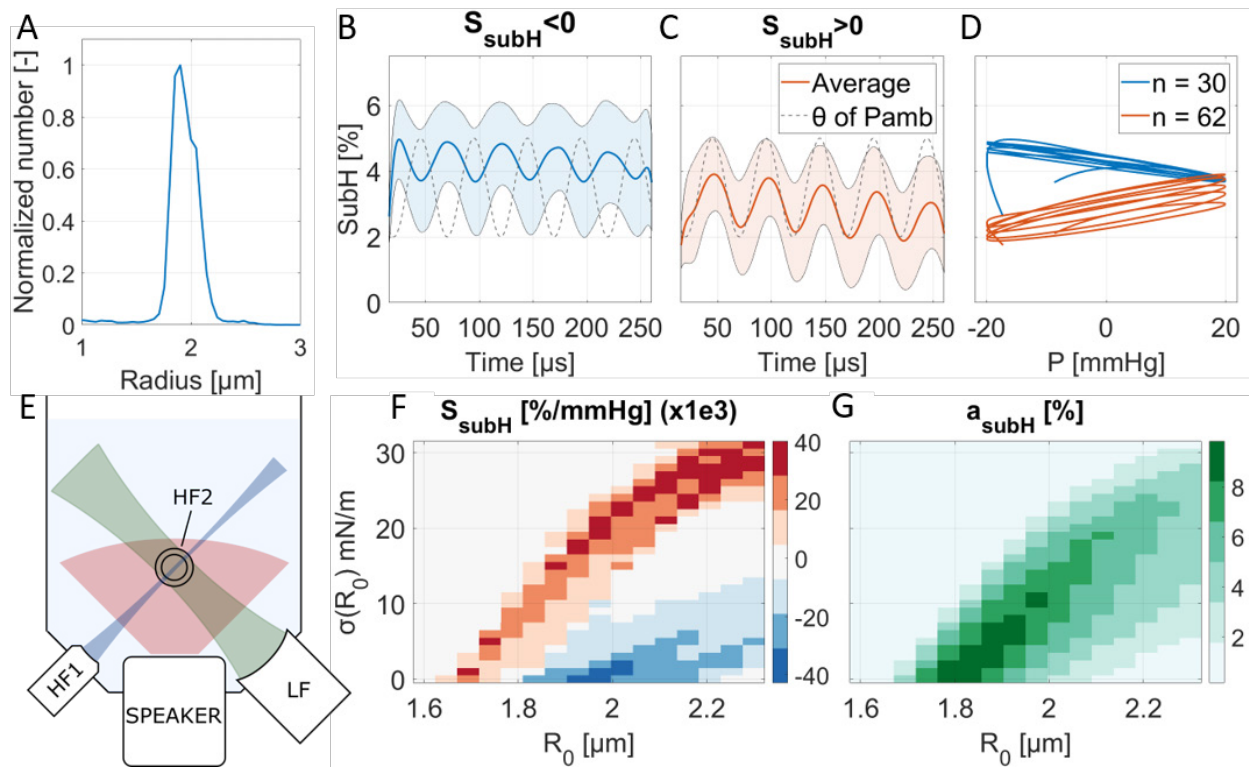
Figure 1. Microbubble population as measured by Coulter counter (A). Measured averaged subharmonic amplitude SubH as a function of time with transparant regions indicating standard deviation and dashed black line indicating phase θ of applied ambient pressure *Pamb*, for all (B) negative sensitivity ($S_{subH}<0$) and (C) positive sensitivity responses. Average SubH as a function of *Pamb* for negative (blue) and positive sensitivity (red) (D). Schematic of the acoustical camera setup used (E). Simulated sensitivity values *SsubH*, color coded red for positive and blue for negative sensitivity (F) and simulated subharmonic levels a_{subh} at $P_{amb} = 0$ for all R_0 and $\sigma(R_0)$ (G).

References

[1]. Roozbeh H. Azami, Flemming Forsberg, John R. Eisenbrey, and Kausik Sarkar. Ambient Pressure Sensitivity of the Subharmonic Response of Coated Microbubbles: Effects of Acoustic Excitation Parameters. Ultrasound in Medicine & Biology, 49(7):1550–1560, 7 2023.

[2]. Peter A. Frinking, Emmanuel Gaud, Jean Brochot, and Marcel Arditi. Subharmonic scattering of phospholipid-shell microbubbles at low acoustic pressure amplitudes. IEEE Transactions on Ultrasonics, Ferroelectrics and Frequency Control, 57(8):1762–1771, 8 2010.

[3]. Abou-Saleh, R.H., F.J. Armistead, D.V.B. Batchelor, B.R.G. Johnson, S.A. Peyman, and S.D. Evans, Horizon: Microfluidic platform for the production of therapeutic microbubbles and nanobubbles. Review of Scientific Instruments, 92(7): p. 074105, 2021.

[4]. G. Renaud, J. G. Bosch, A. F. W. van der Steen, and N. de Jong. An "acoustical camera" for in vitro characterization of contrast agent microbubble vibrations. Applied Physics Letters, 100(10):101911, 3 2012.

[5]. P. Marmottant, S. Van Der Meer, M. Emmer, M. Versluis, N. De Jong, S. Hilgenfeldt, and D. Lohse, A model for large amplitude oscillations of coated bubbles accounting for buckling and rupture. The Journal of the Acoustical Society of America 118, 3499 (2005).

In vivo microbubble behavior in microvasculature under ultrasound excitation: a high speed, intravital study in rat cremaster muscle

<u>Sae K. Jang[1]</u>, Cheng Chen[1], Xucai Chen[1], Brandon Helfield[2], Flordeliza Villanueva[1]

[1]Center for Ultrasound Molecular Imaging and Therapeutics, University of Pittsburgh, Pittsburgh, USA
[2]Department of Physics, Concordia University, Montreal, Canada
Corresponding author: jangsk@upmc.edu

Introduction

Microbubbles (MBs) are currently being investigated as delivery agents for localized therapeutic interventions. Prior *in vitro* work has shown that ultrasound-targetted MB cavitation can enhance delivery of otherwise impermeant large molecule agents via MB-induced shear force and generation of membrane pores and intercellular gaps [1]. Other *ex vivo* work has shown that MBs behave differently in microvascular environments as compared to free floating *in vitro* environments. For example, *ex vivo* studies in the rat cecum and mesentery showed that MBs became elongated in shape with reduced expansion of bubbles due to the elastic forces of the surrounding microvessel, and could cause vessel expansion, invagination, as well as vessel rupture. The oscillations of the MBs can further create microjets [2, 3].

Studying MBs *in vivo* introduces numerous variables, including blood flow, blood viscosity, interaction with red blood cells, and the dynamic viscoelastic interactions between MBs and the surrounding microvessel and tissue. The biophysical interaction of the MB and the microvasculature *in vivo* has not yet been fully described due to the technical challenges of capturing circulating individual MBs in motion at a high temporal and spatial resolution. Here, we provide the first observations of MB cavitation behavior in the microcirculation *in vivo*.

Methods

Animal experiments were approved by the University of Pittsburgh Institutional Animal Care and Use Committee. Prior to each experiment, a single element ultrasound transducer (model A302S-SU-F1.63-PTF, Olympus NDT) was positioned in a custom temperature-controlled intravital imaging chamber, and was aligned to the optical focal plane. The 3-dB width of the ultrasound beam was 2.5 mm. The UPMC Cam [4], an ultrafast microscopy camera utilizing a helium-driven rotating mirror design and capable of recording up to 25 million frames per second for 128 frames, was used to to capture the dynamic behavior of the microbubble at 8-12 million frames per second (10-20 μs movie duration) at 40-60× magnification.

Wistar male rats weighing 150g-250g were anesthesized with inhaled isoflurane. The cremaster muscle was externalized and prepped for intravital imaging [5]. A polyethylene catheter was placed into the ipsilateral femoral artery and advanced until positioned just proximal to the inferior epigastric artery, which was confirmed with visualization of saline flushing the cremasteric feeding artery. The animal was then placed in the custom stage, with the externalized cremaster tissue mounted in the confocal area for high speed microscopy. Activated Definity (Lantheus) was injected via femoral arterial line in 20-60 μL boluses. For each acquisition, a single pulse of six to ten cycles of ultrasound (f=1 MHz, acoustic pressures = 0.8-1.75 MPa) was delivered to a portion of the cremaster muscle.

Microscopy images were analyzed with MATLAB using a minimum cost algorithm for pixel intensities over a given region of interest for MB border detection [6]. The MB dimensions were determined using the direct linear square fitting method for ellipses to obtain major axis (longitudinal along length of vessel) and minor (radial) axis measurements [7]. The area of the ellipse was used to calculate an equivalent diameter of the MB assuming a circular shape. Aspect ratio was calculated as the major axis of the ellipse divided by the minor axis.

Results

The MBs expanded in response to ultrasound pulses, often taking an ellipsoid shape with more longitudinal expansion along the major axis (**Figure 1**). **Figure 2** shows an example of major and minor axis plotted against time, for a MB exposed to 10 cycles of 1 MHz, 1 MPa ultrasound and imaged at approximately 9 million frames per second. All ten ultrasound cycles can be appreciated in the MB expansions. There was a trend of larger MB areas with increasing acoustic pressure (**Figure 3**).

Similar to prior *ex vivo* studies, microvessel expansion, as well as invagination, was observed with MB contractions. However, new findings were also observed in this *in vivo* study. Some of the MBs were observed to split into lobes (**Figure 4**) with the applied ultrasound pulse. Instead of fragmenting, the MB lobes subsequently merged again. In addition, the expansion and contraction of the MB caused subtle oscillation in position of the adjacent red blood cells.

Conclusions

We describe *in vivo* behavior of MBs in the microcirculation under ultrasound excitation, using the rat cremaster muscle and high speed microscopy. The observations confirm predictions from prior *ex vivo* work that MB expansion is reduced due to the resistance from the surrounding microvasculature and tissue. Unlike a MB without boundary, which would expand spherically, the MB is compressed by the microvessel and elongates into an ellipsoid shape. As it expands against the vessel, the MB exerts normal force back to the microvessel and tissue. These coupling forces of the MB and the microvasculature suggest that the MB behavior not only reflects properties of the MB, but also the viscoelastic properties of the surrounding vessel and tissue.

The oscillations of the MB under ultrasound also create shear stress in the microvasculature, and some of these forces can be visualized by the oscillating positions of surrounding red blood cells. The added viscosity of blood likely attenuates MB expansion and decreases fragmentation [8]. Similarly, the surrounding microvessel and intravascular cells may limit the amplitude of oscillation and provide protection against fragmentation. Lastly, the bioeffects of the microbubble may also affect flow via downstream effects of shear stress on the endothelium and red blood cells, such as nitric oxide release.
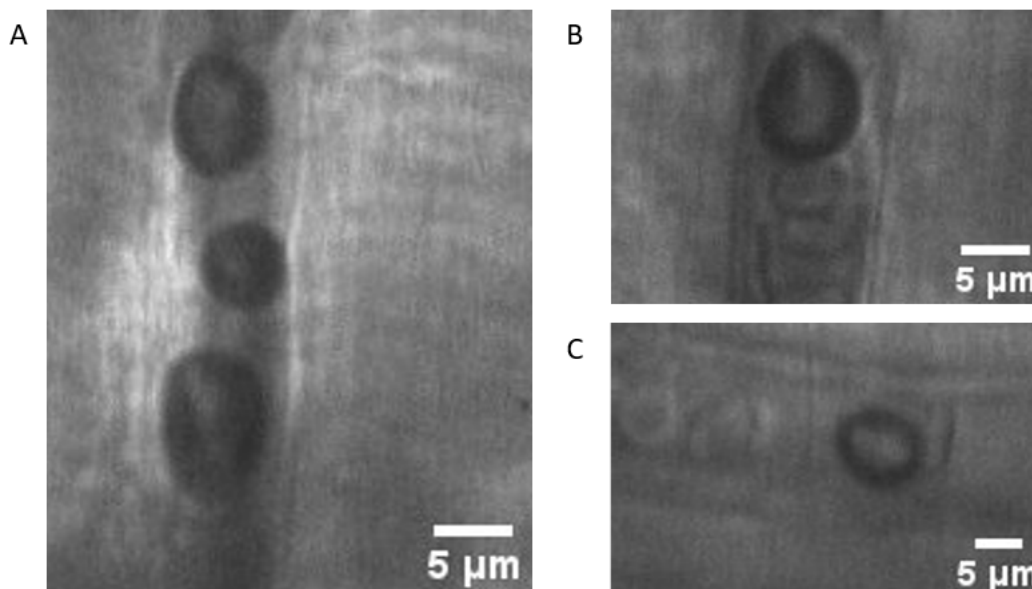
Figure 1. Examples of microbubbles taking elongated ellipsoid shapes due to vessel compression. Surrounding red blood cells can be seen in the microvessels.
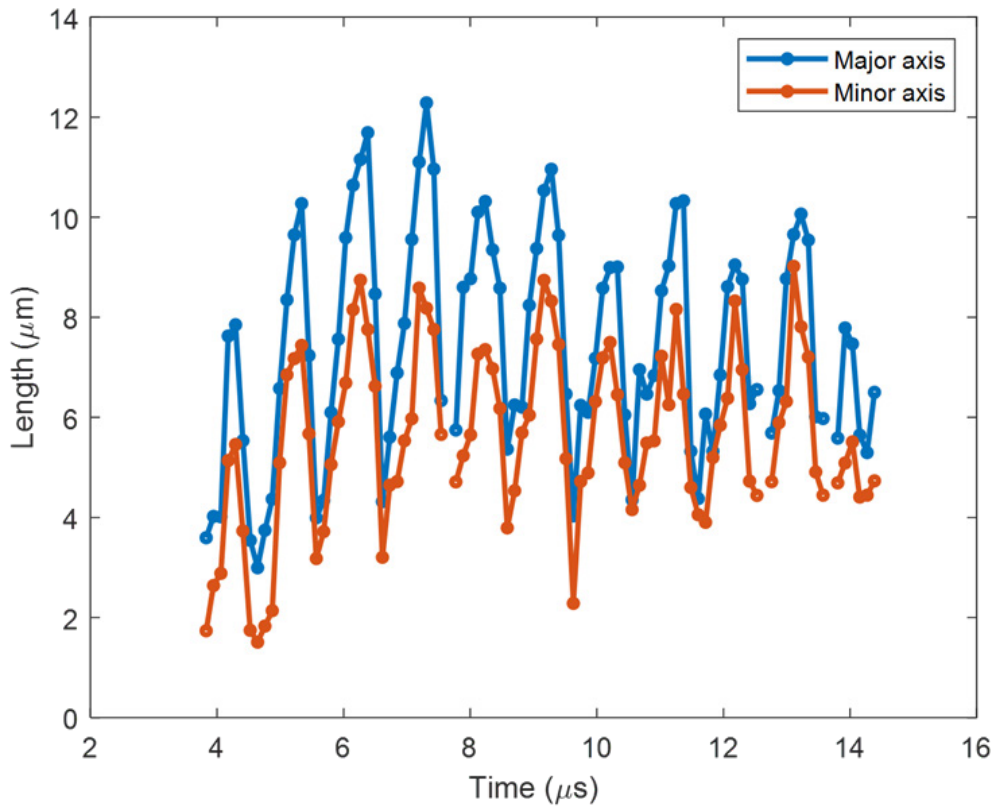
Figure 2. Major and minor axis measurements of a microbubble with 10 cycles of ultrasound at 1 MHz and 1 MPa, imaged at 8.6 million frames per second.
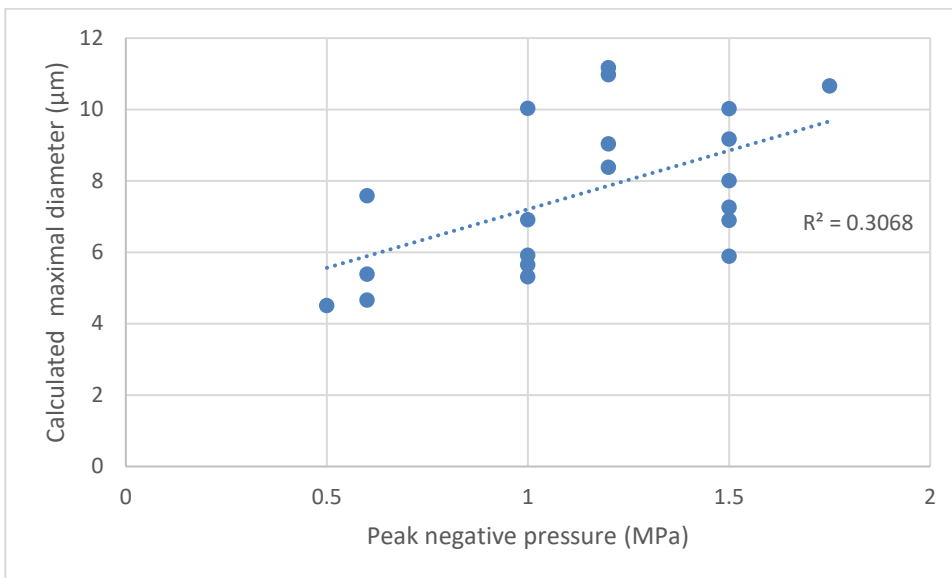
Figure 3. Calculated maximal diameter plotted in microns. Each point represents one microbubble.
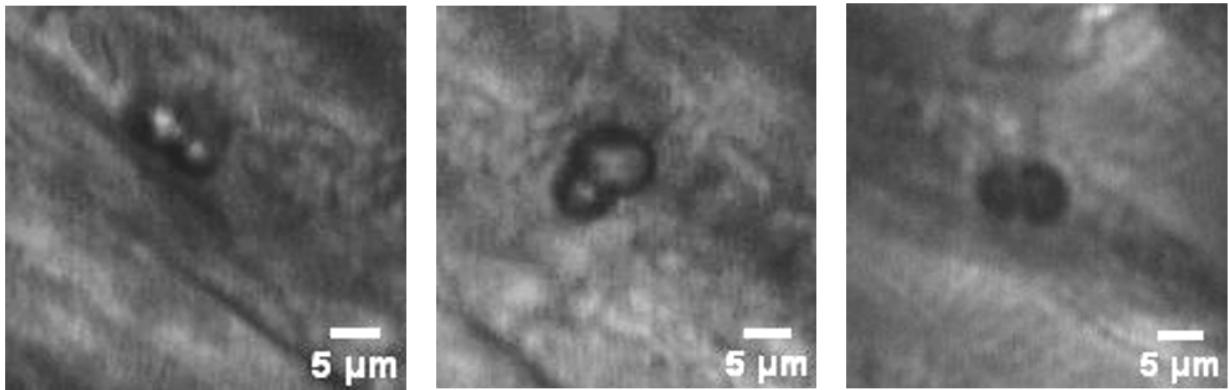
Figure 4. Examples of microbubbles forming multiple lobes.

References

[1]. Helfield B, Chen X, Watkins SC, Villanueva FS: **Biophysical insight into mechanisms of sonoporation**. *Proceedings of the National Academy of Sciences* 2016, **113**(36):9983-9988.

[2]. Caskey CF, Stieger SM, Qin S, Dayton PA, Ferrara KW: **Direct observations of ultrasound microbubble contrast agent interaction with the microvessel wall**. *J Acoust Soc Am* 2007, **122**(2):1191-1200.

[3]. Chen H, Brayman AA, Bailey MR, Matula TJ: **Blood vessel rupture by cavitation**. *Urol Res* 2010, **38**(4):321-326.

[4]. Chen X, Wang J, Versluis M, de Jong N, Villanueva FS: **Ultra-fast bright field and fluorescence imaging of the dynamics of micrometer-sized objects**. *Rev Sci Instrum* 2013, **84**(6):063701.

[5]. Majno G Fau - Gilmore V, Gilmore V Fau - Leventhal M, Leventhal M: **A technique for the microscopic study of blood vessels in living striated muscle (cremaster)**. (0009-7330 (Print)).

[6]. Helfield BL, Cherin E, Foster FS, Goertz DE: **Investigating the subharmonic response of individual phospholipid encapsulated microbubbles at high frequencies: a comparative study of five agents**. *Ultrasound Med Biol* 2012, **38**(5):846-863.

[7]. Fitzgibbon A, Pilu M, Fisher R: **Direct Least-squares fitting of ellipses**, vol. 21; 1996.

[8]. Helfield B, Black JJ, Qin B, Pacella J, Chen X, Villanueva FS: **Fluid Viscosity Affects the Fragmentation and Inertial Cavitation Threshold of Lipid-Encapsulated Microbubbles**. *Ultrasound Med Biol* 2016, **42**(3):782-794.

In vitro Use of Microbubbles for Cell Therapy Biomanufacturing

Samir Cherkaoui, **_Sylvie Henrioud, Deborah Lacombe, Sophie Montandon, Thierry Bettinger_**

Bracco Suisse SA, CH-1228 Plan-les-Ouates, Geneva, Switzerland
Corresponding author: samir.cherkaoui@bracco.com

Introduction

CAR (Chimeric Antigen Receptor) T-cell therapy presents a fast-growing field of cancer immunotherapy. It aims at harnessing the power of T-cells isolated from the cancer patient. In contrast to other cancer treatments such as chemotherapy, the patient's own immune cells are taken out using a process called leukapheresis. Then, after selection and activation of T-cells, these cells are reengineered by introducing a genetic sequence to express the CARs proteins on their surface that allows them to recognize and destroy the cancer cells. Once expanded in the lab, these modified T-cells are re-administered to the patient through the vein to directly fight cancerous cells. As such, genetically modified CAR T-cells are acting as 'living drugs'. Since the commercialization of the first CAR T-cell therapy in 2017 (Kymriah®), other innovative and individualized T-cell drugs were approved by regulatory bodies (FDA, EMA, NMPA) and thousands of global clinical trials are ongoing in the oncology pipeline [1]. However, despite these approvals, there is still an urgent need to overcome some challenges and practical barriers to enable a widespread use of CAR T-cell therapy in the clinical practice [2]. In particular, the manufacturing workflow remains very complex, labor and cost intensive with a vein-to-vein process requiring up to 3-4 weeks with a typical price higher than 300 k$ per dose.

Figure 1: Typical cell therapy workflow

Among the different steps of this complex workflow (See Figure 1), separation/isolation of T-cells from other contaminants (red blood cells, monocytes, granulocytes) is essential to streamline the cell therapy workflow. In fact, it was shown that appropriate T-cell isolation might impact both quality, efficacy and safety, and ultimately the clinical outcome. Until recently, Magnetic-Activated Cell Sorting (MACS) and Fluorescence-Activated Cell sorting (FACS) were the main technologies for cell isolation but these 2 methods suffer from some weaknesses in terms of throughput, scalability and gentleness with the cells which is essential for an efficient use of T-cells as medicines. BACS (Buoyancy-Activated Cell Sorting) represents a novel procedure. In this method, targeted cells are first labeled with a biotinylated specific antibody. The buoyancy agent (functionalized with biotin binding protein such as avidin or streptavidin) is added to the cell mixture. After incubation, the complex (targeted cell/buoyancy agent) is separated by centrifugation allowing the targeted cell recovery (Figure 2).

In this study, we propose to use BACS procedure using specifically designed streptavidin coupled microbubbles to overcome the limitations of the current cell sorting technologies [3]. Comprehensive characterization of the BACS-MB was performed in terms of size, concentration and streptavidin (STV) density. In particular, cell recovery tests were also implemented to assess BACS-MB performances.

Methods

Microbubbles preparation: Streptavidin was coupled to microbubbles using the thiol/maleimide reaction. The final formulation was freeze-dried to enable long term stability, easy storage, and transportation. After redispersion in a saline solution, a milky suspension of BACS-MB was obtained. The microbubbles features were characterized using Coulter counter Multisizer to determine the size distribution and concentration.

A cell recovery test using a human cancerous cell line, namely CCRF-CEM (with CD45 antibody), was established to assess the BACS-MB ability to select targeted cell populations.
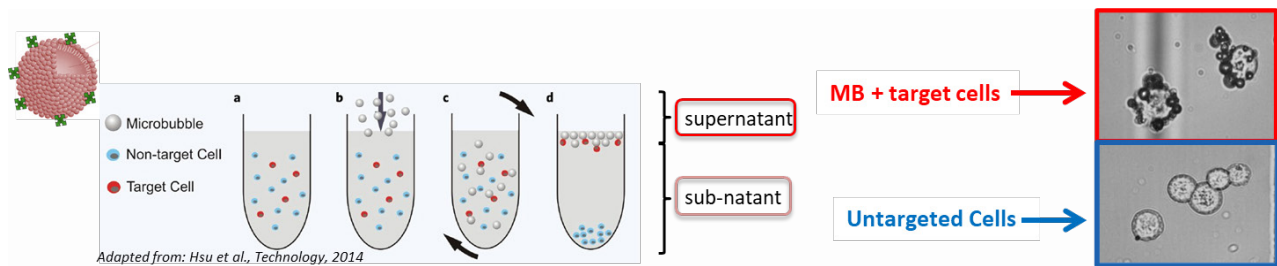
Figure 2: BACS: *in vitro* **Buoyancy-Assisted Cell Sorting (BACS)** [4]

Results

Gas-filled streptavidin functionalized microbubbles were obtained in the form of freeze-dried material. Some key quality attributes were identified to allow efficient flotation of targeted cells (positive selection). The streptavidin density on the MB surface appeared to influence the cell recovery. Higher was the streptavidin density and higher was the cell recovery.

These microbubbles bind specifically to the desired target cells increasing their buoyancy. Subsequent collection of the floating target cells coated with microbubbles provide a highly purified preparation of target cells, with high recovery efficiency and cell viability.

Using a specific CD45 biotinylated antibody to select human lymphoblast cells, a very high cell recovery was achieved, above 95%, with the targeted cells-MBs are collected on the top in the supernatant whereas the rest sinks down in the infranatant. Similar cell recovery data combined with a high purity and viability were accomplished in the case of human primary T-cells (Figure 3). In addition, our BACS process was compared to a MACS method, considered as a gold standard, for T-cells isolation from human blood showing similar to higher performances in terms of cell recovery, purity and viability. In contrast to other cell sorting techniques, BACS is a gravity driven process without the need for a magnet, column, microfluidics or other specific equipment.
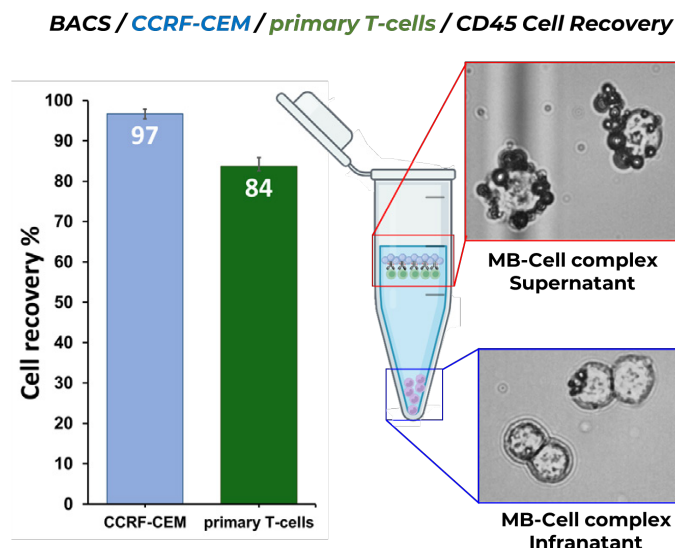
Figure 3: Cell recovery for human lymphoblast cells (CCRF-CEM) and human primary T-cells using BACS-MB

Conclusions

The BACS microbubbles developed by Bracco present competitive benefits over existing cell sorting systems. In fact, the targeted cells can be efficiently collected with a high purity along with a very good recovery. Due to the softness of the process, relying on natural MBs floatability, there is no stress on the cells thus leading to increased cell viability. More importantly, contrary to other methodologies, no debeading is needed and microbubbles can be removed gently by applying overpressure. The BACS process is cost effective, scale independent and easily amenable to automation for CAR T-cell manufacturing purposes. To conclude, this in vitro buoyancy agent holds a great potential in the cell therapy manufacturing space by reducing cell processing time, increasing the yields and making these life-saving therapies accessible and affordable for patients in need.

References

[1]. Ana Rosa Saez-Ibañez et al. "Landscape of cancer cell therapies: trends and real-world data" Nature Reviews | Drug Discovery. 2022, | Sep; Vol 21: 631-632

[2]. ENDPOINTS NEWS "Marks doubles down on urgency to improve gene therapy manufacturing", November 6, 2023

[3]. WO 2020/127816 A1: Gas filled microvesicles with ligand

[4]. Hsu et al. "Fast sorting of CD4+ T cells from whole blood using glass microbubbles "Technology (Singap WorldSci). 2015 Mar;3(1):38-44

Update on CEUS for Carotid Artery

Pintong Huang [1]

[1]Department of Ultrasound, The Second Affiliated Hospital of Zhejiang University School of Medicine
Full Second Author2, Full Third Author1, 2*

Abstract

Carotid plaque, a key contributor to ischemic strokes, presents significant challenges in public health globally. The rupture of vulnerable carotid plaques, leading to thrombus formation, is a primary cause of these strokes. In this context, Contrast-Enhanced Ultrasound (CEUS) has emerged as a vital diagnostic and management tool due to its high temporal resolution and sensitive blood flow imaging capabilities.

CEUS significantly improves the detection rate of hypoechoic plaques on the anterior wall, crucial for early diagnosis. It offers enhanced visualization of carotid lumen stenosis and effectively identifies vulnerable plaques, such as ulcerated plaques and those with intraplaque neovascularization. This ability aids immensely in early intervention strategies. In differential diagnosis, CEUS excels by distinguishing carotid plaques, dissection, and Takayasu's arteritis. Its accuracy in identifying these conditions helps tailor patient-specific management plans. Additionally, CEUS holds predictive value in cerebrovascular events, thereby facilitating proactive patient management and potentially reducing the occurrence of adverse outcomes. Therapeutically, CEUS enhances diagnostic accuracy for pseudo-occlusions. This improvement is particularly beneficial in guiding interventions for symptomatic cases, aiming to reduce the long-term risk of strokes and carotid occlusions. CEUS also plays a crucial role in monitoring treatment progression, especially in pharmacotherapy, by assessing changes in neovascularization within plaques. Furthermore, CEUS is invaluable in prognostic evaluations, particularly following carotid endarterectomy. It also enhances the clarity and resolution of ultrasound images post-vascular stent placement, contributing to better post-procedural care and outcome assessments.

In summary, CEUS stands as a cornerstone in the modern approach to managing carotid artery disease. Its capabilities span across diagnosis, treatment, prediction, prevention, and prognosis, solidifying its essential role in improving patient outcomes in carotid artery-related pathologies.

References

[1]. Grau AJ, Weimar C, Buggle F, et al, Risk factors, outcome, and treatment in subtypes of ischemic stroke: the German stroke data bank [J]. Stroke, 2001, 32(11): 2559-66

[2]. Staub D, Schinkel AF, Coll B, et al. Contrast-enhanced ultrasound imaging of the vasa vasorum: from early atherosclerosis to the identification of unstable plaques [J]. JACC Cardiovascular imaging, 2010, 3(7): 761-71.

[3]. Zamani M, Skagen K, Scott H, et al. Carotid Plaque Neovascularization Detected With Superb Microvascular Imaging Ultrasound Without Using Contrast Media [J]. Stroke, 2019, 50(11): 3121-7.

[4]. Giannoni MF, Vicenzini E, Citone M, et al. Contrast carotid ultrasound for the detection of unstable plaques with neoangiogenesis: a pilot study [J]. Eur J Vasc Endovasc Surg, 2009, 37(6): 722-7.

[5]. Saha SA, Gourineni V, Feinstein SB. The Use of Contrast-enhanced Ultrasonography for Imaging of Carotid Atherosclerotic Plaques: Current Evidence, Future Directions [J]. Neuroimaging clinics of North America, 2016, 26(1): 81-96.

[6]. Horie N, Morofuji Y, Morikawa M, et al. Communication of inwardly projecting neovessels with the lumen contributes to symptomatic intraplaque hemorrhage in carotid artery stenosis [J]. Journal of neurosurgery, 2015, 123(5): 1125-32.

[7]. Ten Kate GL, van den Oord SC, Sijbrands EJ, et al. Current status and future developments of contrast-enhanced ultrasound of carotid atherosclerosis [J]. J Vasc Surg, 2013, 57(2): 539-46.

[8]. Ventura CA, Silva ES, Cerri GG, et al. Can contrast-enhanced ultrasound with second-generation contrast agents replace computed tomography angiography for distinguishing between occlusion and pseudo- occlusion of the internal carotid artery? [J]. Clinics (Sao Paulo, Brazil), 2015, 70(1): 1-6.

[9]. Yoshida K, Nozaki K, Kikuta K, et al. Contrast-enhanced carotid color- coded duplex sonography for carotid stenting follow-up assessment [J]. AJNR American journal of neuroradiology, 2003, 24(5): 992-5.

The development of a clinical implantable ultrasound system for repeatedly disrupting the blood-brain barrier

Michael Canney[1], Guillaume Bouchoux[1], Carole Desseaux[1], Charlotte Schmitt[1], Adam M Sonabend[2], Roger Stupp[2], Ahmed Idbaih[3], Alexandre Carpentier[3]

[1]Carthera, Lyon, France
[2]Department of Neurological Surgery, Feinberg School of Medicine, Northwestern University, Chicago, IL
[3]Hôpital Pitie Salpetriere, AP-HP, Sorbonne Université, Paris, France
Corresponding author: michael.canney@carthera.eu

Introduction

The blood-brain barrier (BBB) limits the efficacy of drug therapies for treatment of brain diseases. Low intensity pulsed ultrasound (LIPU), in combination with administration of microbubbles, can be used to temporarily disrupt the BBB and enhance the delivery of systemic drugs for the treatment of brain tumors and other brain diseases.

Methods

A 1-MHz implantable ultrasound system (SonoCloud, Carthera, Lyon, France) was developed to use LIPU for temporary and repeated BBB disruption [1, 2]. The system consists of an implant with either one [2] or nine [3] circular, 10-mm diameter ultrasound transducers attached to a titanium mesh. The device is implanted in a skull window during surgery. The system is connected to an external radiofrequency generator using a single-use transdermal needle and pulsed ultrasound is applied using a low duty cycle for a duration of several minutes at time of a bolus infusion of microbubbles. The system is accessed in an outpatient infusion suite with no need for imaging guidance, at the time of administration of therapeutic agents, with the BBB opening procedure lasting several minutes. A first-in-human clinical trial was launched in 2014 with the first version of the system (SonoCloud-1) using SonoVue® (Bracco) microbubbles [1, 2] and additional trials with a second generation version with a larger volume of coverage (SonoCloud-9) in 2019 using Definity® microbubbles (Lantheus) [3]. To date, clinical trials using this system have been performed in patients with glioblastoma [1, 2, 3], Alzheimer's Disease [4], and brain metastases using a wide spectrum of therapeutic agents including carboplatin, nab-paclitaxel, and immune checkpoint inhibitors.

Results

Results from the first-in-human clinical trial in glioblastoma patients demonstrated that BBB disruption is safe and well-tolerated by patients. These results were used to establish safe ultrasound parameters (1.03 MPa at 1 MHz) for repeated BBB disruption. Subsequent phase 1/2 trials have further demonstrated the safety of repeatedly disrupting the BBB over a larger volume (>6x6x6 cm^3). Furthermore, results from these trials have demonstrated that disruption can be achieved using either SonoVue® or Definity® microbubbles and that the BBB is rapidly restored within several hours [3]. Thus, there is an optimal window for administration of therapeutic agents to maximize drug delivery to the brain using this approach. Intraoperative sonication and measurement of drug concentrations furthermore showed that drug concentrations are increased by 4-6x in the brain [3]. A phase 3 clinical trial has been launched in patients with recurrent glioblastoma to further explore the efficacy of this approach.

Conclusions

Since 2014, clinical trials have demonstrated the safety of using the SonoCloud System in more than 100 patients treated (>500 sonications to disrupt the BBB). A recently launched, Phase 3, registrational trial in Europe and the United States will further validate the efficacy of this approach in patients with recurrent glioblastoma and may provide a new treatment option for patients with severe brain diseases.

References

[1]. Carpentier, A., Canney, M., Vignot, A., Reina, V., Beccaria, K., Horodyckid, C., Karachi, C., Leclercq, D., Lafon, C., Chapelon, J.Y. and Capelle, L., 2016. Clinical trial of blood-brain barrier disruption by pulsed ultrasound. Science translational medicine, 8(343), pp.343re2-343re2.

[2]. Idbaih, A., Canney, M., Belin, L., Desseaux, C., Vignot, A., Bouchoux, G., Asquier, N., Law-Ye, B., Leclercq, D., Bissery, A. and De Rycke, Y., 2019. Safety and feasibility of repeated and transient blood–brain barrier disruption by pulsed ultrasound in patients with recurrent glioblastoma. Clinical Cancer Research, 25(13), pp.3793-3801.

[3]. Sonabend, A.M., Gould, A., Amidei, C., Ward, R., Schmidt, K.A., Zhang, D.Y., Gomez, C., Bebawy, J.F., Liu, B.P., Bouchoux, G. and Desseaux, C., 2023. Repeated blood–brain barrier opening with an implantable ultrasound device for delivery of albumin-bound paclitaxel in patients with recurrent glioblastoma: a phase 1 trial. The Lancet Oncology, 24(5), pp.509-522.

[4]. Epelbaum, S., Burgos, N., Canney, M., Matthews, D., Houot, M., Santin, M.D., Desseaux, C., Bouchoux, G., Stroer, S., Martin, C. and Habert, M.O., 2022. Pilot study of repeated blood-brain barrier disruption in patients with mild Alzheimer's disease with an implantable ultrasound device. Alzheimer's Research & Therapy, 14(1), p.40.

Newly designed functionalized polymer microbubbles for the targeted treatment of stroke

Louise Fournier[1], _Myriam Abioui-Mourgues[2]_, _Georges Chabouh[3]_, _Rachida Aid[1,4]_, _Olivier Couture[3]_, _Cyrille Orset[2]_ and _Cédric Chauvierre[1]_

[1]_Université Paris Cité, Université Sorbonne Paris Nord, UMR-S U1148 INSERM, Laboratory for Vascular Translational Science (LVTS), Paris, France_
[2]_Normandie University, UNICAEN, INSERM UMR-S U1237, Physiopathology and Imaging of Neurological Disorders (PhIND), GIP Cyceron, Institut BB@C, Caen, France_
[3]_Sorbonne Université, CNRS, INSERM, Laboratoire d'Imagerie Biomédicale, Paris, France_
[4]_Université Paris Cité, UMS 34, Fédération de Recherche en Imagerie Multi-modalité, Paris, France_
Corresponding author: louise.fournier@inserm.fr

Introduction

Cardiovascular diseases are the global burden of contemporary humanity. Described as the leading cause of mortality and disability, it has become a medical priority with the ever-increasing aging of the global population. Among the various pathologies related to the cardiovascular system, our group has focused on thrombotic diseases. They result from the pathological formation of a blood clot (thrombi) due to dysregulation in the hemostatic system and/or atherosclerotic disease. Thrombi are primarily composed of fibrin mesh trapping red blood cells, activated platelets, and circulating inflammatory cells, and they form in both veins and arteries. The major risk is vessel occlusion caused by the displacement of the thrombus to the lungs (pulmonary embolism), the small vessels of the heart (myocardial infarction), and the brain (stroke). Standard thrombolysis relies on the injection of recombinant tissue-type plasminogen activator (rtPA), which activates plasminogen into plasmin, the primary fibrinolytic protease. As a result, plasmin disassembles cross-linked fibrin and releases trapped cells. When administered systemically, rtPA has a relatively short half-life (approximately 4 minutes) due to the presence of its natural inhibitor (PAI-1). Consequently, the drug is injected at a concentration (0.9 mg/kg of body weight) that entails dose-related side effects such as neurotoxicity and hemorrhagic transformation of the event. Overall, the primary unmet medical need for the treatment of thrombotic diseases is an effective, specific therapy that reduces potentially life-threatening side effects. Within the wide spectrum of nanomedicine methods available, our attention was directed towards microbubbles. These micro-scale structures offer the advantage of remaining in the vascular compartement and their adaptability for ultrasound signal add the possibility of specific molecular imaging.

Methods

The synthesis of functionalized polymer MBs relies on three primary components. Isobutyl cyanoacrylate (IBCA) forms the structural basis of the polymeric shell. Perfluorobutane (PFB) contributes to the stability of MBs due to its inert properties. Fucoidan, a sulfated polysaccharide, serves as the targeting agent for activated endothelium and activated platelets, owing to its affinity for P-selectins. This newly patented acoustic cavitation process involves the copolymerization of IBCA and fucoidan at the water/PFB interface under ultrasound (US) insonation. The resulting targeted MBs were thoroughly characterized in terms of size (using laser granulometry), concentration (microscopy), surface charge (Dynamic Light Scattering - DLS), shell width (Focused Ion Beam), morphology (Scanning Electron Microscopy) and cell biocompatibility (assessed through hemolysis, MTT, LDH). The echogenic properties were validated _in vitro_ and _in vivo_ ensuring the contrast enhancer property of those newly developed MBs. Not only these MBs can be burst on demand with US signal, but can also be observed with US imaging in the brain vasculature through the skull. The targeting capabilities of the incorporated fucoidan were validated using a microfluidic assay involving activated human platelets. The thrombolytic drug (rtPA) was incorporated using an adsorption protocol based on charge interaction between the MBs and the serine protease. The

activity of the loaded rtPA was validated through qualitative fibrinolytic assays and quantitative amidolytic assays (PefaFluor® substrate quantification). Subsequently, the rtPA-loaded targeted MBs were tested in a stroke mice model (involving approximately 80 animals) for resolving ischemic lesions compared to the gold standard of systemic rtPA injection. To briefly outline the procedure, stroke was induced by injecting thrombin into the Middle Cerebral Artery (MCA) and monitored using laser speckle imaging. MRI scans were conducted on the mice 24 hours after treatment, and the resulting ischemic lesions were analyzed. Then, organs were harvested to trace the biodistribution of fluorescent residues from the MBs.

Results

In this study, we compared systemic injection of rtPA to rtPA-loaded targeted MBs at the same doses, here, one-tenth of the usual dose used in mice. This choice was motivated by the ultimate goal of limiting the side effects associated with the rtPA dose. This significant constraint did not hinder effective clot resolution thanks to the specific targeting of functionalized MBs. Indeed, 1 mg/kg injection of rtPA loaded on targeted MBs reduced the average size of the ischemic lesion by more than 50% in a group of 18 animals compared to gold standard treatment. Drug loading helped protect the protein, and specific clot targeting led to treatment improvement. This result is all the more promising as treatment with free rtPA at the same concentration was not significantly more effective than the negative control with a saline solution. Furthermore, we monitored the permeability of the Blood-Brain Barrier since the bubbles are micron-sized by injecting Gadoteric Acid (GA) intravenously. This test showed no signs of Blood-Brain Barrier impairment when comparing all groups. Overall, targeted treatment with functionalized MBs was much more effective than the reference treatment, and no collateral bleeding or Blood-Brain Barrier leakage was observed. Fluorescence residues from the MBs were observed through rhodamine labeling on *ex vivo* organs and as expected, the majority of the fluorescence was observed in the liver, fulfilling its role in blood detoxification. Interestingly, specific fluorescence in the stroke area was observed after 24 hours. This supports the validation of the targeting capacity of functionalized MBs *in vivo*.

Conclusions

The process of synthesizing functionalized polymer MBs using acoustic cavitation stands out from hydrodynamic cavitation due to its ability to reduce the synthesis time by a factor of three. Through *in vitro* and *in vivo* assessments, we confirmed the goal of producing stable, biocompatible, and precisely targeted MBs, which proved to be an effective treatment for ischemic stroke. What's particularly encouraging is that the issues related to the dosage of rtPA treatment seem surmountable, as we achieved significant outcomes with a 90% dose reduction without any adverse effects. Furthermore, the observed persistence of ischemic memory unveils new possibilities for monitoring P-selectin expression using US imaging after clot-resolution, and managing potential recurrences.

Figure 1: Graphical abstract of the rtPA-loaded targeting MBs stroke treatment.

Acoustic cavitation synthesis

Activated platelet/endothelium targeting MBs

Stroke treatment
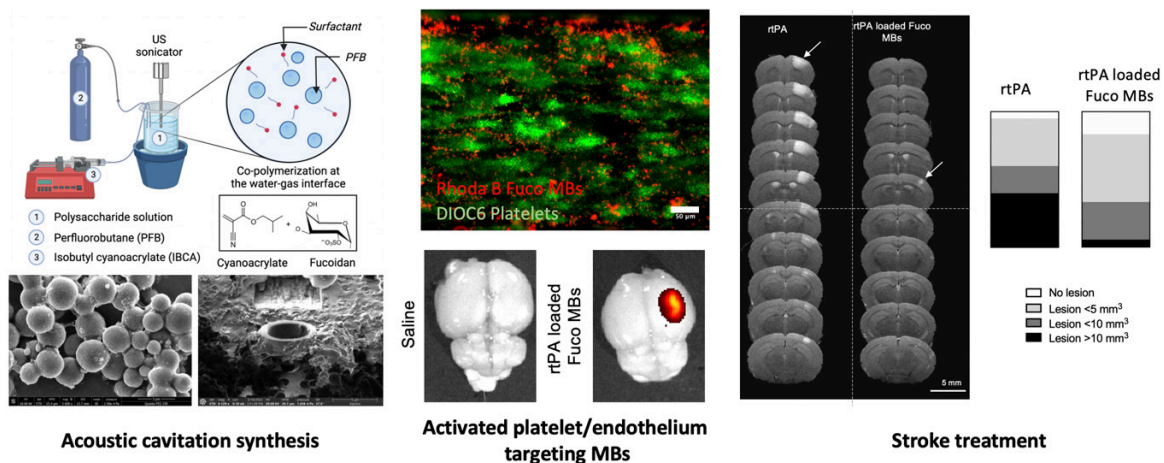
Modulating Sterile Inflammatory Response in Focused Ultrasound and Microbubble-Mediated Blood-Brain Barrier Opening: Impact of Microbubble Size and Sonication Points

Payton Martinez[1], Jane Song[1], Adam Green[2], Mark Borden[1,3]

[1]*Biomedical Engineering, University of Colorado – Boulder, Boulder, USA*
[2]*Pediartic Oncology, University of Colorado – Anschutz, Aurora, USA*
[3]*Mechanical Engineering, University of Colorado – Boulder, Boulder, USA*

Introduction

Microbubbles (MBs) combined with focused ultrasound (FUS) have emerged as a promising noninvasive technique to permeabilize the blood-brain barrier (BBB) for drug delivery to the brain [1–3]. However, the biological effects are not as well understood, particularly a comprehensive understanding of the transcriptomic environment. Kovacs et al. were one of the first to show the genomic results of BBB opening providing an insight that the peak of the acute inflammatory response was around 6 hours [4]. McMahon et al. later investigated the effects of microbubble composition where the idea of microbubble size may affect the SIR was brought up although the use of different microbubble shells and only one population having been size isolated led to the need to perform experiments isolating microbubble size [5]. Previously our group was able to show that the SIR was more dependent on BBB opening intensity rather than the mechanical index or microbubble volume dose alone [6].

This study uses RNA sequencing to investigate the effects of varying microbubble size and number of sonication points on BBB opening using high-resolution ultra-high field MRI-guided FUS and the sterile inflammatory response (SIR).

Methods

In-house microbubbles were size isolated to 1, 3, and 5 µm ± 1 µm as previously described [7], and immunocompetent mice (n=2/3 per size) were injected via tail vein at 10 µl/kg. Right after (10-20 seconds) sonication was started with parameters as follows: center frequency: 1 MHz, peak negative pressure: 0.5 MPa, pulse length: 1 ms, pulse repetition frequency: 1 Hz for 1, 4, or 9 sonication points (all within single pulse repetition cycle). Sonication lasted 3 minutes, and passive cavitation data was collected and analyzed as previously described [8]. Directly after FUS mice were imaged using T1w and T2w MRI sequences to determine the extent of BBBO and edema. After 6 hours mice were sacrificed, and brains were extracted. Using MRI guidance, brains were dissected to isolate the affected area of BBBO and the contralateral region. All samples were sent in for RNA sequencing and analyzed as previously described [6].

Results

Our size-isolated microbubbles showed three separate size distributions with little overlap between adjacent sizes and no overlap between 1 and 5 µm (Fig. 1). We have demonstrated that using multiple pulsing schemes (1, 4, and 9 sonication points) we can achieve a larger volume of opening by only mildly increasing the intensity of BBBO at each point (contrast enhancement, Fig. 2). Our results show at multiple sonication points (4) we do not see significant differences in BBBO volume or contrast enhancement at three different microbubble sizes (Fig. 2).

Upon our investigation into the inflammatory response, we see a linear trend as we increase the sonication points from one to nine (Fig. 3A). This linear trend holds for the three hallmark pathways of the onset of SIR, a sustained response, and damage associated signaling (TNFa signaling, inflammatory response, and apoptosis, respectively) compared to BBBO volume. When comparing the difference in the inflammatory response from different-sized microbubbles, we see a slight trend increasing as we increase

microbubble size. This is most indicated in Fig. 3A where all three sizes have similar BBBO volumes although increasing NES scores for all three pathways.

Conclusions

Our study demonstrates that the inflammatory response from BBB opening is most dependent on the opening volume as indicated by the strong increase when increasing the number of sonication points. We also show that although secondary, there is a trend between microbubble size and the biological effects that result. As the microbubble size increases so does the inflammatory response.
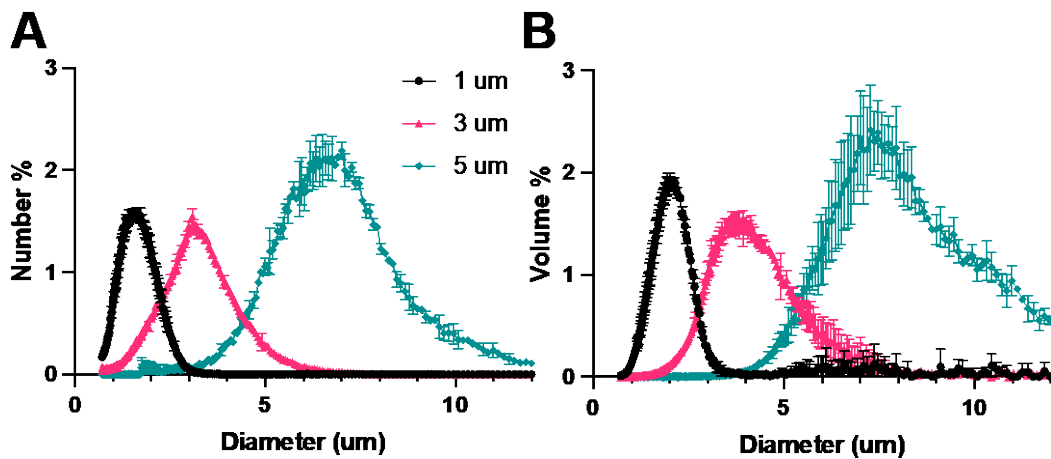
Figure 1. Size Distributions of Size Isolated Microbubbles. (A) Number percent size distributions of 1, 3, and 5 um microbubbles. (B) Volume percent size distributions of same microbubble populations. Data is shown at mean ± standard deviation.
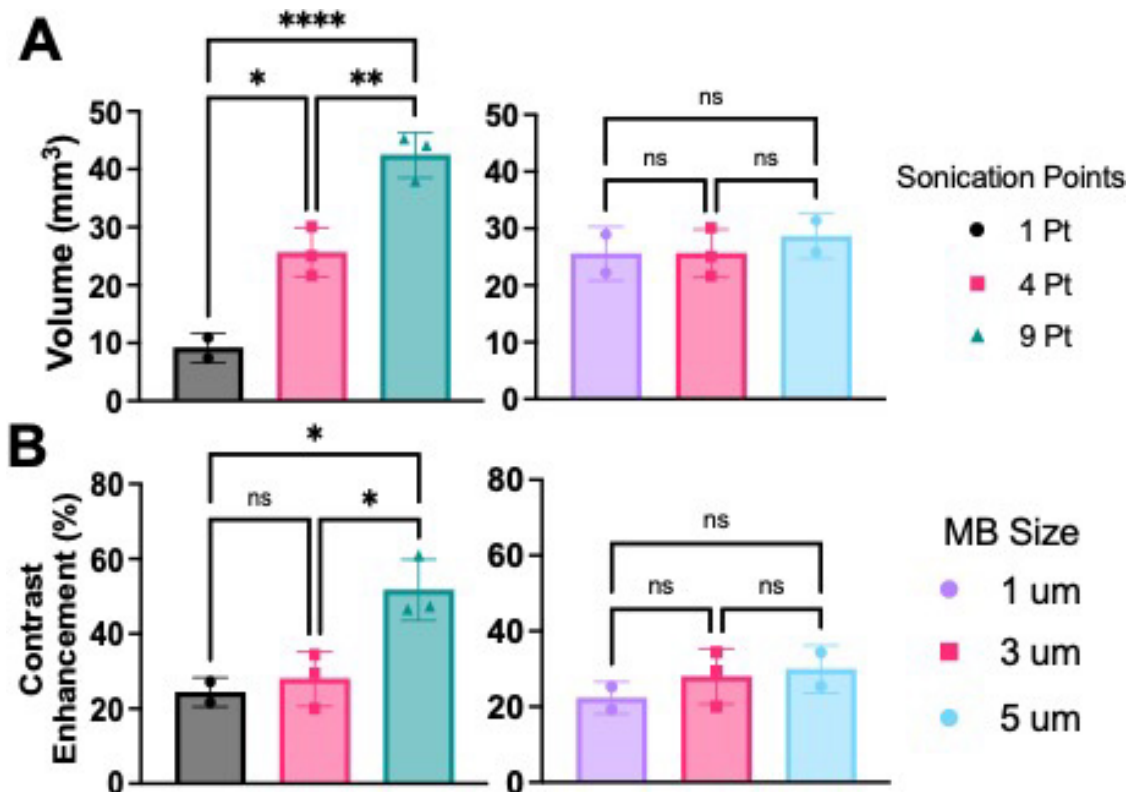
Figure 2. Quantification of BBB opening using T1w MRI. (A) BBBO volume of three sonication point schemes (left) and three microbubble sizes (right). (B) BBBO contrast enhancement of three sonication point schemes (left) and three microbubble sizes (right). Data is shown at mean ± standard deviation. Significance testing was done using a student's t-test (n=6). * Indicates P < 0.05; ** indicates P < 0.0001.**
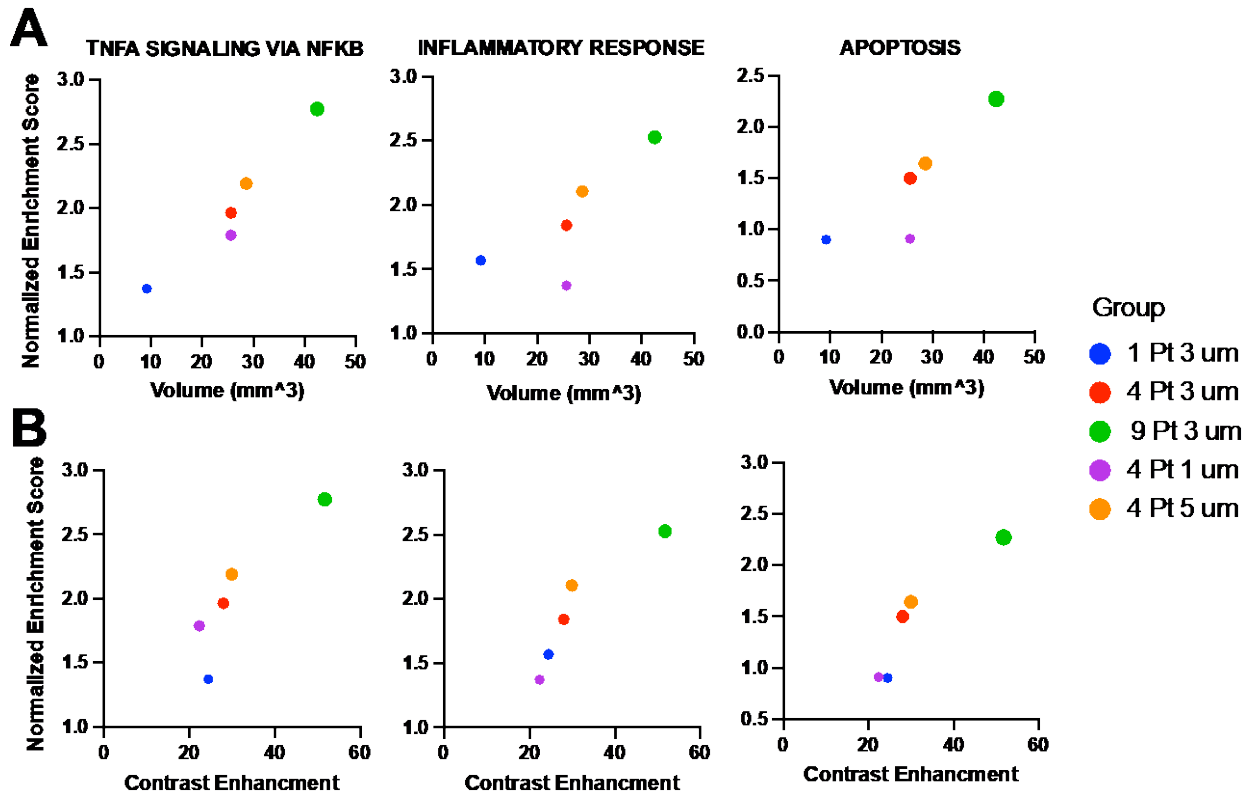
Figure 3. RNA sequencing correlation to extent of BBB opening. Normalized enrichment scores of three major inflammatory pathways (TNFA Signalling, Inflammatory Response, and Apoptosis) compared to BBBO volume (A) and contrast enhancement (B). Data is represented as only means.

References

[1]. Martinez, P. *et al.* MRI-guided focused ultrasound blood–brain barrier opening increases drug delivery and efficacy in a diffuse midline glioma mouse model. *Neuro-Oncology Advances* **5**, vdad111 (2023).

[2]. Ishida, J. *et al.* MRI-guided focused ultrasound enhances drug delivery in experimental diffuse intrinsic pontine glioma. *Journal of Controlled Release* **330**, 1034–1045 (2021).

[3]. Kooiman, K., Vos, H. J., Versluis, M. & de Jong, N. Acoustic behavior of microbubbles and implications for drug delivery. *Advanced Drug Delivery Reviews* **72**, 28–48 (2014).

[4]. Kovacs, Z. I. *et al.* Disrupting the blood–brain barrier by focused ultrasound induces sterile inflammation. *Proc. Natl. Acad. Sci. U.S.A.* **114**, (2017).

[5]. McMahon, D., Lassus, A., Gaud, E., Jeannot, V. & Hynynen, K. Microbubble formulation influences inflammatory response to focused ultrasound exposure in the brain. *Sci Rep* **10**, 21534 (2020).

[6]. Martinez, P. *et al.* Comprehensive Assessment of Blood-Brain Barrier Opening and Sterile Inflammatory Response: Unraveling the Therapeutic Window. http://biorxiv.org/lookup/doi/10.1101/2023.10.23.563613 (2023) doi:10.1101/2023.10.23.563613.

[7]. Feshitan, J. A., Chen, C. C., Kwan, J. J. & Borden, M. A. Microbubble size isolation by differential centrifugation. *Journal of colloid and interface science* **329**, 316–324 (2009).

[8]. Martinez, P., Bottenus, N. & Borden, M. Cavitation Characterization of Size-Isolated Microbubbles in a Vessel Phantom Using Focused Ultrasound. *Pharmaceutics* **14**, 1925 (2022).

Jetting behaviour of ultrasound-driven microbubbles in contact with a cell monolayer

Marco Cattaneo[1], Gazendra Shakya[1], Giulia Guerriero[1], Lisa Krattiger[2], Outi Supponen[1]

[1]_Institute of Fluid Dynamics, ETH Zürich, Zürich, Switzerland_
[2]_Department of Obstetrics, University Hospital Zürich, Zürich, Switzerland_
Corresponding author: mcattaneo@ethz.ch

Introduction

The localised ultrasound stimulation of systemically-administered microbubbles holds great premise for targeted therapeutic delivery by inducing controlled nanodamage to vascular walls. While there is clear clinical evidence demonstrating the effectiveness of this approach [1], the specific physical mechanism responsible for nanodamage is still a subject of debate. Various phenonoma have been proposed, including the pushing and pulling motion of the bubble interface [2], the oscillatory shear stress induced by the bubble oscillation [3], the steady shear stress generated by bubble's microstreaming [4], the acoustic radiation force [5] and the inertial jetting [6]. _In-vitro_ studies have revealed the perforation of the cell membrane occurs starting from an acoustic pressure of around 100 kPa [7]. While inertial jetting is the most energetic mechanism, it also requires the highest driving pressure for activation (~ 1 MPa). Consequently, jetting is not been considered a plausible mechanism for enhanced permeabilization at the lower pressures commonly used in the clinical practice. However, our study unveils, through the use of time-resolved side-view visualizations, that microbubbles in contact with a endothelial cell monolayer can exhibit stable and periodic jets directed towards the cell substrate at driving pressures as low as 100 kPa. Our experiments also provide evidence for the existence of three distinct jetting regimes dependent on the bubble's size and identifies shape deformations as the mechanism that governs and determines the jetting regime. The remarkable speed of these microjets implies a substantial role in causing nanodamage to the surface.

Methods

A. Experimental setup

We conducted two distinct sets of experiments. In the first set we used a PDMS (Polydimethylsiloxane, Young modulus E ≈ 1 MPa) substrate, which offer a greater testing convenience than a biological substrate, to facilitate an extended examination of microbubble jetting behavior. Subsequently, in the second set, we employed a endothelial cell (HUVECs) monolayer cultivated on a PC (polycarbonate) film as a substrate to validate the findings obtained in the previous experiment. In the first experiment, the PDMS substrate is suspended in a water bath filled with deionised water (T ≈ 22°C). Lipid-coated microbubbles manufactured in-house (< 5 μm-radius) are injected underneath the substrate and let adhere to the bottom surface by flotation. The microbubbles are acoustically driven at 1.5 MHz by using an ultrasound transducer (PA1612, Precision Acoustics) positioned in the water bath perpendicular to the horizontal plane. In the second experiment, the cell-cultivated plastic film is installed in a custom-built, acoustically and optically transparent chamber filled with a solution of PBS (phosphate-buffered saline) and microbubbles. The chamber is then placed within the water bath, with the membrane positioned on top to allow contact with microbubbles through flotation. The microbubbles are acoustically driven at 1 MHz by using a HIFU (high-intensity focused ultrasound) transducer (PA1280, Precision Acoustics) positioned in the water bath at a slight angle (15°) relative to the vertical direction to avoid acoustic reflections within the test chamber. A needle hydrophone (0.2 mm, Precision Acoustics) is employed to measure the acoustic pressure and to align the acoustic focal point with the optical field of view. The bubble dynamics is recorded using a custom-built horizontal microscope featuring a f = 2 mm water-immersion microscope objective (CFI Plan 100XC W, Nikon) and a f = 400 mm tube lens (TL400-A, Thorlabs) for a total magnification of 200×. The objective is made waterproof and inserted into the water tank through a sealed window. An ultra-high-speed camera (HPV- X2, Shimadzu) is used to perform recordings at 10 million frames per second, covering a span of

25.6 microseconds and offering a 160 nm-pixel resolution. For backlight illumination, a continuous halogen illuminator (OSL2, Thorlabs) is used for live imaging, while two Xenon flash lamps used sequentially (MVS-7010, EG&G) are employed for video recording. Only bubbles located over 50 μm from the substrate's edge are tested to avoid corner proximity effects.

B. Microbubble synthesis

The lipid-coated microbubbles are prepared in-house. The gas core is made of C_4F_{10} (perfluorobutane, Fluoromed) and the lipid coating consists of 90 mol% DPPC (1,2- distearoyl-sn-glycero-3-phosphocholine, NOF EUROPE) and 10 mol% of DSPE-PEG2K (1,2-distearoyl-sn-glycero- 3-phosphoethanolamine-N-[methoxy(polyethylene glycol)- 2000]), Larodan). The microbubbles are produced by probe-sonicating the surface of the lipid solution while simultaneously flowing C_4F_{10} gas over it. Large bubbles and lipid residuals are removed through centrifugation.

C. Substrate fabrication

The PDMS substrates are fabricated using a standard soft-lithography technique. PDMS prepolymers (Elastosil RT 601 A/B) are mixed in a 9:1 weight ratio, degassed in a vacuum chamber, cast into a cleaned silicon wafer and cured at room temperature overnight. The PDMS substrates are plasma-treated to make the surface hydrophilic before use.

D. Endothelial cell culture

Primary human umbilical vein endothelial cells (HUVECs, PromoCell GmbH) were cultured in EMG-2 (Lonza Bioscience AG) medium supplemented with 10% Fetal Bovine Serum (FBS, Gibco™, Thermo Fisher Scientific) at 37°C and 5% CO_2. HUVECs were seeded on polycarbonate membranes (thickness 50 μm, surface area 1 cm^2) cut from a CLINIcell (MABIO, France) and incubated for 4 days to form confluent cell monolayers. The culture medium was replaced on day 3, and HUVECs used were below passage 12.

Results

The first experiment with a PDMS substrate reveals that the behavior of a coated microbubble in contact with a surface depends on the microbubble's size. Fig. 1 illustrates a qualitative classification of bubble behaviour as a function of the bubble size. Following an initial phase of purely spherical oscillations, large over-resonant bubbles naturally progress into a period-doubled (half-harmonic) shape mode induced by the Faraday instability mechanism (green-labelled regime in Fig. 1). As the size of the bubble decreases, the shape mode intensity increases, causing a pronounced folding of the bubble's tip during the oblate phase of the shape mode, ultimately leading to the formation of a jet directed towards the substrate. The jet occurence is periodic and intertwined with the cyclic nature of the shape mode. As a result, its frequency is half of the ultrasound frequency, i.e., it is half-harmonic (blue-labelled regime in Fig. 1). In the case of resonant microbubbles, the extremely intense shape deformations cause the pinching-off of a daughter bubble following the rapid shrinking of the bubble's neck during the prolate phase of the shape mode. The mother bubble, now being under-resonant, is too small to sustain shape modes but its interface velocity during the compression phase is high enough to induce the formation of a jet. Since the occurrence of jetting is now unrelated to the shape modes but instead linked to volumetric oscillation, its frequency is the same as that of the acoustic driving, i.e., it is harmonic (violet-labelled regime in Fig. 1). Lastly, sub-resonant bubbles, owing to their small size, cannot sustain shape modes and only experience volumetric oscillations. Therefore, bubble manifest no splitting. Nevertheless, the interface's velocity is again enough to generate harmonic microjets during the bubble compression phases (pink-labelled regime in Fig. 1). Fig. 2 provides a more quantitative analysis of bubble behavior, illustrating how the various regimes depend on both bubble size and the applied acoustic pressure.
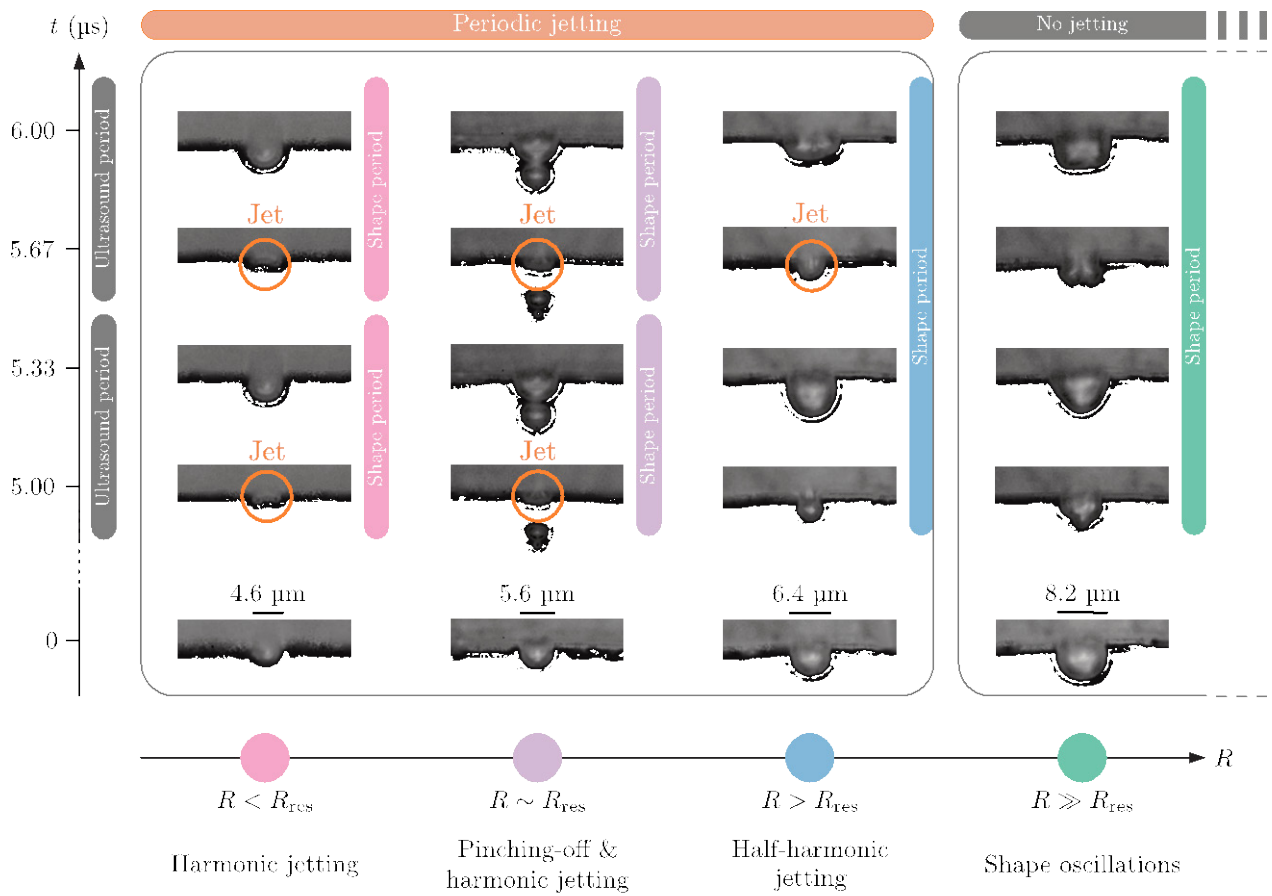
Figure 1: Classification of the behaviour of a bubble in contact with a substrate as a function of its size. Three different regimes of stable and repeated jetting can be identified.
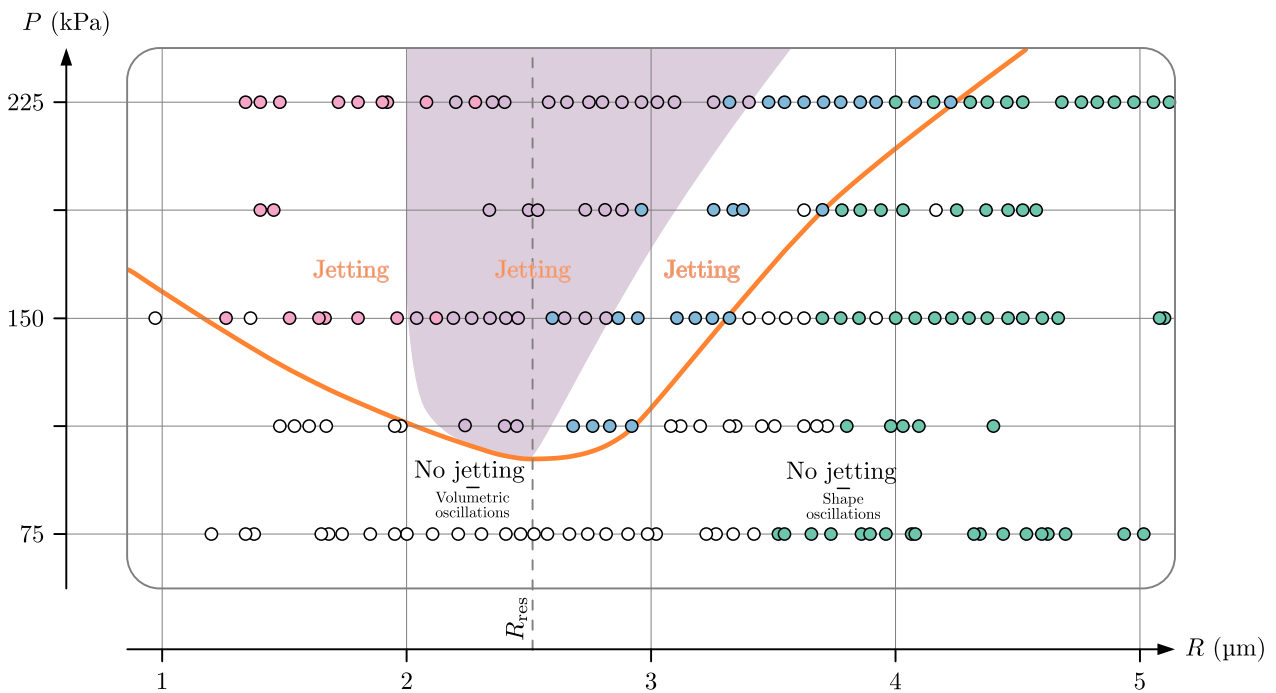
Figure 2: Bubble behaviour regime map based on bubble size and driving acoustic pressure.

The emergence of jetting is observed to initiate at approximately 100 kPa of acoustic pressure when bubbles are at their resonance size. As the pressure increases, the spectrum of bubble sizes capable of producing jets widens toward both smaller and larger bubbles, covering the entire range of bubble sizes typically used in therapy at a pressure of around 200-250 kPa. We also note that the pinching-off regime (in violet) extends toward larger bubbles as the increase in acoustic pressure intensifies the shape mode amplitude but not toward small bubbles since the shape mode occurrence is solely contingent on the bubble size.

The second experiment with the endothelial cell monolayer confirms the observations reported so far. In Fig. 3, a slightly over-resonant bubble in contact with a cell after an initial cycle of spherical oscillation (first row of images) develops an intense shape mode which triggers the formation of a jet directed toward the cell during the compression phase of the oblate stage (second row of images). Conversely, in the prolate stage, the neck of the bubble contracts, causing its division (third row of images). However, the splitting is not permanent, and the bubble ultimately reunites and continues to manifest a shape mode and half-harmonic jetting in the subsequent ultrasound cycles (fourth and fifth rows of images). Hence, this bubble behaviour can be classified within the "half-harmonic jetting" regime.
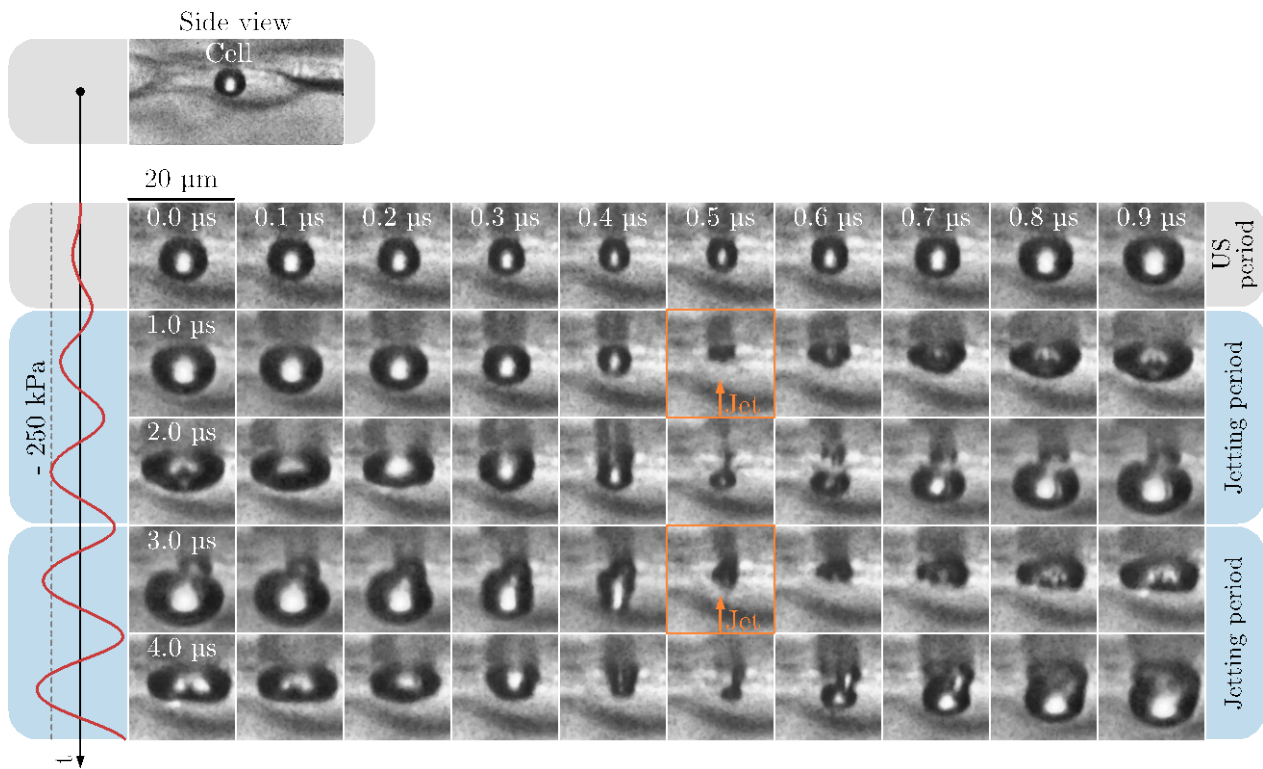
Figure 3: Image sequence of an ultrasound-driven microbubble in contact with an endothelial cell, featuring half-harmonic jetting.

In Fig. 4, an under-resonant bubble sitting on top of a cell is too small to exhibit any shape mode but nontheless it does manifest repeated jets directed toward the cell due to the strong asymettric compression it undergoes at every ultrasound cycle (third, fourth and fifth rows of images) after an initial ramping-up period (first and second rows of images). Therefore, this bubble behaviour can be classified within the "harmonic jetting" regime.
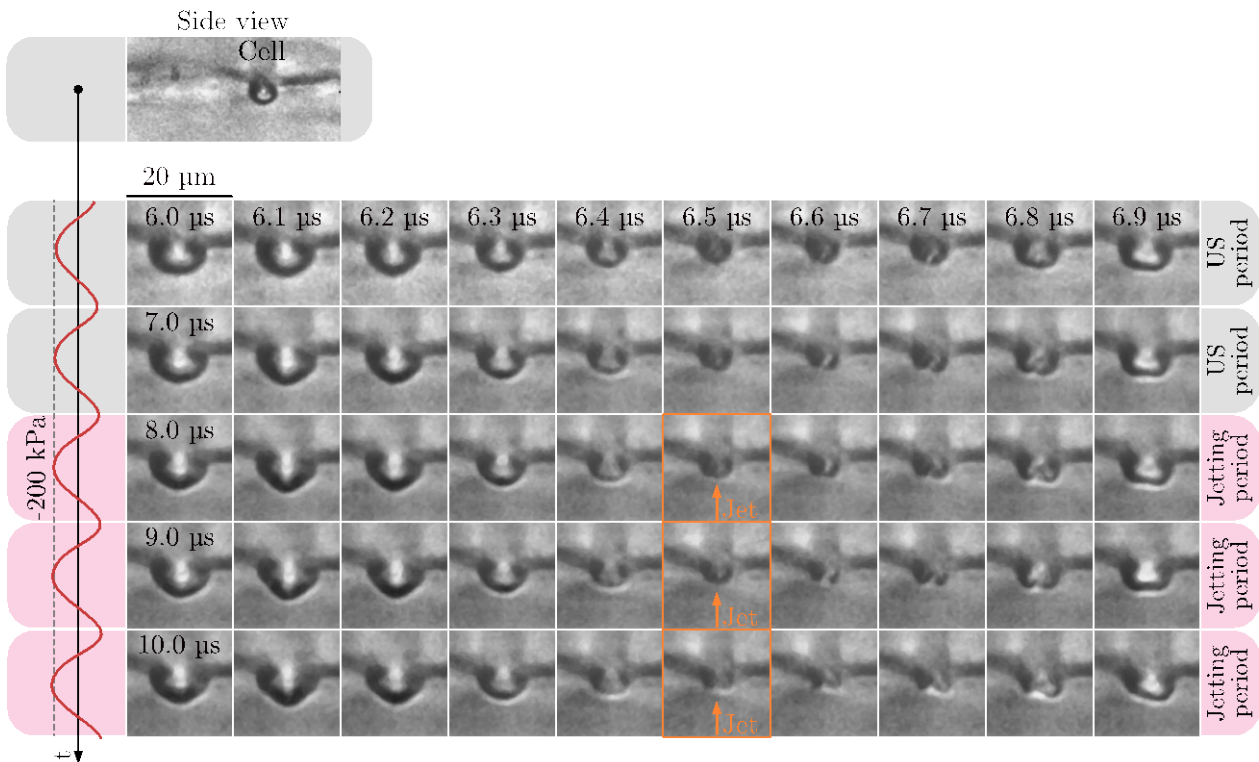
Figure 4: Image sequence of an ultrasound-driven microbubble in contact with an endothelial cell, featuring harmonic jetting.

Conclusions

Using time-resolved side-view visualizations, we elucidate the interactions between single coated microbubbles and an endothelial cell monolayer when exposed to ultrasound. Our investigation reveals the stable and repeated occurrence of jets directed toward the cell substrate at acoustic driving pressures as low as 100 kPa for resonant bubbles and 200-250 kPa regardless of the bubble size. Given the damage potential of liquid jets, this finding suggests that the main contributing factor to enhanced cell permeabilization may be the occurrence of periodic jets. We also provide evidence for the existence of three distinct jetting regimes dependent on the bubble's size: half-harmonic jetting for over-resonant bubbles, transition from half-harmonic to harmonic jetting following bubble splitting for resonant bubbles and harmonic jetting for under-resonant bubbles. Finally, we pinpoint shape modes as the pivotal factor that governs and dictates the jetting regime.

Acknowledgments

References

[1]. Sierra C, *et al*., Lipid microbubbles as a vehicle for targeted drug delivery using focused ultrasound-induced blood-brain barrier opening, Journal of Cerebral Blood Flow and Metabolism*, 37.4, 2017.

[2]. Van Wamel A, *et al*., Vibrating microbubbles poking individual cells: Drug transfer into cells via sonoporation, Journal of Controlled Release, 112.2, 2006.

[3]. Helfield B, *et al*., Biophysical insight into mech- anisms of sonoporation, Proceedings of the National Academy of Sciences, 113.36, 2016.

[4]. Philippe M and Hilgenfeldt S, Controlled vesicle deformation and lysis by single oscillating bubbles, Nature, 423.6936, 2003.

[5]. Zhou Y, *et al.*, Controlled permeation of cell membrane by single bubble acoustic cavitation, Journal of Controlled Release, 157.1, 2012.

[6]. Prentice P, *et al*., Membrane disruption by optically controlled microbubble cavitation, Nature Physics, 1.2, 2005.

[7]. Kooiman K, *et al.*, Sonoporation of endothelial cells by vibrating targeted microbubbles, Journal of Controlled Release, 154.1, 2011.

Ultrasound and Biodegradable Cavitation Nuclei for Needle-Free Transdermal Vaccination

**Joel P. R. Balkaran**[1], Brian Lyons[1], Johanna K. Hettinga[1], Darcy Dunn-Lawless[1], Michael D. Gray[1], Constantin C-Coussios[1], Robert C. Carlisle[1]

[1]_Institute of Biomedical Engineering (IBME), University of Oxford, Oxford, U.K._
Corresponding author: joel.balkaran@eng.ox.ac.uk

Introduction

Despite the advent of improved vaccine technologies like mRNA therapeutics, immunisation still primarily targets muscle tissue using needle and syringe (N+S) delivery. [1] In contrast to the 'immune desert' that is muscle tissue, the rich immune millieu within the skin makes it a much more desirable target organ. However, reproducible transdermal/transcutaneous delivery remains elusive. [2,3] N+S delivery also remains painful, and needlephobia persists as one of the primary reasons people abstain from regular vaccinations. [4] Cavitation nuclei (CN) could allow for ultrasound (US)-mediated needle-free vaccination into the skin, however current CN are unsuitable due to their short activity-life (vaccines must be stable over long periods of time), non-biocompatibility, or varied response. [5,6] We thus hypothesised that a new biodegradable CN species could be designed to be applied topically and produce sustained inertial cavitation, quantified in real-time by Passive Cavitation Detection (PCD) during focused US exposure, to deliver a vaccine agent transcutaneously. [7] Reporter plasmid DNA (pLuc) was chosen to take advantage of the multiplicative effect of genetic delivery, and this allowed quantification of gene expression by bioluminescence and of gene delivery by qPCR. Finally, the adaptive immune response was assessed by measurement of antibodies raised against the expressed protein, with the aim of demonstrating the potential for a non-invasive vaccine delivery alternative.

Methods

- Protein-derived biodegradable CN were made by sonication with an organic volatile phase followed by lyophilisation, then characterised by size, zeta potential, concentration, and cavitation profile.

- Focused US (FUS) was used (265kHz, 10% duty cycle, 10Hz PRF, 1.7MPa PNP) to insonify the CN together with pLuc topically to anaesthetised (shaved and depilated) mice for 2 minutes (Fig 1).

- Passive cavitation detection was performed using a single-element focused 5-MHz receiver transducer confocally and co-axially aligned with the FUS source, with signals high-pass-filtered above 1.8 MHz.

- DNA expression was quantified by IVIS after 24 hours, and delivery efficacy assessed by qPCR of skin at 0 and 24 hours post pDNA administration.

- Antibody response to luciferase protein was assessed by ELISA of tail-bleeds drawn in 7-day intervals.
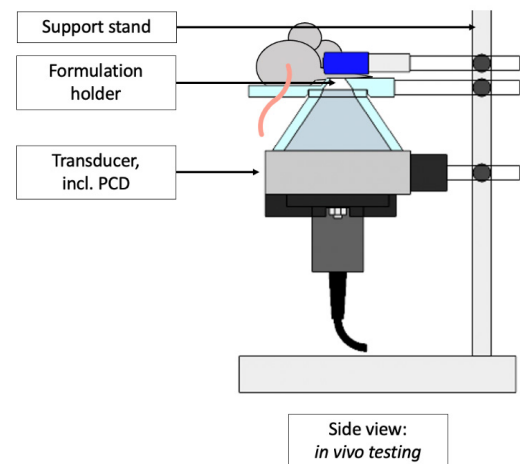
Fig. 1: Schematic of ultrasound setup for _in vivo_ application

Results

Our synthesis approach was able to produce a novel solid biodegradable CN species, with a median hydrodynamic diameter of 154 ± 10nm per DLS measurements verified by single-particle nanoparticle tracking analysis (NTA). The particle concentration by NTA was found to be 3E10 ± 4E9 particles per mL

(Fig 2a). *In vivo* delivery quantification following cavitation-enhanced transdermal delivery showed that only 0.08% of the DNA administered entered the skin, compared to 92% for N+S ID injection (Fig 2b). However, DNA expression quantified by IVIS luminescence for the cavitation-enhanced transdermal delivery mice (1.5E6 ± 5E5 A.U.) was on par with N+S intradermal injection (1.7E6 ± 1.9E6). Antibody quantification (Fig 2c) showed that US-treated mice had significantly (p=0.02) more systemic antibodies after 42 days (78ng/mL ± 44ng/mL) than ID injected mice (7ng/mL ± 2ng/mL). Notably, this therapeutic outcome was not observed in US-only controls, indicating that the acoustic stimulation of the novel CN was responsible for this enhanced delivery, expression and immune response.
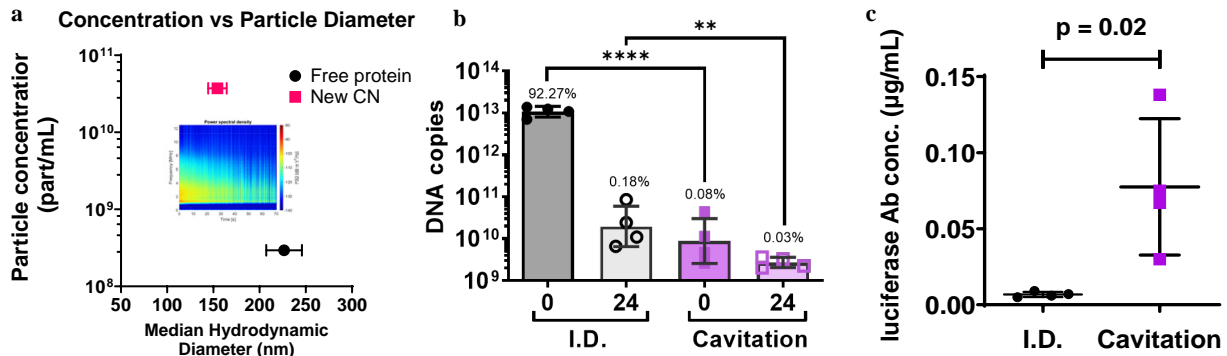
Fig 2. a- Concentration vs size characterisation of unreacted protein and novel CN with spectrogram for 60s of US stimulation of CN inset; b- DNA copies detected by qPCR at 0hr and 24hr timepoints for ID injection and cavitation delivery, c- absolute anti-luciferase antibody concentration in blood 42-days post treatment with boost at 21-days for ID injection and cavitation

Conclusions

New solid biodegradable CN were produced, characterised, and used for cavitation-enhanced transdermal DNA delivery with US. In spite of less DNA vector crossing the skin, the level of local gene expression was comparable to intradermal delivery , and a superior systemic immune response was observed after 42 days. Cavitation-enhanced, cavitation-monitored delivery therefore potentially provides a viable platform for needle-free vaccination that could require significantly lower doses of genetic vaccines to be produced.

References

[1] W. Zhang and S. Wang, "Effect of vaccine administration modality on immunogenicity and efficacy," Exp Rev of Vac, 2015.

[2] D. Chaplin, "Overview of the immune response," J of Allergy and Clin Imm, 2010.

[3] P. H. Lambert and P. E. Laurent, "Intradermal vaccine delivery: will new delivery systems transform vaccine administration?," Vaccine, 2008.

[4] J. Hamilton, "Needle Phobia: A Neglected Diagnosis," Journal of Family Practice, 1995

[5] H. Tang, et al, "An Investigation of the Role of Cavitation in Low-Frequency Ultrasound-Mediated Transdermal Drug Transport," Pharm Res, 2002.

[6] S. Bhatnagar, H. Schiffter and C. Coussios, "Exploitation of Acoustic Cavitation-Induced Microstreaming to Enhance Molecular Transport," J of Pharm Sci, 2014.

[7] J. Hettinga, B. Lyons, J. Balkaran, P. Rijal, D. Dunn-Lawless, L. Caproni, M. Gray, K. Suslick, C. Coussios, and R. Carlisle, "Cavitation-Mediated Transcutaneous Delivery of Protein and Nucleotide-based Antigen for Rapid High-level Immune Responses," Advanced Therapeutics, 2023.

Ultrasound Targeted Microbubble Cavitation (UTMC) for the treatment of Myocardial Microvascular Obstruction (MVO)

*Muhammad Wahab Amjad, Soheb Anwar Mohammed, Xucai Chen, Flordeliza S. Villanueva, John J. Pacella*1*

Center for Ultrasound Molecular Imaging and Therapeutics, Heart and Vascular Medicine Institute, University of Pittsburgh, Pittsburgh, PA, USA

Introduction

Cardiovascular disease (CVD) is the leading cause of global death. In 2019, 17.9 million people died from CVD, 85% of which were due to acute myocardial infarction (AMI) [1]. Post-AMI congestive heart failure is increasing due to microvascular obstruction (MVO). MVO is the blockage of the microcirculation by atherothrombotic debris and tends to occur after coronary stenting for AMI, resulting in hypoperfusion. Current therapeutic strategies for MVO are not consistently effective. Hence, we have been developing ultrasound (US)-targeted microbubble cavitation (UTMC) as a potential treatment for MVO.

Methods

Initially, we demonstrated the efficacy of UTMC in a rat hindlimb model of MVO [2]. Given these promising findings, in the current work, we expanded our investigation to a clinically relevant large animal model. Rapacz familial hypercholesterolemic (RFH) pigs were used to carry out the experiments [3]. The study protocol is shown in Figure 1. On day 1, left anterior descending (LAD) microcirculation was embolized with a clot mixture after mid-LAD balloon occlusion (20 min), to cause a reduction in microvascular perfusion (assessed by myocardial contrast echocardiography, MCE) and thus to create MVO. The MVO in the LAD bed was then treated with UTMC therapy during concurrent infusion of Definity® contrast agent. The therapeutic ultrasound was delivered with a customized ultrasound imaging system (Philips EpiQ with S5-1 probe) with long tone bursts (1.3 MHz center frequency, 1.3 MPa peak negative pressure, 1 ms pulse duration). The perfusion was reassessed with MCE post UTMC. Cardiac MRI was obtained at 36 hours to measure infarct size and area of MVO. At 48 hours post UTMC therapy, MCE was repeated, the heart was stained with Evans Blue, the animals were euthanized, and the hearts were sectioned for tetrazolium chloride (TTC) analysis of infarct size. There were 4 MCE measurement time points i.e., baseline, during balloon occlusion, during MVO, and 48 hours post UTMC treatment (*n*=6). Analysis was conducted with 2D echocardiography, MCE, measurement of infarct size using MRI and measurement of risk area/infarct size using TTC/Evans Blue. Control animals did not receive UTMC (MVO, no treatment) (*n*=5).
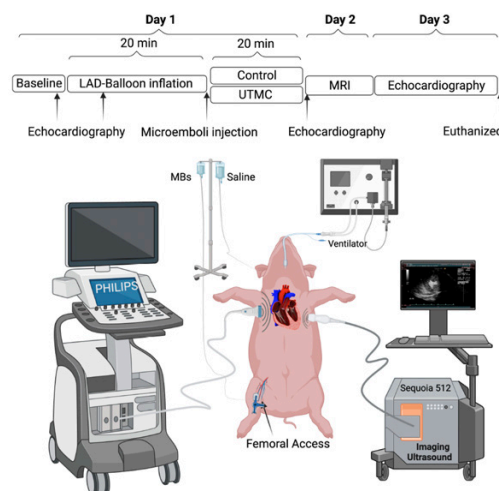
Figure 1. Schematic showing key time points of the study and pictorial representation of experimental setup.

Results

LAD angiographic flow was improved at 48 hours post UTMC treatment in comparison to control. 2D echographic imaging revealed that the UTMC treatment significantly improved LV systolic performance, measured by fractional left ventricular area change, as compared to control. Also, compared to control, UTMC was found to significantly enhance LAD blood volume 48 hours post treatment (Figure 2). MRI clips showed that UTMC ameliorated MVO. MRI derived left ventricular (LV) segmental wall motion and ejection fraction (EF) also improved after UTMC treatment versus control. Infarct size was reduced as shown by both Evans Blue/TTC staining and MRI.
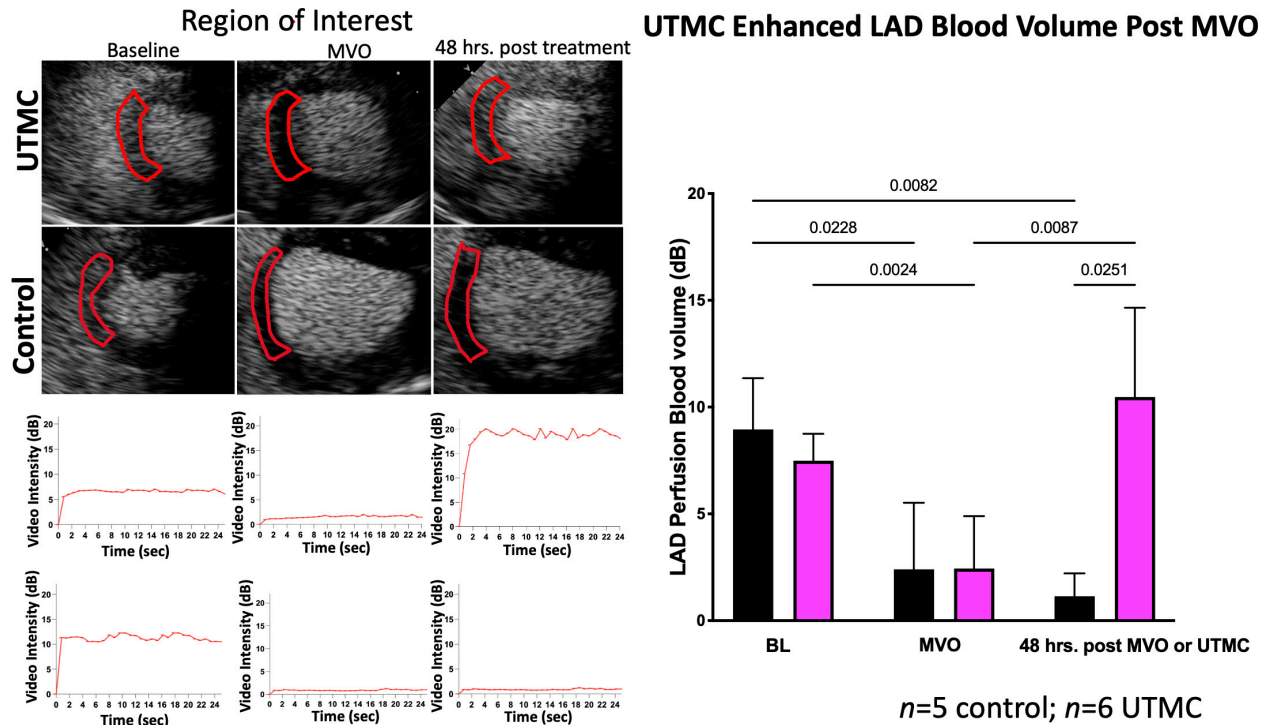
Figure 2. MCE images showing the LAD bed (outlined in red) and video intensity curves of baseline, MVO and 48h post treatment at different time points. The graph on the right shows LAD bed microvascular blood volume.

Conclusions

This is the first study to demonstrate the efficacy of UTMC for the treatment of isolated myocardial MVO in a clinically relevant large animal model. This was determined through a comprehensive analysis comprising cineangiography, 2D echocardiography, MCE, MRI, and Evans Blue/TTC staining. Taken together, we demonstrated that UTMC significantly reduced infarct size, enhanced LAD microvascular perfusion and improved LV systolic performance, and should enable clinical translation of this promising therapy.

References

[1]. World Health Organization, Cardiovascular diseases (CVDs) key facts, (2021). https://www.who.int/news-room/fact-sheets/detail/cardiovascular-diseases-(cvds).

[2]. Yu FTH, Amjad MW, Mohammed SA, Yu GZ, Chen X, Pacella JJ, Effect of Ultrasound Pulse Length on Sonoreperfusion Therapy, Ultrasound in Medicine & Biology, Volume 49, Issue 1, 2023.

[3]. Porras AM, Shanmuganayagam D, Meudt JJ, Krueger CG, Reed JD, Masters KS. Gene Expression Profiling of Valvular Interstitial Cells in Rapacz Familial Hypercholesterolemic Swine. Genom Data. 2014 Dec 1;2:261-263.

Microbubble-mediated endothelial cell-cell contact opening is induced by F-actin stress fiber severing and recoil

B. Meijlink[1], H.R. van der Kooij[1], Y. Wang[1], H. Li[1], S. Huveneers[2], K. Kooiman[1]

[1] _Department of Biomedical Engineering, Erasmus MC, Rotterdam, the Netherlands_
[2] _Department of Medical Biochemistry, Amsterdam UMC, Amsterdam, the Netherlands_
Corresponding author: k.meijlink@erasmusmc.nl

Introduction

The delivery of drugs to diseased tissue can be enhanced by increasing the vascular permeability using ultrasound (US) activated microbubbles (MBs). Understanding the mechanism behind this treatment is crucial for safe and efficient use in the clinic. Treating endothelial cells with ocsillating MBs can induce sonoporation, subsequently followed by opening of cell-cell contacts [1,2], and tunnel formation [3] through the cell. Although MB behaviour could predict sonoporation in these studies [1-3], it could not explain the other cellular responses. This suggests a cellular component may be involved in this process. A possible component could be the filamentous (F)-actin cytoskeleton, and specifically stress fibers, since these are directly linked to cell adhesion proteins as well as involved in the creation thereof [4]. Besides, the F-actin network is involved in transcellular tunnel formation [5]. Recently, a US and MB study showed that the F-actin network can be disrupted and was involved in the subsequent recovery of the cell membrane upon sonoporation [6]. However, the role of F-actin during MB-mediated cell-cell contact opening and tunnel formation has not been reported and was the aim of our study.

Methods

The F-actin network of human umbilical vein endothelial cells was genetically labelled using a lentiviral Lifeact-GFP construct after which the cells were grown to full confluency in a CLINIcell (50 µm membrane, Mabio). Homemade DSPC-based MBs stained with Biotracker Blue dye were added. Cells were incubated with Propidium Iodide and Cell Mask Deep Red dye to visualize sonoporation, cell membranes, and cellular junctions. Cells were incubated without or with Y-27632 (10 µM final concentration) for 1 h before imaging to diminish F-actin stress fibers [7]. The sample was placed in a 37° C waterbath which was part of a custom build imaging setup consisting of a Nikon A1R+ confocal microscope, to record cellular behaviour, coupled with a Shimadzu HPV-X2 ultra-high-speed camera (10 Mfps), to record microbubble behaviour. The cellular response and microbubble behaviour were simultaneously imaged during a 4-min timelapse in which US (2 MHz, 10 cycles, 350 kPa PNP) was applied at t=0. Additionally, a 3D z-stack confocal microscopy image was made before and after the timelapse. MB radius (R) over time and excursion amplitude ($R_{max}-R_0$) were analyzed. The distance between the MB and the stress fibers in the cell of interest was analysed using the intersection of a stress fiber with a spherical coordinate system centered at the MB. Significance was assessed using Welch's t-test in SPSS.

Results

The cellular response of cells to a US and a single MB treatment without Y-27632 was investigated in 31 cells. Fig 1A shows a typical example of a cell upon treatment where disruption of the F-actin network and severing of stress fibers was observed at the location of the MB. This was followed by the recoil of the severed fibers, opening of cell-cell junctions, and retraction of the cell within 15 s after treatment. The recoil of the stress fibers always occurred along the longitudinal direction of the fibers. In other cells, the ultrasound-activated MB induced F-actin disruption only or disruption and recovery. F-actin remodeling was only observed upon sonoporation. (Fig. 1B). Opening of cell-cell contacts within 15 s after sonoporation was mainly observed in cells with recoiling stress fibers (occurrence of 54%). With non-resealing membrane pores, F-actin remained disrupted whereas all resealing pores showed F-actin disruption and recovery. For non-sonoporated cells, the MB excursion was significantly lower compared to all disrupted F-actin

conditions. No significant differences in MB excursion were observed between the F-actin remodeling types. The severed stress fibers were at a mean distance of 2.1 μm (IQR = 1.6) from the MB center, which was significantly lower than 5.7 μm (IQR = 6.3) for non-severed stress fibers. When cells were incubated with Y-27632, the F-actin stress fibers decreased as shown in Fig. 1C. In 17 cells incubated with Y-27632, disruption only (Fig. 1 C) and disruption and recovery were observed upon MB oscillation. However, no F-actin stress fiber severing and recoil and opening of cell-cell contacts were observed (Fig. 1D).

Conclusions

To the best of our knowledge, this is the first study showing that cell-cell contact opening within 15 s upon sonoporation is a result of F-actin stress fiber severing. In addition, F-actin remodeling was only observed upon sonoporation. Although the MB excursion could not predict the type of F-actin remodeling upon sonoporation, the location of the MB in relation to the stress fibers was a significant factor. In the absence of stress fibers, cell-cell contact opening was abolished, which further emphasizes the importance of F-actin stress fibers in the process of cell-cell contact opening. These new insights can be used to predict where cell-cell opening will occur, thereby aiding in improving the controllability of microbubble-mediated drug delivery.
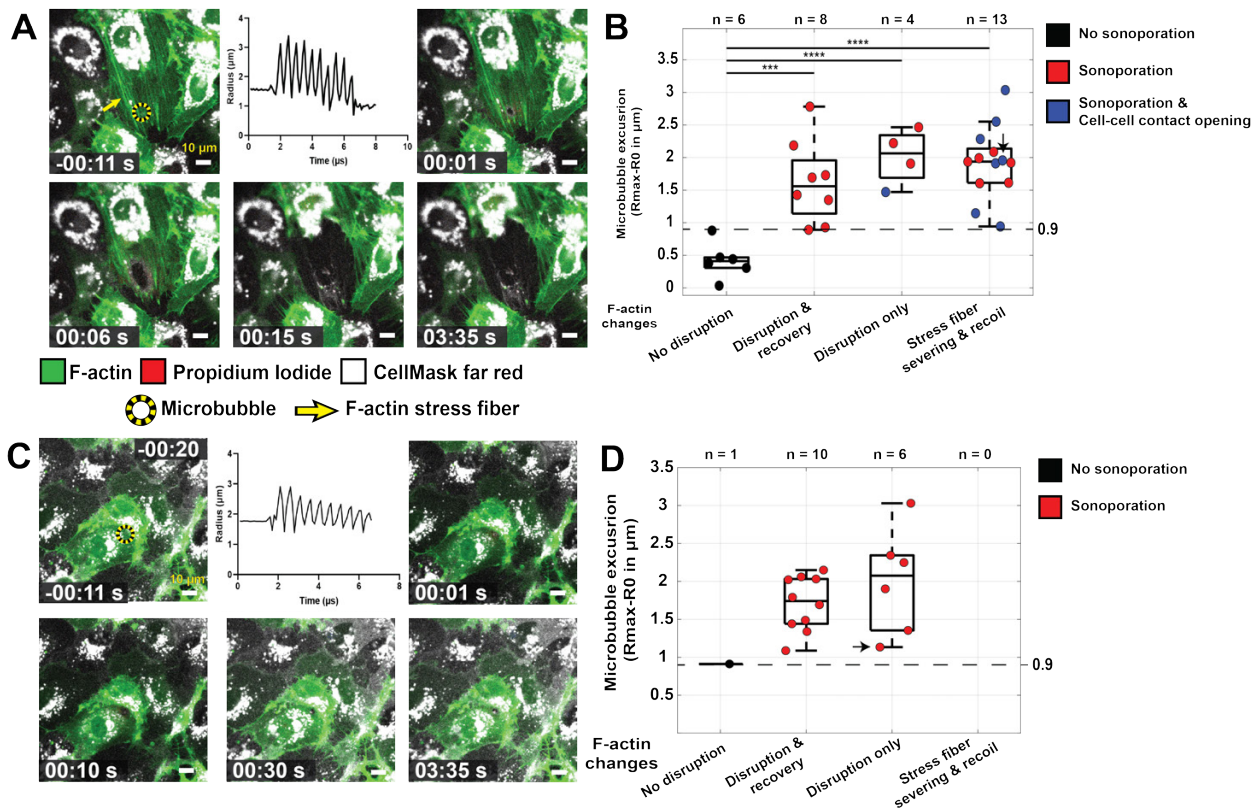
Figure 1: F-actin remodelling upon ultrasound and single MB treatment. A) Example of cellular response (fluorescent images) and MB behaviour at t=0 (radius-time curve) showing F-actin disruption and stress fiber (one example at yellow arrow) severing at the MB location (yellow dotted circle) upon sonoporation. This severing induced the recoil of stress fibres resulting in cell-cell contact opening within 15 sec after US treatment. **B)** Quantification of the MB excursion, F-actin changes, and cellular effects (point colours). **C)** Example of cellular response (fluorescent images) and MB behaviour at t=0 (radius-time curve) showing F-actin disruption only in absence of stress fibres in Y- 27632 treated cells. **D)** Quantification of the MB excursion, F-actin changes, and cellular effects (point colours) in Y- 27632 treated cells. Significance is shown with ***= p< 0.001, ****= p< 0.0001. Bar graphs show the median, interquartile range, and 5-95% interval with whiskers. The dotted lines in B and D show the 0.9 μm sonoporation threshold [3]. Arrows in B and D indicate the examples shown in A and C.

References

[1]. Helfield B, Chen X, Watkins SC, Villanueva FS, Biophysical insight into mechanisms of sonoporation. Proc Natl Acad Sci, 113(36):9983-8, 2016

[2]. Beekers I, Vegter M, Lattwein KR, Mastik F, Beurskens R, van der Steen AFW, de Jong N, Verweij MD, Kooiman K, Opening of endothelial cell-cell contacts due to sonoporation. J Control Release, 322:426-438, 2020

[3]. Beekers I, Langeveld SAG, Meijlink B, van der Steen AFW, de Jong N, Verweij MD, Kooiman K, Internalization of targeted microbubbles by endothelial cells and drug delivery by pores and tunnels, J Control Release, 347:460-475, 2022

[4]. Burridge K, Guilluy C, Focal adhesions, stress fibers and mechanical tension, Exp Cell Res, 343(1):14-20, 2016

[5]. Ng WP, Webster KD, Stefani C, Schmid EM, Lemichez E, Bassereau P, Fletcher DA, Force-induced transcellular tunnel formation in endothelial cells, Mol Biol Cell, 28(20):2650–60, 2017

[6]. Jia C, Shi J, Han T, Yu ACH, Qin P, Spatiotemporal Dynamics and Mechanisms of Actin Cytoskeletal Remodeling in Cells Perforated by Ultrasound-Driven Microbubbles, Ultrasound Med Biol, 48(5):760-777, 2022

[7]. Katoh K, Kano Y, Amano M, Onishi H, Kaibuchi K, Fujiwara K, Rho-kinase-mediated contraction of isolated stress fibers. J Cell Biol, 153(3):569-84, 2001

3D Ultrafast amplitude modulation for molecular ultrasound imaging of stationary microbubbles targeted to inflammation

G. Chabouh[1], L. Fournier[2], M. Abioui-Mourgues[3], L. Denis[1], D. Vivien[3,4], C. Orset[3], C. Chauvierre[2], O. Couture[1]

[1]_Sorbonne Université, CNRS, INSERM, Laboratoire d'Imagerie Biomédicale, Paris, France_
[2]_Université Paris Cité, Université Sorbonne Paris Nord, UMR-S U1148 INSERM, Laboratory for Vascular Translational Science (LVTS), Paris, France_
[3]_Normandie University, UNICAEN, INSERM UMR-S U1237, Physiopathology and Imaging of Neurological Disorders (PhIND), GIP Cyceron, Institut BB@C, Caen, France_
[4]_Department of clinical research, Caen-Normandie University Hospital, Caen, France_
Corresponding author: georges.chabouh@sorbonne-universite.fr

Introduction

Central nervous system (CNS) inflammation is a prominent trait seen in neurodegenerative diseases, including common conditions such as Alzheimer's disease. Microbubbles (MBs) find extensive utility in the medical field beyond their imaging capabilities. They can be functionalized by attaching ligands to their surfaces, facilitating binding to specific target molecules (**Kooiman, 2014**). Previously, we introduced polymer-coated MBs with fucoidan functionalization that are sensitive to inflammation (**Li et al., 2019**), resulting in the demonstration of effective and targeted stroke treatment (**Fournier et al., 2023**). These functionalized MBs were shown to be ultrasound sensitive and compatible with 3D Ultrasound Localization Microscopy (ULM) through intact mouse brain with a multiplexed 32x32 matrix probe (**Chavignon et al., 2021**).

Ultrasound molecular imaging remains challenging as the signal from the adhered MBs can be mixed with the one of the tissues with the current spatiotemporal filters. In this work, we developed a 3D ultrafast amplitude modulation ultrasound sequence that would enable volumetric ultrasound imaging of stationary targeted microbubbles.

Methods

Polymer MBs functionalized with fucoidan are produced through an acoustic cavitation protocol that relies on three primary components. Isobutyl cyanoacrylate (IBCA) forms the structural basis of the polymeric shell. Perfluorobutane (PFB) contributes to the stability of fucoMB due to its inert properties. Fucoidan, a sulfated polysaccharide, serves as the targeting agent for activated endothelium and activated platelets, owing to its affinity for P-selectins. The targeting capabilities of the incorporated fucoMBs were validated in-vitro using a microfluidic assay involving activated human platelets and in-vivo on a mouse stroke model (**Fournier et al., 2023**).

Ultrasound acquisitions were then performed with a 256-channels research ultrasound scanner (verasonics, Kirkland, USA) and an 5.6 MHz multiplexed 32x32 matrix probe (Vermon, France). The 3D ultrafast amplitude modulation sequence is a modified version of the classical multiplexed sequence. It is characterized by modulated amplitudes: two bursts with half amplitude, achieved by muting the odd and even elements of the transducer, and one burst with full amplitude. Following reception, we apply a subtraction operation to eliminate the linear signal while capturing distinct nonlinear responses of the fucoMB (**Averkou et al., 2020).**

In-vitro validation on stationnary fucoMB were studied through a home-made setup. The US phantom employed was a tissue mimicking Doppler flow phantom (ATS Laboratories, CIRS) with a wall-less channel of 2 mm in diameter at 10 mm depth. Flow rate was modulated using butterfly valves to stop the flow.

Results

The fucoMBs were ultrasound senstive and their signal was even captured through the skull of a healthy mice in-vivo (**Fig1a**). With multiple bolus injection of 50 µL/min for a total of 8 minutes, 3D ULM was construced revealing the microvsculature of the mouse brain.

In-vitro, the non-linear signal of the fucoMBs is enhanced with a CTR up to 10 dB **Fig1c-d** compared to almost no signal in the Bmode image (**Fig1b**). Beyond certain driving amplitude (8V in this case), the targeted MBs undergo disruption (**Fig1e** before burst and **f** after burst) with the intensity peaking at 32 dB before dropping back to the noise level (**Fig1g**).
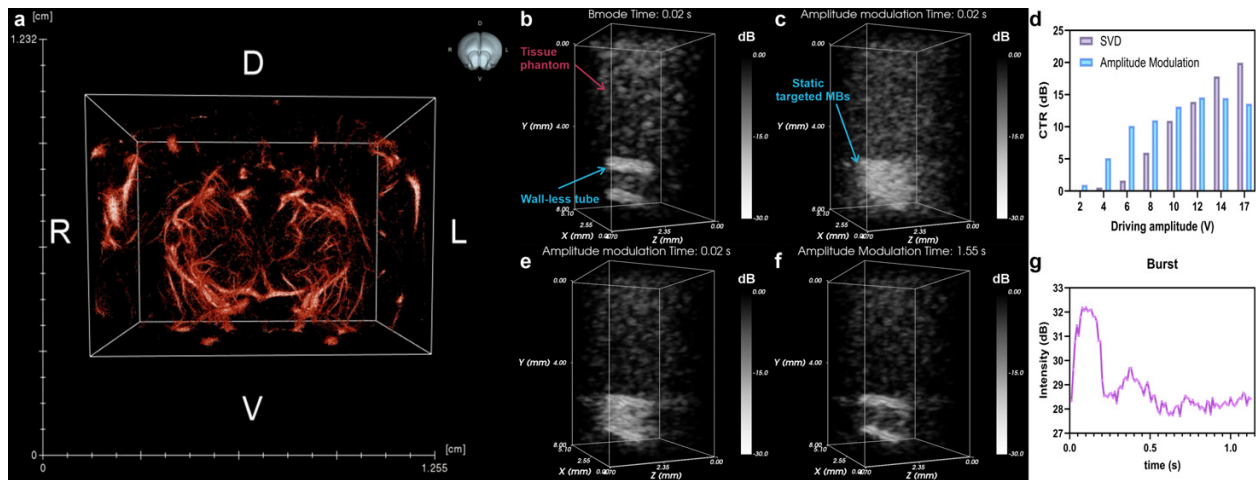
Figure 1 a) 3D in-vivo transcranial ULM on healthy mouse brain with Fucoidan polymer MBs. 3D in-vitro tissue mimicking phantom **b)** Bmode **c)** Amplitude modulation (AM) signal of stationary MBs **e)** AM signal before burst and **f)** after burst, **g)** Intensity of the burst AM signal during one acquisition bloc and **d)** Contrast-to-tissue ratio (CTR) for AM signal of stationary MBs Vs singular value decomposition (SVD) in function of different driving voltages.

Conclusions

The singular value decomposition (SVD) is so far the most used clutter filter in ULM. Unfortunately, it cannot distinguish slow-moving or stationnary MBs from tissues, thus it hinders the ultrasound molecular imaging since the adhered microbubble will be removed.

Here, we developed a 3D non-linear pulsing schemes that enables imaging slow-moving and stationnary MBs as well as an on-demand burst of the adhered MBs.

We showed that fucoidan polymer microbubbles that can target P-selectin are ultrasound sensitive through intract mouse brain and permit 3D ULM. The final goal is to perform transcranial molecular ULM (mULM) of neuro-inflammation.

References

[1]. Kooiman, K., Vos, H. J., Versluis, M., & De Jong, N. Acoustic behavior of microbubbles and implications for drug delivery. *Advanced drug delivery reviews*, *72*, 28-48, 2014.

[2]. Li, B., Aid-Launais, R., Labour, M. N., Zenych, A., Juenet, M., Choqueux, C., ... & Chauvierre, C. Functionalized polymer microbubbles as new molecular ultrasound contrast agent to target P-selectin in thrombus. *Biomaterials*, *194*, 139-150, 2019.

[3]. Fournier L, Abioui-Mourgues M, Chabouh G, Aid R, De La Taille T, Couture O, Vivien D, Orset C, Chauviere C, rtPA-loaded fucoidan polymer microbubbles for the targeted treatment of stroke. Biomaterials, (https://doi.org/10.1016/j.biomaterials.2023.122385), 2023.

[4]. Chavignon A, Heiles B, Hingot V, Orset C, Vivien D, Couture O, 3D transcranial ultrasound localization microscopy in the rat brain with a multiplexed matrix probe. IEEE TBE, 69, 2021.

[5]. Averkiou, M. A., Bruce, M. F., Powers, J. E., Sheeran, P. S., & Burns, P. N. Imaging methods for ultrasound contrast agents. *Ultrasound in medicine & biology*, *46*(3), 498-517, 2020.

Ultrasound particle image velocimetry to investigate potential hemodynamic causes of limb thrombosis after endovascular aneurysm repair with the Anaconda endograft

**H. Mirgolbabaee**[1,2], **L. van de Velde**[1,2,3], **R. H. Geelkerken**[1,4], **M. Versluis**[2], **E. Groot Jebbink**[1,3], **M. M. P. J. Reijnen**[1,3]

[1]_Multi-Modality Medical Imaging (M3I) Group, Technical Medical Centre, University of Twente, Enschede, The Netherlands_
[2]_Physics of Fluids (PoF) Group, Technical Medical Centre, University of Twente, Enschede, the Netherlands_
[3]_Department of Vascular Surgery, Rijnstate Hospital, Arnhem, the Netherlands_
[4]_Section of Vascular Surgery, Department of Surgery, Medisch Spectrum Twente, Enschede, The Netherlands_
Corresponding author: h.mirgolbabaee@utwente.nl

Introduction

Endograft limb thrombosis (LT) is a clinical relevant complication following endovascular aneurysm repair (EVAR) [1, 2]. Patients suffering from LT may be asymptomatic, but do often develop symptoms such as intermittent claudication or acute limb threatening ischemia, impacting the quality of life and therefore LT regularly requires a reintervention [3]. The Anaconda endograft (Terumo Aortic, Inchinnan, Scotland, UK) has been reported to have a high limb occlusion rate [1]. Its independent ring design makes it kink-resistant and flexible; however, this may also cause cribs and valley's to form that may induce unfavorable local flow patterns (e.g., fluid stasis and recirculation zones), eventually causing thrombus formation and LT [4].

Methods

An in-vitro flow setup consisting of a thin-walled patient-specific AAA flow phantom was fabricated. This phantom was designed using the latest post-operative computed tomography angiography scan of the patient before an occlusion occurred in the left graft limb. Contrast-enhanced ultrasound particle image velocimetry (echoPIV) was performed to quantify time-resolved velocity fields of both iliac arteries. Measurements were performed in the same phantom with and without the Anaconda endograft, to investigate the impact of the endograft on the local flow fields. Representing hemodynamic parameters vector complexity (VC) and residence time (RT) were calculated for both iliac arteries.

Results

In both limbs, the vector fields were mostly unidirectional during systolic and end-systolic velocity phases before and after endograft placement (Fig. 1 and Fig. 2, respectively). Local vortical structures and complex flow fields were observed at the diastolic and transitional flow phases. The average VC was higher (0.11) in the phantom with endograft, compared to the phantom without endograft (0.05). Notably, in both left and right iliac arteries, the anterior wall regions corresponded to a two- and four-fold increase in VC in the phantom with endograft, respectively. A higher RT (up to 25 s) was observed in the phantom with endograft, in which the left iliac artery, with LT in follow-up, showed two fluid stasis regions.

Conclusions

This in-vitro study shows that unfavorable hemodynamics are present in the limb that presented with LT, compared to the non-thrombosed side, with higher VC and longer RT. These parameters might thus be valuable in predicting the occurrence of LT. Future studies with larger sample sizes must be done to further evaluate these hemodynamic norms.
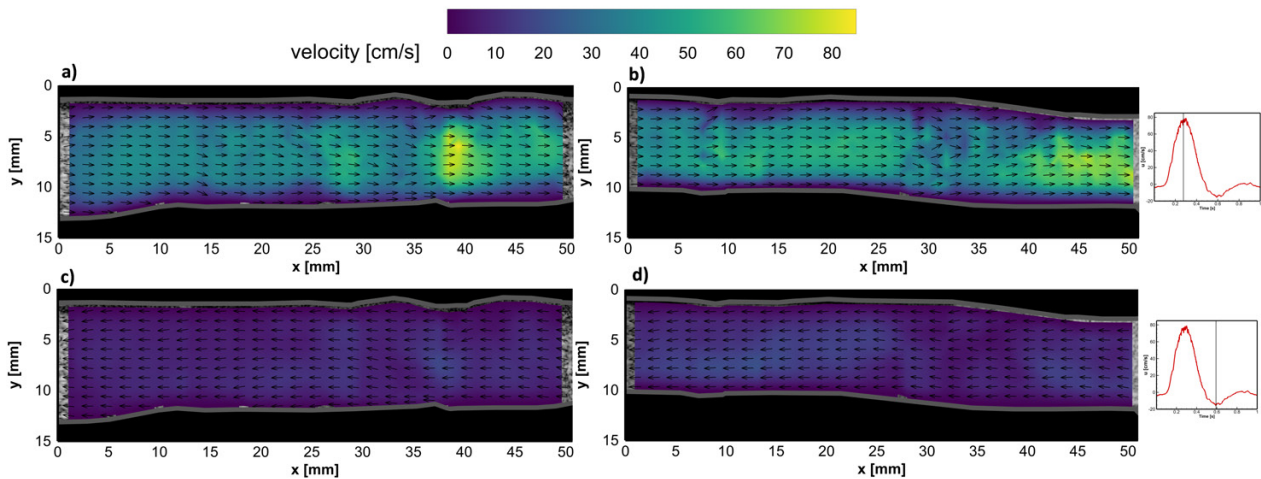
Figure 1. (left) Flow fields in the left iliac artery at PSV (a) and ESV (c) time points before endograft placement. (Right) Flow fields in the right iliac artery at PSV (b) and ESV (d) time points before endograft placement. Velocity vector magnitudes are depicted by the colorbar; while vector lengths are kept equal for better visualization of flow direction. PSV: peak systolic velocity; ESV: end systolic velocity
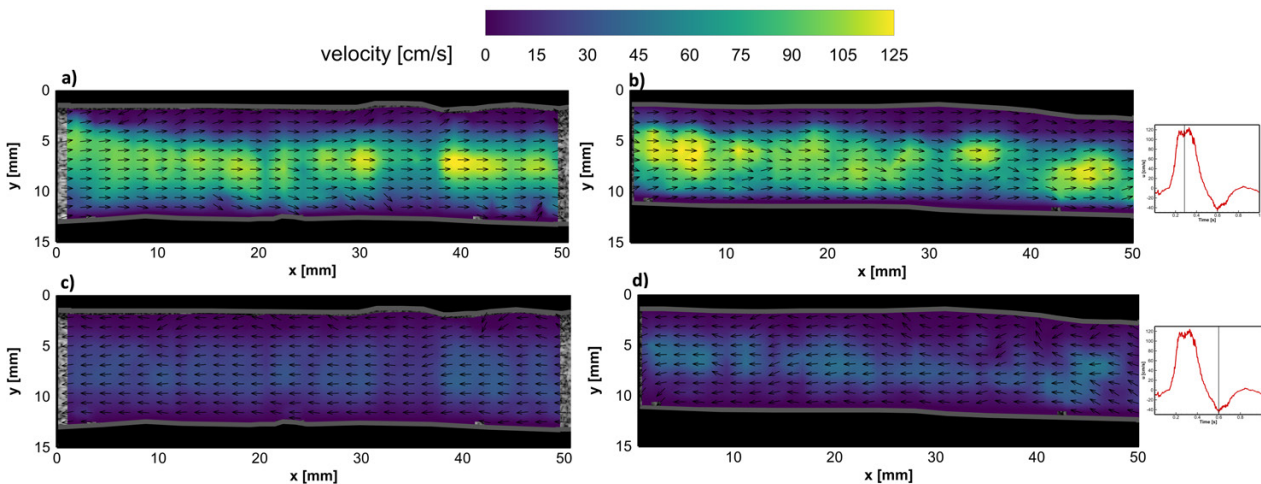
Figure 2. (left) Flow fields in the left iliac artery at PSV (a) and ESV (c) time points after endograft placement. (Right) Flow fields in the right iliac artery at PSV (b) and ESV (d) time points after endograft placement. Velocity vector magnitudes are depicted by the colorbar; while vector lengths are kept equal for better visualization of the flow direction. PSV: peak systolic velocity; ESV: end systolic velocity

References

[1]. Rödel SGJ, Zeebregts CJ, Meerwaldt R, van der Palen J, Geelkerken RH. Incidence and Treatment of Limb Occlusion of the Anaconda Endograft After Endovascular Aneurysm Repair. Journal of Endovascular Therapy. 2019;26(1):113-120. doi:10.1177/1526602818821193

[2]. Bogdanovic M, Stackelberg O, Lindström D, et al. Limb Graft Occlusion Following Endovascular Aneurysm Repair for Infrarenal Abdominal Aortic Aneurysm with the Zenith Alpha, Excluder, and Endurant Devices: a Multicentre Cohort Study. European Journal of Vascular and Endovascular Surgery. 2021;62(4):532-539. doi:https://doi.org/10.1016/j.ejvs.2021.05.015

[3]. Cochennec F, Becquemin JP, Desgranges P, Allaire E, Kobeiter H, Roudot-Thoraval F. Limb graft occlusion following EVAR: Clinical pattern, outcomes and predictive factors of occurrence. European Journal of Vascular and Endovascular Surgery. 2007;34(1):59-65. doi:10.1016/j.ejvs.2007.01.009

[4]. Simmering JA, de Vries M, Haalboom M, Reijnen MMPJ, Slump CH, Geelkerken RH. Geometrical Changes of the Aorta as Predictors for Thromboembolic Events After EVAR With the Anaconda Stent-Graft. Journal of Endovascular Therapy. 2022;30(6):904-919. doi:10.1177/15266028221105839

Size-Selected Microbubbles for Superharmonic Imaging

**Jing Yang**[1,2], **Amin Jafari Sojahrood**[2], **David E. Goertz**[1,2],
**F. Stuart Foster**[1,2], **Christine E.M. Demore**[1,2]

[1]Department of Medical Biophysics, University of Toronto, Toronto, Canada
[2]Physical Sciences Platform, Sunnybrook Research Institute, Toronto, Canada
Corresponding author: jingj.yang@mail.utoronto.ca

Introduction

Superharmonic contrast imaging (SpHI) takes advantage of higher order nonlinear components in the broadband microbubble (MB) response, including the superharmonics, which boosts the contrast-to-tissue ratio with almost complete suppression of tissue clutter. This technique utilizes dual-frequency (DF) probes that transmit low-frequency pulses to initiate MBs' nonlinear behaviour and receive the higher order signals (up to >10th harmonic) backscattered from MBs. Thus, SpHI allows visualization of the vasculature containing MBs while inherently removing signals from the surrounding tissue. Our previous SpHI demonstrations used an array-based DF transducer (2 and 20 MHz) and a commercially available polydisperse MB agent [1], [2]. In this work, we investigate *in vitro* the contrast signal intensity and longevity with in-house polydisperse MBs and size-selected MBs of ~1.5, 2.2, and 4.3 µm in diameter, comparing to commonly used MicroMarker MB solutions.

Methods

Two VevoF2 systems (FUJIFILM Visualsonics, Toronto, Canada) were used to drive the 2 and 20 MHz transducer arrays. Synchronization in the VADA programming mode enabled transmit (Tx) at 2 MHz and receive (Rx) at 20 MHz on separate systems. Conventional line-by-line imaging with a walking aperture and a single cycle pulse was used to generate acoustic beams with an effective focal depth of ~9 mm. *In vitro* imaging was performed on a contrast-filled channel (1.27 mm diam.) which was embedded in a tissue-mimicking matrix. The channel was aligned vertically and positioned to image the transverse cross section within the focal region of the probe. MB solutions were fed into the channel by a syringe and the flow was stopped prior to imaging.

The in-house polydisperse MBs (volume-weighted median diameter: 1.5 µm) were produced as decribed in [3], and centrifugation was performed to produce size-selected MBs [4] with volume-weighted median diameters of 1.5, 2.2, and 4.3 µm. Gas volume matching to MicroMarker (median diameter: 2.3 µm) was performed, and solutions corresponding to 2×10^6 and 5×10^5 MBs/mL were made for each of the five MB size distributions (MicroMarker; in-house polydisperse, three size-selected MBs).

Fifty SpHI frames were acquired at 63 frames per second at Tx powers from 10% to 100% (10% step; corresponding pressures in water were measured with a calibrated hydrophone). Mean SpHI intensities within the channel region-of interest (ROI) were normalized to the mean background signal intensity found within the channel when filled with PBS, followed by logarithmic compresison.

Results

As shown in Figure 1a, backscattered signals from the tissue-mimicking matrix was suppressed to the noise level at three representative Tx powers. The contrast-filled channel becomes visually brighter as the Tx power increases from 10% to 50%. Quantitative analyses showed a rise in mean contrast intensity for all five MB distributions for Tx powers increasing from around 20% to 70% before reaching a plateau near 80% Tx power (Figure 1b). Above 80% Tx power (489 kPa), RF signal saturation was observed, except for the 4.3 µm MBs, which had lower mean contrast intensities than the other distributions. Overall, the in-house polydisperse MBs and the 2.2 µm MBs showed comparable trends in mean contrast intensity to the MicroMarker MBs. Mean contrast signal decay (Figure 1c) was observed at intermediate and high Tx powers (>40%) for all MB distributions. Greatest signal decay was found for the highest Tx power, as

expected. At 70% Tx power (440 kPa), the polydisperse MBs (MicroMarker and in-house) as well as the 2.2 µm MBs showed slower decay relative to the other two size-selected MBs (Figure 1d).

Conclusions

Both the polydisperse and size-selected MBs showed good contrast intensity at high acoustic pressures (MI > 0.3) for the 2/20 MHz frequency pair used for transmit and receive. The large (4.3 µm) MBs may not be preferrable for use with this frequency combination for superharmonic imaging, as reflected by the consistently lower contrast intensity observed at relevant pressure ranges (MI: 0.19-0.42). The commercial and in-house polydisperse MBs as well as the 2.2 µm MBs offer superiority in signal longevity over the other size-selected MBs, making them a potentially more suitable option for superharmonic imaging.
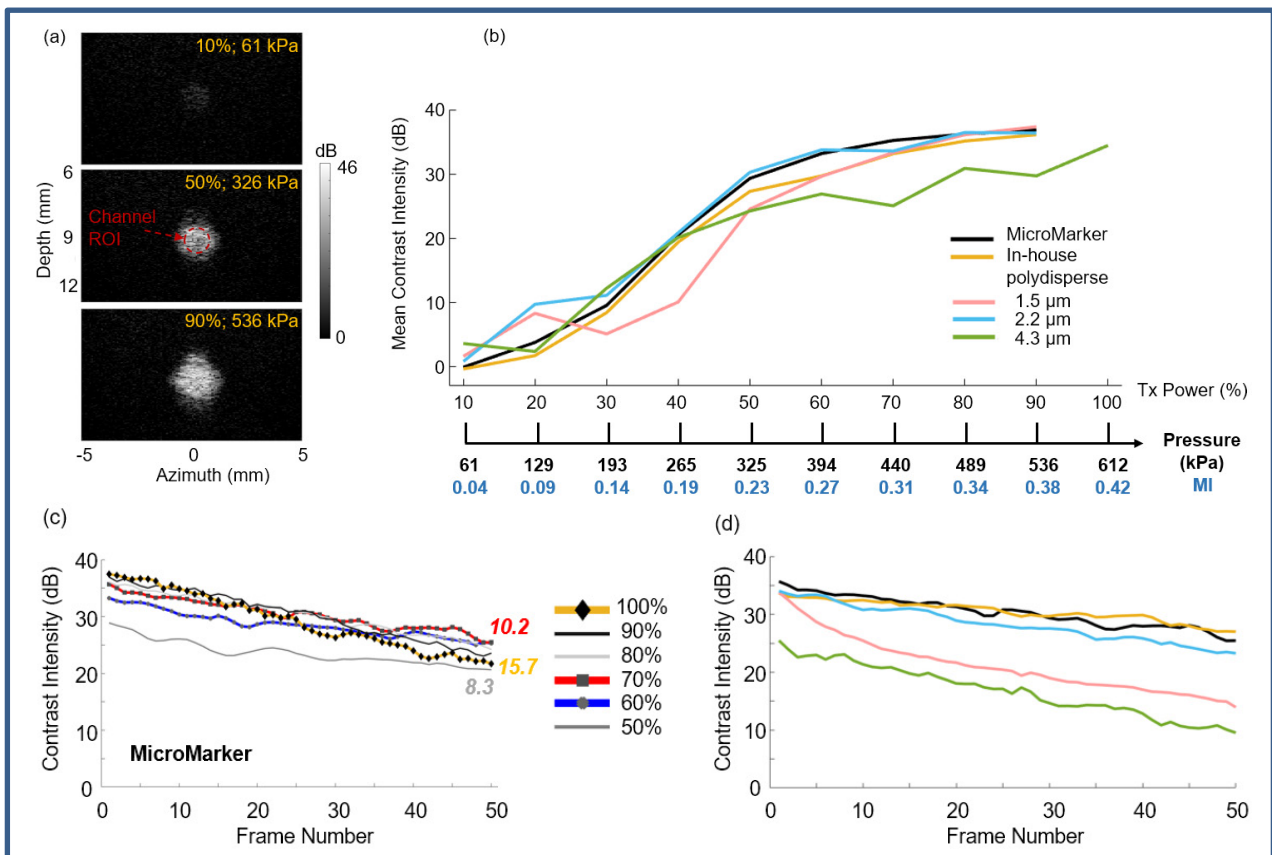
Figure 1. (a) First frame of the SpHI data set at three representative Tx powers of 10%, 50% and 90% when the channel was filled with MicroMarker MBs at 5×10^5 MBs/mL. (b) Mean contrast intensity on the first SpHI frame at increasing Tx powers for all MB distributions at the cocnentration of 5×10^5 MBs/mL for MicroMarker. Data points with significant saturation at 100% Tx power were removed. (c) Mean contrast intensity for 50 frames at 326 – 612 kPa when the channel was filled with MicroMarker MBs at 5×10^5 MBs/mL; difference between the first and last frames for 50%, 70% and 100% Tx power are labelled. (d) Mean contrast intensity for 50 frames at 440 kPa (70% Tx power) for all five MB distributions.

References

[1]. Yang J et al., "Characterization of an Array-Based Dual-Frequency Transducer for Superharmonic Contrast Imaging", IEEE TUFFC, vol. 68(7), pp. 2419-2431, July 2021, doi: 10.1109/TUFFC.2021.3065952

[2]. Yang J et al., "Superharmonic Imaging with Plane Wave Beamforming Techniques", IEEE TUFFC, vol. 70(11), pp. 1442-1456, November 2023, doi: 10.1109/TUFFC.2023.3316120

[3]. de Leon A et al., "Contrast Enhanced Ultrasound Imaging by Nature-Inspired Ultrastable Echogenic Nanobubbles," Nanoscale, vol. 11, no. 33, pp. 15647–15658, Sep. 2019, doi: 10.1039/c9nr04828f

[4]. Feshitan JA, Chen CC, Kwan JJ, and Borden MA, "Microbubble size isolation by differential centrifugation," Journal of Colloid and Interface Science, vol. 329, no. 2, pp. 316–324, Jan. 2009, doi: 10.1016/j.jcis.2008.09.066.

Waveform characteristics for AI-based ultrasound super-resolution using microbubbles

Rienk Zorgdrager[1], Nathan Blanken[1], Michel Versluis[1], Guillaume Lajoinie[1]

[1]*Physics of Fluids Group, Technical Medical (TechMed) Centre, University of Twente, Netherlands*
Corresponding author: r.c.zorgdrager@utwente.nl

Introduction

Contrast-enhanced ultrasound imaging is clinically well adopted for diagnosing cardiovascular diseases. Typically, clinical workflows use Doppler techniques to image blood flow as blood flow is intrinsically linked to the pathology of cardiovascular diseases. More recently, vector flow imaging techniques based on speckle tracking have gained scientific attention due to their improved ability to image flows in terms of resolution, speed and accuracy [1,2]. However, the underlying conventional beamforming algorithms of both the Doppler and vector flow imaging techniques are diffraction-limited and therefore their resolution is limited to the wavelength of the pulses. To overcome this limitation, ultrasound localization microscopy (ULM) has been introduced, which is based on localizing and tracking non-overlapping point spread functions [3]. Moreover, recent studies have been successful in localizing microbubbles using deep learning algorithms which perform the beamforming step after deconvolving the RF signals, thereby not relying on point spread function separation and free from beamforming inaccuracies [4]. As these approaches rely on deconvolved signals, it breaks with the paradigm that links pulse length and imaging resolution. The following question now arises: are there waveforms that, despite their increased time duration, yield a higher resolution than a short imaging pulse, due to their distinctive temporal features or the enhanced nonlinear features of the microbubbles response are more effectively detected and deconvolved by a convolutional neural network (CNN)?

Methods

This study comprises two main steps: i) raw element RF data is acquired using a fast simulator for different waveforms and ii) a CNN is trained for each waveform to estimate the location of single microbubbles relative to each transducer element using the single-element RF signals.

The synthetic RF data will be formed by propagating a plane wave in a homogeneous medium where monodisperse bubbles (10 to 1000 bubbles) are randomly seeded. The waveforms vary in terms of pulse length, temporal frequency spread (both continuous frequency as well as frequency sweep) and delay- or polarity encoded number of repetitions. Figures 1a-c) show schematics of the different waveforms. The single-frequency pulses will have different center frequencies (1.7 MHz, 2.5 MHz and 3.4 MHz) to evoke different microbubble responses. Additionaly, each of these pulses will be investigated with a short (2.9 µs) and a long (4.7 µs) variant. Both up- and downsweep chirps will be investigated (with a frequency range of 1.2 MHz – 4.0 MHz) of which each have a short (6.1 µs) and a long variant (16.1 µs). The delay- or polarity-encoded pulse trains consist of four repetitions of a single-frequency pulse (2.5 MHz, short and long). Acoustic pressure amplitude of each simulation is randomly chosen between 5 and 250 kPa. For each waveform, a CNN is trained with 5000 simulated RF-channels to localize the microbubbles. To optimize the network's performance, a dilated convolutional architecture and a dual-loss function are used as described in [4]. Finally, the microbubble localization performance of all CNNs will be compared to assess which waveform type has the greatest super-resolution potential.
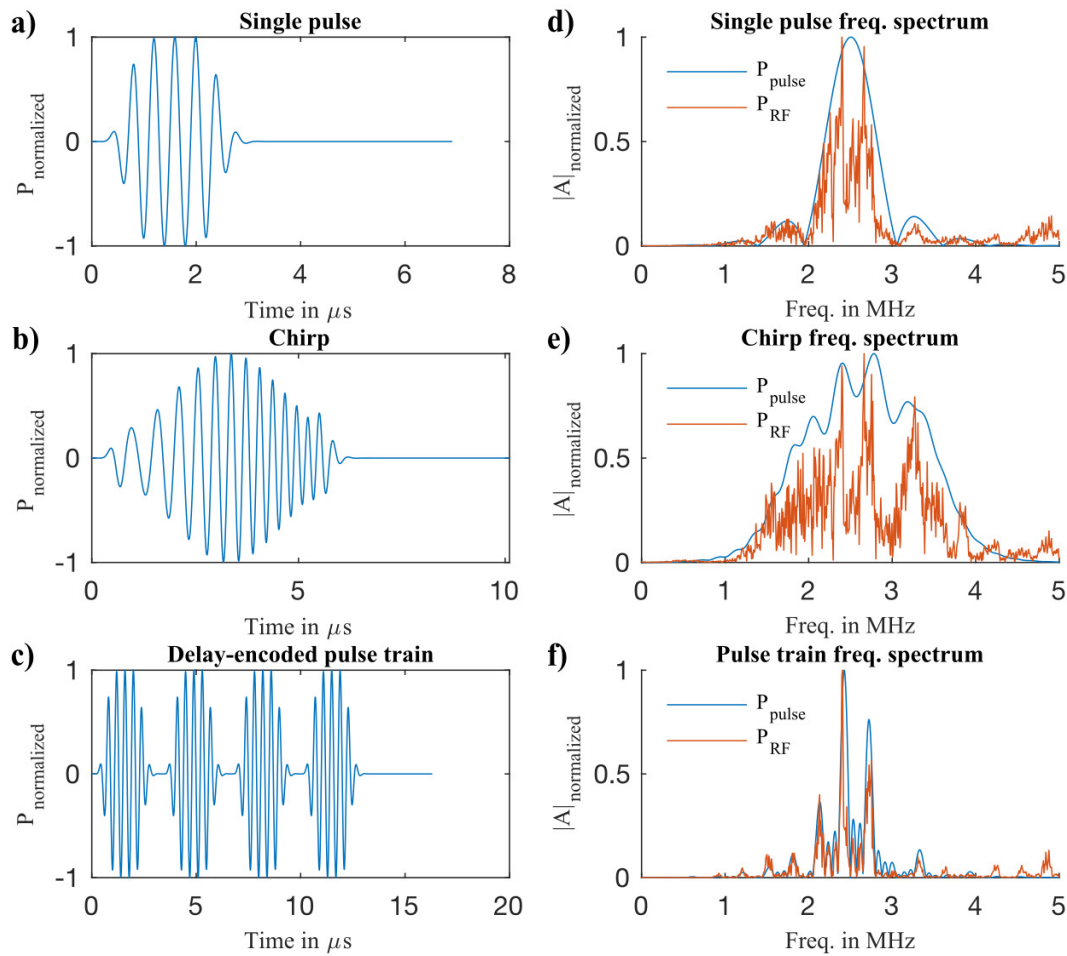
Figure 1: Examples of investigated waveform types, their frequency content, and the frequency content of the received RF signal. Figure 1a), b) and c) are schematic representations of the waveforms investigated in this study. a) Continuous frequency pulse of 2.5 MHz (2.9 μs), b) upsweeping chirp from 1.2 – 4.0 MHz (6.1 μs), c) delay-encoded pulse train (13.6 μs) of four times the reference, single-frequency pulse with delays encoded of respectively 0.5, 1.0 and 1.5 microseconds. The delays used are for conceptualization only and do not correspond to the actual delays used for the simulations. Figure 1d), e) and f) show the frequency content of the waveforms (respectively a), b) and c)) and the received RF signal after plane wave emission. The microbubble cloud contained 307 microbubbles and the transmitted pressure was 214 kPa.

Results

At the time of writing this abstract, the training of the neural networks has not yet been completed. However, we can already present the effect of the different waveform types on the received RF signals from the microbubble cloud and we can demonstrate the super-resolution performance of a trained neural network for a short imaging pulse [4]. Figures 1d-f) show the frequency spectra of the waveforms described in Figure 1a-c) and the frequency spectra of its respective received RF signal. The difference between the frequency spectrum of the waveform and the received RF signal can be attributed to the nonlinear propagation, the nonlinear response of the microbubbles and the random fluctuations in microbubble density, making it difficult to interpret the data.

Figure 2 shows the superior resolution of the proposed strategy compared with a conventional beamforming algorithm for a single short imaging pulse at a transmit pressure of 205 kPa. Previously, a neural network with a the same architerture as ours was able to detect microbubbles with an order-of-

magnitude gain in resolution [4]. As the use of waveforms with a different duration, frequency or time-frequency fingerprint can alter both the frequency as well as the phase response of the microbubbles, we expect to be able to enhance the localization accuracy of the in [4] developed CNN.
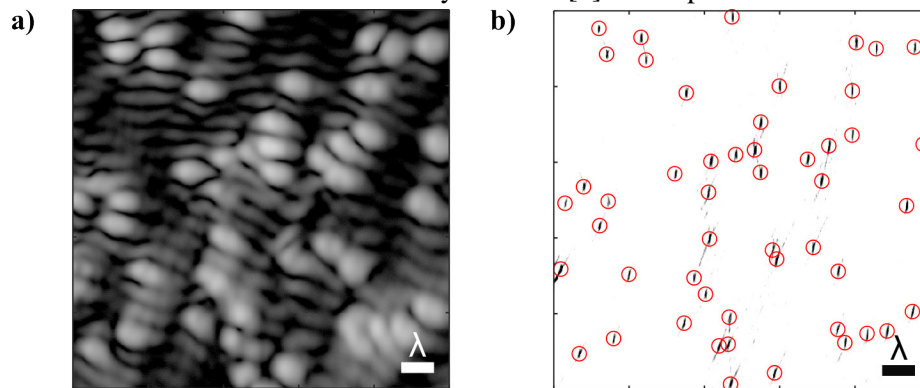
Figure 2: Demonstration of deep learning-based super-resolution [4]. This figure shows a subregion of ultrasound images obtained using a) direct beamforming and envelope detection of element RF signals and b) beamforming of devonvolved element RF signals with a single short imaging pulse (2.0 μs). The transmit pressure was 205 kPa. The scalebars represent the wavelength λ (0.87 μm).

Conclusions

The proposed study will aid understanding in the use of ultrasound waveform characteristics for enhancing performance of deep-learning-accelerated direct deconvolution in super-resolution CNNs. The results of this study, which are expected in the near future, will guide future studies towards optimizing waveforms for resolution in deep-learning based approaches.

References

[1]. Zhou X, Vincent P, Zhou X, Leow CH, Tang MX. Optimization of 3-D Divergence-Free Flow Field Reconstruction Using 2-D Ultrasound Vector Flow Imaging. Ultrasound Med Biol. 2019 Nov;45(11):3042-3055. doi: 10.1016/j.ultrasmedbio.2019.06.402. Epub 2019 Aug 2. PMID: 31378550.

[2]. Engelhard S, van Helvert M, Voorneveld J, Bosch JG, Lajoinie G, Groot Jebbink E, Reijnen M, Versluis M, "Blood Flow Quantification with High-Frame-Rate, Contrast-Enhanced Ultrasound Velocimetry in Stented Aortoiliac Arteries: In Vivo Feasibility" in Ultrasound in Medicine & Biology. 2022;48(8):1518-1527, doi: 10.1016/j.ultrasmedbio.2022.03.016.

[3]. Couture O, Hingot V, Heiles B, Muleki-Seya P, Tanter M, "Ultrasound Localization Microscopy and Super-Resolution: A State of the Art." in IEEE Trans Ultrason Ferroelectr Freq Control. 2018 Aug;65(8):1304-1320. doi: 10.1109/TUFFC.2018.2850811. Epub 2018 Jun 26. PMID: 29994673.

[4]. Blanken N, Wolterink JM, Delingette H, Brune C, Versluis M and Lajoinie G, "Super-Resolved Microbubble Localization in Single-Channel Ultrasound RF Signals Using Deep Learning," in IEEE Transactions on Medical Imaging, vol. 41, no. 9, pp. 2532-2542, Sept. 2022, doi: 10.1109/TMI.2022.3166443.

A Capillary-scale Microvascular Phantom — Demonstration of Multi-stage Vessel Branching and 3D Super-resolution Ultrasound Imaging

Shusei Kawara[1], Brian Cunningham[1,2], Jingwen Zhu[1], James Bezer[1], Meng-Xing Tang[1], James Choi[1], Sam Au[1,2]

[1]*Department of Bioengineering, Imperial College London, London, UK*
[2]*Convergence Science Centre, Institute of Cancer Research, London, UK*
Corresponding authors: j.choi@imperial.ac.uk and s.au@imperial.ac.uk

Introduction

Microbubbles are used in ultrasound imaging to provide contrast for better diagnostic capacity. Microvascular phantom is a useful tool for the optimisation of image processing algorithms and has been used across the field. Hydrogel-based "wall-less" phantom is desirable compared to widely-used silicone tubes given that the density of hydrogel is typically close to that of water. While hydrogel has an excellent acoustic property matching with water and tunable mechanical stiffness, their diameters are often limited to > 100 μm making it unsuitable for rapid prototyping. Also, leakage is a non-trivial problem when the diameter gets capillary-scale since hydrodynamic resistance increases with the inverse of the fourth power.

To overcome these problems, we invented a method to manufacture a leakage-free microfluidic phantom with a capillary scale down to 6.2 μm in diameter through wire-templating. We then developed multi-stage fractally branching microchannels with our invented dipper rig for generating a bifurcating wire template. This method is suitable for rapid prototyping and studying ultrasound imaging.

Methods

Our phatoms were fabricated by wire-templating involving three phases; 1) surface-treatment of guide glass capillaries 2) template wire coating, and 3) assembly and channel formation as previously described [1] (Figure 1). For the bifurcating wire template, we developed a dipper rig (Figure 2a) to selectively dip-coat multiple wires with polyurethane. The dipped wires were bundled by surface tension of polyurethane while slowly extracted from the reservoir generating bifurcating wire bundles after multiple dip sequences (Figure 2b) [1]. They were then loaded on the custom-made alignment rig (Figure 2c).

Super-resolution imaging of the phantom was attempted with the single channel of 100 μm and bifurcating channels of the mother channel of 130 μm and the daughter channels of 70 μm diameters were made in polyacrylamide hydrogel (3.24 kPa and 8.73 kPa in Young's moduli respectively) as described above. The phantom was placed on a sheet of acoustic absorber (AptFlex F28, Precision Acoustics, UK) and below 32x32 matrix array imaging probe (Mat 8.0/1024 2068, Vermon, France) (Figure 4a). Verasonics 256 system (Vantage 128, Verasonics, USA) was used to drive and receive with the 32x32 matrix probe. Ultrasound super-resolution images were constructed as previously described [2].

Results

Our manufacturing phantom accommodated flow at 6.1 μm diameter (Figure 1a-c). Bifurcated phantom was shown to accommodate flow with round cross-section where diameters of respective parental, daughter and granddaughter microchannels were measured as 99.1 ± 4, $58.9 \pm 11/59.0 \pm 2$ and $29.6 \pm 2/32.0 \pm 0.8/34.5 \pm 4/32.2 \pm 1.4$ μm (Figure 3d,e). Optical (Figure 4c top) and ultrasound super-resolution images (Figure 4b,c middle and bottom) were successfully acquired with our phantom.

Conclusions

Our microvascular model has shown compatibility with *in vitro* studies of ultrasound imaging. Both single and bifurcating channels were manufactured in a simple and inexpensive manner. Detailed manufacturing methods can be found in the recent publication by S, Kawara *et al*, 2023, *Small* [1]
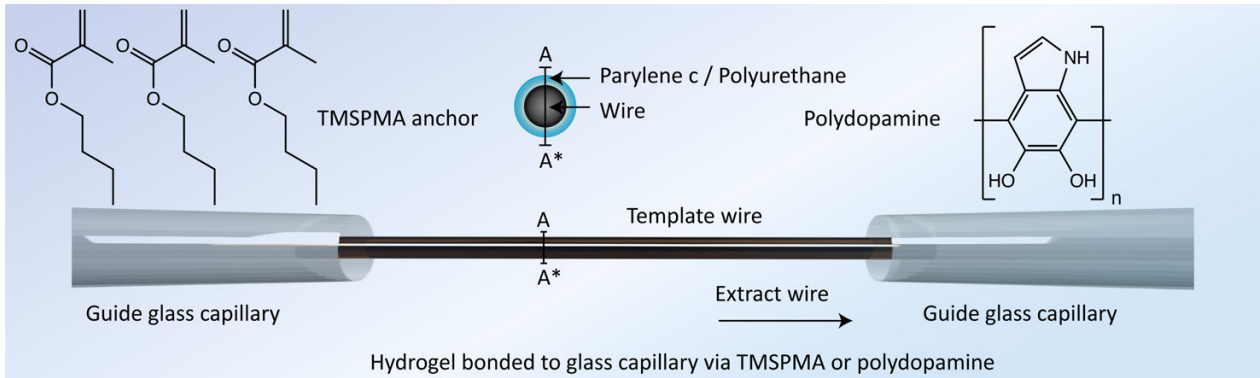
Figure 1. Wire templating technology. A guide glass capillary was bonded to a hydrogel, providing a strong interface at the inlet and outlet. The wire template was coated to make it hydrophobic. After the hydrogel forms, pulling the wire out left a smooth, non-leaking microchannel down to 6.2 µm in diameter.
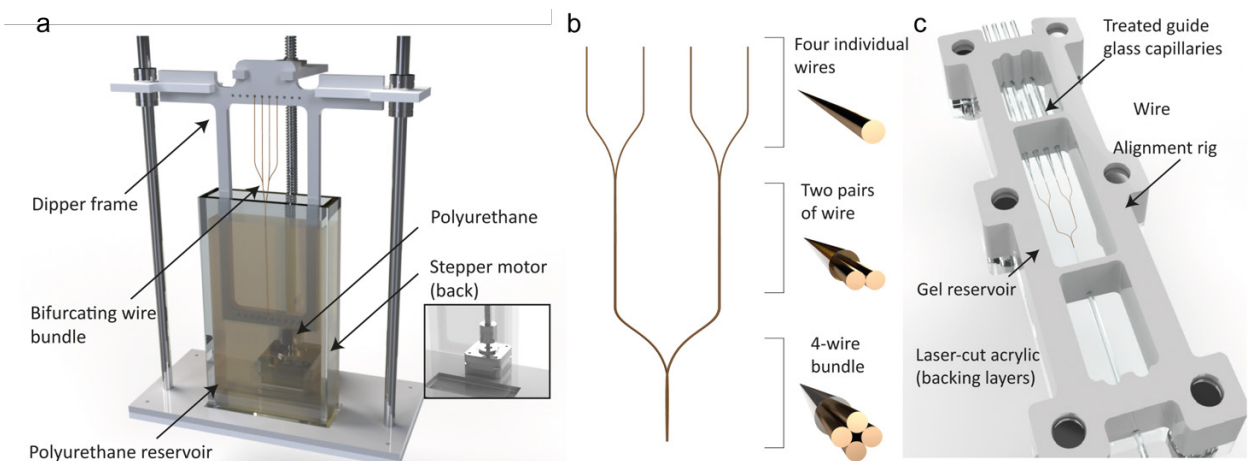
Figure 2. Bifurcating microchannel technology. (a) Dipper rig for dip coating, (b) 1-2-4 bifurcating template wire, and (c) wire-loaded alignment rig.
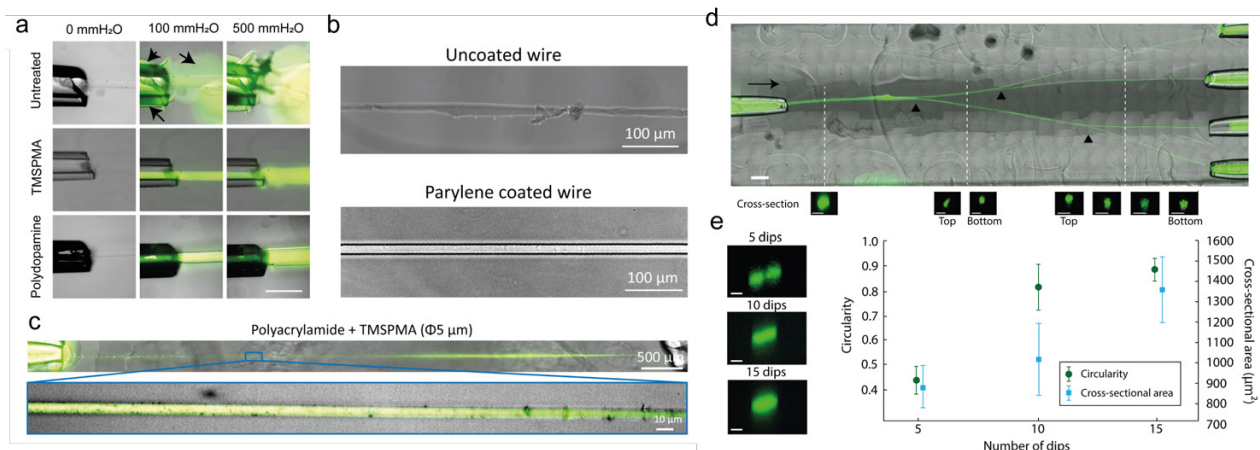
Figure 3. Microchannel structure. (a) Micrograph of gel-glass interface during pressure-ramp, (b) channel formed with and without parylene-c coating, (c) 6.1µm-diameter single channel, (d) bifurcations, and (e) cross-sections of channels.
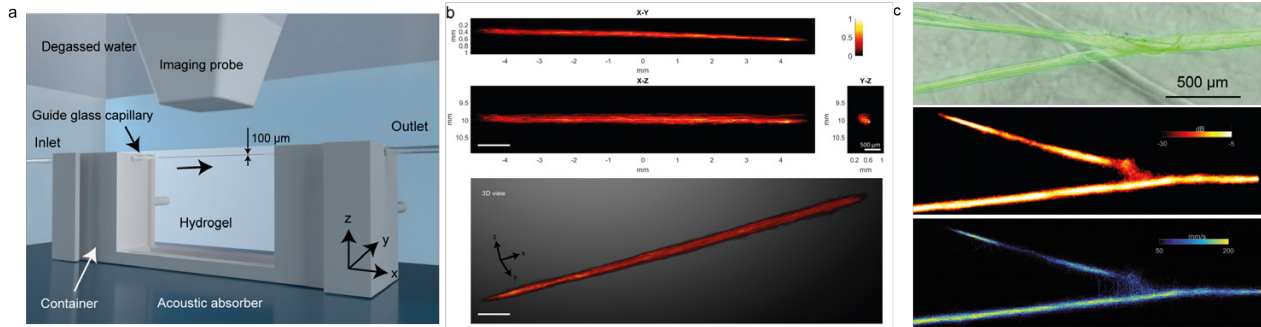
Figure 4. Super-resolution imaging of microchannels. (a) experimental setup, and (b) single (density map in decibels), and (c) bifurcating channels; micrograph (top), density map in decibels (middle) and flow speed map in mm/s (bottom).

References

[1]   S. Kawara *et al.*, "Capillary-Scale Hydrogel Microchannel Networks by Wire Templating," *Small*, 2023, doi: 10.1002/smll.202301163.

[2]   J. Yan *et al.*, "Transthoracic super-resolution ultrasound localisation microscopy of myocardial vasculature in patients," *IEEE Trans. Med. Imaging*, Mar. 2022, Accessed: Apr. 06, 2023. [Online]. Available: https://arxiv.org/abs/2303.14003v2.

Multi-parametric Assessment of Contrast and Molecular Ultrasound to Predict Response to anti-PD-L1 Immune Checkpoint Inhibitor

Mahsa Bataghva, Farbod Tabesh, Arutselvan Natarajan, Ramasamy Paulmurugan, Ahmed El Kaffas

Molecular Imaging Program at Stanford (MIPS), Stanford University School of Medicine, Stanford, CA, USA.
The Canary Center at Stanford for Cancer Early Detection, Stanford University School of Medicine, Palo Alto, CA, USA.
Corresponding author: mbataghv@stanford.edu

Introduction

Immune checkpoint inhibitor (ICI) therapy has revolutionized cancer treatment by unleashing powerful immune responses that result in significant and lasting clinical improvements. Nonetheless, ICIs are only effective in 20-50% of cancer patients; it would be ideal to have tools to help select which patients will respond to ICTs. Hisptopathological assessment of tissue expression of PD-L1 can potentially provide this, but are highly invasive. Contrast-enhanced and molecular ultrasound imaging techniques offer robust means to analyze tumor vasculature and characterize EC surface markers, potentially delivering decision-support information to guide clinicians managing patients receiving ICTs. In this study, we investigate whether quantitative parameters from 2D and 3D molecular and 2D contrast-enhanced ultrasound (CEUS) can help predict ICT treatment response in the pre-clinical setting.

Method

A total of n = 25 mice (nine-week-old) had CT26 colon cancer cell implantation on their upper hindlimb. Tumors were allowed to grow to ~6 mm/diameter, measured by manual caliper every 2 days. Mice were separated into two groups of treated and non-treated with PD-L1 antibody. Three doses of 10mg/kg ICI therapy were given to the treated group (n=20 mice) on days 8, 11, and 14 after tumors reached ~6 mm diameter. Tumor volume measurements collected on day 8th, 11th, 14th, 17th and 21st post implantation were used to determine the tumor growth rate as a surrogate of treatment response.

For the imaging procedures, mice were anesthetized with 1-3% isoflurane. Microbubbles were injected by placing a catheter in the tail vein. The mice were injected with anti-PD-L1 targeted microbubbles (TMBs). Ultrasound imaging was performed with a preclinical Vevo2100 system (Visualsonics, Toronto, Canada), with M250 transducer. Microbubbles were prepared based on the manufacturer protocol using target-ready TBS MBs. A destructive pulse was applied after the acquisition of perfusion signals and tumors were imaged dynamically during contrast wash-in and wash-out.

Prior to the treatment, on day 8 of the tumor growth, perfusion parameters of peak-enhancement (PE) and area-under-the-curve (AUC), which correlate to blood volume, and wash-in-rate (WiR), time-to-peak (TP) which correlate to blood flow from the time intensity curves (TIC) of the 2D contrast-enhanced ultrasound (CEUS) images as well as the differential targeted enhancement (dTE) from 2D molecular ultrasound images were acquired. Also, mean volumetric dTE was calculated based on the subtraction of the intensity of the tumor volume before injection and before destruction of the TMBs. Tumor volume was generated through interpolation of selected 10 regions of interest on the 2D planes.

Result

Variations in the tumor growth rate were observed within the treated group, likely attributed to the immunocompetent nature of the mice under investigation. Treated animals were stratified into responders (n=18) and non-responders (n=2) based on normalized tumor volumes on day 10 to their respective volume

on day 1 (i.e., the implantation day) and k-means clustering algorithm; the non-responder group had a tumor growth delay of 4 days, similar to the control group (7.5 days).

A one-way ANOVA test was conducted on the dTE of targeted microbubbles, calculated based on 2D and 3D images, between the none responsive and the very responsive groups yielded a test statistic of 12.1 and 24.1, indicating a significant difference between the two groups with a p-value of 0.005 and 0.0006, respectively. This suggests that dTE from both 2D and 3D molecular ultrasound images are descriptive of the tumor response, but that the 3D-derived dTE may enhance descrimination beteween different groups.

On the other hand, the CEUS AUC and PE parameter between the responder and non-responder groups exhibited a considerable disparity, with the value of 23.5 and 3.8 with p-values of 0.000.8 and 0.05 respectively. This indicate these 4 parameters can distinguish the two group and that all there parameters are good predictors for treatment response. However, Pearson correlation results shows relatively high correlation between the PE and AUC with coefficient of 0.74, meaning that the one of these features is highly descriptive of the other and only one of them is enough to be used as a predictive feature from 2D CEUS. We also applied descision tree rule based model and results indicates that with lower values of 3D dTE, lower AUC determines non-responder groups and higher AUC determines responders group, while with higher values of dTE, PE is the descriminative feature.

Conclusion

Our preliminary results suggest the effectiveness of combined CEUS and molecular US to assess tumor treatment response to PD-L1 immunosuppressive therapy prior to the administration of the treatment. The results indicates that AUC of the time TIC from 2D CEUS images which shows the intra-tumor blood volume as well as the dTE from 2D and 3D molecular US shows significant differences between the responsive and non-responsive group and can be further investigated to study the immunotherapy treatment response.
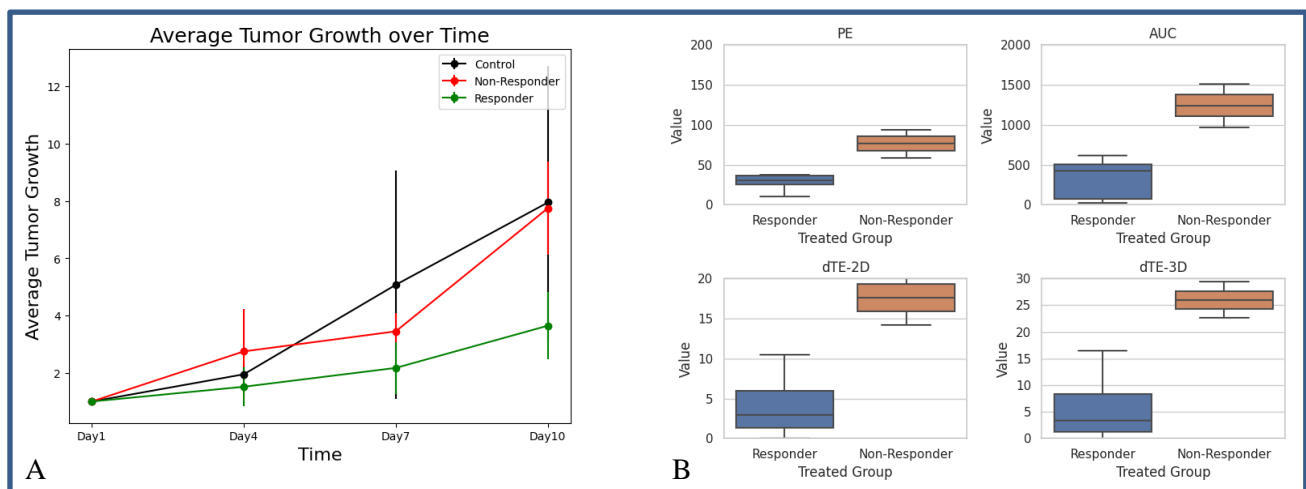
Figure 1. A. Represents the average tumor growth in different groups of mice. B. Shows the difference between the averaged values of PE, AUC, 2D dTE and 3D dTE between the two groups of responders and non-responders.

References

[1]. Vareki, S. M., Garrigós, C., and Duran, I., "Biomarkers of response to PD-1/PD-L1 inhibition.", Critical reviews in oncology/hematology 116 (2017): 116-124.

[2]. Sun, L., Zhang, L., Yu, J. *et al.* "Clinical efficacy and safety of anti-PD-1/PD-L1 inhibitors for the treatment of advanced or metastatic cancer: a systematic review and meta-analysis.", *Sci Rep* **10**, 2083 (2020).

Comparison of a novel agitation method for microbubble production with established preparation technologies

J. Katrinka Mavrak [1], L. Bau [1], J. Rivera [1], A. Sedgwick [2], E. Stride [1]

[1]*Institute of Biomedical Engineering, University of Oxford, Oxford, UK*
[2]*Department of Chemistry, Kings College London, London, UK*

Corresponding author: jovana.katrinka@hertford.ox.ac.uk

Introduction

The most widely-used microbubble (MB) agents consist of a gas core stabilized with a phospholipid shell, and have been successfully used for both imaging and therapy [1, 2, 3]. Multiple methods for production of MBs have been developed. Sonication or mechanical agitation are the most commonly used; although novel techniques such as microfluidics have also been successfully utilized for MB production [4, 5, 6, 7]. Each method has its advantages and disadvantages. A key advantage of mechanical agitation is the ease with which it can be used in the clinic for *in situ* production of MBs in pre-prepared sterile vials. However, currently available agitators can only process small volumes and are prone to breakage. To address these challenges, we investigated whether a more robust agitation protocol could be developed using a well established bench-top instrument available in most research and clinical laboratories for tissue sample preparation. Furthermore, we compared this method to established protocols for MB production, namely sonication and agitation with commercial agitator.

Methods

Lipid suspension production

Suspensions of DPPC (6 mg/mL), DPPA (10 mg/mL), DPPE-PEG5k (15 mg/mL) were prepared by dissolving the lipids in propylene glycol at 55 °C for 20 min. The stock suspensions (2.67 mL of DPPC, 0.18 mL of DPPA and 0.81 mL of DPPE-PEG5k) were mixed in an 8 mL glass vial and added dropwise to 20 mL of an 80:10:10 water/propylene glycol/glycerol mixture under vigorous stirring at 55 °C. Then, 1 mL of lipid suspension was transferred to a 2 mL freeze drying vial, capped with a rubber stopper, and crimped with aluminum cap for further use in agitation protocols.

Microbubble production, sizing, and stability studies

Headspace gas exchange was performed in vials containing lipid suspension prior to agitation. While kept on ice, perfluorobutane was introduced into the vials through a needle. MBs were produced by the following procedures:

- Tissue homogenizer agitation protocol: Following headspace gas exchange, the lipid suspension was placed in a tissue homogenizer (Precellys Evolution). Vials were inserted in custom-made inserts and agitated on 10.000 rpm for 45 seconds, unless otherwise stated.

- Clinical agitation protocol: Following headspace gas exchange, the lipid suspension was agitated in an amalgam capsule mixing machine (3M ESPE Capmix). Vials were placed in the machine and agitated at 4500 rpm for 39 seconds.

- Sonication protocol: 5 mL of lipid suspension was transferred to a 7 mL glass vial and a 3 mm sonicator probe tip was placed deep into the liquid and sonicated with 35% amplitude for 2.5 minutes. Then, the tip was placed at the air/water interface and sonicated at 85% amplitude for 30 seconds, while perfluorobutane gas was simultaneously introduced to the vial headspace (no prior gas exchange was performed in this case).

MBs were removed from vials with an 18g needle and syringe to a clean vial and kept on ice until use. MB quality was monitored by measuring concentration and size distribution after production with a Coulter Counter Multisizer 4e (Beckman Coulter). MB stability was assessed by repeating the measurement of concentration and size distribution every hour from production for 8 hours (and after 24 hours). Samples were kept on ice between measurements.

Results

MBs prepared by using the tissue homogenizer protocol were smaller with a narrower size distribution compared to MBs made by sonication and clinical agitation (Figure 1A). They also had a higher concentration (Figure 1B) and were stable for over 8 hours in storage at 4ºC, with minimal variation in size and concentration over the measuring period (data not shown). Other two methods showed higher intersample variation in size over the measured period, while concentration remained relatively constant. Varying the time (for more than 10 seconds) and speed of production was found to influence both concentration and size distribution, allowing for tuning of MB properties (data not shown).
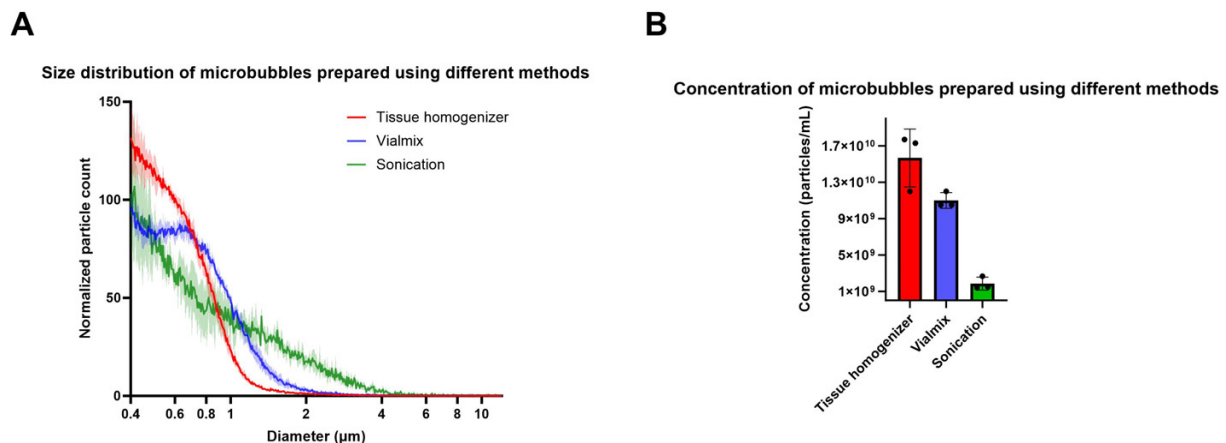
Figure 1. – Characterization of MBs produced with different methods. Size distribution (A) and concentration (B) of MBs were obtained by Coulter Counter. All groups had n=3 and plotted is the mean and standard deviation.

Conclusions

We compared the size, concentration and stability of MBs produced using 3 different methods: sonication, mechanical agitation using a commercial vial shaker and agitation using a tissue homogenizer. The tissue homogenizer was found to yield bubbles at a higher concentration and with a narrower size distribution than sonication or the commercial shaker. Stability measured as a concentration and size over the 8 hours (on 4ºC) was found to be best in tissue homogenizer MBs, with smallest intersample variation. The tissue homogenizer is also capable of processing larger volumes and numbers of samples, which may be important for therapeutic applications of microbubbles. It can be operated at different speeds and for different durations to tune the MB size distribution if required.

References

[1]. W Villanueva, Flordeliza S., et al. "Targeted ultrasound imaging using microbubbles." Cardiology clinics 22.2 (2004): 283-298.

[2]. Unger, Evan C., et al. "Therapeutic applications of lipid-coated microbubbles." Advanced drug delivery reviews 56.9 (2004): 1291-1314.

[3]. Cosgrove, David, and Chris Harvey. "Clinical uses of microbubbles in diagnosis and treatment." Medical & biological engineering & computing 47 (2009): 813-826.

[4]. Dixon, Adam J., et al. "Enhanced intracellular delivery of a model drug using microbubbles produced by a microfluidic device." Ultrasound in medicine & biology 39.7 (2013): 1267-1276.

[5]. Hettiarachchi, Kanaka, et al. "On-chip generation of microbubbles as a practical technology for manufacturing contrast agents for ultrasonic imaging." Lab on a Chip 7.4 (2007): 463-468.

[6]. Hall, Ronald L., et al. "Formulation and characterization of chemically cross-linked microbubble clusters." Langmuir 35.33 (2019): 10977-10986.

[7]. Zhou, Meifang, Francesca Cavalieri, and Muthupandian Ashokkumar. "Tailoring the properties of ultrasonically synthesised microbubbles." Soft Matter 7.2 (2011): 623-630.

Coalescence-free monodisperse microbubble produced at room temperature using Pluronic F68: acoustic response and shelf stability

Yuchen Wang[1], _Sander Spiekhout[1]_, _Ana Walgode[1]_, _Antonius F. W. van der Steen[1]_, _Benjamin R. G. Johnson[2]_, _Klazina Kooiman[1]_

[1]_Department of Biomedical Engineering, Thoraxcenter, Erasmus MC, Rotterdam, NL_
[2]_Molecular and Nanoscale Physics Group, School of Physics and Astronomy, University of Leeds, Leeds, UK_
Corresponding author: y.wang@erasmusmc.nl

Introduction

Clinically available microbubbles have a broad resonance spectrum owing to their polydisperse size distribution. Monodisperse microbubbles (mMBs) have a more uniform acoustic response and can be generated using a microfluidic flow-focusing chip [1]. However, this production process is prone to coalescence at room temperature, limiting the production rate. A previous study showed effective suppression of mMB coalescence after adding 82.7 mol% Pluronic F68 (PF68) [2]. However, the evaluation of size stability was only limited to 10 minutes post-production so the effects on shelf stability are unknown. Furthermore, the mMB were not acoustically characterized. Therefore, this study explores the impact of incorporating PF68 in the mMB production process on size stability for up to seven days, and characterizes the acoustic properties of these mMB using attenuation measurements.

Methods

The lipid film consisting of DSPC and DPPE-PEG5000 (9:1 mol ratio) was rehydrated in PBS to a lipid concentration of 20 mg/ml. Subsequently, PF68 was added to the solution to reach varying molar percentages of 0 (0PF-MB), 5 (5PF-MB), 7.2 (7.2PF-MB), 10 (10PF-MB) or 30 (30PF-MB) in separate experiments. The mMBs were produced at room temperature in the microfluidic platform Horizon [3]. A high-speed-camera was coupling to the Horizon to monitor the production process (Figure 1A) by measuring the on-chip size distribution using a customized MATLAB script. During production, the C_4F_{10} gas pressure was set to 800 mbar, and the lipid solution flow rate adjusted to reach a 6 µm on-chip radius. The produced mMBs were collected and stored in a gas tight medical vial pre-filled with C_4F_{10}. The shelf stability was assessed by measuring the mMB size distribution over 7 days using Coulter Counter Multisizer 3 (number-weighted). Acoustic attenuation measurements were performed two days after production by transmitng a sequence of 12-cycle pulses with frequencies ranging from 1 to 5 MHz in 100 kHz steps at acoustic pressures of 10, 25, 75 and 150 kPa. The shell stiffnes was derived from the measured resonance curve at 10 kPa and the peak mMB size using a linearized Rayleigh-Plesset equation.

Results

Figure 1B-F shows the on-chip size and 7 days size distribution of 5 mMB formed with different molar ratios of PF68. In the absence of PF68, the MB coalesced on chip, which resulted in a wide size distribution with multiple peaks. When PF68 was added, on-chip coalescence was suppressed, resulting in a mMB population with a single peak radius around 6 µm. For 5PF-MB (Figure 1C), 7.2PF-MB (Figure 1D) and 10PF-MB (Figure 1E), they shrank to approximately 2 µm in 2 hours and remained stable for up to 7 days. However, the stability of 30PF-MB was compromised, disappearing in 2 hours post-production (Figure 1F). The shrinkage rate, calculated from the ratio of on-chip mMB radius to the mMB radius as measured by the Coulter Counter, increased with the molar percentage of PF68. This shrinkage ratio was 2.8, 2.99, and 3.04 for 5PF-MB, 7.2PF-MB, and 10PF-MB, respectively.

Furthermore, the concentration of mMB increased from 2 hours, and peaked after 1 day (10PF-MB) or after 2 days (5PF-MB and 7.2PF-MB), followed by a gradual decline up to 7th day. The initial increase in bubble concentration can be attributed to large foam bubbles due to Ostwald ripening which eventually dissolve to the same smaller mMB radii [4].
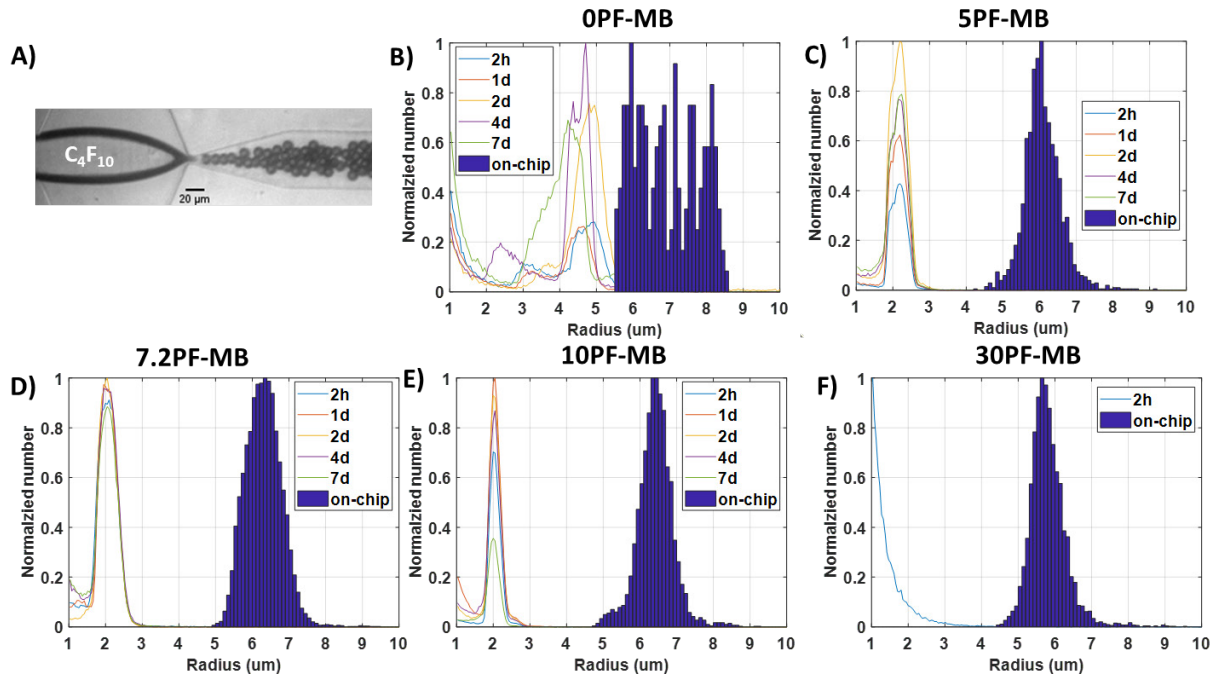
Figure 1. A) Bright-filed image of 30PF-MB production in a flow-focusing chip. On-chip and 7-day size distribution of B) 0PF-MB, C) 5PF-MB, D) 7.2PF-MB, E) 10PF-MB and F) 30PF-MB.

The attenuation spectra of the 5PF-MB, 7.2 PF-MB and 10PF-MB are shown in Figure 2. The resonance frequency decreased from 2.8 MHz to 2.5 MHz for 5PF-MB with increasing pressures from 10 to 150 kPa. For the 7.2PF-MB it decreased from 3 to 2.75 MHz, and 3.2 to 2.9 MHz for 10PF-MB. The obtained stiffness values of the stable bubbles were 0.85 N/m, 0.81 N/m and 0.86 N/mfor 5PF-MB, 7.2PF-MB, and 10PF-MB, respectively.
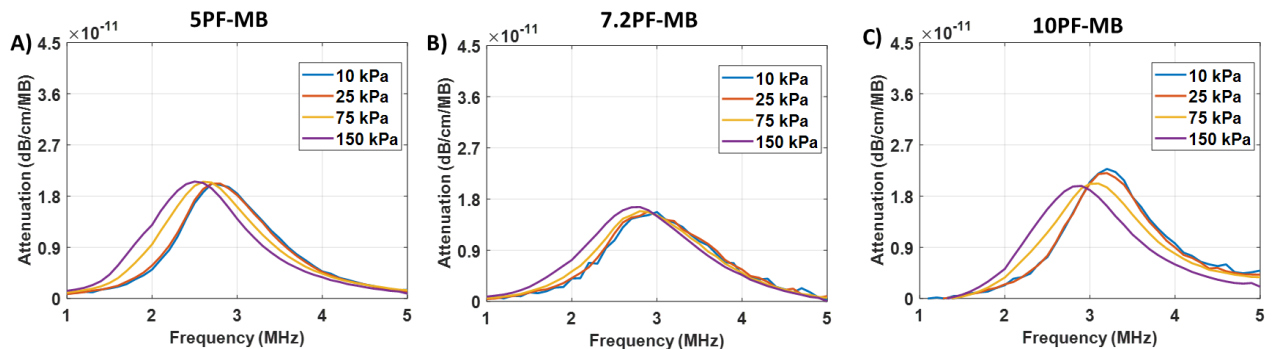
Figure 2. Attenuation measurements of A) 5PF-MB, B) 7.2PF-MB and C)10PF-MB from 1 to 5 MHz at pressure of 10-150 kPa.

Conclusions

In conclusion, our results show that adding PF68 suppresses coalescence in the production of mMB at room temperature. The 5PF-MB, 7.2PF-MB, and 10PF-MB exhibited stable size distribution over 7 days, while the 30PF-MB did not, suggesting an upper limit of PF68 addition for reaching stable mMB. Attenuation measurements revealed a comparable stiffness value for 5PF-MB, 7.2PF-MB, and 10PF-MB, that is higher than comparable mMB without PF added [4]. These findings underline the benefits of adding PF68 to scale-up the production of coalescence-free monodisperse microbubbles.

References

[1].Segers, T., P. Kruizinga, M.P. Kok, G. Lajoinie, N. De Jong, and M. Versluis, Monodisperse Versus Polydisperse Ultrasound Contrast Agents: Non-Linear Response, Sensitivity, and Deep Tissue Imaging Potential. Ultrasound in Medicine & Biology, **44**(7): p. 1482-1492, 2018.

[2].Shih, R., D. Bardin, T.D. Martz, P.S. Sheeran, P.A. Dayton, and A.P. Lee, Flow-focusing regimes for accelerated production of monodisperse drug-loadable microbubbles toward clinical-scale applications. Lab on a Chip, **13**(24): p. 4816, 2013.

[3].Abou-Saleh, R.H., F.J. Armistead, D.V.B. Batchelor, B.R.G. Johnson, S.A. Peyman, and S.D. Evans, Horizon: Microfluidic platform for the production of therapeutic microbubbles and nanobubbles. Review of Scientific Instruments, **92**(7): p. 074105, 2021.

[4].Segers, T., E. Gaud, G. Casqueiro, A. Lassus, M. Versluis, and P. Frinking, Foam-free monodisperse lipid-coated ultrasound contrast agent synthesis by flow-focusing through multi-gas-component microbubble stabilization. Applied Physics Letters, **116**(17), 2020.

Monodisperse targeted microbubbles: bound versus unbound

Martin R.P. van den Broek[1], Michel Versluis[2], Albert van den Berg[1], Tim Segers[1]

[1]_BIOS / Lab on a Chip Group, Max Planck Center Twente for Complex Fluid Dynamics, University of Twente, Enschede, The Netherlands_
[2]_Physics of Fluids Group, University of Twente, Enschede, The Netherlands_

Corresponding author: m.r.p.vandenbroek@utwente.nl

Introduction

Lipid-coated microbubbles are routinely used in the clinic as ultrasound contrast agents (UCAs) [1]. An emerging application of microbubbles and ultrasound is molecular ultrasound imaging using functionalized microbubbles with targeting ligands incorporated in the bubble shell. However, the polydisperse size distribution of current UCAs complicates quantitative molecular ultrasound imaging due to their non-uniform acoustic response, which inhibits the acoustic discrimination of freely floating, non-specifically bound, and specifically bound bubbles [2,3]. Narrowing down the size distribution of functionalized microbubble suspensions is therefore a promising pathway to quantitative molecular ultrasound imaging. Here, we show that monodisperse biotinylated microbubbles can be produced using microfluidics, and that they can be used for high-precision acoustic measurements of resonance frequency changes upon their flotation and specific binding to a wall.

Methods and results

Microbubble formation and washing. Monodisperse microbubbles were formed in the flow focusing device shown in Fig. 1A. The lipid dispersion contained DSPC mixed with DSPE-PEG5000 and DSPE-PEG5000-Biotin at a molar fraction of 90 : 9 : 1, respectively. Stable microfluidic bubble formation requires a total lipid concentration of at least 12.5 mg/mL. As such, approximately only 1 in every 10.000 lipid molecules self-assemble in the bubble shell. The excess lipids need to be removed as these occupy the available binding sites thereby preventing the molecular binding of the bubbles. The common method to remove excess lipids is centrifugation. However, centrifugation affects microbubble stability due to the increased hydrostatic pressure during centrifugation, which compresses the bubbles and thereby potentially results in lipid shedding and a decreased bubble size, see Fig. 1C. To maintain the monodispersity of the bubbles, we devised a novel and fully automated microfluidic washing method that can be used to reduce the excess lipid concentration by at least 10.000 times (Fig. 1B). The method allows washing to be performed within minutes while the microbubble size distribution remains unaffected (Fig. 1C).

To verify that the produced microbubbles were biotinylated and that excess lipid was removed, fluorescently labeled streptavidin (Streptavidin-AlexaFluor488) was added to a washed microbubble suspension. After a 10-minute incubation period, the dye was washed away. The concurrent fluorescence and brightfield images shown in Fig. 1D show that all bubbles are biotinylated and, based on the low background intensity, that the excess lipid was successfully cleared.

Acoustic characterization. A 50-μm thick polystyrene film incorporated in a 3D printed closed sample holder was coated with streptavidin through physisorption. Washed microbubbles were then brought in contact with the surface through floatation. Unbound microbubbles were flushed out of the sample holder by applying a flow while the sample holder was flipped upside down. Microscope images were then taken to verify that the bound microbubbles were spaced by at least 10 times their diameter to minimize acoustic bubble-bubble interactions.

The resonance behavior of microbubbles in the unbounded fluid, floating to the polystyrene surface, and specifically bound to the surface was measured using 12-cycle narrowband ultrasound attenuation

measurements at an acoustic pressure of 3 kPa. The sample holder with an uncoated polystyrene surface was used to determine the ultrasound attenuation of microbubbles floating against the wall. The obtained attenuation spectra shown in Fig. 1F demonstrate that the resonance frequency (frequency of maximum attenuation) of the microbubbles decreased by 15% upon their flotation from the unbounded fluid to the wall, and by an additional 10% upon their molecular binding to the wall.

Conclusions

Monodisperse biotinylated microbubbles can be produced by microfluidic flow focusing. The excess lipids can be washed away using a novel automated washing method that maintains microbubble monodispersity. Preliminary results show that the resonance frequency of the 3-µm radius microbubbles studied here decreases by 15% upon their flotation from the unbounded fluid to the wall, and by an additional 10% upon their molecular binding to the wall. As such, the results are a first indication that monodisperse functionalized microbubbles are a route to the acoustic discrimination of freely floating, non-specifically bound, and specifically bound microbubbles.
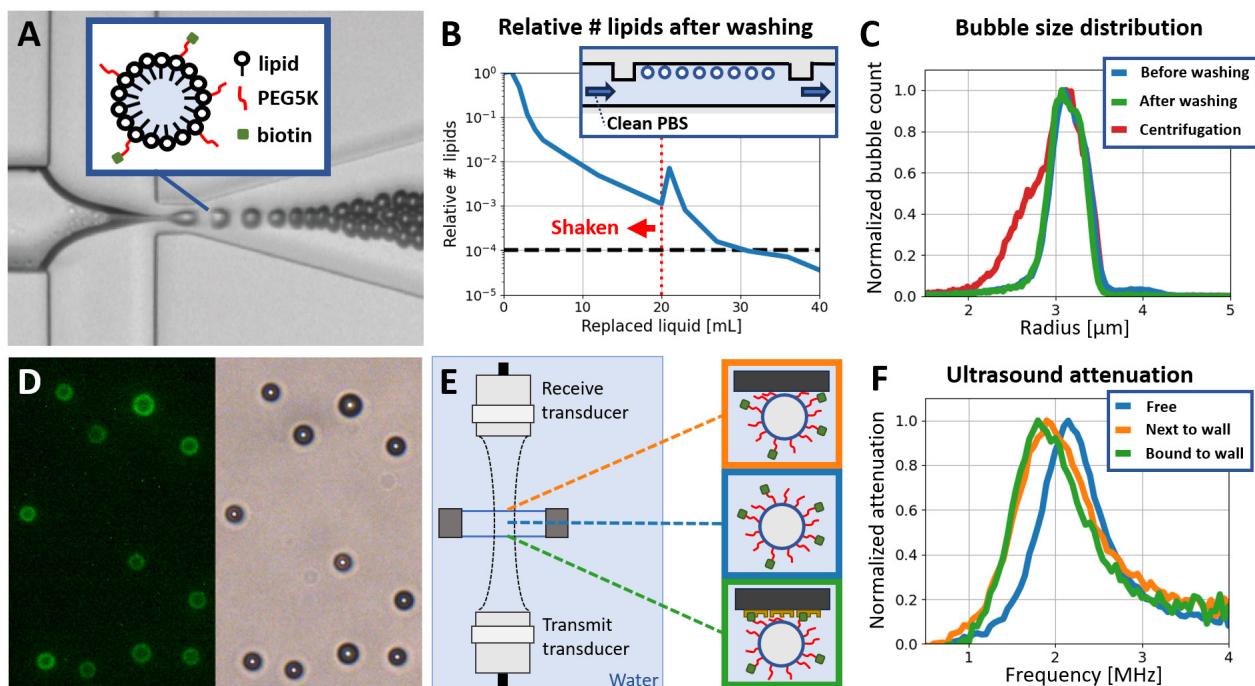
Figure 1: (A) Biotinylated microbubble formation by flow focusing. (B) Relative number of excess lipids as a function of liquid volume pumped through the washing chamber (inset). (C) Microbubble size distribution before and after washing and centrifugation. (D) Corresponding fluorescent and brightfield images of fluorescently labeled streptavidin attached to the biotinylated microbubbles. (E) Schematic of the ultrasound setup for the acoustic attenuation experiments. (F) Ultrasound attenuation spectra for the same microbubble suspension homogeneously distributed in the sample holder, floating against the top wall of the sample holder, and bound to the bottom wall of the sample holder.

References

[1]. Frinking P., Segers T., Luan Y., Tranquart, F., Three Decades of Ultrasound Contrast Agents: A Review of the Past, Present and Future Improvements, Ultrasound in Medicine & Biology, 4: 892-908, 2020.

[2]. Dollet B., Marmottant P., Garbin V., Bubble dynamics in soft and biological matter, Ann. Rev. Fluid Mech. 51, 331 (2019).

[3]. Smeenge M. *et al.* (2017). First-in-human ultrasound molecular imaging with a VEGFR2-specific ultrasound molecular contrast agent (BR55) in prostate cancer: a safety and feasibility pilot study. *Investigative radiology*, *52*(7), 419-427.

The Effect of Poly(ethylene glycol) Configuration on Microbubble Pharmacokinetics

J. Angel Navarro-Becerra[1,2] and Mark Borden[1,2]

[1]*Biomedical Engineering Program, University of Colorado Boulder, Boulder, CO, USA*
[2]*Mechanical Engineering Department, University of Colorado Boulder, Boulder, CO, USA*
Corresponding author: jose.navarro@colorado.edu

Introduction

Microbubble volume dose (MVD) represents a standardized metric that unifies the MB size distribution and concentration into a single dose parameter (µL/kg) for predicting MB biological effects, acoustic response and pharmacokinetic behavior [1-3]. Poly(ethylene glycol) (PEG), a commonly used non-ionic hydrophilic polymer within the MB shell, can adopt either a brush or mushroom configuration depending on the PEG molecular weight and surface density [4]. PEG is thought to prevent coalescence and shield the MB from opsonization and rapid clearance, although it is also known to induce an antibody response after multiple injections [5]. However, the effect of PEG configuration on MB pharmacokinetics remains unexplored. Hence, this study aimed to investigate the effect of different PEG configurations on MB pharmacokinetics as a function of MVD.

Methods

3 µm lipid-coated MBs (DBPC: PEG2000 and PFB gas) with mushroom, intermediate and brush configuration were obtained by varying the PEG molar ratio at 2%, 5% and 10%. Three Wistar rats (300-400 g) were intravenously injected with 20 and 40 µL/Kg MVD of each MB configuration. Then, blood samples were withdrawn at different times (1–30 min) and analyzed by image processing. The order of pharmacokinetics profile, half-life ($t_{1/2}$) and area-under-the-curve (AUC_1) for each configuration were determined by fitting the one-compartment model ($C_1=C_0e^{-k_et}$) and two-compartment model ($C_1=C_0[\alpha e^{-\lambda_1 t}+(1-\alpha)e^{-\lambda_2 t}]$).

Results

The mushroom, intermediate and brush size-isolated MBs exhibited a mean volume-weighted diameter of 3.2 µm. For 20 MVD and 40 µL/Kg MVD, MB clearance followed first-order kinetics (Figure 1A) and biexponential kinetics (Figure 1B). The exponential decay curves indicate that at low MVD, MBs were eliminated from circulation 20 min post-administration (Fig. 1A-a), whereas at high MVD, circulation time extended until 30 min (Fig. 1B-b). Surprisingly, the brush and intermediate configurations displayed a slightly faster MVD decay over time than the mushroom configuration.

Interestingly, for both kinetic profiles, the $t_{1/2(1)}$ (Fig. 1A-b and Fig. 2B-b) and AUC_1 (Fig. 1A-c and Fig. 2B-c) values in the central compartment (C_1) decreased with increasing PEG concentration from mushroom to brush and remained similar for intermediate and brush configurations. The $t_{1/2(1)}$ decreased from 2.3 ± 0.3 to 1.4 ± 0.2 min and from 0.40 ± 0.05 to 0.20 ± 0.03 min for 20 and 40 µL/kg MVD. Freely circulating MBs, represented by the AUC_1, decreased from 66.9 ± 9.9, 32.6 ± 3.3 and 40.8 ± 6.8 µL×min/kg and from 105.3 ± 13.6 to 41.8 ± 10.3 min µL×min/kg, respectively.

Conclusions

In conclusion, the findings from our study provide valuable insights into the pharmacokinetics of MBs with various PEG configurations. These results suggest that a lower PEG fraction is recommended to prolong circulation time, enhance bioavailability and reduce the retention of lipid-coated MBs.

A. One-compartment model (20 MVD)
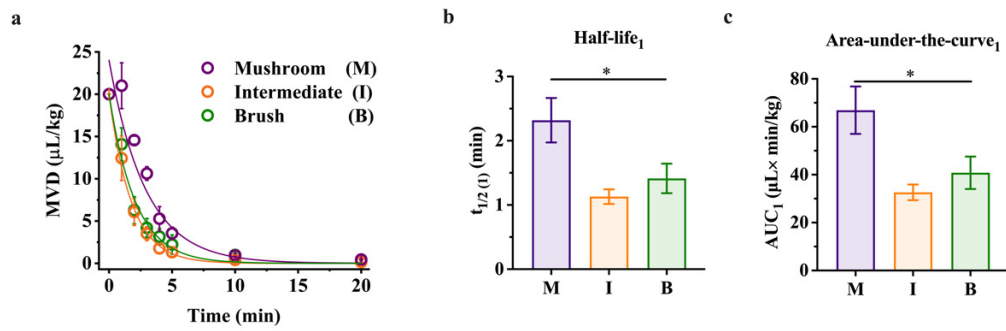
B. Two-compartment model (40 MVD)
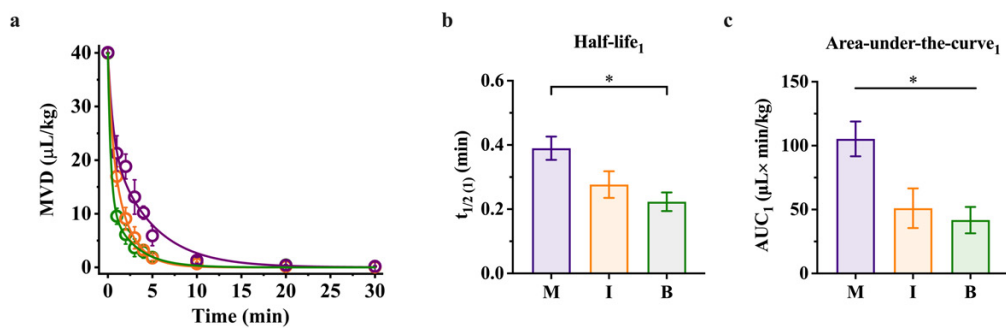
Figure 1. Pharmacokinetic characterization within the central compartment (C_1) for mushroom (M), intermediate (I) and brush (B) PEG microbubble (MB) configurations. A-B) Pharmacokinetic analysis in a one- and two-compartment model for MBs administered at 20 and 40 µL/kg MVD, respectively. a) Pharmacokinetic profiles are depicted with solid lines representing monoexponential and biexponential decay fits, with $R^2 \geq 0.98$, b) half-life ($t_{(1/2)}$) and area-under-the curve (AUC_1). *$p \leq 0.05$. The data represent the mean ± standard deviation from three different experiments.

References

[1]. Song, K. H., Fan, A. C., Hinkle, J. J., Newman, J., Borden, M. A., & Harvey, B. K. (2017). Microbubble gas volume: A unifying dose parameter in blood-brain barrier opening by focused ultrasound. *Theranostics*, *7*(1), 144.

[2]. Martinez, P., Bottenus, N., & Borden, M. (2022). Cavitation characterization of size-isolated microbubbles in a vessel phantom using focused ultrasound. *Pharmaceutics*, *14*(9), 1925.

[3]. Navarro-Becerra, J. A., Song, K. H., Martinez, P., & Borden, M. A. (2022). Microbubble size and dose effects on pharmacokinetics. *ACS biomaterials science & engineering*, *8*(4), 1686-1695.

[4]. De Gennes, P. G. (1987). Polymers at an interface; a simplified view. *Advances in colloid and interface science*, *27*(3-4), 189-209.

[5]. Chen, B. M., Cheng, T. L., & Roffler, S. R. (2021). Polyethylene glycol immunogenicity: theoretical, clinical, and practical aspects of anti-polyethylene glycol antibodies. *ACS nano*, *15*(9), 14022-14048.

Differential Sensitivity of F98 Glioma Tumors and Adjacent Healthy Spinal Cord Tissue in Response to Focused Ultrasound and Microbubbles

Mahsa Mokhlesabadi[1,2], Danielle Charron[1], Meaghan O'Reilly[1,2]

[1] *Sunnybrook Research Institute, Sunnybrook Health Sciences Centre, Toronto, ON, M4N 3M5, Canada*
[2] *Department of Medical Biophysics, Faculty of Medicine, University of Toronto, Toronto, ON*
Corresponding author: mahsa.mokhlesabadi@mail.utoronto.ca

Introduction

Intramedullary spinal cord tumors (IMSCTs), despite their low incidence[1], impose a significant challenge in clinical settings due to the ineffective, highly invasive, and toxic treatment options[2]. Surgical resection, as the current standard of care, is limited by the infiltration pattern of some tumors such as astrocytomas[3]. Moreover, most of the newly developed and tested treatments target the IMSCT brain counterparts resulting in spinal cord tumor treatments being left as an underexplored research area. Thus, there is a need to innovate new interventions for treating tumors in the spinal cord.

Focused ultrasound (FUS) in combination with ultrasound contrast agents is a relatively new, localized, and non-invasive treatment modality which has demonstrated broad clinical adaptability[4]. Intense interaction of ultrasound field with microbubbles can induce vascular disruption and lead to tumor growth delay subsequent to cell starvation[5,6]. Despite FUS-induced anti-vascular therapy being preclinically tested for various non-CNS tumor types, it has been studied to a lesser degree in the CNS. While in non-CNS tissue the tumors have shown to be more sensitive to this treatment due to their underdeveloped vasculature, there is a lack of corresponding data for CNS tumors. Thus, this study focuses on testing FUS and microbubble-induced anti-vascular therapy in spinal cord tumors for the first time to compare sensitivity of tumor versus healthy spinal cord tissue in a rat IMSCT model.

Methods

F98 glioma cells were injected directly in the midplane of the rat spinal cord to establish IMSCT[7]. A spherically focused PZT transducer with a center frequency of 580 kHz (10ms bursts, 1 Hz PRF, 40s duration) was used to deliver FUS under MRI guidance. After intravenous injection of house-made lipid-shelled microbubbles (MBs, composed of DSPC and DSPE-PEG2000, measuring 1.00 ± 0.85 um in diameter and dosed at 2.4×10^7 MBs per 100 grams of rat body weight), animals were treated both in the tumor tissue and the adjacent healthy spinal cord tissue over four different experiment arms of sham ultrasound (n=3) and ultrasound pressures (non-derated) of 0.4 MPa (n=5), 0.8 MPa (n=4) and 1.2 MPa (n=5). Animals were then sacrificed at 24h post-treatment, and the spinal cord tissue was harvested and processed for histology.

Results

Red blood cell extravasation, petechiae, and hemorrhagic lesions were detected in the H&E-stained slides of the samples. While damage to the tumor seems to be more localized, usually showing up as a proteinaceous fluid-filled cavity with floating red blood cells, the healthy tissue suffers from more extensive bleeding, in the form of many isolated areas of damage which are closely spaced but not contiguous, and sometimes extend beyond the FUS target size. A total damage rate of 62% for healthy tissues and 50% for tumor tissue was achieved; however, different pressures yielded different damage rates with 1.2 MPa pressure causing 100% damage rate in both healthy and tumor tissue, 0.8 MPa pressure causing damage in all healthy targets but only 25% of the treated tumors, and 0.4 MPa pressure giving rise to mild damage in 60% of both healthy and tumor tissue.

Moreover, qualitative comparison of damage in tumor versus healthy spinal cord tissue demonstrates the greater relative sensitivity of the healthy spinal cord tissue in response to FUS-induced anti-vascular therapy compared with the F98 tumors.

Conclusions

Similar or greater susceptibility of healthy spinal cord tissue to FUS-induced damage accentuates the importance of safety measures even in less intense FUS treatments such as blood spinal cord barrier opening for drug delivery as the ultrasound parameters which are adequate to acquire the desired bioeffects in tumor might bring about hazardous bioeffects in the surrounding vitally important healthy spinal cord tissue. It also underscores the need to confine the treatment based on the tissue type.

References

[1]. G. Capo, A. Vandenbulcke, and C. Y. Barrey, "Intramedullary Spinal Tumors," in Central Nervous System Tumors-Primary and Secondary, IntechOpen, 2022.

[2]. M. K. Tobin, J. R. Geraghty, H. H. Engelhard, A. A. Linninger, and A. I. Mehta, "Intramedullary spinal cord tumors: a review of current and future treatment strategies," Neurosurg Focus, vol. 39, no. 2, p. E14, 2015.

[3]. D. Samartzis, C. C. Gillis, P. Shih, J. E. O'Toole, and R. G. Fessler, "Intramedullary spinal cord tumors: part II—management options and outcomes," Global Spine J, vol. 6, no. 2, pp. 176–185, 2016.

[4]. S.-K. Wu, C.-L. Tsai, Y. Huang, and K. Hynynen, "Focused ultrasound and microbubbles-mediated drug delivery to brain tumor," Pharmaceutics, vol. 13, no. 1, p. 15, 2021.

[5]. D. E. Goertz, "An overview of the influence of therapeutic ultrasound exposures on the vasculature: high intensity ultrasound and microbubble-mediated bioeffects," International Journal of Hyperthermia, vol. 31, no. 2, pp. 134–144, 2015.

[6]. Y.-J. Ho and C.-K. Yeh, "Concurrent anti-vascular therapy and chemotherapy in solid tumors using drug-loaded acoustic nanodroplet vaporization," Acta Biomater, vol. 49, pp. 472–485, 2017.

[7]. Caplan, J. et al. "A novel model of intramedullary spinal cord tumors in rats: functional progression and histopathological characterization," Neurosurgery, vol. 59, pp. 193–200, 2006.

Delivery of Anti-Cancer Drugs using Microbubble-Assisted Ultrasound in a 3D Spheroid Model

Marie Roy[1], Corentin Alix[1], Julien Burlaud-Gaillard[2], Damien Fouan[1], William Raoul[3], Ayache Bouakaz[1], Emmanuelle Blanchard[2], Thierry Lecomte[3,4], Marie-Claude Viaud-Massuard[5], Noboru Sasaki[6], Sophie Serrière[1,7], Jean-Michel Escoffre[1]

[1]_UMR 1253, iBraiN, Université de Tours, Inserm, 37032 Tours, France_
[2]_Inserm U1259, MAVIVH, Université de Tours & Plateforme IBiSA des Microscopies, PPF ASB, CHRU de Tours, Tours, France_
[3]_Inserm UMR 1069, N2C, Université de Tours, France_
[4]_Department of Hepato-Gastroenterology & Digestive Oncology, CHRU de Tours, France_
[5]_UMR 1100, CEPR, Université de Tours, Inserm, Tours, France_
[6]_Faculty of Veterinary Medicine, Hokkaido University, Sapporo, Japan_
[7]_Département d'Imagerie Préclinique, PPF ASB, Université de Tours, 37032 Tours, France_

Corresponding author: marie.roy@univ-tours.fr

Introduction

Tumor spheroids are promising 3D _in-vitro_ tumor models for the evaluation of drug delivery methods [1]. Indeed, their architectures reflect partly the 3D organization of tumor, tumoral heterogeneity and microenvironment, resulting in a greater resistance to drugs than that observed in 2D _in-vitro_ models [2,3]. The design of noninvasive and targeted drug methods is required to improve the intratumoral bioavailability of chemotherapeutic drugs and to reduce their adverse off-target effects. Among such methods, microbubble-assisted ultrasound (MB-assisted US) is an innovative modality for noninvasive targeted drug delivery. This method enhances the local drug extravasation and penetration in the tumor tissue while reducing their nonspecific accumulation in healthy tissue and their side effects [4]. The aim of the present study is to evaluate the influence of acoustic pressure and MB concentration on the delivery of a drug model into colorectal cancer (CRC) spheroids and to investigate the efficacy of this US modality for the delivery of bleomycin, doxorubicin and irinotecan in colorectal cancer (CRC) spheroids.

Methods

Spheroid permeabilization – The CRC spheroids were placed in the cuvette and incubated with a fluorescent dye, propidium iodide (PI; 100 μM), and Vevo MicroMarker MBs (range from 2.10^7 to 8.10^7 MB/mL) in a deionized water tank at 37°C. Subsequently, the spheroids were exposed to 1 MHz sinusoid US waves with a pulse repetition period of 100 μs, 40 cycles/pulse, for 1 min with a peak negative pressure (PNP) range from 100 to 400 kPa. The PI penetration into spheroid was assessed using a fluorescence microscope. Spheroid growth and viability were evaluated by measuring spheroid area for 10 days under optical microscope and by a trypan blue assay at the 13th day, respectively.

Impact of MB-assisted US on spheroid structure – Ultrastructural modifications of CRC spheroids were investigated using histological analysis and transmission electron microscopy (TEM), immediately and 20 min after MB-assisted US.

Drug delivery using MB-assisted US – Three chemotherapeutic drugs, including bleomycin (0.1 μM and 1 μM), doxorubicin (1 μM and 10 μM) and irinotecan (0.1 μg/mL and 1 μg/mL), were acoustically delivered (400 kPa; 4.10^7 MB/mL) into the spheroids. Spheroid growth and viability was evaluated as described above.

Results

Spheroid permeabilization – The exposure of CRC spheroids to an PNP range of 100 kPa to 400 kPa significantly induced an increase of the fluorescence intensity compared to PI treatment alone, reaching a plateau from 300 kPa. Surprisingly, the doubling or quadrupling of the MB concentration resulted in similar permeabilization of spheroids as for an MB concentration of 2.10^7 MB/mL. Regardless of the PNP value or MB concentration, MB-assisted US had no significant influence on spheroid growth or viability.

Impact of MB-assisted US on spheroid structure – Histological analysis showed that the spheroids appeared less cohesive in structure immediately and 20 min after MB-assisted US exposure compared to the control spheroids. Indeed, the intercellular junctions of tumor cells located in the peripheral layers of spheroids were significantly disrupted in comparison to the control spheroids (37 ± 2 % immediately after MB-assisted US *versus* 12 ± 2 % for the control condition). TEM analysis confirmed these histological observations. Indeed, the sonicated spheroids exhibited changes in cell morphology and organization (i.e, wide intercellular gaps) in the peripheral layer of CRC spheroids compared to the control condition.

Drug delivery using MB-assisted US – The bleomycin treatment alone (0.1 or 1 µM) induced a decrease in spheroid growth compared to the control condition. This cytotoxic effect became more important when the bleomycin was delivered using MB-assisted US. Indeed, the acoustically mediated delivery of bleomycin at 0.1 µM resulted in a significant reduction of spheroid growth, which was close to that obtained with bleomycin treatment alone at 1 µM. In addition, the exposure of spheroids to MB-assisted US with 1 µM of bleomycin completely inhibited the spheroid growth. The trypan blue exclusion assay confirmed these results at the 13th day. However, this US modality did not improve the therapeutic efficacy of doxorubicin and irinotecan on CRC spheroids.

Conclusions

MB-assisted US induced an efficient permeabilization of colorectal cancer (CRC) spheroids to small molecules without affecting their viability and their growth. Histological analysis and electron microscopy revealed that MB-assisted US affected only the peripheral layer of CRC spheroids. MB-assisted US enhanced the therapeutic efficacy of bleomycin on CRC spheroids but not that of doxorubicin and irinotecan. Finally, this study demonstrates that tumor spheroids are a relevant model to evaluate the efficacy of MB-assisted US for the delivery of chemotherapeutics.

Acknowledgements

References

[1]. Roy, M.; Alix, C.; Bouakaz, A.; Serrière, S.; Escoffre, J.-M. Tumor Spheroids as Model to Design Acoustically Mediated Drug Therapies: A Review. Pharmaceutics 2023, 1;15(3):806

[2]. Torisawa, Y.-S., Takagi, A., Shiku, H., Yasukawa, T. & Matsue, T. A multicellular spheroid-based drug sensitivity test by scanning electrochemical microscopy. Oncol Rep 2005 13, 1107–1112

[3]. Ward, J. P. & King, J. R. Mathematical modelling of drug transport in tumour multicell spheroids and monolayer cultures. Mathematical Biosciences 2003, 181, 177–207

[4]. Snipstad, S.; Vikedal, K.; Maardalen, M.; Kurbatskaya, A.; Sulheim, E.; Davies, C. de L. Ultrasound and Microbubbles to Beat Barriers in Tumors: Improving Delivery of Nanomedicine.Adv Drug Deliv Rev 2021,177, 113847.

Improving Radiosensitization of Intrahepatic Cholangiocarcinoma and Metastatic Disease in the Liver Using a Microbubble-Based Approach: Initial Results from a Clinical Trial

_Corinne E. Wessner[1,2], Ji-Bin Liu[1], Kibo Nam[1], Kristen Bradigan[1],
Cristina Kuon Yeng Escalante[1], Tania Siu Xiao[1], Flemming Forsberg[1],
Andrej Lyshchik[1], Patrick O'Kane[1], Stephen Topper[1], Kevin Anton[1], John R. Eisenbrey[1]_

_Department of Radiology, Thomas Jefferson University Hospitals, Philadelphia, PA
School of Biomedical Engineering, Science and Health Systems, Drexel University, Philadelphia, PA
Corresponding author: John.Eisenbrey@jefferson.edu_

Introduction

Intrahepatic cholangiocarcinoma (ICC) is an aggressive epithelial cell malignancy that arises from the biliary tree in the liver and accounts for approximately 20% of all primary liver cancers, while hepatocellular carcinoma (HCC) accounts for the remaining 80% [1]. Moreover, the liver is a particularly common location for metastatic disease. In patients that have ICC or metastatic disease in the liver, 5-year relative survival rates are poor, ranging from 11-42% [2] [3]. Unfortunately, most patients present with disease that puts them outside the transplant criteria, so locoregional therapies such as transarterial radioembolization (TARE) are used as a bridge to transplant or to delay disease progression [4], [5]. TARE utilizes small glass beads approximately 30 μm in diameter that enclose the radioactive material yttrium-90 (Y90) [6]. Y90-TARE provides a localized and sustained release of radiation to the tumor with high delivered doses (approximately 110-200 Gy) [6]. Treatment efficacy is currently determined by a 2-6 month CT/MRI, and unfortunately, patients often have to wait months after Y90-TARE procedure to determine if the treatment was effective.

Contrast-enhanced ultrasound (CEUS) uses gas-filled microbubbles approximately 1-10 μm in diameter. At higher acoustic pressures (but still under the United States Food and Drug Administration limit of mechanical index < 1.9), these microbubbles undergo ultrasound-triggered microbubble destruction (UTMD), which can produce bioeffects on tumor endothelial cells [7]. UTMD induces mechanical perturbation on tumor endothelial cells, upregulating the production of ceramide, which acts as a second messenger for apoptosis and augments radiosensitization [8], [9]. Our group has shown the potential benefits of UTMD in a randomized clinical trial of hepatocellular carcinoma patients undergoing Y90-TARE. The aim of this clinical trial is to evaluate the safety and potential efficacy of using volumetric UTMD to improve outcomes in patients with ICC and metastatic disease in the liver who receive Y90-TARE.

Methods

In this pilot clinical trial, recruitment started in April 2022 under NCT# 05328167. Eligible participants with ICC or metastatic disease in the liver scheduled for a sub-lobar Y90-TARE treatment with tumors > 1 cm provided informed consent to participate in this IRB-approved study at Thomas Jefferson University. As part of the research protocol, each participant received four CEUS examinations. The first CEUS examination occurred one to two weeks prior to TARE at the time of the planning procedure, the second examination 1-4 hours post-Y90-TARE, and the third and fourth CEUS examinations were one- and two weeks post-Y90-TARE, respectively. Microbubble infusions consisted of 5 ml of activated Optison (GE Healthcare, Princeton, NJ) mixed in 50 ml saline and infused over a 10-minute period at a rate of 120 ml/hour through a peripheral arm vein. After confirmation of contrast enhancement, 2D and 3D CEUS imaging was performed with a modified Logiq GE E10 scanner (GE HealthCare, Waukesha, WI) using a RAB6-D probe with transmitting frequencies ranging from 3.3-5.0 MHz.

For all CEUS examinations, participants were asked to temporarily halt respiration (approximately 5-10 seconds) to acquire CEUS imaging over the 10-minute infusion. For CEUS examination 1, imaging consists of baseline 2D and 3D CEUS to evaluate pre-treatment tumor enhancement. In CEUS examinations 2-4 (post Y90-TARE), volumetric UTMD (approximately 4 seconds) with flash-replenishment imaging was repeated approximately 3-5 times at the tumor midline. For 2D imaging, UTMD destructive pulses (approximately 4 seconds) were acquired to sweep through the tumor volume. For safety evaluation, vital signs pre and post-UTMD sessions, adverse events, and liver function tests at baseline and 1-2 months post Y90-TARE were evaluated. For treatment response, participants' long-term outcomes and cross-sectional follow-up imaging are being evaluated and will eventually be matched to historical controls.

Results:

To date, seven participants have been enrolled with no serious adverse events recorded for any of the CEUS examinations. Five cases were diagnosed as ICC, and two cases as colorectal cancer metastases. Mean tumor diameter was 4.3 cm (range: 2.2-8.3 cm). The mean age and BMI were 60 ± 5.8 years and 28.8 ± 3.8 kg/m^2, respectively. Contrast enhancement was present in all CEUS cases, and 3D volume acquisition rates ranged from 0.3 to 3.0 volumes/second. The mean mechanical index and intensity peak spatial peak temporal average (IPSTA) during coded-harmonic imaging was 0.2 ± 0.1 and 7.8 ± 7.2 mW/cm^2 with UTMD destructive pulses 0.9 ± 0.3 and 170.7 ± 24.1 mW/cm^2. The mean Y90-TARE radiation dose was 141.7 Gy (range: 130-150 Gy). To date, four participants have completed all CEUS examinations. One participant withdrew from the study after CEUS examination 1, one completed three of the four CEUS examinations with no follow-up cross-sectional imaging, and one participant remains on active follow-up CEUS imaging.

Currently, cross-sectional imaging post-Y90-TARE is available for two participants. In these two participants (both with ICC), the 2-6 month cross-sectional imaging determined that one participant had a non-viable tumor. This participant had no further liver-directed therapy (Figure 1). The other participant had viable tumor and underwent Y90-TARE retreatment of the same tumor seven months post-CEUS imaging. In both participants, the treatment cavity was assessed by the study team. In the patient with the non-viable tumor on cross-sectional imaging, the treatment cavity showed no residual or internal enhancement on CEUS imaging. The participant found to have viable disease post-Y90-TARE on cross-sectional imaging showed post-treatment residual enhancement on CEUS, indicating that CEUS may also be useful for monitoring treatment response in these participants immediately post-Y90-TARE. Two participants recently completed all CEUS examinations and are awaiting cross-sectional imaging.

Conclusions:

Early results demonstrate that the addition of UTMD in participants with ICC and metastatic disease to the liver receiving Y90-TARE is safe and well tolerated. Microbubble cavitation may help sensitize tumors to improve treatment response to Y90-TARE. However, recruitment and data analysis are ongoing.
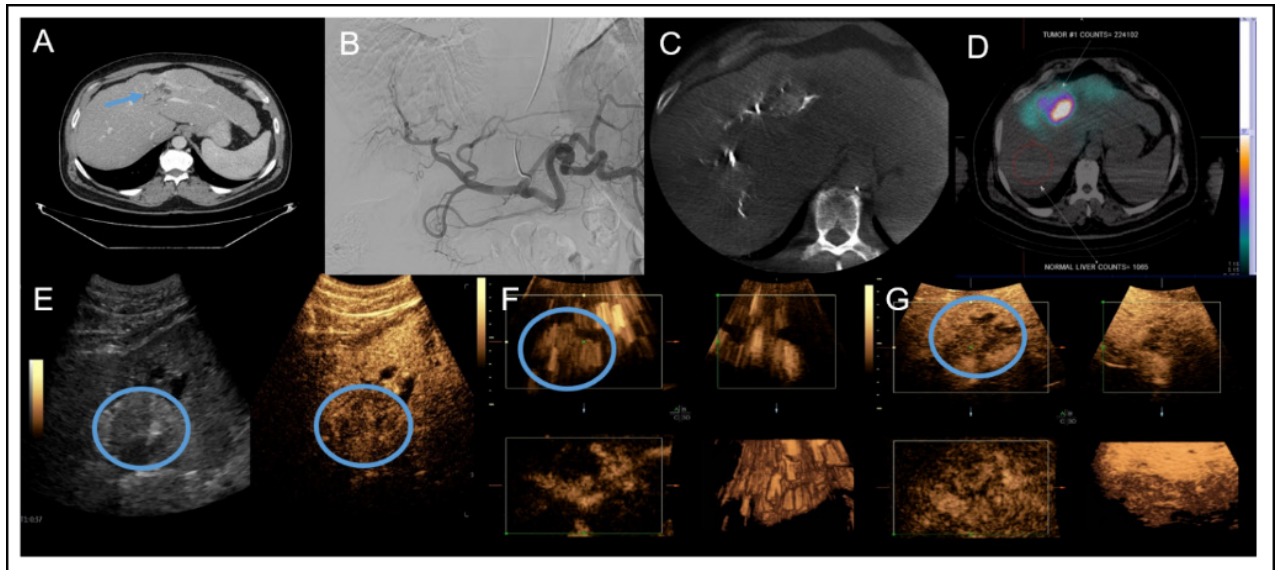
Figure 1. Intrahepatic cholangiocarcinoma in the left lobe of the liver on a pre-treatment contrast-enhanced CT (A). During the treatment planning, angiography (B), cone-beam CT (C), and Tc-99m MAA (macroaggregated albumin) SPECT-CT (D) was performed to evaluate hepatic and tumor feeding vasculature. Dual 2D CEUS imaging immediately post-Y90 TARE treatment (E) 3D UTMD pulse sequences (F) and 3D harmonic imaging to evaluate tumor reperfusion (G). The blue circle indicates the corresponding tumor.

References:

[1]. N. Razumilava and G. J. Gores, "Cholangiocarcinoma," *Lancet*, vol. 383, no. 9935, pp. 2168–2179, Jun. 2014, doi: 10.1016/S0140-6736(13)61903-0.

[2]. J. Yang and L.-N. Yan, "Current status of intrahepatic cholangiocarcinoma," *World J Gastroenterol*, vol. 14, no. 41, pp. 6289–6297, Nov. 2008, doi: 10.3748/wjg.14.6289.

[3]. A. I. Valderrama-Treviño, B. Barrera-Mera, J. C Ceballos-Villalva, and E. E. Montalvo-Javé, "Hepatic Metastasis from Colorectal Cancer," *Euroasian J Hepatogastroenterol*, vol. 7, no. 2, pp. 166–175, 2017, doi: 10.5005/jp-journals-10018-1241.

[4]. K. E. Zane, J. M. Cloyd, K. S. Mumtaz, V. Wadhwa, and M. S. Makary, "Metastatic disease to the liver: Locoregional therapy strategies and outcomes," *World J Clin Oncol*, vol. 12, no. 9, pp. 725–745, Sep. 2021, doi: 10.5306/wjco.v12.i9.725.

[5]. J. Bridgewater *et al.*, "Guidelines for the diagnosis and management of intrahepatic cholangiocarcinoma," *Journal of Hepatology*, vol. 60, no. 6, pp. 1268–1289, Jun. 2014, doi: 10.1016/j.jhep.2014.01.021.

[6]. A. Al-Kalbani and Y. Kamel, "Y-90 Microshperes in the Treatment of Unresectable Hepatocellular Carcinoma," *Saudi J Gastroenterol*, vol. 14, no. 2, pp. 90–92, Apr. 2008, doi: 10.4103/1319-3767.39627.

[7]. [G. J. Czarnota *et al.*, "Tumor radiation response enhancement by acoustical stimulation of the vasculature," *Proc. Natl. Acad. Sci. U.S.A.*, vol. 109, no. 30, Jul. 2012, doi: 10.1073/pnas.1200053109.

[8]. [A. El Kaffas and G. J. Czarnota, "Biomechanical effects of microbubbles: from radiosensitization to cell death," *Future Oncology*, vol. 11, no. 7, pp. 1093–1108, Apr. 2015, doi: 10.2217/fon.15.19.

[9]. [A. El Kaffas, A. Al-Mahrouki, A. Hashim, N. Law, A. Giles, and G. J. Czarnota, "Role of Acid Sphingomyelinase and Ceramide in Mechano-Acoustic Enhancement of Tumor Radiation Responses," *J Natl Cancer Inst*, vol. 110, no. 9, pp. 1009–1018, Feb. 2018, doi: 10.1093/jnci/djy011.

Enhancement of radiation-induced cell death using ultrasound-stimulated microbubbles

Hannah Bargh-Dawson[1], Carol Box[1], John Civale[1], Graeme Birdsey[2], Jessica Downs[3], Jeffrey Bamber[1], Emma Harris[1]

[1]Radiotherapy & Imaging, Institute of Cancer Research, London, UK
[2]National Heart & Lung Institute, Imperial College London, UK
[3]Cancer Biology, Institute of Cancer Research, London, UK
Corresponding author: hannah.bargh-dawson@icr.ac.uk

Introduction

Stereotactic body radiotherapy (SBRT) is a type of hypofractionated radiotherapy in which radiation doses, larger than conventional radiotherapy doses (typically >6 Gy), are precisely delivered to tumours. SBRT has shown clinical success in several cancer types; however, its use in treating head and neck cancers (HNC) is limited by the risk of damage to the surrounding vital normal tissues. Independent vascular injury is reported to enhance the tumour cytotoxicity of SBRT and improve clinical response to treatment. As a result, tumour vasculature targeting agents are proposed as adjunct therapies to radiotherapy, with the aim of reducing the radiation dose required to achieve a given level of tumour cytotoxicity. Extensive preclinical evidence supports the use of ultrasound-stimulated microbubbles (USMB) as mechanically acting radiosensitisation agents, with equivalent cell death and tumour growth control observed following the combination of USMB and low dose radiotherapy (2 to 6 Gy) compared to higher doses of radiation alone (>8 Gy) [1, 2, 3]. This work aimed to assess the therapeutical potential of USMB as radiosensitisation agents in HNC using pre-clinical models and explore the mechanism of action responsible for achieving the radioenhancement effects.

Methods

Female C57BL/6 mice bearing subcutaneous MOC2 (murine oral carcinoma) tumours (n=24) were randomly allocated into i) no treatment ii) 8 Gy or iii) USMB and 8 Gy treatment groups once tumours reached 150 mm^3. For USMB, intravenously administered Luminity® (Pharmanovia, Burgemeester, Netherlands) were stimulated by a 1 MHz single-element transducer (Precision Acoustics, Dorchester, UK) emitting a 50 ms tone-burst pulse of 16-cycles at 3 kHz PRF and 500 kPa, repeated every 2 s to allow for MB recirculation. A single radiation dose of 8 Gy was delivered using a Small Animal Radiation Research Platform (Xstrahl Ltd, Suwannee GA, USA). Radiation was delivered 6 hours post USMB. Tumour size was assessed with callipers every 2 days post-treatment until tumours reached the humane size limit of the project licence.

To assess vascular changes, longitudinal DCE-US imaging was performed at 48 hours and 7 days post-treatment and at the humane endpoint. Time-amplitude curves (TACs) were generated using DCE-US imaging data to derive semi-quantitative metrics of tumour perfusion such as peak enhancement (PE) and MB wash-in and wash-out time. Tumour morphology and neovascularisation were assessed by a pathologist using Haematoxylin and Eosin (H&E) and CD-31staining of tumours excised at study endpoint.

Results

USMB enhanced MOC2 tumour response to radiotherapy. Tumours treated with the combination of USMB and 8 Gy exhibited a growth delay relative to the 8 Gy and untreated controls, with the median doubling time increasing to 11.4 days for USMB and 8 Gy tumours compared to 7.9 and 4.9 days for the 8 Gy and untreated tumours respectively, Figure 1.

Analysis of longitudinal DCE-US imaging revealed changes in metrics associated with enhanced tumour perfusion in tumours treated with USMB and 8 Gy. At seven days post treatment, the median PE increased, and wash-in time decreased (2224 a.u and 15.8 s respectively) compared to measurements taken of the same tumours 48 hours post-treatment (1492 a.u and 42.4 s) and at endpoint (773 a.u and 69.3 s). In

addition, median PE was higher and wash-in time lower in USMB and 8 Gy tumours compared to the 8 Gy (1082 a.u and 25.7 s) and untreated control (1020 a.u and 55.2 s) tumours at the same 7-day time point, Figure 2.

H&E staining revealed that cells within the untreated tumours had morphological characteristics associated with poor cell differentiation and a more mesenchymal phenotype. In contrast, tumours treated with 8 Gy or USMB and 8 Gy comprised of a mixture of two distinct cell populations with different morphological features, Figure 3. One population was regular in cell and nuclear size and more closely resembled normal squamous mucosa, which are features associated with well-differentiated squamous carcinoma cells. Whereas the second population had large and abnormal nuclei and increased mitotic activity, appearing only moderately differentiated. Tumours treated with USMB and 8 Gy had a higher proportion of well-differentiated cells than the tumours treated with 8 Gy alone, Figure 3. Furthermore, CD31 staining revealed that the vessels within the well-differentiated regions were less chaotic and more similar in morphology to vessels within non-cancerous tissues, Figure 3.

Conclusions

These results demonstrate that USMB can be used as a localised adjunct treatment to enhance response of HNC to radiotherapy. A higher proportion of the cells within tumours treated with USMB and 8 Gy appeared morphologically well-differentiated and similar to normal epithelial cells.   Well-differentiated tumours are associated with a less aggressive disease phenotype, better treatment response and survival. Additionally, an increase in blood volume and blood flow into tumours was observed seven days after treatment with USMB and 8 Gy. Future work will utilise multimodality imaging, further histological analysis, and immune profiling to determine the molecular mechanisms responsible for radiosensitisation using USMB in HNC.
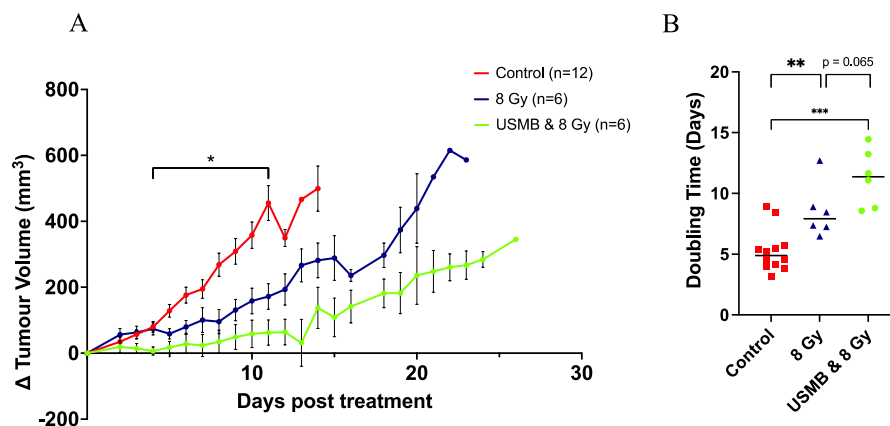
Figure 1. **A.** Mean MOC2 tumour growth curves per treatment group, expressed as change in tumour volume relative to tumour volumes at treatment (*p < 0.05, Multiple Mann-Whitney t tests between control and USMB and 8 Gy). **B.** Tumour doubling times (calculated using an exponential (Malthusian) fit) per treatment group (*** p = 0.0004, ** p = 0.005, Mann-Whitney t tests).
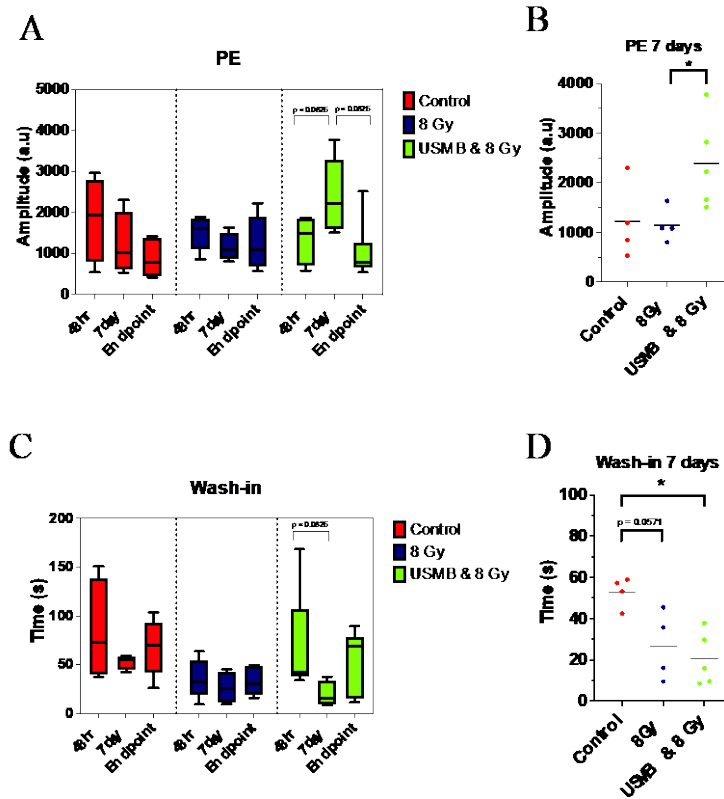
Figure 2. DCE-US metrics of MOC2 tumours at 48 hours and 7 days post-treatment and at end point. **A & C.** Changes in peak enhancement (PE) and wash-in time for MOC2 tumours over time. **B & D.** Differences in PE and wash-in time between groups 7 days post-treatment (*P = <0.05, Mann Whitney t tests).
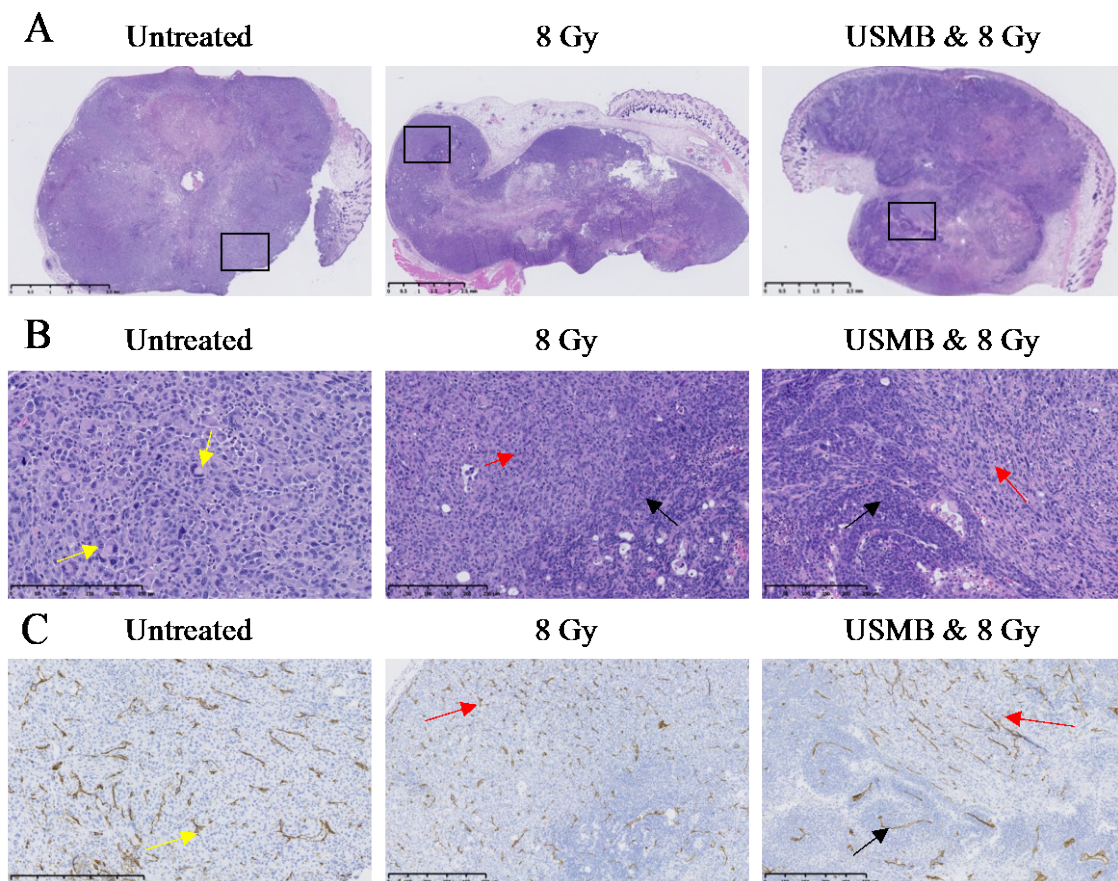
Figure 3. **A.** H&E staining of representative tumours from the untreated, 8 Gy and USMB and 8 Gy treatment groups. Bar = 2.5 mm. **B.** High magnification images of ROIs from **A**. Poorly differentiated cells with large and abnormal nuclei (yellow arrows) observed in the untreated tumour. Two distinct populations observed in 8 Gy, and USMB and 8 Gy tumours: darker stained cells = well-differentiated (black arrow) and paler cells = moderately differentiated (red arrow) carcinoma cells. Bar = 250 μm. **C.** Immunohistochemical staining of CD31 on endothelial cells within ROIs from **A**. Images show morphological differences between the blood vessels in poorly- (yellow arrow), moderately- (red arrow) and well- (black arrow) differentiated tumour regions. Bar = 500 μm.

References

[1]   El Kaffas A, Gangeh MJ, Farhat G, Tran WT, Hashim A, Giles A, et al. Tumour Vascular Shutdown and Cell Death Following Ultrasound-Microbubble Enhanced Radiation Therapy. Theranostics. 2018;8(2):314-27.

[2]   Lai P, Tarapacki C, Tran WT, El Kaffas A, Lee J, Hupple C, et al. Breast tumor response to ultrasound mediated excitation of microbubbles and radiation therapy in vivo. Oncoscience. 2016;3(3-4):98-108.

[3]   McNabb E, Al-Mahrouki A, Law N, McKay S, Tarapacki C, Hussein F, et al. Ultrasound-stimulated microbubble radiation enhancement of tumors: Single-dose and fractionated treatment evaluation. PLoS One. 2020;15(9):e0239456.

Effect of ultrasound and microbubbles on nanoparticle delivery and functional vasculature in three tumor models

Caroline Einen[1,2], Håkon Wesche[1], Andrea B. Kastellet[1], Anna Kurbatskaya[1], Jessica Lage[1], Veronica Nordlund[1], Catharina de Lange Davies[1], Sofie Snipstad[1,3]

[1]Department of Physics, Norwegian University of Science and Technology (NTNU), Trondheim, Norway
[2]Porelab, Trondheim, Norway
[3]Cancer Clinic, St. Olavs Hospital, Trondheim, Norway
Corresponding author: caroline.einen@ntnu.no mailto:

Introduction

Nanoparticles are used as drug carriers in cancer therapy, but present limited and variable tumor accumulation [1]. The delivery of nanoparticles to tumors can be improved by cavitation of microbubbles with ultrasound [2]. However, the mechanisms and biological effects of this treatment are not fully understood. Thus, there is a need to explore the effect of ultrasound and microbubbles on the tumor microenvironment in general, for instance the tumor vasculature, as well as nanoparticle uptake. It is also necessary to understand the role of the tumor microenviroment in the success or failure of nanoparticle delivery with ultrasound and microbubbles, to asses whether a tumor/patient group could benefit from such a treatment.

Methods

Three murine tumor models, 4T1 (breast cancer), CT26 (colon cancer) and KPC (pancreatic cancer) were grown subcutaneously in the hind leg of mice. Contrast Enhanced Ultrasound (CEUS) imaging with MicroMarker was done to characterize the tumor vasculature and perfusion (Fig. 1).

Animals were treated with pulsed ultrasound over 9 minutes, with intraveneous SonoVue injections at 0, 3 and 6 minutes. A frequency of 1 MHz, a mechanical index of 0.5 and a pulse repetition frequency of 0.25 Hz with 10 000 cycles was used, parameters previously shown to increase delivery of both free and nanoparticle encapsulated drugs to tumors [3]. Passive cavitation detection was used to confirm SonoVue activity.

Animals were injected with FITC-labeled lectin directly after ultrasound treatment to label functional blood vessels, followed by euthanazia after 5 minutes. Polymeric nanoparticles were injected prior to ultrasound treatment to evaulate effects on particle delivery, where whole animal optical imaging was used to monitor particle uptake in tumors over time. Confocal imaging was used to image all blood vessels (CD31), functional vessels (FITC-lectin), hyaluronic acid (HA, HA-binding protein) and cell nuclei (DAPI), and fibrillar collagen was imaged by second harmonic generation microscopy. The fraction of functional blood vessels in the tumor was evaluated by the ratio between functional and all vessels.

Results

CEUS imaging revealed that the CT26 tumors presented slower perfusion and a higher blood volume compared to the 4T1 and KPC tumors. In the case of all blood vessels, both functional and non-functional, confocal imaging revealed similar amounts between the three tumor models, with a great degree of variation from tumor to tumor. The CT26 and KPC tumors presented comparable cell densities, with 4T1 trending lower than the other two. Further, CT26 had the lowest amount of HA of the three tumor models. Additionally, the KPC tumors showed a trend toward increased amounts of fibrillar collaged compared to 4T1 and CT26.

There was a reduction in the fraction of functional blood vessels in all three tumor models directly after treatment with ultrasound and microbubbles, however the reduction was more pronounced in the 4T1 and CT26 tumors compared to KPC. Further, the effect of ultrasound and microbubbles on nanoparticle uptake varied between the three tumor models.

Conclusions

The CT26, 4T1 and KPC tumors presented different tissue characteristics and responded differently to treatment wih ultrasound and microbubbles. Notably, the KPC tumors had higher amounts of collagen and a smaller reduction in the fraction of functional blood vessels compared to 4T1 and CT26, potentially indicating that collagen-rich tumors are more resistant to vascular effects from ultrasound and microbubbles. These results highlight the importance of evaluating treatment suitability and effects in the specific cancer tissue of interest.
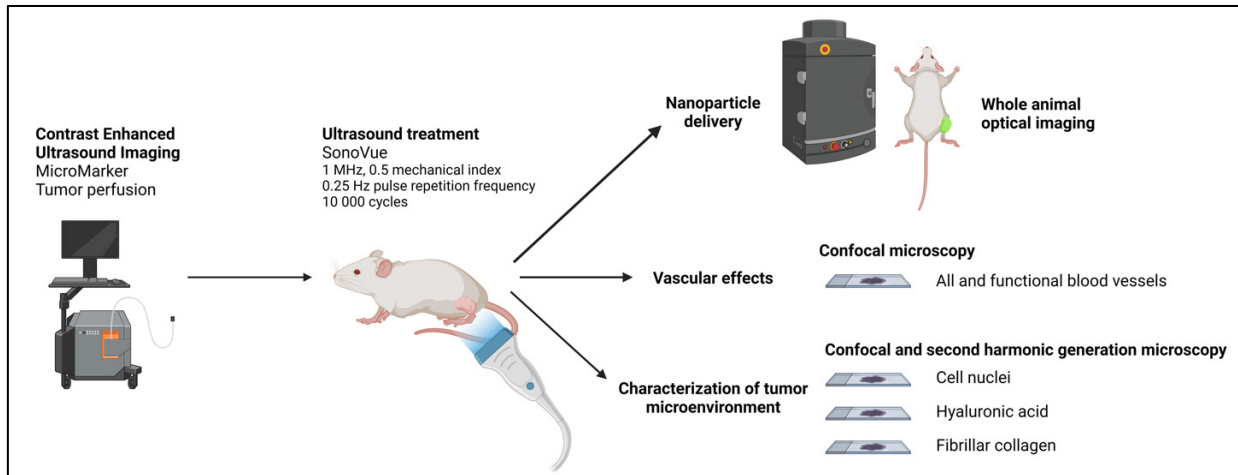
Figure 1. Simplified schematic overview of the study. Figure created with BioRender.com

References

[1]. Wilhelm, S.; Tavares, A.J.; Dai, Q.; Ohta, S.; Audet, J.; Dvorak, H.F.; Chan, W.C.W. Analysis of Nanoparticle Delivery to Tumours. *Nat. Rev. Mater.* **2016**, *1*, 16014, doi:10.1038/natrevmats.2016.14.

[2]. Snipstad, S.; Vikedal, K.; Maardalen, M.; Kurbatskaya, A.; Sulheim, E.; Davies, C. de L. Ultrasound and Microbubbles to Beat Barriers in Tumors: Improving Delivery of Nanomedicine. *Adv. Drug Deliv. Rev.* **2021**, 113847, doi:10.1016/J.ADDR.2021.113847.

[3]. Snipstad, S.; Mørch, Ý.; Sulheim, E.; Åslund, A.; Pedersen, A.; Davies, C. de L.; Hansen, R.; Berg, S. Sonopermeation Enhances Uptake and Therapeutic Effect of Free and Encapsulated Cabazitaxel. *Ultrasound Med. Biol.* **2021**, *47*, 1319–1333, doi:10.1016/j.ultrasmedbio.2020.12.026.

Uptake and microdistribution of doxorubicin in murine tumors treated with SonoVue and focused ultrasound

Veronica Nordlund[1], _Margrete Haram[2,3,4]_, _Jenny Josefine Lorck Bjørgen[1]_, _Sofie Snipstad[1,4]_, _Caroline Einen[1]_, _Catharina de Lange Davies[1]_

[1]_Department of Physics, Norwegian University of Science and Technology, Trondheim, Norway_
[2]_Department of Radiology and Nuclear Medicine, Norwegian University of Science and Technology, Trondheim, Norway_
[3]_Department of Clinical and Molecular Medicine, St. Olav's Hospital, Trondheim University Hospital, Trondheim, Norway_
[4]_Cancer clinic, St. Olav's Hospital – Trondheim University Hospital, Trondheim, Norway_
Corresponding author: veronica.nordlund@ntnu.no

Introduction

Using microbubbles (MB) in combination with focused ultrasound (FUS) has shown to improve the tumor uptake and therapeutic effect of standard chemotherapy in both preclinical and clinical trials [1-4]. In a preclinical study, Haram et al. found that MB + FUS treatment of orthotopic pancreatic tumors in mice increased the uptake of the chemotherapeutic agent FOLFIRINOX, as presented in Fig. 1 [5].
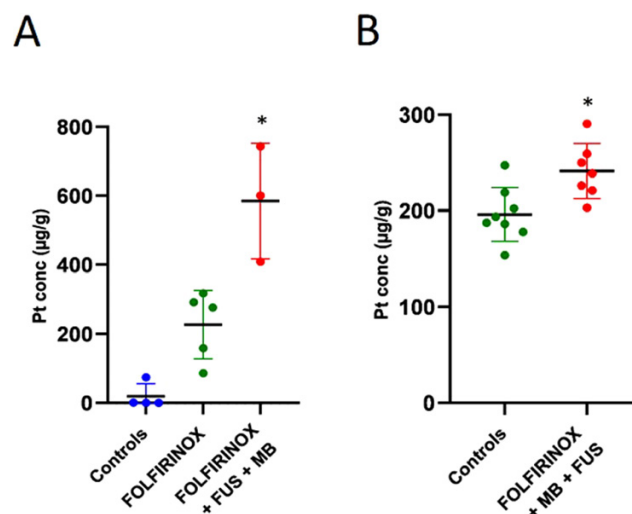
Figure 1. Tumor uptake of platinum in pancreatic tumor tissue after (A) five treatments and (B) one single treatment [5].

However, there was not a significant difference in tumor growth between the groups which received FOLFIRINOX alone compared to those treated with FOLFIRINOX in combination with MB + FUS. In a subsequent clinical trial, patients with inoperable pancreatic ductal adenocarcinoma (PDAC) were treated with standard chemotherapy either with or without MB + FUS [6]. The tumor growth varied greatly between patients within both the treated and control group, and no significant difference was observed between the groups. It should be mentioned that only 20 patients were included and randomized for either treatment with FUS+MBs or control. A prerequisite for successful chemotherapy is that the drug reaches all tumor cells.

Therefore, overall tumor uptake of drugs needs to be supplemented with information on the microdistribution within the tumor. In our work, confocal laser scanning microscopy was used to image the microdistribution of the fluorescent cancer drug doxorubicin in murine tumors treated with and without MB + FUS.

Methods

Subcutaneous murine KPC and CT26 tumors in the hind leg of mice were chosen as tumor models. On treatment day, the mice were anesthetized and placed on a water tank with an ultrasound setup as shown in Fig. [2].
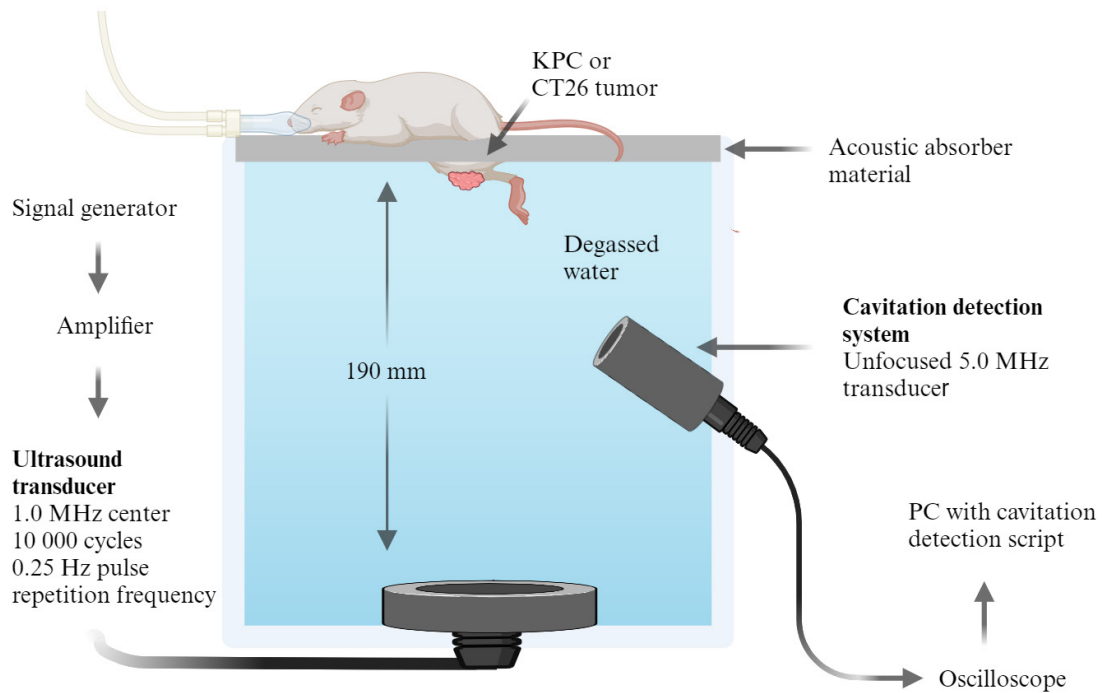
Figure 2. Schematic illustration of the ultrasound setup. Created with BioRender.com.

Before sonication, 10 mg/kg doxorubicin was injected intravenously. Immediately after, the tumor was sonicated with FUS for 6 minutes. 50 μL SonoVue was injected intravenously immediately after initiation of sonication and after 3 minutes. 25 minutes after the initial SonoVue injection, 50 μL lectin conjugated with a fluorochrome was injected intravenously to label functional vessels. Five minutes later, mice were euthanatized, and tumors were harvested. The fluorescence of doxorubicin from the whole tumor was imaged ex vivo in the IVIS whole animal imaging system.

Tumor sections were imaged using confocal laser scanning microscopy. 25 μm frozen tumor sections were prepared with a cover glass and the mounting medium VectaShield PLUS with DAPI nucleic acid stain. Tile scans were captured using a 20x/0.8 air objective. The images were processed and analyzed using ImageJ.

Results

Representative confocal laser scanning images from one KPC and one CT26 tumor treated with doxorubicin and MB + FUS are shown in Fig. 3. The tile scans illustrate that CT26 tumors have more functional blood vessels (green) throughout their center than KPC tumors. Ex vivo fluorescence imaging from tumors in the whole-animal imaging system shows that the total uptake of doxorubicin is higher in CT26 tumors than in KPC tumors, probably due to the higher amount of blood vessels in CT26 tumors. From the confocal laser scanning images, the average fluorescence intensity and sum of pixel values of

doxorubicin (yellow) are measured in ongoing work and gives an indication of the total doxorubicin uptake in the tumor section. The zoomed-in areas show that there is more fluorescence from doxorubicin in areas close to blood vessels, and the intensity decreases with increased distance from the blood vessel. To quantitate this concentration gradient and the effect of MB + FUS, the number of cells with doxorubicin as a function of distance from the nearest blood vessel are determined. Furthermore, doxorubicin accumulated within the cell nuclei, which was confirmed by colocalization with DAPI (not shown).
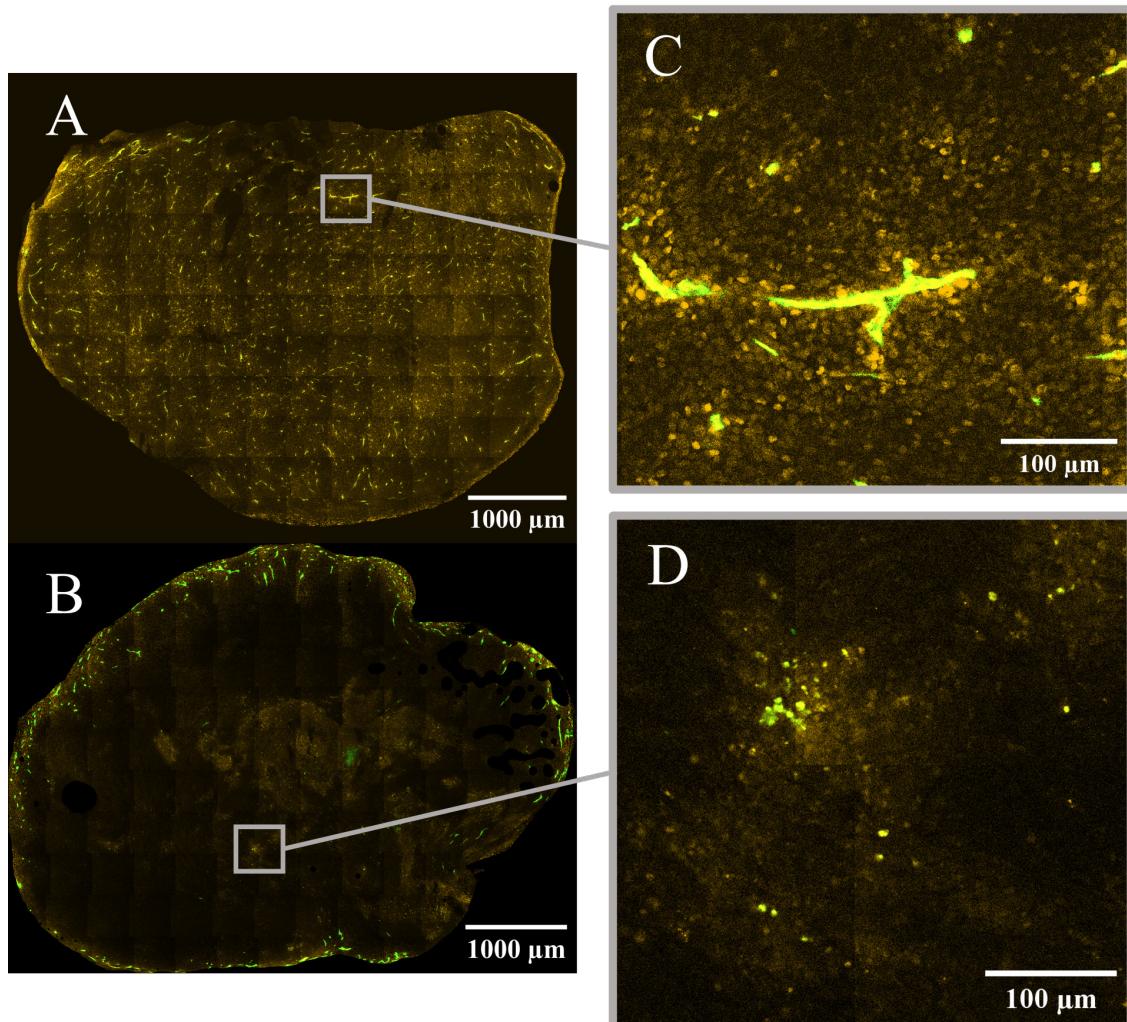
Figure 3. Whole-tumor tile scans of doxorubicin (yellow) and blood vessels stained with FITC-labeled lectin (green) in CT26 (A) and KPC (B) tumors, together with zoomed-in snapshots (C, D) from select regions of each tumor.

Conclusions

Whole-tumor fluorescent imaging shows a higher uptake of doxorubicin in CT26 tumors than in KPC tumors, in accordance with a higher amount of blood vessels in CT26 tumors. More doxorubicin was seen in close vincinity to blood vessels, and the uptake of doxorubicin in cells decreased with distance from the blood vessel. Ongoing analyses investigate differences in uptake and microdistribution of doxoubicin in tumors treated with and without FUS+MB.

References

[1]. Kotopoulis S, Delalande A, Popa M, Mamaeva V, Dimcevski G, Gilja OH, Postema M, Gjertsen BT, McCormack E, Sonoporation-enhanced chemotherapy significantly reduces primary tumour burden in an orthotopic pancreatic cancer xenograft, Molecular Imaging and Biology, 16: 53–62, 2013.

[2]. Snipstad S, Mørch Ý, Sulheim E, Åslund A, Pedersen A, Davies CDL, Hansen R, Berg S, Sonopermeation enhances uptake and therapeutic effect of free and encapsulated cabazitaxel, Ultrasound in Medicine & Biology, 47: 1319–1333, 2021.

[3]. Kotopoulis A, Dimcevski G, Gilja OH, Hoem D, Postema M, Treatment of human pancreatic cancer using combined ultrasound, microbubbles, and gemcitabine: a clinical case study, Medical Physics, 40: 072902, 2013.

[4]. Han F, Wang Y, Dong X, et al. Clinical sonochemotherapy of inoperable pancreatic cancer using diagnostic ultrasound and microbubbles: a multicentre, open-label, randomised, controlled trial [published online ahead of print, 2023 Oct 5]. Eur Radiol.

[5]. Haram M, Snipstad S, Berg S, Mjønes P, Rønne E, Lage J, Mühlenpfordt M, Davies CDL, Ultrasound and Microbubbles Increase the Uptake of Platinum in Murine Orthotopic Pancreatic Tumors, Ultrasound in Medicine & Biology, 49: 1275-1287, 2023.

[6]. Haram M, Hansen R, Myhre OF, Solberg S, Amini N, Angelsen BA, Davies CDL, Hofsli E, Treatment of inoperable pancreatic adenocarcinoma with focused ultrasound and microbubbles in patients receiving chemotherapy [submitted 2023]

Real-time catheter optimisation for radioembolisation using Dynamic Contrast Enhanced Ultrasound: proof-of-concept in an ex-vivo perfused porcine model

J.L. van der Hoek[1], **A. Visser[1], T.J. Snoeijink[1,5], M.E. Krommendijk[1], H.R. Liefers[2], J.G.M. Greve[2], M. Versluis[3], J. Arens[4], S. Manohar[1], E. Groot Jebbink[1]**

[1]*Multi-Modality Medical Imaging group, University of Twente, Enschede, The Netherlands*
[2]*TechMed Simulation Centre, University of Twente, Enschede, The Netherlands*
[3]*Physics of Fluids group, University of Twente, Enschede, The Netherlands*
[4]*Engineering Organ Support Technologies group, University of Twente, Enschede, The Netherlands*
[5]*Department of Medical Imaging, Radboud University Medical Center, Nijmegen, The Netherlands*
Corresponding author: j.l.vanderhoek@utwente.nl

Introduction

Radioembolisation is a treament option for liver cancer at an unresectable stage. In this treatment, radioactive microspheres are injected via a catheter into the hepatic arterial vasculature, which allows for local irradiation. In practice, results often show unpredicted underdosage of the targeted tumours and off-site toxicity in healthy tissue[1]. A considerable limitation of the current procedure is the lack of real-time visualisation of the microspheres during treatment. To overcome this limitation, we propose a new treatment strategy that uses contrast microbubbles as inert microsphere precursors. This is based on earlier in-vitro experiments where similar particle trajectories were observed[2]. The quantitative analysis of microbubble presence at the target site can be performed by using dynamic contrast enhanced ultrasound (DCE-US) and time intensity curves (TICs). This technique enables the assessment of cathether locations for optimal targeting of a tumour. Furthermore, the saturation of a tumour by microsphere embolisation could be measured with TICs of microbubble injections before and after microsphere injections, which could enhance the quality of current dosimetry. A proof-of-concept of this novel radioembolisation treatment plan using DCE-US visualisation is presented in this work.

Methods

An in-house developed liver machine perfusion platform was used for normothermic ex vivo perfusion of a porcine liver. At the start of perfusion, a target location at one of the liver lobes was selected and a 9L4 linear transducer (Siemens Acuson S2000, Siemens Healthineers, Erlangen, Germany) was fixed at this location. A microcatheter was inserted in the hepatic artery under X-ray guidance (ARTIS pheno, Siemens Healthineers, Erlangen, Germany). An overview of the complete setup is shown in Figure 1. Prior to the injection of non-irradiated holmium-165 microspheres (Quirem Medical B.V., Deventer, The Netherlands), BR-14 microbubbles (Bracco Suisse, Geneva, Switzerland) were injected at several catheter locations and analysed by a TIC analysis tool developed in-house. Real-time analysis was realised by feeding the ultrasound images directly into a Matlab (MathWorks, Natick, Massachusetts, United States) algorithm via a framegrabber. Based on the peak intensity values of the TIC analysis, the optimal catheter position was chosen for the microsphere injection. A successive microbubble injection was used to measure tissue saturation. The holmium-165 microsphere deposition was assessed by exploiting the paramagnetic properties of these microspheres using a T_2^* multi-gradient MR scan after the experiment[3].

Results

TICs of multiple microbubble injections were generated real-time and provided direct feedback about the influence of the catheter configuration. Peak intensities increased as the catheter was positioned closer to the target site. The feeding artery to this location was identified by DCE-US and the catheter was positioned close to this artery, resulting in the highest peak intensity. After injection of the microspheres, analysis of an additional microbubble injection showed a significant decrease in peak intensity. The MR scan showed a microsphere deposition in both the target lobe and a smaller adjacent lobe.

Conclusions

The real-time feedback provided by TICs in our new approach enabled efficient optimization of the catheter position in targeting the designated area. A microsphere deposition was observed in the target lobe, which shows that DCE-US can provide real-time feedback during the experimental radioembolisation procedure. Microspheres were also deposited outside the target area in a smaller adjacent lobe, and further optimisation of the catheter position could have resulted in a deposition limited to the target area. The TIC signal intensity decrease after the microsphere injection could indicate that microbubbles can be used to measure tumour saturation.

Figure 1. Overview of the experimental setup for development of the DCE-US radioembolisation protocol. From left to right: a) a display showing the analysed ultrasound data in TICs for multiple injection locations, b) an ACUSON S2000 ultrasound system showing both a contrast mode and a B-mode image, c) a perfused porcine liver on top of the reservoir including a 9L4 ultrasound transducer, d) the in-house developed perfusion apparatus for normothermic oxygenated blood perfusion of a porcine liver, e) X-ray images for microcatheter guidance using a digital subtraction angiography (DSA).
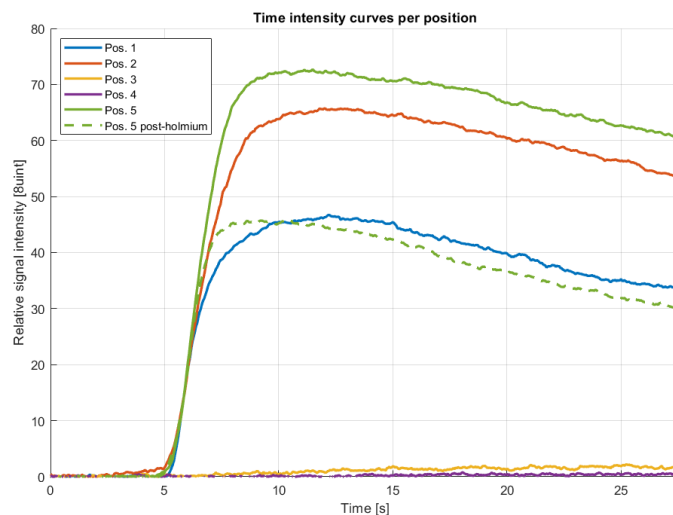
Figure 2. TICs of the microbubbles at the target location for different catheter positions (pos.), including a post-holmium microbubble injection for tumour saturation analysis

References

[1]. Smits ML, Nijsen JF, van den Bosch MA, Lam MG, Vente MA, Mali WP, van het Schip AD, Zonnenberg BA. Holmium-166 radioembolisation in patients with unresectable, chemorefractory liver metastases (HEPAR trial): a phase 1, dose-escalation study. The lancet oncology. 2012;13(10):1025-1034.

[2]. Van der Hoek JL, Snoeijink TJ, Mirgolbabaee H, Groot Jebbink E. Analysis of microbubble and holmium-165 microsphere behaviour in a 2D in-vitro liver vasculature phantom. [Unpublished manuscript]

[3]. Nijsen JF, Seppenwoolde J-H, Havenith T, Bos C, Bakker CJ, van het Schip AD. Liver tumors: MR imaging of radioactive holmium microspheres—phantom and rabbit study. Radiology. 2004;231(2):491-499.

Antibubbles as a new method for ultrasound-triggered local drug delivery

Nicolas Moreno-Gomez[1], Athanasios G. Athanassiadis[1], <u>Albert T. Poortinga[2]</u>, Thijs van den Broek[3], Mario Ries[3], Noboru Sasaki[4]
Peer Fischer[1]

[1]*Institute for Molecular Systems Engineering and Advanced Materials, Im Neuenheimer Feld 225, 69120 Heidelberg, Germany and Max Planck Institute for Medical Research, Jahnstr. 29, 69120 Heidelberg, Germany.*
[2]*Department of Mechanical Engineering, Eindhoven University of Technology, Eindhoven, The Netherlands.*
[3]*UMCU/PMC Utrecht, The Netherlands*
[4]*Hokkaido University. Sapporo, Japan*

Introduction

The ability to precisely shape ultrasound fields has made it possible to remotely trigger responses in localized regions on demand, while benefiting from ultrasound's unique characteristics compared to other methods of remote stimulation. For instance, ultrasound provides higher spatial resolution than magnetics, while propagating further than light through complex and opaque media [1]. Nevertheless, despite the benefits of ultrasound, there are few materials that can be triggered or controlled with ultrasound. In many examples, high-intensity ultrasound is required to release a payload from a carrier such as microbubbles [2], liposomes [3, 4], or phase-change droplets [5] using acoustic pressures on the order of MPa and frequencies of tens of kHz up to a few MHz [1,6]. However, the use of high-intensity ultrasound can lead to undesirable effects that limit its application in sensitive material or biological systems. In order to be useful in a wide range of contexts without inducing unwanted damage, there is therefore a need for ultrasound-responsive materials that respond to low intensity ultrasound, ideally in the range of 200 kPa or below. An additional challenge when using existing ultrasound-responsive systems is their release response. There is typically a narrow range of excitation pressures, above which the carrier is destroyed and the payload is released in a single event [2,7]. While such behavior might be desirable in some applications, e.g. for rapid delivery of a payload, there are other settings where more control is required. For instance, when the payload should be precisely dosed in response to real-time feedback [8], or when the payload needs to be slowly delivered over an extended period of time [9]. In this work, we identify Pickering-stabilized antibubbles as a new carrier for triggered release and show that they respond robustly to low-intensity ultrasound. Antibubbles consist of one [10-12] or more liquid droplets [13, 14] surrounded by a gas layer. Unlike microbubble-based carriers, which require specially-modified payloads that can be attached to the outer shell [15], the internal droplets in an antibubble can carry large volumes of payload without special preparation. Because of these benefits, antibubbles are a new class of ultrasound contrast agents that have recently been proposed for ultrasonic drug delivery [14]. Here we demonstrate, for the first time, that payload delivery via antibubbles can be triggered by low-intensity ultrasound with controllable temporal release profiles. We find that, unlike with existing carriers, it is possible to change the release behavior from single release to multiple-release by varying the composition of the antibubble. Our results open the door to designing tailored antibubble formulations for specific applications, making antibubbles a valuable and versatile component for the design of new low-intensity ultrasound-activated smart materials.

As an application example we show that antibubbles in an ultrasound field can permeabilize cells to facilitate the uptake of drugs.

Methods

Antibubbles are fabricated [14] by creating a water-in-oil-in-water (W/O/W) Pickering emulsion template with the desired payload dissolved in the inner water phase. The solvent is then extracted by freeze-drying, creating a stable powder template with a very long shelf life. Before use, the antibubbles are re-constituted from the powder in an aqueous solution of sodium chloride. Four different formulations were prepared by varying the size of the template and the composition of the outer shell, while keeping the inner cores the same for all formulations (see Table 1). The sizes are varied by homogenizing the W/O/W emulsion at either 7000 or 14000 rpm. The outer shell is varied by using two distinct types of commercially-available fumed silica particles. One type (Aerosil 200) was predominantly hydrophilic, while the other (Aerosil R972) has a modified surface with carbon content of 0.6-1.2%, making it predominantly hydrophobic.

To determine the response of antibubbles to ultrasound, we measured the change in fluorescence caused by the release of calcein after exposure to ultrasound. The experimental setup is shown in Figure 1a. Antibubbles were observed in a quartz spectroscopy cuvette that had an ultrasonic transducer bonded to one side of the cuvette. Fluorescence was measured by illuminating the sample with 460 nm light from a fiber-coupled LED, and collecting the emitted light with a fiber-coupled spectrometer oriented 90◦ to the excitation fiber. The fluorescence intensity at 520 nm, corresponding to the calcein emission peak, was used as an indicator of antibubble bursting.

To investigate the ability of cell permeabilization using antibubbles, antibubbles loaded with Dylight 649 conjugated Tomato lectin were produced according to the procedure described above. These antibubbles were first exposed to mild acoustic exposure (750kHz, MI=0.4, bust-tone pulse 20x10000cycles) to permeabilize the bladder cancer cells and subsequently "collapsed" with a strong acoustic pulse of MI>2. Subsequently, the cells were either directly observed using fluorescence microscopy or the cells were first incubated with propidium iodide.

Table 1. : Different antibubble formulations and their response to ultrasonic excitation at 1 MHz

Shell composition	Homogenization rate	Size	Release type	Release threshold
Hydrophilic	14000 rpm	34 ± 8 μm	Single	<7 kPa
Hydrophilic	7000 rpm	51 ± 13 μm	Single	80 kPa
Hydrophobic	14000 rpm	19 ± 5 μm	Multi	40 kPa
Hydrophobic	7000 rpm	58 17 μm	None	>250 kPa

Results

Antibubbles with hydrophilic outer shells demonstrate single-release behavior, with the release pressure dependent on the size (see Table 1). The larger (51 μm) hydrophilic antibubbles (Figure 1b) release calcein already at a low pressure of 88 kPa (equivalent intensity 258 mW cm−2), with fluorescence release increasing to saturation at 109 kPa. The smaller (34 μm) antibubbles (Figure 1c) demonstrated a similar release behavior, yet starting from a lower pressure below 7 kPa (equivalent intensity 2 mW cm−2), with the amount of calcein release increasing until 53 kPa, where the fluorescence signal saturates, indicating no further release from the core. These differences in the response indicate that by changing the size, the required acoustic pressure for release can be shifted.

In contrast to the hydrophilic antibubbles, those with the hydrophobic shell demonstrate more varied size-dependent behavior in response to ultrasound. As shown in Figure 1d, the larger (58 μm) antibubbles do not release appreciable amounts of calcein after irradiation. The formulation with a smaller diameter (19 μm), however, shows that above 49 kPa (equivalent intensity 80 mW cm−2) the fluorescence intensity increases linearly with each ultrasound pulse to at least 250 kPa (Figure 1e), indicating an ongoing release

process that does not saturate. To test this behavior further, we measured the calcein released by these small, hydrophobic antibubbles across multiple pulses at 70 kPa (Figure 1g). We find that even at a single excitation pressure, the antibubbles release small amounts of calcein after each pulse, reflecting a stepwise release process rather than a single one.

Our results clearly demonstrate that the response of antibubbles to ultrasound is strongly dependent on outer shell composition and antibubble size. While the hydrophilic antibubbles release the core contents in a single bursting event upon ultrasound exposure, the hydrophobic antibubbles release less of their core contents per exposure, providing on-demand dosing of the payload. In both cases, the bubble sizes determine the pressure threshold, above which the antibubbles begin releasing their contents. This behavior, however also shows different trends depending on the shell composition. For the hydrophilic antibubbles, smaller bubbles exhibit a higher release threshold, while for the hydrophobic antibubbles, the larger bubbles do not exhibit any release behavior within the range of pressures investigated. These ressults indicate a more complex interplay between size and shell composition in determining the acoustic response of antibubbles
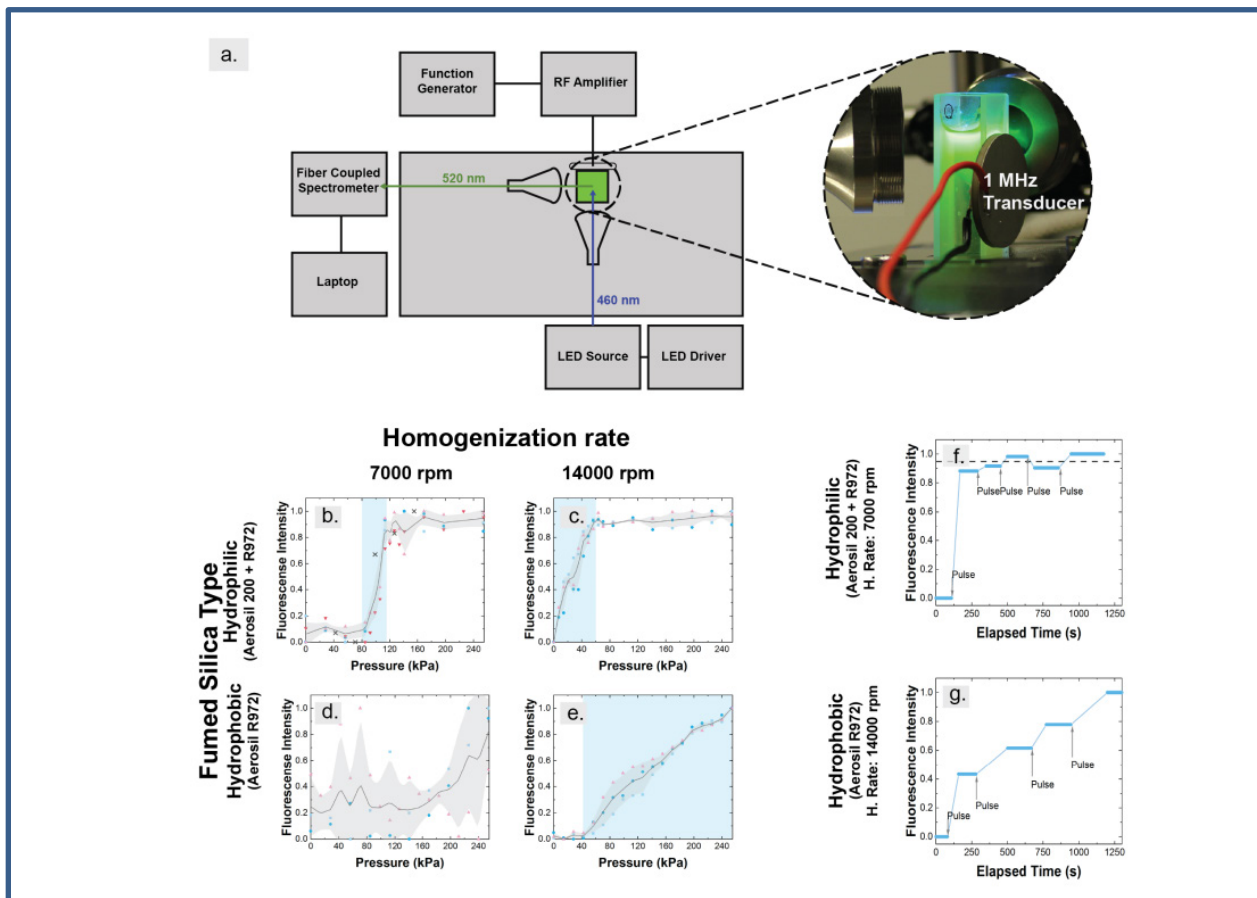
Figure 1. Experimental setup and results for fluorescence measurements as a function of ultrasound exposure. (a) Antibubbles were loaded into a cuvette and exposed to ultrasound using an integrated transducer at 1 MHz. Fluorescence signals at 520 nm were measured using a fiber-coupled spectrometer, oriented perpendicular to the excitation light (460 nm). (b)-(e) The antibubble response to ultrasonic pressure depends on antibubble composition. The pressure response for (b) 51 μm hydrophobic antibubbles and (c) 34 μm hydrophilic antibubbles both demonstrate a clear threshold behavior with fluorescence intensities saturating above the threshold. The response of (d) 58 μm and (e) 19 μm hydrophobic antibubbles show differing behaviors, with a low-intensity threshold only observable in the smaller antibubbles. (f) The hydrophilic antibubbles release all the fluorescence after a single ultrasound pulse, with no significant release after subsequent pulses at the same pressure (140 kPa). (g) The hydrophobic antibubbles release the core fluorescence incrementally across multiple pulses at the same pressure (70 kPa)

Figure 2a shows an electron microscopy image of the antibubbles used to study cell permeabilization. The size of the antibubbles is around 5-10 μm. Figure 2b and 2c show fluorescence microscopy images of cell layers exposed to antibubbles and ultrasound. Cell permeabilisation is evidenced by propidium iodide

uptake into the cells (Figure 2b). By contrast, exposing the cells to ultrasound in the absence of antibubbles did not show this permeabilization effect (results not shown). Drug load release was observed by binding of TL-Dylight 649 to the cell membranes (Figure 2c)
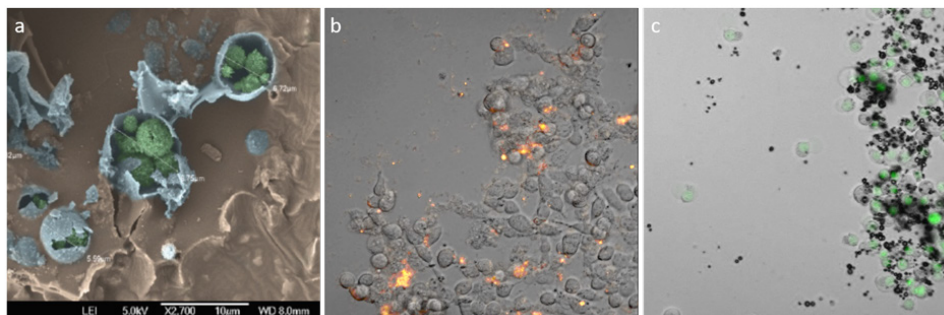
Figure 2. (a) Electron microscope image of antibubbles consisting of drug loaded cores encapsulated in a gas filled bubble. (b) Cell membrane bound TL-Dylight649 fluorescense after acoustic release of the Antibubble payload. (c) The fluorescense of the propidium iodine uptake into the cells evidences the permeabilisation of the cell membranes.

Conclusions

We have demonstrated that antibubbles respond to low-intensity ultrasound by releasing their payload in a controllable manner. By varying the antibubble size and composition, the release pressure can be tuned within the 10-100 kPa range, and different release profiles can be achieved. Hydrophilic antibubbles displayed a characteristically sharp pressure release threshold, and ejected the majority of the payload after a single ultrasound pulse. By contrast, the smaller hydrophobic antibubbles exhibited a unique stepwise release profile, making it possible to precisely dose the payload delivery over time.

The ability to deliver payloads at low pressures, as well as the ability to tune the delivery profile between single and stepwise release, make antibubbles a unique carrier for payload delivery in diverse settings. As an application example we have shown that antibubbles in the presence of an ultrasound field can permeabilize cells in order to enhance the uptake of drugs.

References

[1]. A. G. Athanassiadis, Z. Ma, N. Moreno-Gomez, K. Melde, E. Choi, R. Goyal, P. Fischer, Chemical Reviews 2021, 122, 5 5165.

[2]. E. Stride, C. Coussios, Nature Reviews Physics 2019, 1, 8 495.

[3]. M. Afadzi, C. d. L. Davies, Y. H. Hansen, T. Johansen, Ø. K. Standal, R. Hansen, S.-E. M˚asøy, E. A. Nilssen, B. Angelsen, Ultrasound in medicine & biology 2012, 38, 3 476.

[4]. F. El Hajj, P. F. Fuchs, W. Urbach, M. Nassereddine, S. Hamieh, N. Taulier, Langmuir 2021, 37, 13 3868.

[5]. O. Couture, M. Faivre, N. Pannacci, A. Babataheri, V. Servois, P. Tabeling, M. Tanter, Medical physics 2011, 38, 2 1116.

[6]. L. J. Delaney, S. Isguven, J. R. Eisenbrey, N. J. Hickok, F. Forsberg, Materials Advances 2022.

[7]. D. Baresch, V. Garbin, Prog. Biophys. Mol. Biol. 2020, 117, 15490.

[8]. A. Y. Rwei, J. L. Paris, B. Wang, W. Wang, C. D. Axon, M. Vallet-Regí, R. Langer, D. S. Kohane, Nat. Biomed. Eng. 2017, 1, 644.

[9]. A. Kar, N. Ahamad, M. Dewani, L. Awasthi, R. Patil, R. Banerjee, Biomaterials 2022, 283, 121435.

[10]. A. T. Poortinga, Langmuir 2011, 27, 2138.

[11]. J. E. Silpe, J. K. Nunes, A. T. Poortinga, H. A. Stone, Langmuir 2013, 29, 8782.

[12]. J. Jiang, A. T. Poortinga, Y. Liao, T. Kamperman, C. H. Venner, C. W. Visser, Adv. Mater. 2023, 2208894.

[13]. A. T. Poortinga, Colloids Surf., A 2013, 419, 15.

[14].   S. Kotopoulis, C. Lam, R. Haugse, S. Snipstad, E. Murvold, T. Jouleh, S. Berg, R. Hansen, M. Popa, E. Mc
        Cormack, O. H. Gilja, A. Poortinga, Ultrason. Sonochem. 2022, 85, 105986.

[15].   I. Lentacker, S. C. De Smedt, N. N. Sanders, Soft Matter 2009, 5, 2161.

Ultrasound and microbubble mediated T cell modulation

Ana Baez[1], Davindra Singh[1], Stephanie He[1], Brandon Helfield[1,2]

[1]*Department of Biology, Concordia University, Montreal, Canada*
[2]*Department of Physics, Concordia University, Montreal, Canada*
Corresponding author: brandon.helfield@concordia.ca

Introduction

While biomedical ultrasound (US) and intravascular microbubbles are clinically used for anatomical assessment (*e.g.* echocardiography), they are increasingly being recognized as tools for targeted therapies. The most established application of therapeutic potentiation of microbubbles is the reversible opening of the blood-brain-barrier for targeted cancer drug delivery into the brain, already in the clinical trial stage in North America and recently started being tested on pediatric patients in Canada. In parallel, the field of cellular immunotherapy has shown promise in the last few years for blood-borne cancers, but has met limited success in solid tumors due to the physiologically hostile tumor milieu and cancer-based immune evasion (*e.g.* the dampening of a Th1 response). Microbubbles have the potential to revolutionize targeted cellular immunotherapy, as they have been shown under conditions to make cells more permeable, locally deliver therapeutics, and modulate the immune microenvironment. However, the biophysical interactions between microbubbles and immune cells, particularly T cells, remain largely unexplored. The overall goal is to explore the effects of microbubble-mediated permeability and modulation of T cells. In this preliminary study, we start by investigating the acoustic conditions capable of increasing T cell permeability while preserving cellular viability.

Methods

Naïve Jurkat cells (Clone E6) were grown in RPMI supplemented with 10% FBS. Firstly, we tested T cell activation efficiency using two stimulants: *i)* anti-CD3/PMA and *ii)* anti-CD3/anti-CD28 (1 ug/mL; 3ug/mL) to measure the secretion of IL-2. Next, cell suspensions were incubated with Definity^{TM} (38 ul into 3 mL; Lantheus Medical Imaging, N. Billerica, MA, USA) and fluorescein dextran (10KDa; ThermoFisher, USA, CA), used here as a surrogate drug. Samples were treated in our custom US setup at 1 MHz for 1000 cycles at a PRI of 5 ms over a range of acoustic peak-negative pressure (208-563 kPa). After washing to remove bubbles and excess dextran, samples were then incubated with propidium iodide (PI) as a marker for cell viability, and subsequently at least 10000 cells per sample were analysed using flow cytometry (FACS Melody; BD Biosciences, CA). T cells that exhibited a FITC+ PI- signal were considered reversibly and viably permeated, and we quantified the effectiveness ratio η for each treatment, defined here as ratio of the FITC+PI- population to the PI+ population.

Results

Our preliminary results indicate a stronger activation via anti-CD3/PMA versus anti-CD3/anti-CD28 ($p<0.0001$), as expected. Further, we have demonstrated an increase in the number of viably sonoporated T cells (up to $41.0 \pm \mathbf{6.3}$%) with increasing acoustic pressure, along with a concurrent loss of overall viability (up to $16.2 \pm \mathbf{7.3}$ %; Fig 1). From this data, we estimate the effectiveness of this approach under these conditions to range from $\mathbf{0.3} \leq \boldsymbol{\eta} \leq \mathbf{4.1}$, with a maximum value achieved at an acoustic peak-negative pressure of 416 kPa. We will move forward with this treatment paradigm as it represented the condition in which delivery was most successful while minimizing T cell loss of viability.
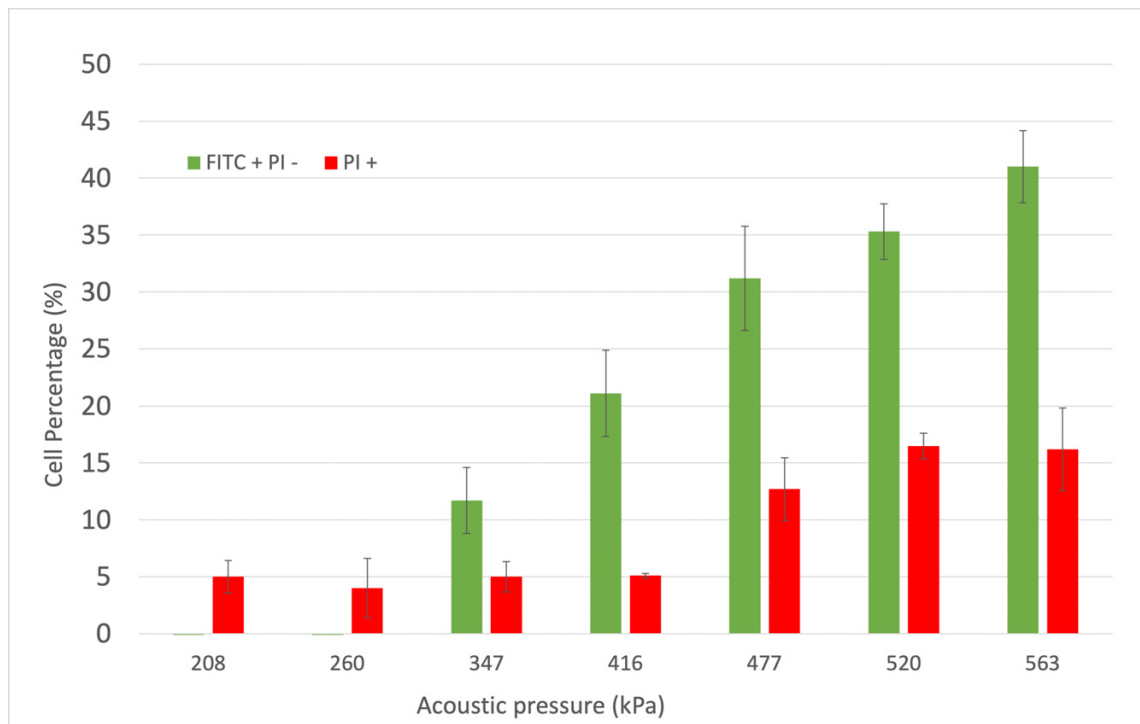
Figure 1. Ultrasound-assisted delivery of an otherwise impermeable macromolecule to T cells. Data is represented as mean ± standard error of the mean at least n=4 samples.

Conclusions

We have demonstrated ultrasound-assisted T-cell delivery of a large macromolecule and its dependence on acoustic pressure. This preliminary dataset has implications on microbubble-mediated T cell immunomodulation, and is the subject of our future work.

References

[1]. Burgess, A., Shah, K., Hough, O., & Hynynen, K. (2015). Focused ultrasound-mediated drug delivery through the blood-brain barrier. *Expert Review of Neurotherapeutics, 15*(5), 477–491. https://doi.org/10.1586/14737175.2015.1028369

[2]. Janwadkar, R., Leblang, S., Ghanouni, P., Brenner, J., Ragheb, J., Hennekens, C. H., Kim, A., & Sharma, K. (2022). Focused Ultrasound for pediatric diseases. *Pediatrics, 149*(3). https://doi.org/10.1542/peds.2021-052714 3.

[3]. Juffermans, L. J. M., et al. (2008). Low-intensity ultrasound-exposed microbubbles provoke local hyperpolarization of the cell membrane via activation of BKCA channels. *Ultrasound in Medicine & Biology, 34*(3), 502–508. https://doi.org/10.1016/j.ultrasmedbio.2007.09.010

[4]. Mehta, R. I., Carpenter, J. S., Mehta, R. I., Haut, M. W., Wang, P., Ranjan, M., Najib, U., D'Haese, P.-F., & Rezai, A. R. (2023). Ultrasound-mediated blood–brain barrier opening uncovers an intracerebral perivenous Fluid Network in persons with Alzheimer's disease. *Fluids and Barriers of the CNS, 20*(1). https://doi.org/10.1186/s12987-023-00447-y 6.

[5]. Przystupski, D., & Ussowicz, M. (2022). Landscape of Cellular Bioeffects Triggered by Ultrasound-Induced Sonoporation. *International Journal of Molecular Sciences, 23*(19), 11222. https://doi.org/10.3390/ijms231911222

Acoustofluidic-mediated transfection of T cells to improve manufacturing of cellular immunotherapies

Connor S. Centner[1], Madison C. Colebank[1], Mariah C. Priddy[1], Omar S. Sarkar[2,3], Kavitha Yaddanapudi[2,3], Jonathan A. Kopechek[1,3]

[1]*Department of Bioengineering, University of Louisville, Louisville, Kentucky, USA*
[2]*Department of Microbiology and Immunology, University of Louisville, Louisville, Kentucky, USA*
[3]*UofL-Health Brown Cancer Center, Louisville, Kentucky, USA*
Corresponding author: jonathan.kopechek@louisville.edu

Introduction

Cellular immunotherapies are rapidly emerging as a promising approach for treatment of many diseases, including cancer and cardiovascular diseases. Non-viral methods for molecular delivery and transfection of T cells are currently in development to improve patient safety and reduce varability during manufacturing of immunotherapies. Ultrasound-mediated microbubble cavitation has been utilized as an effective non-viral approach to enhance intracellular delivery of biomolecules. However, most ultrasound-mediated molecular delivery studies have utilized static sample chambers, which have limited throughput and are generally not practical for cell therapy manufacturing processes. To address these limitations, we are developing novel acoustofluidic platforms to enable intracellular delivery of biomolecules as cells continuously pass through an ultrasound field in a 3D-printed flow chamber [1]. In this study, we assessed biological parameters that influence molecular delivery and transfection in human T cells.

Methods

Primary human T cells were isolated from whole blood donations collected from healthy donors following protocols approved by the institutional review board at the University of Louisville. Human Jurkat T cells were also tested for comparison. Cationic phospholipid-coated microbubbles were added to T cell solutions prior to ultrasound treatment in a static chamber or in a flow system [2]. B-mode ultrasound pulses were generated using a P4-1 probe on a Verasonics Vantage ultrasound system. Continuous flow acoustofluidic treatment was performed using 3D-printed plastic flow chambers. Molecular delivery, transfection efficiency, and cell viability were assessed using flow cytometry and confocal microscopy.

Results

Acoustofluidic treatment enhanced delivery of FITC-dextran and GFP plasmids to human T cells while maintaining viability, as indicated by flow cytometry measurements and confocal microscopy imaging. Our study revealed that cell cycle phase influences acoustofluidic molecular delivery efficiency to T cells, with higher delivery observed during the S phase compared to the G2/M phase ($p < 0.001$) or G0/G1 phase ($p < 0.01$). In addition, low cell plating densities (100,000 cells/mL) during cell culture enhanced molecular delivery compared to higher cell plating densities ($p < 0.001$), even though all groups were resuspended at equal concentrations for acoustofluidic treatment.

Conclusions

This study provides new insights into biological parameters that influence ultrasound-mediated molecular delivery and transfection in human T cells using a novel 3D-printed plastic acoustofluidic device requiring only ~2-3 seconds of treatment time. These results demonstrate that acoustofluidic treatment with cationic microbubbles induces rapid uptake of biomolecules and enables transfection of DNA plasmids in human T cells. In addition, the results indicate that biological parameters such as cell cycle phase and initial cell plating density have implications on the efficiency of acoustofluidic-mediated molecular delivery. This

study demonstrates that acoustofluidic technology holds promise for improved non-viral transfection and manufacturing of human T cell therapies.
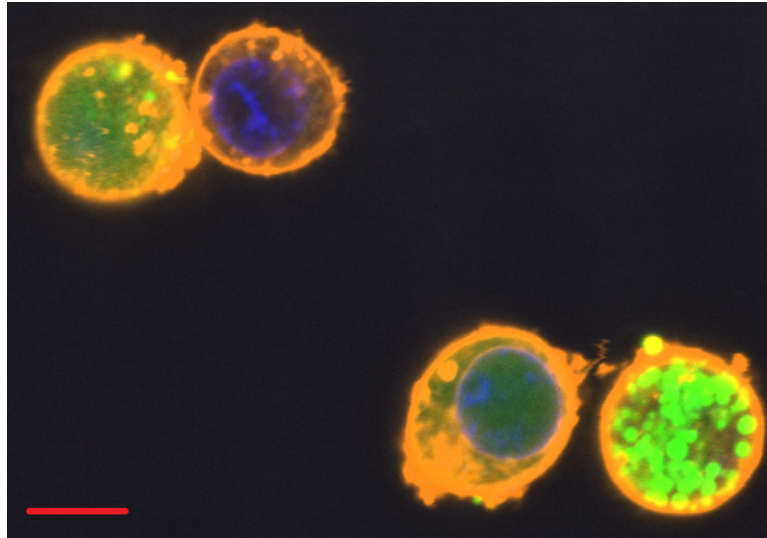
Figure 1. Representative confocal microscopy image of human T cells after acoustofluidic-mediated delivery of 150 kDa FITC-dextran, demonstrating intracellular molecular delivery. Green stain = FITC-dextran delivered into the cell via acoustofluidic treatment with cationic microbubbles, blue stain = DAPI (nuclei), red stain = DiD (cell and organelle membranes). Scale bar represents 5 µm.

References

[1]. Centner, C.S., et al., Acoustofluidic-mediated molecular delivery to human T cells with a three-dimensional-printed flow chamber. J Acoust Soc Am, 2021. **150**(6): p. 4534.

[2]. Centner, C.S., et al., *Comparison of Acoustofluidic and Static Systems for Ultrasound-Mediated Molecular Delivery to T Lymphocytes.* Ultrasound Med Biol, 2023. **49**(1): p. 90-105.

In-vivo IL-12 plasmid delivery using microbubble-assisted ultrasound in a mouse melanoma model

Edward Oujagir[1], Coralie Mousset[1,2], Valérie Schubnel[1], Marie Roy[1],
Damien Fouan[1], Ayache Bouakaz[1], Sophie Serrière[1], Laurent Machet[1,3],
Valérie Gouilleux-Gruart[2], Jean-Michel Escoffre[1]

[1]*UMR 1253, iBrain, Université de Tours, Inserm, Tours, France*
[2]*GICC, EA 7501, Université de Tours, Tours, France*
3*Department of Dermatology, Tours University Hospital, Tours, France*
Corresponding authors: jean-michel.escoffre@inserm.fr and valerie.gouilleux@univ-tours.fr

Introduction

In recent years, immunotherapy and in particular vaccination based on dendritic cells (DCs), has emerged as a promising therapeutic strategy for cancer treatment. These vaccines are mainly generated *ex-vivo* from autologous DCs, which must be tailor-made for each patient. This process is complex and expensive, preventing the generalization of this immunotherapy. The *in-vivo* delivery of immunostimulatory molecules (*i.e.,* tumor antigens, cytokines) could thus make it possible to circumvent the laborious and costly procedures encountered in the development of these vaccines. Among these molecules, interleukin-12 (IL-12) is a very attractive molecule in oncology due to its ability to stimulate not only the adaptive immune system but also the innate immune system. Some clinical studies show that systemic administration of recombinant IL-12 induces serious side effects in patients with advanced melanoma while its local administration helps reduce these side effects maintaining its therapeutic efficacy [1]. Other studies advocate delivery of a plasmid encoding IL-12 (pIL-12) by electroporation. Although this strategy allows the effective regression of primary and advanced melanoma, electroporation remains an invasive method associated with local side effects [2]. In this context, this project therefore aims to design a therapeutic approach based on the local delivery of pIL-12 in mouse melanoma model using a noninvasive method, the microbubble-assisted ultrasound (MB-assisted US) [3].

Methods

In vitro experiments – The pIL-12 was designed with InvivoGene (Toulouse, France). This pDNA was prepared from transformed *Escherichia coli* using a Endofree plasmid purification system. Then, its quantity and quality were assessed using spectrophotometry and an agarose gel electrophoresis. A restriction map was produced to ensure the pIL-12 identity. Finally, pIL-12 (5 or 10 µg) was transfected into B16F10 melanoma cells using MB-assisted US (1 MHz, 10 kHz PRF, 40% DC, 0.4 MPa, 30s; Vevo Micromarkers^{TM} MB/cell ratio of 5). The secretion of IL-12 in the cell culture medium was assessed using an ELISA assay and the cell viability was evaluated using MTT assay 48 hours after gene delivery.

In vivo experiments – *In vivo,* a plasmid encoding the luciferase reporter gene (pLuc) was used in order to design and to validate the gene delivery protocol. The pLuc (50 µg) was acoustically delivered MB-assisted US (1 MHz, 10 kHz PRF, 40% DC, 0.4 MPa, 3 min; 2×10^6 MBs) in mouse melanoma model. The luciferase expression was measured using bioluminescence imaging 24 and 48 hours post-transfection. Using optimized protocol, pIL-12 (50 µg) was then delivered intratumorally and the therapeutic efficacy was evaluated by monitoring the tumor growth using B-mode US imaging.

Results

In vitro experiments – The pIL-12 was produced and purified with excellent quality (no contamination by bacterial genomic DNA and lipopolysaccharides) and with a high yield. The restriction mapping confirmed the pIL-12 identity. MB-assisted US significantly increased the production and the secretion of IL-12 in the cell medium compared to the incubation of cells with pIL-12 on its own ($p<0.001$). The delivery of 10 µg pIL-12 significantly increased the IL-12 concentration in the cell medium in comparison with a

dose of 5 μg (2352 ± 125 pmol/mL *versus* 1430 ± 45 pmol/mL; p<0.05). The acoustically-mediated pIL-12 delivery slightly affected the cell viability compared to the control groups (80 ± 2 % *versus* 95 ± 5%).

In-vivo experiments – The intratumoral injection of pLuc did not result in luciferase expression in the tumor tissue. However, the acoustically-mediated pLuc delivery significantly increased the luciferase expression in the tumor tissue 24 hours ($6{\times}10^5 \pm 2{\times}10^5$ photons/sec) and 48 hours ($4{\times}10^5 \pm 1{\times}10^5$ photons/sec) later compared to the control group ($4{\times}10^4 \pm 2{\times}10^3$ photons/sec ; p<0.001). No side effect was observed during and after the procedure of acoustically-mediated pLuc delivery. In addition, the delivery of pIL-12 using MB-assisted US induced a 2.5-fold decrease in tumor growth compared to the intratumoral pIL-12 administration alone (p<0.001).

Conclusions

MB-assisted US is a safe and efficient modality for the *in-vivo* delivery of immunostimulatory molecules (*i.e.,* tumor antigens, cytokines) in cancer immunotherapy.

Acknowledgements

References

[1]. Gollob JA, Mier JW, Veenstra K, McDermott DF, Clancy D, Clancy M, Atkins MB, Phase I trial of twice-weekly intravenous interleukin 12 in patients with metastatic renal cell cancer of malignant melanoma: ability to maintain IFN-gamma induction is associated with clinical response, Clin. Cancer Res., 2000, 6:1678-92.

[2]. Daud AI, DeConti RC, Andrews S, Urbas P, Riker AI, Sondak VK, Munster PN, Sullivan DM, Ugen KE, Messina JL, Heller R, Phase I trial of interleukin-12 plasmid electroporation in patients with metastatic melanoma, J. Clin. Oncol., 2008, 26:5896-903.

[3]. Oujagir E, Mousset C, Schubnel V, Fouan D, Bouakaz A, Serrière S, Machet L, Gouilleux-Gruart V, Escoffre JM, Therapeutic efficacy of *in-vivo* IL-12 plasmid delivery using microbubble-assisted ultrasound in a mouse melanoma model, Mol. Pharm., under review.

Comprehensive Assessment of Blood-Brain-Barrier Opening and Sterile Inflammatory Response: Unraveling the Therapeutic Window

Jane J. Song[1] and Payton J. Martinez[1], Francis G. Garay[2], Kang-Ho Song[1], Toni Mufford[2], Jenna Steiner[2], John DeSisto[3], Nicholas Ellens, Natalie J. Serkova[2], Adam L. Green[3], Mark Borden[1]

[1] _Biomedical Engineering, University of Colorado Boulder, Boulder, USA_
[2] _Pedatric Oncology, Anschutz Medical Campus, Aurora, USA_
[3] _Radiology, Anschutz Medical Campus, Aurora, USA_

Corresponding author: jaso1167@colorado.edu

Introduction

The permeabilization of the blood-brain barrier (BBB) through microbubbles stimulated by focused ultrasound (MB+FUS) has been widely adopted as a reversible and noninvasive technique to transport drugs into the brain. While significant attention has been paid to optimizing the BBB opening (BBBO) for drug delivery, less has been explored regarding the bioeffects following BBBO. One of the most significant discoveries up to this point has been the sterile inflammatory response (SIR), a local immune response that is stimulated upon BBBO[1]–[3]. Microbubbles (MBs) actuated by focused ultrasound offers a solution to the challenge of drug delivery by reversibly permeabilizing the BBB [4], [5]. Multiple studies have optimized parameters such as mechanical index (MI), microbubble volume dose (MVD), pulse repetition frequency (PRF), and sonication length in order to understand its effect on brain permeability [5], [6]. As a result, direct biological consequences warrant further investigation. Our study aims to understand the extent of the SIR by examining the two key acoustic and microbubble parameters: MI and MVD. Selecting a range of low to high MIs (0.2 - 0.6) and MVDs (0.1- 40 μL/kg), mice were sonicated in the right striatum, and brains were dissected 6 hours later for bulk RNA sequencing. By assessing the MI and MVD dose effects on BBBO and SIR, we were able to establish a "therapeutic window" for these parameters in mice.

Methods

Lipid films were prepared with a 90:10 ratio of lipid 1,2-disteraroyl-sn-glycero-3-phosphocholine (DSPC), purchased from Avanti Polar Lipids and a poly(oxy ethylene)$_{40}$ stearate PEG40S (Cat: P3440-250G, Sigma Aldrich) emulsifier. Lipid films were hydrated and diluted to a final concentration of 2 mg/mL. Afterwards, films were homogenized using a 20 kHz probe on a low power setting (Model 250A, Branson Ultrasonics; Danbury, CT) and once cooled re-sonicated with perfluorobutane (PFB, FluoroMed TX) to produce polydisperse microbubbles. Microbubbles were then differentially centrifuged to obtain a 3-μm volume-weighted diameter [7]. CD-1 ISG mice were imaged with a Bruker Biospec 9.4 Tesla MR scanner (Bruker, Billerica, MA). Anesthesia was given to animals receiving FUS treatment and MRI images were acquired for targeting in the right striatum (T1w fast spin echo RARE and T2-turboRARE). Before FUS, mice were retro-orbitally co-injected with monodispersed microbubbles (0.1-40 μL/kg) and a gadolinium-based contrast agent, MultiHance at 0.2 mmol/kg (Bracco, Princeton, NJ). Focused ultrasound parameters were as follows: 10-ms pulse length, 1.0-Hz pulse repetition frequency, 300-s treatment time, and a range of peak negative pressures (0.246, 0.492 or 0.738 MPa derated _in situ_). Six hours post FUS treatment brain samples were dissected out and RNA was extracted using the RNAeasy kit (Cat: 74004, Qiagen) per the manufacturer's instructions. Post sequencing, FASTQ files were analyzed on Pluto (https://pluto.bio) where differential gene expression (DEG) was performed between the control isoflurane group versus FUS-treated animals. From this, a Gene Set Enrichment Analysis (GSEA) was performed comparing the log2 fold changes from the DEG results to rank genes.

Results

DEGs for all 12 conditions were analyzed through GSEA using the hallmark pathways covering the 50 most essential biological pathways. The 12 most significantly enriched pathways were all related to inflammatory processes with highest enriched pathway being TNFα signalling and the lowest IL2 STAT5 signalling (Figure 1). These trends are more prevalent in the 0.6 MI and 40 MVD doses versus the lower groups. Significant correlations were observed between BBBO parameters and RNA expression. Gene Set Enrichment of Hallamrk Pathways.
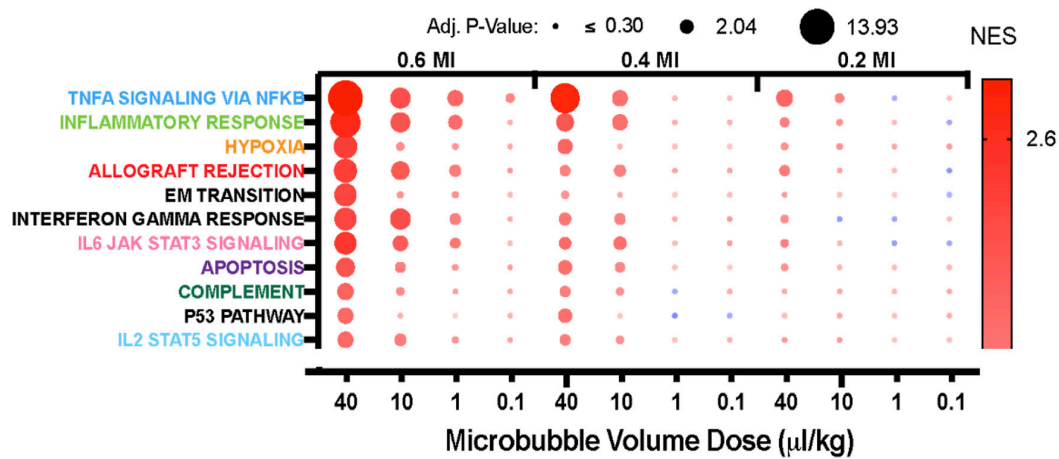
Figure 1. Gene Set Enrichment of Hallamrk Pathways. (A) A dot plot of the 12 most significant pathways out of the 50 hallmark pathways ranked based on significance. Dots indicate adjusted p-value scores while color indicates NES (Red = high NES, Blue = low NES).

Figure 2A displays the window of BBBO where the red areas indicate conditions capable of inducing significant BBBO while blue is considered insignificant BBBO. As the MVD and MI increased, so did the area in which opening was detected and contrast enhancement was increased. With this window of BBBO determined, we combined our data from the RNA sequencing and determined three classes of SIR (Fig. 3B): class I being only the activation of TNFα signalling via NFκB (NES >1.65), class II being the significant enrichment of TNFα signalling via NFκB and Inflammatory response (NES >1.65), and class III being the activation of TNFα signalling via NFκB, Inflammatory response and Apoptosis (NES >1.65).
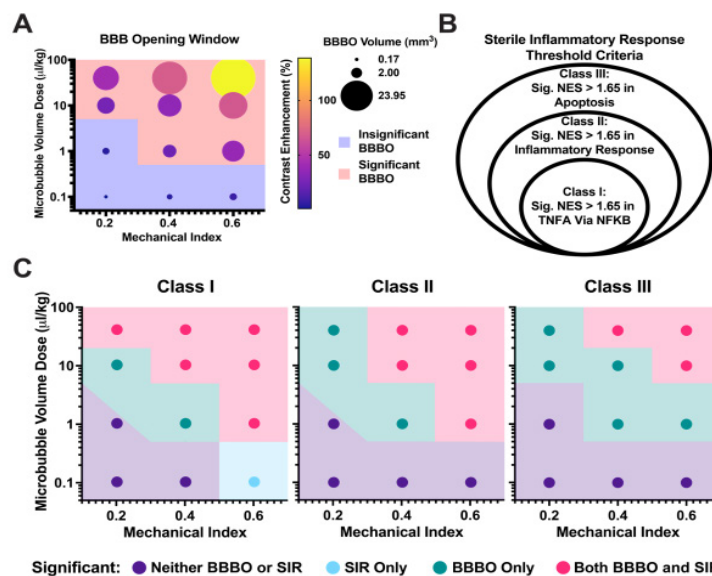
Figure 2. Establishing the Therapeautic Window Between BBBO and the Sterile Inflammatory Response. (A) A dot plot representing the window of BBBO where size of the circle indicates volume of BBBO and

color indicates level of contrast enhancement. Regions in red indicate where significant BBBO has been achieved while blue indicates insignificant BBBO. (B) Our classifications of SIR were categorized into 3 groups where each circle represents a classification. (C) In the three classes, areas in purple are where no BBBO or SIR occurs, light blue as SIR only, green as only BBBO and pink as regions where both BBBO and SIR are occuring.

Combining our classification of SIR with our window of BBBO, we were able to define three therapeutic windows (Figure 2C). With purple indicating neither BBBO nor SIR, both blue and pink regions highlight regions where BBBO is occurring, however, SIR is only observed in the pink regions which correlate to regions where the MI and MVD are higher. It is important to note that the only instance where SIR occurs without significant BBBO is in class I indicated by the region in light blue. These regions shift between the classes where the therapeutic window, which we define, is where successful BBBO is achieved without SIR and is illustrated in green. In class I, the therapeutic window is seen to only encompass two conditions (10 MVD + 0.2 MI and 1 MVD + 0.4 MI), whereas in class II, due to the addition of significant enrichment in an inflammatory response, the therapeutic window widens to include 40 MVD + 0.2 MI. Finally, in our most stringent definition of SIR, the therapeutic window has now 5 candidates and conditions to operate within if BBBO is to be achieved without significant cellular damage (40 MVD + 0.2 MI, 10 MVD + 0.2 MI, 10 MVD + 0.4 MI, 1 MVD + 0.4 MI, 1 MVD + 0.6 MI).

Conclusions

Overall, the study demonstrated that MI and MVD crucial roles in BBBO. RNA sequencing results from all 12 conditions testing low to high MI and MVD granted insight into the transcriptomic changes occurring with major upregulated pathways being related to inflammation and damage. With this data, three classifications of SIR were able to be defined, offering multiple windows and conditions to operate within based on experimental specifications and approaches. In conclusion, we have proposed 3 therapeutic windows for optimal BBBO which hopefully address important concerns regarding the safety and effectiveness of focused ultrasound-mediated drug delivery to the brain.

References

[1] Z. I. Kovacs *et al.*, "Disrupting the blood–brain barrier by focused ultrasound induces sterile inflammation," *Proc. Natl. Acad. Sci.*, vol. 114, no. 1, Jan. 2017, doi: 10.1073/pnas.1614777114.

[2] D. McMahon and K. Hynynen, "Acute Inflammatory Response Following Increased Blood-Brain Barrier Permeability Induced by Focused Ultrasound is Dependent on Microbubble Dose," *Theranostics*, vol. 7, no. 16, pp. 3989–4000, 2017, doi: 10.7150/thno.21630.

[3] O. Jung *et al.*, "Neuroinflammation associated with ultrasound-mediated permeabilization of the blood–brain barrier," *Trends Neurosci.*, vol. 45, no. 6, pp. 459–470, Jun. 2022, doi: 10.1016/j.tins.2022.03.003.

[4] K.-H. Song, B. K. Harvey, and M. A. Borden, "State-of-the-art of microbubble-assisted blood-brain barrier disruption," *Theranostics*, vol. 8, no. 16, pp. 4393–4408, 2018, doi: 10.7150/thno.26869.

[5] K. Gandhi, A. Barzegar-Fallah, A. Banstola, S. B. Rizwan, and J. N. J. Reynolds, "Ultrasound-Mediated Blood–Brain Barrier Disruption for Drug Delivery: A Systematic Review of Protocols, Efficacy, and Safety Outcomes from Preclinical and Clinical Studies," *Pharmaceutics*, vol. 14, no. 4, p. 833, Apr. 2022, doi: 10.3390/pharmaceutics14040833.

[6] D. McMahon and K. Hynynen, "Acute Inflammatory Response Following Increased Blood-Brain Barrier Permeability Induced by Focused Ultrasound is Dependent on Microbubble Dose," *Theranostics*, vol. 7, no. 16, pp. 3989–4000, 2017, doi: 10.7150/thno.21630.

Sonoporation of pancreatic adenocarcinoma: interim analysis from a Phase II clinical trial

Priscilla Machado[1], Trang Vu[1], John R Eisenbrey[1], James Posey III[2], Spiros Kotopoulis[3], Babar Bashir[2], Patrick Mille[2], Atrayee BasuMallick[2], Daniel Lin[2], Rajan Singla[2], Audun M Trelsgård[3], Ingrid K Nordaas[3], Georg Dimcevski[3], Odd Helge Gilja[3], Kirk Wallace[4], <u>Flemming Forsberg[1]</u>

[1]*Department of Radiology, Thomas Jefferson University, Philadelphia, PA, 19107, USA*
[2]*Department of Medical Oncology, Sidney Kimmel Cancer Center, Thomas Jefferson University, Philadelphia, PA 19107, USA*
[3]*National Centre for Ultrasound in Gastroenterology, Haukeland University Hospital, Bergen, Norway*
[4]*3GE HealthCare, Niskayuna, NY 12309, USA*

Introduction

Pancreatic ductal adenocarcinoma (PDAC) is 3% of cancers diagnosed in the United States with 64,050 new cases expected in 2023, but it is the fourth leading cause of cancer-related deaths in both men and women with 50,550 expected deaths in 2023 [1]. Five year survival rates have climbed to around 12%, but improvement in survival for PDAC patients over the past 30+ years have been very slow; especially for patients with metastatic disease [1-3]. One of the reasons that the mortality rate nearly parallels the incidence is that only 15 to 20% of patients are considered resectable at the time of diagnosis, while the remaining have locally advanced and surgically unresectable PDAC or PDAC with metastatic disease [2-6]. Despite the "curative" intent of treatment for those patients who present with surgically amenable PDAC and undergo resection followed by adjuvant systemic therapy (with or without radiation) their median overall survival is around 15.5 to 24 months [4]. The five year overall survival for these resected patients is 25 to 30% for those with lymph node negative disease and only 10% in patients with lymph node positive disease. Hence, there is an urgent clinical need to improve chemotherapy delivery to PDAC and, thus, improve outcomes for these patients.

The dense desmoplastic stroma surrounding PDAC combined with their poor blood supply make these cancers notoriously unresponsive to chemotherapy [6]. Nonetheless, the angiogenic vasculature is sufficient to produce marked signal enhancement when imaged with contrast enhanced ultrasound (CEUS) [5-8]. CEUS relies on the IV administration of gas-filled microbubbles in the 1-10 μm size range as ultrasound contrast agents (UCAs) [9]. Imaging UCAs a sufficiently high acoustic pressures (typically > 200 kPa) have the potential to temporarily alter vascular structures through radiation force, shock waves, microstreaming (including liquid jets) and the activation of various intracellular signaling responses in a process known as sonoporation[10, 11]. Thus, sonoporation will briefly (on the order of 24 hours) increase the local vascular permeability, allowing more chemotherapy drugs to extravasate into the targeted PDAC.

Our group conducted a Phase I clinical trial aimed at augmenting standard of care chemotherapy efficacy for PDAC, which led to significant improvements in 10 patients receiving sonoporation treatment compared to 63 historical controls [4, 5]. The results included tumor regression in 50% of the patients and a significant increase in median overall survival from 8.9 months in the controls to 17.6 months (p = 0.011) [4, 5]. Subsequently, we used xenograft mouse models of PDAC to investigate sonoporation with all four clinically-approved UCAs and two ultrasound regimens to identify the ideal parameters to increase therapeutic efficacy [12]. Treatment with high power utilizing Sonazoid (GE HealthCare, Oslo, Norway) as the UCA most consistently caused an increase in permeabilization across different experiments [12].

Hence, our group has initiated a Phase II clinical trial of sonoporation treatment of PDAC (i.e., standard of care chemotherapy augmented with CEUS and Sonazoid microbubbles). The objective of this study was to perform an interim analysis of this ongoing Phase II clinical trial.

Materials and Methods

Subjects are eligible to be enrolled in this ongoing, prospective, multi-center, Phase II clinical trial, if they are patients with PDAC (stage 2 or higher) and are scheduled to start standard of care chemotherapy

treatment. The total enrolment goal is 120 subjects randomly assigned to one of two equally large groups (i.e., 60 subjects per group) receiving either standard of care chemotherapy or chemotherapy followed by sonoporation. The two standard of care chemotherapy regimens for treating PDAC are FOLFIRINOX (prescribed in about 80% of patients) and Gemcitabine/Nab-Paclitaxel (given to the remaining approximately 20% of cases) [2-4]. The choice of chemotherapy treatment will be decided independently by the clinical oncology teams at the respective sites.

The study has been approved by the participating Universities' Institutional Review Boards as well as the United States Food and Drug administration (IND no. 153,874). The full protocol and statistical analysis plan are available at *https://clinicaltrials.gov/ct2/show/NCT04821284* (trial registration number: NCT04821284). The primary objective is to evaluate the safety and therapeutic efficacy of sonoporation on PDAC treatment based on local progression-free and overall survival (PFS and OS, respectively).

The sonoporation treatment consisted of 20 minutes of ultrasound imaging sweeping slowly through a single primary PDAC tumor (Figure 1) using a modified Logiq E10 ultrasound scanner (GE HealthCare, Waukesha, WI, USA) with a C1-6 probe transmitting 20 µs pulses at 2.0 MHz during infusion of Sonazoid (rate: 0.18 mL/kg hour). The choice of acoustic settings for sonoporation of PDAC as well as the use of Sonazoid were based on our prior animal studies [12]. Treatment followed the timeline and guidelines of the standard of care chemotherapeutic regimen for PDAC, with sonoporation performed immediately following each administration of chemotherapy (when the concentration of drugs was maximum).

For statistical analyses Wilcoxon rank sum tests, unpaired two-way t-tests and Cox survival curves with log-rank tests were employed to compare the groups with and without sonoporation. Tests were performed using Stata 15.1 (StataCorp, College Station, TX, USA) with p-values less than 0.05 indicating statistical significance.
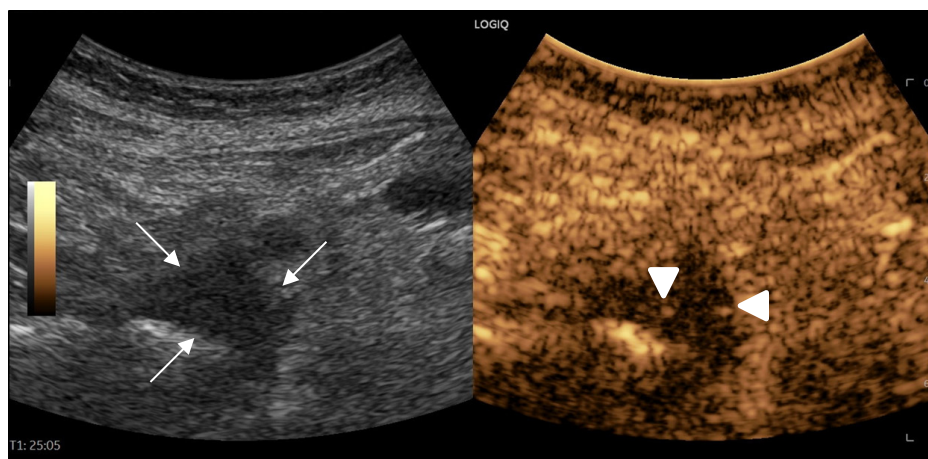
Figure 1: Example of dual-imaging B-mode and CEUS of a PDAC (arrows) during sonoporation with a few microbubbles seen within the tumor (arrowheads).

Results

To date, 45 out of 120 subjects (37.5%) have been enrolled, since this clinical trial opened for enrolment on December 3rd, 2021. The mean age of the subjects was 63 years (range: 28 - 84 years) and 22 (48.9% of the 45) were randomized to the sonoporation group, while 17 (or 37.7% out of 45) were allocated to the control group (6 subjects or 13.3% out of the total 45 were considered screen fails).

Neither the PFS nor the OS survival curves showed any significant differences between groups with and without sonoporation augmentation (p > 0.58), but it should be noted that only 20 and 13 subjects, respectively, have reached the PFS and OS end-points at this early stage. Interim results showed improvements with sonoporation in median PFS (132 days vs 111 days) and in median OS (208 days vs 181 days), while the number of chemotherapy cycles delivered, time on study and CA19-9 levels showed no or very limited improvements (cf., Table 1). None of these differences were statistically significant (p > 0.34). No adverse events were considered related to the administration of Sonazoid (i.e., related to sonoporation),

but we encountered 22 serious adverse events (grade 3 or higher; 10 in the chemotherapy group and 12 in the chemotherapy with sonoporation group). All serious adverse events were grade 3; except one grade 4 and two grade 5 events in two of the control subjects receiving standard of care chemotherapy only (p = 0.047).

Table 1: *Interim comparison of sonoporation and chemotherapy versus chemotherapy alone groups.*

(median values)	Sonoporation	Controls
No of chemotherapy cycles	6	7
Study duration (days)	105	98
PFS (days)	132	111
OS (days)	208	181
Δ CA19-9 (U/mL)	-1.0	0.0

Conclusions

An interim analysis of an ongoing, multi-center, Phase II clinical trial evaluating sonoporation treatment of PDAC (i.e., standard of care chemotherapy augmented with CEUS and microbubbles) has been conducted. Results showed almost a 20% improvement in median PFS and OS; albeit not statistically significant. There was a statistically significant difference between groups with and without sonoporation with respect to serious adverse even rates, but as no adverse events were associated with the sonoporation treatment this result is probably due to variation in the underlying disease. Nonetheless, these initial results are encouraging and suggest that sonoporation treatment of PDAC may improve patient care by increasing the PDAC response to standard of care chemotherapy.

Acknowledgements

References

[1] Siegel RL, Miller KD, Wagle NS, Jemal A. Cancer statistics, 2023. *CA Cancer J Clin*. 2023; 73:17–48.
[2] Klein AP. Identifying people at a high risk of developing pancreatic cancer. *Nat Rev Cancer* 2013; 13(1):66-74.
[3] Rawla P, Sunkara T, Gaduputi V. Epidemiology of pancreatic cancer: global trends, etiology and risk factors. *World J Oncol* 2019; 10(1):10-27.
[4] Mintziras I, et al. Postoperative morbidity following pancreatic cancer surgery is significantly associated with worse overall patient survival; systematic review and meta-analysis. *Surg Oncol* 2021; 38:101573.
[5] Kotopoulis S, Dimcevski G, Gilja OH, Hoem D, Postema M. Treatment of human pancreatic cancer using combined ultrasound, microbubbles, and gemcitabine: a clinical case study. *Med Phys* 2013; 40(7):072902.
[6] Dimcevski G, et al. A human clinical trial using ultrasound and microbubbles to enhance gemcitabine treatment of inoperable pancreatic cancer. *J Control Release*, 2016; 243:172-181.
[7] Wang Y, et al. Clinical value of contrast-enhanced ultrasound enhancement patterns for differentiating focal pancreatitis from pancreatic carcinoma: a comparison study with conventional ultrasound. *J Ultrasound Med* 2018; 37(3):551-559.
[8] Forsberg F, et al. Subharmonic and endoscopic contrast imaging of pancreatic masses – a pilot study. *J Ultrasound Med*, 2018; 37(1):123-129.
[9] Lyshchik A. *Specialty Imaging: Fundamentals of CEUS*. 2019. Elsevier Health Sciences:Manitoba, Canada.
[10] Helfield B, Chen X, Watkins SC, Villanueva FS, Biophysical insight into mechanisms of sonoporation. *Proc Natl Acad Sci USA*. 2016; 113(36):9983-9988.
[11] Kooiman K, et al. Ultrasound-responsive cavitation nuclei for therapy and drug delivery. *Ultrasound Med Biol* 2020; 46(6):1296-1325.
[12] Schultz CW, et al. Selecting the optimal parameters for sonoporation of pancreatic cancer in a pre-clinical model. *Cancer Biol Ther* 2021; 22(3):204-215.

Assessing sonoporation efficiency under controlled flow rates in *ex vivo* mesenteric arteries

Stephanie He[1], Davindra Singh[1], Brandon Helfield[1,2]

[1]*Department of Biology, Concordia University, Montreal, Canada*
[2] *Department of Physics, Concordia University, Montreal, Canada*
Corresponding author: stephanie.he@mail.concordia.ca

Introduction

Ultrasound and microbubbles (USMB)-mediated therapies are currently being explored in both cardiovascular and oncological fields. Leveraging the intravascular nature of microbubbles, these therapies involve strategies such as modulating vessel permeability or inducing sonoporation of individual endothelial cells. In-depth studies regarding the physical interactions of microbubbles and blood vessels have taken place in a range of vessels (*e.g.* mesenteric vessels [1], [2], the aorta [3], [4], and in chorioallantoic membrane vessels [5]). In this context, we have developed a novel system to study the bioeffects of USMB within a pressurized, viable and physiologically intact mesenteric artery. In the present study, we explore the effect of microbubble flow rate on the efficiency of sonoporation.

Methods

Third order mesenteric arteries were isolated from healthy male and female Sprague-Dawley rats (Charles River Laboratories, Senneville, QC, Canada) in accordance to Concordia University's Animal Research Ethics Committee. Excess tissues were carefully cleaned from the vessels and cannulated to a pressure myograph (Living Systems Intrumentation, Fairfax, VT, USA). The vessels were then maintained at 60 mmHg and 37°C in Krebs-Hepes buffer. To confirm vessel viability from our handling, the vessels were subjected to increasing phenylephrine (Sigma-Aldrich, St-Louis, MO, USA) concentrations, an adrenergic agonist, to induce vasoconstriction, and vasodilation was achieved by removing the phenylephrine solution to ensure proper vasoreactivity. Vessel diameters were analysed on MATLAB (Mathworks, Natick, MA, USA).

The pressurized vessels were then treated with USMB at 2.25 MHz, 150 kPa, PRI of 1 ms and 500 or 250 cycles (duty cycles (DC) of 22.2% or 11.1%, respectively). Definity™ (Lantheus Medical Imaging, N. Billerica, MA, USA) microbubbles were perfused intralumenally at constant flow rates of 0.83 cm/s, 1.47 cm/s or 1.89 cm/s, assuming a maximum average vessel diameter of 391 μm (n=10). To quantify sonoporation, the vessels were incubated in propidium iodide (PI; 150 nM; Sigma-Aldrich), and frames spanning the entire vessel were recorded with a Basler Ace 2 camera (Basler, Ahrensburg, Germany) before and after USMB treatments on a Leica microscope equipped with an X-Cite™ (Excelitas Technologies, Waltham, MA, USA) light source for fluorescence microscopy. Controls were exposed to the same ultrasound parameters without microbubbles. The number of PI-positive cells was quantified through MATLAB (Mathworks). Finally, a subset of data were subjected to a vessel viability assay post USMB treatment.

Results

All of the vessels studied achieved at least a 60% vasoconstriction capacity following 10^{-5} M phenylephrine incubation, and promptly returned to at least 90% of their maximum vessel diameter after phenylephrine removal (n≥4 for each group). This indicates that our isolation methodology and handling ensures viable arteries. Our sonoporation results indicate that at higher intralumenal flow rates and duty cycles, we observe a higher number of PI-positive cells, which is in line with our previous *in vitro* work [6]. Specifically, under the stronger US condition (DC of 22.2%), we confirmed that the ratio of PI-positive cells increased with increasing flow rate; from 2.6 (n=4, p<0.05) to 2.8 (n=4, p=0.001), to 6.0 (n=3, p<0.001) compared to the controls at flow rates of 0.83 cm/s, 1.47 cm/s and 1.89 cm/s respectively. A similar trend

was observed at the lower DC setting, where the proportion of PI-positive cells increased from 1.98 (n=3, p<0.001), to 2.15 (n=3, p=0.002), to 2.39 (n=3, p<0.001) with increasing flow rate. The latter treatment regime also resulted in an adequate vessel response to vasoconstriction, confirming vessel viability post treatment.

By comparing the fold change in sonoporation between the two USMB conditions at a given flow rate, we noted interesting observations. Specifically, at the slower flow rates (0.83 cm/s and 1.47 cm/s), the harsher USMB condition elicited a 1.3x increase in sonoporation, whereas at the higher flow rate (1.89 cm/s) this resulted in a 2.5x increase. The noticeable increase in the PI-positive cells under the 22.2% DC treatment regime at a flow rate of 1.89 cm/s may be indicative of vessel damage.

Conclusions

We have shown that microbubble flow rate is an important factor in the sonoporation efficiency within an individual physiologically intact vessel. This data has implications in the broader success of USMB therapies within different disease contexts.

References

[1]   H. Chen, A. A. Brayman, M. R. Bailey, and T. J. Matula, "Blood vessel rupture by cavitation," *Urol. Res.*, vol. 38, no. 4, pp. 321–326, 2010, doi: 10.1007/s00240-010-0302-5.

[2]   H. Chen, A. A. Brayman, W. Kreider, M. R. Bailey, and T. J. Matula, "Observations of translation and jetting of ultrasound-activated microbubbles in mesenteric microvessels," *Ultrasound Med. Biol.*, vol. 37, no. 12, pp. 2139–2148, 2011, doi: 10.1016/j.ultrasmedbio.2011.09.013.

[3]   J. A. Navarro-Becerra, G. A. Caballero-Robledo, C. A. Franco-Urquijo, A. Ríos, and B. Escalante, "Functional Activity and Endothelial-Lining Integrity of Ex Vivo Arteries Exposed to Ultrasound-Mediated Microbubble Destruction," *Ultrasound Med. Biol.*, vol. 46, no. 9, pp. 2335–2348, 2020, doi: 10.1016/j.ultrasmedbio.2020.05.004.

[4]   C. A. Franco-Urquijo, J. Á. Navarro-Becerra, A. Ríos, and B. Escalante, "Release of vascular agonists from liposome-microbubble conjugate by ultrasound-mediated microbubble destruction: effect on vascular function," *Drug Deliv. Transl. Res.*, vol. 12, no. 5, pp. 1175–1186, 2022, doi: 10.1007/s13346-021-00994-7.

[5]   B. Meijlink, I. Skachkov, A. F. W. van der Steen, N. de Jong, and K. Kooiman, "The preparation of chicken ex ovo embryos and chorioallantoic membrane vessels as in vivo model for contrast-enhanced ultrasound imaging and microbubble-mediated drug delivery studies," *J. Vis. Exp.*, vol. 2021, no. 168, pp. 1–27, 2021, doi: 10.3791/62076.

[6]   E. Memari, F. Hui, H. Yusefi, and B. Helfield, "Fluid flow influences ultrasound-assisted endothelial membrane permeabilization and calcium flux," *J. Control. Release*, vol. 358, pp. 333–344, Jun. 2023, doi: 10.1016/j.jconrel.2023.05.004.

Contrast-Enhanced Molecular Imaging of Endothelial PD-L1 as a Key Role in Immune Checkpoint Therapy

Farbod Tabesh, *Negar Sadeghipour, Arutselvan Natarajan, Ramasamy Paulmurugan*, Ahmed El Kaffas**

Molecular Imaging Program at Stanford (MIPS), Stanford University School of Medicine, Stanford, CA, USA.
The Canary Center at Stanford for Cancer Early Detection, Stanford University School of Medicine, Palo Alto, CA, USA
Corresponding authors: paulmur8@stanford.edu, elkaffas@stanford.edu

Introduction and Purpose

Immune checkpoint therapies (ICT) have had high success rates in cancer patients [1,2]. However, such therapies only succeed in less than 20% of solid tumors. Programmed death-1 ligand (PD-L1) as an immunosuppressive marker on tumors and their endothelial cells (ECs) is a proposed potent biomarker for predicting therapy response; however, characterizing PD-L1 is currently only possible via invasive biopsies [3]. Our group is developing non-invasive contrast-enhanced ultrasound molecular imaging (CEUMI) methods to monitor the expression of immune markers in the context of ICT [4]. This work presents pilot results demonstrating that the immunosuppressive PD-L1 marker can be imaged longitudinally with CEUMI.

Methods

In this work, we aimed to develop a PD-L1-targeted contrast agent to demonstrate CEUMI for longitudinal imaging and precisely measuring vasculature PD-L1 on ECs. For this reason, we first evaluated the expression of PD-L1 *in vivo* using ECs of murine tumors exposed to immune modulators such as IFN-γ by immunostaining. We then confirmed the expression of PD-L1 on ECs of the syngeneic murine colorectal cancer model in immunocompetent mice. We used commercially available target-ready MBs (Vevo MicroMarker target-ready contrast agent kit; VisualSonics Inc, Toronto, ON) and targeted them with anti-PD-L1 antibody (MB_{Targ}) for CEUMI of vascular PD-L1. To ensure the binding specificity of MB_{Targ} to PD-L1, we also used Isotype MBs (MB_{iso}). We first assessed the binding specificity of MB_{Targ} to PD-L1 expressed on tumor-specific ECs using a CT-26 mouse flank tumor model (Fig. 1A). We imaged baseline expression of EC-specific PD-L1 in Balb/C mice (n=9) bearing CT-26 tumors using MB_{Targ} and MB_{iso} (intravein injection) with a pre-clinical Vevo2100 system using an M250 transducer (Fig. 1B). Furthermore, we modulated the expression of PD-L1 using anti-PD-L1 antibodies (block) or interferon-γ (IFN-γ) (promote) *in vivo* (Fig. 1C) and longitudinally imaged for the expression of PD-L1 using MB_{Targ}. We examined whether CEUMI could capture longitudinal changes in PD-L1 expression on ECs upon exposure of tumors to immune modulators (IFN-γ to increase expression and anti-PDL1 to decrease). The signals were quantified by calculating the differential targeted enhancement (dTE) values and correlated the results with the treatment conditions. We also aimed to predict the PD-L1 treatment response using CEUMI of endothelial PD-L1 to eliminate the need for other painful methods for the first time by imaging endothelial PD-L1 CEUMI. We imaged 25 mice (having CT-26 tumor cell line) before starting the treatment (pre-treatment imaging). Post-treatment images were recorded after administering three doses of anti-PD-L1 antibodies (10 mg/kg) and measuring the tumor volumes every three days. After categorizing the treatment response based on the tumor growth rate of treated and non-treated mice, we related the treatment response to the dTE values of the pre-treatment imaging.

Results

CEUMI of tumor using PD-L1 targeted MBs showed a significant increase in dTE (7.4 a.u.) compared to that of MB_{iso} (2.7 a.u.) (Fig. 1D). In addition, CEUMI of MB_{Targ} demonstrated significant higher PD-L1 expression in the ECs of tumors upon treatment using IFN-γ, resulting in a higher dTE value (1.15 ± 0.14). At the same time, the anti-PD-L1 antibody-treated group showed a significantly lower dTE value (0.55 ± 0.21) (p= 0.0017) (Fig. 1E). Our results suggest that MB_{Targ} can image absolute and longitudinal changes in PD-L1 expression exclusively on ECs using CEUMI. To differentiate the response in treatment, we normalized the tumor growth to their initial tumor size for both treated and non-treated mice. Then, we grouped them based on the resemblance in growth behavior to the non-treated mice. We then realized that increasing dTE values (because of higher expression of PD-L1) weakened the response to the treatment. Therefore, we divided the treated mice into responders and non-responders, in which the growth rate of the non-responder group was close to that of the non-treated group. Finally, we have also investigated whether the response to PD-L1 can be stratified in these immunocompetent mice and found evidence of a trend where mice having

higher expression of PD-L1 pre-therapy are less likely to respond to therapy. Based on the results, the average dTE of the responder group was 4.3±3.7 while that of non-responders was 9.1±6.0

Conclusions

This work proved that the expression of PD-L1 on murine tumor vascular ECs can be measured using CEUMI. The enhanced binding of PD-L1-MB$_{Targ}$ to the expressed PD-L1 in the vascular ECs (bound to vasculature PD-L1) achieved a higher contrast signal than those recorded from isotype MBs (MB$_{iso}$). More contrast signals were observed when the mice were treated with IFN-γ than in the anti-PD-L1 antibody-treated group. These results can help guide the development of clinically relevant MBs for imaging EC-specific PD-L1 expression in the tumor vasculature and ultimately provide decision-support to clinicians managing patients receiving ICT therapy. We also found that we can predict the PD-L1 treatment response using CEUMI of endothelial PD-L1. Studies of other immune diseases like multiple sclerosis and other autoimmune diseases such as Type I diabetes might also be possibly studied through this imaging technique, given the reported role of immunosuppressive markers on these diseases.

Figure 1. (A) Schematic illustration showing the CEUMI of EC-specific PD-L1 expression using MB$_{Targ}$; **(B)** B-mode and contrast images of CT26 tumors using MB$_{Targ}$ and MB$_{iso}$. A destructive pulse was applied 6 minutes after the bolus injection of each microbubble to acquire images to calculate the differential targeted enhancement (dTE); **(C)** Pictorial representation showing the expression of PD-L1 on vascular endothelial cells and the associated inhibition on T cell infiltration into the tumor tissues. Therefore, blockage of PD-L1 using anti-PD-L1 monoclonal antibodies allows infiltration of T cells into the tumor for cell-mediated antitumor effect; **(D)** CEUMI comparing the specificity of PD-L1 expression in the ECs using MB$_{Targ}$ and MB$_{iso}$ before and after anti-PD-L1 antibody and IFN-γ treatment. The colored-scale images show the dTE signal on the tumor region. Top: CEUMI images of animals treated using anti-PD-L1 antibody and bottom: CEUMI images of animals treated with IFN-γ. MB$_{iso}$ (left column) and MB$_{Targ}$ (middle column), treated mice (right column); and **(E)** Quantitative graph showing the normalized dTE values for PD-L1 markers imaged in pre- and post-treated mice that received IFN-γ and anti-PD-L1 antibody. The PD-L1 dTE in pre and post-treatment were normalized by taking the ratio of PD-L1 to isotype dTEs. The final ratio shown in the plot is the post-to-pre-treatment comparison (i.e., post-treatment normalized dTE/pre-treatment normalized dTE). The control group was left untreated. The IFN-γ treated group received three doses of 50 µg IFN-γ injected via the tail vein every 24 hours. The PD-L1 blocked group received two doses of 250 µg anti-PD-L1 antibody every 24 hours before being imaged. ** $p < 0.01$.

References

[1]. Huinen ZR, et al., Anti- angiogenic agents—overcoming tumour endothelial cell anergy and improving immunotherapy outcomes, Clinical Oncology, 18: 527-540, 2021.

[2]. Nowak-Sliwinska P, et al., Proinflammatory activity of VEGF-targeted treatment through reversal of tumor endothelial cell anergy, Angiogenesis, 26: 279-293, 2023.

[3]. Vaishampayan P, et al., PD-L1 as an emerging target in the treatment and prevention of keratinocytic skin cancer, Symposium Journal, 62: 52-61, 2023.

[4]. Kumar US, et al., FN3 linked nanobubbles as a targeted contrast agent for US imaging of cancer-associated human PD-L1, Journal of Controlled Release, 346: 317-327, 2022.

Ultrasound Localization Microscopy in Identifying Symptomatic Carotid Plaque

Tingting Wang[1], Ying Zhang[1], Ferenc Kandi[2], Simona Turco[2], Massimo Mischi[2*], Pintong Huang[1]**

[1] 1 Department of Ultrasound in Medicine, The Second Affiliated Hospital of Zhejiang University School of Medicine, Zhejiang University, No. 88 Jiefang Road, Shangcheng District, Hangzhou, 310009, People's Republic of China.
[2] Lab of Biomedical Diagnostics, Department of Electrical Engineering, Eindhoven University of Technology, Eindhoven, The Netherlands.
Corresponding author: [*]M.Mischi@tue.nl, [**]huangpintong@zju.edu.cn

Introduction

Intraplaque neovascularisation is an active biomarker of vulnerable carotid plaques, which can predict the occurrence of stroke independent of the stenosis degree. Ultrasound localization microscopy (ULM) represents a cutting-edge technique that capitalizes on the imaging potential of microbubbles via contrast-enhanced ultrasound (CEUS). Here, we aimed to perform vasa vasorum ULM of the carotid plaque and demonstrate that ULM can provide quantitative imaging markers to identify the symptomatic carotid plaque.

Methods

Based on clinical manifestations or the detection of acute/subacute strokes via head MRI/CT scans within a two-week frame, patients were stratified into symptomatic and asymptomatic cohorts. Offline-saved carotid plaque CEUS recordings were scrutinized, with plaques meticulously delineated. A curated subset of 300 frames, characterized by minimal pulsation, was earmarked for in-depth analysis. The data processing phase entailed the discernment of microbubbles from tissue signals utilizing singular value decomposition techniques and point spread function of the system. Each optimized frame underwent ULM to localize and chronicle microbubble movement. Sequential microbubble trajectories were consolidated, enabling an overarching view across the entire data spectrum. The finale involved a rigorous juxtaposition of ULM-derived metrics across symptomatic and asymptomatic clusters, zeroing in on parameters like microbubble count, track count, and microbubble path.

Table 1. Patients' characteristics and parameters measured by ultrasound.

Name	Symptomatic (n=34)	Asymptomatic (n=24)	_p_-value
Age (year)	65 [62–67]	71 [65–75]	0.034
Gender (men)	23 (67.6)	21 (87.5)	0.121
Smoking	17 (50.0)	14 (58.3)	0.599
Hypertension	25 (73.5)	20 (83.3)	0.526
Hyperlipidemia	2 (5.8)	2 (8.3)	1
Diabetes mellitus	12 (35.3)	7 (29.2)	0.778
Body mass index (kg/m2)	24.1 [21.9–25.4]	22.9 [21.3–24.3]	0.136
C-reactive protein (mg/L)	1.2 [1–4.5]	2.1 [1–4.9]	0.427
Investigated wall area (mm2)	25.3 [19.4–31.6]	25 [20.5–30.8]	0.636
Microbubbles (n) per second per mm^2	4.96 [4.15–5.86]	1.2 [0.54–2.11]	< 0.001
Tracks (n) per second per mm^2	0.36 [0.31–0.42]	0.08 [0.05–0.1]	< 0.001
Microbubble path (mm) per second per mm^2	0.74 [0.34–1.17]	0.16 [0.09–0.22]	< 0.001

Results

The cohort comprised 58 individuals diagnosed with carotid plaques, of which 34 were symptomatic, and 24 were asymptomatic. Among them, 44 (75.9%) were male, with age of 68.75 ± 6.21 years. Symptomatic plaques (n = 34) manifested a median microbubble count per second per mm^2 of 4.96 [4.15–5.86], track count per second per mm^2 0.36 [0.31 – 0.42] and a microbubble path per second per mm^2 21 [13–37] mm (Table 1). In stark contrast, asymptomatic plaques (n = 24) registered a microbubble count of 1.2 [0.54–2.11], track count 0.08 [0.05 – 0.1], and a microbubble path 0.16 [0.09–0.22] mm. The variance in ULM metrics between the cohorts bore statistical significance, evidenced by P-values < 0.05, underscoring the distinct ultrastructural attributes of symptomatic versus asymptomatic plaques.

Conclusions

ULM enables in vivo visualization of intraplaque neovascularization, distinguishing symptomatic carotid plaques with diagnostic relevance, yet requires motion compensation for improved results.

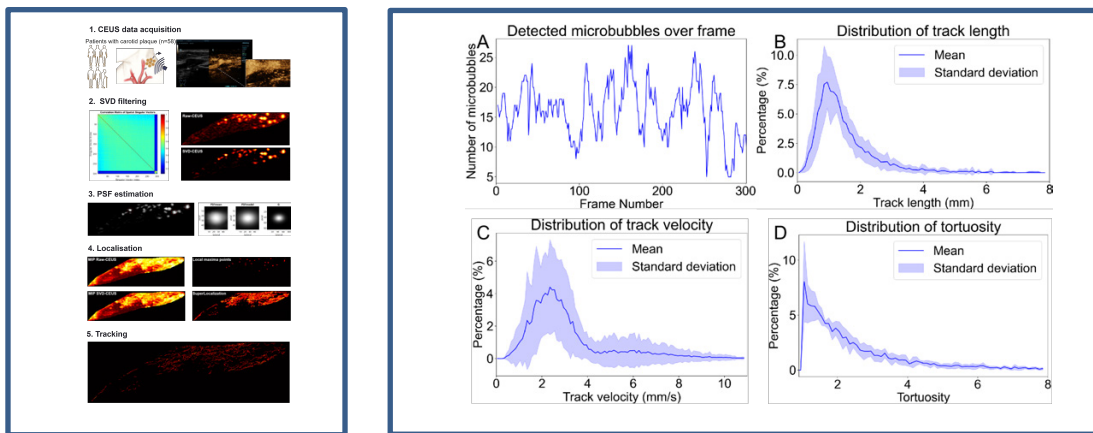Figure 1. Summary diagram of the processing method.

Figure 2. Detected microbubbles over frame (A) in a case. Distribution of track length (B), track velocity (C), tortuosity (D) within the symptomatic carotid plaque patients.

References

[1]. Errico C, Pierre J, Pezet S, et al. Ultrafast ultrasound localization microscopy for deep super-resolution vascular imaging. Nature. 2015;527(7579):499-502.

eATP Release Kinetics following Microbubble Cavitation in cultured HUVECs

<u>Marie Amate</u>[1,2], Ju Jing Tan[1,3], Francis Boudreault[1], Ryszard Grygorczyk[1,3], Thomas Gervais[1,4], François Yu[1,2,5].

[1]*Centre de recherche du Centre hospitalier de l'Université de Montréal, Montreal, Canada*
[2]*Biomedical Engineering Institute, Université de Montréal, Montreal, Canada*
[3]*Department of Medicine, Université de Montréal, Montreal, Canada*
[4]*Department of Engineering Physics, Polytechnique Montréal, Montreal, Canada*
[5]*Department of Radiology, Radio-oncology and Nuclear Medicine, Université de Montréal, Montreal, Canada*
Corresponding author: marie.amate@montreal.ca

Introduction

Ultrasound Targeted Microbubble Cavitation (UTMC) can induce a localized provascular response that can improve cancer radiotherapy [1]. Indeed, UTMC has been shown to trigger directly and indirectly [2] the Nitric Oxide (NO) pathways, which can lead to a localized vasodilation response [3]-[5].

The role of extracellular Adenosine-5'-Triphosphate (eATP) has been underlined in vascular tone regulation via the activation of the purinergic pathways [6], [7]. Indeed, the activation of the purinergic pathways leads to NO production in endothelial cells, making eATP a critical molecule involved in vasodilation. UTMC has been shown to cause eATP release via lytic and non-lytic paths [2], [8]-[10].

In the present study, we are interested in observing and quantifying the eATP release at the cellular scale to better understand the mechanisms of vasodilation *in vivo*. We propose a method to quantify eATP release kinetics by single cells, classified as sonoporated or dead cells, following UTMC *in vitro* using microscopy techniques.

Methods

Microfluidic model and cell culture. HUVEC cells were grown on the ceiling of PDMS microfluidic chips. We designed the microfluidic chip with three parallele rectilinear square-section channels (600 μm x 600 μm x 2 cm). The dimensions were chosen to fall inside the -6dB area of our therapy transducer. Cells were seeded (500 cells/mm^2) in chips previously coated with fibronectin (100 μg/mL; 1h; room temperature). The chips were flipped upside down and incubated for 28 h (37°C; 5% CO2) to allow cell sedimentation and attachment on their ceiling.

Luciferin-Luciferase bioluminescent assay. eATP was measured in real-time with a bioluminescent Luciferin-Luciferase (LL) assay. Immediately before the experiment, a microbubble solution (Definity™, final concentration of 10^7 MB/mL in RPMI phenol red free) was mixed at equal volume (25 μL each) with an isotonically adjusted Luciferin-Luciferase (isotonic LL) solution (Millipore-Sigma commercial kit, cat: FLAAM). The MB-LL solution was supplemented with Propidium Iodide (PI; 25 μg/mL final concentration) to be able to track sonoporation and cell death. This solution was injected into the chip before UTMC.

Ultrasound set up. The ultrasound probe (A303S-SU, 1MHz, 0.5 Inch, Olympus) was positioned above the chip, 2.7 cm away from the channels with an angle of 60° with the chip. A single ultrasound pulse was applied at a pressure of 300kPa and a pulse length varying between 10, 100, and 1000 cycles (Fig. 1B).

eATP release imaging and quantification. The bioluminescence signal of eATP was captured with an EMCCD detector camera (Evolve 512, Teledyne Photometrics, Tucson, AZ, 512 x 512 pixels, 13 μm pixel size). A standard c-mount lens was mounted on the camera objective, to achieve a magnification of 0.33, allowing a field of view of 20mm x 20mm. The bioluminescence signal was acquired for 5 min with a frame rate of 0.5fps (1s interval between frames plus 1s signal integration). A binning of 2 x 2 was applied to

----

ensure an optimal signal which leads to a final resolution of 78 x 78 μm^2 per pixel. The signal was quantified with the method described by Tan et. al., 2019 [11]. The quantification was normalized by measuring the enzyme activity on the day of the experiment to take into account the decay of the enzyme with time.

Fluorescence microscopy. A PI scan of the chips was done before and 5 min after the pulse with a fluorescent microscope equipped with a 2-axis computer-driven stage. In the end, a viability assay was done with calcein-AM (4 $\mu g/mL$ in HBSS; 30min; 37°C; 5% CO_2), and a Calcein-AM/PI scan was done.

Cell classification. PI, Calcein-AM, and eATP images were processed with an in-house Matlab® program. This program is able to classify cells into "sonoporated cell" vs "dead cell" categories based on calcein-AM/PI colocalization and PI intensity. As the EMCCD camera resolution is 30.2 times coarser than the fluorescence image camera (2,58 μm x 2,58 μm per pixel), a bicubic interpolation of the eATP images was done to make the resolution of the eATP image and the fluorescence images consistent.

Isolated cell analysis. We first analyzed isolated cells, i.e. cells with an eATP signal "cloud" that did not merge with other eATP clouds during the entire image sequence. A circular ROI of radius 300 μm was drawn on the eATP signal image which encompassed the entire cloud. The parameters taken into account are:

- Total eATP release per cell (mol) (Fig. 1A).
- The eATP time to peak (s) for every cell, ie. the time between the pulse and the total eATP release (Fig. 1A).
- eATP release rate (mol/s) for every cell, ie. the difference of the summation of eATP signal in an ROI from an image to the previous one, divided by the time between two frames (2s) (Fig. 2A).
- The mean eATP release per sonoporated $q_{mean\ sc}$ and dead $q_{mean\ dc}$ cells separatly (mol/cell) on the chip of interest.
- The possible maximum eATP released measured in a sonoporated $q_{max\ sc}$ and a dead $q_{max\ dc}$ cell (mol/cell) on the chip of interest.

Cell cluster analysis. Based on these individual measurements made on isolated cells, we tried at first to quantify eATP released by cell clusters (ie. when the clouds of eATP coming from different cells are merging at some point in the eATP image sequence) with two strategies.

First strategy: We assumed that both sonoporated and dead cells are a source of eATP, therefore we can tell that the total eATP released q_{total} (mol) in an area is the sum of the eATP released by each of the sonoporated and dead cells in the area. As we cannot measure the eATP coming from each cell in a cell cluster we are simplifying the equation by the formulae:

$$q_{total} = q_{dc} \cdot n_{dc} + q_{sc} \cdot n_{sc} \qquad (1)$$

With n_{sc} and n_{dc} the number of sonoporated and dead cells respectively, and q_{sc} and q_{dc} the quantity released by sonoporated and dead cells respectively (in mol/cell). We calculated the total ATP released q_{total} by drawing an ROI including the eATP signal of the entire cluster and q_{sc} and q_{dc} were replaced by the couples ($q_{mean\ sc}$; $q_{mean\ dc}$) (Fig. 3A dark green dots and line) or ($q_{max\ sc}$; $q_{max\ dc}$) (Fig. 3A light green dots and line). A total of 9 cell clusters were analyzed with this method (Fig. 3B).

Second strategy: Since differences appeared between sonoporated and dead cell eATP release rates for individual cells, we analyzed a cell cluster to see if we could find the same pattern between sonoporated and dead cell release rate in an eATP cloud merging several eATP releases.

In this analysis, we focused on images at early time points after the pulse because the rate difference were already significant in the isolated cells analysis, and the eATP clouds were not yet merged which allowed us to draw ROI more accurately. We used circular ROI (radius 117 μm ie. 1.5-pixel radius in the eATP signal images) around the eATP clouds to minimize overlapping.

Statistical analysis. Data were analyzed with a Two-way ANOVA test with a Tukey multicomparison test and a parametric Student T-test (Prism 8, GraphPad). $p < 0.05$ was considered significant.

Results and discussion

In individual cells, the eATP release was significantly higher in dead cells than in sonoporated cells for chips 1, 2, and 3 (Fig. 1C). Nevertheless, the eATP time to peak was not different from sonoporated and dead cells in all chips (Fig. 1D). Our data presented a degradation in signal between chips, which was observed despite compensating for luciferase activity decay with time. Thus, we restricted our analyses on a per-chip basis onwards.

In Figure 2, we compare the eATP released rates with a large (300 μm radius - Fig. 2A) and a small (117 μm radius - Fig. 2B) ROI as a function of time after the pulse. In all chips, the eATP release rate was higher for dead cells in the first 10s after UTMC with both ROI sizes. As expected the larger ROI yielded slightly better results but differences could still be detected with the smaller ROI.

The analysis of cell clusters with the first strategy (Fig. 3A) showed a linear correlation between both sides of equation (1). The couple ($q_{max\,sc}$; $q_{max\,dc}$) underestimated the total eATP released by 22% and ($q_{mean\,sc}$; $q_{mean\,dc}$) by 55%. One possible explanation for this may be a cellular detachment between the eATP imaging and PI/Calcein-AM image acquisitions.

We started exploring the analysis of the cell cluster with the second strategy which as expected was noisier than with isolated cells (Fig. 4C). We can note that the sonoporated cells with a high release rate (>4 fmol/s) between the second 4 and 6 after the pulse, which are the cells 9, 10, 11, 12, 23, are mostly placed in the middle of the eATP cloud formed by the cell cluster (Fig. 4A and B). The signal around these cells may thus be affected by nearby dead cells. Also, the relatively coarse resolution of the eATP signal acquisition makes it hard to draw the ROI without overlap.

Conclusions

We developed an approach that gives a quantification of the eATP released per sonoporated and dead cells separately. Overall, we can tell that eATP release kinetic is different between sonoporated and dead cells. The significant difference between release rates at the early time points is promising for analyzing eATP clouds from clusters of cells. In the future, a better estimation of the eATP release in the case of a cell cluster treated by UTMC will be investigated. We expect this work to provide a greater understanding of sonoporation mechanisms to optimize UTMC *in vivo* and improve the outcome of anti-cancer radiotherapy.

Abbreviations

UTMC: Ultrasound Targeted Microbubble Cavitation; eATP: extracellular Adenosine-5'-Triphosphate; NO: Nitric Oxide; HUVEC: Human Umbilical Vein Endothelial Cells; PDMS: Polydimethylsiloxane; EMCCD: Electron Multiplying Charge-Coupled Device; LL: Luciferin-Luciferase; PI: Propidium Iodide; SEM: Standard Error of the Mean; ROI: Region of Interest.
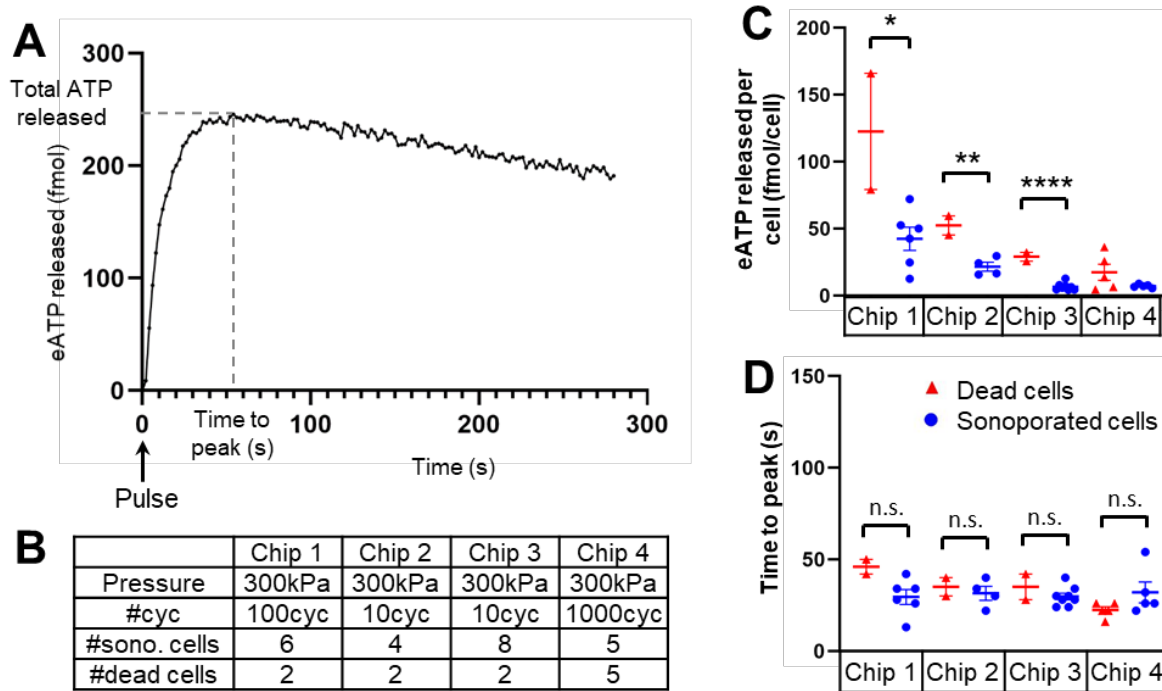
Figure 1. A. Example of the kinetic of eATP release with time in an ROI. The pulse is given at t=0s, the maximum of the curve is considered as the total eATP released in the ROI. **B.** Table of pulse and the number of isolated PI-positive cells analyzed per chip. **C.** Total eATP release per isolated cell. **D.** Time to peak for every isolated cell. C and D, display: Mean and SEM with single cell values. Parametric Student t-test. The stars represent sono. vs. dead. ****: $p < 0,0001$; ***: $p < 0,001$; **: $p < 0,01$; ; *: $p < 0,05$.
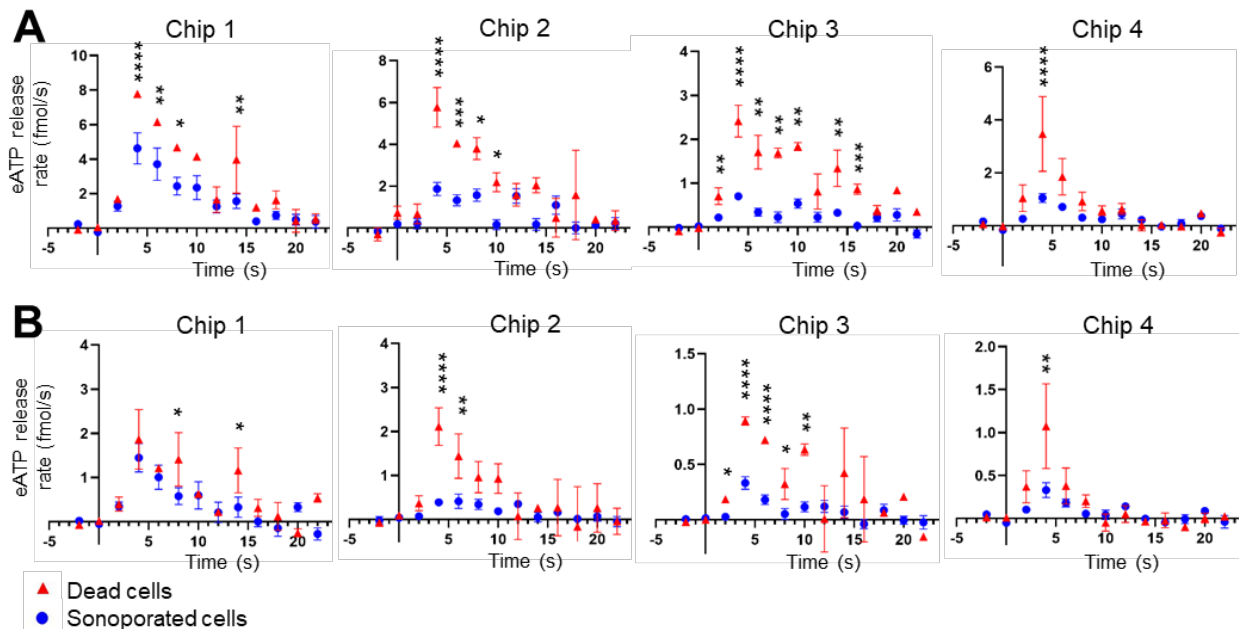
Figure 2. A. eATP release rate in time for each chip with an ROI of radius 300μm. **B.** eATP release rate in time for each chip with an ROI of radius 117μm (i.e. radius of 1.5 pixels in the eATP release signal images). Display: Mean of the eATP release rate averaged by sonoporated and dead cells separately and SEM. Two-way ANOVA with Tukey multicomparison test. The stars represent sono. vs. dead. ****: $p < 0,0001$; ***: $p < 0,001$; **: $p < 0,01$; ; *: $p < 0,05$.
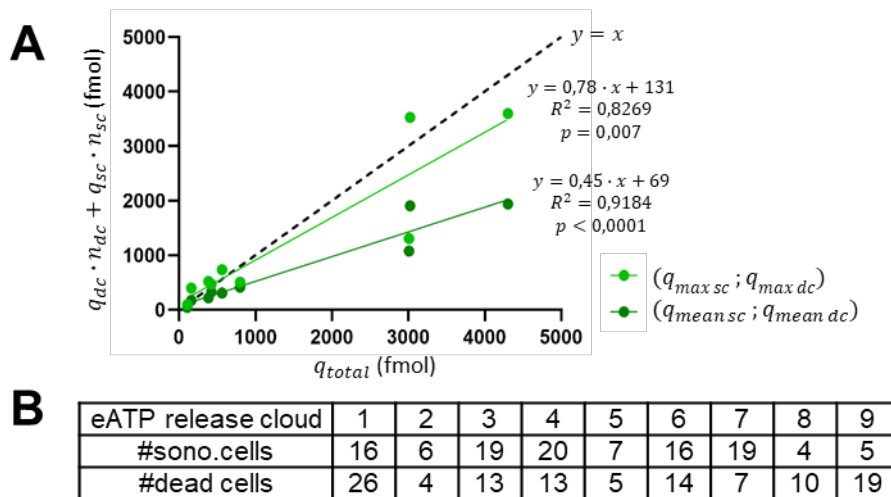
Figure 3. A. Correlation map of the eATP measured and the eATP quantity calculated using eATP/cell values calculated on isolated cells. **B.** Table of eATP release clouds and the number of cells corresponding.
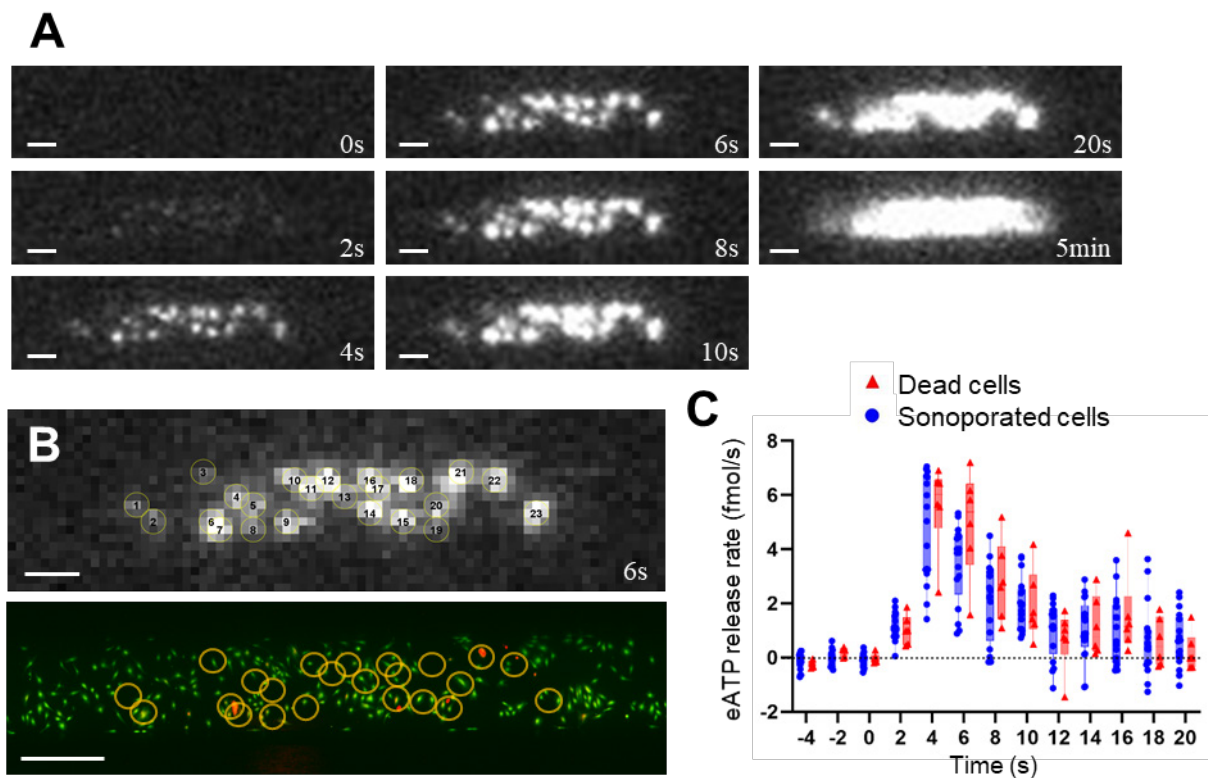
Figure 4. A. Typical eATP release frame sequence captured with the EMCCD camera at different time points. **B.** eATP signal frame 6s after the pulse and corresponding PI/Calcein-AM fluorescent image (magnification 5x). A 1.5-pixel-radius circle is drawn around every PI-positive cell. A and B, scale bars: 500μm. **C.** eATP release rate for every ROI drawn in B (ROI 6, 7, 14, 19, 21, 22: dead cells in red triangles; ROI 1, 2, 3, 4, 5, 8, 9, 10, 11, 12, 13, 15, 16, 17, 18, 20, 23 sonoporated cells in blue dots).

References

[1]. S. Michon, F. Rodier, and F. T. H. Yu, "Targeted Anti-Cancer Provascular Therapy Using Ultrasound, Microbubbles, and Nitrite to Increase Radiotherapy Efficacy," *Bioconjug. Chem.*, vol. 33, no. 6, pp. 1093–1105, Jun. 2022, doi: 10.1021/acs.bioconjchem.1c00510.

[2]. J. T. Belcik *et al.*, "Augmentation of Muscle Blood Flow by Ultrasound Cavitation Is Mediated by ATP and Purinergic Signaling," *Circulation*, vol. 135, no. 13, pp. 1240–1252, Mar. 2017, doi: 10.1161/CIRCULATIONAHA.116.024826.

[3]. J. T. Belcik *et al.*, "Augmentation of Limb Perfusion and Reversal of Tissue Ischemia Produced by Ultrasound-Mediated Microbubble Cavitation," *Circ. Cardiovasc. Imaging*, vol. 8, no. 4, Apr. 2015, doi: 10.1161/CIRCIMAGING.114.002979.

[4]. F. T. H. Yu, X. Chen, A. C. Straub, and J. J. Pacella, "The Role of Nitric Oxide during Sonoreperfusion of Microvascular Obstruction," *Theranostics*, vol. 7, no. 14, pp. 3527–3538, 2017, doi: 10.7150/thno.19422.

[5]. Y. Zhang *et al.*, "Sononeoperfusion effect by ultrasound and microbubble promotes nitric oxide release to alleviate hypoxia in a mouse MC38 tumor model," *Ultrason. Sonochem.*, vol. 100, p. 106619, Nov. 2023, doi: 10.1016/j.ultsonch.2023.106619.

[6]. G. Burnstock, "Local Control of Blood Pressure by Purines," *J. Vasc. Res.*, vol. 24, no. 3, pp. 156–160, 1987, doi: 10.1159/000158691.

[7]. [R. S. Sprague, M. L. Ellsworth, and H. H. Dietrich, "Nucleotide release and purinergic signaling in the vasculature driven by the red blood cell.," vol. Curr Top Membr 54, 2003, pp. 243–268.

[8]. J. Goldgewicht, J. J. Tan, R. Grygorczyk, T. Gervais, and F. T. H. Yu, "A multiplexed microfluidic and microscopy study of vasodilation signaling pathways using microbubble and ultrasound therapy," IEEE, Sep. 2020, pp. 1–4. doi: 10.1109/IUS46767.2020.9251762.

[9]. R. Grygorczyk *et al.*, "Lytic Release of Cellular ATP: Physiological Relevance and Therapeutic Applications," *Life*, vol. 11, no. 7, p. 700, Jul. 2021, doi: 10.3390/life11070700.

[10]. F. Moccetti *et al.*, "Flow Augmentation in the Myocardium by Ultrasound Cavitation of Microbubbles: Role of Shear-Mediated Purinergic Signaling," *J. Am. Soc. Echocardiogr.*, vol. 33, no. 8, p. 1023–1031.e2, Aug. 2020, doi: 10.1016/j.echo.2020.03.016.

[11]. J. Tan, O. Ponomarchuk, R. Grygorczyk, and F. Boudreault, "Wide field of view quantitative imaging of cellular ATP release," *Am. J. Physiol.-Cell Physiol.*, vol. 317, no. 3, pp. C566–C575, Sep. 2019, doi: 10.1152/ajpcell.00096.2019.

Whole organ volumetric sensing Ultrasound Localization Microscopy for characterization of kidney structure

G. Chabouh[1#], _L. Denis[1#]_, _S. Bodard[1,2]_, _F. Lager[3]_, _G. Renault[3]_, _A. Chavignon[1]_, _O. Couture[1]_

1Sorbonne Université, CNRS, INSERM, Laboratoire d'Imagerie Biomédicale, Paris, France.
2AP-HP, Hôpital Necker Enfants Malades, Service d'Imagerie Adulte, F-75015, Paris, France.
3Université de Paris, Institut Cochin, INSERM, CNRS, F-75014 PARIS, France
 # These authors contributed equally
Corresponding author: georges.chabouh@sorbonne-universite.fr

Introduction

Nephrons are the filtration units of the kidney and their function relies heavily on their microcirculation. In particular, glomeruli are bundles of fenestrated capillaries which thighly control liquid and toxins excretion and, consequently, overall blood volume and homeostasis. Pathological modifications of the glomeruli are currently assessed through indirect perfusion imaging and biological samples to yield metrics such as glomerular filtration rate.

Despite its obvious diagnostic importance, an accurate estimation of blood flow in the capillary bundle within glomeruli defies the resolution of conventional imaging modalities. Ultrasound Localization Microscopy (ULM) has demonstrated its ability to image in-vivo deep organs in the body (**Errico et al. 2015, Christensen et al., 2020, Song et al., 2023**). Recently, the concept of sensing ULM or sULM (**Denis et al., 2023**) was introduced to classify individual microbubble behavior based on the expected physiological conditions at the micrometric scale. In the kidneys of both rats and humans, it revealed glomerular structures in 2D but was severely limited by planar projection. In this work, we aim to extend sULM in 3D to image the whole organ and in order to perform an accurate characterization of the entire kidney structure and its functional units.

Methods

Experiments were conducted according to European and French regulations. They have been approved by the local ethics committee on animal experimentation (CEEA34) and registered by the French ministry of research under number #33913. To perform the ultrasound acquisition, the left kidney was externalized through an incision in the abdomen. The organ was then placed on an acoustic absorber and fixed with a needle to avoid movement. A 25G catheter was placed in the tail vein to perform microbubbles injections (SonoVue, Bracco, Italy) needed for volumetric sULM. The animal was under isoflurane anesthesia (4% for induction, 2.5% for maintenance) with appropriate analgesia (subcutaneous injection of 0.1 mg/Kg of buprenorphine 30 minutes prior to experiments).

Ultrasound acquisitions were then performed with a 256- channels research ultrasound scanner (verasonics, Kirkland, USA) and an 8 MHz multiplexed matrix probe (Vermon, France). Five hundred blocks were acquired, with 200 images per block and a framerate of 130Hz. Each image being the result of a compounding of 5 plane-waves oriented according to +- 5° (in the elevation axis and in the lateral axis). The sequence was decomposed according to a light configuration (**Chavignon et al., 2021**), and lasted for 8 minutes, with repeated bolus injections of 50 μL/min every 1 minute. The pulse duration is about 2 cycles with a pulse repetition frequency (PRF) of 13.5 kHz. The data were then reconstructed with a classical delay and sum beamforming on a [98.5, 150, 150] μm grid, before reaching the final sULM resolution of [9.85, 9.85, 9.85] μm.

The construction pipeline of the 3D sULM mapping follows a classical ultrasound Bmode volume reconstruction, a clutter filtering using a low-threshold Singular Value Decomposition (SVD) where the first six singular values were annulled, microbubble localization using radial symmetry algorithm (**Heiles**

et al., 2022), and tracking using the Hungarian algorithm. It is worth to mention that in this work; the localization and tracking were done on an unique dataset. Thanks to the volumetric acquisition, we were able to precisely track the microbubble along its entire path within the blood vessels without any loss of visual continuity due to the microbubble velocity changes.

To correct motion induced by breathing, heartbeat and muscle contraction, in our study, we generalized phase correlation in 3D with subwavelength motion, a technique that has previously demonstrated its effectiveness in improving ULM resolution in 2D (**Hingot et al., 2017**).

sULM is built upon an a-priori knowledge of the local environment based on previous invasive microscopy studies such as histology. To highlight specific microbubble behaviour, we employed two different metrics that we define hereafter. Microbubble velocity, characterized as the mean displacement magnitude between every two successive points along a trajectory, divided by the corresponding time interval. The Pathway Angular Shift (PAS), delineated as the angular difference computed between sets of three consecutive points along a track.

Results

To estimate physiological parameters like the glomerular filtration rate, it is essential to carefully pinpoint glomeruli within the cortex. This task is achieved through a systematic two-step approach. Firstly, cortical tracks (afferent and efferent arteioles + glomeruli) are extracted by applying a velocity threshold (3 < track speed < 6 mm/s).
This velocity parameter serves as a discriminant, effectively distinguishing various segments of the kidney's structure. In order to substract only glomeruli in the cortex, the Pathway Angular Shift (PAS) metric is employed on the tracks established via the dual velocity cutoff. If the computed PAS value surpasses a designated threshold of 40 degrees, all data points exhibiting PAS > 40° are identified as localizations within the glomerulus. Note that the threshold value used in PAS is empirical. In Fig.1a, 3D sULM rendering of the kidney is displayed, with a closer view provided in b. Here, glomeruli are highlighted in blue, main vessels in orange, and the medulla in green. In Fig. 1 c demonstrates the probability function for the total traveled distance, which reaches its peak at 18 μm. Notably, due to the complex presence of various vessel loops within the capsule, determining the size of the glomeruli through microcirculation is impractical. To approximate a size-related metric, we propose utilizing the total traveled distance within the glomeruli. Upon statistical analysis encompassing all the glomeruli across the rat population, a total traveled distance of 7.5 +- 0.6 μm is obtained. This measurement is notably smaller than the actual glomerular size (which boasts a 50- micron diameter).
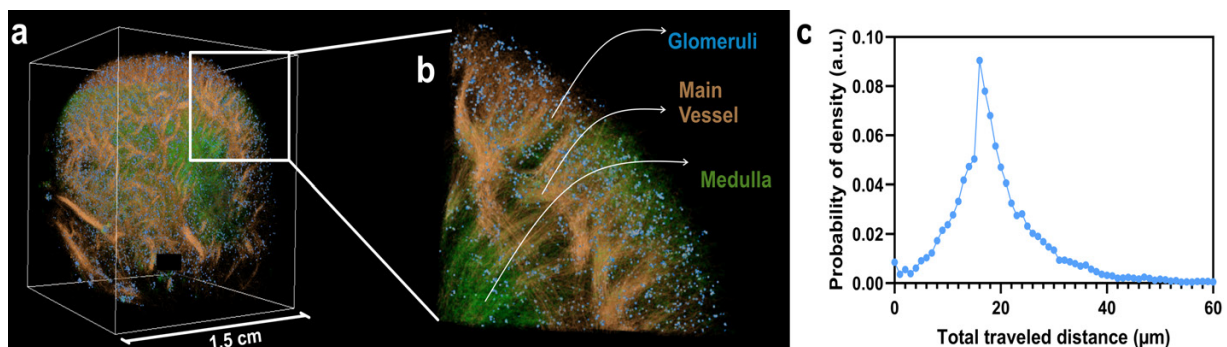
 Figure 1. **Whole organ volumetric sULM reveals accurate estimation of glomeruli physiology: a Volumetric sULM rendering with three different families encoded in color. Medulla in green, main vessels in orange and glomeruli in blue. b shows a zoom on a part of the kidney. The probability of density of all the glomeruli tracks (in blue) of the total traveled distance c.**

Conclusions

The extension of sULM into the 3D domain combined with a 3D subwavelength motion correction algorithm allow better localization and more robust tracking. The 3D metrics of velocity and pathway

angular shift made glomerular mask possible. This approach facilitated the quantification of glomerular physiological parameter such as an interior traveled distance of approximately 7.5 +- 0.6 microns within the glomerulus. This study introduces a technique that characterize the kidney physiology which could serve as a method to improve pathology assessment. Furthermore, such study demonstrates that sULM is sensitive to the functional units of organs and, hence, bridge the gap between imaging at the millimetric scale and exploration of the microstructure of organs.

References

[1]. Errico C, Pierre J, Pezet S, Desailly Y, Lenkei Z, Couture O, Tanter M, Ultrafast ultrasound localization microscopy for deep super-resolution vascular imaging, Nature, 499-502, 2015.

[2]. Christensen-Jeffries, K., Couture, O., Dayton, P. A., Eldar, Y. C., Hynynen, K., Kiessling, F., ... & Van Sloun, R. J. Super-resolution ultrasound imaging. *Ultrasound in medicine & biology*, *46*(4), 865-891, 2020.

[3]. Song, P., Rubin, J. M., & Lowerison, M. R. Super-resolution ultrasound microvascular imaging: Is it ready for clinical use?. *Zeitschrift für Medizinische Physik, 2023*.

[4]. Denis L, Bodard S, Hingot V, Chavignon A, Battaglia J, Renault G, Lager F, Abderrahmane A, Helenon O, Correas JM, Couture O, Sensing ultrasound localization microscopy for the visualization of glomeruli in living rats and humans, eBiomedicine, 91, 2023.

[5]. Chavignon A, Heiles B, Hingot V, Orset C, Vivien D, Couture O, 3D transcranial ultrasound localization microscopy in the rat brain with a multiplexed matrix probe. IEEE TBE, 69, 2021.

[6]. Heiles B, Chavignon A, Hingot V, Lopez P, Teston E, Couture O, ormance benchmarking of microbubble-localization algorithms for ultrasound localization microscopy. Nature BME, 6-5, 2022.

[7]. Hingot, V., Errico, C., Tanter, M., & Couture, O. Subwavelength motion-correction for ultrafast ultrasound localization microscopy. *Ultrasonics*, *77*, 17-21, 2017.

Single-bubble measurement of absolute drug loading on protein-conjugated microbubbles

Jocelyne Rivera[1,2], Luca Bau[1], Bradford J. Wood[2], Eleanor Stride[1]

[1]Institute of Biomedical Engineering, University of Oxford, Oxford, UK
[2]Center for Interventional Oncology, National Cancer Institute, Bethesda, Maryland, USA
Corresponding author: jocelynerivera@stcatz.ox.ac.uk

Introduction

Phospholipid-coated microbubbles are already clinically approved as ultrasound contrast agents and it has been shown that conjugating therapeutic proteins to microbubbles can able them to be used as delivery vehicles [1-3]. In order to investigate the effect of microbubbles as delivery agents, it is first necessary to accommodate a set of strict requirements: a therapeutic dose of antibody must be loaded on a tolerated and safe dose of microbubbles ($<10^9$ microbubbles/mouse). The development of such formulations can also involve complex manufacturing procedures, which require accurate assays for process development and quality control. An absolute measure of drug loading (weight of conjugated drug per dose of microbubbles), arguably one of the most important specifications in a target product profile, is particularly difficult to determine on microbubbles.

Absolute drug loading is typically either not reported, or measured after centrifugal separation of unbound drug from drug-loaded microbubbles. In most instances, the amount of conjugated drug is determined either indirectly by subtracting the unbound drug from the total or directly after dissolution of the purified microbubbles. Drug concentration has been measured by methods including HPLC[4], Bradford assay[3], bicinchonic acid assay[5] and fluorescence[6], all of which can suffer from lipid interference. Additionally, centrifugation can result in partial destruction of the microbubbles and therefore transfer of drug-conjugated lipids to the subnatant. In some cases, relative loading was measured by flow cytometry for the purpose of process optimisation [7, 8], but, to the best of our knowledge, absolute loading has never been determined.

In this work, we first investigate the extent to which centrifugation can affect absolute drug loading measurements using a fluorescent payload as a model drug and quantifying the loss of payload after each centrifugation cycle. We then describe an optimised protocol for the determination of absolute drug loading on antibody-loaded microbubbles by flow cytometry, which does not require sample processing steps such as centrifugation or bubble dissolution and provides single-bubble information including distribution of drug surface density.

Methods

Fabrication of microbubbles. A 2 mL freeze drying vial (Adelphi VCDIN2R) was charged with 1 mL of lipid suspension (0.8 mg/mL DPPC, 0.09 mg/mL DPPA, 0.6 mg/mL DPPE-PEG5K in PBS/glycerol/propylene glycol 8:1:1 v/v) and sealed. The headspace was filled with perfluorobutane by 4 vacuum/refill cycles. After cooling at 4°C, the vial was shaken for 45s in a VialMix. The vial was cooled at 4°C for 1 minute and 1 mL of microbubbles transferred into a syringe using an 18G needle with a 5 μm filter. Concentration and size distribution were measured in a Multisizer 4e Coulter counter (Beckmann Coulter, USA). For the flow cytometry experiments DPPE-PEG5K was entirely replaced by DPPE-PEG5K-maleimide, while for the centrifugation experiments 0.04 mg of DPPE-PEG5K were replaced by the same amount of DPPE-PEG5K-AF488.

Preparation of antibody-loaded bubbles. Cetuximab was fluorescently labeled with Alexa Fluor 647 NHS ester, purified by size exclusion in a Zeba spin column, and subsequently thiolated with Traut's reagent and purified again to obtain 5 mg/ml of antibody with a dye-to-antibody ratio and thiol-to-antibody of 1 (as

measured by Ellman's assay). The thiolated antibodies were immediately mixed with the microbubbles and reacted for 1 hr at room temperature.

Microbubble centrifugation study. Fluorescently labelled microbubbles (9 separate batches) were centrifuged 300 g for 5 min at 4 °C in a 3 mL plastic syringe (3 replicates per batch). After removal of the subnatant, the cake was resuspended. For the first cycle of centrifugation, cake and subnatant from three of the batches were mixed with an equal volume of isopropanol and sonicated, and their fluorescence emission measured in an Omega Fluostar plate reader. Of the remaining six batches, three were subjected to a second cycle and the other three to a second and a third cycle of centrifugation before dilution with isopropanol, sonication and fluorescence measurement.

Flow cytometry measurements. A BD LSRFortessa™ flow cytometer was used to count and analyse populations of fluorescent microbubbles. Flow cytometer parameters were optimized to accumulate 700,000 counts in less than 5 minutes. The flow cytometer was run at 35 μL/min until 700,000 events were recorded per measurement, with voltages of 200 V (FSC) and 200 V (SSC) and thresholds of 15000 (FSC) and 1000 (SSC). All samples were diluted to 1:100 with PBS immediately before analysis. The fluorescence signal was calibrated with Quantum™ MESF (molecules of equivalent soluble fluorochrome) 647 beads (Bangs Laboratories) suspended in 400 μL PBS according to the manufacturer's protocol.

FlowJo was used to analyze the flow cytometry data. A bubble gate was applied in the FSC-H vs SSC-H plane, followed by a singlet gate in the FSC-A vs FSC-H. The distribution of fluorescence signal in the R670_14.A channel was used to quantify the fluorophore on bubbles and calibration beads. The geometric mean fluorescent intensity (GMFI) for the calibration standards was estimated by fitting a mixture of gaussian distributions to the log-transformed fluorescence signal. The signal was then calibrated by fitting a linear regression to the log-transformed GMFI vs. log-transformed number of dye molecules (as provided by the manufacturer). The absolute drug loading on microbubbles (μg Ab/10^9 MB) was obtained from the arithmetic mean of the number of antibodies per bubble.

$$\text{Loading [μg Ab/}10^9\text{ MB]} = 10^{15} \frac{\sum_i^N n_{\text{Dye}_i}}{N \cdot DAR} \frac{MW_{\text{Ab}}}{N_{AV}}$$

where DAR is the dye-to-antibody ratio, N is the total number of events in the bubble gate, n_{Dye_i} is the number of dye molecules for each event (obtained from the calibration described above), MW_{Ab} is the molecular weight of the antibody and N_{AV} is Avogadro's number.

Results

The transfer of functionalised lipids onto microbubbles following amalgamation was first investigated. We found that less than 10% of PEGylated lipids were incorporated into microbubble shell following bubble formation (Figure 1), much lower than previously reported for DSPC/DSPE-PEG formulations [9]. Surprisingly, after two additional purification cycles, the fraction of PEGylated lipids did not increase over 20%. Moreover, large batch-to-batch and replicate-to-replicate variations were observed, suggesting that centrifugation-based methods can be prone to measurement artifacts due to microbubble destruction. To address this challenge, a direct characterisation method based on flow cytometry to selectively detect signal from microbubbles without further sample processing steps was developed. This direct characterisation method provides single-bubble measurements and therefore distribution of loading as well as average loading on a safe dose of bubbles. Additionally, dilution and lower scattering thresholds were required to remove negative bias on fluorescence due to high background signal. An antibody loading of 60 μg/10^9 MB was obtained for bubbles loaded by maleimide-thiol addition (Figure 2).
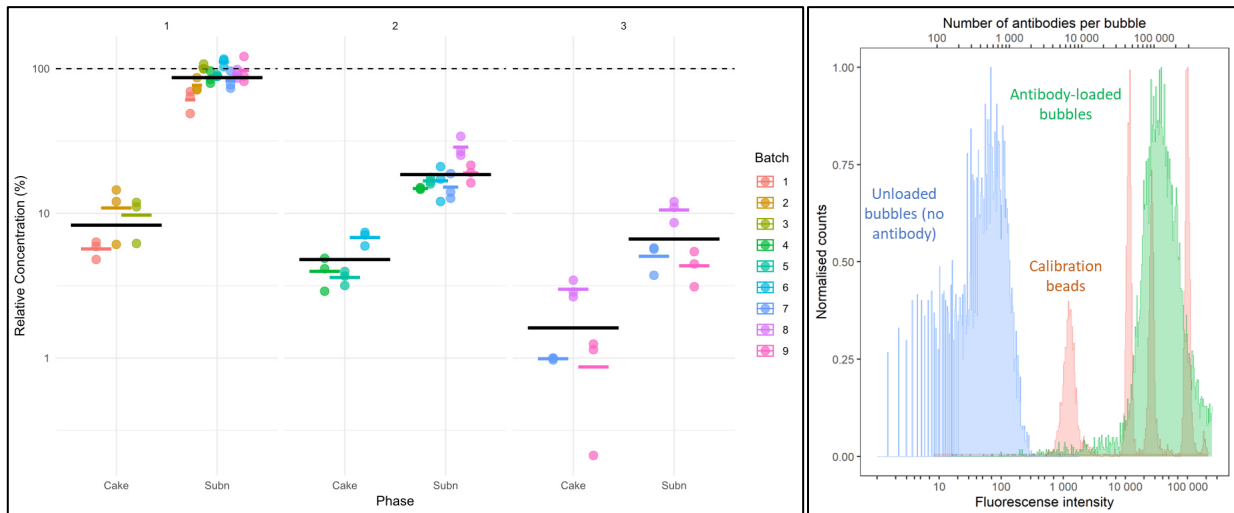
Figure 1. Fraction of PEGylated lipids on microbubble shell surface after each centrifugation phase (9 batches, 3 centrifugation steps).

Figure 2. Flow cytometry measurements on unloaded and antibody-loaded bubbles.

Conclusions

Adequate drug loading is a prerequisite of microbubble-based delivery systems. An accurate measurement of loaded dose is necessary to characterise the final pharmaceutical product, and highly desirable to guide process optimisation towards achieving a loading that is as close as possible to the theoretical maximum based on microbubble surface area. The development of reliable quality control protocols is therefore an important step towards the clinical translation of drug-loaded microbubbles. We showed that centrifugation-based methods are prone to measurement artifacts due to the destruction of microbubbles and describe a flow cytometry protocol for the determination of absolute drug loading on protein-conjugated microbubbles, which we believe will facilitate the development of these promising constructs.

References

[1]. Ma, Y., et al., Ultrasound targeting of microbubble-bound anti PD-L1 mAb to enhance anti-tumor effect of cisplatin in cervical cancer xenografts treatment. Life Sci, 2020. **262**: p. 118565.

[2]. Lustig, A., et al., Lipid Microbubble-Conjugated Anti-CD3 and Anti-CD28 Antibodies (Microbubble-Based Human T Cell Activator) Offer Superior Long-Term Expansion of Human Naive T Cells In Vitro. Immunohorizons, 2020. **4**(8): p. 475-484.

[3]. Yuan, H., et al., Ultrasound Microbubble Delivery Targeting Intraplaque Neovascularization Inhibits Atherosclerotic Plaque in an APOE-deficient Mouse Model. In Vivo, 2018. **32**(5): p. 1025-1032.

[4]. Li, T., et al., PD-L1-targeted microbubbles loaded with docetaxel produce a synergistic effect for the treatment of lung cancer under ultrasound irradiation. Biomater Sci, 2020. **8**(5): p. 1418-1430.

[5]. Kim, D., et al., PD-L1 Targeting Immune-Microbubble Complex Enhances Therapeutic Index in Murine Colon Cancer Models. Pharmaceuticals (Basel), 2020. **14**(1).

[6]. Bekeredjian, R., et al., Augmentation of cardiac protein delivery using ultrasound targeted microbubble destruction. Ultrasound Med Biol, 2005. **31**(5): p. 687-91.

[7]. Otani, K. and K. Yamahara, Development of antibody-carrying microbubbles based on clinically available ultrasound contrast agent for targeted molecular imaging: a preliminary chemical study. Mol Imaging Biol, 2011. **13**(2): p. 250-6.

[8]. Wang, X., et al., Novel single-chain antibody-targeted microbubbles for molecular ultrasound imaging of thrombosis: validation of a unique noninvasive method for rapid and sensitive detection of thrombi and monitoring of success or failure of thrombolysis in mice. Circulation, 2012. **125**(25): p. 3117-26.

[9]. Unnikrishnan, S., et al., Formation of Microbubbles for Targeted Ultrasound Contrast Imaging: Practical Translation Considerations. Langmuir, 2019. **35**(31): p. 10034-10041.

Shape Oscillation and Microstreaming Profile of a Phospholipid-coated Wall-attached Microbubble

Hongchen Li[1], Yuchen Wang[1], Ruisheng Su[2], Christian Cierpk[3], Michel Versluis[4], Antonius F. W. van der Steen[1], Martin D. Verweij[1,5], Nico de Jong[1,5], Klazina Kooiman[1]

[1]_Department of Biomedical Engineering, Erasmus MC, Rotterdam, the Netherlands_
[2]_Department of Radiology & Nuclear Medicine, Erasmus MC, Rotterdam, the Netherlands_
[3]_Institute of Thermodynamics and Fluid Mechanics, Technische Universität Ilmenau, Ilmenau, Germany_
[4]_Physics of Fluids Group, Techmed Centre, University of Twente, Enschede, the Netherlands_
[5]_Section of Medical Imaging, Department of Imaging Physics, Delft University of Technology, Delft, the Netherlands_
Corresponding author: h.li@erasmusmc.nl

Introduction

The intricate dynamics of microbubbles in response to ultrasound, encompassing shape oscillations and microstreaming, hold importance across various applications, ranging from surface cleaning to particle transport and interactions with tissues and/or bacteria [1-3]. Previous studies on microbubble shape oscillation and microstreaming [4-6] predominantly focused on uncoated air bubbles exceeding 10 μm in radius, utilizing kHz ultrasound, a condition not representative of clinical scenarios. However, shape oscillations in combination with microstreaming have not yet been investigated for clinically relevant microbubble sizes. This study therefore aimed to address the existing gap by investigating the shape oscillation and microstreaming profile of phospholipid-coated microbubbles attached to a wall under varying acoustic parameters.

Methods

Fig. 1a depicts the experimental configuration and Fig. 1b illustrates the experimental timeline. Two ultra-high-speed cameras (Shimadzu HPV-X2) were integrated with a custom-built upright Eclipse Ni-E microscope (Nikon Instruments, the Netherlands) set at $60\times$ magnification. The cameras operated at frame rates of 5 Mfps (Camera 1) and 10 kfps (Camera 2) to capture microbubble shape oscillation and cavitation microstreaming, respectively. A cylindrical lens was placed in front of Camera 2 to induce astigmatic aberration for astigmatic particle tracking velocimetry (APTV) [7,8]. Biotinylated DSPC-based microbubbles (radius: 3-8 μm) were generated through a microfluidic flow-focusing device and targeted to streptavidin-coated glass. Insonification was applied to each microbubble across an acoustic pressure range of 85-425 kPa at 25,000 cycles and $f_0 = 1.25$ MHz. The microbubble contour was tracked by image processing based on the gray value distribution using MATLAB. Subsequently, the contour underwent modal decomposition based on Legendre polynomials. The temporal changes in the amplitude of each surface mode were then extracted at frequencies f_0 and $f_0/2$. APTV [7,8] was used to measure the 3D trajectories of particles (500 nm, polymer beads, Thermo Scientific) from the 10 kfps camera recordings.
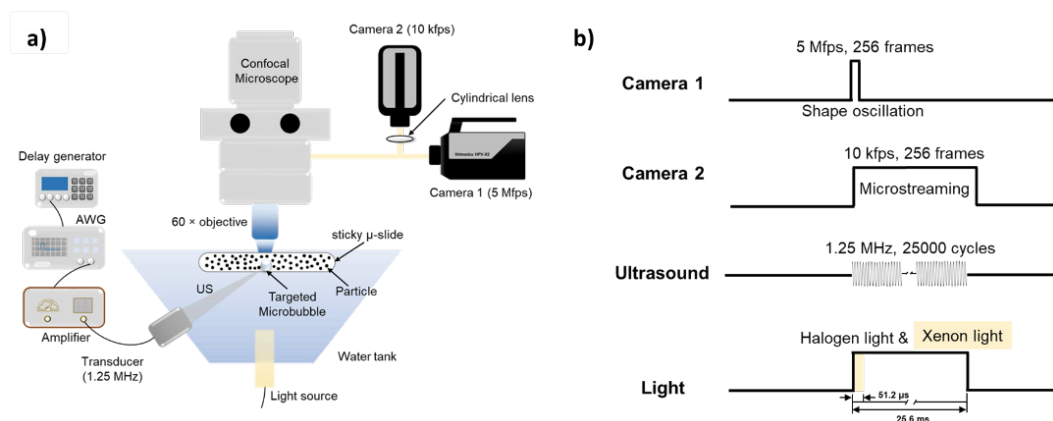
Figure 1. (a) Schematic representation of the experimental setup (not drawn to scale). (b) Corresponding experimental timelines.

Results

Fig. 2 illustrates two typical examples (from a total of 79 cases) of microbubble shape oscillation and their corresponding microstreaming profiles for microbubbles with radii of 5.12 μm and 4.35 μm, insonified at 425 kPa and 255 kPa, respectively.
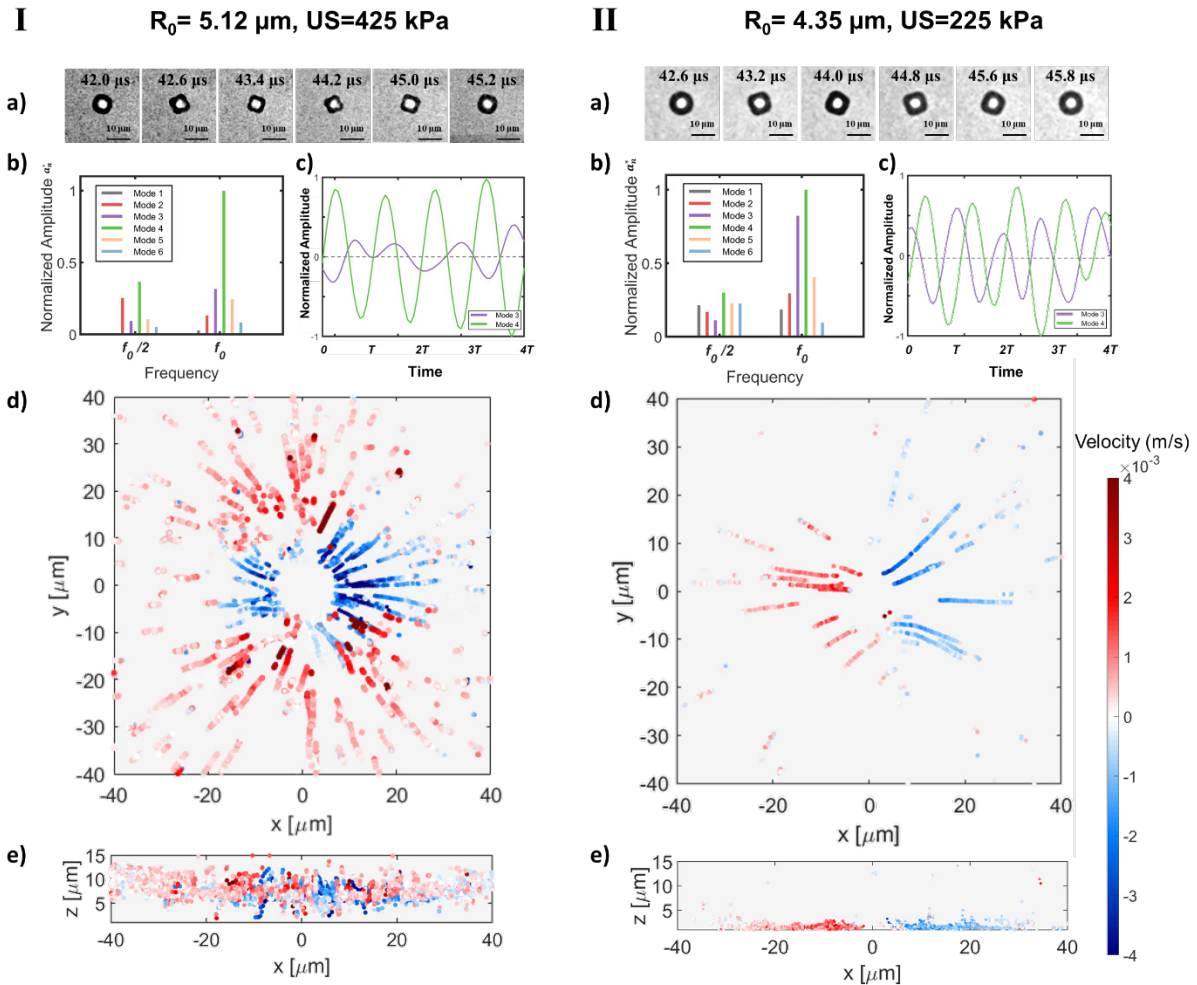
Figure 2. Two examples of microbubble shape oscillation and corresponding microstreaming profiles (I-II). For each example: (a) Selected frames of microbubble oscillation from four ultrasound cycles (0 to 4T). (b) Spectrum of the modal decomposition on the frequency of f0/2 and f0. (c) Temporal evolution of the normalized amplitude, emphasizing predominant shape oscillations, particularly modes 3 and 4. (d) The 2d projection of the microstreaming profile in the (x, y) plane with the streaming velocity indicated by colour. (e) The 2D projection of the microstreaming profile in the (x, z) plane.

In Fig. 2Ia and 2IIa, six selected frames of microbubble oscillation are shown from four ultrasound cycles. In both cases, the microbubbles become square (or cross) shape, i.e. exhibiting a 4th-order dominant shape oscillation. Figs. 2Ib and 2IIb further detail the normalized amplitude of 4th-order and other surface modes at half of the driven frequency $f_0/2$ and the driven frequency f_0. Notably, microbubble shape oscillations appeared after several cycles (4 to 40 cycles) of spherical oscillation, and gradually stabilized to a specific mix of different surface modes with possibly one dominating surface mode. In example I, mode 4 at f_0 dominates, displaying a quadrupole shape microstreaming pattern (Fig. 2Id) with a streaming velocity on the order of 10^{-3} m/s ($|v_{xy}| < 6.2 * 10^{-3}$ m/s). In example two, mode 4 at f_0 is prominent, while mode 3 at f_0 constitutes 80% of mode 4 at f_0, resulting in a dipole shape microstreaming pattern (Fig. 2IId) with a slightly lower streaming velocity ($|v_{xy}| < 2.5 * 10^{-3}$ m/s). In the streaming figures 2Id, 1Ie, 2IIb, and 2IIc, positive velocity values (in red) indicate flow moving away from the microbubble, while negative velocity values (in blue) indicate flow moving towards the microbubble. The information from Figs. 2Ib and 2Ic suggest that example I exhibits a strong self-interaction of mode 4 at f_0, leading to a quadrupole pattern [9]. Conversely, example II, due to a pronounced mix of mode 3 and mode 4 with a 3π/4

phase shift, displays a dipole pattern dominated by the interaction between surface mode 3 and mode 4 at f_0 [9]. Within the entire dataset (79 cases), 21 cases featured a dipole microstreaming pattern, while 18 cases displayed a quadrupole microstreaming pattern. Regarding microstreaming in the direction perpendicular to the wall (z direction), in example I, particles move to a higher z position near the microbubble center ($(x, y) = (0, 0)$), forming a volcano-shaped pattern (Fig. Ie), which indicates a gentle recirculation in the z direction ($v_z < 2.3 * 10^{-2}$ m/s). In contrast, in example II (Fig. IIe), the inwards and outwards flow around the microbubble is nearly in the same z plane, implying a weaker motion in the z direction ($v_z < 1.1 * 10^{-2}$ m/s).

Conclusions

In this study, we successfully conducted simultaneous monitoring of the shape oscillation and the corresponding 3D microstreaming patterns of phospholipid-coated microbubbles attached to a wall. Using ultra-high-speed microscopic imaging and astigmatic particle tracking velocimetry, we elucidated two distinct microstreaming patterns—namely, quadrupole and dipole patterns and we discussed the mechanism behind their formation. The distinct 3D characteristics of the microstreaming patterns will lead to different outcomes in mechanical impact. These insights enhance our understanding of microbubble behavior under ultrasound and also hold the promise of advancing the efficiency of microbubble-assisted ultrasound imaging and therapeutic applications based on additional control over microbubble oscillation.

References

[1]. Yamashita, Tatsuya & Ando, Keita. (2019). Low-intensity ultrasound induced cavitation and streaming in oxygen-supersaturated water: Role of cavitation bubbles as physical cleaning agents. Ultrasonics - Sonochemistry 52 (2019) 268–27.

[2]. Marmottant, P., Hilgenfeldt, S. Controlled vesicle deformation and lysis by single oscillating bubbles. (2003). Nature 423, 153–156 (2003).

[3]. Kooiman, K., S. Roovers, S.A.G. Langeveld, R.T. Kleven, H. Dewitte, M.A. O'Reilly, J.M. Escoffre, A. Bouakaz, M.D. Verweij, K. Hynynen, I. Lentacker, E. Stride, and C.K. Holland. (2020). Ultrasound-Responsive Cavitation Nuclei for Therapy and Drug Delivery. Ultrasound Med Biol, 2020. 46(6): p. 1296-1325.

[4]. Tho, P., Manasseh, R., & Ooi, A. (2007). Cavitation microstreaming patterns in single and multiple bubble systems. Journal of Fluid Mechanics, 576, 191-233.

[5]. Cleve, S., Guédra, M., Mauger, C., Inserra, C., & Blanc-Benon, P. (2019). Microstreaming induced by acoustically trapped, non-spherically oscillating microbubbles. Journal of Fluid Mechanics, 875, 597-621.

[6]. Fauconnier, M., Mauger, C., Béra, J., & Inserra, C. Nonspherical dynamics and microstreaming of a wall-attached microbubble. Journal of Fluid Mechanics, 935, A22.

[7]. Cierpka C, Hain R and Kahler C J. (2010). A simple single camera 3C3D velocity measurement technique without errors due to depth of correlation and spatial averaging for micro fluidics Meas. Sci. Technol. 21 045401.

[8]. Barnkob R., Kähler C. J., and Rossi M. (2015). General defocusing particle tracking, Lab Chip, 2015, 15, 3556-3560

[9]. Gabriel Regnault, Cyril Mauger, Philippe Blanc-Benon, Alexander A. Doinikov, Claude Inserra. (2021). Signatures of microstreaming patterns induced by non-spherically oscillating bubbles. J. Acoust. Soc. Am. 1 August 2021; 150 (2): 1188–1197.

Quantitative evaluation of anti-biofilm cavitation activity seeded from microbubbles or solid gas-stabilizing nuclei by passive acoustic mapping

Sara B. Keller[1], Gareth LuTheryn[2], Michael Gray[1], Brian Lyons[1], Robin Cleveland[1], Eleanor Stride[1,2], Constantin Coussios[1]

[1]*Institute of Biomedical Engineering, University of Oxford, Oxford, United Kingdom*
[2]*Nuffield Department of Orthopaedics, Rheumatology, and Musculoskeletal Sciences, University of Oxford, Oxford, United Kingdom*
*Corresponding author: sara.keller@eng.ox.ac.uk*

Introduction

Bacterial biofilms present a major challenge to achieving effective antibiotic therapy, as these sessile communities of microbes promote both physical and functional changes that protect bacteria from their environment. Because of this, bacteria within biofilms are known to be between 10-1000 times more resistant to antibiotics than their planktonic counterparts [1]. Focused ultrasound in combination with cavitation nuclei can mechanically disrupt biofilms, potentially offering a novel 'drug-free' antibiotic paradigm. The aim of this work was to evaluate the role of acoustic cavitation in the biofilm disruption process, through quantitative passive acoustic mapping (PAM) of cavitation activity using both microbubbles and a novel protein cavitation nuclei (PCaN). Two different pathogenic bacteria were evaluated: methicillin-resistant *Staphylococcus aureus* (MRSA) and *Pseudomonas aeruginosa* (PAO1), both of which are on the World Health Organization's priority list for new antibiotic research and development and are known to form robust biofilms. The outcome of this work could inform development of optimized cavitation-based antibiotic therapies that may be broadly applicable to a variety of bacterial species.

Methods

Two different strains representing Gram-positive and Gram-negative bacteria were evaluated as single-species biofilms: *S. aureus* isolated from osteomyelitis and *P. aeruginosa* (PAO1) isolated from a chronic wound. Bacteria were added to an Ibidi μ-Slide at an OD_{600} of 0.2 and then cultured for 48 hours to form a biofilm. The ultrasound exposure setup and acoustic field within the μ-Slide may be seen in Figure 1.
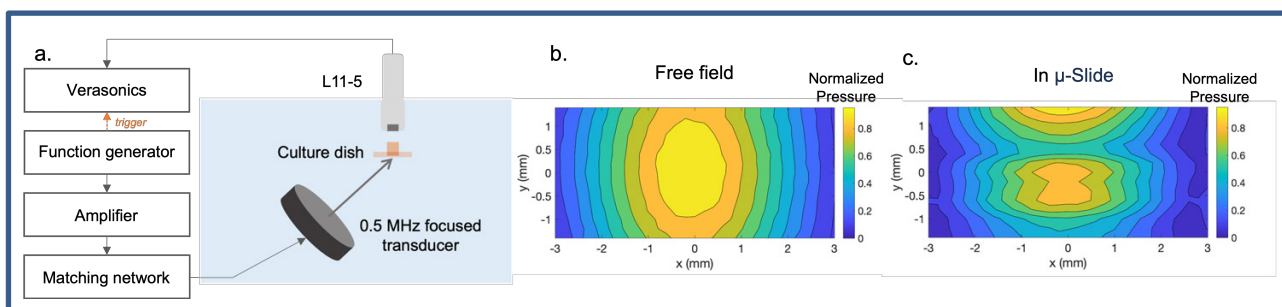
Figure 1. (a) Experimental setup of ultrasound exposure and cavitation detection through the Ibidi μ-Slide. (b) and (c) show the acoustic field in the free field and within the μ-Slide, respectively, both normalized to the maximum pressure in the free field.

Before ultrasound exposure, biofilms were live/dead stained with Syto 9 and propidium iodide and imaged with fluorescence microscopy. 1×10^8 microbubbles/mL diluted into sterile water, 1×10^{10} PCaN/mL diluted into sterile water, or sterile broth alone was added to the biofilms. Biofilms were placed into the water tank where they were exposed to 0.5-1.5 MPa peak rarefactional pressure (derated), 200 cycles, at a 5 Hz PRF for 30 seconds. To evaluate the effect of ultrasound without any added cavitation nuclei, just the highest pressure (1.5 MPa) was tested. Each scattered microbubble cavitation signal was

passively received by a calibrated L11-5 linear array located 28 mm above the biofilm for quantitative analysis of cavitation energy and spatial extent over time.

Calibrated pressure data were beamformed into PAM energy maps using Robust Capon Beamforming [2] after applying a 4 MHz high pass filter. Each transmit pulse resulted in one PAM image. To enable quantification of cavitation activity for each individual replicate, the sum of all pixels per frame was plotted against time, and the area under the curve was calculated [3]. This was used to correlate against reduction in biofilm coverage area. To get a map of the total accumulated cavitation energy in acoustic uJ experienced by the biofilm, all frames acquired were summed into a single PAM map. This was used to compare to the width of biofilm removal.

Results

An increase in transmit pressure/cavitation energy resulted in an increase in biofilm removal, seen both qualitatively and quantitatively (Fig. 2). A positive correlation was observed between cavitation energy and biofilm removal that could be fit to an exponential curve to describe the rate of biofilm destruction. There were slight differences observed between cavitation nuclei and between species which can be attributed to differences in cavitation activity, host-pathogen interactions, and biofilm morphology.
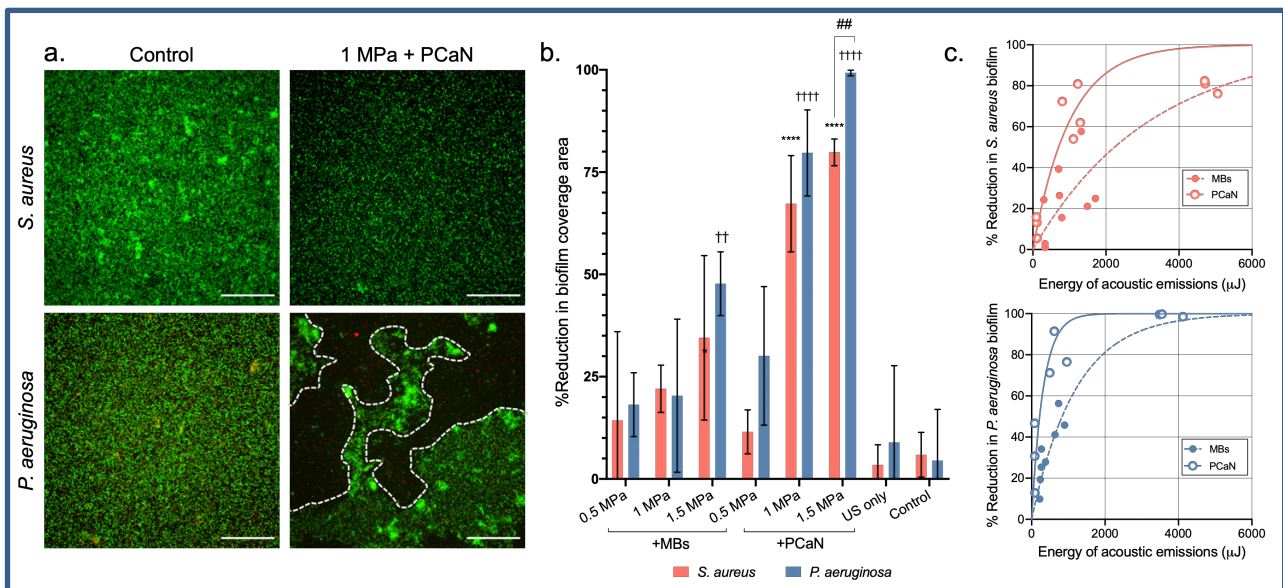
Figure 2. (a) representative microscopy images from control biofilms and biofilms exposed to 1 MPa ultrasound with PCaN (scale bars represent 100 μm). (b) reduction in biofilm presence determined with semi-quantitative image analysis. (c) Correlation between %biofilm reduction and energy of acoustic emissions in *S. aureus* and *P. aeruginosa* biofilms, respectively. **=difference between* S. aureus *experimental conditions and control, †=difference between* P. aeruginosa *experimental conditions and control, #=difference between S. aureus and P. aeruginosa conditions, p<0.05 indicates significance*

Examples of the comparison between PAM energy maps for two different ultrasound transmit conditions (1 MPa and 1.5 MPa with PCaN) and the resulting microscopy images of *P. aeruginosa* biofilms can be seen in Figure 3. The lateral PAM line at 28 mm (the location of the biofilm in the axial imaging plane) was compared with a smoothed image intensity profile through the central region of the microscopy image. The boundaries of the biofilm destruction area were used to identify the lowest accumulated PAM energies that still resulted in clearance, represented by the two vertical grey lines. The PAM energies were averaged to determine the lowest average cavitation energy for each condition that still resulted in biofilm removal. The minimum PAM energy required to remove bacteria remained consistent despite differences in exposure parameters.
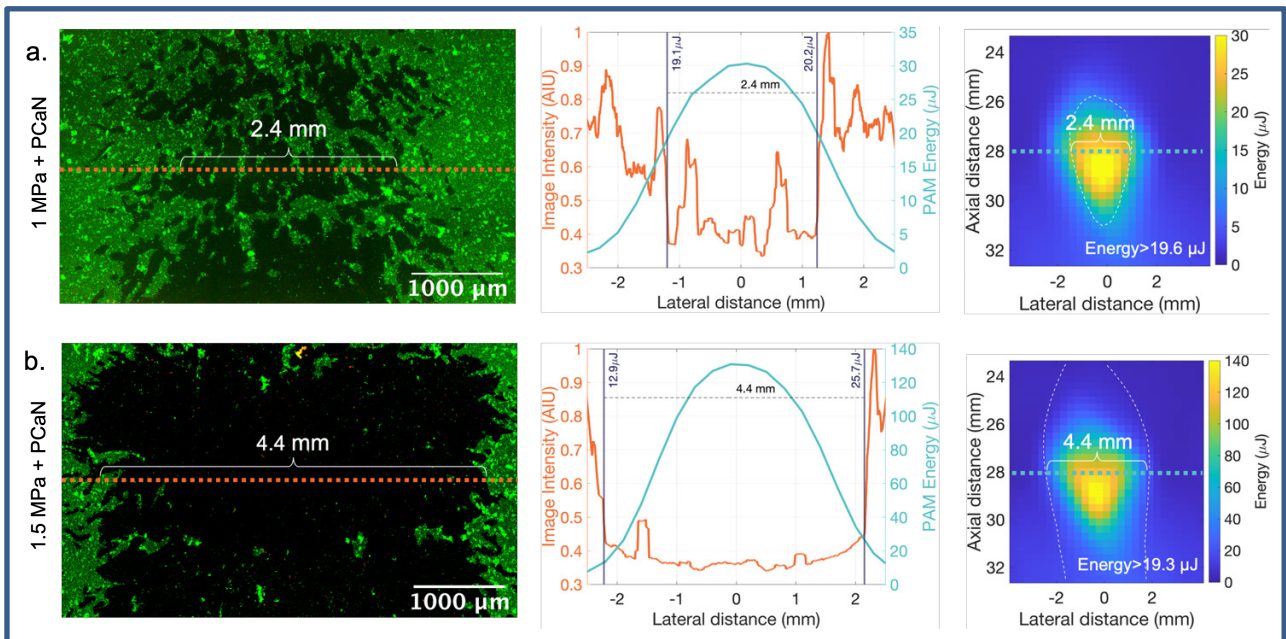
Figure 3. Large image scans of *P. aeruginosa* biofilm disruption at (a) 1 and (b) 1.5 MPa with PCaN compared to the summed PAM spatial energy for each pressure condition, respectively. The PAM energy corresponding to the width of the biofilm clearance zone is consistent between pressure settings

Conclusions

The goal of this work was to investigate the use of cavitation to eliminate biofilms of two priority pathogens, *Pseudomonas aeruginosa* and *Staphylococcus aureus*. We utilized passive acoustic mapping (PAM) to provide quantitative analysis of cavitation energy which we then correlated with reduction in biofilm presence and overall extent of biofilm destruction. We also compared two different cavitation agents, microbubbles as well as a solid protein cavitation nuclei. We found a positive correlation between cavitation dose and biofilm reduction in all cases except for using microbubbles on *S. aureus* biofilms, which we attribute to variations in biofilm morphology. Finally, the minimum PAM energy required to eliminate biofilms was consistent across transmit pressures and bacterial species. Cavitation-enhanced biofilm removal is a potentially promising form of antibiotic therapy.

References

[1]   D. Sharma, L. Misba, and A. U. Khan, "Antibiotics versus biofilm: an emerging battleground in microbial communities," *Antimicrobial Resistance & Infection Control 2019 8:1*, vol. 8, no. 1, pp. 1–10, May 2019, doi: 10.1186/S13756-019-0533-3.

[2]   C. Coviello *et al.*, "Passive acoustic mapping utilizing optimal beamforming in ultrasound therapy monitoring," *J Acoust Soc Am*, vol. 137, no. 5, pp. 2573–2585, May 2015, doi: 10.1121/1.4916694.

[3]   C. A. B. Smith and C. C. Coussios, "Spatiotemporal Assessment of the Cellular Safety of Cavitation-Based Therapies by Passive Acoustic Mapping," *Ultrasound Med Biol*, vol. 46, no. 5, pp. 1235–1243, May 2020, doi: 10.1016/J.ULTRASMEDBIO.2020.01.009.

Shell characterization of single microbubbles using a novel stress-strain analysis

Charlotte Nawijn[1], Sander Spiekhout[2], Jason Voorneveld[2], Hans Bosch[2], Michel Versluis[1], Tim Segers[3], and Guillaume Lajoinie[1]

[1]*Physics of Fluids Group, Technical Medical (TechMed) Center, University of Twente, The Netherlands*
[2]*Department of Biomedical Engineering, Thorax Center, Erasmus MC University Medical Center, Rotterdam, the Netherlands*
[3]*BIOS Lab-on-a-Chip group, Max-Planck Center Twente for Complex Fluid Dynamics, MESA+ Institute for Nanotechnology, University of Twente, The Netherlands*
Corresponding author: c.l.nawijn@utwente.nl

Introduction

Microbubbles are of great interest for ultrasound imaging, both for diagnosis as contrast agents, and for ultrasound therapy to locally deliver drugs or genes or to employ a mechanical stress to cells to induce sonoporation. A full characterization of the nonlinear response of microbubbles to ultrasound is crucial to fully exploit the specific features of these bubbles. The most interesting feature resides in nonlinear scattering, which is heavily enhanced by the viscoelastic shell, especially at low driving amplitudes [1]. While acoustic attenuation measurements can be used to characterize bubble populations at low acoustic pressure, these need to be performed on an ensemble of microbubbles, and thus high-precision characterization is only possible by using monodisperse bubbles [2, 3]. In contrast, single microbubbles can be characterized using ultra-high-speed optical imaging [4], but this requires relatively large oscillation amplitudes (~100 nm), and measurements in the free-field are very challenging [5].

Here, we propose a novel method to characterize the viscoelastic shell properties of single microbubbles measured with high-frequency scattering in an 'acoustical camera' setup [6, 7]. Detailed knowledge of the acoustic driving pressure and frequency combined with a precise measurement of the resulting strain and strain rate of the bubble interface allows us to derive the elastic and viscous properties of single microbubbles. This approach does not require any a priori knowledge on the constitutive laws of the monolayer shell. In addition to providing detailed information of single bubble dynamics, it also opens new possibilities to unravel the dissipation mechanisms within the interface as a function of strain and strain rate.

Methods

The elastic and viscous pressure contributions of the bubble surface can be equated to the contributions of inertia, gas thermodynamic behavior, sound re-radiation, atmospheric pressure, and incident acoustic pressure by reorganizing the Keller-Miksis equation [1]:

$$f = -\rho_L\left(R\ddot{R} + \frac{3}{2}\dot{R}\right) + \left(P_0 + \frac{2\sigma(R_0)}{R_0}\right)\left(\frac{R_0}{R}\right)^{3\kappa}\left(1 - \frac{3\kappa}{c_L}\dot{R}\right) - P_0 - P_{ac}, \qquad (1)$$

with $R = R(t)$ the bubble radius, $\dot{R}$ and $\ddot{R}$ its time derivatives, R_0 the initial radius, $\sigma(R_0)$ the initial surface tension, ρ_L the density of the medium, κ the polytropic exponent of the gas, c_L the speed of sound in the medium, P_0 the atmospheric pressure, and P_{ac} the incident acoustic pressure. In general terms, f can be written as:

$$f = f_{elas} + g_{visc}\dot{R}. \qquad (2)$$

Through nondimensionalization, the viscous and elastic pressure contributions can be written as a function of the radial strain $dR = (R(t) - R_0)/R_0$, and its time derivative. The elastic contribution is independent of the strain rate and can thus be determined from the nondimensionalized function $\tilde{f}$ at $d\dot{R} = 0$, where all viscous terms (due to the viscosity of the shell and of the medium) disappear. From the elastic contribution we determine the surface tension as a function of dR. The remainder of $\tilde{f}$ after subtraction of the elastic contribution then constitutes the viscous contribution.

To validate this novel approach, we characterize $\tilde{f}$ for a single microbubble as a function of dR and $d\dot{R}$. The incident acoustic pressure is ramped up and down (over 2×100 µs), while we measure the radial strain and strain rate with an 'acoustical camera' [6, 7], see Fig. 1A. Briefly, the bubbles are suspended in a tank where they are insonified at a frequency of 1.9 MHz transmitted by a low-frequency transducer (LF). Single-bubble strain is measured by a high-frequency transducer (HF2) through geometrical scattering of a 25 MHz ultrasound wave transmitted by another high-frequency transducer (HF1) [7]. We use lipid-shelled (DSPC mixed with DPPE-PEG5k, 9:1 molar ratio) monodisperse C_4F_{10}-filled microbubbles, made in-house using a flow-focusing device [8, 9]. The bubbles had a radius of 2.2 ± 0.27 µm.

From the single-bubble strain, the surface tension as a function of bubble radius is recovered by applying an error minimization routine on 4 parameters: the initial radius R_0, the initial surface tension $\sigma(R_0)$, the time of flight of the ultrasound to the exact bubble location, and the pressure amplitude within calibration margins.

Results

The total viscoelastic pressure contribution f as a function of the strain and strain rate of a single microbubble is shown in Fig. 1B. Starting at $[dR, d\dot{R}] = [0, 0]$, the hyperplane is travelled in successively larger spirals as the driving pressure increases. A typical surface tension curve extracted for a single bubble is shown Fig. 1C. The orange dashed line depicts the surface tension curve measured experimentally for a monodisperse bubble suspension, with a similar formulation (DPPC:DPPE-PEG5k, 9:1 molar ratio) and with the same mean size [3]. Good agreement is found between our single-bubble results and the curves measured on the monodisperse suspension. The median surface tension curve obtained from 64 bubbles is shown in Fig. 1D, where the shaded region indicates the standard deviation. The shell elasticity (0.6 N/m) matched the one from the attenuation experiments [3]. The waist of the curve at $dR = 0$ provides the distribution in initial surface tension: $\sigma(R_0) = 29 \pm 5.6$ mN/m. The size distribution determined through error minimization ($R_0 = 2.1 \pm 0.18$ µm) also has an excellent match with Coulter Counter measurements (data not shown here).
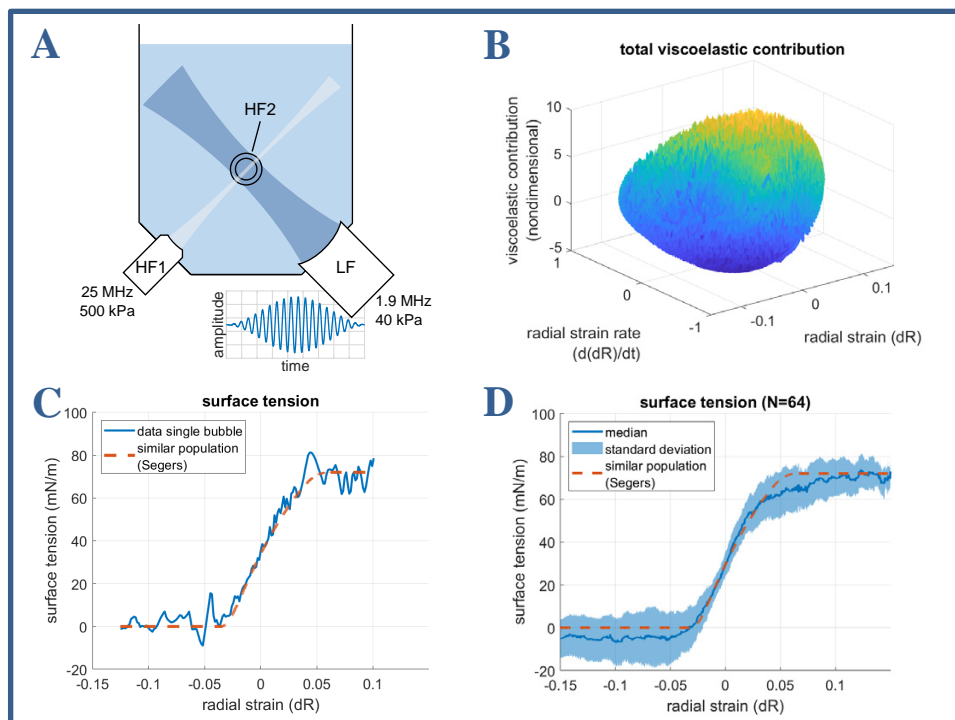
Figure 1. A) Schematic of the acoustical camera, with its low-frequency (LF) and high-frequency (HF) transducers. B) Viscoelastic pressure contribution of a single microbubble as a function of strain and strain rate. C) Strain-dependent surface tension extracted from panel B. The orange dashed line shows the surface tension curve measured for an ensemble of monodisperse microbubbles by Segers et al. [3]. D) Median surface tension curve (64 bubbles). The orange dashed line again shows the measurement from Segers et al. [3].

Conclusions

The combined viscoelastic pressure contribution of lipid-shelled microbubbles is determined from the radial strain of single microbubbles recorded by an acoustical camera. The elastic contribution, obtained at zero strain rate, provides the surface tension as a function of the bubble radius. The measured surface tension is in good agreement with earlier measurements on a monodisperse bubble population, for small radial amplitude oscillations. The stress-strain analysis and error minimization also provide statistics on the size and the initial surface tension of single microbubbles. Future work will investigate the dependence of the viscous contribution of the shell on the strain and strain rate.

References

[1]. M. Versluis, E. Stride, G. Lajoinie, B. Dollet, and T. Segers, "Ultrasound Contrast Agent Modeling: A Review", Ultrasound in Medicine & Biology, 46.9: 2117-2144, 2020.

[2]. M. A. Parrales, J. M. Fernandez, M. Perez-Saborid, J. A. Kopechek, and T. M. Porter, "Acoustic characterization of monodisperse lipid-coated microbubbles: Relationship between size and shell viscoelastic properties", The Journal of the Acoustical Society of America, 136.3: 1077-1084, 2014.

[3]. T. Segers, E. Gaud, M. Versluis, and P. Frinking, "High-precision acoustic measurements of the nonlinear dilatational elasticity of phospholipid coated monodisperse microbubbles", Soft Matter, 14.47: 9550-9561, 2018.

[4]. M. Overvelde, V. Garbin, J. Sijl, B. Dollet, N. de Jong, D. Lohse, and M. Versluis, "Nonlinear shell behavior of phospholipid-coated microbubbles", Ultrasound in Medicine & Biology, 36.12: 2080-2092, 2010.

[5]. V. Garbin, D. Cojoc, E. Ferrari, R. Z. Proietti, S. Cabrini, and E. Di Fabrizio, "Optical micro-manipulation using Laguerre-Gaussian beams", Japanese Journal of Applied Physics, 44.7S: 5773, 2005.

[6]. G. Renaud, J. G. Bosch, A. F. W. Van Der Steen, and N. De Jong, "Low-Amplitude Non-linear Volume Vibrations of Single Microbubbles Measured with an 'Acoustical Camera'", Ultrasound in Medicine & Biology, 40.6: 1282–1295, 2014.

[7]. S. Spiekhout, J. Voorneveld, B. van Elburg, G. Renaud, T. Segers, G. Lajoinie, M. Versluis, M. D. Verweij, N. de Jong, and J. G. Bosch, "Time-resolved absolute radius estimation of vibrating contrast microbubbles using an acoustical camera", The Journal of the Acoustical Society of America, 151.6: 3993-4003, 2022.

[8]. T. Segers, A. Lassus, P. Bussat, E. Gaud, and P. Frinking, "Improved coalescence stability of monodisperse phospholipid-coated microbubbles formed by flow-focusing at elevated temperatures," Lab on a Chip, 19.1: 158-167, 2019.

[9]. T. Segers, E. Gaud, G. Casqueiro, A. Lassus, M. Versluis, and P. Frinking, "Foam-free monodisperse lipid-coated ultrasound contrast agent synthesis by flow-focusing through multi-gas-component microbubble stabilization", Applied Physics Letters, 116.17: 173701, 2020.

Characterisation of Gas Vesicles as Cavitation Nuclei for Ultrasound Therapy using Passive Acoustic Mapping and High-Speed Optical Imaging

Cameron A. B. Smith[1], Avinoam Bar-Zion[1], Qiang Wu[2], Luca Bau[2], Eleanor Stride[2], Mikhail G. Shapiro,[1,3,4] and Constantin C. Coussios[2)]

[1]*Division of Chemistry and Chemical Engineering, California Institute of Technology, Pasadena, California, USA*
[2]*Department of Engineering Science, University of Oxford, Oxford, UK*
[3]*Andrew and Peggy Cherng Department of Medical Engineering, California Institute of Technology, Pasadena, California, USA*
[4]*Howard Hughes Medical Institute, California Institute of Technology, Pasadena, California, USA*
Corresponding author: csmith3@caltech.edu

Introduction

Gas Vesicles (GVs) are protein-shelled gas-filled particles[1] that can be expressed by genetically engineered bacteria[2] and mammalian[3,4] cells. They have been investigated as contrast agents for high frequency[5] ultrasound imaging with encouraging results[6] and excitingly it has also been shown that GV-producing cells are capable of infiltrating the cores of tumours[7]. Since these cells can also be engineered such that they only produce GVs under certain conditions[8,9] they offer a high degree of molecular specificity, as well as enabling GVs to populate regions of tumours which are traditionally the hardest to reach with conventional cavitation nuclei[4,10]. They thus could be of great potential value as agents for ultrasound therapy. An initial study exploring their use as nuclei for mechanical ablation has shown promise[10]. In this work we conduct a thorough characterization of the cavitation dynamics of GVs to inform their further development as potential therapeutic agents.

Methods

For cavitation mapping, the experimental set-up was comprised of a single therapeutic transducer that could be driven at either 0.5 or 1.6 MHz. GVs were suspended in 0.5 ml of water in 2 ml Eppendorf tubes positioned at the transducer focus. Acoustic emissions were received using two perpendicular co-planar L7-4 linear arrays which were calibrated using a wire scatterer[11]. These signals were recorded using a programmable ultrasound engine (Vantage 256, Verasonics) and then beamformed using the RCB-PAM algorithm[12] in a 10 mm lateral by 15 mm axial region of interest, with a pixel size of 0.4 mm square, $\varepsilon = 5$.

For high-speed optical imaging the set-up was modified so that the GVs were injected into a polyethylene tube of 180 μm inner diameter and 10 μm wall thickness (Advanced Polymers, Salem NH, USA). An 40X objective lens with a numerical aperture of 0.8 and working distance 3 mm (LUMPLFLN 40XW Olympus) was focused on the mid-plane of the tube and coupled to a high-speed camera (HPV-X2, Shimadzu, Tokyo, Japan). Illumination was provided by a high intensity light source (480 nm, SOLIS-1C, Solis® High-Power LEDs, Thorlabs LTD. Ely, United Kingdom). Bubble oscillations were captured imaging at 1, 5 or 10 million frames per second for a range of different GV concentrations and peak negative pressures.

Results

First, we investigated the persistence of cavitation. Emissions could be detected throughout the entire duration of the first ultrasonic pulse of up to 5000 cycles. However, the emissions produced by exposure to subsequent pulses were greatly diminished, with very little cavitation detectable after 4 pulses. This was found to be true over the range of pressures tested, down to 200 kPa. The effect of peak negative driving pressure on the harmonic-broadband transition of the GV's was also explored at 0.5 and 1.6 MHz. A sharp threshold was discovered at low sample volumes both in terms of applied acoustic pressure and GV concentration. To gain a better understanding of the GV behavior, spectrograms of the received acoustic signals were compared to Keller-Miksis models (Figure 1). These results suggested that the cavitation emissions received came not from individual GVs but instead from larger bubbles formed by the coalescence of gas released by the GVs.

This hypothesis motivated the high-speed imaging experiments, the results of which confirmed the existence of a delay between GV destruction, which occurred at the arrival of the therapeutic pulse, and the generation and collapse of large bubbles formed by coalescence, which were responsible for the acoustic emissions (Figure 2).

Conclusions

From the combined simulations and experimental evidence, it appears that the acoustic emissions detected from GVs under therapeutic ultrasound exposure conditions come not from individual GVs but instead from bubbles formed by the coalescence of gas released from collapsed GVs. These results provide mechanistic insight into how GVs are capable of acting as cavitation nuclei, though their irreversible collapse and gas release will require careful selection of the pulsing regime to achieve the required biological effect.
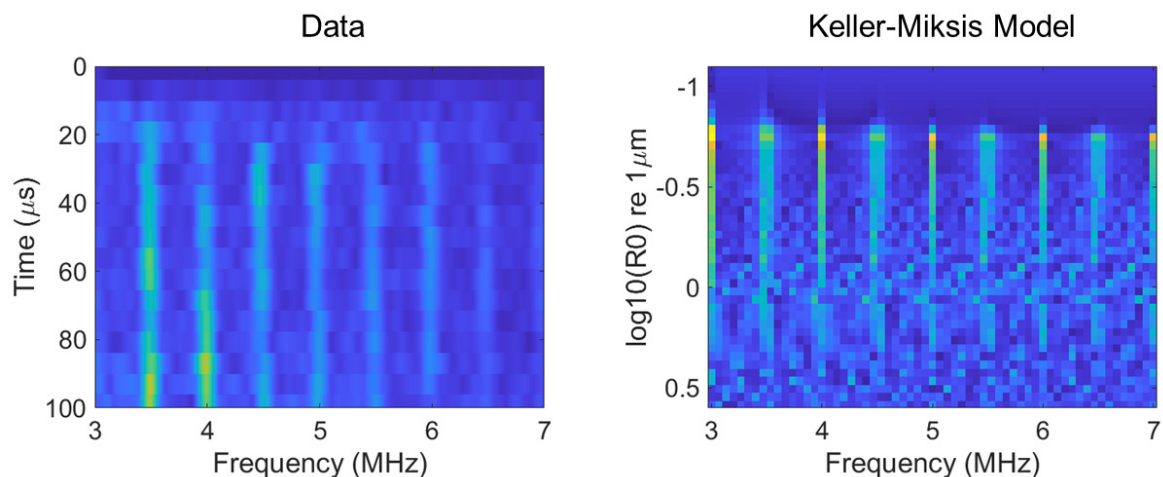
Figure 1: (Left) Average spectrogram (n=5) showing the frequency distribution of cavitation emissions over the pulse duration for 0.5 MHz and 1.4x10^{10} particles per ml concentration, cropped to more clearly show the cavitation emissions during the first 50 transmitted cycles, Time = 0 corresponds to the timepoint at which cavitation emissions are expected to be received from the center of the Eppendorf. **(Right)** the results for a Keller-Miksis bubble simulation showing the frequency distribution of cavitation emissions at a range of bubble resting sizes (R0) with the same ultrasound parameters as in the experimental dataset.
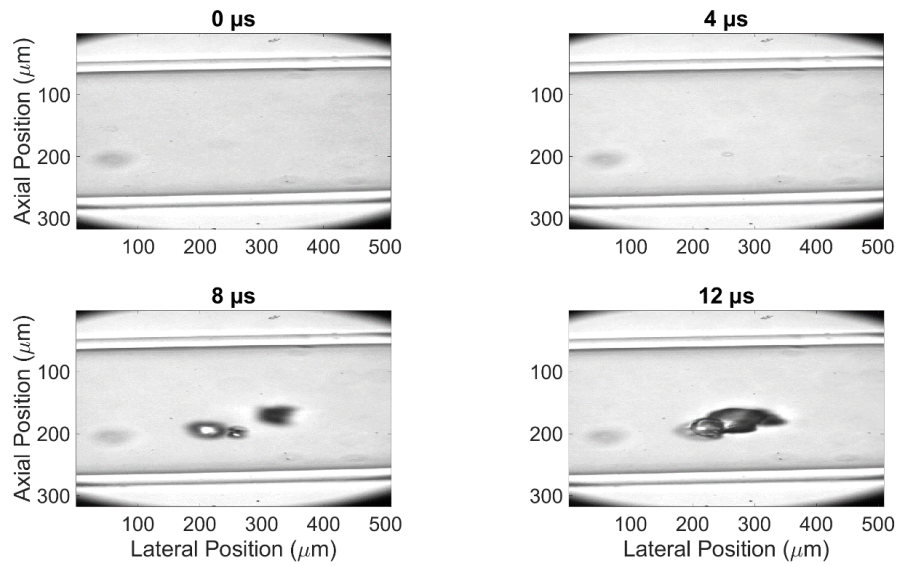
Figure 2: **Frames from a high-speed camera acquisition showing the destruction of sub-micrometer gas vesicles at the arrival of the therapeutic pulse (0 - 4 μs) and the subsequent coalescence and cavitation of larger bubbles (4 – 12 μs).**

References

[1]. G.J. Lu, A. Farhadi, A. Mukherjee, and M.G. Shapiro, "Proteins, air and water: reporter genes for ultrasound and magnetic resonance imaging," Current Opinion in Chemical Biology **45**, 57–63 (2018).

[2]. M.G. Shapiro, P.W. Goodwill, A. Neogy, M. Yin, F.S. Foster, D.V. Schaffer, and S.M. Conolly, "Biogenic gas nanostructures as ultrasonic molecular reporters," Nature Nanotechnology **9**(4), 311–316 (2014).

[3]. R.W. Bourdeau, A. Lee-Gosselin, A. Lakshmanan, A. Farhadi, S.R. Kumar, S.P. Nety, and M.G. Shapiro, "Acoustic reporter genes for noninvasive imaging of microorganisms in mammalian hosts," Nature **553**(7686), 86–90 (2018).

[4]. R.C. Hurt, M.T. Buss, M. Duan, K. Wong, M.Y. You, D.P. Sawyer, M.B. Swift, P. Dutka, P. Barturen-Larrea, D.R. Mittelstein, Z. Jin, M.H. Abedi, A. Farhadi, R. Deshpande, and M.G. Shapiro, "Genomically mined acoustic reporter genes for real-time in vivo monitoring of tumors and tumor-homing bacteria," Nat Biotechnol, 1–13 (2023).

[5]. E. Cherin, J.M. Melis, R.W. Bourdeau, M. Yin, D.M. Kochmann, F.S. Foster, and M.G. Shapiro, "Acoustic Behavior of Halobacterium salinarum Gas Vesicles in the High-Frequency Range: Experiments and Modeling," Ultrasound in Medicine and Biology **43**(5), 1016–1030 (2017).

[6]. Y. Yang, Z. Qiu, C. Liu, Y. Huang, L. Sun, and J. Dai, "Acoustic characterization of nano gas vesicles," 2015 IEEE International Ultrasonics Symposium, IUS 2015, 1–4 (2015).

[7]. A. Bar-Zion, A. Nourmahnad, D. Mittelstein, S. Yoo, D. Malounda, M. Abedi, A. Lee-Gosselin, D. Maresca, and M. Shapiro, "Acoustically Detonated Biomolecules for Genetically Encodable Inertial Cavitation," bioRxiv, 620567 (2019).

[8]. D.P. Sawyer, A. Bar-Zion, A. Farhadi, S. Shivaei, B. Ling, A. Lee-Gosselin, and M.G. Shapiro, "Ultrasensitive ultrasound imaging of gene expression with signal unmixing," Nature Methods **18**(8), 945–952 (2021).

[9]. A. Lakshmanan, Z. Jin, S.P. Nety, D.P. Sawyer, A. Lee-Gosselin, D. Malounda, M.B. Swift, D. Maresca, and M.G. Shapiro, "Acoustic biosensors for ultrasound imaging of enzyme activity," Nature Chemical Biology **16**(9), 988–996 (2020).

[10]. A. Bar-Zion, A. Nourmahnad, D.R. Mittelstein, S. Shivaei, S. Yoo, M.T. Buss, R.C. Hurt, D. Malounda, M.H. Abedi, A. Lee-Gosselin, M.B. Swift, D. Maresca, and M.G. Shapiro, "Acoustically triggered mechanotherapy using genetically encoded gas vesicles," Nature Nanotechnology **33**, (2021).

[11]. M.D. Gray, and C.C. Coussios, "Broadband Ultrasonic Attenuation Estimation and Compensation With Passive Acoustic Mapping," 497–516 (2018).

[12]. C. Coviello, R. Kozick, J. Choi, M. Gyöngy, C. Jensen, P.P. Smith, and C.-C. Coussios, "Passive acoustic mapping utilizing optimal beamforming in ultrasound therapy monitoring.," The Journal of the Acoustical Society of America **137**(5), 2573 (2015).

Left ventricular vector flow imaging: in vivo comparison of echoPIV against 4D flow MRI

Yichuang Han[1], Daniel J. Bowen [1], Bernardo Loff Barreto [1], Robert. R. Zwaan [1],
Mihai Strachinaru[2,1], Rob J. van der Geest [4], Alexander Hirsch [1,3],
Annemien E. van den Bosch [1], Johan G. Bosch [1] and Jason Voorneveld [1]

[1]*Department of Cardiology, Cardiovascular Institute, Thorax Center, Erasmus MC, Rotterdam, the Netherlands*
[2]*Department of Cardiology, Brussels University Hospital - Erasme Hospital, Brussels, Belgium*
[3]*Department of Radiology and Nuclear Medicine, Erasmus MC, Rotterdam, the Netherlands*
[4]*Department of Radiology, Leiden University Medical Center, Leiden, the Netherlands*

Corresponding author: y.han@erasmusmc.nl

Introduction

Accurately measuring blood flow patterns in the heart could provide insights in the pathophysiology of cardiac disease, and may provide additional diagnostic and prognostic information. At present, 4D flow MRI is considered the gold standard of intracardiac flow imaging. EchoPIV is a more recent technique that uses high frame rate contrast enhanced ultrasound imaging to quantify blood flow patterns. This study aimed to assess the agreement between echoPIV and 4D flow MRI for in vivo intracardiac flow imaging.

Methods

This study evaluated 26 patients referred for a cardiac MRI. 4D flow MRI was acquired for each patient as a reference. We acquired 2-angle pulse inversion sequences (P4-1 probe, Vantage 256 Verasonics) during SonoVue infusion (1ml/min). Registration between the two modalities was done manually using landmarks (mitral annulus and apex) in the three standard views (apical 2-, 3-, and 4-chamber) and a rigid transformation. We compared the results of both modalities for various cardiac flow parameters, including flow velocity, flux, kinetic energy, and rate of energy loss.

Results

For the acquisitions with sufficient Bmode image quality and sufficiently aligned plane with MRI, we observed good correspondence between echoPIV and MRI regarding spatial flow patterns and derived flow parameters. The velocity profile at the base level (mitral valve) had cosine similarity of 0.92 ± 0.06 and normalized mean absolute error of 0.14 ± 0.05. The kinetic energy and rate of energy loss also showed a high level of cosine similarity (0.89 ± 0.10 and 0.91 ± 0.06) with normalized mean absolute error of 0.25 ± 0.10 and 0.52 ± 0.15.

Conclusions

With sufficient-quality B-mode imaging, echoPIV proves to be an effective method for estimating left ventricular flow, offering spatial-temporal velocity distributions similar to those obtained with 4D flow

MRI. Each modality has its strengths and weaknesses. EchoPIV has the ability to capture inter-beat variability and fine flow details in the apex, whereas MRI is not limited by patient BMI and poor acoustic windows.
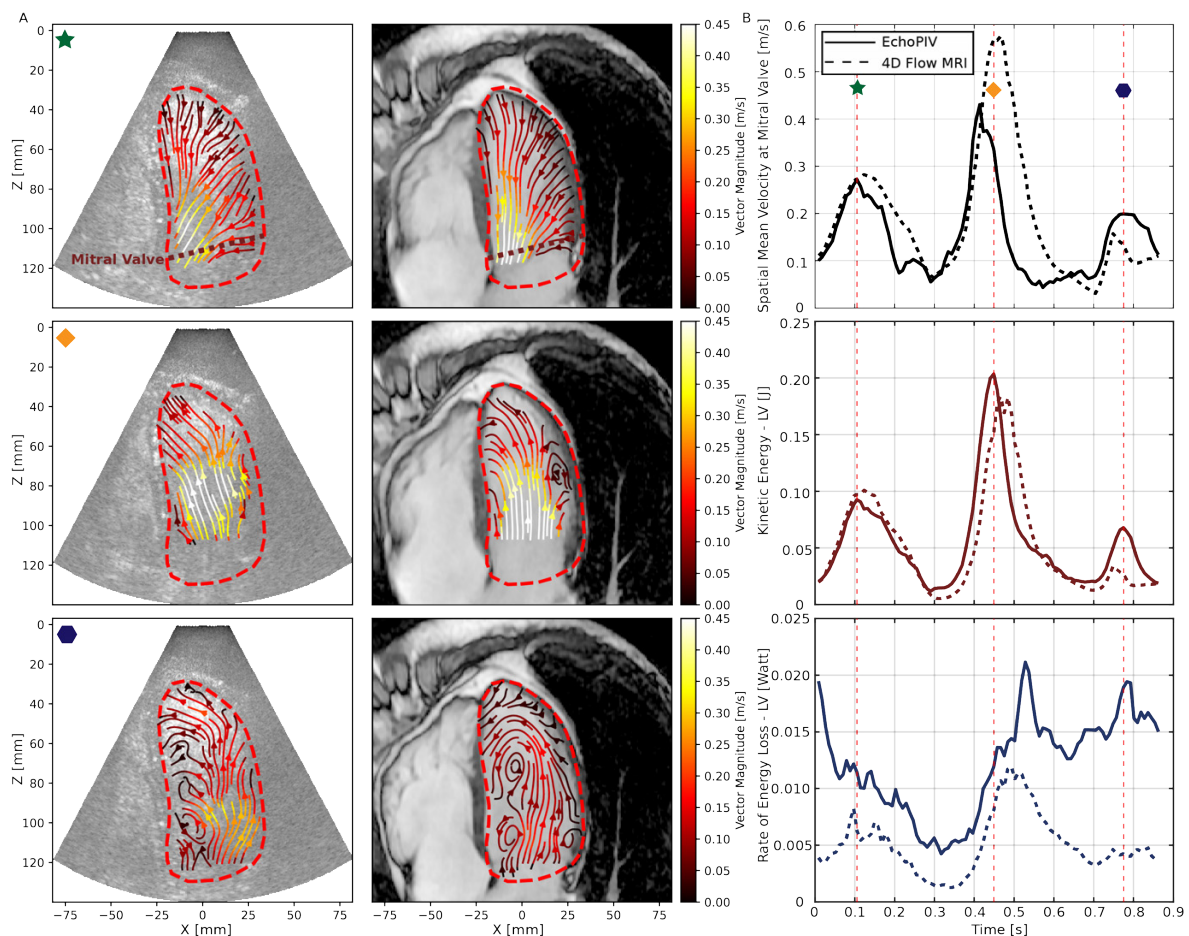
Acknowledgement

Figure 1. (A) Flow streamlines of EchoPIV (left) and MRI (right) at $t = 105ms$ (ejection phase), $t = 449ms$ (early filling) and $t = 775ms$ (late filling). (B) Spatial mean velocity at the level of mitral valve and derived flow parameters (kinetic energy, rate of energy loss) of the full left ventricle for echoPIV (solid) and MRI (dash)

Ultrasound Velocimetry of Blood Flow in a Helical Stent *In vivo*

Ashkan Ghanbarzadeh-Dagheyan[1,2], Majorie van Helvert[1,3]. Michel M.P.J. Reijnen[1,3], Michel Versluis[2], Erik Groot Jebbink[1,3]

[1]*Multi-Modality Medical Imaging (M3i), University of Twente, Enschede, The Netherlands*
[2]*Physics of Fluid (PoF), University of Twente, Enschede, The Netherlands*
[3]*Department of Vascular Surgery, Rijnstate Hospital, Arnhem, The Netherlands*
Corresponding author: a.dagheyan@utwente.nl

Introduction

3D helical stents have been developed for the treatment of peripheral arterial disease (PAD) in the lower limb to induce swirling flow in the stented arteries. Early results show better outcomes when compared to straight stents [1]. Straight stents, due to their geometry, disrupt the native swirling flow that exists in the arteries; thus, it is hypothesized that the helical shape of these new stents restores part of the native swirling flow. This could enhance arterial wall shear stress and improve treatment outcomes. In a previous study *in vitro*, we used contrast-enhanced ultrasound (CEUS) velocimetry (echoPIV) to characterize flow in the inlet and outlet of a helical stent model [2]. We showed that in comparison with the inlet, the flow in the outlet of the helical stent is more complex and the velocity profile is more skewed, two signatures of a swirling flow. In this study, we report flow characterization inside a helical stent *in vivo*, in a patient who had received the stent.

Methods

This retrospective study was approved by the ethical board NL80130.091.21. Initially, fifteen patients had received the BioMimics 3D helical stent (Veryan Medical, Horsham, UK); however, only one patient (male, 57 years old) was eligible and provided informed consent. Prior to contrast-enhanced ultrasound (CEUS) imaging, an intravenous injection of 0.75 mL Sonovue microbubbles was given to the patient (Bracco, Milan, Italy). Next, high-frame-rate CEUS acquisitions were made using Verasonics Vantage 256 (Kirkland, WA, USA) at 4 MHz and 2000 frames per second, for three seconds.

The data was collected in the upstream, downstream, and middle of the stent in two different leg postures, flexed and straight. After singular-value-decomposition (SVD) filtering, the acquired images were postprocessed to generate vector fields using a correlation-based echoPIV algorithm [3]. As it turned out, among the six processed image sets, only in three cases — inlet and middle of the straight leg and middle of the flexed leg — the ultrasound signal was strong enough for the data to be processed into vector fields. In these cases, twelve regions were selected for analysis, and vector complexity (VC) and skewedness were calculated for each case. VC is defined as [4]

$$VC = 1 - \sqrt{\bar{x}^2 + \bar{y}^2} \tag{1}$$

where

$$\bar{x} = \frac{1}{n}\sum_{i=1}^{n} \cos \beta_i \tag{2a}$$

$$\bar{y} = \frac{1}{n}\sum_{i=1}^{n} \sin \beta_i \tag{2b}$$

$$\beta_i = \tan^{-1}(v_i, u_i). \tag{2c}$$

Here, u_i and v_i denote the axial and lateral velocity of each vector i within the selected region. In this study, we modified the definition of β_i (2c) to
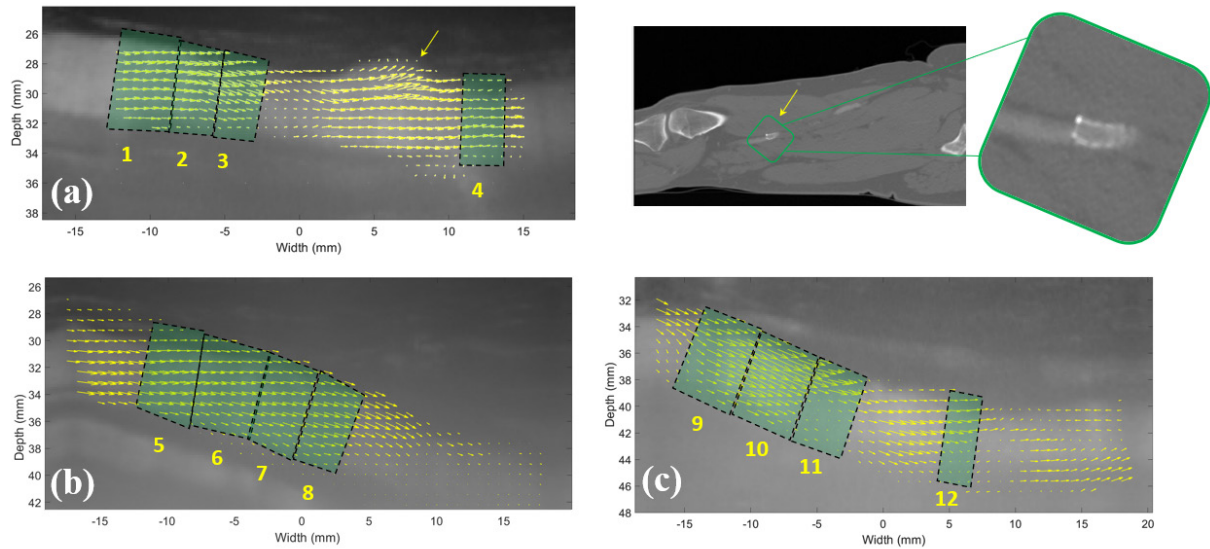
Figure 1. The shape of the time-averaged vector fields (output of echoPIV) in the superficial femoral artery (SFA), stented with a Biomimic 3D helical stent: (a) straight leg, upstream of the stent, (b) straight leg, middle of the stent, (c) flexed leg, middle of the stent. On the right side of (a), a CT scan of the stent shows that the inlet of the stent had malapposition, causing extra flow patterns to form as shown by the arrow in (a). The twelve regions analyzed for vector complexity and skewedness are shown as masks over the images. The brighter region of each image is the strong average signal due to the contrast bubbles, clearly showing the boundaries of the SFA.

$$\hat{\beta}_i = \tan^{-1}(v_i/u_i) \tag{2d}$$

so that all vectors are mapped into the first and fourth quartiles of the unit circle, not taking into account vector complexity due to the change in the direction of the blood flow. We called this definition modified vector complexity (MVC). Skewedness (S) was defined as the location of the maximum velocity in the velocity profile with respect to the centerline of the selected region in mm [5]. To calculate S, each region was first rotated so that its centerline matched the horizontal line (x-axis). Note that S can accept positive and negative values.

Results and Discussion

Figure 1 shows the time-averaged vector fields (over three cycles) in the three analyzed image sets. As only the shape and relative magnitude of the vector fields are important to calculate MVC and S, the magnitude of the vectors is not shown here. In Fig. 1-(a), it can be seen that there is a region with a more complex vector field. As the figure on the right of Fig. 1-(a) reveals, in that location, the stent inlet was misplaced a bit, causing extra flow patterns to (deviations from the streamlines in the native vessel) to form. In overall, twelve regions are marked and numbered for analysis. As Fig. 1 shows, Regions 1-3 are in the proximal of the stent, straight leg; Region 4 is at the inlet and inside the stent, past the spot of the misplaced stent, Regions 5-8 are inside the stent, straight leg; and Regions 9-12 are inside the stent, flexed leg.

Figure 2 shows the analysis result for each region with its respective number. First of all, in Fig. 2-(a), it can be seen that MVC is the highest at the stent inlet in the straight leg, past where the stent does not have full apposition. This was predictable by looking at the shape of the vector field in Fig. 1-(a). S is, however, the lowest in this region, as Fig. 2-(b) shows. MVC in the regions proximal of the stent are generally lower than the regions inside the stent, both in the straight and flexed leg. This can be seen in Fig. 2-(c), where the data is averaged over Regions 1-3, 5-8, and 9-12, showing mean value of the data and its standard error in each case, corresponding to Fig. 1, (a)-(c). Region 4 is excluded from the average as an outlier.

In Figure 2-(b), one can see that S changes signs from one location to the next inside the stent. This behavior is expected from a strong helical flow, causing the maximum velocity of the flow to move from one side to the other as it progresses through the stent. This was reported in a simulation study of a curved
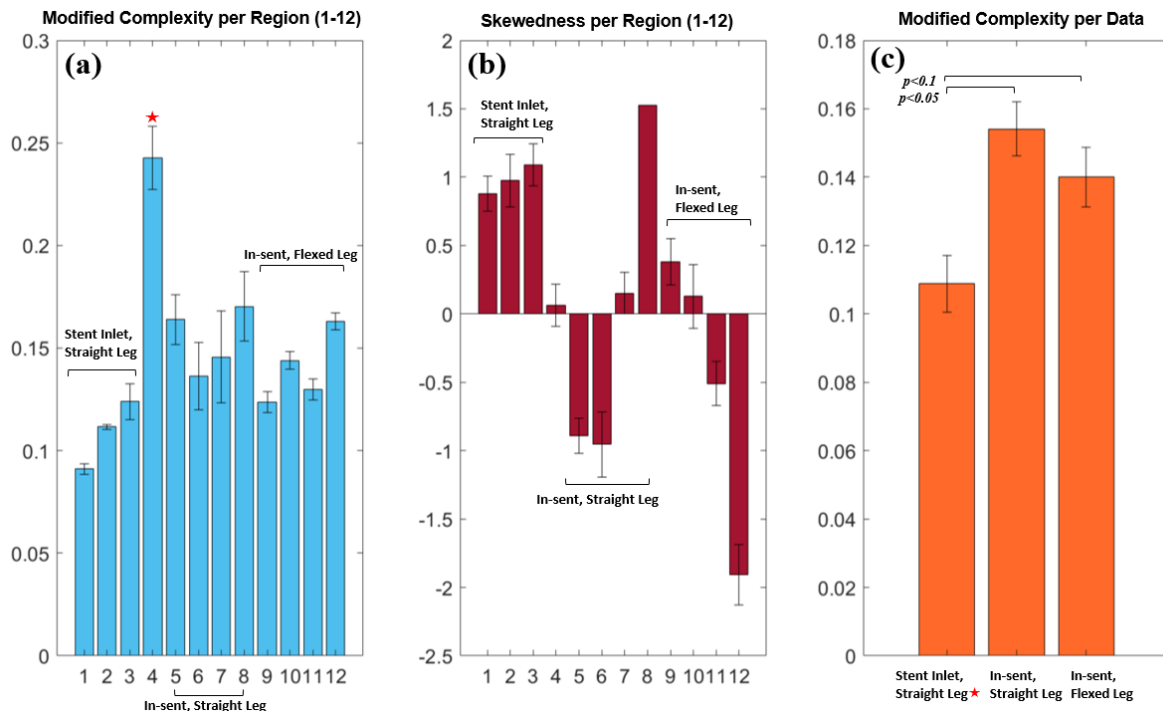
Figure 2. Analysis results: (a) modified vector complexity per region (1-12), (b) skewedness per region (1-2), (c) modified vector complexity per data (stent inlet-straight leg, in-sent-straight leg, in-stent-flexed leg). The red star marks Region 4 as an outlier. Standard errors are shown on top of the bars.

tube in [6], where the maximum velocity also moves in the cross section of the tube as flow progresses. In [2], where we only looked at the flow in the proximal and distal of the stent, this change in the sign of S was not observed. This is due to the fact that at the outlet of the stent, the swirling flow is already dampened; yet, inside the stent, it keeps being induced by the shape of the stent. Therefore, inside the stent, in both straight and flexed leg, variations in S and its sign are noticeable. Note that S in the proximal of the stent (Region 1-3) does not vary much, but it is not small. This may be due to the native geometry of the vessel, which is not completely straight.

Although echoPIV was not feasible in the remaining datasets due to weak ultrasound signal in deep tissue, in the three cases discussed above, echoPIV enabled quantifying the blood flow inside and in the proximal of the helical stent.

Conclusions

Our analysis shows that the helical stent causes the blood flow to have higher vector complexity (VC) and variations in skewedness (S) when compared to the proximal of the stent. Higher VC and S are signatures of swirling flow. To achieve these results, we applied contrast-enhanced ultrasound velocimetry (echoPIV) to characterize flow inside a helical stent *in vivo*. This study shows that echPIV enables quantifying the flow and the shape of the vector field in the proximal of and inside the stent. Despite the fact that echoPIV was not feasible in some of the datasets due to being deeper in the tissue, this study shows that echoPIV is a suitable tool to quantify and analyze how blood flow behaves due to the implantation of stents. Further studies on swirling flow inside helical stents, including more patients are warranted.

References

[1]. Piorkowski, M., Zeller, T., Rammos, C., Deloose, K., Hertting, K., Sesselmann, V., ... & Lichtenberg, M. (2023). BioMimics 3D Stent in Femoropopliteal Lesions: 3-Year Outcomes with Propensity Matching for Drug-Coated Balloons. Journal of Cardiovascular Development and Disease, 10(3), 126.

[2]. Ghanbarzadeh-Dagheyan, A., van de Velde, L., Reijnen, M., Versluis, M., & Jebbink, E. G. (2023, April). Comparing flow in helical and straight stents using 2D ultrasound particle image velocimetry. In Medical Imaging 2023: Ultrasonic Imaging and Tomography (Vol. 12470, pp. 206-210). SPIE.

[3]. Engelhard, S. A. J., Voorneveld, J., Vos, H. J., Westenberg, J. J., Gijsen, F. J., Taimr, P., ... & Bosch, J. G. High-frame-rate contrast-enhanced ultrasound particle image velocimetry in the abdominal aorta: First human results. Radiology.

[4]. Saris, A. E., Hansen, H. H., Fekkes, S., Menssen, J., Nillesen, M. M., & de Korte, C. L. (2019). In vivo blood velocity vector imaging using adaptive velocity compounding in the carotid artery bifurcation. Ultrasound in medicine & biology, 45(7), 1691-1707.

[5]. Ghanbarzadeh-Dagheyan, A., Jebbink, E. G., Reijnen, M., & Versluis, M. (2022, October). Skewedness as a Signature of Dean Flow Measured by Echo-PIV. In 2022 IEEE International Ultrasonics Symposium (IUS) (pp. 1-4). IEEE.

[6]. Kadyirov, A. (2013, October). Numerical investigation of swirl flow in curved tube with various curvature ratio. In Proceedings of the 2013 COMSOL Conference in Rotterdam.

Optical investigation of the dynamics of ultrasound contrast agents during insonification in the kHz range

A. Feasson[1], G. Chabouh[2], B. van Elburg[3], M. Versluis[3], T. Segers[4], E. Bossy[1] , C. Quilliet[1], G. Coupier[1]

[1]*Laboratoire Interdisciplinaire de Physique (Liphy), Université Grenoble Alpes , Grenoble, France*
[2] *Laboratoire d'imagerie biomédicale (LIB), Sorbonne Université, Paris, France*
[3]*Physics of Fluids group, Technical Medical (TechMed) Center, University of Twente, Enschede, The Netherlands.*
[4]*Bios/Lab-on-a-chip Group, Max Planck Center Twente for Complex Fluid Dynamics, MESA+ Institute of Nanotechnology, University of Twente, Enschede, The Netherlands.*

Corresponding author: andrea.feasson@univ-grenoble-alpes.fr

Introduction

Most of the artificial microswimmers up to date, whether they are bio-inspired, acoustically, or magnetically driven, do not go faster than their biological counterparts. This can become an issue if we want an efficient way to transport cargo through the blood vasculature for targeted drug delivery. Indeed, most of the artificial microswimmers are too slow to go against the blood flow and are advected. Passive advection of micro or nanocarriers results in only 1% of them successfully reaching a target [1]. Thus, it would become necessary to develop faster microswimmers to gain efficiency and selectivity.

It has been demonstrated in previous studies [2,3] that an ultrasound contrast agent (UCA) can swim via a pressure-driven instability activated at a frequency of order 1 Hz. The swimming mechanism is represented in Figure 1. When subjected to a pressure wave of varying amplitude at a given frequency, the UCA will buckle when the amplitude of the pressure wave reaches a critical pressure. Then if the amplitude of the wave is lowered back to ambient pressure, the UCA will deform back to the spherical shape. Such a deformation cycle done at a frequency of 1 Hz is responsible for a swimming motion with a net displacement of around one-third of the UCA radius per cycle [4]. If this net displacement per cycle is fixed for one type of UCA and does not depend on the wave's frequency, then increasing the frequency should increase the speed of the microswimmer as more cycles can be done in the same amount of time. However, a question remains. Does this pressure instability hold at high frequencies? Some papers have shown indirect evidence of what they call buckling during insonification of UCA in the kHz range [5]. In addition, simulations have demonstrated that the kHz range would be optimal for the swimming of the UCA [4]. Thus, I will explore experimentally with the homemade setup that I designed, the effect of an ultrasound wave at a frequency of around 20-40 kKz on the buckling of different types of UCA.
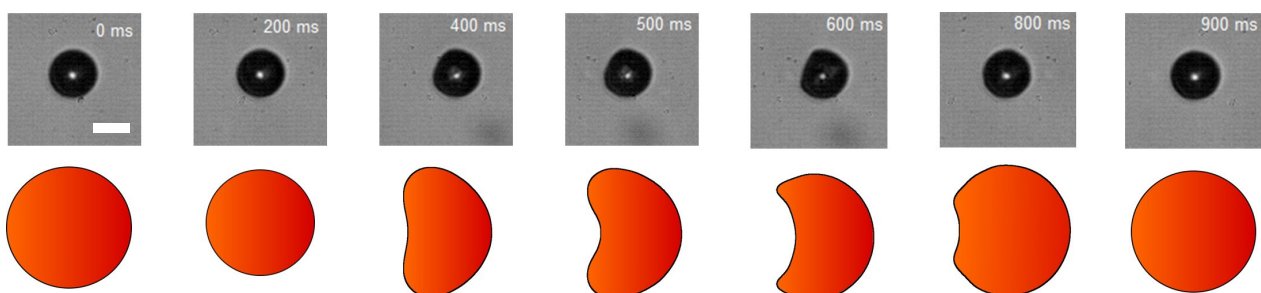

Figure 1. Example of a pressure cycle at 1 Hz by increasing external pressure to buckling pressure, then decreasing pressure again to atmospheric pressure. The scale bar is 5 µm.

Methods

Homemade and commercial UCAs were probed by the experimental setup depicted in Figure 2. Homemade UCAs have a compression modulus χ_{2d} of 4 N/m and the commercial ones (SonoVue® Bracco Spa, Milan, Italy) of 0.5 N/m. A rectangle glass capillary (CM scientific) used as a flow cell is connected to, on one end a Falcon microfluidic reservoir of 15 ml (Fisher Scientific, USA) where the UCA are put in saline solution, and the other end is plugged into a valve. The reservoir is connected to an Elveflow® pressure controller (Elvesys®, France). At the beginning of the experiment, the valve is open to allow the UCA to flow into the cell, and then it is closed. The glass capillary is placed horizontally in a tank full of water in such a way as to be in an antinode of the tank at the frequency of the transducer. The transducer (TC1026, Teledyne RESON, Slangerup, Denmark) is on one side of the tank and can emit frequencies between 16 to 37 kHz. The UCAs are excited by the standing wave and their deformations are looked at through a microscope Olympus® BX51 with a 60x water-immersible objective (Olympus® LUMPlanFL N, Japan). Positioning the tank under the microscope was ensured by the removal of the stage and the condenser.
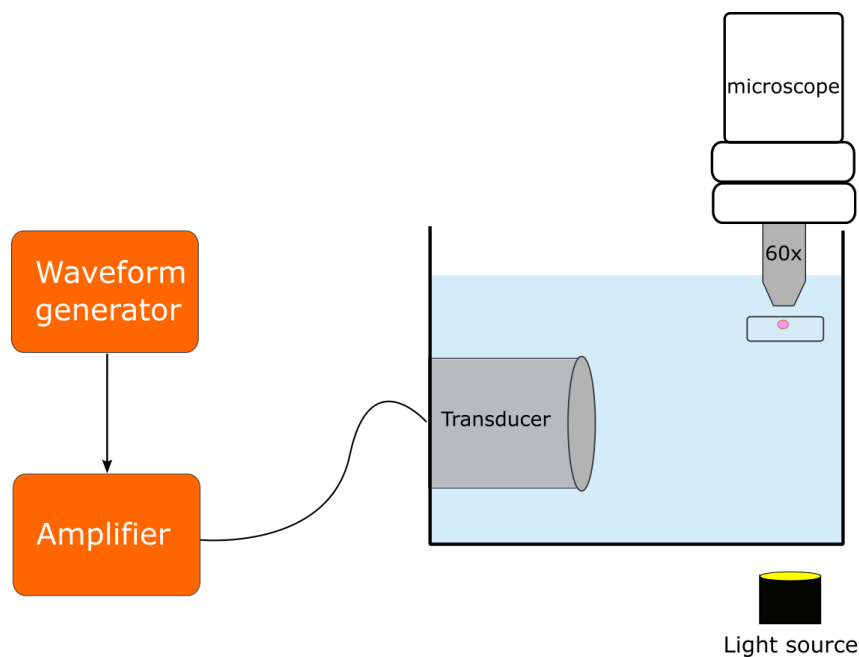
Figure 2. Experimental setup. The flow cell represented by a blue rectangle with a UCA inside is connected to a pressure controller and a valve on the other end.

Results

Previous simulations have shown that multiple parameters were to be considered to make the UCA swim faster. Firstly, the exciting pressure wave frequency and the compression modulus χ_{2d} of the UCA [4]. In Figure 3, the amplitude of the pressure is set to 800 mbar and the frequency is varied for different compression modulus. For each case, the speed increases up to a point before collapsing. The UCA with a χ_{2d} of 2 N/m goes faster and its speed collapses after the one with a χ_{2d} of 0.5 N/m. In the case of the χ_{2d} of 4 N/m, it does not go faster than the $\chi_{2d} = 2$ N/m because the 800 mbar of amplitude is below its buckling

pressure. Experimentally, we will check if we see buckling and swimming for an exciting ultrasound wave of around 20-40 kHz. The experience is still underway.
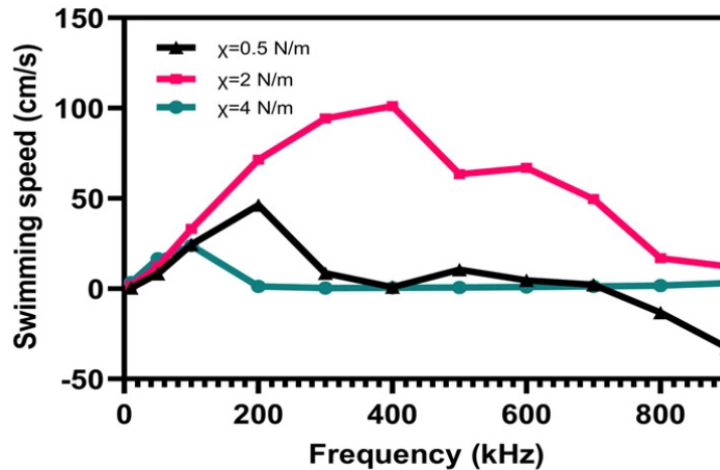
Figure 3. The estimated swimming velocity is a function of the varying excitation frequency for three different compression moduli χ_{2d} = 0.5, 2, and 4 N/m with the amplitude of the pressure wave fixed at 800 mbar [4].

Conclusions

We are about to confirm experimentally that buckling is possible in the kHz range. This would lead to making the UCA swim faster and possibly make them move up the bloodstream.

References

[1]. Anchordoquy T. J., Barenholz Y., Boraschi D., Chorny M., Decuzzi P., Dobrovolskaia M. A., ... , Simberg D, Mechanisms and Barriers in Cancer Nanomedicine: Addressing Challenges, Looking for Solutions, ACS Nano, 11: 12-18, 2017.

[2]. Chabouh G., Quilliet C., Dollet B., Marmottant P., Coupier G, Ultrasound contrast agents: From buckling dynamics to swimming., The Journal of the Acoustical Society of America, 151(4), A109-A109, 2022.

[3]. Chabouh G., van Elburg B., Versluis M., Segers T., Quilliet C., Coupier G., Buckling of lipidic ultrasound contrast agents under quasi-static load, Philosophical Transactions of the Royal Society A, 381(2244), 20220025, 2023

[4]. Chabouh G., Mokbel M., van Elburg B., Versluis M., Segers T., Aland S., ... , Coupier, G., Coated microbubbles swim via shell buckling. Communications Engineering, 2(1), 63, 2023

[5]. Renaud G., Bosch J. G., van der Steen A. F., de Jong N, Dynamic acousto-elastic testing applied to a highly dispersive medium and evidence of shell buckling of lipid-coated gas microbubbles, The Journal of the Acoustical Society of America, 138(5), 2668-2677, 2015

A new approach to assess the mechanical properties and gas permeability of microbubbles

Hedar H Al-Terke[1], Gregory Beaune [1], Jaakko V. I. Timonen[1], Françoise Brochard-Wyart[2], Robin H. A. Ras[1]

[1] *Department of Applied Physics, Aalto University School of Science, Puumiehenkuja 2, 02150, Espoo, Finland*
[2] *Sorbonne –Université Paris 05, CNRS UMR 168, Institut Curie, 26 rue d'Ulm, 75248 Paris*
Corresponding authors: francoise.brochard@curie.fr and robin.ras@aalto.fi

Introduction

Microbubbles are the main ultrasound-enhanced contrast agents (UECAs). However, they are highly sensitive and their lifetime is quite short.[1] The key issue in developing high-quality UECAs is to find a balance between the lifetime of the bubbles inside the body and their echogenicity. Both parameters depend on the nature of the gas core and the mechanical properties of the shell. Here we present the micropipette aspiration technique to characterize protein-coated bubbles.[2]

Methods

The micropipette aspiration technique has long been used to examine incompressible vesicles, such as emulsions and living cells.[3] However, when it comes to compressible bubbles, current models are inadequate for analysis. To address this limitation, we have developed a model that accounts for the compressibility of bubbles, derived from the existing model for incompressible vesicles. Moreover, we have introduced a sealing parameter (Q) to characterize the gas leakage through the bubble membrane.

By exerting a pressure differential between the micropipette and the membrane of the bubble, we aspirate a tongue into the pipette. This action effectively increases the surface area while maintaining a near-constant volume. By measuring the length of the tongue over time, we are able to characterize both the mechanical properties (elastic modulus and surface viscosity) of the membrane and the gas permeability.

Results

The primary outcome of our study entails the introduction of a sealing parameter denoted as Q. For $Q \gg 1$, the stationary tension exhibited by the membrane adheres to Laplace's law. Conversely, for $Q \ll 1$, the stationary tension diminishes substantially and declines in proportion to Q. It is worth noting that this particular range of behavior has never been observed in lipid membranes adorned with protein pores.

Conclusions

The micropipette aspiration technique is employed to assess the mechanical properties of protein-coated gas bubbles. This technique allows for the determination of a sealing parameter (Q), which is crucial for evaluating gas permeability.We successfully tested this new micropipette aspiration model on a new type of microbubbles. This new model will be useful in developing and testing microbubbles for *i.e.* UECA in a range of biomedical applications, including drug delivery and tissue engineering. These well-characterized bubbles hold promising potential as UECAs in a range of biomedical fields for various biomedical applications, including drug delivery and tissue engineering.
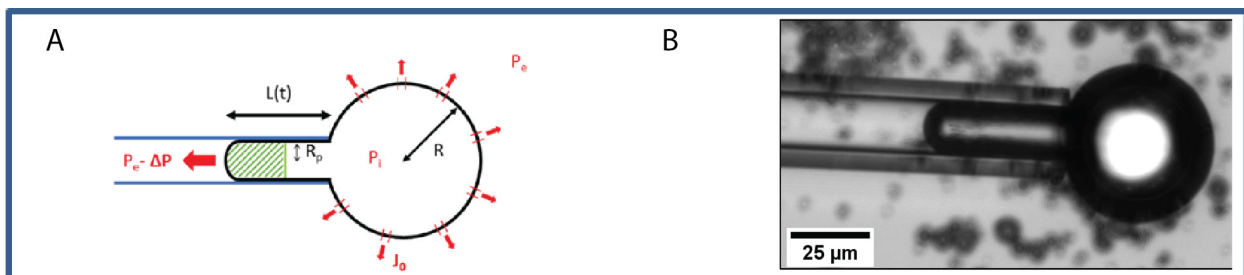
Figure 1. (A) Schematics of the micropipette aspiration experiment. (B) A bright-field microscopy image of aspirated protein-coated bubble.[2]

References

(1) Frinking, P.; Segers, T.; Luan, Y.; Tranquart, F. Three Decades of Ultrasound Contrast Agents: A Review of the Past, Present and Future Improvements. *Ultrasound Med. Biol.* **2020**, *46* (4), 892–908. https://doi.org/10.1016/j.ultrasmedbio.2019.12.008.

(2) Al-Terke, H. H.; Beaune, G.; Junaid, M.; Seitsonen, J.; Paananen, A.; Timonen, J. V. I.; Joensuu, J.; Brochard-Wyart, F.; Ras, R. H. A. Compressibility and Porosity Modulate the Mechanical Properties of Giant Gas Vesicles. *Proc. Natl. Acad. Sci.* **2023**, *120* (4), e2211509120. https://doi.org/10.1073/pnas.2211509120.

(3) Evans, E.; Rawicz, W. Entropy-Driven Tension and Bending Elasticity in Condensed-Fluid Membranes. *Phys. Rev. Lett.* **1990**, *64* (17), 2094–2097. https://doi.org/10.1103/PhysRevLett.64.2094.

Enhanced control of cavitation phenomena in ultrasound mediated drug delivery using monodisperse microbubbles

D. Fouan[1], *L. te Winkel[2]*, *J.M. Escoffre[1]*, *W. van Hoeve[2]*, *A. Bouakaz[1]*

1. UMR 1253, iBrain, Université de Tours, Inserm, Tours, France
2. Solstice Pharmaceuticals, Enschede, Netherlands

Introduction:

In the medical field, the controlled use of cavitation induced by ultrasound in the presence of microbubbles presents a promising avenue for targeted drug delivery. Cavitation, is a critical phenomenon that must be finely tuned to ensure the safety and efficacy of ultrasound mediated therapies. This study aims to elucidate the cavitation characteristics of monodisperse versus polydisperse microbubble populations to improve control in drug delivery applications.

Objective:

The primary objective of this research is to answer to the following question: Can the cavitation behavior of monodisperse microbubbles be more precisely controlled compared to polydisperse microbubbles, thereby enhancing the predictability and safety of ultrasound-mediated drug delivery systems.

Methods:

Monodisperse microbubble populations were synthesized with a primary size distribution analogous to the mean size of the polydisperse microbubbles to facilitate direct comparison. The polydisperse samples were composed of four distinct microbubble contrast agent solutions, each with a different mean diameter, to cover a broad resonance frequency spectrum.

The experimental setup comprised a calibrated ultrasound system designed to evaluate the cavitation behavior of microbubbles. We measured the resonance frequencies and cavitation thresholds of both monodisperse and polydisperse microbubble populations. For resonance frequency determination, we employed the attenuation method in a transmit-receive mode, utilizing a series of single-element transducers with varying frequencies to identify the resonant peaks of the microbubbles. The transducers were carefully selected to match the expected resonance range of the microbubbles, ensuring accurate and sensitive detection.

To assess the cavitation properties of the microbubbles, we utilized a single-element transducer operating at 1 MHz for transmission (50 cycles pulse). This frequency was chosen because most drug delivery research, including studies on blood brain barrier opening, is conducted at this frequency range. For cavitation threshold measurements, the transmit and receive transducer were positioned orthogonally at 90 degrees to each other to capture the acoustic emissions from the microbubbles. For receive, a 2.25 MHz single element transducers were used. This setup was designed in detecting the onset of both stable and inertial cavitation events. The cavitation index was derived by analyzing the spectrum of the scattered ultrasound signal, with particular attention paid to the subharmonic frequencies indicative of stable cavitation and the broad band noise associated with inertial cavitation. The acoustic pressure levels were incrementally increased from 100 to 800 kPa, and the corresponding cavitation activity was recorded. This method allowed for the precise determination of the pressure threshold at which cavitation commenced for each microbubble population.

Results:

The resonance frequency of the various monodisperse microbubbles extended from 2 to 5 MHz while the 4 polydisperse microbubbles had resonance frequencies of 3, 3.5, 4 MHz and above 8 MHz. As expected, our findings indicate that monodisperse microbubbles exhibit a narrower resonance curve and a higher quality factor (Q-factor), suggesting a more predictable and stable response to ultrasound excitation. In contrast, polydisperse microbubbles showed broader resonance curves and lower Q-factors, leading to a less controlled cavitation response. The cavitation thresholds measured corroborated these observations, with monodisperse microbubbles demonstrating uniform behavior and polydisperse samples exhibiting a wide variability. The results showed also that for the same resonance frequency, the inertial cavitation of the monodisperse samples initiates at much higher applied acoustic pressures than for polydisperse microbubbles of the same resonance frequency. Also, the stable cavitation characteristics in terms of the threshold is relatively consistent for monodisperse microbubbles, as they all resonate similarly under the acoustic field as they are excited below their resonance frequencies. For polydisperse microbubbles, the threshold varies, with some bubbles entering stable cavitation at different acoustic pressures due to their size dispersity.

Conclusion:

The study confirms that monodisperse microbubbles offer superior control over cavitation phenomena due to their consistent size and resonant properties. This predictability is paramount for the safe application of ultrasound in drug delivery, where precise dosing and minimal off-target effects are critical. To validate these results, additional investigations involving cell cultures and animal models are planned.

Dynamics of ultrasound-driven coated microbubbles confined in viscoelastic tubes

__Fleur Vialle__[1], Michel Versluis[1], Guillaume Lajoinie[1]

[1]*Physics of Fluids group, Techmed Centre, University of Twente, Enschede, The Netherlands*
Corresponding author: f.vialle@student.utwente.nl

Introduction

The dynamics of ultrasound-driven coated microbubbles have been primarily investigated in unbounded fluids. The resonance behaviour of these free microbubbles is well-described by Rayleigh-Plesset-type equations, where the nonlinear effect of the shell can be described by the Marmottant model [1]. However, when microbubbles are located in capillaries, which have a typical diameter of approximatley 4 to 8 µm [2], the assumption of an unbounded fluid no longer holds. To increase the sensitivity of diagnostic and therapeutic ultrasound, the resonance behaviour of microbubbles in small vessels should be understood.

Few experimental studies have been performed on microbubbles confined in capillary tubes, and these were mainly based on optical high speed imaging [3]–[5]. Existing experimental studies typically use rigid capillaries, and/or high pressures for therapeutic applications. Up to now thus, mainly numerical studies have been performed on the effect of soft viscoelastic confinement on the resonance of microbubbles at low diagnostic pressures. These studies show that confinement of bubbles in rigid vessels decreases the natural frequency, while the frequency is increased in the case of compliant vessels. The resonance frequency is predicted to depend on both vessel size and vessel stiffness [2], [6]–[8]. These numerical studies, however, still require experimental validation and do not take into account the effect of the bubble shell on the resonance behaviour.

To gain insight into the resonance behaviour of microbubbles confined in capillaries for diagnostic ultrasound, we propose to use a combination of optical and acoustic measurements. We study both the effect of vessel diameter and vessel stiffness on the natural frequency. Moreover, to overcome the limitation of small SNR at lower ultrasound pressures relevant for diagnostic ultrasound, we will be using monodisperse bubbles which we characterize using both chirps and short imaging pulses.

Methods

The experimental setup used to study the microbubble dynamics both optically and acoustically is shown in Fig. 1A. For the optical measurements the phantom is illuminated from the left. A high speed camera together with a microscope are used to record the oscillations of the microbubbles during ultrasound actuation at a framerate of 10 million frames/s. The GE C1-6D ultrasound transducer is used to transmit two types of ultrasound waveforms: a broad band imaging pulse and a down-chirp covering a frequency range equal to the bandwidth of the transducer, i.e. from 6 MHz down to 1 MHz. These waveforms are shown in Fig. 1C. The nonlinear behaviour of the bubbles is investigated through a pulse inversion pulsing scheme.

Capillary phantoms with diameters ranging from 15 too 100 µm are created in an optically and acoustically transparent polyvinyl chloride plastisol (pvcp). The stiffness of the PVCP can further be tuned to investigate the effect of increasing elasticity on bubble resonance. Measurements are performed using both hollow glass beads and monodisperse microbubbles as acoustic scatterers. The hollow glass beads are used as linear reference.

Results

The first acoustic measurements of microbubbles and hollow glass beads flowing through a tube with a diameter of 100µm are shown in Fig. 1. Fig. 1C and E show the Fast Fourier Transform (FFT) of the acoustic responses measured when using the imaging pulse and chirp, respectively. Differences can be seen between the microbubble response and the glass beads response. The microbubbles show a smaller response at lower

frequencies than the linear beads when insonified by a chirp, while the microbubbles show a slightly smaller response at higher frequencies when driven by a broad band imaging pulse.
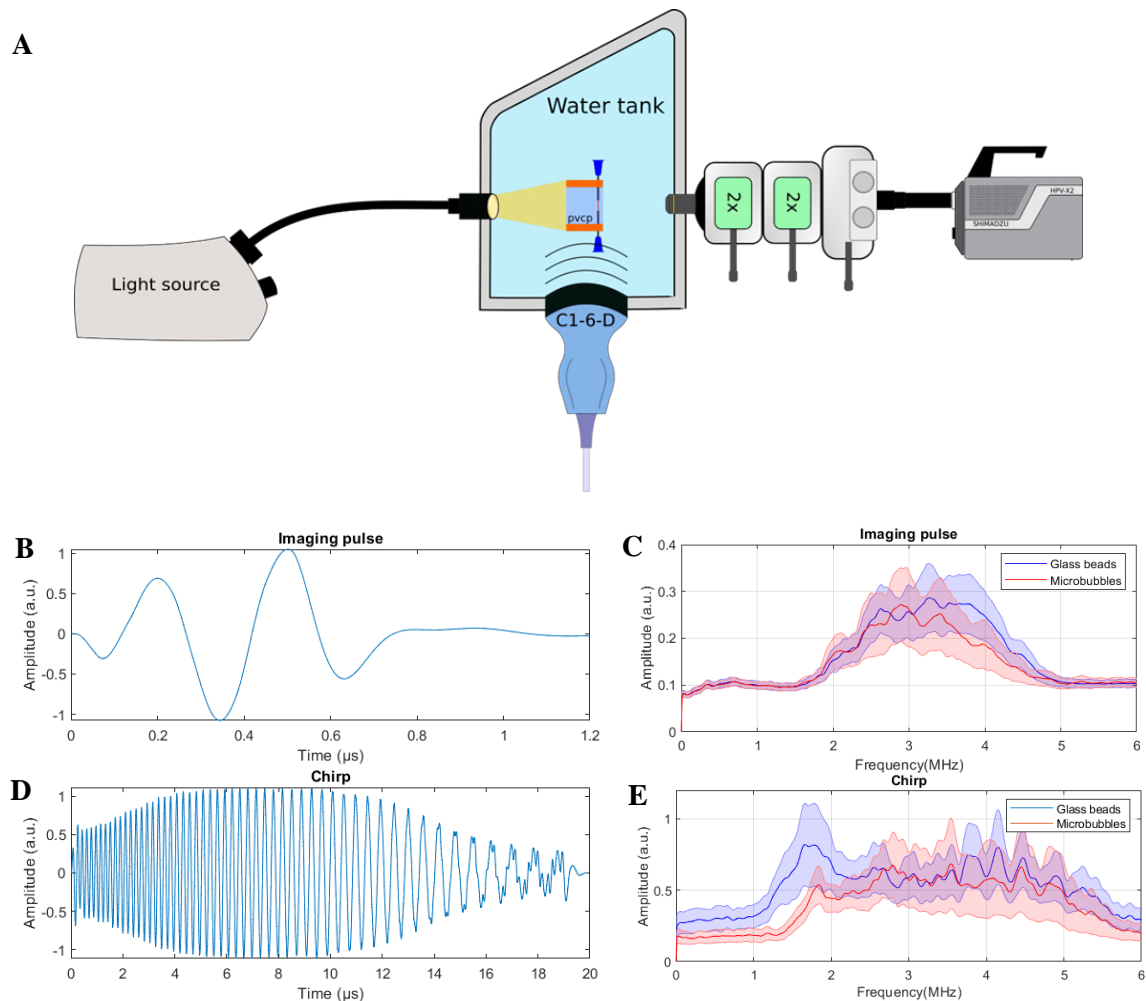
Figure 1. A) Schematic overview of the experimental setup (top view). Imaging pulse (B.) and chirp (D.) transmitted by GE C1-6D transducer. Fast Fourier transform (FFT) of the imaging pulse (C.) and chirp (E.) scattered by the hollow glass beads and microbubbles flowing through a 100 µm tube.

Conclusions

We have produced capillary vessel phantoms that are optically and acoustically transparent. The tubes have diameters below 100 µm and can be perfused with a microbubble solution. The first acoustic measurements show differences between the signal received from the microbubbles and the glass beads. This method will be further developed to investigate the resonance behaviour of microbubbles in viscoelastic capillaries.

References

[1] M. Versluis, E. Stride, G. Lajoinie, B. Dollet, and T. Segers, 'Ultrasound Contrast Agent Modeling: A Review', *Ultrasound Med. Biol.*, vol. 46, no. 9, pp. 2117–2144, Sep. 2020, doi: 10.1016/j.ultrasmedbio.2020.04.014.

[2] S. Qin, C. F. Caskey, and K. W. Ferrara, 'Ultrasound contrast microbubbles in imaging and therapy: Physical principles and engineering', *Phys. Med. Biol.*, vol. 54, no. 6, pp. R27–R57, Mar. 2009, doi: 10.1088/0031-9155/54/6/R01.

[3] C. F. Caskey, D. E. Kruse, P. A. Dayton, T. K. Kitano, and K. W. Ferrara, 'Microbubble oscillation in tubes with diameters of 12, 25, and 195 microns', *Appl. Phys. Lett.*, vol. 88, no. 3, p. 033902, Jan. 2006, doi: 10.1063/1.2164392.

[4] D. H. Thomas, V. Sboros, M. Emmer, H. Vos, and N. De Jong, 'Microbubble oscillations in capillary tubes', *IEEE Trans. Ultrason. Ferroelectr. Freq. Control*, vol. 60, no. 1, pp. 105–114, Jan. 2013, doi: 10.1109/TUFFC.2013.2542.

[5] H. Zheng, P. A. Dayton, C. Caskey, S. Zhao, S. Qin, and K. W. Ferrara, 'Ultrasound-Driven Microbubble Oscillation and Translation Within Small Phantom Vessels', *Ultrasound Med. Biol.*, vol. 33, no. 12, pp. 1978–1987, Dec. 2007, doi: 10.1016/j.ultrasmedbio.2007.06.007.

[6] S. Qin and K. W. Ferrara, 'The Natural Frequency of Nonlinear Oscillation of Ultrasound Contrast Agents in Microvessels', *Ultrasound Med. Biol.*, vol. 33, no. 7, pp. 1140–1148, Jul. 2007, doi: 10.1016/j.ultrasmedbio.2006.12.009.

[7] H. N. Oğuz and A. Prosperetti, 'The natural frequency of oscillation of gas bubbles in tubes', *J. Acoust. Soc. Am.*, vol. 103, no. 6, pp. 3301–3308, Jun. 1998, doi: 10.1121/1.423043.

[8] S. Martynov, E. Stride, and N. Saffari, 'The natural frequencies of microbubble oscillation in elastic vessels', *J. Acoust. Soc. Am.*, vol. 126, no. 6, pp. 2963–2972, Dec. 2009, doi: 10.1121/1.3243292.

Resolving sonoluminescent flux per bubble in multi-bubble sonoluminescence using photon number statistics

Richard S. K. Lane[1], Niclas Westerberg[1], Eleanor Stride[2], Daniele Faccio[1]

[1]Extreme Light, School of Physics & Astronomy, University of Glasgow, Glasgow G12 8QQ, UK
[2]Institute of Biomedical Engineering, University of Oxford, Oxford, UK
Corresponding author: richard.lane@glasgow.ac.uk

Introduction

The periodic collapse of gas microbubbles in a liquid at the focus of an ultrasonic field leads to the emission of broadband radiation, known as multi-bubble sonoluminescence (MBSL). Due to the chaotic conditions within a bubble cloud, quantitative study of this emission has typically been carried out on a single bubble, SBSL. That is however, typically considered to be a different regime in terms of the collapse dynamics and sonoluminescence emission. The conical bubble cloud structure generated by a kHz horn can contain several thousand bubbles, each with an equilibrium radius of ~5 μm, and a maximum radius of ~40 μm [1]. The efficiency of photon generation in MBSL has been found to be significantly lower than in SBSL [2]. As individual bubble flashes are not synchronised, time-correlated single photon counting can be used to obtain the flash duration for a statistically average bubble [3]. High speed imaging can only resolve bubble clusters [4], and has shown that bubble flashing is distributed inhomogenously across the cloud [5].

Here we show, through photon number statistics, that an estimation of the photon flux from a single bubble within a multi-bubble cloud, can be extracted by imaging the emission under an ultrasonic horn tip onto a photon number resolving camera. An emission rate of ~75 photons/s is found from the full conical bubble structure. A photon flux of 0.6–1.0 photons/s is estimated for a single bubble within the cloud.

Sonoluminescence has been suggested as a possible mechanism for sonodynamic therapy [6] but remains controversial. This work is a step towards ascertaining if the photon flux from cavitating bubbles in the MHz domain can photoactivate drugs coated on microbubbles, as is currently performed by a laser in photodynamic therapy (PDT).

Methods

A 20 kHz ultrasonic horn can be used as a benchtop reactor for sonoluminescence imaging with a scientific grade camera [7]. We constructed a homebuilt system comprising a Sonicator with a 6mm horn (Fisher Scientific FB120) inserted in a 3d-printed tank, filled with ultrapure water, and imaged using a $4f$ fused-silica aspheric lens 1:1 relay (f=50) onto a photon counting camera (QCMOS, Hamamatsu). Photon statistics of broadband light can be analysed by reducing degrees of freedom such as polarisation, spatial modes, and spectral modes [8]. Filtering of the emission to statistically isolate a single bubble was achieved by inserting filters in the Fourier plane of the optical path.

Quantum retrodiction is a method which back-propagates quantum mechanics, i.e. photon modefunction evolution in time [9], and gives the most likely initial quantum state given a measurement result and prior knowledge. We use this to correct for background noise, and to recover the photon statistics of the light emitted from the bubble cloud. Alongside the Fourier filtering, this allows us to determine the photon emission statistics of a single (statistical) bubble, which we find to be compatible with thermal emission.

Results

Assuming that each photon is emitted as a spherical wave, the total number of unfiltered photons emitted by the bubble cloud (accounting for detector efficiency and solid angle) is ~75 photons/s. For photons filtered sufficiently spectrally (temporally) and spatially (using a 6 mm iris and 35 nm bandpass filter centered at 469 nm), the photon emission rate for a single (statistical) bubble is found to be 0.6–1.0 photons/s.
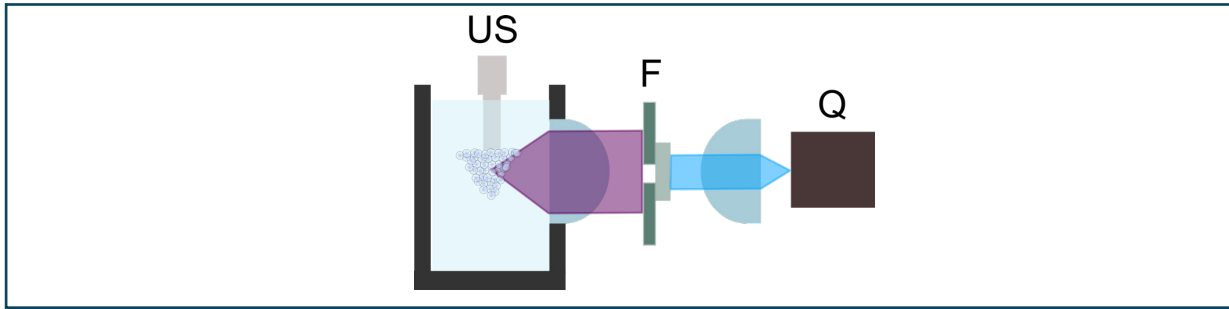
Figure 1. Schematic of the acoustic-luminescence setup, with 20kHz ultrasonic horn sonotrode (US) producing a bubble cloud, Fourier plane spatial/spectral filtering (F), and photon counting camera (Q).
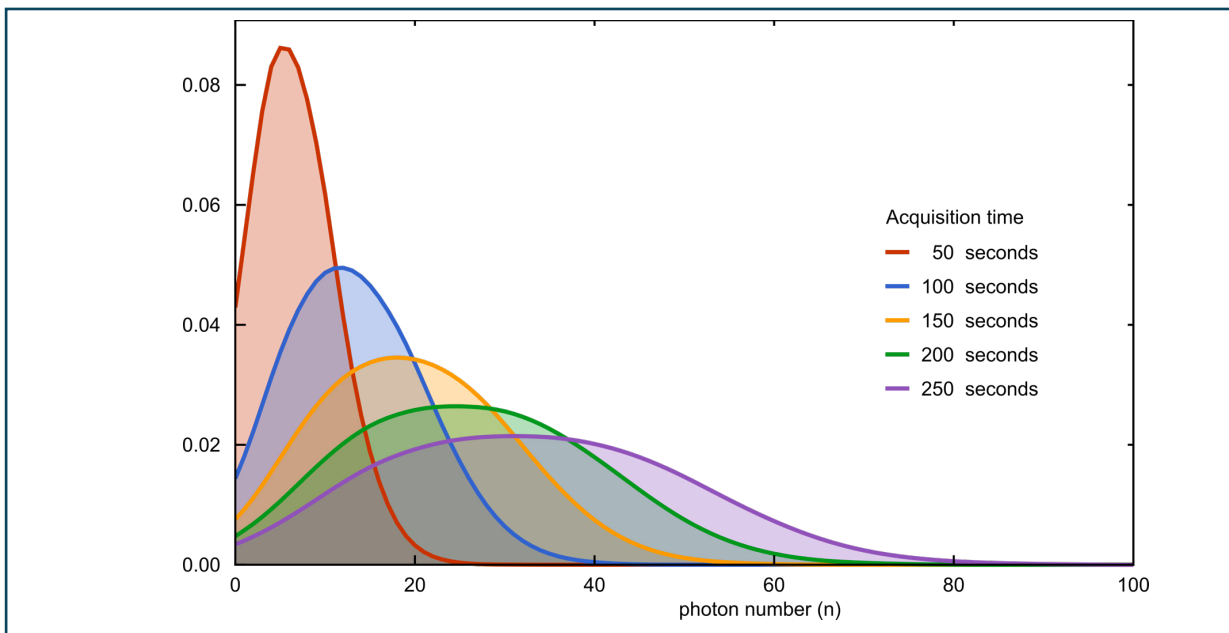
Figure 2. Retrodicted photon emission probability of a single (statistical) bubble into the solid angle of the optical system.

Conclusions

Optical imaging, and photon statistics have successfully been used to determine the photon flux of a single bubble in a horn-generated chaotically-cavitating MBSL cloud.

References

[1]. Ilgon KO, Kwak HY, "Measurement of Pulse Width from a Bubble Cloud under Multibubble Sonoluminescence Conditions", J. Phys. Soc. Japan, 79, No. 1, 2010.

[2]. Kazachek MV, Gordeychuk TV, "Using Photon Correlation Counter for Determining the Amount of Emitting Bubbles and Number of Photons per Flash of Multibubble Sonoluminescence", Tech. Phys. Lett., 46, 263-267, 2020.

[3]. Kazachek MV, Gordeychuk TV, "Resolving duration and sequence of Na and continuum flashes during MBSL with time-correlated single photon counting", arXiv:2005.00105.

[4]. Deng HY, Wang H, Ding X, Duan ZC, Qin J, Chen MC, He Y, He YM, Li JP, Li YH, Peng LC, Matekole ES, Byrnes T, Schneider C, Kamp M, Wang DW, Dowling JP, Höfling S, Lu CY, Scully MO, Pan JW, "Quantum Interference between Light Sources Separated by 150 Million Kilometers". Phys. Rev. Lett., 123, 080401, 2019.

[5]. Cairós C, Mettin R, "Simultaneous High-Speed Recording of Sonoluminescence and Bubble Dynamics in Multibubble fields", Phys. Rev. Lett., 118, 064301, 2017.

[6]. Beguin E, Shrivastava S, Dezhkunov N, McHale AP, Callan JF, Stride E, "Direct Evidence of Multibubble Sonoluminescence Using Therapeutic Ultrasound and Microbubbles", ACS Appl. Mater. Interfaces, 11(22), 19913-19919, 2019.

[7]. Wood RJ, Bertin A, Lee J, Bussemaker MJ, "The application of flow to an ultrasonic horn system: Phenol degradation and sonoluminescence". Ultrason. Sonochem., 71, 105373, 2021.

[8]. Yusuf L, Symes MD, Prentice P, "Characterising the cavitation activity generated by an ultrasonic horn at varying tip-vibration amplitudes", Ultrason. Sonochem., 70, 105273, 2021.

[9]. Barnett SM, "Quantum Retrodiction", Andersson E, Öhberg P (eds), Quantum Information and Coherence, Scottish Graduate Series. Springer, Cham., 2014.

The role of the compression phase of ultrasound waves in acoustic droplet vaporization

Samuele Fiorini[1], Anunay Prasanna[1], Gazendra Shakya[1], Outi Supponen[1]

[1]*Institute of Fluid Dynamics, ETH Zürich, Zürich, Switzerland*
Corresponding author: sfiorini@ethz.ch

Introduction

In the past years, there has been a growing interest in investigating ultrasound-based therapies for applications such as embolotherapy [1] and targeted drug delivery [2]. The use of ultrasound-activatable agents like microbubbles has shown great potential in terms of specificity of the treatment and reduction of the needed ultrasound peak pressure. Acoustic Droplet Vaporization (ADV) is an emerging technique that employs ultrasound-activatable phase-change micron- and sub-micron-sized liquid droplets as cavitation nuclei. The liquid cores act as precursors of microbubbles, providing longer *in-vivo* circulation lifetimes and the possibility for the nanodroplets to naturally extravasate through the leaky vasculature of tumor tissues, which is advantageous for targeted drug delivery. Moreover, droplets are activated only if a defined ultrasound negative pressure value (usually referred to as vaporization threshold) is reached, providing an almost neutral behaviour below the threshold value and a strong response above it.

Here, we present a novel insight into the physics of the acoustic interaction between ultrasound and droplets by highlighting the significant role played by the compression phase of the ultrasound wave in generating tension within the droplet. We theoretically and numerically demonstrate that a so-called *Gouy Phase Shift* can occur in the acoustic focal point of the droplet, leading to a sign reversal of the incoming pressure wave. In this way, tension in the liquid can arise due to the tight focusing of a purely compression wave, potentially achieving cavitation without the need of a rarefaction phase. The narrow compression peak of distorted ultrasound waves, created by nonlinear propagation within the medium surrounding the droplets, are found to have a primary role in the creation of localized tension regions in the droplet bulk, since they typically undergo highly pronounced phase shifts.

The results are supported by ultra-high-speed visualizations showing the localized nucleation location in the droplet bulk in correspondence to the calculated global pressure minimum.
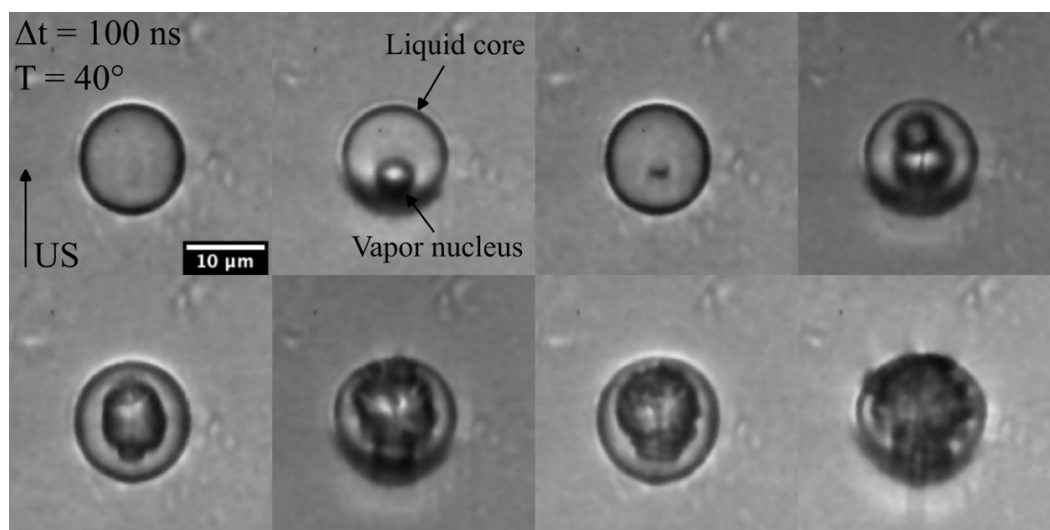

Figure 1. Snapshots showing acoustic vaporization of a perfluoropentane droplet. The incident peak negative pressure is *P* = -5 MPa, and the wave fundamental frequency is f_0 = 5 MHz.

Methods

Experimental Setup

The droplets used in the experiments are composed of perfluoropentane (C_5F_{12}) liquid cores stabilized with fluorosurfactant (Capstone™ FS-30). To ensure monodispersity of the population, a custom-made flow-focusing microfluidic device is used to produce the emulsion.

A 5 MHz high-intensity focused ultrasound transducer is used to initiate vaporization. The acoustic pressure waveform is recorded at the transducer's focal point using a 75-μm needle hydrophone. The time-resolved vaporization process of a single droplet upon ultrasound exposure is imaged using a custom-built ultra-high-speed videomicroscopy facility composed of a 200X magnification microscope coupled with a 10 million frames per second high-speed camera (Shimadzu HPV-X2). The droplet sample is kept on an agarose platform immersed in a water bath at 40 °C, at the location of the transducer's focal point. The experimental nucleation location is then extracted from the video frames. Snapshots of a typical vaporization experiment are shown in Fig. 1.

Simulations

Simulations of ultrasound wave propagation within the droplet are performed with k-Wave MATLAB toolbox [3]. Due to the small size of the droplet (9.0 μm) with respect to the transducer focal area, the incoming wave is regarded as a plane wave, with a pressure variation over time provided by the hydrophone measurements. Thermodynamic parameters for perfluoropentane and water are extracted from the NIST database [4]. The results of the simulation show very good agreement with the theoretical solution, originally formulated by Anderson et al. [5] and adapted to our test case.

Theory

Gouy phase shift indicates the variation in phase, which is increasingly obtained by a focusing beam in close proximity of the focal point. Gouy phase shift has been originally discovered in the field of optics, although the physical principle applies to all kind of waves. Direct observation of the phase shift for a converging pressure wave has been performed recently [6]. For a Gaussian beam, an analytical expression of the phase shift can be obtained as $\emptyset(z) = tan^{-1}(z/z_R)$, with z being the distance from the focal point along the propagation axis and z_R the Rayleigh length, expressed as $z_R = \pi f w_0^2/c$, with f and c being the frequency of the wave and the phase velocity respectively and w_0 the beam waist at the focus. As can be seen from the expression for $\emptyset(z)$, a wave travelling from $z \ll z_R$ to $z \gg z_R$ will undergo a phase shift of $\Delta\emptyset = \pi$, meaning that the wave will reverse its sign. When focusing a wave with a harmonic content included between 5 MHz and 50 MHz travelling in perfluoropentane (sound speed $c_s = 405$ ms^{-1}), the Rayleigh length assumes values ranging from $z_R \sim 100$ μm to $z_R \sim 10$ μm. Since its magnitude is roughly of the same order as the diameter of the microdroplets considered in this study and the employed ultrasound wave's spectrum shows significant energy up to 50 MHz due to nonlinear distortion, there is the possibility to observe phase shift in the focal point located inside the droplet core.

Results

Previous works [7] have shown that the acoustic wave is focused inside the droplet bulk, creating a very localized tension region in which nucleation is more likely to occur. To assess the distinct contributions of the compression and tensile portions of the wave to the global pressure minimum, two different calculations are carried out – one limited to the compression and one to the rarefaction phase of the original incoming wave. Due to the linearity of the wave equation, the sum of the two solutions reconstructs the complete propagation dynamics inside the droplet core. The snapshots shown in Fig. 2, captured at the time instant in which the complete solution has a global minimum, present the two partial solutions and the undisturbed incoming wave compared with the result of the full simulation. It is worth

noting that the rarefaction wave at this instant is focused on the distal side of the droplet (see Fig. 2C). On the other hand, the purely compression solution presents a strong negative pressure in a region consistent with the location of the global minimum and with a contribution in magnitude roughly equal to the one of the rarefaction solution (Fig. 2D). The position of the pressure minimum is confirmed experimentally by the first nucleation locations in the droplet core, presented in Fig. 2B. We believe that the creation of tension from a purely compression wave is due to the occurrence of Gouy phase shift during the focusing inside the droplet core of the incoming acoustic wave. It is important to notice that the characteristic specific acoustic impedance for perfluoropentane is lower than the one for water. Therefore, no change in pressure sign is expected for an acoustic wave travelling in the droplet core and reflecting at the interface. The characteristic length for the phase shift is the Rayleigh length, which in turn is dependent on the beam waist. We numerically estimate the beam waist for the main harmonic components of the incoming wave, finding that the Rayleigh length reduces with increasing excitation frequency, reaching values that are below the droplet radius considered for the experiments. Therefore, we expect to observe a very pronounced phase shift for higher harmonic components. This prediction is confirmed by the numerical simulation shown in Fig. 2D, in which the compression portion of the incoming wave, whose harmonic content is broader with respect to the rarefaction phase (and thus contains higher frequencies), undergoes a clear sign reversal when passing through the focus located in the rear of the droplet. Later, the generated tension wave is refocused on the proximal side, where the global pressure minimum is reached.
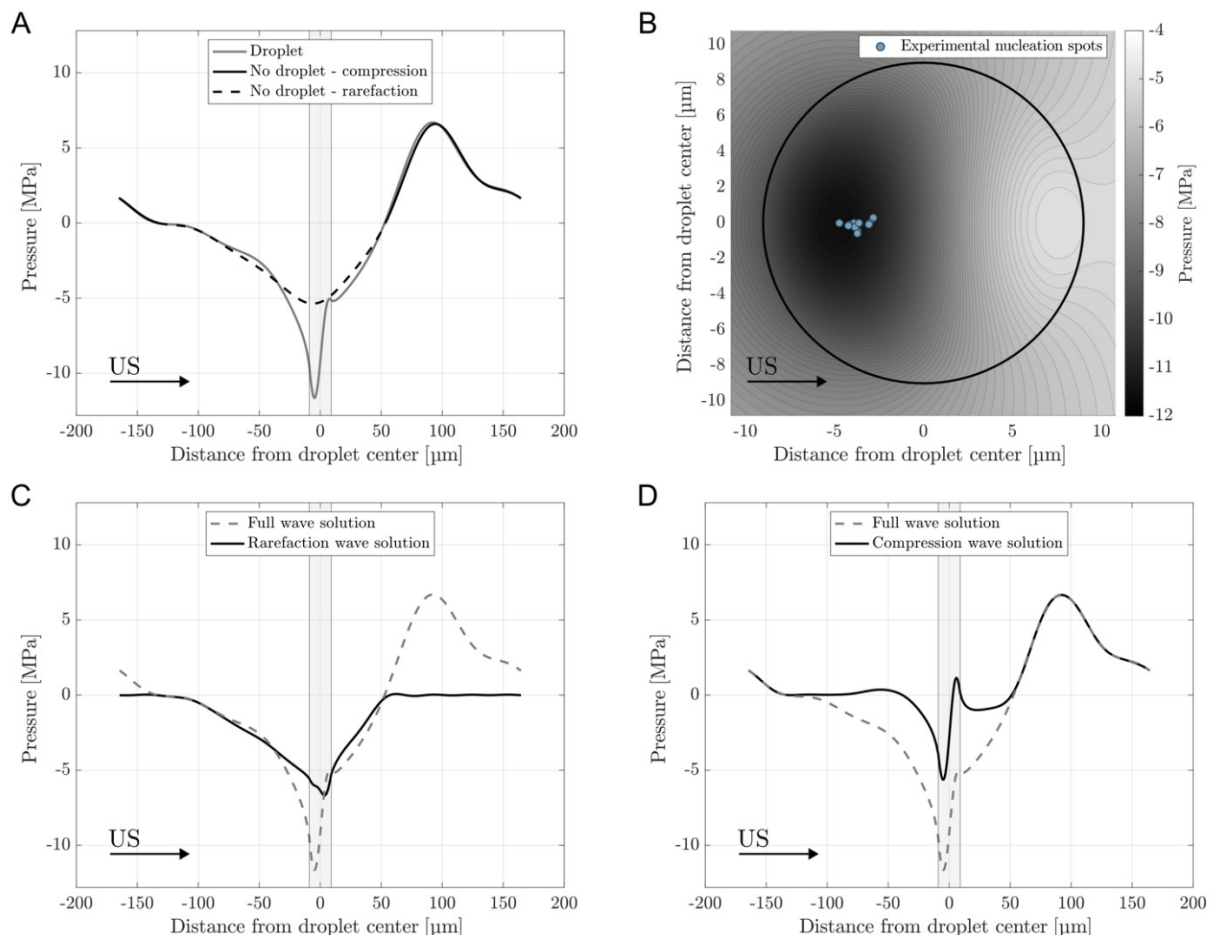
Figure 2. Computed pressure fields inside the droplet and in its surrounding at the time instant in which the global minimum in pressure is reached. The gray shaded areas show the droplet position. Axial symmetry is assumed in all the calculations. The dashed and solid lines in A, C and D represents the pressure on the droplet centerline. (A) Comparison between the undisturbed incident wave (black line) and the effect of introducing a droplet in the calculation domain (gray line). (B) Pressure map on the droplet center plane with the experimentally detected nucleation spots. (C) and (D) Purely rarefaction and compression solution compared with the full solution. It can be observed that the location of the global minimum is dictated by the compression solution due to phase shift of the compression peak.

Conclusions

In this work, we demonstrate the significance of the compression phase of an ultrasound wave in acoustic droplet vaporization. We show that the distorted compression part of the incoming wave, which includes a broader spectrum of frequencies, presents a pronounced phase shift while crossing the focal point. The extent of such a shift is sufficient to change the sign of the wave, actively creating a tension region in the droplet bulk. The rarefaction part of the wave does not present the same behaviour, and sign reversal is not expected. Therefore, we believe that new parameters to define the vaporization threshold should be considered, as the minimum pressure alone does not effectively represent the rich dynamics occurring in the droplet bulk in the case of distorted waves. This finding also opens a new avenue for optimizing the acoustic driving for micro- and nanodroplets, with the possibility to achieve vaporization exploiting ultrasound waves with high peak positive pressures and with reduced peak negative pressures, thus improving the overall safety of the treatment by effectively reducing the Mechanical Index.

Acknowledgements

References

[1]. Harmon et al., Minimally invasive gas embolization using acoustic droplet vaporization in a rodent model of hepatocellular carcinoma, Scientific Reports, 2019.

[2]. Chen et al., Targeted drug delivery with focused ultrasound-induced blood-brain barrier opening using acoustically-activated nanodroplets, Journal of Controlled Release, 2013.

[3]. Treeby and Cox, k-Wave: MATLAB toolbox for the simulation and reconstruction of photoacoustic wave-fields, Journal of Biomedical Optics, 2010.

[4]. Lemmon et al., NIST reference fluid thermodynamic and transport properties-REFPROP.

[5]. Anderson, Sound scattering from a Fluid Sphere, Journal of the Acoustical Society of America, 1949.

[6]. Lee et al., Origin of Gouy Phase Shift Identified by Laser-Generated Focused Ultrasound, ACS Photonics, 2020.

[7]. Shpak et al., Acoustic droplet vaporization is initiated by superharmonic focusing, Proceedings of the National Academy of Sciences, 2014.

Acoustic vaporization of droplet aggregations

Anunay Prasanna[1], Samuele Fiorini[1], Gazendra Shakya[1], Outi Supponen[1]

[1]Institute of Fluid Dynamics, ETH Zürich, Zürich, Switzerland
Corresponding author: aanunay@ethz.ch

Introduction

Ultrasound-responsive agents, such as microbubbles and nanodroplets, have demonstrated their powerful capabilities in theranostics. Micron- and sub-micron-sized droplets have been employed as microbubble precursors, since they can be converted into microbubbles upon exposure to ultrasound. This phase-change process, called acoustic droplet vaporization (ADV), is a novel technique that can be employed for contrast enhanced ultrasound imaging [1], gas embolotherapy [2], targeted drug delivery [3], and other ablation techniques such as histotripsy [4] and thermal ablation [5]. Droplets, compared to microbubbles, provide increased stability against dissolution, and therefore, longer circulation times *in vivo* [6]. The smaller size of droplets allows them to extravasate deep into the leaky vasculature of tumor tissues, thus creating highly localized microbubbles that enable better specificity and targeting for therapeutic applications [7].

Currently, the incident peak negative pressure (PNP) – commonly known as the acoustic vaporization threshold – required to achieve droplet vaporization *in vivo* are prohibitively high [8]. Therefore, suitable techniques need to be devised in order to reduce the vaporization threshold and efficiently vaporize smaller droplets. Introducing clusters of droplets and creating droplet aggregations have been shown to reduce the required incident pressure for vaporization, as opposed to vaporizing separate, single droplets [9, 10]. However, the underlying physics explaining why aggregations reduce the vaporization threshold is currently not well understood. Here, we investigate this phenomenon through spatiotemporally resolved experiments, and further elucidate which aggregations are desirable for maximum threshold reduction.

Methods

A. Droplet aggregation preparation

Micron-sized droplets containing perfluoropentane (C_5F_{12}) liquid core were prepared in-house either through amalgamation or a flow-focusing microfluidic device. Lipid solution containing 1,2-distearoyl-sn-glycero-3-phosphocholine (DSPC), 1,2-distearoyl-phosphoatidyl ethanolamine-polyethyleneglycol sodium salt (DSPE-PEG2000), and 1,2-distearoyl-sn-glycero-3-phosphoethanolamine-N-[biotinyl(polyethylene glycol)-2000] (DSPE-PEG2000-Biotin) in a 90:5:5 molar ratio, with a concentration of 10 mg/ml, was used as the surfactant. Biotinylated droplets were then extracted through gravitational sedimentation, and the collected droplets were mixed with a 0.5 mg/ml streptavidin solution to make use of the biotin-streptavidin conjugation scheme, allowing the droplets to form randomized aggregations.

B. Experimental setup

Ultra-high-speed video microscopy was performed to visualize the vaporization dynamics of the droplet aggregations. A 60 X Olympus objective was coupled to a tube lens of focal length 600 mm, (Thorlabs, TL-600A) to provide a total magnification of 200X. The tube lens was coupled to a high-speed camera (Shimadzu HPV-X2) with a recording rate of 10 million frame per second. The aggregations were placed in an optically and acoustically transparent 1% w/v agarose chamber, with the chamber positioned at the optical focus of the objective and the acoustic focus of the high-intensity focused ultrasound transducer (see Fig. 1). High-intensity ultrasound transducers having central frequencies of 5 MHz (Precision Acoustics, UK) and 3.5 MHz (Olympus Corporation) were used, and were powered by a 200 W amplifier (E&I 1020L) with the signal being provided by an arbitrary wave generator (Teledyne LeCroy LW 420B). The agarose chamber was immersed in a water bath that was heated by an immersion heater and maintained at a temperature of $37°$ C.
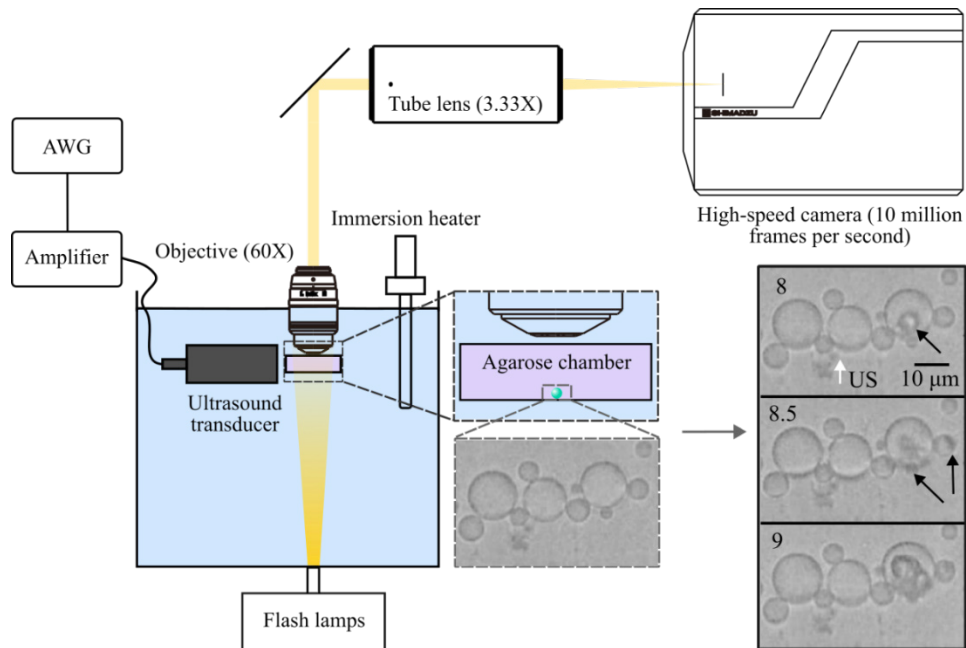
Figure 1. Experimental setup for time-resolved imaging of the vaporization dynamics of droplet aggregations. The inset shows snapshots of the vaporization dynamics of a typical multi-drop aggregation, with the white arrow indicating the direction of propagation of ultrasound, and the black arrows highlighting vapor bubble nucleation. The snapshots are labelled with their non-dimensional times, t/T_d, where T_d is the time-period of the incoming ultrasound. Here, the frequency is, f = 5 MHz, and the applied peak negative pressure is $p_a = 2.68$ MPa.

Results

Fig. 2 depicts the vaporization threshold, p_a, as a function of the drop radius for single droplets and droplet aggregations sonicated with the 5 MHz transducer and maintained at 37° C. It is important to note that single droplets having an initial radius less than 6.5 µm did not vaporize in our setup (shaded area in Fig. 2), even at the highest applied peak negative pressure ($p_a = 3.76$ MPa). However, Fig. 2(a) shows that much smaller droplets were repeatedly and successfully vaporized when they were part of an aggregation. Additionally, the figure suggests that the required negative pressure for these droplets is lower when they are part of an aggregation. It can be noted from Fig. 2(b) that the threshold of larger droplets in an aggregation corresponds well with the threshold for single droplets. It must also be emphasized that usually the largest drop in an aggregation, apart from certain exceptions, vaporizes first (see also Fig. 3).

Instants of the vaporization dynamics for different aggregation configurations are shown in Fig. 3. Two important points can be highlighted for all three cases. The first nucleation position is quite localized, similar to the case of single droplets as predicted by Shpak et al. [11]. This is consistent with Fig. 2(b), which indicates that the threshold of the largest drop in an aggregation is equivalent to that of single droplet vaporization. Secondly, subsequent nucleation events seem to occur after the collapse of the initial vapor bubble. We hypothesize that once the larger droplet in an aggregation vaporizes, the acoustic scattering from the created vapor bubble, and the tension generated by the initial collapse and expansion cycle of the first vapor bubble, interacts with the incoming acoustic wave. This creates regions of high negative pressure in the smaller droplets of an aggregation, thereby aiding their vaporization at much lower incident pressures.
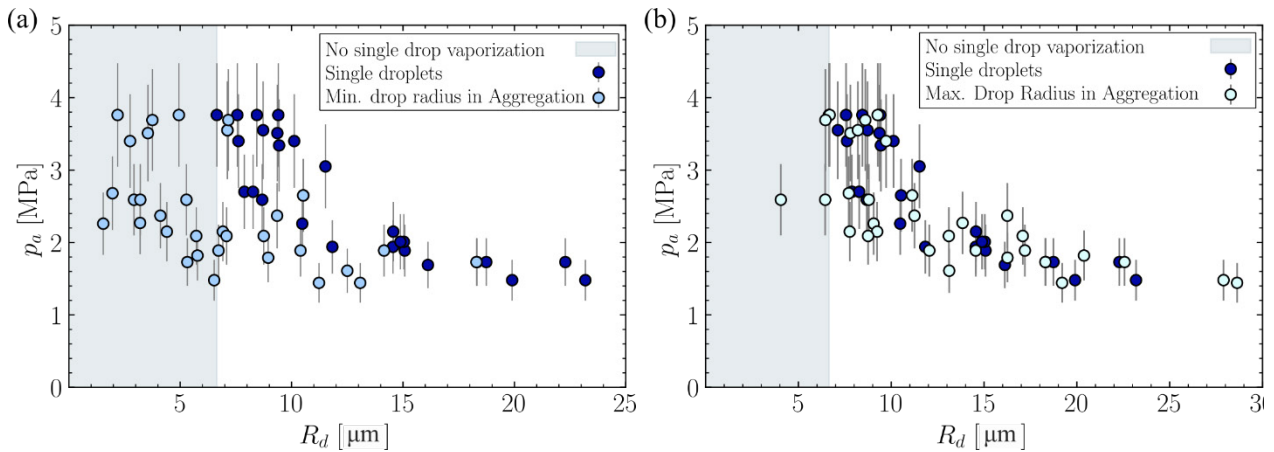
Figure 2. Vaporization threshold for single droplets versus (a) the minimum droplet radius in an aggregation and (b) the maximum droplet radius in an aggregation. The applied frequency here is *f* = 5 MHz.
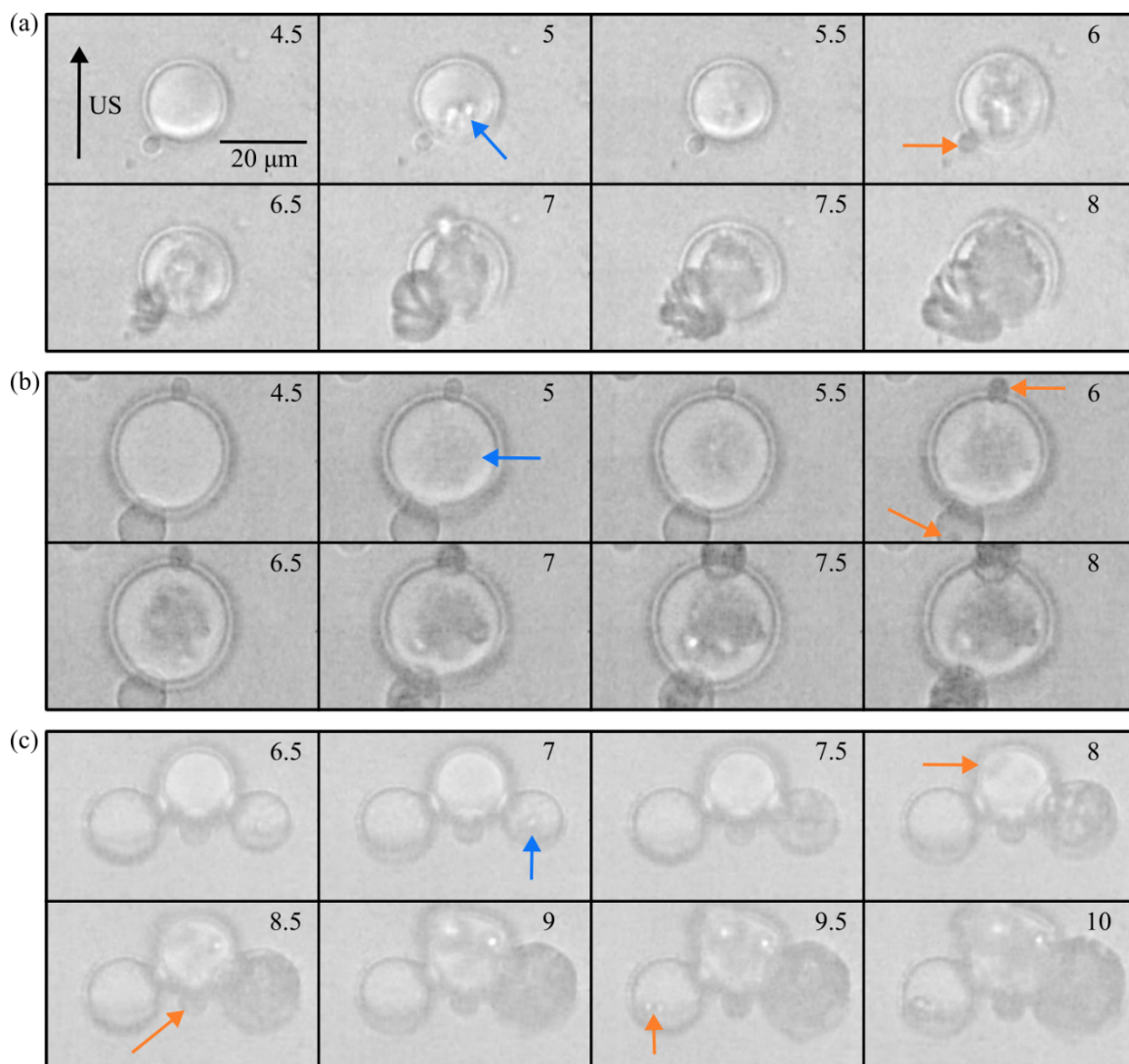
Figure 3: Snapshots of the vaporization dynamics of droplet aggregations labelled with their non-dimensional times, t/T_d. The blue arrow shows the location of the first nucleation, while the orange arrows indicate the location of subsequent nucleation events. The applied frequency is *f* = 5 MHz. (a) A 2-droplet aggregation with the first nucleation location coinciding with the values predicted by Shpak et al. [11]. Here, $p_a = 3.4$ MPa. (b) A 3-droplet aggregation with $p_a = 2.27$ MPa.. (c) A 4-droplet aggregation with $p_a = 2.15$ MPa. It is interesting to note that while the first nucleation spot corresponds with the predictions by Shpak et al. [11], the subsequent nucleation locations are arbitrary and not localized.

In Figs. 3(b) and 3(c), it can also be seen that the smallest droplet in the aggregation vaporizes before certain larger droplets within the same aggregation. It must also be emphasized that not all droplets in an aggregation necessarily vaporize, and it is not always the case that the first nucleation event is localized, even when localized nucleation is expected [11]. This indicates that there are complex acoustic lensing effects in play, with different droplet configurations either promoting or demoting the vaporization of droplets. In particular, the orientation of the biggest and the smallest droplet with respect to each other and the incoming ultrasound seems to play an important role in lowering the vaporization threshold for the smaller droplet.

Conclusions

Droplet aggregations were successfully prepared and shown to reduce the required incident peak negative pressure for droplets. Once the larger droplet in an aggregation vaporizes, the smaller droplet also tends to vaporize at the same applied peak negative pressure. Complex lensing effects due to the physical geometry of the configuration, and the acoustic scattering and high pressure generated by the collapse and expansion of the first vapor bubble contribute to the subsequent nucleation events. Further numerical simulations to study the effect of different droplet sizes in an aggregation, the number of droplets, and different aggregation geometries will be conducted to provide deeper insight into the vaporization dynamics of droplet aggregations.

References

[1]. Albrecht T et al., Renal, hepatic, and cardiac enhancement on Doppler and gray-scale sonograms obtained with EchoGen, Academic Radiology, 1996, vol. 3

[2]. Harmon JN et al., Minimally invasive gas embolization using acoustic droplet vaporization in a rodent model of hepatocellular carcinoma, Scientific Reports, 2019, vol. 9, no. 1, p. 11040

[3]. Chen CC et al., Targeted drug delivery with focused ultrasound-induced blood-brain barrier opening using acoustically-activated nanodroplets, Journal of Controlled Release, 2013, vol. 172, no. 3, p. 795-804

[4]. Vlaisavljevich et al., Effects of ultrasound frequency on nanodroplet-mediated histotripsy, Ultrasound in Medicine and Biology, 2015, vol. 41, no. 8, p. 2135-2147

[5]. Zhang M. et al., Acoustic droplet vaporization for enhancement of thermal ablation by high intensity focused ultrasound, Academic Radiology, 2011, vol. 18, no. 9, p. 1123-1132

[6]. Borden et al., Acoustic nanodrops for biomedical applications, Current Opinion in Colloid and Interface Science, 2020, vol. 50, p. 101383

[7]. Zhou X et al., Ultrasound-responsive highly biocompatible nanodroplets loaded with doxorubicin for tumor imaging and treatment *in vivo,* Drug Delivery, 2020, vol. 27, p. 469-481

[8]. Burgess MT and Porter TM, On-demand cavitation from bursting droplets, Acoustics Today, 2015, vol. 11, no. 4

[9]. Guo S et al., Lowering of acoustic droplet vaporization threshold via aggregation, Applied Physics Letters, 2017, vol. 111, no. 25, p. 254102

[10]. Guo S et al., Manipulation of nanodroplets via a nonuniform focused acoustic vortex, Physical Review Applied, 2020, vol. 13, no. 3, p. 034009

[11]. Shpak et al., Acoustic droplet vaporization is initiated by superharmonic focusing, Proceedings of the National Academy of Sciences, 2014, vol. 11, no. 5, p. 1697-1702

Characterisation of Perfluoropentane Droplets: Nitric Oxide Capacity and Acoustic Droplet Vaporisation Threshold

Christopher K. Campbell[1], Tanveer A. Tabish[2], Luca Bau[3], Davide De Grandi[3], Kirsten O'Brien[4], Gareth LuTheryn[1], Peter Glynne-Jones[4], Jeremy S. Webb[5], Nicholas D. Evans[4], Eleanor Stride[3], Dario Carugo[1]

[1]Nuffield Department of Orthopedics, Rheumatology and Musculoskeletal Sciences (NDORMS), University of Oxford, Oxford, UK
[2]Division of Cardiovascular Medicine, Radcliffe Department of Medicine, University of Oxford, Oxford, UK
[3]BUBBL group, IBME, University of Oxford, Oxford, UK
[4]School of Engineering, University of Southampton, Southampton, U.K
[5]National Biofilms Innovation Centre (NBIC), School of Biological Sciences, University of Southampton, Southampton, U.K.
Corresponding author: christopher.campbell@ndorms.ox.ac.uk

Introduction

Perfluorocarbon droplet (PD) emulsions are of increasing interest for their potential in a variety of applications in biomedical ultrasound. The liquid perfluorocarbon (PFC) core of PDs can be stabilised by a polymer, protein or lipid shell, and can dissolve bioactive gases including oxygen and nitric oxide (NO) [1]. PDs are also responsive to ultrasound and can be converted into gas-filled microbubbles through acoustic droplet vapourisation (ADV) of sufficient intensity [2]. Subsequent microbubble cavitation can deliver mechanical disruption or allow for temporal control in the release of loaded therapeutic molecules. Consequently there is extensive interest in the use of liquid PFCs as gas transporters and stimuli responsive delivery systems [3]. In the context of antimicrobial therapy, NO is a key signalling molecule known to regulate biofilm dispersal. However, conventionally used NO pro-drugs (e.g. glyceryl trinitrate) or direct inhalation of the gas can lead to unwanted side-effects. Furthermore,the scavenging and inactivation of NO by oxygen-centered species and heme-containing proteins restrict its half-life in biological systems to less than 5 seconds [4]. Due to the short half-life and fast diffusion rate *in vivo*, its localised and controlled delivery is yet to be realised. There is also limited research quantifying the loading capacity of PFC droplet emulsions. To address these needs, this study aims to quantify the capacity and determine the ADV threshold of PD emulsions for NO delivery.

Methods

Perfluorocarbon droplet manufacture

Droplets were manufactured by sonication, emulsifiying a lipid solution with perfluoro-n-pentane (PFP, Strem Chemicals, UK) in a two-step process. In the first sonication step, a Model 120 Sonic Dismembrator (Fisher Scientific, UK) was used to disperse 1,2-distearoyl-sn-glycero-3-phosphocholine (DSPC) and polyoxyethylene (40) stearate (PEG40S) in a 9:1 molar ratio within Dulbecco's phosphate-buffered saline (DPBS, Corning). Preceding the second sonication step, PFP was added in a 10:1 or 2:1 Lipids:PFP volumetric ratio (4.76% and 33.3% v/v PFP, respectively) and vortexed for 15 s to create precursor droplets. The second sonication step utilised pulsed sonication (2 s on - 15 s off, duty cycle: ~11.8%, 60 s total ON time) to make PDs, with a water-ice bath to maintain sample temperature <15 °C, necessary due to the low boiling point of 28 °C for PFP.

Particle Characterisation

Particle diameter was measured using a Multisizer 4e Coulter Counter (Beckman Coulter, USA). A 1:10 dilution in DPBS of each PD sample was added to a 10 ml volume of ISOTON diluent (Beckman Coulter, USA). Assuming spherical particle geometry, particle diameter vs concentration was measured.

Nitric Oxide Loading and Quantification

Due to the rapid reaction of NO with oxygen, samples were first sparged using N_2 gas to remove all dissolved oxygen. To prevent foam production, 1 ml aliquots of PFP droplet emulsion (1:10 and 2:1 Lipid:PFP), Lipid-only (DSPC, PEG40S) and MilliQ Water were gently agitated with a N_2 headspace for 30 mins on ice. Subsequently, an oxygen-free NO-source (400 ppm NO in Nitrogen, BOC, UK) was flowed over each sample for 5 min before sealing. The MilliQ water and Lipids only samples were rested at 4 °C for 2 h before measuring. The PD samples were left sealed overnight (14 h) at 4 °C prior to measuring.

NO-oxide (NOx) concentrations were detected by using a chemiluminescence NO analyzer (NOA) (CLD 88, ECO MEDICS AG, Switzerland). Total NOx (μM) was determined using an instrument-specific calibration constant. Briefly, the amount of NO evolved from the test solution was calculated based on the calibration curves of the NOA, which were regularly obtained by plotting the NOA signal peaks (volts, V) during calibration vs. the introduced amount of $NaNO_2$ standards into the system via nitrite reduction in an acidified vanadium chloride solution.

Determining Acoustic Droplet Vaporisation Threshold

The ADV threshold of droplet emulsions of varying PFP volumetric will be assessed using a focused ultrasound (US) setup. Briefly, a HIFU transducer (H107, 0.5 MHz fundamental frequency, 63.2 mm geometrical focus, 64 mm active element diameter, rectangular cut out 22×57 mm, Sonic Concepts Inc., Washington, USA) will be used to stimulate a range of PD formulations manufactured with between 5% and 50% v/v PFP at a driving frequency of 1.5 MHz, PRF of 5 Hz and 3000 cycle bursts (1% duty cycle) at peak negative pressures (PNP) between 0.5 and 4 MPa. PDs will be exposed to US for 60 s at 37 °C.

Results

The median diameter of PDs with 4.75% and 33.3% v/v PFP was 0.62 ± 0.25 μm and 1.39 ± 1.17 μm, respectively (**Fig.1**). The NO concentration was measured in water, lipids and both 4.75% and 33.3% v/v PFP PD samples, with n=3 for all samples (**Fig. 2**). The mean NOx concentrations (± 1 S.D.) for NO-water, NO-lipids, NO-PDs (4.75% v/v) and NO-PDs (33.3% v/v) were 58.9 ± 17.7 μM, 129 ± 24.9 μM, 108 ± 11.7 μM and 109 ± 16.9 μM, respectively. The ΔNOx between NO-water and NO-lipids was 69.9 μM (95% CI range 48.3 to 91.4) The ΔNOx between NO-PDs (4.75% v/v) and NO-PDs (33.3% v/v) was 1.04 μM (95% CI range -14.3 to 16.4).

Conclusions

Both PD and lipid-only samples were able to dissolve a significantly higher concentration of NO than water alone. There was a small difference in NOx-concentration between NO-PDs (4.75% v/v) and NO-PDs (33.3% v/v), suggesting that the lipid component of the PDs may be the key contributor to their NO carrying capacity. However, although an oxygen-free environment was maintained, the long incubation time for PDs (14h) could have affected the NOx-concentration measured within the samples. Future testing will reduce incubation times and assess the effect of a wider range of PFP volumetric concentration.
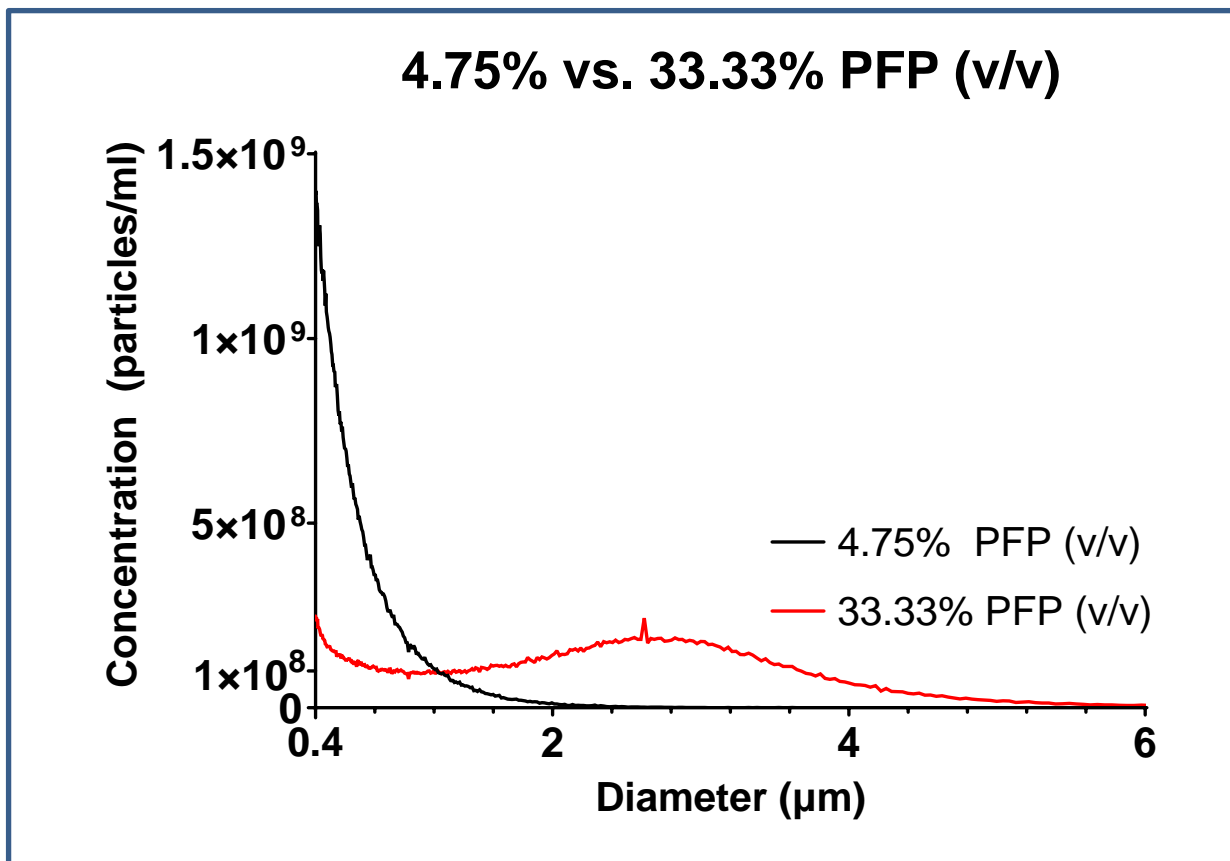
Figure 1. Multisizer data of particle diameter vs. concentration for two types of PD sample manufactured with either 4.75% (black) or 33.3% (red) v/v PFP. The median diameter of PDs with 4.75% was 0.62 ± 0.25 μm. The median diameter of PDs with 33.3% v/v PFP was 1.39 ± 1.17 μm (mean ± S.D. of 3 measurements).

Figure 2. Chemiluminescence data showing mean NOx concentration. Mean concentrations of NO-oxides were 58.9 ±17.7 μM, 129 ± 24.9 μM, 108 ± 11.7 μM and 109 ± 16.9 μM for NO-water, NO-Lipids, NO-PDs (4.75% v/v) and NO-PDs (33.3% v/v), respectively. ΔNOx of NO-water vs. NO-lipids 69.9 μM (95% CI range 48.3 to 91.4). ΔNOx of NO-PDs (4.75% v/v) vs. NO-PDs (33.3% v/v) was 1.04 μM (95% CI range -14.3 to 16.4).
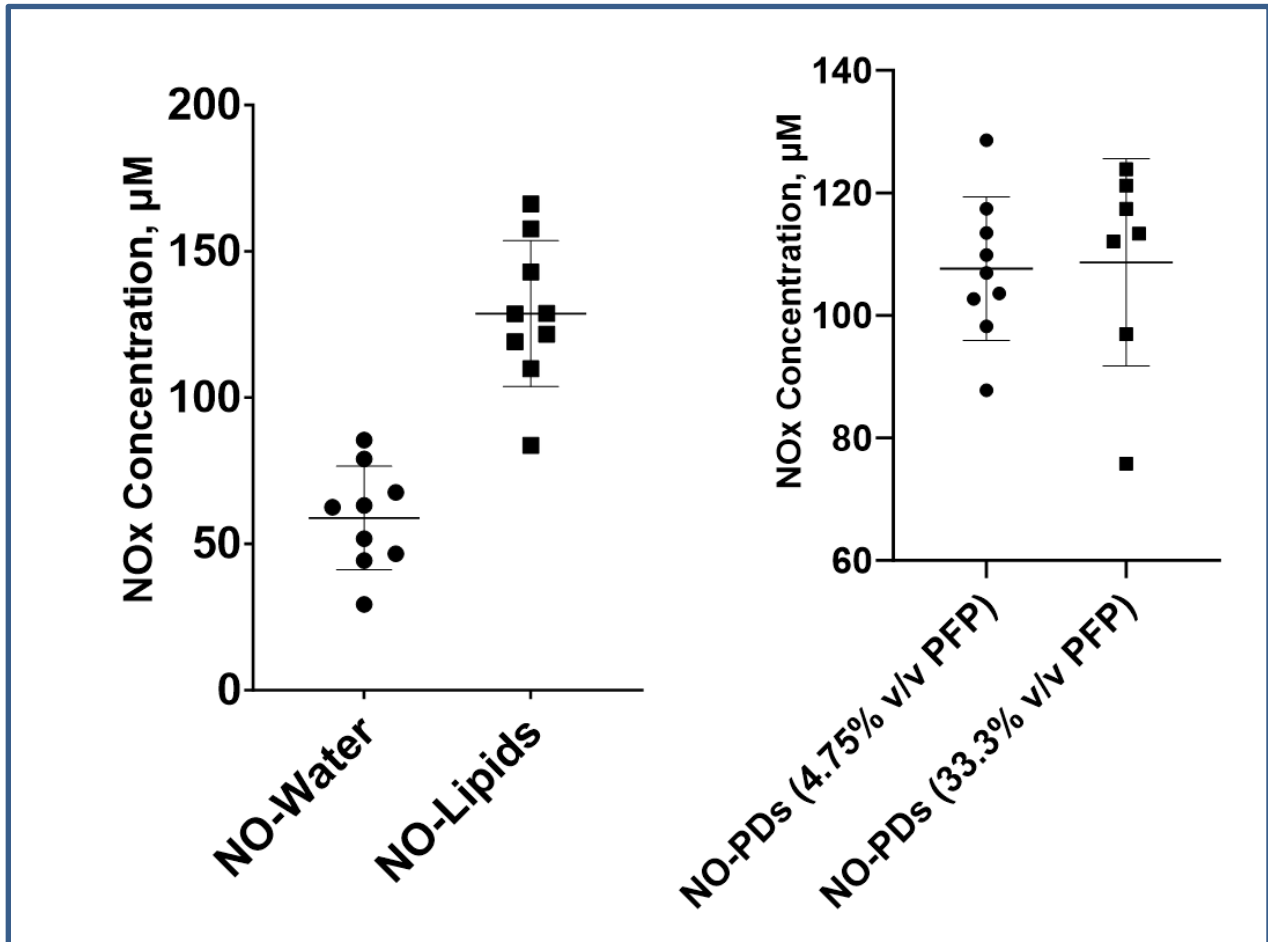
References

[1]. Choi, M., Jazani, A.M., Oh, J.K. and Noh, S.M., 2022. Perfluorocarbon Nanodroplets for Dual Delivery with Ultrasound/GSH-Responsive Release of Model Drug and Passive Release of Nitric Oxide. Polymers, 14(11), p.2240.

[2]. Zhou, Y., 2015. Application of acoustic droplet vaporization in ultrasound therapy. Journal of therapeutic ultrasound, 3(1), pp.1-18.

[3]. Jägers, J., Wrobeln, A. and Ferenz, K.B., 2021. Perfluorocarbon-based oxygen carriers: from physics to physiology. *Pflügers Archiv-European Journal of Physiology*, *473*, pp.139-150.

[4]. Tuteja, N., Chandra, M., Tuteja, R. and Misra, M.K., 2004. Nitric oxide as a unique bioactive signaling messenger in physiology and pathophysiology. *Journal of Biomedicine and Biotechnology*, *2004*(4), pp.227-237.

Bone Cell Response to Perfluoropentane Nanodroplets for Bone Repair

Kirsten E O'Brien[1], _Christopher K Campbell[2], Robin Rumney[3], Eleanor Stride[2], Dario Carugo[2], Nicholas D Evans[1]_

[1]_School of Engineering, University of Southampton, Southampton, UK_
[2]_Nuffield Department of Orthopaedics, Rheumatology and Musculoskeletal Sciences, University of Oxford, Oxford, UK_
[3]_School of Pharmacy & Biomedical Sciences, University of Portsmouth, Portsmouth, UK_

Corresponding author: k.e.obrien@soton.ac.uk

Introduction

Low oxygen tension has been shown to decrease bone forming activity and increase bone resorbing activity [1],[2]. This imbalance results in decreased or reversed bone fracture healing. It is, therefore, integral to restore normal oxygen conditions. Perfluorocarbons are capable of dissolving large amounts of oxygen (approximately 50 times that of water)[3]. However, they are immiscible in most fluids and so they need to be stabilised by a phospholipid membrane to form particulate carriers – such as nanodroplets. The aim of this project was to assess whether the nanodroplets have a non-cytotoxic dose in vitro on cells of osteoblastic and osteoclastic lineage. Additionally, to assess whether nanodroplets are capable of delivering oxygen to bone cells in vitro.

Methods

For nanodroplet fabrication, first lipid films were made by evaporpating chloroform solutions of 18.5 moles of 1,2-distearoyl-sn-glycero-3phosphocoline (DSPC) and 2.05 moles of polyoxyethylene (40) stearate (PEG(40)s) overnight in fume hood. The lipid film was rehydrated using phosphate buffered saline (PBS) to create a final total lipid concentration of 4 mg/mL. The resulting solution was then homogenised by sonicating continuously for 2.5 minutes at the 40% amplitude setting using a Model 120 Sonic Dismembrator with a 3.22 mm diameter sonicator tip. 800 μL of the resulting lipid solution was then placed in a 1.5 mL eppendorf with 40 μL of perfluoropentane (PFP), which was then placed in an ice-water bath. The solution was then pulse sonicated for 1.5 minutes (total on time) at 60% amplitude with a 2 seconds on, 15 seconds off pulse regime. Where loaded nanodroplets were used, oxygen or nitrogen was bubbled through 300 μL of the nanodroplet solution for 1 minute followed by filling the headspace with oxygen or nitrogen for 30 seconds.

To determine oxygen delivery to cells, the relative concentration of hypoxia inducible factor-1α (HIF-1α) in lysates of SAOS-2 cells grown at 1% oxygen were compared to those grown at normoxia in the presence and absence of nanodroplets was measured by SDS-PAGE western blot. HIF-1α and β-actin were detected using antibody chemiluminescence. The HIF-1α expression was measured using densiometry and normalised to β-actin. These results were validated using a vascular endothelial growth factor (VEGF) ELISA.

To test cell viability, alamar blue and DAPI (4′,6-diamidino-2-phenylindole) staining were performed. Bone marrow stromal cells (BMSC) and peripheral blood mononuclear cells (PBMCs) were seeded at 2.5×10^4 and 7.6×10^5 cells/cm^2 respectively and placed overnight in an incubator to adhere. The cells were then treated with a dilution of nanodroplets (0, 0.01, 0.1 and 1% v/v) and placed in either normoxia or hypoxia for 24 or 72 hours. An alamar blue assay was then performed to investigate cell metabolism. DAPI staining was also performed on MC3T3-E1 cells to investigate cell proliferation.
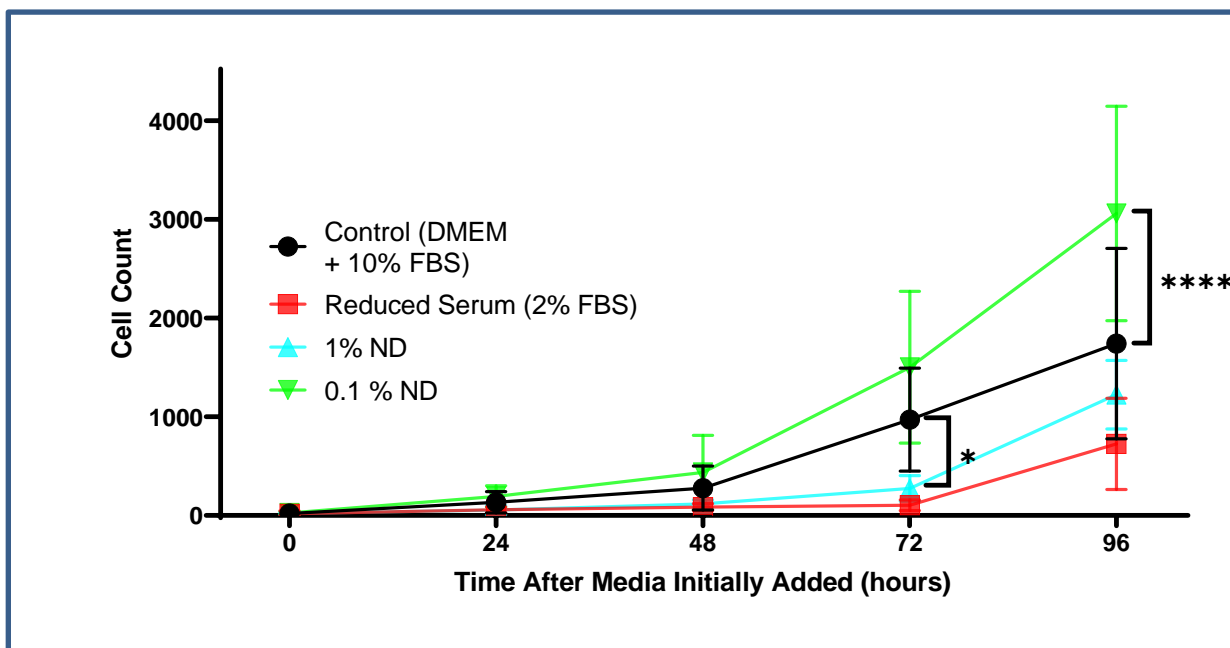
Results

HIF-1α concentration in the presence of air-saturated nanodroplets was found to be 71.8 % ± 10.3 compared ot the absence of droplets in hypoxia (n = 3, p = 0.0414). Interestingly, this was not observed in the oxygen- (113.2% ± 18.6, n=3, P > 0.05) and nitrogen-saturated (95.8% ± 21.1, n=2) groups. This may be due to nanodroplet instability caused by the oxygen and nitrogen loading processes. However, there was no difference in the VEGF expression between the hypoxic control and hypoxic air-saturated nanodroplet groups (n = 3).

The highest concentration (1% v/v) of nanodroplets was found to have a detrimental effect on cell viability in normoxia with decreases in metabolism compared to the no nanodroplet control observed in PBMC and BMSCs (PBMCs: 83.6% ± 9.5, n = 3 p = 0.0648; BMSC: 86.1% ± 16.1, n = 3, p = 0.0702). In MC3T3E1 cells, a decrease in cell proliferation as measured using DAPI was observed in the presence of 1% v/v nanodroplets compared to the control (see Figure 1). Interestingly, in hypoxia, there were no significant decreases in cell metabolism in either BMSCs and PBMCs (97.1% ± 10.3, n = 1; 100.1% ± 16.4, n = 3, p > 0.9999 respectively). Below 1% v/v the nanodroplets were found to have increased or no effect on cell viability.

Conclusions

Nanodroplets were found to have a dose-dependent effect on bone cell viability, with higher concentrations usually leading to reduced metabolism and proliferation. Cells treated with 0.01% v/v air-saturated nanodroplets in hypoxia demonstrated reduced HIF-1α concentration compared to the hypoxic control, suggesting the nanodroplets may be effective in relieving the hypoxic conditions experienced by the cells. However, further work must be done to understand the effect of gas loading on nanodroplet stability .

Figure 1. Results of cell proliferation experiments. The number of nuclei counted using DAPI staining of the nuclei. The 1% and 0.1% ND are percentage volumes added to the DMEM with 10% FBS. The reduced serum was used to demonstrate a growth curve with a reduced growth rate. (n=9).
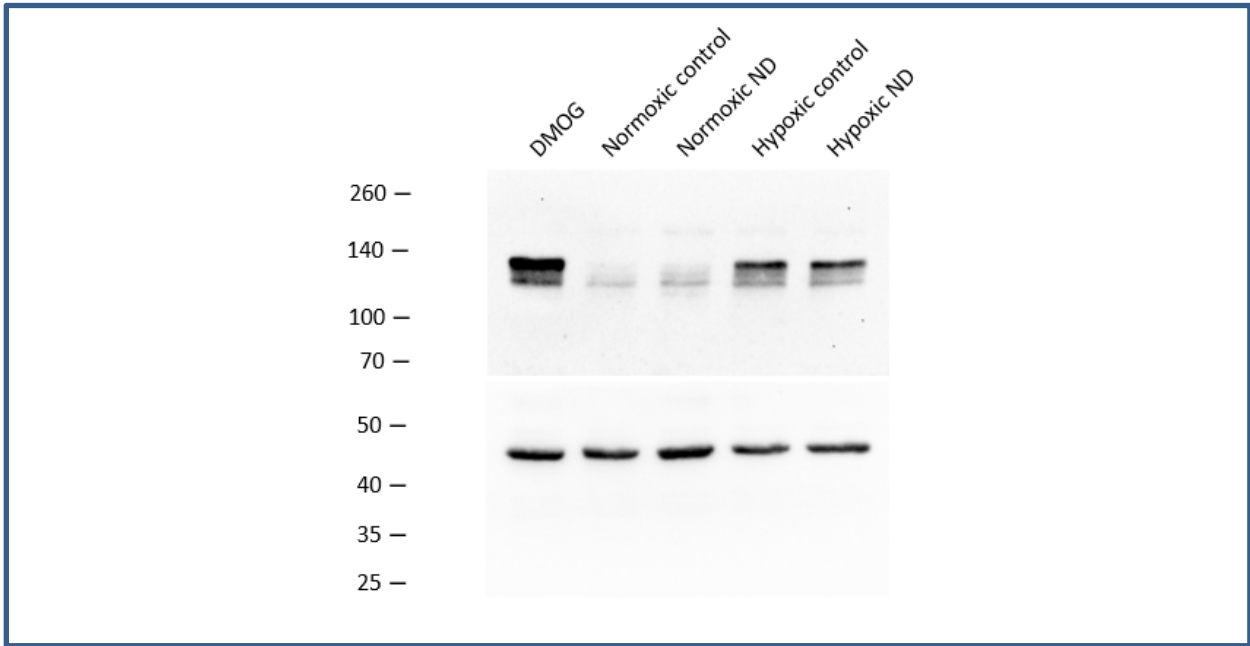
Figure 2. Representative western blot analysing the relative levels of HIF-1α (molecular weight of 120 kDa) and β-actin (molecular weight of 42 kDa)

References

[1]. Utting, J.C., Robins, S.P., Oh, J.K., Brandao-Burch, A., Orriss, I.R., Behar, J and Arnett, T.R., 2006. Hypoxia inhibits the growth, differentiation and bone-forming capacity of rat osteoblasts. Experimental Cell Research, 312(10), p.1693-1702.

[2]. Knowles H.J., Athanasou N.A., 2009. Acute hypoxia and osteoclast activity: a balance between enhanced resorption and increased apoptosis, The Journal of Pathology, 218(2), p256–264.

[3]. Wesseler E.P., Iltis R., Clark L.C., 1977.The solubility of oxygen in highly fluorinated liquids, Journal of Fluorine Chemistry. 9(2), p137–146.

Design of an *ex vivo* Perfusion Chamber for Studying the Effects of Microbubble-Enhanced Ultrasound-Mediated Drug Delivery to Bone

Sam Sloan[1], Simon Tilley[2,3], Fabrice Pierron[1], Dario Carugo[4], Eleanor Stride[4], Richard Oreffo[2], Janos Kanczler[2], Nicholas D Evans[1,2]

[1] *Faculty of Engineering and Physical Sciences, University of Southampton, Southampton, UK;*
[2] *Faculty of Medicine, University of Southampton, Southampton, UK;*
[3] *University Hospital Southampton, Southampton, UK;*
[4] *Nuffield Department of Orthopaedics Rheumatology and Musculoskeletal Sciences (NDORMS), University of Oxford, Oxford, UK*

Introduction

2-5% of all bone fractures result in non-union [1]. Growth factors, such as bone morphogenetic proteins (BMPs), have been proven to induce bone formation and repair; however, a reliable targeted delivery system is needed [1]. Microbubble (MB)-enhanced ultrasound-mediated drug delivery through the vasculature offers a promising strategy for minimally-invasive, targeted delivery of bioactive compounds [2]. Embryonic chick femurs have previously been used as an *ex vivo* model to study delivery of bioactive compounds during fracture healing [3]. Here, we have designed an acoustically and biologically compatible perfusion chamber to house an embryonic chick femur with a fracture to study drug delivery and gene transfection *ex vivo* using ultrasound and microbubbles and MBs. We intend to use this device to study how stimulation of MBs loaded with bone specific therapeutics affects the regeneration of bone in the fracture model.

Methods

Polydimethylsiloxane (PDMS) was used for fabrication of the chamber due to its favourable acoustic and optical properties and biological compatibility. The chamber was manufactured by replica moulding. Design for the PDMS moulds and holder were created in Autodesk Inventor and 3D printed in polylactic acid (PLA). The moulds were then filled with degassed PDMS and cured. Both halves were permanently sealed with super glue (Loctite, Westlake, Ohio, USA) containing an embryonic chick femur, isolated at day 11, with an imposed fracture (Fig. 1A). Flow through the chamber was enabled by a syringe pump connected via 1 mm diameter silicone tubing (Fig. 1B). The system was immersed in a system for acoustic transfection (SAT) for ultrasound exposure (Fig. 1B) [4].

MBs were generated through sonication of 1,2-distearoyl-sn-glycero-3-phosphocholine (DSPC) and polyoxyethylene (40) stearate (PEG40s) in a 9:1 molar ratio. The chamber was exposed to ultrasound of frequency 900 kHz, duty cycle 30%, and pulse length 300 μs. Peak negative pressures of 0.1, 0.4, 0.7 and 1 MPa (in the absence of flow) were tested. A peak negative pressure of 1 MPa was used for tests with perfusion at flow rates of 1, 2 and 4 mL/min. A peak negative pressure of 1 MPa and a flow rate of 4 mL/min were used to test microbubble concentrations of 1.57×10^6, 7.9×10^6 and 1.57×10^7 MBs/mL (100×, 50×, and 10× dilutions of the stock concentration respectively). The ultrasound response of MBs was detected by passive cavitation detection (PCD) using an immersion transducer (5 MHz Imersion Transducer V326-SU, Olympus Panametrics, Southend-on-Sea, Essex, UK). From the detected acoustic signals, the 2nd, 3rd and 4th harmonics of the power spectrum were isolated and the total power was also compared between experiments.

Results

In the no flow condition with increasing peak negative pressures, a corresponding increase in the amplitude of the harmonics was detected at pressures 0.1 ($p < 0.05$), 0.4 ($p < 0.001$), 0.7 ($p < 0.01$) and 1.0 MPa ($p < 0.01$) indicating successful bubble stimulation within the chamber within a therapeutically relevent pressure range. A significant increase was also detected in the harmonics at a peak negative pressure of 1.0

MPa and flowrates of 1 ($p < 0.05$), 2 ($p < 0.01$) and 4 mL/min ($p < 0.001$) and this remained steady over time, indicating successful perfusion of bubbles through the chamber enabling constant replenishment. Similarly, a significant increase was also observed in the harmonics at a peak negative pressure of 1 MPa and a flowrate of 4 mL/min at concentrations of 1.57×10^7 ($p < 0.05$), 7.9×10^6 ($p < 0.05$) and 1.57×10^6 MBs/mL ($p < 0.05$) wth a no significants observed between the various concentrations, indicating successful stimulations at therapeutically relevant concentrations, flow rates and pressures.

Conclusions

An acoustically compatible perfusion chamber has been designed for the study of enhanced drug delivery to an embryonic chick femur using ultrasound and MBs. MBs could be stimulated acoustically and their response detected within the chamber at therapeutically relevant acoustic pressures, perfusion flow rates, and MB concentrations. This chamber will be used in future research to study the delivery of model therapeutics, such as green fluorescent protein plasmids (pm-eGFP,) whose enhanced uptake in bone due to ultrasound responsive MBs has been previously observed *in vivo* [5]. Further to this, the chamber will be used to study the delivery of bone specific therapeutics, such as BMP genes, which have previously been shown to induce bone regeneration [6].
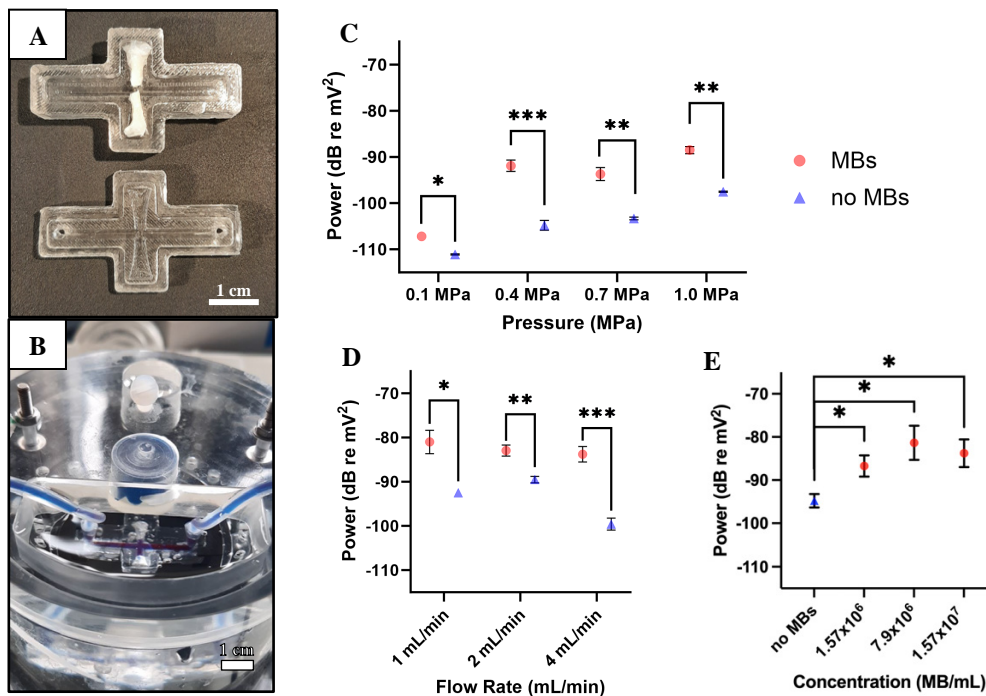
Figure 1. A) Top and bottom halves of the perfusion chamber, moulded in PDMS and containing a embryonic chick femur, isolated at day 11 and fixed in paraformaldehyde (PFA), positioned across the channel. B) PDMS chamber and housing mounted within the SAT with silicone tubing for perfusion inserted. The blue food colouring indicates the perfusion channel through the chamber. The contribution of the harmonics to the power spectrum is shown at C) the no flow conditions at peak negative pressures of 0.1 MPa, 0.4 MPa, 0.7 MPa and 1.0 MPa,; at D) a peak negative pressure of 1.0 MPa and flowrates of 1 mL/min, 2 mL/min and 4 mL/min; and at E) a peak negative pressure of 1 MPa, flowrate of 4 mL/min and concentrations of 1.57×10^7 MBs/mL, 7.9×10^6 MBs/mL and 1.57×10^6 MBs/mL. Data points represent mean ± SD. * $p < 0.05$, ** $p < 0.01$, *** $p < 0.001$.

References

[1]. B. Wildemann, A. Ignatius, F. Leung, L. A. Taitsman, R. M. Smith, R. Pesántez, M. J. Stoddart, R. G. Richards, and J. B. Jupiter, "Non-union bone fractures," 12 2021, https://doi.org/10.1038/s41572-021-00289-8

[2]. Mitragotri, S. (2005). "Healing sound: the use of ultrasound in drug delivery and other therapeutic applications. Nature Reviews Drug Discovery", 4, 255–260, https://doi.org/10.1038/nrd1662

[3]. Smith, E. L., Kanczler, J. M., Gothard, D., Roberts, C. A., Wells, J. A., White, L. J., Qutachi, O., Sawkins, M. J., Peto, H., Rashidi, H., Rojo, L., Stevens, M. M., el Haj, A. J., Rose, F. R. A. J., Shakesheff, K. M., & Oreffo, R. O. C. (2014). "Evaluation of skeletal tissue repair, Part 1: Assessment of novel growth-factor-releasing hydrogels in an ex vivo chick femur defect model". *Acta Biomaterialia*, *10*(10), 4186–4196. https://doi.org/10.1016/j.actbio.2014.06.011

[4]. Gray, M., Vasilyeva, A. V., Brans, V., Stride, E. Studying Cavitation Enhanced Therapy. J. Vis. Exp. (170), e61989, http://doi:10.3791/61989 (2021).

[5]. Bez, Maxim, et al. "In situ bone tissue engineering via ultrasound-mediated gene delivery to endogenous progenitor cells in mini-pigs." Science translational medicine 9.390 (2017): eaal3128.

[6]. Wegman, F., et al. "Osteogenic differentiation as a result of BMP-2 plasmid DNA based gene therapy in vitro and in vivo." Eur Cell Mater 21 (2011): 230-242.

Ultrasound-Targeted Microbubble Cavitation-Mediated Blood-Brain Barrier Opening for Drug Delivery in Alzheimer's Disease

Grace E. Conway[1], _Xucai Chen[1]_, _Stacey J. Sukoff Rizzo[2,3]_, _Afonso C. Silva[2]_, _Flordeliza S. Villanueva[1]_

[1]_Center for Ultrasound Molecular Imaging and Therapeutics, University of Pittsburgh, Pittsburgh, PA, USA_
[2]_Department of Neurobiology, University of Pittsburgh, Pittsburgh, PA, USA_
[3]_Department of Geriatric Medicine, Aging Institute, University of Pittsburgh, Pittsburgh, PA_
Corresponding author: villanuevafs@upmc.edu

Introduction

Drug delivery for neurological diseases, such as Alzheimer's disease (**AD**), is challenging due to restricted diffusion across the blood-brain barrier (**BBB**). One method for transiently penetrating the BBB is ultrasound-targeted microbubble cavitation (**UTMC**), where focused ultrasound (**FUS**) is applied to the brain as intravenously injected microbubbles (**MB**s) traverse the microcirculation. We hypothesized that opening the BBB with UTMC would increase the brain concentration of an orally administered drug previously developed for AD (LY2886721, a β-site amyloid precursor protein cleaving enzyme 1 [**BACE1**] inhibitor) using a murine model of AD.

Methods

Male and female 5XFAD mice at 6 months of age (JAX stock#034848) were used in the following three studies. These mice overexpress human familial mutations in the *APP* and *PSEN1* genes resulting in an early onset phenotype of accumulation of Aβ plaques in the brain.

First, to define the pharmacokinetics and half life ($t_{1/2}$) of the drug, 5XFAD mice ($n=8$ per sex) were dosed with LY2886721 (10 mg/kg p.o.), and blood was collected at 15, 30, 60, 120, 240, and 480 min. The concentrations of LY2887821 in plasma and terminal brain homogenates were measured via liquid chromatography with tandem mass spectrometry.

Second, to determine the correlation between plasma and brain drug concentrations, 5XFAD mice ($n=6$) were administered LY2886721 (10 mg/kg or 30 mg/kg p.o.), and terminal brain and plasma samples were collected at $t_{1/2}$ (2.5 h). Simple linear regression and Pearson correlation coefficient were performed.

In the third series of experiments, we opened the BBB in the right brain hemisphere of 5XFAD mice using an RK-50 system (FUS Instruments Inc, Toronto, ON, Canada) equipped with a passive cavitation detection probe. Definity microbubbles (0.25 µL/g) (Lantheus, N Billerica, MA) were injected i.v. and FUS (1.45 MHz, 2 Hz pulse repetition frequency, 10 ms pulse length, 0.6 MPa for 30 s) was applied to each of 11 spots across the right hemisphere. The cavitation dose was quantified in the 0.7250 ± 0.0002 MHz subharmonic bandwidth. 30 minutes after BBB opening, mice ($n=8$) were administered LY2886721 (30 mg/kg p.o.). After 45 minutes, terminal brain hemispheres were collected and analyzed for the concentration of LY2886721. A two-sided paired t-test was performed for comparison of UTMC-treated and un-treated hemispheres. Significance was defined as $p<0.05$.

Results

The half-life ($t_{1/2}$) of LY2886721 in 5XFAD mice was determined to be 2.5 h. There was a positive correlation between terminal plasma and brain concentrations of LY2886721 across doses in 5XFAD mice ($r=0.96$; $R^2=0.92$). For BBB experiments, the subharmonic cavitation dose was similar across the 11 treatment spots (**Figure 1A**). After BBB opening, there was an increase in the concentration of LY2886721 in the UTMC-treated hemisphere compared to the non-UTMC treated hemisphere ($p=0.021$; **Figure 1B**). Sex related differences will be discussed. Data on the effect of enhanced LY2886721 with UTMC on Aβ plaque burden are forthcoming.

Conclusions

UTMC can be used to open the BBB in 5XFAD mice and increase the brain concentration of LY2886721, a BACE1 inhibitor that has previously been reported to decrease pathologic Aβ brain concentrations in preclinical studies of AD. Ultimately, using UTMC to open the BBB and to concentrate drugs in the brain may not only enhance the therapeutic effect of otherwise impermeant drugs but also lower the systemic dose requirements for therapeutic efficacy, diminishing the risk for toxicity and off-target effects.
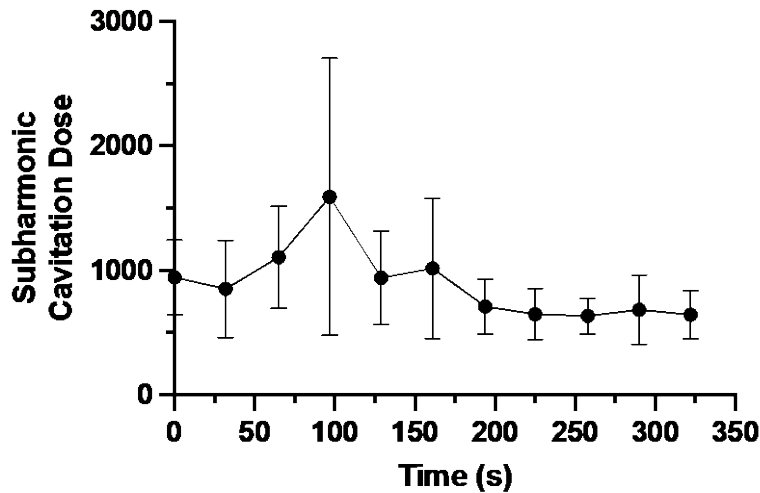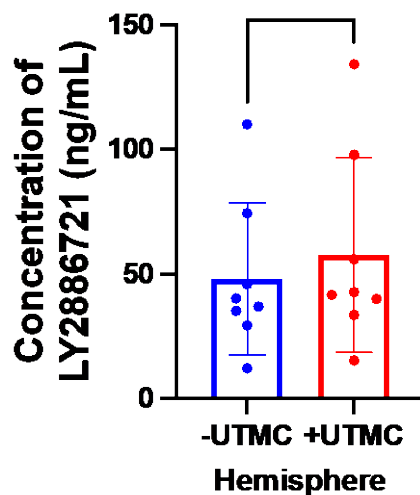
Figure 1. UTMC opened the BBB to deliver LY2886721 to the brain. Data represents mean ± SD (n=8). *p<0.05. (A) Subharmonic cavitation dose was consistent across the 11 treatment locations in the right brain hemisphere. (B) There was an increase in brain concentration of LY2886721 in the UTMC-treated hemisphere compared to non-UTMC treated hemisphere in 5XFAD mice.

Feasibility of ultrasound-mediated oral biopharmaceutical delivery: In-vitro gastrointestinal stability of microbubbles

Colm S. O'Reilly[1], Abdul Basit[2], Mine Orlu[2], Eleanor Stride[1,3], Gareth LuTheryn[1], Michael Gray[3], Dario Carugo[1]

[1]*NDORMS, Medical Sciences Division, University of Oxford, Oxford, United Kingdom*
[2]*UCL School of Pharmacy, University College London, London, United Kingdom*
[3]*Institute of Biomedical Engineering, University of Oxford, Oxford, United Kingdom*
Corresponding author: colm.oreilly@ndorms.ox.ac.uk

Introduction

Despite a century of research, oral biopharmaceutical formulations are largely absent in the clinical setting [1].

Ultrasound-mediated gastrointestinal (GI) delivery has recently demonstrated potential to improve macromolecule uptake ex-vivo and in-vivo using ultrasound alone [2]. Ultrasound responsive agents, like shelled gas microbubbles, undergo volumetric oscillations (or cavitation) when exposed to ultrasound and can transiently permeabilise biological barriers to improve drug absorption. These agents could therefore potentially promote GI delivery, reduce the ultrasound intensities required, and enable drug encapsulation or targeting.

To the best of the authors' knowledge, microbubble behaviour in the gastrointestinal tract has not been widely investigated. Hence the aim of this study was to assess the stability of microbubbles in simulated gastrointestinal media.

Methods

Dried films, comprising DSPC and PEG-40-Stearate with a molar ratio of 9:1, were suspended at a concentration of 4 mg/ml in simulated gastrointestinal media. Microbubbles, encapsulating room air, were generated using a tissue homogeniser. Microbubble suspensions were incubated at 37 °C and the size and concentration were measured at timepoints over 24 hours via optical microscopy and image analysis using an ImageJ macro.

The protocol was refined to enable removal of unincorporated lipids and phosphate buffered saline from the microbubble suspension via centrifugal washing and then resuspending the microbubble cake in simulated gastrointestinal media to solely examine stability rather than formation and stability in the previous protocol. Microbubble suspensions were again stored at 37 °C and the size and concentration measured over 24 hours via a Coulter counter (Multisizer, Beckman-Coulter).

Results

In both studies, the mean microbubble diameter increased over time while the microbubble concentration decreased over time which is the typical change of a microbubble population due to Ostwald ripening. In the first study, 0.1M Hydrochloric acid (pH 1.2), simulating the acidic environment of the stomach, had a statistically significant effect on microbubble concentration, indicating that acidic pH may influence microbubble formation during agitation. The subsequent study found no significant changes in concentration stability profiles between PBS and simulated gastrointestinal media as seen in Figure 1.

Work is in progress examining the effect of fasted and fed state simulated gastrointestinal media on microbubble stability.

Conclusions

DSPC-PEG-40-Stearate (9:1) room air microbubbles manufactured via tissue homogenisation were found to be sufficiently stable over a period of 24 hours in biorelevant simulated gastrointestinal media, with microbubble concentration remaining above 10^9 particles/ml.
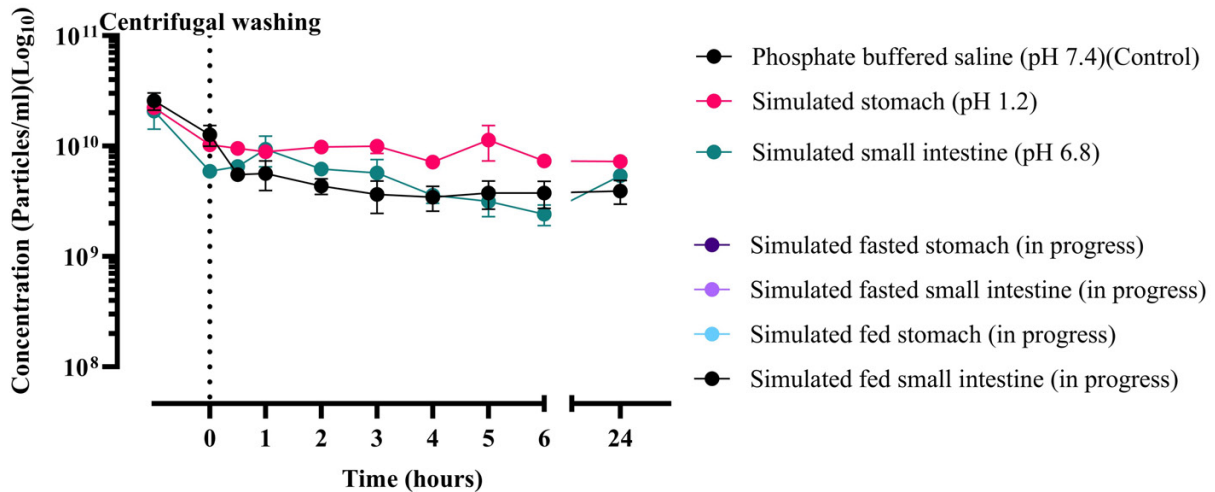
Figure 1. Stability profile of DSPC-PEG-40-Stearate (9:1) room air microbubbles in simulated gastrointestinal media.

References

[1]. Vllasaliu D, Thanou M, Stolnik S, Fowler R. Recent advances in oral delivery of biologics: nanomedicine and physical modes of delivery. Expert Opinion on Drug Delivery [Internet]. 2018;15(8):759–70. Available from: https://dx.doi.org/10.1080/17425247.2018.1504017

[2]. Schoellhammer CM, Schroeder A, Maa R, Lauwers GY, Swiston A, Zervas M, et al. Ultrasound-mediated gastrointestinal drug delivery. Science Translational Medicine [Internet]. 2015;7(310):310ra168–. Available from: https://dx.doi.org/10.1126/scitranslmed.aaa5937

Microbubble Mediated Mechanical Removal Of Oral Biofilms *In-Vitro*

D. De Grandi[1], G. LuTheryn[2], M. Stoffels[3], M. Born[3], B. Gottenbos[3], D. Carugo[2], E. Stride[1]

[1]BUBBL group, IBME, University of Oxford, Oxford, UK
[2]Nuffield Department of Orthopedics, Rheumatology and Musculoskeletal Sciences (NDORMS),
University of Oxford, Oxford, UK
[3]Philips Oral Healthcare, Eindhoven, Netherlands
Corresponding author: davide.degrandi@eng.ox.ac.uk

Introduction

Most bacteria can live both in sessile (attached) and planktonic (in suspension) states. In their sessile state, bacteria undergo phenotypic modifications that allow them to live in surface-attached multicellular communities defined as 'biofilms', where bacteria are encased in a self-produced matrix of extracellular polymeric substances (EPS). Biofilms stratified structure, ability to chemically communicate by quorum sensing (QS) and adapt to survive in adverse conditions, determine significantly increased resistance to traditional chemotherapy. It has been estimated that up to 80% of chronic human infections are determined by surface attached biofilms [1], and oral biofilm-related infections are among the most common diseases worldwide.

The oral microbiota is comprised of both commensal and pathogenic bacteria, that live attached to teeth and soft tissue surfaces forming complex and long-lasting biofilms. When the homeostasis of the oral microbiota is broken (*e.g.* due to prolonged exposure to saccharose and low pH), there is a shift in the microbial community composition that lead to pathogenic plaque formation. Pathogenic oral biofilms are linked to the onset of most infectious oral diseases. Despite some promising anti-plaque methods being developed [2], the lack of truly efficacious and widely available therapeutic options to eradicate and prevent plaques constitutes an unmet need for safe and effective treatment of oral infections.

At present, the gold standard treatments for plaque related pathologies, are mechanical debridement and planing of the teeth surface and root. Most treatment cycles include surgical removal of the damaged tissue and mechanical occlusion of the exposed tissue with specialized resins. Although such treatments can effectively limit the impact of dental biofilm-related pathologies, they show several limitations, such as gum recession, enamel thickness reduction, root and dentine sensitization, difficulty in debriding / scaling / planning of the subgingival and interstitial space, modified enamel and dentine surface roughness following treatment, and dispersion of viable bacteria from the biofilm that often lead to secondary infections.

Streptococcus mutans is a facultatively anaerobic, gram-positive coccus. It is generally a commensal bacterium of the oral cavity but when the homeostasis of the microbiome is broken, it can express pathogenicity determinants and induce damage to surrounding tissues. At least 25 species of *Streptococcus* are normally present in the oral cavity, but *S. mutans* is the most prevalent, accounting for up to ~40% of the total *Streptococci* in the oral microbiome. For this reason, monospecies *S. mutans* biofilms are widely accepted as a simple oral-biofilm model in the scientific community, with the caveat that a short lived and monospecies biofilm cannot represent adequately the biodiversity and mechanical properties of the plaque, and for this reason should be considered as a starting point for optimization rather than a representation of the *in vivo* conditions.

Given the high human and economic impact of oral biofilm-related infectious pathologies worldwide, alternative methods for dental plaque removal are a research area of great interest. In this work we hypothesise that ultrasound induced cavitation of gas microbubbles can be employed as an effective modality for mechanical removal of oral biofilms from the tooth surface. To test this hypothesis we developed an in-vitro apparatus that can apply a well-defined ultrasound field to oral biofilm models grown on tooth-mimicking surfaces.

Methods

The work can be divided into three main sections: ultrasonic set-up design and characterization, relevant biofilm model selection, and treatment optimization.

For this work a single species biofilm composed of *S. mutans* (ATCC-25175, LGC Limited, Queen's Road, TW11 0LY, United Kingdom), was grown on a hydroxyapatite (HA) disc (HAD70, HIMED, 148 Sweet Hollow Road, NY 11804, USA), which was used as a tooth mimicking surface. Bacteria were cultured on brain heart infusion (BHI) agar for 48 hours (37 °C, 90% humidity, 5% CO_2). A single colony was selected from the plate and transferred into 5 ml of BHI spiked with 1% sucrose in 75 mM HEPES (pH 7.5) for 24 h. The liquid culture was then diluted to 0.01 OD (600 nm) and seeded over the HA substrate, in a 24 well-plate. The biofilm was grown statically for 24 h.

Microbubbles were prepared by dissolving dipalmitoylphosphatidylcholine (DPPC) and polyoxyethylene-(40) stearate (PEG40S) in chloroform in 9:1 molar ratio. Chloroform was then evaporated and the obtained lipid film redispersed in DPBS:propylene glycol:glycerol (8:1:1 volume ratio) at 85 °C, to a final concentration of 1 mg/ml of lipids. The lipid mix was then placed in gas tight 2 ml vials (1 ml of suspension in each vial), which can be stored at 4°C for up to a month. For microbubbles production, the head space of the vial was saturated with perfluorobutane (PFB), the vial was shaken using a tissue homogenizer (Precellys® Evolution Homogenizer, Bertin Exensor UK) for 45s at 10,000 rpm. During the production process and after manufacturing, the microbubble suspension must be kept in an ice bath. Microbubble concentration and size were estimated using a Multisizer 4e Coulter Counter (Beckman Coulter, IN 46268, United States). Microbubbles were diluted to a final concentration of 10^8 bubbles/ml immediately before usage. The obtained microbubbles had a 0.89 μm ± 0.02 μm mean equivalent spherical diameter.

The treatment consisted of submerging the HA disc in ~2 ml of bubbles suspension, in the configuration represented in Figure 1B. The disc is placed at the focus of a HIFU transducer (H107,0.5 MHz fundamental frequency, 63.2 mm geometrical focus, 64 mm active element diameter, custom rectangular cut out of 22×57 mm, Sonic Concepts Inc., Washington, USA). Ultrasound (US) parameters for this work were: driving frequency of 0.5 MHz, 1000 cycles per burst, pulse repetition frequency (PRF) of 5 Hz, duty cycle (DC) of 1%, and peak negative pressure (pnp) between 0.2 and 2.0 MPa. Total treatment time was fixed at 60 seconds. The negative control was treated in the same way as all the other sample but without US exposure.

Treatment outcomes were evaluated through fluorescence imaging (Nikon Eclipse Ti2 inverted microscope, Nikon digital sight 50M camera, CFI Plan Fluor 4X objective, Nikon UK, Branch of Nikon Europe B.V.). The bacteria were stained before each imaging session using two DNA binding stain, Syto9 and Propidium Iodide (PI) (Filmtracer™ LIVE/DEAD™ Biofilm Viability Kit, Fisher Scientific UK Ltd) following manufacturer instructions. Excitation and emission wavelength windows used for Syto9 and PI were 465-495 nm and 528-553 nm, 515-555 nm and 577-630 nm, respectively.

After imaging, a custom Python script was developed and used to process the images and evaluate the number and area of bacterial clusters covering the HA disc surface.
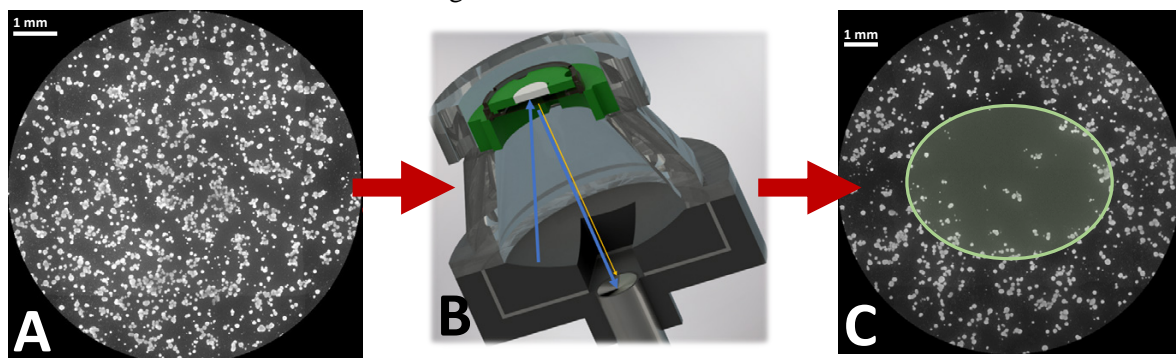
Figure 1. A) Live/dead stained biofilm pre-treatment (in this image only Syto9 channel is shown) B) Experimental set-up developed for the exposure of biofilms (grown on tooth-mimicking susbtrates) to ultrasound and/or ultrasound-responsive particles and C) Live/dead stained biofilm post-treatment (in this image only Syto9 channel is shown). The green area at the centre represents the dimension of the focal region (half maximum region) of the US field.

Results

We developed a reproducible protocol for *S. mutans* biofilm formation on a HA surface. The protocol yielded a surface coverage of ~ 13.6% ± 3.4. Only clusters consisting of more than ~40 cells (~8 pixels diameter) were considered in the calculation, to exclude fluorescent signals coming from "salt and pepper" noise, which is hardly discerned from signals from small bacterial clusters at the magnification used in this work.

After some preliminary tests (not presented here), we determined a suitable set of parameter values for initial US treatments to be: 10^8 bubbles/ml, 0.5 to 1.5 MPa pnp, 1000 cycles per burst, and PRF 5 Hz (1% DC). As presented in Figure 2 and 3, there is a positive correlation between the total energy of acoustic emissions generated by cavitating microbubbles and the percentage of biofilm removed from the substrate. Exposure of the biofilm to 0.5 MPa pnp did not affect the biofilm adhesion to the substrate, whereas samples treated at 1.0 and 1.5 MPa pnp were significantly different in appearance from the control (which is exposed to the same microbubble dispersion for 60 seconds, but without US).
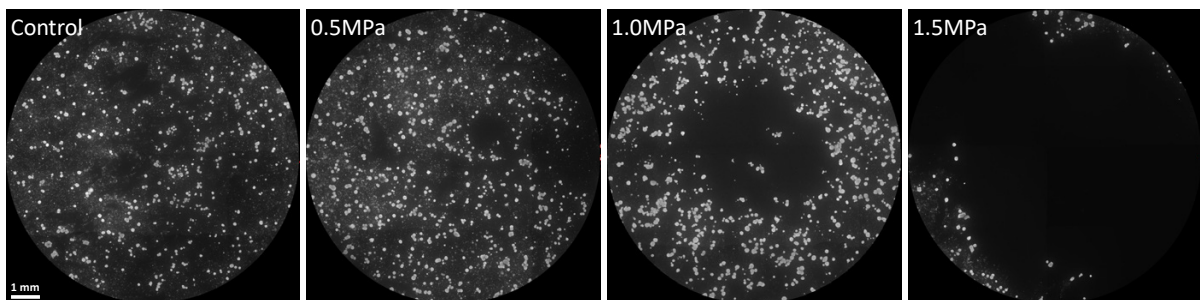

Figure 2. Syto9 stained biofilm post-treatment. Interestingly, at 1.0 MPa pnp, the region showing complete biofilm removal overlays with the half maximum focal region of the US field, whereas when the pressure is increased to 1.5 MPa pnp the area of removal extends significantly.
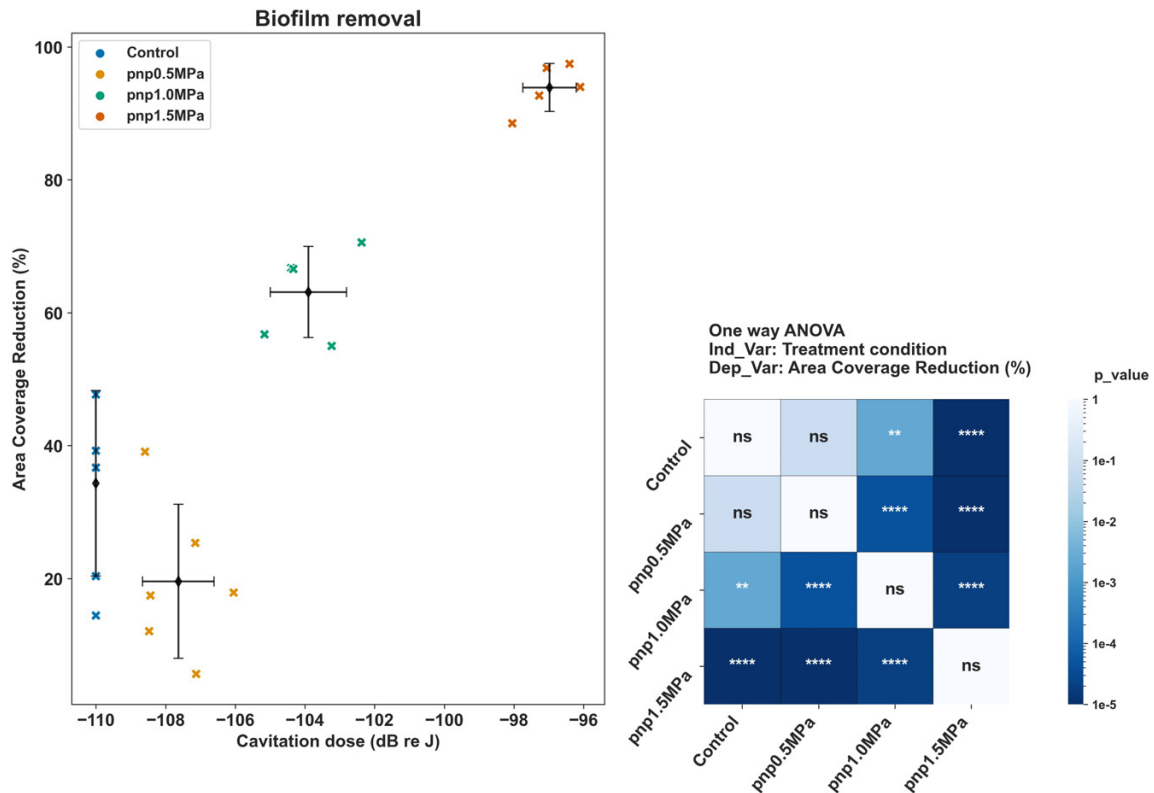
Figure 3. Biofilm reduction from HA substrate following microbubble cavitation. In the plot, the "X" represent a single data point, the diamond represent the mean energy and mean reduction in area covered by bacteria for each treatment condition, the brakets represent the mean ± std. pvalue<0.0001 is represented as ****, pvalue<0.01 is represented as **.

Conclusions

We demonstrated that exciting microbubbles at low duty cycles and relatively low acoustic pressures can mechanically damage biofilms formed on a tooth mimicking hard surface. We also demonstrated that the effect of cavitation can be either restricted to the focal spot of the US field or affect a much larger area, depending on the peak negative pressure applied. This finding is promising as US induced cavitation could improve the removal of plaque in hard-to-reach crevices in the oral cavity.

References

[1]. M. Jamal et al., 'Bacterial biofilm and associated infections', J. Chin. Med. Assoc., vol. 81, no. 1, pp. 7–11, Jan. 2018, doi: 10.1016/j.jcma.2017.07.012.

[2]. D. Berger, A. Rakhamimova, A. Pollack, and Z. Loewy, 'Oral Biofilms: Development, Control, and Analysis', High-Throughput, vol. 7, no. 3, Art. no. 3, Aug. 2018, doi: 10.3390/ht7030024.

The antibiofilm effects of nitric oxide donors in combination with an ultrasound-responsive system for the treatment of chronic wound infections

Aaron Crowther[1], Gareth LuTheryn[2], Davide De Grandi[3], Sara Keller[3], Tanveer Tabish[4], Christopher K. Campbell[2], Maryam Parhizkar[1], Dario Carugo[1,2]

[1]School of Pharmacy, Department of Pharmaceutics, University College London, London, United Kingdom
[2]Nuffield Department of Orthopaedics, Rheumatology and Musculoskeletal Sciences (NDORMS), University of Oxford, Oxford, United Kingdom
[2]Institute of Biomedical Engineering, University of Oxford, Oxford, United Kingdom
[4]Division of Cardiovascular Medicine, Radcliffe Department of Medicine, University of Oxford, Oxford, United Kingdom
Corresponding author: aaron.crowther.21@ucl.ac.uk

Introduction

Bacterial biofilms are a major global health concern, responsible for approximately 80% of all recorded chronic and recurrent microbial infections. One example of a clinically significant biofilm-associated infection is the chronic wound. Biofilms in chronic wounds disrupt the normal healing process, giving rise to infection-related morbidity and mortality. Many novel antibiofilm agents have been reported in the literature, notably nitric oxide (NO) gas which has shown efficacy in biofilm dispersal and wound healing through lipid peroxidation, DNA cleavage, and protein dysfunction but has limited clinical applicability due to its short half-life, instability, and fast diffusion rate *in vivo*. There has also been a growing interest in the antibiofilm effects of microbubbles (MBs), with some promising results on NO-loaded MBs; however, the antibiofilm efficacy of these formulations have been limited by various drawbacks, e.g. limited stability, and burst release over short durations. To overcome these limitations, in this study we evaluate the antibiofilm effects of NO donors including propylamine propylamine NONOate (PA-NO) and spermine NONOate (SP-NO), which release NO in an acid-catalyzed manner, for the prospective integration into an ultrasound-responsive system.

Methods

The Griess assay was used to confirm NO release from candidate NONOates and investigate the pH-dependence of decomposition, investigating pH levels 5.5, 6.5, and 7.5. A chemiluminescence NO analyzer (NOA) was used to quantify the total amounts of NO released from NONOates. To assess the antibiofilm effects of the NO donor candidates, *Pseudomonas aeruginosa* (PAO1) biofilms were grown for 24 hours in 96-well microplates. Biofilms were treated with 250 µM PA-NO and SP-NO at pH levels 5.5, 7.5, and 8.5, for 60- and 120-min. Biofilms were then stained with crystal violet solution and absorbance was measured to represent total biomass. Antibiofilm efficacy was assessed at both 37 °C and, the more wound-relevant temperature, 32 °C. Minimum inhibitory concentration (MIC) and minimum biofilm eradication concentration (MBEC) experiments are ongoing to assess the efficacy of antibiotics gentamicin and tobramycin in combination with candidate NONOates. The stability of cationic MBs (comprising DSPC, DSEPC, and PEG40S) was evaluated for 2 hours at room temperature by measuring MB diameter and concentration. The spatial parameters of the acoustic field for a 1.1 MHz focused transducer coupled to an Ibidi dish through a water-filled cone, were calibrated to estimate the acoustic pressure delivered to the biofilm at the base of the dish. Passive cavitation detection (PCD) tests are ongoing to determine the effects of incubation time on microbubble cavitation activity in proximity to a biofilm.

Results

The Griess assay showed decreasing amounts of NO detected as the pH of the NONOate solution was increased. No biofilm dispersal was observed after 60-min treatment, at all pH levels assessed; however, extending the treatment time to 120 min showed significant biomass reductions for 250 μM PA-NO, and SP-NO, at 37 °C and pH 7.5. Assessing biofilm dispersal at 32 °C also showed 120-min treatment with 250 μM PA-NO and SP-NO at pH 7.5 to be the most optimal conditions for biomass reduction. Initial MIC and MBEC data show significantly higher concentrations of antibiotic-only solutions are required to produce an inhibitory effect on bacterial cells in biofilm compared to planktonic cells. As NONOate treatment timescale requirements were observed to be at least 120 minutes, the effect of a pre-exposure MB incubation period of 120 minutes on MB stability was assessed. MB stability studies showed MB diameter increased from 2.2 μm to 3.3 μm, and MB concentration decreased from 2.3×10^8 MB/mL to 6.8×10^7 MB/mL within 120 minutes. Experiments are ongoing to determine the effects of a pre-exposure incubation period on microbubble cavitation activity.

Conclusions

The work presented here highlights the potential for NONOates to be used as an antibiofilm therapy in combination with an ultrasound-responsive system, for the first time. The antibiofilm effects of NONOates have been assessed in wound-relevant conditions, assessing pH as a variable, and investigating a temperature that is more consistent with those reported *in vivo*. Ongoing work is assessing the potentiation effects of NONOates on antibiotic efficacy, and the effect of a pre-exposure incubation period on the antibiofilm efficacy of MBs. Future work will investigate both the antibiofilm and antimicrobial effects of a combination therapy consisting of NONOate, antibiotic, and MBs for the treatment of chronic wound biofilms.

Mechanisms regulating ultrasound targeted microbubble cavitation-induced endothelial hyperpermeability

Anurag N. Paranjape, Xucai Chen, Flordeliza S. Villanueva

Center for Ultrasound Molecular Imaging and Therapeutics, University of Pittsburgh, Pittsburgh, PA, USA
Corresponding author: villanuevafs@upmc.edu

Introduction

Ultrasound (US)-targeted Microbubble Cavitation (UTMC) plays a crucial role in improving drug delivery through the endothelial barrier. To successfully apply this technique in clinical settings, we need a deeper understanding of the molecular mechanisms that govern UTMC-induced hyperpermeability. Here we explored the involvement of calcium and endothelial nitric oxide synthase (eNOS) pathways in regulating UTMC-induced endothelial hyperpemeability.

Methods

Human coronary artery endothelial cells were seeded abluminally on transwells with 0.4 μm pores, and US was applied using a single-element transducer (A302S-SU, 1-inch diameter) submerged in a water tank for 10 seconds (1 MHz, 250 kPa PNP, 10 cycles, 10 ms interval). Permeability was gauged through transendothelial electrical resistance (TEER) and 10 kDa dextran transfer. Immunostaining for VE-cadherin was done to quantify inter-endothelial gaps. Visualization of Ca^{2+} with Fluo4-AM, and sonoporation with propidium iodide were done with live-cell imaging. Stress fibers were visualized using phalloidin staining, while s-nitrosylation was assessed with Biotin switch assay.

Results

Transwell-based assays revealed that UTMC induced hypermeability, as shown by a significant reduction in transendothelial electrical resistance and an elevation in 10 kDa Texas red dextran flux. UTMC induced a notable influx of Ca^{2+}, a response that was effectively inhibited by blocking Piezo1 channels ($p<0.0001$) using GsMTx4. Immunostaining demonstrated that under the influence of UTMC, VE-cadherin underwent a reorganization from a predominantly linear to an interrupted pattern, a well-known characteristic associated with hyperpermeability. This reorganization was concurrent with increased stress fiber formation, a process dependent on Ca^{2+} influx, suggesting heightened cell contraction as a contributing factor to gap formation. Furthermore, our observations indicate that UTMC increases the production of nitric oxide (NO), and the inhibition of endothelial nitric oxide synthase (eNOS) using L-NAME nullifies the hyperpermeability induced by UTMC. Preliminary findings suggest that UTMC induces a rise in overall S-nitrosylation, a phenomenon that was dependent on Ca^{2+} influx. Notably, colocalization studies reveal an increased S-nitrosylation of both β-catenin and VE-cadherin proteins in response to UTMC, potentially contributing to the destabilization of adherens junctions. This study underscores the role of Ca^{2+} influx, eNOS activation, and heightened S-nitrosylation of adherens junction proteins in the regulation of endothelial hyperpermeability.

Conclusions

UTMC enhances drug delivery by inducing endothelial hyperpermeability. Here we show that UTMC causes influx of Ca^{2+}, eNOS activation, increased S-nitrosylation and reorganization of VE-cadherin. Further exploration of these pathways will aid in clinical translation and optimization of UTMC for delivering cell-impermeant drugs.

Contrast Ultrasound-Mediated Targeted Delivery of Cardioprotective Factors in Ischemia Reperfusion Injury of the Heart

Asli Akin[1], Lifen Xu[1], Lucile Genty[1], Amanda Ochoa Espinoza[1], Albert Neutzner[1], Gabriela Kuster[1,2], Beat Kaufmann[1,2]

[1]*Department of Biomedicine, University of Basel, Basel, Switzerland*
[2]*Department of Cardiology and Cardiovascular Research Institute Basel (CRIB), University Hospital Basel, University of Basel, Basel, Switzerland*
Corresponding author: asli.akin@unibas.ch

Introduction

Ischemia reperfusion (IR) injury and left ventricular remodelling after myocardial infarction (MI) may lead to heart failure.[1,2] Recent research suggests that inhibition of left ventricular remodelling could be achieved via mechanisms such as anti-apoptotic signaling through Fms-like tyrosine kinase 3 ligand (FLT3L), acting via AKT and ERK pathways.[3]

Limited availability in target tissues is an obstacle for effective therapies using small protein drugs.[4,5] Microbubbles (MB) have been developed for molecular imaging as well as gene and drug delivery in recent years. Ultrasound mediated destruction of MB carrying drug payload could lead to maximized site-targeted drug delivery, while minimizing systemic exposure. We hypothesized that delivery of FLT3L coupled to microbubbles would reduce infarct size and improve left ventricular ejection fration (LVEF) in a clinically relevant model of myocardial IR.

Methods

Lipid shelled (DSPC 2mg/ml, PEG stearate 1mg/ml, DSPE-PEG-biotin 0.28mg/ml) microbubbles (MBs) with a gas core (decafluorobutane) were produced. FLT3L was conjugated to the microbubble surface using biotin-streptavidin linkage. Fluorescence labeling (NHS-Fluorescein) of FLT3L was used to measure and optimize drug payload. Biological activity of FLT3L after exposure to ultrasound (1.5 MHz, MI of 1.9, 30 fps for 10 minutes) and of ultrasound mediated destruction of microbubbles carrying FLT3L was measured in OCI-AML5 cell cultures using an XTT assay. In vivo biological activity of MBs carrying FLT3L (MB_{FLT3L}, $3x10^8$, iv injection) with ultrasound destruction (1.5MHz, MI 1.4, 1 frame every 5 sec, 30 minutes) was compared to FLT3L (1.8μg, iv injection) only, to controls and to sham operated animals (n=4-6 per group) in a murine model of myocardial IR. On day 7 after IR, infarct size was measured on picrosirius staining and LVEF on high frequency echocardioagaphy by investigators blinded for treatment assignment.

Results

Incubation of $1x10^8$ microbubbles with 2.5μg or 5μg FLT3L resulted in similar amounts of drug payload conjugated to MBs (2.0±0.1μg vs. 2.0±0.3μg per $1x10^8$ MB). Increased amounts of DSPE-PEG-biotin (0.42mg/ml) used for MB production did not increase drug payload. XTT assays confirmed similar activity of FLT3L and FLT3L exposed to ultrasound (ED50 29.7±32.1 ng vs. 20.6±21.6 ng), while activity of MB_{FLT3L} after ultrasound destruction was lower (ED50 128.1±4.8 ng). Results of in vivo experiments are shown in Figure 1. In control animals about 30% of the myocardium were infarcted whereas sham animals had no infarcts (p<0.01). However, neither animals treated with FLTL3 nor animals treated with MB_{FLT3L} showed a reduction in infarct size compared to controls. On high frequency echocardiography, LVEF was significantly lower in control animals (p=0.019), whereas this was not the case for animals treated with FLT3L or MB_{FLT3L}.

Conclusions

Conjugation of FLT3L to MBs is possible in dosages relevant for antiapoptotic effects. In a cell assay, MB_{FLT3L} show biologic effects attributable to FLT3L after ultrasound destruction. However, in vivo effects are modest and related to ejection fraction, while there was no effect on infarct size.
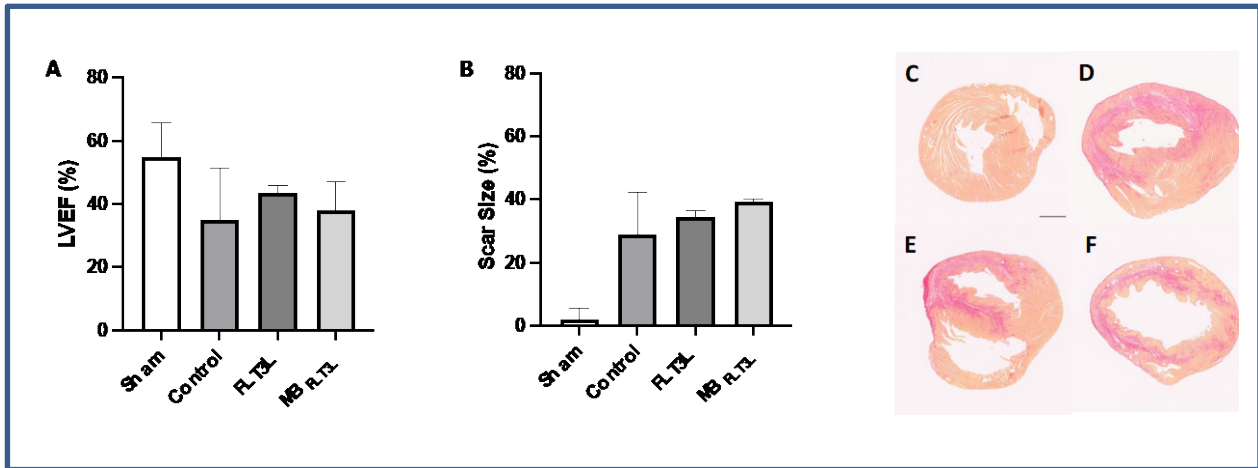
Figure 1. LVEF (A) and infarct size (B) 7 days after IR in sham (n=5), control (n=6), FLT3L (n=5) and MB_{FLT3L} (n=5) treated mice. Representative cross-sectional heart images from sham (C), control (D), FLT3L (E), and MB_{FLT3L}(F)-treated mice after picrosirius staining. Bar 0.5mm.

References

[1]. Townsend N, Wilson L, Bhatnagar P, Wickramasinghe K, Rayner M and Nichols M. Cardiovascular disease in Europe: epidemiological update 2016. Eur Heart J. 2016;37:3232-3245.

[2]. Mann DL and Bristow MR. Mechanisms and models in heart failure: the biomechanical model and beyond. Circulation. 2005;111:2837-49.

[3]. Pfister O, Lorenz V, Oikonomopoulos A, Xu L, Hauselmann SP, Mbah C, Kaufmann BA, Liao R, Wodnar-Filipowicz A and Kuster GM. FLT3 activation improves post-myocardial infarction remodeling involving a cytoprotective effect on cardiomyocytes. J Am Coll Cardiol. 2014;63:1011-9.

[4]. Primeau AJ, Rendon A, Hedley D, Lilge L and Tannock IF. The distribution of the anticancer drug Doxorubicin in relation to blood vessels in solid tumors. Clin Cancer Res. 2005;11:8782-8.

[5]. Baker JH, Lindquist KE, Huxham LA, Kyle AH, Sy JT and Minchinton AI. Direct visualization of heterogeneous extravascular distribution of trastuzumab in human epidermal growth factor receptor type 2 overexpressing xenografts. Clin Cancer Res. 2008;14:2171-9.

Influence of Extracellular Matrix Stiffness on Endothelial Sonoporation Under Flow Conditions

Zoe D. Katz[1], Elahe Memari[2], Brandon Helfield[1,2]

[1]*Department of Biology, Concordia University, Montreal, Canada*
[2]*Department of Physics, Concordia University, Montreal, Canada*

Introduction

Cancer immunotherapy has faced challenges in the treatment of solid cancers due to the complex tumor microenvironment (TME) [1]. The TME is composed of variable elements *i.e.* stromal cells, immune cells, cytokines, signalling factors, and extracellular matrix (ECM) scaffolding [2]. One challenge to overcome in the development of cancer immunotherapy is represented by TME physical barriers that prohibit immune cell infiltration [3]; ultrasound (US) stimulated microbubbles present a novel way to potentiate the use of cancer immunotherapy in tumors by permeabilizing the tumor vasculature [4]. Although there are studies on the increased efficacy of the dual treatment of US-stimulated microbubble and immunotherapy [5][6], there is much to discover about the effect of individual TME parameters on US-assisted bioeffects. Here, we focus on the biophysical interactions of different stiffnesses of ECM on US-assisted vascular permeabilization.

The ECM composition and stiffness changes throughout cancer progression [7], where less stiff matrices promote cancer invasion and metastasis [8], and stiffer matrices can lead to fibrosis, angiogenesis, and cancer cell proliferation [8]. Further, microbubble vibration dynamics, and the subsequent bioeffects, are also very sensitive to boundary effects, including the viscoelastic nature of the surrounding tissue [9]. Understanding the effect of the stiffness of the matrix environment on the efficacy of US-microbubble assisted vascular permeabilization through sonoporation, it is possible to design individual tumor-specific parameters. Here, we will address the effect of ECM stiffness on sonoporation by assessing a variety of different ECM stiffnesses and compositions.

Methods

In order to explore different flow conditions of the aberrant tumor vasculature, we used a novel fluidic system to grow human umbilical vein endothelial cells (HUVECs) under flow. The endothelial monolayers were seeded on a range of collagen matrices (0.5, 2, and 3.5mg/mL) corresponding to estimated stiffnesses of 5, 25, and 75 Pa (Young's Modulus), and cultured under shear-flow (10 dyn/cm^2) for three days. We then co-perfused the HUVEC monolayers with a fluorescent surrogate sonoporation maker (propidium iodide; PI) and Definity^{TM} microbubbles at either of two physiologically relevant flow rates (5 or 30 ml/min). Using our custom acoustically coupled microscope system, samples were treated under flow with a 1 MHz frequency (300 kPa, 20 cycles, PRI=1 ms, duration of 4 s). Real-time images were recorded and data analysis was conducted using an in-house MATLAB program to quantify the number of PI positive cells.

Results

Sonoporation efficiency under the same acoustic stimulus was significantly affected by collagen substrate concentration (*i.e.* stiffness). Under the faster flow rate (30ml/min), the percentage of treated cells was 1.3%, 4.2% and 6.1% for samples cultured on 0.5, 2.0 and 3.5 mg/ml respectively, signifying a relative increase in sonoporation from a stiffer substrate (3.2 fold increase, p<0.01 for 2.0 mg/ml; 4.7-fold increase, p<0.001 for 3.5 mg/ml) as compared to the least stiff condition. We observed a very similar trend under the lower microbubble flow rate (5ml/min), where the same model ECM stiffnesses showed HUVEC sonoporation rates increasing from 0.2%, 2.0%, and 5.7% (10-fold increase, p<0.001 for 2.0 mg/ml; 28.5-fold increase, p<0.01 for 3.5 mg/ml). From this dataset, we also observed that for a given collagen substrate,

there is a significant increase in sonoporation efficiency with increasing flow rate (6.6-fold increase, $p<0.05$ for 0.5; 2.1-fold increase, $p<0.01$ for 2.0; 1.1-fold increase, $p>0.05$ for 3.5).

Preliminary results of similar experiments using different polyacrylamide hydrogels to explore a wider range of stiffnesses (Young's modulus: 100, 800, 1600 kPa) show a similar trend.

Conclusions

In this study, we demonstrate that ECM stiffness has a large effect on US-assisted endothelial sonoporation propensity when subjected to the same US condition. Stiffer matrix environments result in greater endothelial sonoporation rates, and we corroborate our previous work [10] confirming an increase in sonoporation rate with increasing microbubble flow rate. These data can be used to fine-tune parameters according to different TMEs; further, our findings have applications in designing US parameters for targeted drug delivery and other clinical contexts that consider a variety of tissue stiffnesses.

References

[1]. Tang L, Huang Z, Mei H, Hu Y. 2023. Immunotherapy in hematologic malignancies: achievements, challenges and future prospects. Signal Transduct Target Therapy. 8(1):306. Available from: http://dx.doi.org/10.1038/s41392-023-01521-5

[2]. Guha P, Heatherton KR, O'Connell KP, Alexander IS, Katz SC. 2022. Assessing the future of solid tumor immunotherapy. Biomedicines. 10(3):655. Available from: http://dx.doi.org/10.3390/biomedicines10030655

[3]. Beyer I, van Rensburg R, Lieber A. 2013. Overcoming physical barriers in cancer therapy. Tissue Barriers. 1(1):e23647. Available from: http://dx.doi.org/10.4161/tisb.23647

[4]. Wang M, Zhang Y, Cai C, Tu J, Guo X, Zhang D. 2018. Sonoporation-induced cell membrane permeabilization and cytoskeleton disassembly at varied acoustic and microbubble-cell parameters. Sci Rep. 8(1):3885. Available from: http://dx.doi.org/10.1038/s41598-018-22056-8

[5]. Ilovitsh T, Feng Y, Foiret J, Kheirolomoom A, Zhang H, Ingham ES, et al. 2020. Low-frequency ultrasound-mediated cytokine transfection enhances T cell recruitment at local and distant tumor sites. Proceedings of the National Academy of Sciences. 117(23):12674–85. doi:10.1073/pnas.1914906117

[6]. Gao X, Nan Y, Yuan Y, Gong X, Sun Y, Zhou H, et al. 2018. Gas-filled ultrasound microbubbles enhance the immunoactivity of the HSP70-MAGEA1 fusion protein against magea1-expressing tumours. Molecular Medicine Reports. doi:10.3892/mmr.2018.9003

[7]. Najafi M, Farhood B, Mortezaee K. 2019 Extracellular matrix (ECM) stiffness and degradation as cancer drivers: NAJAFI et al. J Cell Biochem [Internet].120(3):2782–90. Available from: http://dx.doi.org/10.1002/jcb.27681

[8]. Deng B, Zhao Z, Kong W, Han C, Shen X, Zhou C. 2022. Biological role of matrix stiffness in tumor growth and treatment. Journal of Translational Medicine. 20(1). doi:10.1186/s12967-022-03768-y

[9]. Helfield BL, Leung BY, Goertz DE. 2014. The effect of boundary proximity on the response of individual ultrasound contrast agent microbubbles. Phys. Med. Biol. 59:1721–1745

[10]. Memari E, Hui F, Yusefi H, Helfield B. 2023. Fluid flow influences ultrasound-assisted endothelial membrane permeabilization and calcium flux. Journal of Controlled Release. 358:333–44. doi:10.1016/j.jconrel.2023.05.004

Ultrasound-Stimulated Microbubble Mediated Modulation of Endothelial Immunogenicity

Wei Chen Lo, _Farbod Tabesh, Mahsa Bataghva, Arutselvan Natarajan,_
Ramasamy Paulmurugan*, Ahmed El Kaffas*

Molecular Imaging Program at Stanford (MIPS), Stanford University School of Medicine, Stanford, CA, USA.
The Canary Center at Stanford for Cancer Early Detection, Stanford University School of Medicine, Palo Alto, CA, USA.
Corresponding author: elkaffas@stanfordl.edu, paulmur8@stanford.edu.

Introduction

Endothelial cells (ECs) play a key regulating role as part of the tumor microenvironment, where they can either promote or impede immune responses, and that can subsequently interfer with several types of immunotherapies[1] [2]. Mechanical forces, such as shear stress, can influence EC behavior, and have been shown to modulate EC inflamation and immunogencity. Ultrasound-stimulated microbubbles (USMB) provide a source of mechanical stimulation that can be targeted specifciatlly to ECs [3][4]. Here, we explore mechanically-induced modulation of immune-relevant EC surface markers, such as PD-L1, ICAM-1, VCAM-1, and FasL, folowing USMB treatment (Fig. 1(a)).

Methods

We used Mile Sven 1 (MS1) cells that were seeded in collagen-IV-coated 0.8 mm Ibidi chamber slides with a 2.5 cm² growth area. The initial seeding concentration was 1M cells/mL one day prior to the experiments. Usphere were used, diluted to a 1:1000 ratio. Concentration measurements yielded a native concentration of 40×10^9 microbubbles/ml with a volume peak distribution at (1 ± 0.2) µm. Fluorescent markers used included DAPI and PD-L1 antibody. The study implemented a long pulse modality treatment using a Vantage system equipped with a P4-2 phased array. Treatment pulses insonified the slides for 10 seconds with a 2 MHz center frequency, 50 µs pulse length, a 500 kPa pressure, and a 200 Hz pulse repetition frequency (PRF). Post quanfication, the slides were fixed, blocked, and stained with primary and secondary antibodies for confocal imaging to assess expression of PD-L1 and other pro-immune markers (i.e. E/P-selecting).

Results

Fig. 1(b) presents a representative overlay of fluorescence microscopy illustrating the effects of shear flow induced by USMB on MS1 membranes. Preliminary results indicate that exposure of MS1 to USMB markedly modifies the expression of the MS1 marker. Morphological analysis, relative to controls without ultrasound exposure, reveals no significant detachment or damage, suggesting that the cavitation of microbubbles induces mild microstreaming rather than intense jetting flows. Initial quantitative assessments show that USMB treatment results in a 12% decrease in PD-L1 marker expression, substantiating the hypothesis that irregular mechanical shear stress can alter MS1 expression of differing immune markers, thereby altering their biological functions and characteristics.

Conclusions

The principal innovation of this exploratory proof-of-concept study lies in the development of USMB-based mechanotransduction targeting EC immunogenicity. The longterm aim is to determine if USMB could augment immunotherapeutic efficacy across all cancer patient populations through mild mechanical stimulation of ECs specifically. Preliminary results indicate a reduction in PD-L1 marker expression in _in vivo_ ECs (which mimics tumor ECs), suggesting an inhibitory effect on this critical immune checkpoint protein. Nevertheless, the complexity and heterogeneity of the tumor microenvironment require

a sophisticated understanding of these interactions. Future investigations will refine ultrasound parameters, explore complex fluid dynamics in culture[5], and assess a broader spectrum of surface markers.
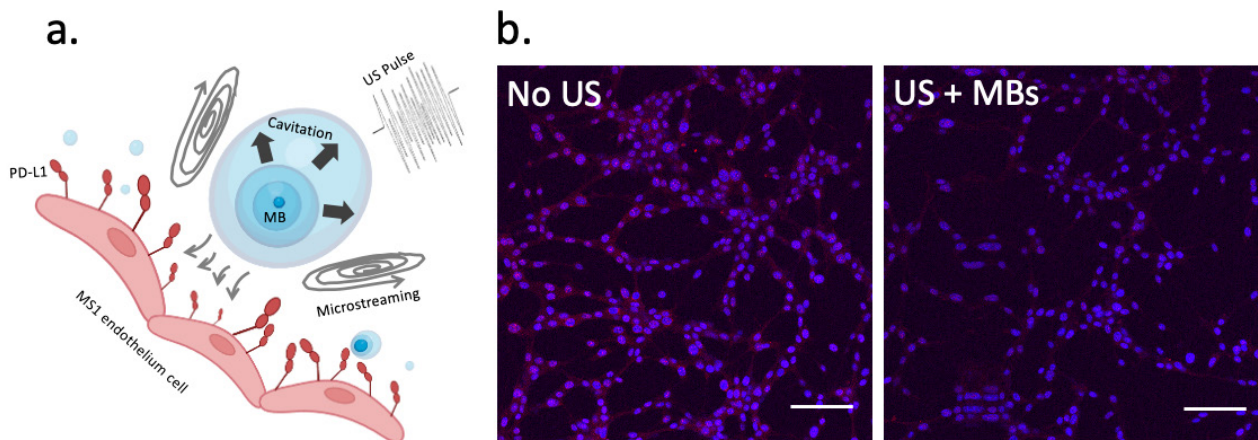

Fig 1. (a) Schematic illustration of microbubbles induced microstreaming to modulate the PD-L1 marker (b) Confocal imaging shows PD-L1 expression before and after exposure to US + MBs, PD-L1 in red, and DAPI in blue. The scale bar is 50 μm.

References

[1]. Fukurnura, D., et al., *Enhancing cancer immunotherapy using antiangiogenics: opportunities and challenges.* Nature Reviews Clinical Oncology, 2018. **15**(5): p. 325-340.

[2]. De Palma, M. and R.K. Jain, *CD4 T Cell Activation and Vascular Normalization: Two Sides of the Same Coin?* Immunity, 2017. **46**(5): p. 773-775.

[3]. Wu, J. and W.L. Nyborg, *Ultrasound, cavitation bubbles and their interaction with cells.* Advanced Drug Delivery Reviews, 2008. **60**(10): p. 1103-1116.

[4]. Fan, Z.Z., R.E. Kumon, and C.X. Deng, *Mechanisms of microbubble-facilitated sonoporation for drug and gene delivery.* Therapeutic Delivery, 2014. **5**(4): p. 467-486.

[5]. Memari, E., et al., *Fluid flow influences ultrasound-assisted endothelial membrane permeabilization and calcium flux.* Journal of Controlled Release, 2023. **358**: p. 333-344.

Sonothrombolysis in a Murine Model of Deep Vein Thrombosis Using Microfluidically Produced Microbubbles

Yanjun Xie[1], Yi Huang[1], Hugo C.S. Stevenson[1], Alexander L. Klibanov[2], John A. Hossack[1]

[1]Department of Biomedical Engineering, University of Virginia, Charlottesville, USA
[2]Department of Medicine, University of Virginia, Charlottesville, USA
Corresponding author: jh7fj@virginia.edu

Introduction

It is estimated that the incidence of venous thromboembolism (VTE) is 245 and 316 per 100,000 people in Europe and in the United States, respectively [1], [2]. Deep vein thrombosis (DVT) occurs when a thrombus obstructs blood flow and induces clinical manifestations. Pulmonary embolism, one of the sequelae of DVT, is life-threatening and causes a mortality rate of 30% if untreated [3]. The removal of a thrombus in the acute stage has been shown to be critical in terms of long-term outcome [4]. Previous research has shown that sonothrombolysis using microbubbles (MBs) from a flow-focusing microfluidic device, cavitated by ultrasound (US), increases the *in vitro* thrombolysis rate by more than 4 fold compared to the clinical dose of tissue plasminogen activator (tPA) [5]. Transiently stable MBs from a microfluidic device dissolve in minutes, and thus do not cause adverse effects. However, blood flow and vein wall remodeling after DVT in animals/humans can be complicated [6]. *In vivo* validation of the efficacy of sonothrombolysis is needed towards further clinical translation. In this abstract, we present the preliminary results of sonothrombolysis using microfluidically produced MBs in an *in vivo* murine model of DVT.

Methods

Four 8-week-old C57BL/6 mice (Jackson Laboratory, Bar Harbor, ME, USA) were partially ligated in inferior vena cava to develop DVT, following the protocol described in [7], on day 0. Three days after surgery, all mice were anesthetized on a 37°C platform and imaged using a Vevo 2100 ultrasound imaging system (VisualSonics, Bothell, WA, USA), where an MS-550D transducer was mounted at a 3D acquisition motor. The imaging parameters are listed in Table. 1.

Mice were divided into (I) 2 mg/kg tPA + US + microfluidically produced microbubbles, (II) 2 mg/kg tPA (Activase, Genentech, South San Francisco, CA, USA) groups. Thrombolytic drugs and microbubbles were administered through a tail vein catheter. One tenth of the tPA dose was injected and the remaining 90% was infused for 30 minutes. A flow-focusing microfluidic device was supplied with a nitrogen gas phase (Linde Gas, Richmond, VA, USA) and a 24 µL/min liquid phase of 4% w/v bovine serum albumin, 10% w/v dextrose and 0.9% saline. MBs of approximately 15 µm were generated at a production rate of 100×10^3 MB/s (Fig. 1c), and delivered to the catheter every 5 min for 30 s. During a 30 min treatment, an A303S panametrics transducer (1 MHz, Olympus, Center Valley, PA, USA) of 2% duty factor and 570 kPa peak-negative-pressure was applied on abdominal area to cavitate the MBs. Another imaging session was performed using the same ultrasound imaging parameters on day 14.

Table 1. Ultrasound Imaging Parameters

Transducer	MS-550D
Center frequency/MHz	40
Imaging width/mm	14
Imaging depth/mm	12
Step size/mm	0.03 (Long axis)/0.1 (Short axis)

The blood clot volume was manually segmented in 3D Slicer. The volume reduction percentage was calculated using the formula below for each mouse and plotted.

$$Volume\ Reduction\ Percentage\ (\%) = (V_{day3} - V_{day14})/V_{day3}$$

Results

On day 3, the initial blood clot volume was 4.3 and 19.8 mm^3 in the experimental group, whereas the control group was 13.2 and 16.8 mm^3. On day 14, the final volume decreased to 0 and 6.1 mm^3 in the experimental group, 7.6 and 7.6 mm^3 in the control group. The therapeutic efficacy of the tPA + US + microfluidically produced MBs outperformed the tPA only group by 37%.

Conclusions

The stenosis model allows partial flow, enabling the delivery of thrombolytic drugs and MBs to DVT. Therefore, it is an appropriate model for sonothrombolysis. This is the first work to demonstrate the use of microfluidically produced MBs facilitating the removal of DVT in a murine model. Future work will examine the use of this method with a larger number of animals.
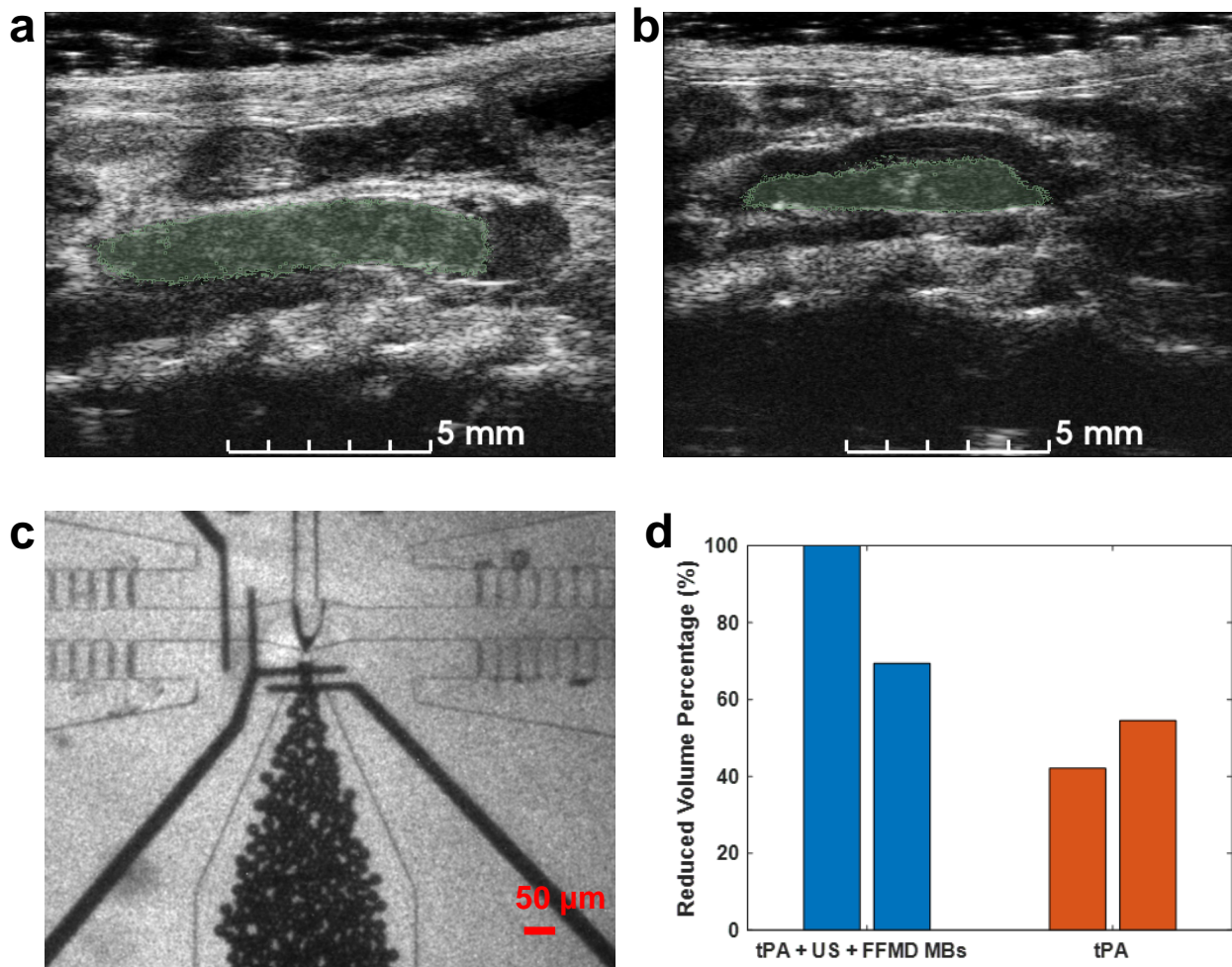
Figure 1. Sonothrombolysis results using the proposed method. Exemplar US imaging slices of a mouse in group I on day 3 and day 14 are shown in (a) and (b), respectively. The superimposed green mask represents the blood clot region. (c) Photo of microfluidically produced MBs was taken at a high-speed camera. (d) The bar plot displays the percentage of reduced volume of tPA + US + microfluidically produced MBs and tPA groups, where 100% is the complete removal of blood clot.

References

[1] A. T. Cohen *et al.*, "Venous thromboembolism (VTE) in Europe," *Thromb Haemost*, vol. 98, no. 10, pp. 756–764, 2007, doi: 10.1160/TH07-03-0212.

[2] C. W. Tsao *et al.*, "Heart Disease and Stroke Statistics—2023 Update: A Report From the American Heart Association," *Circulation*, vol. 147, no. 8, pp. e93–e621, Feb. 2023, doi: 10.1161/CIR.0000000000001123.

[3] J. Bělohlávek, V. Dytrych, and A. Linhart, "Pulmonary embolism, part I: Epidemiology, risk factors and risk stratification, pathophysiology, clinical presentation, diagnosis and nonthrombotic pulmonary embolism," *Exp Clin Cardiol*, vol. 18, no. 2, pp. 129–138, 2013.

[4] L. Watson, C. Broderick, and M. P. Armon, "Thrombolysis for acute deep vein thrombosis," *Cochrane Database of Systematic Reviews*, no. 11, 2016, doi: 10.1002/14651858.CD002783.pub4.

[5] A. J. Dixon, J. M. R. Rickel, B. D. Shin, A. L. Klibanov, and J. A. Hossack, "In Vitro Sonothrombolysis Enhancement by Transiently Stable Microbubbles Produced by a Flow-Focusing Microfluidic Device," *Ann Biomed Eng*, vol. 46, no. 2, pp. 222–232, Feb. 2018, doi: 10.1007/s10439-017-1965-7.

[6] K. B. Deatrick *et al.*, "Postthrombotic vein wall remodeling: Preliminary observations," *Journal of Vascular Surgery*, vol. 53, no. 1, pp. 139–146, Jan. 2011, doi: 10.1016/j.jvs.2010.07.043.

[7] A. Brill *et al.*, "von Willebrand factor–mediated platelet adhesion is critical for deep vein thrombosis in mouse models," *Blood*, vol. 117, no. 4, pp. 1400–1407, Jan. 2011, doi: 10.1182/blood-2010-05-287623.

Reversal of doxorubicin resistance in human colon cancer cells using microbubble-assisted sonoporation

Dawid Przystupski[1], Dagmara Baczyńska[2], Marek Ussowicz[1]

[1]*Department of Paediatric Bone Marrow Transplantation, Oncology and Haematology, Wroclaw Medical University, Wroclaw, Poland*
[2] *Department of Molecular and Cellular Biology, Wroclaw Medical University, Wroclaw, Poland*
Corresponding author: dawid.przystupski@student.umw.edu.pl

Introduction

Since multidrug resistance phenomenon (MDR) is partially driven by membrane proteins responsible for effective drug efflux, it has been believed that ultrasound-mediated sonoporation may alter the drug sensitivity of cancer cells. Microbubble-based sonoporation has been shown to reduce the expression of Pgp in the blood-brain barrier in rats. Aryal et al. observed a downregulation of Pgp that lasted more than 72 hours [1]. The reduction in Pgp activity was also revealed in sonoporated breast cancer cells [2]. Similar findings were reported by Bjånes et al. who investigated the gemcitabine efficacy in sonoporated pancreatic cancer cells [3]. To explore this phenomenon further, we determined the effect of microbubble assisted sonoporation on human colon cancer cells sensitive and resistant to doxorubicin.

Methods

The effect of sonoporation combined with doxorubicin and SonoVue microbubbles was examined in this study. As a research model, we used human colon cancer cells sensitive (LoVo) and resistant to doxurubicin (LoVoDx). At the beginning, we exposed LoVo and LoVoDx cells to ultrasound (2 W/cm^2, DC 50%, 1MHz, 30 sec) without and with microbubbles and administered doxorubicin at the following time points: 0h, 2h, 4h, 8h, 16h, 24h, 48h and 72h after the ultrasound (US) exposure. Next, we examined the drug cytotoxicity by MTS assay and intracellular doxorubicin concentration by flow cytometry at the chosen time points. Moreover, P-gp activity was determined by measuring intracellular accumulation of rhodamine 123 in LoVo and LoVoDx cells at the defined time points. Finally, we checked expression of the selected drug-resistance-mediated genes: ABCB1, ABCC1, ABCG2, TOP2A, FOXO3, NFKB1 and NFKB2. Additionaly, we measured the level of ABCB1, ABCC1 and ABCG2 proteins in LoVo and LoVoDx cells by flow cytometry following the US exposure.

Results

We noticed that ultrasound treatment combined with microbubbles altered the drug resistance of LoVo and LoVoDx cells. We observed the highest intracellular doxorubicin concentration when the drug was administered 8h-16h following the exposure that resulted in the highest toxicity of the chemotherapeutic at the mentioned time points. Moreover, this was accompanied by the lowest Pgp activity measured by rhodamine 123 assay. Our experiments also revealed the reduced levels of ABCB1, ABCC1 and ABCG2 proteins up to 24 hours in doxurubicin-resistant LoVoDx cells – the lowest level of cell membrane ABCB1, ABCC1 and ABCG2 was observed 8-16 hours following the ultrasound treatment. Additionally, we confirmed that ultrasound exposure altered the expression of MDR-related genes, especially when microbubbles were used: we noticed the highest reduction of ABCC1 and ABCG2 mRNA levels up to 24h following the treatment. However, the reduction of ABCB1 mRNA level was only observed in LoVo cells. Interestingly, we found that microbubble-assisted sonoporation caused the reduced expression of transcription factors responsible for doxorubicin resistance: FOXO3, NFKB1 and NFKB2, both in LoVo and LoVoDx cells. Interestingly, ultrasound exposure also increased the expression of TOP2A – a target for dexorubicin treatment making malignant cells, especially in LoVoDx cells, much more susceptible to the chemotherapeutic.

Conclusions

This study demonstrated an effective strategy for modulating drug resistance in cancer cells by microbubble-mediated sonoporation. Our analyses confirmed that ultrasound may affect MDR-related proteins level and activity as well as gene expression. The enhanced intracellular delivery of doxorubicin was confirmed both in drug-sensitive and resistant colon cancer cells. We believe that the decreased level and activity of Pgp was caused by the ultrasound "shaving" effect leading to the removal of extracellular domains of membrane proteins as well as US-assisted DNA damage during sonoporation, which suppresses transcription and translation.

References

[1]. Aryal, M.; Fischer, K.; Gentile, C.; Gitto, S.; Zhang, Y.-Z.; McDannold, N. Effects on P-Glycoprotein Expression after Blood-Brain Barrier Disruption Using Focused Ultrasound and Microbubbles. PLoS One 2017, 12, e0166061, doi:10.1371/journal.pone.0166061.

[2]. Deng, Z.; Yan, F.; Jin, Q.; Li, F.; Wu, J.; Liu, X.; Zheng, H. Reversal of Multidrug Resistance Phenotype in Human Breast Cancer Cells Using Doxorubicin-Liposome-Microbubble Complexes Assisted by Ultrasound. J. Control. Release 2014, 174, 109–116, doi:10.1016/j.jconrel.2013.11.018.

[3]. Bjånes, T.; Kotopoulis, S.; Murvold, E.T.; Kamčeva, T.; Gjertsen, B.T.; Gilja, O.H.; Schjøtt, J.; Riedel, B.; McCormack, E. Ultrasound- and Microbubble-Assisted Gemcitabine Delivery to Pancreatic Cancer Cells. Pharmaceutics 2020, 12, 1–15, doi:10.3390/pharmaceutics12020141.

FIRST ANNOUNCEMENT 2025

30th EUROPEAN SYMPOSIUM ON ULTRASOUND CONTRAST IMAGING

16-17 JANUARY 2025

ROTTERDAM, THE NETHERLANDS

Information on the 30th **EUROPEAN SYMPOSIUM ON ULTRASOUND CONTRAST IMAGING: Sharon Sewell, info@echocontrast.nl**

The 29ᵗʰ European Symposium on Ultrasound Contrast Imaging Rotterdam is sponsored by:

Bracco Suisse SA

Marco Graf, Senior
Communication Events Manager
Cadempino, Switzerland

Philips Healthcare

James D'Amico
Senior Product Marketing
Manager
General Imaging Ultrasound
Eindhoven, The Netherlands

Erasmus University MC - Thorax Center

Prof.dr Rudolf de Boer
Head of the department
Rotterdam
The Netherlands

Fujifilm VisualSonics

Adrie Gubbels, Sales Manager
Visualsonics
Amsterdam, the Netherlands

GE Healthcare

Christopher (Scott) Lee
Product Leader – Optison
Missouri USA

Samsung Medison

Luc van Dalen, account
manager HME of the
Samsung Electronics Benelux

Solstice Pharmaceutic Managing directorals

Wim van Hoeve, Sales Manager
Enschede, the Netherlands

Verasonics, Inc

Toni Baumann, Associate
Director, Product Marketing &
Communications
Kirkland, WA

Oldelft Ultrasound

Stefan Roggeveen
Commercial Manager
Delft, the Netherlands

Hartstichting

Den Haag, the Netherlands

Siemens Healthineers

SHS US IN ADGI
United Kingdom

sponsors:

Golden sponsor

PHILIPS

GOLD

Silver sponsor

BRACCO
LIFE FROM INSIDE

SIEMENS
Healthineers

SILVER

SAMSUNG

GE HealthCare

Erasmus MC

THORAX CENTRUM

Bronze sponsor

Solstice
pharmaceuticals

FUJIFILM
VISUALSONICS

BRONZE

Hartstichting

Oldelft
Ultrasound

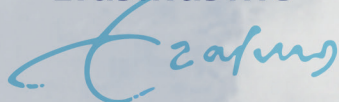Verasonics
The leader in Research Ultrasound™

The 29th European Symposium on Ultrasound Contrast Imaging, Rotterdam is sponsored by:

PHILIPS

Erasmus MC

THORAX CENTRUM

BRACCO

LIFE FROM INSIDE

GE HealthCare

SAMSUNG

SIEMENS Healthineers

Oldelft Ultrasound

Verasonics
The leader in Research Ultrasound™

Hartstichting

Solstice pharmaceuticals

FUJIFILM
VISUALSONICS